Thermo-mechanical Fatigue Behavior of Materials

THIRD VOLUME

HUSEYIN SEHITOGLU
AND HANS J. MAIER, EDITORS

STP 1371

ASTM

STP 1371

Thermo-mechanical Fatigue Behavior of Materials: Third Volume

Huseyin Sehitoglu and Hans J. Maier, editors

ASTM Stock Number: STP1371

ASTM
100 Barr Harbor Drive
West Conshohocken, PA 19428-2959

Printed in the U.S.A.

Library of Congress Cataloging-in-Publication Data

Thermo-mechanical fatigue behavior of materials. Third volume / Huseyin Sehitoglu and Hans J. Maier, editors.
p. cm. -- (STP ; 1371)
ASTM Stock Number: STP1371.
Includes bibliographical references and index.
ISBN 0-8031-2853-3
1. Alloys--Thermomechanical properties. 2. Composite materials--Thermomechanical properties. 3. Fracture mechanics. I. Title: Thermomechanical fatigue behavior of materials. II. Sehitoglu, Huseyin, 1957- . III. Maier, Hans J., 1960- . IV. Symposium on Thermomechanical Fatigue Behavior of Materials (3rd: 1998: Norfolk, Va.) V. ASTM special technical publication; 1371.
TA483.T48 2000
620.1'126--dc21 00-020035

Peer Review Policy

Each paper published in this volume was evaluated by two peer reviewers and at least one editor. The authors addressed all of the reviewers' comments to the satisfaction of both the technical editor(s) and the ASTM Committee on Publications.

To make technical information available as quickly as possible, the peer-reviewed papers in this publication were prepared "camera-ready" as submitted by the authors.

The quality of the papers in this publication reflects not only the obvious efforts of the authors and the technical editor(s), but also the work of the peer reviewers. In keeping with long-standing publication practices, ASTM maintains the anonymity of the peer reviewers. The ASTM Committee on Publications acknowledges with appreciation their dedication and contribution of time and effort on behalf of ASTM.

Printed in Baltimore, MD
March 2000

Foreword

This publication, *Thermo-mechanical Fatigue Behavior of Materials: Third Volume*, contains papers presented at the symposium of the same name held in Norfolk, Virginia, on 4–5 November 1998. They symposium was sponsored by ASTM Committee E8 on Fatigue and Fracture. The symposium co-chairmen were Huseyin Sehitoglu, University of Illinois, and Hans J. Maier, Universität Paderborn.

Contents

COMPOSITES

EXPERIMENTAL TECHNIQUES

Overview

The area of thermal and thermo-mechanical fatigue of structural alloys has been a topic of intense interest to scientists and engineers. ASTM has sponsored two successful symposia on this topic in the last seven years. The current symposium is aimed at exposing the deformation and damage mechanisms in thermo-mechanical fatigue in all materials. Papers published represent contributions in the disciplinary areas of materials science, mechanics and engineering applications. Specifically, the symposium focused on the study of stress-strain response in a number of technologically important materials, damage mechanisms in thermo-mechanical fatigue (creep, oxidation effects), microscopic investigations of materials subjected to thermo-mechanical fatigue, life prediction under thermo-mechanical fatigue (including fracture mechanics, damage mechanics, and initiation life approaches), solutions to thermo-mechanical fatigue problems in industry (including gas turbines, automotive engines), and novel experimental techniques for thermo-mechanical fatigue (high frequency, multiaxial testing, and round robin results). Materials studied included metals, intermetallics, and composites. Critical isothermal experiments that shed insight into thermo-mechanical fatigue were presented as well as thermal fatigue tests on different component geometries.

The 20 contributions in this STP range from gaining a deeper understanding of crack initiation and growth as influenced by the underlying microstructure to studies on developing engineering relationships and mathematical models for macroscopic behavior. The authors have been active researchers in high-temperature fatigue and have all made notable contributions in their specific areas of interest. The participation from outside U.S. was very strong reflecting the world wide interest in this field. A collection of recent articles on the topic would be of considerable value for the preparation of new design criteria, standards, and new texts in this field. We hope that, taken all together, this STP will be of considerable interest to the engineering and scientific community.

We would like to thank the international advisory board which included: Dr. John Allison, Ford Motor Company, USA; Dr. J. Bressers, Institute for Advanced Materials- JRC Petten, The Netherlands; Professor H. J. Christ, Universität-GH-Siegen, Germany; Dr. Gary Halford, NASA Lewis, USA; Prof. D. Löhe, Universität Karlsruhe, Germany; Professor H. Mughrabi, Universität Erlangen-Nurnberg, Germany; Prof. R. Ohtani, Kyoto University, Japan; Dr. L. Remy, Ecole Nationale Superieure des Mines de Paris Armines, France; and Dr. Peter Skelton, Imperial College, United Kingdom. We would like to express our gratitude to all authors, reviewers, and ASTM staff for their contribution to the publication of this STP.

Huseyin Sehitoglu
University of Illinois
Urbana, Illinois
Symposium Chairman and Editor

Hans J. Maier
Univerität Paderborn
Paderborn, Germany
Symposium Chairman and Editor

Microstructure

Ralf Kowalewski[1,2] and Haël Mughrabi[1]

Thermo-mechanical and Isothermal Fatigue of a Coated Columnar-Grained Directionally Solidified Nickel-Base Superalloy

Reference: Kowalewski, R. and Mughrabi, H., **"Thermo-mechanical and Isothermal Fatigue of a Coated Columnar-Grained Directionally Solidified Nickel-Base Superalloy,"** *Thermo-mechanical Fatigue Behavior of Materials: Third Volume, ASTM STP 1371,* H. Sehitoglu and H. J. Maier, Eds., American Society for Testing and Materials, West Conshohocken, PA, 2000.

Abstract: The isothermal low-cycle fatigue (LCF) and the out-of-phase thermomechanical fatigue (TMF) behaviours of the directionally solidified nickel-base superalloy DS CM 247 LC, coated with a plasma-sprayed NiCrAlY-coating (PCA-1), were studied in detail. The investigations were performed on the uncoated, the coated substrate material and also on the pure coating material, in contrast to most existing work. The results of the isothermal LCF tests show that the fatigue life of the substrate/coating-composite is governed by the fatigue behaviour of the bulk coating material. The out-of-phase TMF cyclic deformation behaviour of the substrate/coating-composite reflects that of the components and is well described by an isostrain composite model. When the mechanical strain amplitudes experienced by the coating material are plotted against the fatigue life, the data on the coated material in isothermal LCF tests at the upper and lower temperatures of the TMF cycle, respectively, and in the TMF tests coincide. This gives further evidence that the behaviour of the coating materials governs that of the coated composite.

Keywords: directionally solidified nickel-base superalloy, DS CM 247 LC, NiCrAlY-coating, thermomechanical and isothermal fatigue, microstructure, fatigue damage/life

Introduction

Because of their superior high-temperature strength properties, nickel-base superalloys are the most important materials used for high-temperature components in gas turbines. However, because of their limited oxidation resistance at high temperatures, their strength potential can only be fully exploited in hot sections of gas turbines by the application of oxidation-resistant protective coatings [1,2].

[1] Research Associate and Professor, respectively, Institut für Werkstoffwissenschaften, Lehrstuhl I, Universität Erlangen-Nürnberg, Martensstr. 5, D-91058 Erlangen, Federal Republic of Germany

[2] Present address: Siemens AG, A&D, LD, QM 31, D-90441 Nürnberg, Federal Republic of Germany

The effect of diffusion coatings is mainly based on an enrichment of the surface contact zone of the superalloy components with the surrounding hot gas atmosphere with chemical elements (above all: aluminium, chromium, yttrium) which are suitable for the formation of thermodynamically stable, dense and adherent oxide layers. The latter serve as a diffusion barrier to slow down the reaction between the substrate and the aggressive environment [3-5].

Beside the diffusion coatings, the so-called MCrAlY-overlay coatings (M = Ni and/or Co and/or Fe) are also widely used to protect turbine components against hot gas corrosion, occasionally as bond coats in combination with ceramic thermal barrier coatings [4,6]. The coating process (low-pressure plasma spraying) permits the application of a variety of compositions of MCrAlY-overlay coatings to the relevant substrates [7,8]. The differences in chemical composition between the coating and the substrate material lead to an inevitable mismatch in their physical and mechanical properties [9,10].

To rate a given coating/substrate-composite under the complex conditions of thermomechanical loading, which prevail during start-up or shut-down operation of land-based gas turbines, it is essential to have a detailed insight into the microstructural changes and the damaging processes. It is therefore insufficient to look only at easily accessible data such as the thermal expansion coefficients, the Young's moduli and standard mechanical data. This is particularly relevant to modelling, compare [11].

Hence, the motivation for the present work was to perform a systematic and fundamental study on the behaviour of an industrial nickel-base superalloy substrate-coating composite under thermomechanical cyclic loading conditions. Here, we report the results of an investigation of the low-cycle fatigue (LCF) and the thermomechanical fatigue (TMF) properties of a NiCrAlY-coated directionally solidified nickel-base superalloy. An important feature of the present study is that, in addition to the investigations performed on the substrate-coating composite, similar separate studies were performed on both the bulk substrate and on the bulk coating materials. It was hoped that this approach would facilitate the understanding and interpretation of the complex behaviour of the substrate-coating composite. The work reported here is part of a more comprehensive study [12]. Excerpts from this work concerning the low-cycle fatigue [13] and the thermomechanical fatigue [14] behaviour have been reported previously.

Experimental Details

The directionally solidified superalloy DS CM 247 LC with the nominal composition (in wt.%): Ni bal., Cr 8.1, Co 9.2, Mo 0.5, W 9.5, Ta 3.2, Ti 0.7, Al 5.6, Zr 0.01, B 0.01, C 0.07, Hf 1.4 was provided in the form of casting slabs. Cylindrical specimens with a diameter of 8 mm and a gauge length of 14 mm (Figure 1a) were taken from these casting slabs in such a manner that the crystallographic <001> directions of the columnar grains were aligned within 15° parallel to the specimen axes.

The microstructure of the heat-treated alloy consisted of different types of carbides with a volume content close to 2% and cuboidal γ' particles (volume content 69%), having an average edge length of 0.44 μm. The specimens were coated over their gauge length by low-pressure plasma spraying with a NiCrAlY-alloy, called PCA-1, consisting of (in wt. %): Ni bal., Cr 25, Al 5, Y 0.5 and unspecified amounts of Ta and Si in a thickness of 200 μm.

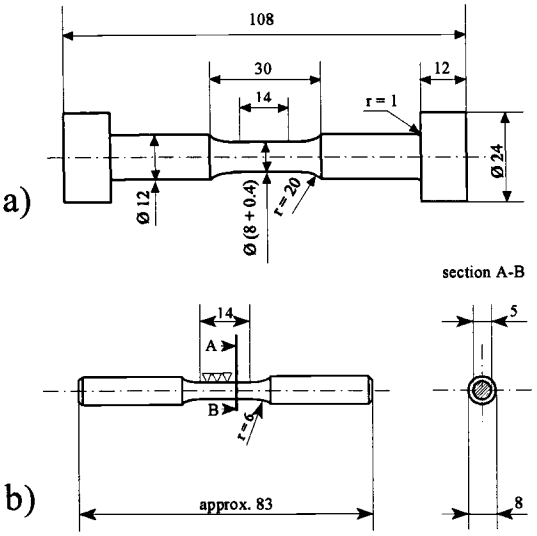

Figure 1 - *Geometry of the LCF- and TMF-specimens of (a) uncoated and coated (200μm PCA-1) nickel-base superalloy DS CM 247 LC and (b) bulk coating material PCA-1.*

The coating material was fine-grained with a grain size of about 1 μm. Also, cylindrical specimens of the bulk coating material with a diameter of 5 mm and a gauge length of 14 mm were prepared from continuously deposited coating material (Figure 1b). Both types of specimens were standard heat-treated, and their surfaces were finally mechanically polished.

The isothermal and thermomechanical fatigue tests were performed on a closed-loop servohydraulic testing machine (MTS 810 with a digital controller) which is equipped with a 200 kHz induction furnace. Strain was measured with a high-temperature axial extensometer with a 12 mm gauge length. Temperature control was conducted with a strip thermocouple, which was wound round the circumference of the specimen (cf. Figure 2).

The isothermal LCF tests were performed under total strain control in symmetrical push-pull with a fixed total strain range $\Delta\varepsilon_t$ of 1.2% at a constant total strain rate $\dot{\varepsilon}_t$ of $10^{-3}s^{-1}$. The TMF test cycle shape was selected so as to simulate the critical conditions prevailing in a near-surface volume element of a turbine blade in a land-based gas turbine during start-up and shut-down operation. The tests were carried out in a particular unsymmetrical out-of-phase cycle at different total strain ranges $\Delta\varepsilon_t$ in the temperature range ΔT from the lower temperature 400°C to the upper temperature 1000°C with a constant frequency of $\nu = 3.17 \times 10^{-3}s^{-1}$. Hence, the strain rates varied accordingly. The tests were started at the lower temperature of 400°C and at zero total strain ε_t.

A schematic presentation of the out-of-phase cycle used in this study is shown in Figure 3a which displays the time dependence and the phase relationships of temperature T and of the strain amplitudes $\Delta\varepsilon_t/2$, $\Delta\varepsilon_{th}/2$ and $\Delta\varepsilon_{mech}/2$, where the total strain ε_t is the sum of the mechanical strain $\varepsilon_{mech} = \varepsilon_{el} + \varepsilon_{pl}$ (ε_{el}: elastic strain, ε_{pl}: plastic strain) and the thermal strain ε_{th}. It should be noted that this TMF cycle is unsymmetrical with respect to

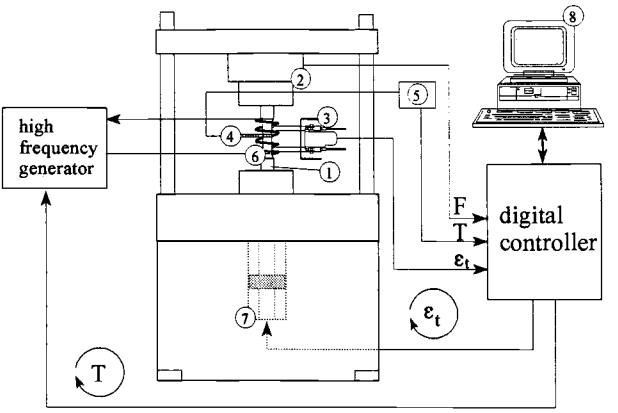

Figure 2 - *Graphic representation of the servohydraulic testing system MTS 810 with a digital controller; (1) specimen, (2) load cell (50 kN), (3) high-temperature extensometer (air cooled), (4) PtRh-Pt-strip thermocouple, (5) temperature-voltage transformer, (6) induction coil, (7) hydraulic actuator, (8) personal computer with controller software (MTS TESTSTAR and TESTWARE-SX).*

ε_{mech}. For comparison, the more commonly used symmetrical out-of-phase TMF cycle, compare [15-18], is shown in Figure 3b.

For the unsymmetrical out-of-phase TMF cycle applied in this study, the mechanical strain ε_{mech} given by the difference between ε_t and ε_{th}, is shifted with respect to the temperature by a phase angle of 180° and varies between zero and some negative value throughout the test. As a consequence, the specimen (blade) experiences a high (damaging) tensile stress at lower temperatures during this out-of-phase TMF cycle.

In addition, the elastic and the thermal properties of the bulk coating and substrate materials were investigated. Furthermore, detailed microstructural studies were conducted on the specimens in the initial state and after fatigue by standard metallographic techniques.

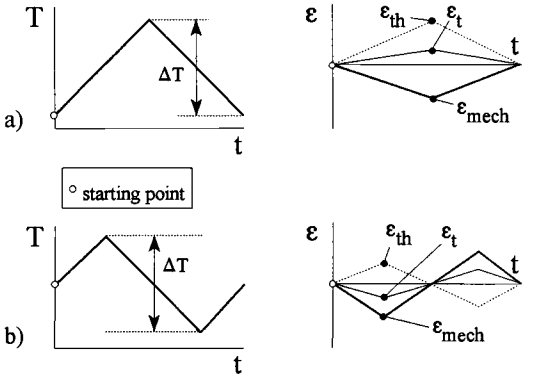

Figure 3 - *Comparison between (a) the unsymmetrical (with respect to the mechanical strain $\Delta\varepsilon_{mech}$) out-of-phase TMF test cycle used in this work and (b) the more common symmetrical out-of-phase TMF cycle. Time is denoted by the symbol t.*

Experimental Results and Discussion

Low-Cycle Fatigue Tests

LCF tests were performed on both the coated nickel-base superalloy DS CM 247 LC and on the bulk coating material PCA-1 at different temperatures and a fixed total strain range $\Delta\varepsilon_t$ of 1.2%. Here, we show the cyclic stress response curves for the substrate-coating composite (Figure 4). With respect to the fatigue behaviour of the bulk coating material, we refer to an earlier report [13]. The DS CM 247 LC/PCA-1 composite shows in the temperature range from 400°C up to 1000°C a minimum in fatigue lifetime at about 600°C. This temperature is near that temperature at which the coating material changes its deformation mode from brittle to ductile with increasing temperature (ductile-to-brittle transition temperature DBTT: approx. 650°C). This is an indication of the fact that the fatigue life of the composite is affected strongly by the fatigue properties of the coating material. In this context, we note that the fatigue lifetime of the bulk coating material tested under the same experimental conditions reveals the same dependence on temperature [13]. The observation of a minimum in the fatigue lifetime of the coating material can be explained by the fact that different deformation mechanisms operate above and below the DBTT [12,13,19,20].

At all temperatures investigated, the cracks in the LCF-specimens of the DS CM 247 LC/PCA-1 composite start from the surface of the composite, i.e. from the surface of the coating material. At lower temperatures, when the coating shows brittle deformation behaviour, the obvious crack initiation sites are micropores (the volume fraction of micropores in the coating material is about 1%), cf. Figure 5a. At temperatures well above the DBTT, at which oxidation gains influence, the brittle oxide scale lying above the ductile coating material breaks, and cracks originate there (Figure 5b).

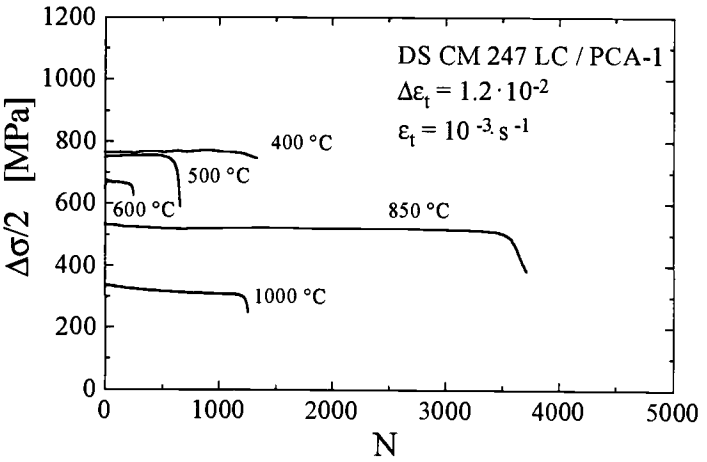

Figure 4 - *Isothermal cyclic stress response curves at different temperatures for the DS CM 247 LC/PCA-1-composite at a fixed total strain range $\Delta\varepsilon_t$ of 1.2% at a constant total strain rate $\dot{\varepsilon}_t$ of $10^{-3}s^{-1}$; $\Delta\sigma/2$: stress amplitude; N: number of cycles.*

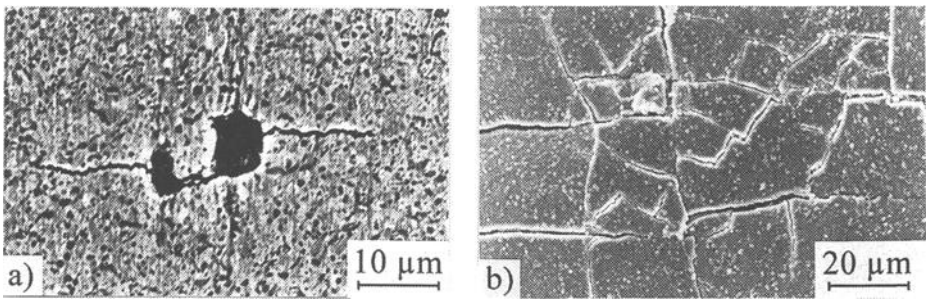

Figure 5 - *SEM micrographs of crack initiation under LCF fatigue loading at the surface of the DS CM 247 LC/PCA-1-composite; $\Delta\varepsilon_t$ = 1.2%; (a) at a coating micropore at 500°C; (b) at oxide scale cracks at 1000°C; stress axis vertical.*

Thermomechanical Fatigue Tests

Results of the TMF tests are shown as cyclic stress (maximum/minimum stress) response curves (Figure 6a) and in the form of the shape of the corresponding hysteresis loops (stress σ vs. mechanical strain ε_{mech}) of the first cycle (Figure 6b) for the DS CM 247 LC/PCA-1-composite at different total strain ranges $\Delta\varepsilon_t$. It should be noted that the compressive stress during increasing compressive total strain goes through a maximum and then decreases. This behaviour is attributed to the combined effect of the decreasing strength and Young's modulus and the enhanced dynamic recovery with increasing temperature.

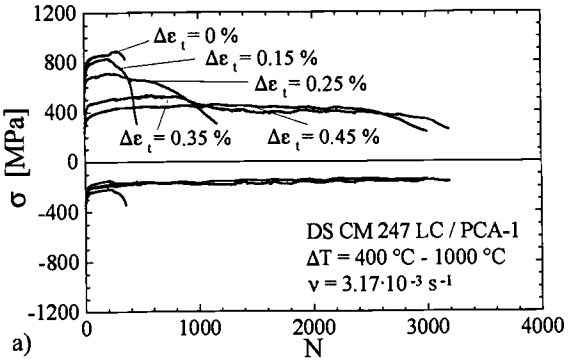

Figure 6 – *(a) Cyclic stress response curves of thermomechanical out-of-phase testing of the DS CM 247 LC/PCA-1-composite at different total strain ranges $\Delta\varepsilon_t$ and a temperature range ΔT from 400°C - 1000°C; test frequency $\nu = 3.17 \times 10^{-3} s^{-1}$. The total strain ranges $\Delta\varepsilon_t$ of 0%, 0.15%, 0.25%, 0.35% and 0.45% correspond to mechanical strain ranges $\Delta\varepsilon_{mech}$ of 1.03%, 0.91%, 0.80%, 0.67% and 0.58%, respectively.*

(continued next page).

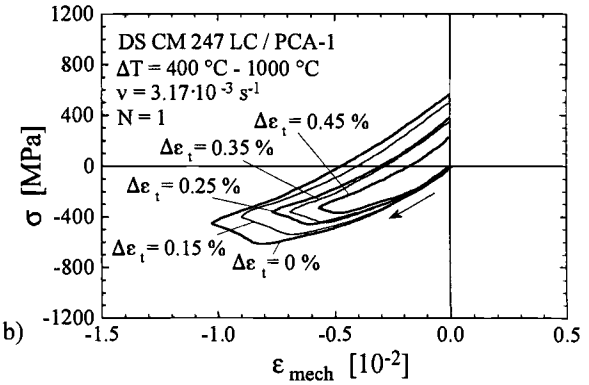

Figure 6 – (continued) *(b) Shape of the hysteresis loops (stress σ vs. mechanical strain $\Delta\varepsilon_{mech}$) for the first cycle.*

The states of the surface after TMF-cycling till failure of specimens with the total strain ranges $\Delta\varepsilon_t$ of 0%, 0.25% and 0.35% (mechanical strain ranges $\Delta\varepsilon_{mech}$ = 1.03%, 0.80%, 0.67%, respectively) reflect significantly different fatigue damage patterns. High mechanical strain amplitudes cause short, widely opened cracks, low mechanical strain amplitudes result in long, narrow cracks (Figure 7). In order to obtain more information about the growth of cracks in the coating during TMF-cycling, a series of identical TMF experiments were performed, which were stopped after a certain number of cycles.

The resulting cyclic stress response curves (maximum/minimum stresses versus number of cycles) of three thermomechanically fatigued specimens of the DS CM 247 LC/

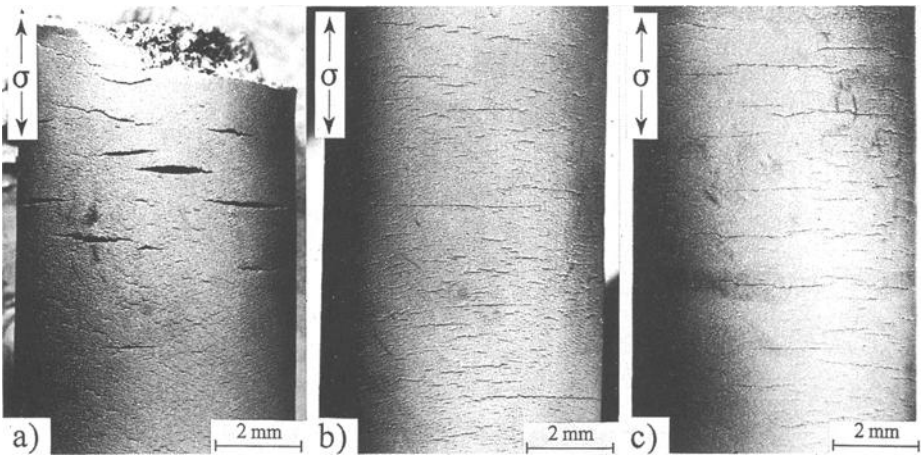

Figure 7 - *Optical micrographs showing the state of the gauge length of three TMF-specimens after testing, temperature range ΔT from 400°C – 1000°C, test frequency $\nu = 3.17 \times 10^{-3} s^{-1}$ (a) total strain range $\Delta\varepsilon_t$ = 0% (mechanical strain range $\Delta\varepsilon_{mech}$ = 1.03%), (b) $\Delta\varepsilon_t$ = 0.25% ($\Delta\varepsilon_{mech}$ = 0.80%) and (c) $\Delta\varepsilon_t$ = 0.45% ($\Delta\varepsilon_{mech}$ = 0.67%).*

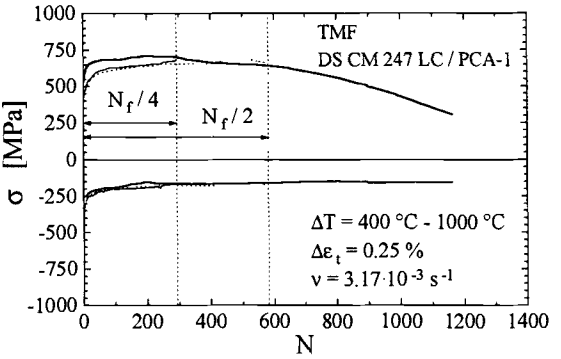

Figure 8 - *Comparison of the cyclic stress response curves of three thermomechanically fatigued specimens of the DS CM 247 LC/PCA-1-composite with increasing number of-cycles $N_f/4$, $N_f/2$ and N_f; total strain range $\Delta\varepsilon_t$ =0.25%, ($\Delta\varepsilon_{mech}$=0.80%) temperature range ΔT = 400°C – 1000°C; frequency $\nu = 3.17 \times 10^{-3} s^{-1}$.*

/PCA-1-composite, fatigued to respective numbers of cycles $N_f/4$, $N_f/2$ and N_f at a total strain range $\Delta\varepsilon_t$ of 0.25% are shown in Figure 8. Figure 9 shows optical micrographs of the surface and near-surface longitudinal sections of the DS CM 247 LC/PCA-1-composite after TMF testing for the same test parameters for different numbers of cycles.

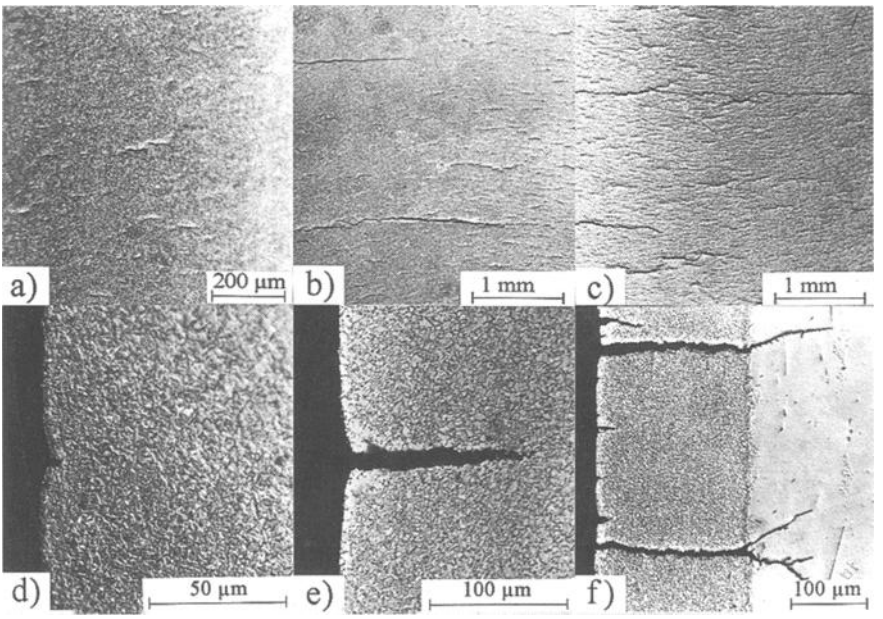

Figure 9 - *Optical micrographs showing the development of crack initiation and propagation on the surface (a)-(c) and in longitudinal sections of near-surface regions (d-f) of the coated composite after TMF-loading (as in Figure 8); (a,d) $N_f/4$; (b,e) $N_f/2$; (c,f) N_f.*

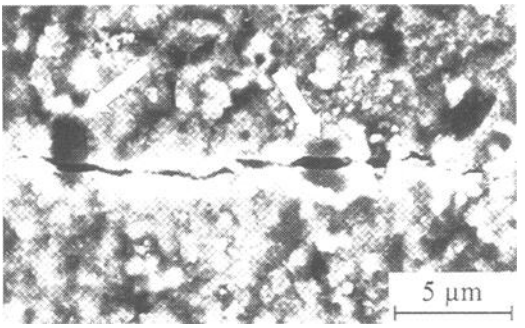

Figure 10 - *SEM micrograph showing crack initiation at the surface of the bulk coating material at the yttrium-rich phase M_5Y. Stress axis perpendicular. TMF test conditions: $\Delta\varepsilon_t = 0.25\%$ ($\Delta\varepsilon_{mech} = 1.18\%$), $\Delta T = 400°C - 1000°C$.*

Damaged grains of the oxidized yttrium-rich M_5Y-phase (M stands for Ni+Cr+Al, cf. [21]) could be identified in TMF tests on the coated substrate material DS CM 247 LC/PCA-1 and on the bulk coating material PCA-1 (Figure 10) as an important origin for the surface cracks of the thermomechanically fatigued specimens of the DS CM 247 LC/PCA-1-composite.

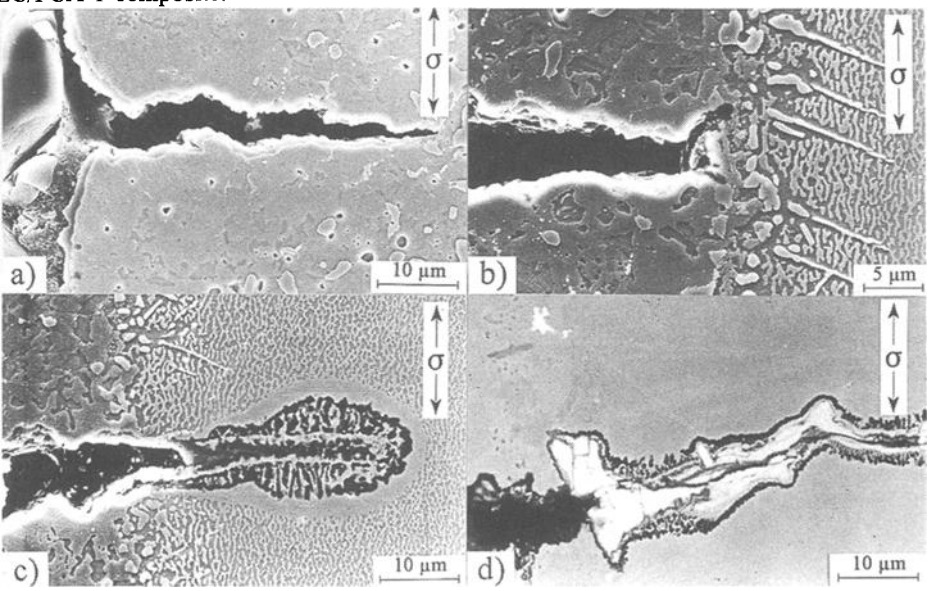

Figure 11 - *SEM micrographs showing the spreading of cracks (a) in the coating near the surface (b) stopping at the coating-substrate border and (c) and (d) cracks crossing the coating-substrate interface due to oxidation of the γ/γ'-structure of the substrate as well as cracks entering the substrate at oxidized, cracked carbides; longitudinal sections; TMF test conditions: total strain range $\Delta\varepsilon_t = 0.25\%$ ($\Delta\varepsilon_{mech} = 0.80\%$), temperature range $\Delta T = 400°C - 1000°C$, test frequency $\nu = 3.17 \times 10^{-3} s^{-1}$, stress axes vertical.*

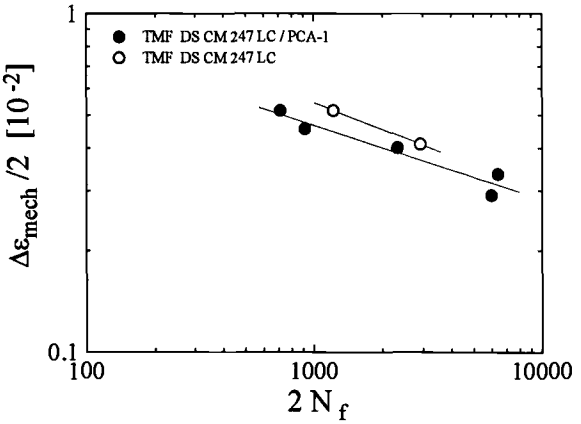

Figure 12 - *Double-logarithmic plot of the mechanical strain amplitude $\Delta\varepsilon_{mech}/2$ versus twice the number of cycles to failure, 2 N_f, for the uncoated and for the coated substrate DS CM 247 LC for TMF-tests for different total strain amplitudes and a temperature range ΔT of 400°C – 1000°C, test frequency $v = 3.17 \times 10^{-3} s^{-1}$.*

It is obvious from the micrographs (Figure 9) that the crack propagation through the coating lasts a certain number of TMF-cycles and therefore influences the fatigue lifetime of the composite. The SEM micrographs (Figure 11) show the growth of cracks in the coating and the subsequent penetration into the substrate material.

To decide whether the coating affects the TMF fatigue life of the composite or not, two exemplary TMF-tests with uncoated DS CM 247 LC-specimens were performed (Figure 12). The comparison of the TMF life data for the uncoated substrate and the composites, plotted in a double-logarithmic plot of the mechanical strain amplitude $\Delta\varepsilon_{mech}/2$ as a function of twice the number of cycles to failure, 2 N_f, shows that, under the TMF conditions described, the fatigue life of the coated alloy is smaller than that of the uncoated material.

It is not surprising that oxidized carbides which help cracks to surmount the coating-substrate interface in the case of the fatigued composite are also preferred sources of cracks in the surface of the uncoated substrate material (Figure 13).

Both the results of the interrupted experiments on the coated composite material and the comparison of the fatigue life data of the uncoated substrate and the composite suggest that the crack propagation in the coating material governs the fatigue properties of the composite to a certain extent.

In order to pursue this question further, some TMF experiments were made on the bulk coating material, using the same parameters as in the TMF tests on the composite. An important finding is that severe microstructural changes occur in the coating material during the temperature cycles and that the TMF behaviour of the coating material cannot be described on the basis of its isothermal behaviour. Thus, measurements of the thermal expansion behaviour of the bulk coating material in a temperature cycle between 400°C and 1000°C yielded a pronounced hysteresis. The latter is related to a time-dependent phase reaction, associated with a volume change which can be understood by inspection of isothermal sections of the ternary NiCrAl phase diagram, shown in Figure 14 for tem

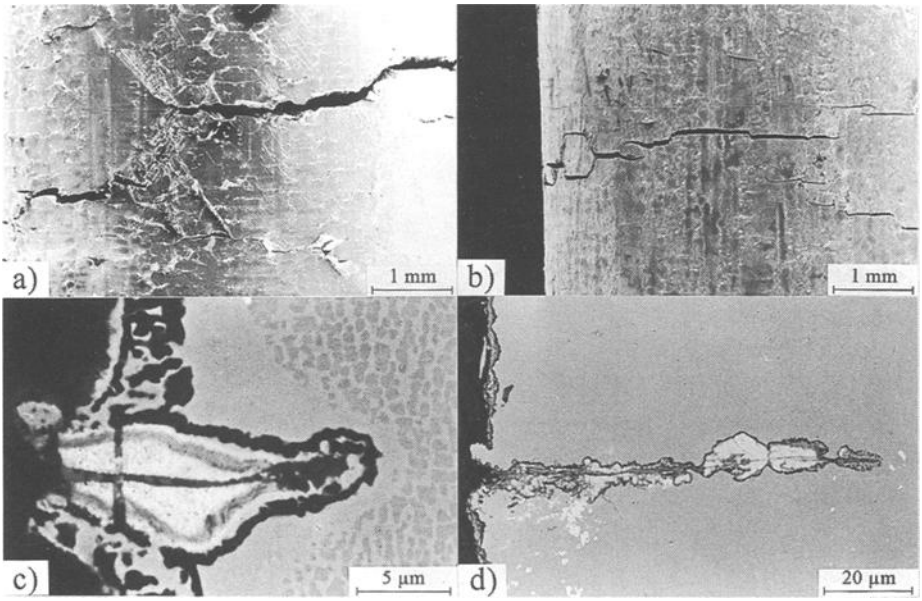

Figure 13 - *SEM micrographs showing crack initiation at oxidized carbides at the surface (a,b) of uncoated substrate material DS CM 247 LC and in longitudinal sections (c,d) after TMF testing. a) and b) $\Delta\varepsilon_t$ = 0% ($\Delta\varepsilon_{mech}$ = 1.03%), c) and d) $\Delta\varepsilon_t$ = 0.25% ($\Delta\varepsilon_{mech}$ = 0.80%), stress axes vertical.*

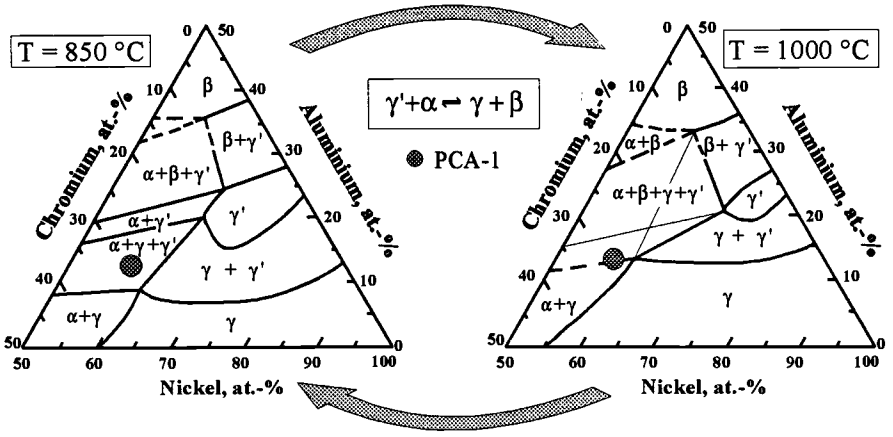

Figure 14 - *Isothermal sections of the ternary nickel-chromium-aluminium system at 850°C and 1000°C, after [22]. The drawn-in point represents the composition of the NiCrAlY-alloy PCA-1, lying in the (α+β+γ+γ') phase field at 1000°C.*

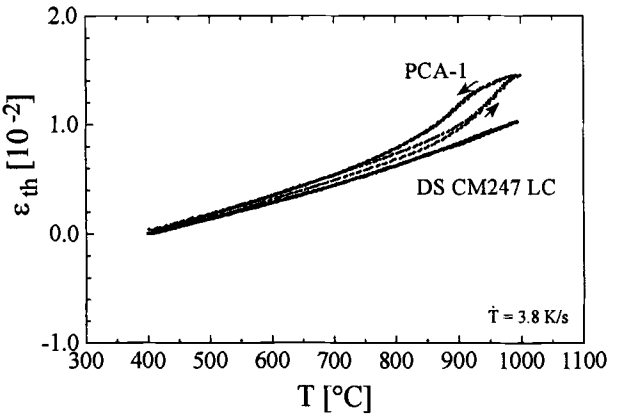

Figure 15 - *Thermal expansion ε_{th} vs. temperature T of the substrate material DS CM 247 LC and of the bulk coating material PCA-1 in the temperature range ΔT of 400°C– 1000°C, frequency $\nu = 3.17 \times 10^{-3} s^{-1}$ (corresponds to $\dot{T} = \pm 3.8$ K/s).*

peratures of 850°C and 1000°C, compare [22]. The composition according to the major constituents of the coating material PCA-1 consists of the following three phases (disregarding the yttrium-rich M_5Y-phase): the body-centred cubic α-phase, the face-centred cubic γ-phase and the ordered γ'-phase with $L1_2$-structure (compare Figure 14). At about 1000°C during the heating branch of the TMF cycle a fourth phase, the ordered face-centred cubic β-phase with B2-structure appears.

Due to the fact that the alloy composition lies in a three-phase region at lower temperatures and in a four-phase region at the highest temperatures of the TMF cycle, respectively, the coating material undergoes a change of its microstructure for every single TMF cycle. Since the microstructural variations of the coating material are accompanied by volume changes [23], an opened hysteresis loop (thermal expansion vs. temperature) is observed during thermal cycling of the bulk coating material PCA-1 (Figure 15), which is coupled with the formation and dissolution of the γ- and the β-phase (according to the equation $(\alpha+\gamma' \leftrightarrow \beta+\gamma)$, depending on the rate of heating and cooling. On the other hand, the thermal expansion ε_{th} versus the temperature T of the substrate material DS CM 247 LC exhibits no hysteresis during cycling in the temperature range ΔT from 400°C – 1000°C (Figure 15).

In Figure 16, stress versus temperature curves are shown for the first TMF cycle of the uncoated substrate, the coated substrate and the bulk coating material, all fatigued under the same experimental conditions. The curve obtained for the substrate-coating composite resembles closely that of the uncoated substrate material, since the cross section of the coating material is only a small fraction of the total cross section. Furthermore, one recognizes that the mechanical responses of the substrate and the coating material differ significantly under identical thermomechanical straining conditions. Thus, whereas the substrate material experiences significant compressive stresses at the upper temperature during the TMF cycle, the compressive stresses in the coating material at the upper temperature are very small as a consequence of severe stress relaxation, associated with reduced strength, of the coating material. On the other hand, the coating material experiences increasing larger tensile stresses during cooling than the substrate material (Figure

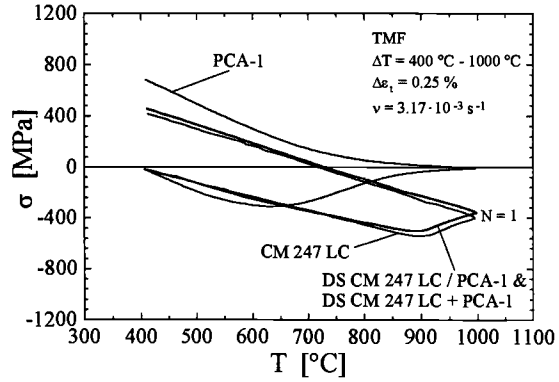

Figure 16 - *Comparison of first stress versus temperature TMF cycle for the bulk alloy DS CM 247 LC, the bulk NiCrAlY coating PCA-1, the coated alloy composite CM 247 LC/PCA-1 and the calculated dependence for the composite CM 247 LC/PCA-1 for a total strain range $\Delta\varepsilon_t$ of 0.25% ($\Delta\varepsilon_{mech}$ = 0.81%) and a temperature range ΔT of 400°C – 1000°C, frequency $\nu = 3.17 \times 10^{-3} s^{-1}$.*

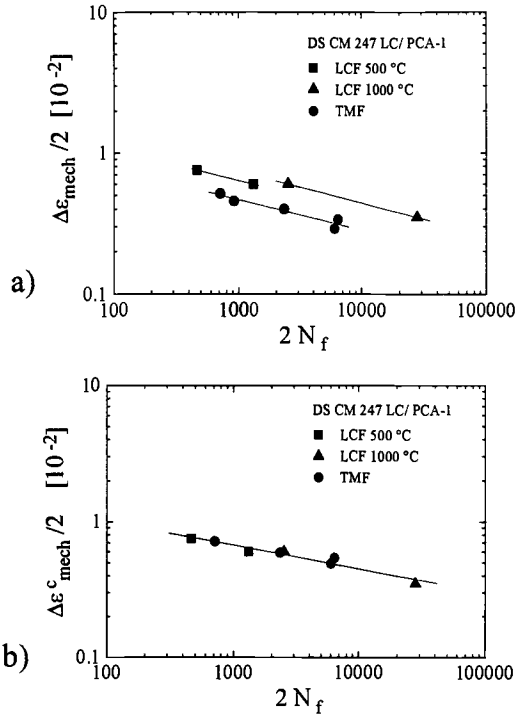

Figure 17 - *Double-logarithmic plot of a) the mechanical strain amplitude $\Delta\varepsilon_{mech}/2$ of the composite and b) the mechanical strain amplitude of the coating $\Delta\varepsilon^{c}_{mech}/2$ versus twice the number of cycles to failure, 2 N_f, for TMF tests and for isothermal LCF-tests.*

16). Additionally, it could be shown that the stress-temperature response of the coated material corresponds closely to that predicted by the superposition of the responses of the substrate and the coating material in a simple iso-strain composite model (coating and substrate are combined in parallel with respect to the total strain, cf. two-bar model [24]).

Finally, it is interesting to note that, in a double-logarithmic plot of the mechanical strain amplitude experienced by the coating, $\Delta\varepsilon^{c}_{mech}/2$, against $2N_f$ for the coated material, the fatigue life data for the coated composite material for isothermal fatigue tests performed near the lower and at the upper temperatures of the TMF cycle, respectively, and for thermomechanical fatigue tests fall on the same common line (Figures 17a and b). It is concluded that the TMF life of the coated alloy is dictated by that of the coating. These findings correspond precisely to the earlier results obtained for the fatigue lives in isothermal LCF tests on the composite [12,13], when compared with the data for the bulk coating material PCA-1.

Acknowledgments

Sincere thanks are extended to ABB Corporate Research Centre, Heidelberg, for substantial financial support and to Dr. Manfred Bayerlein and Dr. Christoph Sommer for their continued interest.

References

[1] Endres, W., "Design Principles of Gas Turbines," in *High-Temperature Materials in Gas Turbines*, P. R. Sahm and M. O. Speidel, Eds., Elsevier Scientific Publishing Company, Amsterdam, 1974, pp. 1-14.

[2] Gell, M., Duhl, D. N., Gupta, D. K., Sheffler, K. D., "Advanced Superalloy Airfoils", *Journal of Metals*, Vol. 39, 1987, pp. 11-15.

[3] Wood, J. H. and Goldman, E. H., "Protective Coatings," in *Superalloys II*, C. T. Sims, N. S. Stoloff and W. C. Hagel, Eds., John Wiley & Sons, 1987, pp. 359-384.

[4] Mèvrel, R., "State of the Art on High-Temperature Corrosion-Resistant Coatings," *Materials Science and Engineering*, Vol. A120, 1989, pp. 13-24.

[5] Smialek, J. L. and Meier, G. H., "High-Temperature Oxidation," in *Superalloys II*, C. T. Sims, N. S. Stoloff and W. C. Hagel, Eds., John Wiley & Sons, 1987, pp. 293-325.

[6] Duret, C. and Pichoir, R., "Chemical Vapor Deposition and Pack Cementation Processes," in *Coatings for High Temperature Applications*, E. Lang, Ed., Elsevier Applied Science Publishers, London, 1986, pp. 33-78.

[7] Gill, B. J. and Tucker, R. C., "Plasma Spray Coating Processes," *Materials Science and Technology*, Vol. 2, 1986, pp. 207-213.

[8] Pettit, F. S. and Goward, G. W., "Gas Turbine Applications," *in Coatings for High Temperature Applications*, E. Lang, Ed., Elsevier Applied Science Publishers, London, 1986, pp. 341-359.

[9] Grünling, H. W., Schneider, K. and Singheiser. L., "Mechanical Properties of Coated Systems," *Materials Science and Engineering*, Vol. 88, 1987, pp. 177-189.

[10] Wood, M. I., "The Mechanical Properties of Coatings and Coated Systems," *Materials Science and Engineering*, Vol. A 121 , 1989, pp. 633-643.

[11] Kadioglu, Y. and Sehitoglu, H., "Modeling of Thermomechanical Fatigue Damage in Coated Alloys," in *Thermomechanical Fatigue Behavior of Materials*, H. Sehitoglu, Ed., ASTM STP 1186, 1993, pp. 17-34.

[12] Kowalewski, R., "Thermomechanische Ermüdung einer beschichteten, stengelkristallinen Nickelbasis-Superlegierung," *Doctorate thesis*, Universität Erlangen-Nürnberg, 1997.

[13] Kowalewski, R. and Mughrabi, H., "Influence of a Plasma-sprayed NiCrAlY Coating on the Low-cycle Fatigue Behaviour of a Directionally Solidified Nickel-base Superalloy," *Materials Science and Engineering*, Vol. A247, 1998, pp. 259-299.

[14] Kowalewski, R. and Mughrabi H., "Thermomechanical Fatigue of a Coated Directionally Solidified Nickel-Base Superalloy," in *Proceedings of 4th International Conference on Low-Cycle Fatigue and Elasto-Plastic Behaviour of Metals and Alloys (LCF-4)*, K.-T. Rie and P. D. Portella, Eds., Elsevier, 1998, pp. 149-154.

[15] Kraft, S. A. and Mughrabi, H., "Thermo-Mechanical Fatigue of the Monocrystalline Nickel-Based Superalloy CMSX-6," in *Thermomechanical Fatigue Behaviour of Materials, Second Volume*, ASTM STP 1263, M. J. Verilli and M. G. Castelli, Eds., 1996, pp. 27-40.

[16] Chen, H., Chen, W., Mukherji, D., Wahi, R.P. and Wever, H., "Cyclic Life of Superalloy IN738LC under In-Phase and Out-of-Phase Thermo-Mechanical Fatigue Loading," *Zeitschrift für Metallkunde*, Vol. 86, 1995, pp. 423-427.

[17] Boismier, D.A. and Sehitoglu, H., "Thermo-Mechanical Fatigue of Mar-M247: Part 1 - Experiments," *Transactions of ASME*, Vol. 112, 1990, pp. 68-79.

[18] Skelton, R. P., " The Determination of Hysteresis Loops in Thermomechanical Fatigue Using Isothermal Stress-Strain Data Fatigue", *Fracture and Materials Structure*, Vol. 17, 1994, pp. 479-496.

[19] Smith, R.W., "Mechanical Properties of a Low-Pressure-Plasma-Applied Co-Cr-Al-Y Coating," *Thin Solid Films*, Vol. 84, 1981, pp. 59-72.

[20] Lowrie, R. and Boone, D. H., "Composite Coatings of CoCrAlY plus Platium," *Thin Solid Films*, Vol. 45, 1977, pp. 491-498.

[21] Frances, M., Vilasi, M. Mansour-Gabr, M., Steinmetz, J. and Steinmetz P., "Etude de l'Oxidation à 850 °C de l'Alliage Ni-Co-Cr-Al(-Y)- Ta Coulé et Projeté au Chalumeau Plasma sous Pression Réduite," *Materials Science and Engineering*, Vol. 88, 1987, pp. 89-96.

[22] Taylor, A. u. Floyd, R. W., "The Constitution of Nickel-Rich Alloys of the Nickel-Chromium-Aluminium System," *Journal of the Institute of Metals*, Vol. 81, 1952, pp. 451-463.

[23] Choquet; P., "Etude de L'Oxidation a Haute Temperature de Depots D'Alliages Ni(Co)CrAl Realisés par Pulverisation Cathodique. Influence des Elements D'Addition Y, Hf et Zr ," Doctorate Thesis, Université Paris-Sud, Orsay, 1987.

[24] Heine, J. E., Warren, J. R. and Cowles, B. A., "Thermal Mechanical Fatigue of Coated Blade Materials," Report, Wright-Patterson Air Force Base, Ohio, WRDC-TR-894027, 1989.

Peter Pototzky,[1] Hans Jürgen Maier,[2] and Hans-Jürgen Christ[1]

Behavior of the High-Temperaturse Titanium Alloy IMI 834 Under Thermo-mechanical and Isothermal Fatigue Conditions

Reference: Pototzky, P., Maier, H. J., and Christ H.-J., **"Behavior of the High-Temperature Titanium Alloy IMI 834 Under Thermo-mechanical and Isothermal Fatigue Conditions,"** *Thermo-mechanical Fatigue Behavior of Materials: Third Volume, ASTM STP 1371,* H. Sehitoglu and H. J. Maier, Eds., American Society for Testing and Materials, West Conshohocken, PA, 2000.

Abstract: The high-temperature titanium alloy IMI 834 was studied with regard to the stress-strain response under thermo-mechanical fatigue conditions, the evolution of the microstructure, the relevant damage mechanisms and their implications for fatigue life. For this purpose isothermal and thermo-mechanical fatigue tests were performed in the temperature range from 350°C to 650°C in vacuum and air, respectively, and changes in the microstructure were determined by means of transmission electron microscopy. It was found that planar dislocation slip prevails in all tests in which the temperature does not exceed 600°C. Hence, in this temperature range the stress-strain response under thermo-mechanical conditions can be predicted solely based on the isothermal behavior. By contrast, a transition to wavy slip takes place at higher temperatures, affecting significantly the stresses in the low-temperature part of the corresponding thermo-mechanical fatigue tests. Fatigue life was generally observed to be lower in out-of-phase tests as compared to in-phase loading. Furthermore, the tests performed in high vacuum demonstrated that oxidation strongly affects fatigue life, but does not basically change the influence of testing mode on cyclic life. This can mainly be attributed to the additional effect of the acting mean stress.

Keywords: High-temperature titanium alloy, IMI 834, isothermal fatigue, thermo-mechanical fatigue, microstructural evolution, oxidation, mean stress effect, cyclic life

Introduction

IMI 834 is a high-temperature titanium alloy which was designed for the use as disc and blade material in the hot part of the compressor of jet engines [*1*]. The application to intended service temperatures of up to 600°C [*2*] requires an excellent combination of fatigue and creep strength. For this purpose, a bimodal fine-grained microstruc-

[1]Graduate Research Assistant and Professor, respectively, Institut für Werkstofftechnik, Universität-GH-Siegen, D-57068 Siegen, Germany.

[2]Professor, Lehrstuhl für Werkstoffkunde, Universität Paderborn, D-33095 Paderborn, Germany.

ture consisting of 15 vol.% equiaxed primary α-phase embedded in a matrix of lamellar transformed β is recommended by the alloy manufacturer. In addition to creep and fatigue loading, components of jet engines are subjected to changes in service temperature. It is well-known that the combination of mechanical strain (or load) cycling with temperature cycling may give rise to the so-called thermo-mechanical fatigue (TMF) and may limit the life of such components [*3*]. Despite this knowledge, in many cases life assessment is still based on isothermal data, since TMF testing requires expensive equipment and is very time-consuming. However, as cyclic stress-strain behavior, crack initiation and crack propagation must be considered to depend on test conditions (TMF or isothermal fatigue), this approach to life prediction may give nonconservative results.

Titanium alloys usually exhibit relatively high strength in combination with low elastic modulus. Therefore, they are capable of large elastic strains. Hence, conventional titanium alloys, which are applied at a maximum operating temperature of not more than 500°C, can tolerate thermal strains induced during thermal cycling as elastic strains and a change in the damage mechanisms does not take place [*4*]. As a consequence, a study of the TMF behavior of these alloys seems not to be essential for life prediction [*5*]. However, the maximum service temperature of the most recent high-temperature titanium alloy IMI 834 is about 600°C, as already mentioned above. Thus, TMF has to be taken into account, because thermal stresses can induce both, elastic and plastic strain.

The objective of the present study was to characterize the stress-strain behavior and the cyclic life of IMI 834 under TMF conditions. In order to provide a sound basis for comparison, the isothermal high-temperature fatigue behavior was firstly characterized applying testing conditions which are identical (as far as possible) to the ones used in the TMF tests. Special emphasis was put on the microstructural changes in order to understand the similarities and differences in the evolution of the microstructure under isothermal and TMF conditions, respectively. Furthermore, tests in high vacuum were performed to eliminate damage by environmental attack and hence to allow to assess the importance of this damage contribution.

Experimental Details

The near-α titanium alloy IMI 834 (nominal composition in wt%: Ti-5.8Al-0.4Sn-3.5Zr-0.7Nb-0.5Mo-0.35Si-0.06C) used in this study was supplied in form of hot-forged bars (1 m length, 60 mm diameter). In Figure 1, optical micrographs of the four microstructures investigated are depicted. The as-received condition (Figure 1a) is characterized by a globular microstructure with a non-uniform grain size of the α-grains (average value 12 μm). The bimodal microstructure (Figure 1b), which is recommended for optimum creep and fatigue performance [*1*], was obtained by solution annealing for two hours at 1020°C (within the α+β-phase field) followed by rapid quenching in oil. During quenching the β-phase transforms into lamellar α (transformed β). The average grain size and the volume fraction of the primary α-grains were found to be 12 μm and 15 vol.%, respectively. The average grain size of the lamellar transformed β matrix is about 25 μm. The lamella width is determined by the rate of cooling from the solution annealing temperature. A bimodal microstructure with broad lamellae resulted from cooling in air instead of oil (Figure 1d). This also increases the average grain size of the primary α-grains slightly (15 μm) without affecting their volume fraction. In order to establish a fully

lamellar microstructure (Figure 1c), solution annealing was carried out at 1060°C for 2 h (above the beta transus). Oil quenching led to a fully lamellar microstructure with an average grain size greater than 0.5 mm and a lamella spacing similar to that of the bimodal microstructure. Prior to testing all specimens except those with globular microstructure (as-received condition) were aged for two hours at 700°C and air cooled. This treatment improves the mechanical properties because of the precipitation of fine silicides and ordered Ti_3Al [*6,7*]. It should be noted that all heat treatments were conducted in high vacuum, in order to prevent from strong oxidation.

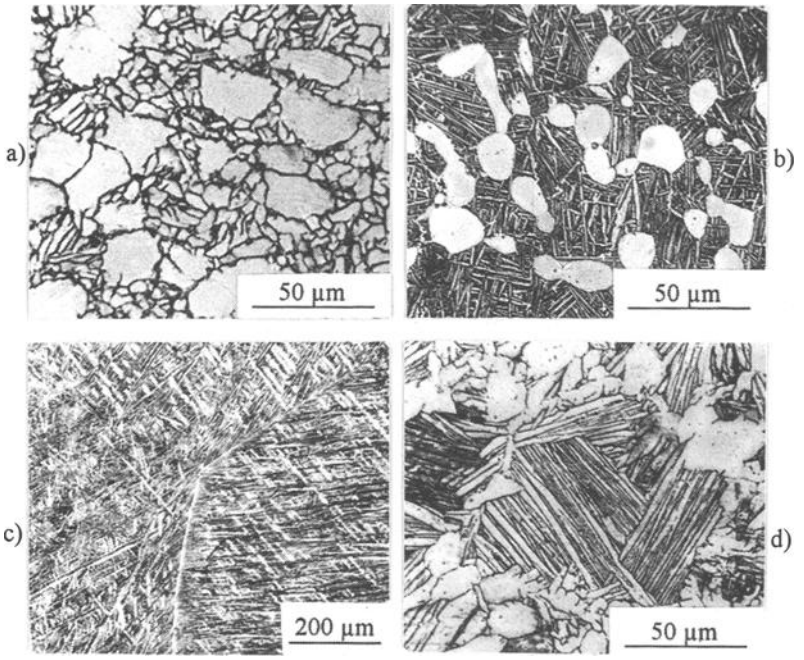

Figure 1 — *Optical Micrographs of IMI 834 with Different Microstructures. a) Globular, b) Bimodal, c) Fully Lamellar and d) Bimodal with Broad Lamellae. Note, that Picture c) Shows a Lower Magnification than a), b) and d).*

For the fatigue tests, specimens with a cylindrical gage length of 14 mm and a gage diameter of 8 mm were machined. To minimize surface effects on fatigue life, the surface within the gage length was electropolished prior to testing. A servo-hydraulic testing system which is equipped with induction heating and a high vacuum chamber was used for the isothermal and thermo-mechnical fatigue tests in air and high vacuum ($p \leq 3 \cdot 10^{-5}$ mbar). The temperature of the samples was measured and controlled by means of thermocouples spot-welded onto the gage length. It should be note that only those tests were considered which have not been affected by spot welding with respect to crack initiation and cyclic life.

In order to facilitate a direct comparison of the stress-strain behavior under thermo-mechanical and isothermal conditions, all fatigue tests were carried out using plastic

strain as feedback signal in the closed control loop of the testing system (plastic strain control [*8*]). A triangular command signal was used for both, the plastic strain and the temperature (Figure 2). All tests were started at zero plastic strain with a positive slope. In the in-phase (IP) tests, the temperature firstly increases and the maximum temperature is reached at the maximum plastic strain, while in the out-of-phase (OP) tests the minimum temperature coincides with maximum plastic strain. The plastic strain signal that cannot be measured directly was determined by means of a self-developed analog circuit which was added to the control electronics of the testing system. The electronic calculation of the plastic strain is based upon the equation:

$$\varepsilon_{pl} = \varepsilon - \varepsilon_{el} - \varepsilon_{th} \tag{1}$$

where ε is the measured total strain, ε_{el} is the elastic strain, and ε_{th} is the thermal strain. ε_{th} was experimentally determined prior to each test by carrying out a thermal cycle at zero stress. Since IMI 834 exhibits a low elastic modulus and a relatively high yield strength, in addition to the temperature dependence of the elastic modulus, deviations from the linearity of the elastic behavior must be taken into account in the calculation of ε_{el} [*9*] from the measured stress. For details see ref. [*10*].

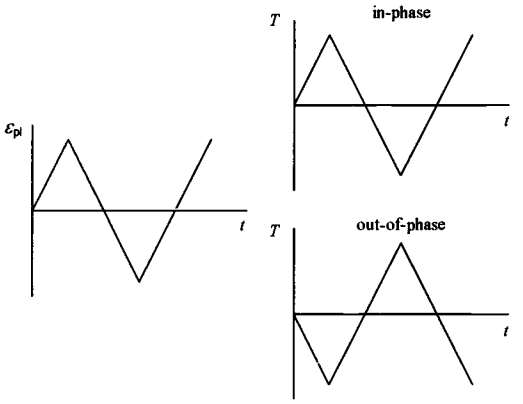

Figure 2 — *Command Signals of Plastic Strain (ε_{pl}) and Temperature (T) for In-Phase and Out-Of-Phase TMF Testing under True Plastic Strain Control.*

Isothermal tests were conducted between room temperature and 650°C at a plastic strain rate of $\dot{\varepsilon}_{pl} = 4 \cdot 10^{-5}$ s^{-1} and at plastic strain amplitudes $\Delta\varepsilon_{pl}/2$ of 0.2% and 0.5%. Thermomechanical fatigue (TMF) behavior was studied in the temperature regime between 350°C and 650°C at identical plastic strain rate and identical plastic strain amplitudes. In order to separate environmental effects on fatigue life from damage due to mechanical and thermal cycling, additional experiments were performed in high vacuum. Furthermore, hardness profiles were measured on cross sections to quantify the formation of an embrittled subsurface zone (α-case) that results from oxygen uptake.

The microstructural changes were studied by means of transmission electron microscopy (TEM) performed at a acceleration voltage of up to 200 kV. TEM specimens

were sectioned perpendicular to the stress axis of the fatigued samples. Electron transparent foils were obtained by conventional twin-jet electropolishing. Crack initiation and initial crack propagation were investigated by scanning electron microscopy (SEM) applied to the gage length surface and the fracture surface of cyclically deformed specimens.

Results

Isothermal Fatigue Behavior

Figure 3 illustrates the cyclic deformation behavior of the bimodal microstructure as a function of test temperature in a representation of the stress amplitude $\Delta\sigma/2$ versus the number of cycles N. The material shows a relatively stable cyclic stress-strain response after a first stage of cyclic softening. At room temperature and at temperatures above 500°C, the stress amplitude was found to continuously decrease, until the growth of a macrocrack leads to a steep drop of $\Delta\sigma/2$. In the tests run at 350°C and 400°C, slight cyclic hardening occurs after initial cyclic softening. As expected, the stress amplitude of the (approximate) cyclic saturation decreases with increasing temperature. However, the number of cycles to failure decreases. Figure 3 shows the results of tests at $\Delta\varepsilon_{pl}/2 = 0.2\%$. A similar behavior was observed at $\Delta\varepsilon_{pl}/2 = 0.5\%$.

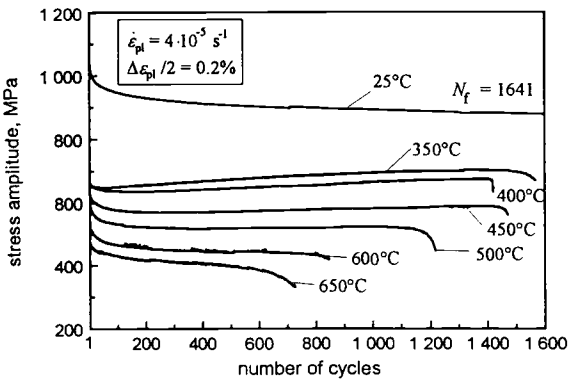

Figure 3 — *Cyclic Deformation Curves of Isothermal Fatigue Tests on Bimodal Specimens at Various Temperatures in Air.*

The effect of microstructure on the fatigue behavior was mainly studied at the temperatures 400°C, 600°C and 650°C. Figure 4 shows in an exemplary fashion the cyclic deformation curves obtained in tests run at 600°C. In principle, all microstructures studied reflect an identical temperature dependence of their cyclic stress-strain response. Therefore at 600°C (Figure 4), a continuous cyclic softening takes place, whereas at 400°C after initial cyclic softening a slight cyclic hardening prevails. The lamellar microstructure exhibits the highest cyclic strength and the bimodal microstructure with the broad lamellae the lowest. Since the high strength of the lamellar microstructure is connected with a relative short cyclic life, the bimodal structure (with fine lamellae) clearly

provides the best compromise of stress amplitude and number of cycles to failure N_f. Although globular and coarse-bimodal microstructure exhibit strongly reduced stress amplitudes, the cyclic life does not increase significantly as compared to the bimodal structure with fine lamellae.

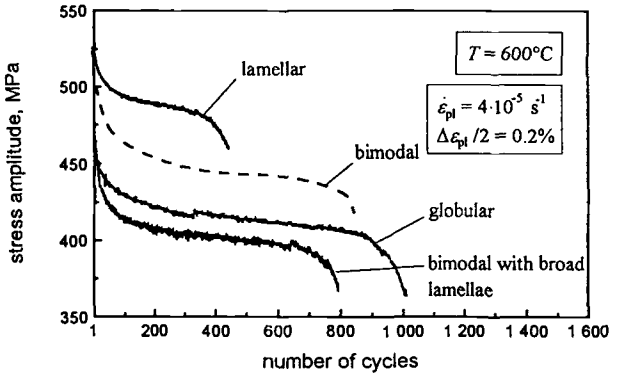

Figure 4 — *Cyclic Deformation Curves of Isothermal Fatigue Tests Carried out at 600°C in Air on Different Microstructures.*

The microstructural study of fatigued samples revealed that the test temperature determines the dislocation slip character. If the test temperature does not exceed 600°C, planar dislocation slip prevails. Consequently, similar dislocation arrangements were formed in this temperature range. As depicted in Figure 5a, inside the primary α-grains planar slip bands exist. The formation of these slip bands is generally attributed to (or at least promoted by) shearing of ordered coherent Ti_3Al precipitates by gliding dislocations [*11,12*]. The existence of Ti_3Al precipitates could be proved by the use of selected area diffraction (SAD) (in accordance with [*13*]). Figure 5b represents the SAD pattern of the primary α-grain shown in Figure 5a, which contains superlattice reflections of Ti_3Al. In contrast to the primary α-grains, the lamellar grains showed only weak or no superlattice reflections. This is caused by the alloy partitioning effect [*14*]. During the solution annealing in the α+β-field, aluminum, which is known to act as an α-stabilizing alloying element, is enriched in the α-phase, whereas the elements Sn, Mo, Zr, Nb and Si diffuse into the β-phase. The higher Al content of the primary α-grains promotes the formation of Ti_3Al during the aging treatment.

Figures 5c and 5d show two grains of the lamellar transformed-β matrix of the same sample which differ significantly in dislocation density (note, that the same imaging conditions were used). Furthermore, these micrographs reveal that cyclic deformation at 400°C does not result in a disintegration of the lamella boundaries. Moreover, only few silicides are visible (*c.f.* Fig. 5c).

At a test temperature of 600°C first indications were found that the lamella boundaries start to disintegrate and that precipitates of silicides decorate these boundaries. At 650°C, this disintegration is clearly appreciable as shown in Figure 6. It should be noted, that this micrograph was taken under such an imaging condition that most dislocations are invisible and the silicides are in contrast. Subgrains within the primary α-grains were found after cyclic deformation at 650°C indicating that above 600°C wavy dislocation

slip starts to prevail and to determine the stress-strain behavior.

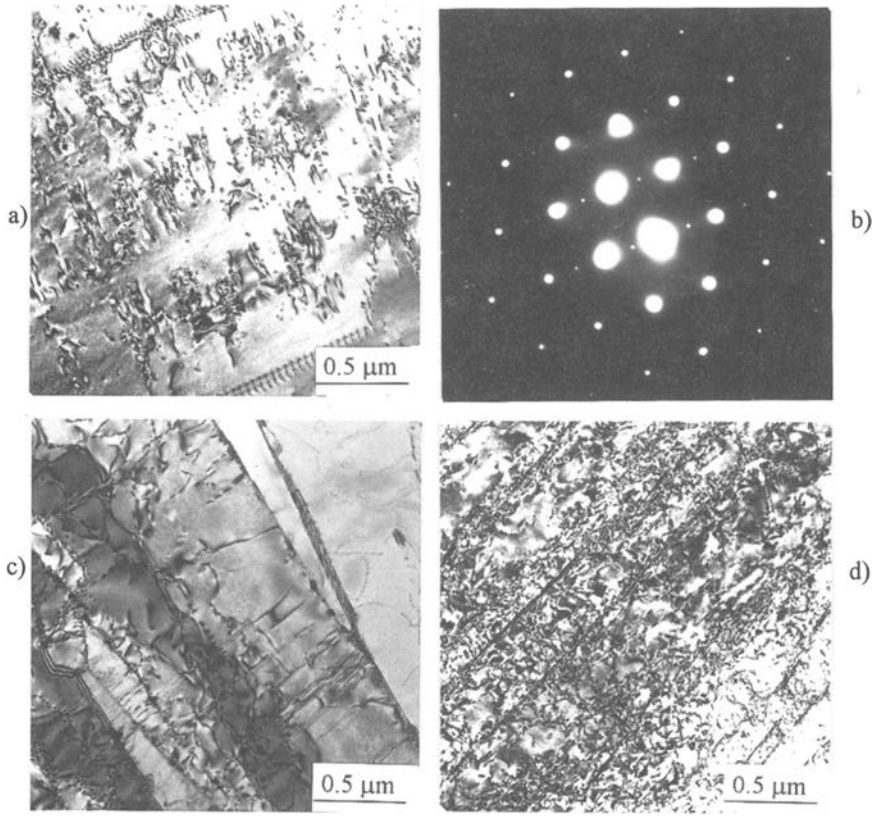

Figure 5 — *TEM Micrographs of a Bimodal Sample, Isothermally Fatigued at 400°C. a) Planar Slip Bands within a Primary α-Grain, b) SAD-Pattern of this Grain Showing Superlattice Reflections, c) and d) Two Different Positions in Lamellar Transformed-β Grains Showing Different Dislocation Densities. Note that g = (10$\bar{1}$ 1) Was Used for All Micrographs.*

The study of the gage length surfaces by means of SEM using back-scattered electron (BSE) contrast showed that at 400°C crack initiation occurred preferentially at primary α-grains and was associated with the planar slip bands formed. An increase of the temperature resulted in fewer, but long cracks on the surface, but these cracks could neither be attributed to the primary α nor to the transformed β in an unambiguous way.

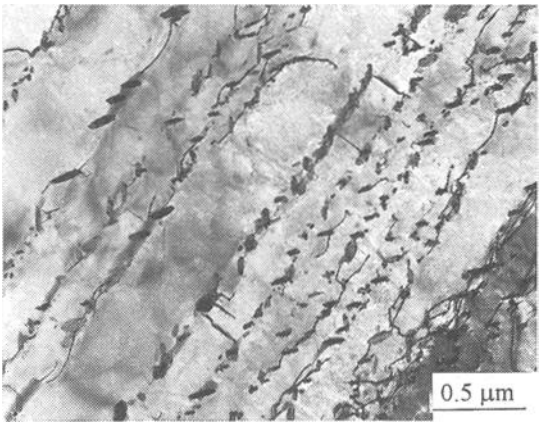

Figure 6 — *Bright-Field Image of a Bimodal Sample, Isothermally Fatigued at 650°C. Silicides Mark the Disintegrated Lamella Boundaries.*

Thermomechanical Fatigue Behavior

This chapter is subdivided in three sections. First, the mechanical behavior under TMF conditions will be dealt with putting special emphasize on the effect of microstructure, of the maximum temperature of the TMF cycle, and of the cycle type (IP or OP). In the second section, the significance of environmental effects for the TMF life will be illustrated by means of comparative TMF tests performed in air and high vacuum. Finally, the results of the microstructural investigations (TEM and SEM) will be presented.

Cyclic Stress-Strain Behavior and Fatigue Life under TMF Conditions — Figures 7a and 7b show cyclic deformation curves of IP tests run in the temperature interval of $T = 400 - 600\,°C$ and $T = 400 - 650\,°C$, respectively. The stress amplitudes and the mean stresses were calculated from the stresses at the maximum and minimum cycle temperature. In some tests, the maximum stress is reached in the high temperature part of the TMF cycle at a temperature lower than the maximum temperature. However, for the conditions represented in Figure 7, the difference between the stress at maximum temperature and the maximum stress is negligible.

IP loading gives rise to a negative (compressive) mean stress (Figure 7). It was found that IP and OP tests lead to stress-plastic strain hysteresis loops which are symmetrical to each other with respect to the origin of the coordinate system. Consequently, a positive mean stress was found under OP conditions. If the maximum cycle temperature T_{max} does not exceed 600°C (Figure 7a), initial cyclic softening occurs which is followed by a (approximate) state of cyclic saturation. Irrespective of the microstructure, the absolute value of the mean stress shows a continuous increase until failure. It is important to note that for $T_{max} \leq 600°C$ the stresses at minimum and maximum cycle temperature of a TMF loop are identical to those of the corresponding isothermal tests (see Figure 3 for comparison; the maximum and minimum stresses of the TMF cycle can easily be calculated from the stress amplitude and the mean stress plotted in Figure 7). In other words,

the thermo-mechanical stress-strain behavior is determined by the immediately acting temperature in the same way as the isothermal one. Hence, a quantitative prediction of TMF hysteresis loops based upon the behavior under isothermal conditions is possible in this temperature regime [*15*].

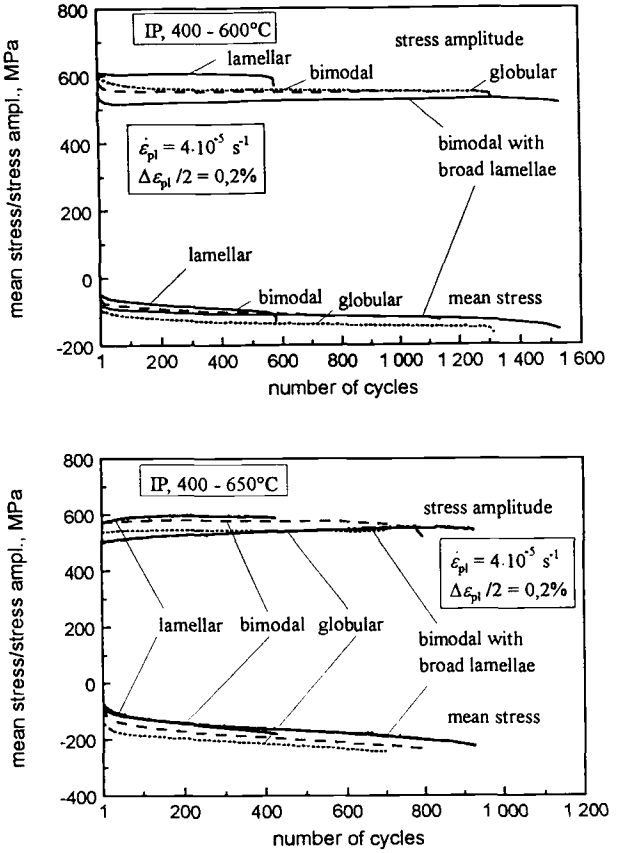

Figure 7 — *Cyclic Deformation Curves of IP TMF Tests in Air at Temperature Intervals of a) 400°C to 600°C and b) 400°C to 650°C.*

If the maximum temperature is increased to 650°C, shorter life and significant higher mean stresses (absolute value) result (Figure 7b). Furthermore, no initial softening but slight continuous cyclic hardening occurs. Again, the cyclic life of the lamellar microstructure is shortest, while the three other microstructures (bimodal, globular and bimodal with broad lamellae) exhibit similar life in agreement with the observations obtained from isothermal tests.

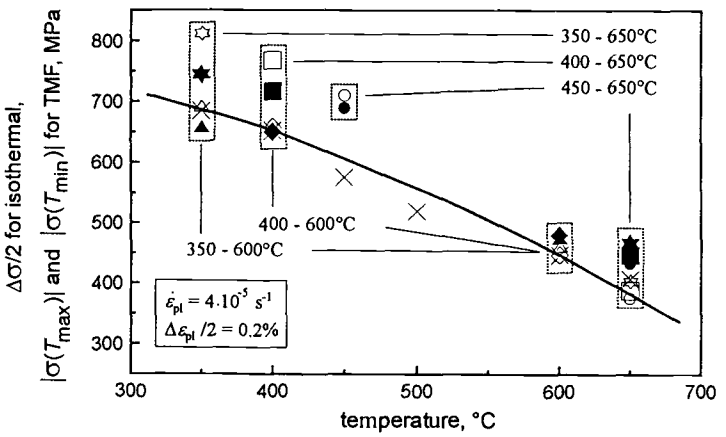

Figure 8 — *Comparison of the Stress Amplitudes of Isothermal Fatigue Tests with the Absolute Values of Stress at Minimum and Maximum Temperature of TMF Tests. Full Symbols Correspond to OP Tests, Open Symbols to IP, and X to Isothermal Conditions (All Test Performed in Air on Bimodal Microstructure).*

Figure 8 tries to illustrate the effect of the maximum cycle temperature on the stress-strain response for the example of the bimodal microstructure. For the isothermal tests, the stress amplitude measured at half life is plotted against the temperature as a solid reference line. The absolute values of the stresses at minimum and maximum temperature (at half life) of the TMF tests are plotted as symbols. Full symbols refer to OP loading and open symbols to IP loading. Figure 8 confirms the statement given above that the corresponding stress values of isothermal and thermo-mechanical fatigue loading coincide, if the maximum cycle temperature of TMF does not exceed 600°C However, in TMF tests with a maximum cycle temperature of 650°C, significant differences are appreciable. It is remarkable, that in particular at the minimum temperature higher stresses than in isothermal tests are found. It will be shown later that this stress increase can be explained by the dislocation arrangement formed under TMF conditions with T_{max} = 650°C, since this arrangement affects significantly the stress-strain response in the low-temperature part of the TMF cycle.

In Table 1 the numbers of cycles to failure for IP and OP tests run on the bimodal microstructure at a plastic strain amplitude of 0.2% are listed. Under all test conditions and irrespective of the microstructure, OP loading was found to be more detrimental than IP testing. Furthermore, a comparison of Table 1 with the corresponding isothermal data listed in Table 2 documents, that the fatigue lives obtained under OP conditions are significantly lower than those observed in isothermal tests even if the maximum temperature of the TMF cycle is considered. The cylic lifetime in vacuum under isothermal conditions is also listed in Table 2. It should be noted that a direct comparison is not possible, since the isothermal tests under vacuum have been performed at a much higher frequency (time per cycle: 10 s). Nevertheless, the important influence of environmental effects is illustrated.

Environmental Effects — Additional TMF tests were carried out in high vacuum keeping the test parameters identical to those used for the tests in laboratory air, in order to characterize the effects of environment on deformation behavior and fatigue life. In Figures 9a and b some results obtained in air and vacuum are compared. As expected, the stress-strain response is not affected by the environment. The only significant change arising from testing in vacuum is a strongly extended life. For the TMF temperature range of 400°C-600°C (Figure 9a) fatigue life is five times longer in vacuum than in air. If the maximum temperature is increased to 650°C (Figure 9b), the corresponding factor is three. It should be emphasized that the ratio of the numbers of cycles to fracture of OP and IP TMF tests is not significantly changed by the environment. Therefore, the more detrimental effect of OP TMF as compared with IP loading may not be attributed solely to stronger damage caused by the embrittled subsurface zone under OP conditions.

Table 1 — *Number of Cycles to Failure for TMF Tests on Bimodal Microstructure at a Plastic Strain Amplitude of 0.2% in Air.*

Temperature [°C]	350-600	350-650	400-600	400-650	450-650
N_f (in-phase)	1100	620	1162	800	950
N_f (out-of-phase)	570	285	482	317	320

Table 2 — *Number of Cycles to Failure for Isothermal Tests on Bimodal Microstructure at a Plastic Strain Amplitude of 0.2% in Air and in Vacuum.*

Temperature [°C]	350	400	450	600	650
N_f (air)	1566	1420	1472	850	685
N_f (vacuum)	—	4927	—	6615	—

Microstructural Changes — TEM studies of the microstructure formed during TMF testing revealed that despite the large differences in cyclic life very similar dislocation arrangements were observed after IP and OP loading. The maximum temperature of the TMF cycle applied seems to be the decisive parameter and can be considered to be responsible for a microstructure development which is identical to the one taking place in the corresponding isothermal test.

If the TMF test is carried out at a temperature range of 400°C-600°C, a microstructure evolves resembling that formed during isothermal cycling at 400°C or 600°C. As shown in Figure 10a for the example of the bimodal microstructure, planar slip bands exist within the primary α-grains (see Figure 5a for comparison). Similarly to samples cyclically deformed at 600°C, in the lamellar regions small silicides decorate the lamella boundaries and a beginning of disintegration of these boundaries is appreciable. By contrast, a different microstructure results, if the TMF tests are conducted with a maximum cycle temperature of 650°C. In both, the primary α-grains (Figure 10b) and the lamellar regions the dislocation density is relatively high. Furthermore, the lamella boundaries have almost completely disappeared, but their initial positions are marked by the silicides

precipitated there. In addition, Figure 10b documents that in the primary α-grains areas with different orientations exist (orientation contrast). This indicates a beginning subgrain formation as a result of wavy dislocation slip.

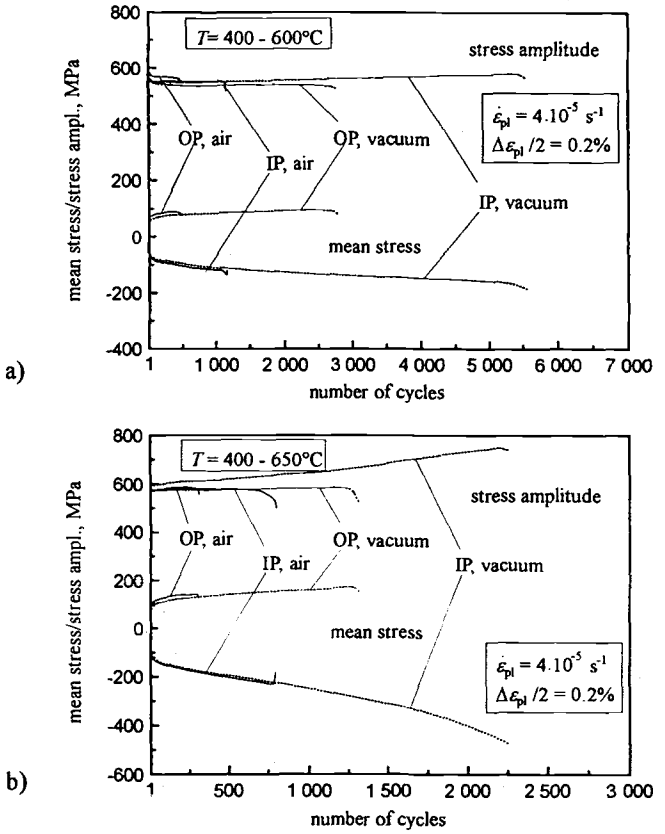

Figure 9 — *Cyclic Stress Response of TMF Tests Performed on Bimodal Specimens in Air and Vacuum, Respectively. a) T = 400°C-600°C, b) T = 400°C-650°C.*

SEM studies of the surface within the gage length of bimodal samples which failed under TMF conditions *in air* revealed that IP loading leads to more, but smaller cracks than OP loading. In contrast to the observations on isothermally cycled specimens, most cracks do not nucleate within the primary α-grains. Rather, these grains seem to act as obstacles to fatigue crack growth.

However, the crack initiation site during TMF testing *in vacuum* was found to be very similar to that of the isothermal experiments. The planar slip bands within the primary α-grains are responsible for crack formation and crack initiation as well as initial crack growth seems to be only slightly affected by the plastic strain/temperature phasing.

More details on crack initiation and propagation and an interpretation of the respective observations are given in separate papers [*16,17*]

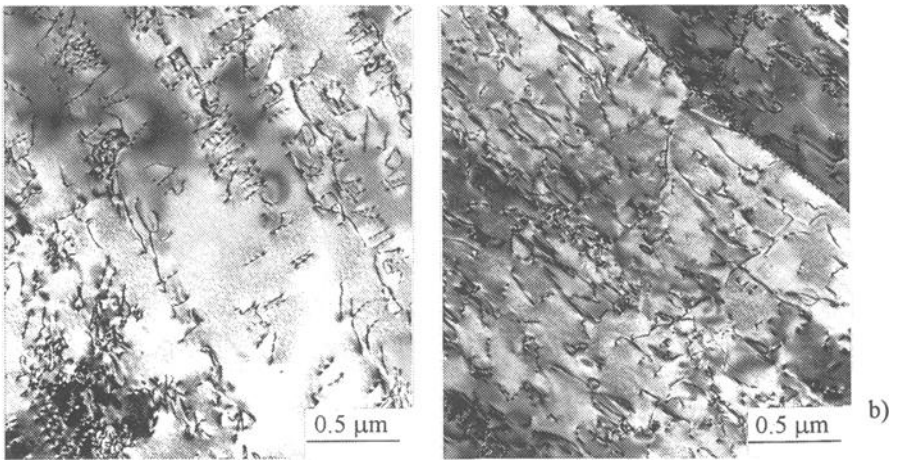

Figure 10 — *TEM Micrographs of Primary α-Grains in Bimodal Samples after TMF at* $\Delta\varepsilon_{pl}/2 = 0.2\%$ *and* $T = 400°C$-$600°C$ *(a) and* $T = 400°C$-$650°C$ *(b);* $g = (10\bar{1}1)$.

Discussion

In this chapter, first the behavior under isothermal conditions will be discussed, since this forms the basis for an understanding of the findings obtained in the study of TMF. As described above, stress response and cyclic lifetime are strongly affected by test temperature (e.g. Figure 3). TEM revealed that three main effects take place in the microstructure and govern the stress-strain response: (i) the formation of planar slip bands, (ii) the coarsening of silicides, and (iii) the disintegration of lamella boundaries.

At temperatures up to 600°C, initial cyclic softening can be attributed to the formation of planar slip bands within the primary α-grains [*18*]. The planarity of slip results from a large difference between the critical resolved shear stress (CRSS) of prismatic slip and the CRSS of basal and pyramidal slip [*11,19*], respectively. In addition, the presence of shearable Ti_3Al promotes the formation of planar slip bands [*18*]. However, if the test temperature exceeds 600°C, the differences in the CRSS of the different slip systems diminishes and dislocation slip changes from planar to wavy. As a result, subgrains start to form within primary α-grains.

At temperatures above 500°C, coarsening of silicides associated with the depletion of silicon in the lamellar matrix [*20,21*] leads to a continuous reduction of the stress amplitude, mainly because of the loss of solid-solution strengthening by Si. Furthermore, the lamellar boundaries start to disintegrate with increasing test temperature (*c.f.* Figure 5c and Figure 6). No direct evidence of dynamic strain aging (DSA) was observed. However, the small difference in the stress amplitudes at 350°C and 400°C indicates that DSA processes take place. Similar results are reported by Neal [*2*], who ob-

served that the stress strain behavior of IMI 834 in the temperature range from 200 to 400°C is only slightly affected by the test temperature. DSA can be considered to result from an interaction between silicon atoms in solid-solution and dislocations [*22*]. Thus, as a consequence of the silicide formation which partially takes place already during the aging pre-treatment of the fatigue specimens, the DSA effect must be expected to be small.

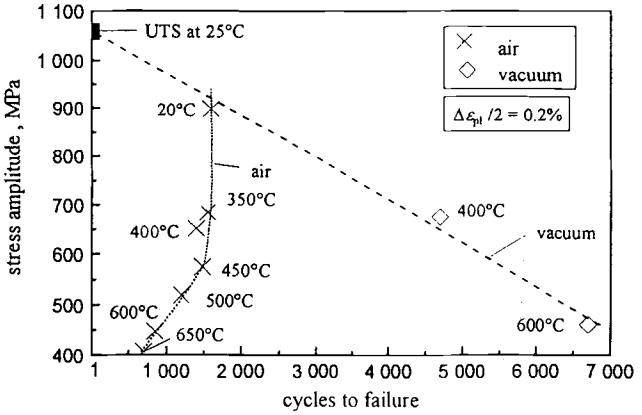

Figure 11 — *Stress Amplitude at $\Delta\varepsilon_{pl}/2$ = 0.2% Plotted versus Cyclic Life for Bimodal Specimens, Isothermally Fatigued at Various Temperatures in Air and Vacuum, Respectively.*

The strong influence of the environment (air/vacuum) on cyclic life is illustrated in Figure 11 representing the stress amplitude (at half life) as a function of N_f. The interaction of the alloy during cycling with the surrounding air leads to a reduction of N_f with increasing temperature, despite the decreasing stress amplitude. In vacuum, however, $\Delta\sigma/2$ (or a corresponding magnitude strongly depending on $\Delta\sigma/2$) seems to be the main life-determining factor. As a first approximation, a straight dashed line is plotted in Figure 11 to describe the tendency of the results of the isothermal tests in vacuum. The ultimate tensile strength (UTS) is used as the stress amplitude of a fatigue test at ambient temperature with $N_f = ¼$.

The observed environmental damage results from the formation of an embrittled subsurface layer. Figure 12 shows the results of hardness measurements on bimodal samples, aged for 100 hours at 550°C, 600°C and 700°C, respectively. The hardness increase in the vicinity of the surface is caused by an inward diffusion of solved oxygen which hardens and stabilizes the α-phase [*23*]. Note that the hardness is roughly proportional to the square root of the oxygen concentration [*24*].

The comparison of the different microstructures (see Figure 4) documents that both, the existence of primary α-grains and the lamella spacing affect the cyclic strength. Since the globular microstructure did not undergo the aging treatment and a texture was observed that is considered to be soft [*25*], this condition may not directly be compared with the three other microstructures. It is known that as a consequence of the alloy partitioning effect the static strength of the lamellar matrix of a bimodal microstructure is lower than that of a fully lamellar microstructure [*14, 26*]. This explains the lower stress

amplitude of both bimodal microstructures in comparison to the lamellar one. Furthermore, the mechanical properties of the lamellar matrix, such as tensile and creep strength or ductility, generally deteriorate with increasing lamella spacing [*6,27*]. Hence, the bimodal condition with broad lamellae showed the poorest fatigue resistance.

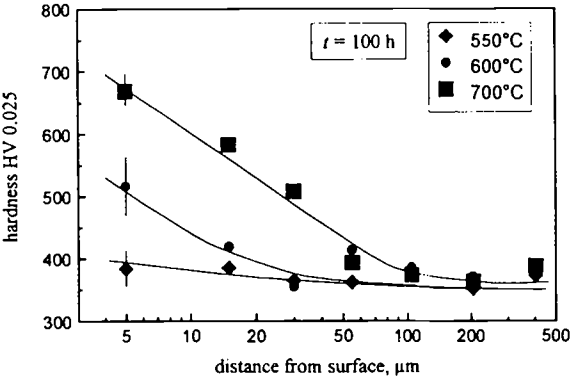

Figure 12 — *Hardness as a Function of Distance from Surface for Bimodal Samples, Aged for 100 Hours in Air at Different Temperatures.*

Cyclic life, however, is strongly affected by the grain size, since both crack initiation and short crack propagation are slower in fine-grained material [*28-30*]. Therefore, similar numbers of cycles to failure were observed for the two bimodal microstructures, whereas the lamellar condition shows significant shorter life as a consequence of its large grain size of greater than 0.5mm.

The behavior under TMF conditions can be discussed on the basis of the isothermal observations. If the temperature does not exceed 600°C, similar microstructures form during isothermal cycling and TMF. This is possible, since no basic change in the dislocation arrangement occurs up to 600°C. Hence, the stress-strain relationship in a TMF hysteresis loop is predictable based upon corresponding isothermal results [*15*].

However, if the maximum temperature of the TMF cycle is increased to 650°C, a microstructure is formed which resembles that found after isothermal cycling at this temperature. Specific tests were devised, in which temperature cycling was interrupted, the temperature was hold constant at the minimum or the maximum temperature, and plastic strain cycling was continued. These tests showed that the dislocation arrangement of the TMF test is relatively stable during subsequent isothermal cycles. Furthermore, the stress amplitude observed for the isothermal part of this test at 400°C (minimum temperature of TMF cycle) was found to be strongly increased [*10*]. Hence, it can be concluded that the more wavy dislocation arrangement developed in TMF tests with T_{max} = 650°C provide an enhanced deformation resistance in the temperature range of planar dislocation glide. This observation is in agreement with the results depicted in Figure 8.

Although IP and OP loading lead to similar microstructures, OP testing was found to be more damaging than IP testing. In the OP tests, high tensile stresses build up during the low-temperature part of the cycle. Consequently, a positive (tensile) mean stress arises, and fatigue cracks initiation and propagation is expected to be faster than under IP

conditions.

Figure 13 shows a representation of the maximum of the absolute stress of TMF tests performed in air as a function of the number of cycles to failure. For each testing mode (IP and OP) the symbols approximately form a straight descending line. Data points which refer to the same value of T_{max} are encircled. Obviously, the TMF life decreases if the magnitude of the maximum stress increases. More interesting is the fact that open and full symbols (IP and OP loading) form clearly discernible groups indicating the important role of the sign of the data plotted.

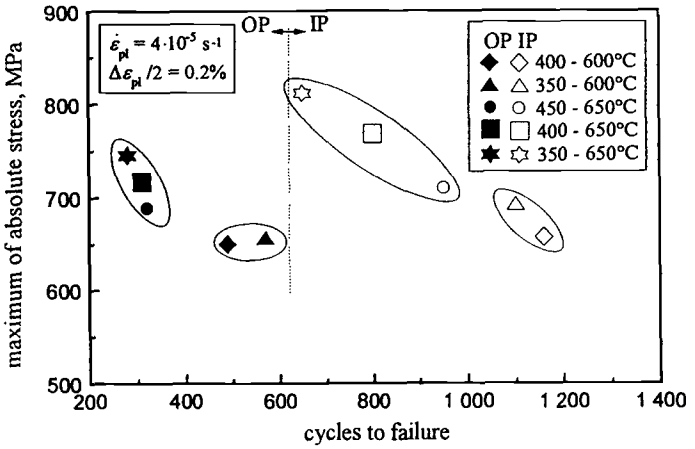

Figure 13 — *The Maximum of the Absolute Values of Stress within a TMF Cycle Plotted against the Cyclic Life (Bimodal, Air).*

It has been mentioned that the site of crack initiation depends in a complex way on the test conditions applied. In most of the isothermal cases, cracks are formed at the planar slip bands of the primary α-grains (in agreement with [*31,32*]). Interestingly enough, these sites seem not to be preferential during TMF testing in air. That means the superimposed temperature cycling changes the crack initiation mechanism. This change can be considered an environmental effect, since TMF in vacuum shows again cracks formed in primary α-grains.

Conclusions

The main results of this study on the isothermal and thermo-mechanical fatigue behavior of the high-temperature titanium alloy IMI 834 can be summarized as follows:

- The isothermal cyclic deformation behavior of IMI 834 is determined by planar dislocation slip at temperatures lower than 600°C. At higher temperatures the slip becomes more wavy, silicides coarsen and the lamella boundaries disintegrate.
- The bimodal microstructure combines high cyclic strength with long cyclic life.
- The reduction of fatigue life with increasing temperature is mainly a consequence of oxidation which leads to an embrittled subsurface zone.

- The deformation behavior under TMF conditions can be understood and predicted solely based on the isothermal observations, if the maximum temperature does not exceed 600°C.
- Higher maximum cycle temperature leads to a change in the dislocation slip character giving rise to an increased stress at low temperatures as compared to isothermal conditions.
- The phasing between plastic strain and temperature under TMF conditions strongly affects fatigue life. In out-of-phase tests generally a lower number of cycles to fracture was observed than in in-phase tests. This can mainly be attributed to the presence of a positive (tensile) mean stress under out-of-phase conditions.
- Different damage mechanisms apply to isothermal and TMF conditions. An assessment of the fatigue life under TMF conditions from data obtained in isothermal tests at the maximum temperature leads to a nonconservative prediction for out-of-phase TMF conditions.

Acknowledgment
Financial support by Deutsche Forschungsgemeinschaft is gratefully acknowledged.

References

[1] Neal, D. F., "Optimization of Creep and Fatigue Resistance in High Temperature Titanium Alloys IMI 829 and IMI 834," *Titanium Science and Technology*, G. Lütjering, U. Zwicker, and W. Bunk, Eds, Deutsche Gesellschaft für Metallkunde e. V., Oberursel, Germany, 1985, pp. 2419-2424.

[2] Neal, D. F., "Development and Evaluation of High Temperature Titanium Alloy IMI 834," *Sixth World Conference on Titanium*, P. Lacombe, R. Tricot, and G. Béranger, Eds, Société Française de Métallurgie, Les édition de physique, Les Ulis, Cedex, 1988, pp. 253-258.

[3] Miller, D. A., and Priest, R. H., "Materials Response to Thermal-Mechanical Strain Cycling," *High Temperature Fatigue, Properties and Prediction*, R. P. Skelton, Ed., Elsevier Applied Science Publishers Ltd, London, New York, 1987, pp. 113-175.

[4] Maier, H. J., "High-Temperature Fatigue of Titanium Alloys," *Materials at High Temperature*, Vol. 15, 1998, pp. 3-14.

[5] Dai, J., Marchand, M. J., and Hongoh, M., "Thermal Mechanical Fatigue Crack Growth in Titanium Alloys: Experiments and Modelling," *Thermomechanical Fatigue of Materials: Second Volume, ASTM STP 1263*, M. J. Verrilli, and M. G. Castelli, Eds, American Society for Testing and Materials, Philadelphia, 1996, pp. 187-209.

[6] Borchert, B., and Daeubler, M. A., "Influence of Microstructure of IMI 834 on Mechanical Properties Relevant to Jet Engines," *Sixth World Conference on Titanium*, P. Lacombe, R. Tricot, and G. Béranger, Eds, Société Française de Métallurgie, Les éditions de physiques, Les Ulis Cedex, 1988, pp. 467-472.

[7] Renner, H., Kestler, H., and Mughrabi, H., "Influence of Heat Treatment and Microstructure on the Low Cycle Fatigue Properties of the Hot Forged Near-α Titanium Alloy IMI 834," *Fatigue '96*, G. Lütjering, and H. Nowack, Eds, Elsevier Applied Science, London, 1996, pp. 935-940.

[8] Christ, H.-J., Mughrabi, H., Kraft, S., Petry, F., Zauter, R., and Eckert, K., "The Use of Plastic Strain Control in Thermomechanical Fatigue Testing," *Fatigue under Thermal and Mechanical Loading-Mechanisms, Mechanics and Modelling*, J. Bressers, and L. Remy, Eds, Kluwer Academic Publishers, Dordrecht, The Netherlands, 1996, pp. 1-14.

[9] Sommer C., Christ H.-J., and Mughrabi H., "Non-linear Elastic Behaviour of the Roller Bearing Steel SAE 52100 During Cyclic Loading," *Acta Metall. et Mater.*, Vol. 39, 1991, pp. 1177-1187

[10] Pototzky, P., Maier, H. J., and Christ, H.-J, "Thermomechanical Fatigue Behavior of the High Temperature Titanium Alloy IMI 834," *Metall. Mater. Trans. A*, Vol. 29A, 1998, pp 2995-3004.

[11] Gysler, A., and Weissmann, S., "Effect of Order in Ti_3Al Particles and of the Temperature on the Deformation of Age-hardened Ti-Al Alloys," *Mater. Science and Engng A*, Vol. 27, 1977, pp. 181-193.

[12] Lütjering, G., and Weissmann, S., "Mechanical Properties of Age-Hardened Titanium-Aluminum Alloys," *Acta Metall.*, Vol. 18, 1970, pp. 785-795.

[13] Blackburn, M. J., "The Ordering Transformation in Titanium-Aluminium Alloys Containing up to 25 at.% Aluminium," Trans. of the Metall. Soc. AIME, Vol. 239, 1967, pp. 1200-1208.

[14] Neal, D. F., "Alloy Development," *Titanium '95: Science and Technology*, P. A. Blenkinsop, W. J. Evans, and H. M. Flower, Eds, The Institute of Materials, London, 1996, pp. 2195-2204.

[15] Maier, H. J., and Christ, H.-J., "Modeling of Cyclic Stress-Strain Behavior and Damage Mechanisms under Thermomechanical Fatigue Conditions," *Intern. J. Fatigue*, Vol. 19, 1998, pp. S267-S274.

[16] Hardt, S., Maier, H. J., and Christ, H.-J., "High-Temperature Fatigue Damage Mechanisms in Near-α Titanium Alloy IMI 834," *Intern. J. Fatigue*, in print.

[17] Maier, H. J., Teteruk, R. G., and Christ, H.-J., "Modeling Thermomechanical Fatigue Life of High-Temperature Titanium Alloy IMI 834," submitted to *Metallurgical and Materials Transactions A*.

[18] Bania, P. J., and Antolovich, S. D., "The High Temperature Low Cycle Fatigue Behavior of a Near Alpha Titanium Alloy," *Titanium Science and Technology*, G. Lütjering, U. Zwicker, and W. Bunk, Eds, Deutsche Gesellschaft für Metallkunde e. V., Oberursel, Germany, 1985, pp. 2305-2312.

[19] Bowen, A. W., "The Preference for <11-20> Slip in Alpha-based Titanium Alloys," *Sixth World Conference on Titanium*, P. Lacombe, R. Tricot, and G. Béranger, Eds, Société Française de Métallurgie, Les éditions de physiques, Les Ulis Cedex, 1988, pp. 93-98.

[20] Donlon, W. T., Allison, J. E., and Lasecki, J. V., "The Influence of Thermal Exposure on Properties and Microstructure of Elevated Temperature Titanium Alloys," *Titanium '92, Science and Technology*, F. H. Froes, and I. Caplan, Eds, TMS, Warrendale, PA, 1993, pp. 295-302.

[21] Cope, M. T., and Hill, M. J, "The Influence of Ageing on the Mechanical Properties of IMI 834," *Sixth World Conference on Titanium*, P. Lacombe, R. Tricot, and G. Béranger, Eds, Société Française de Métallurgie, Les éditions de physiques, Les Ulis Cedex, 1988, pp. 153-158.

[22] Madsen, A., and Ghonem, H. "Effects of Aging on the Tensile and Fatigue Behavior of the Near-α Ti-1100 at Room Temperature and 593°C," *Mater. Science and Engng A*, Vol. 177, 1994, pp. 63-73.

[23] Leyens, C., Peters, M., and Kaysser, W. A., "Oxidation Behaviour of Near-α Titanium Alloys and their Protection by Coatings," *Titanium '95: Science and Technology*, P. A. Blenkinsop, W. J. Evans, and H. M. Flower, Eds, The Institute of Materials, London, 1996, pp. 1935-1942.

[24] Liu, Z., and Welsch, G., "Effects of Oxygen and Heat Treatment on the Mechanical Properties of Alpha and Beta Titanium Alloys," *Metall. Trans. A*, Vol. 19A, 1988, pp. 527-542.

[25] Polmear, I. J., *Light Alloys*, Edward Arnold, second edition, London, 1989.

[26] Andres, C., Gysler, A., and Lütjering, G, "Correlation Between Microstructure and Creep Behavior of the High-Temperature Ti Alloy IMI 834," *Z. Metallkde*, Vol. 88, 1997, pp. 197-203.

[27] Andres, C., Gysler, A., and Lütjering, G, "Correlation Between Microstructure and Creep Behavior of the High-Temperature Ti-Alloy IMI 834," *Titanium '92, Science and Technology*, F. H. Froes, and I. Caplan, Eds, TMS, Warrendale, PA, 1993, pp. 311-318.

[28] Lütjering, G., and Gysler, A., "Fatigue," *Titanium Science and Technology*, G. Lütjering, U. Zwicker, and W. Bunk, Eds, Deutsche Gesellschaft für Metallkunde e. V., Oberursel, Germany, 1985, pp. 2065-2083.

[29] Lütjering, G., Gysler, A., and Wagner, L: "Crack Propagation in Ti-Alloys," *Sixth World Conference on Titanium*, P. Lacombe, R. Tricot, and G. Béranger, Eds, Société Française de Métallurgie, Les éditions de physiques, Les Ulis Cedex, 1988, pp. 71-80.

[30] Torster, F., Gysler, A., and Lütjering, G., "Effect of Microstructure and Test Temperature on Fatigue Properties of IMI 834," *Titanium '95: Science and Technology*, P.A. Blenkinsop, W. J. Evans, and H. M. Flower, Eds, The Institute of Materials, London, 1996, pp. 1395-1402.

[31] Dowson, A. L., Hollis, A. C., and Beevers, C. J., "The Effect of the Alpha-Phase Volume Fraction and Stress Ratio on the Fatigue Crack Growth Characteristics of the Near-Alpha IMI 834 Ti Alloy," *Intern. J. Fatigue*, Vol. 14, 1992, pp. 261-270.

[32] Woodfield, A. P., Postans, P. J., Loretto, M. H., and Smallman, R. E., "The Effect of Long-Term High Temperature Exposure on the Structure and Properties of the Titanium Alloy Ti5331S," *Acta Metall.*, Vol. 36, 1988, pp. 507-515.

Bernd Kleinpass,[1] Karl-Heinz Lang,[2] Detlef Löhe,[3] and Eckard Macherauch[4]

Influence of the Mechanical Strain Amplitude on the In-Phase and Out-of-Phase Thermo-mechanical Fatigue Behaviour of NiCr22Co12Mo9

Reference: Kleinpass, B., Lang, K.-H., Löhe, D., and Macherauch, R., **"Influence of the Mechanical Strain Amplitude on the In-Phase and Out-of Phase Thermo-mechanical Fatigue Behaviour of NiCr22Co12Mo9,"** *Thermo-mechanical Fatigue Behavior of Materials: Third Volume, ASTM STP 1371,* H. Sehitoglu and H. J. Maier, Eds., American Society for Testing and Materials, West Conshohocken, PA, 2000.

Abstract: In total strain controlled in-phase and out-of-phase thermo-mechanical fatigue (TMF) tests on NiCr22Co12Mo9 (Inconel 617, Nicrofer 5520 Co) with a maximum temperature of 1123 K, a minimum temperature of 473 K and different mechanical strain amplitudes the cyclic stress-strain response, the change of the microstructure and the development of damage were analysed. The initial values of the induced stress amplitudes and plastic strain amplitudes, and the amount of cyclic hardening increase with the total mechanical strain amplitude. The observed cyclic hardening results from strong dislocation-dislocation and dislocation-particle interactions during plastic deformation at lower temperatures the latter being enhanced by the precipitation of small semi-coherent carbides at elevated temperatures of the TMF cycles. For each type of TMF tests the lifetime behaviour can be adequately described by the combination of the relationships of Basquin and Coffin-Manson. At equal total mechanical strain amplitudes in-phase tests always yield smaller lifetimes than out-of-phase tests. The difference between the two types of TMF-tests rises with increasing lifetime. This behaviour is caused by different accumulation of creep damage which is favoured by tensile stresses at high temperatures.

Keywords: nickel-base superalloy, thermo-mechanical fatigue, cyclic deformation behaviour, damage development, lifetime behaviour

[1]Dr.-Ing, Linde AG, Seitner Str. 70, D-82049 Höllriegelskreuth, Germany
[2]Dr.-Ing, Institut für Werkstoffkunde I, Universität Karlsruhe (TH), Postfach 6980, D-76128 Karlsruhe, Germany
[3]Prof. Dr.-Ing, Institut für Werkstoffkunde I, Universität Karlsruhe (TH), Postfach 6980, D-76128 Karlsruhe, Germany
[4]Prof. Dr.rer.nat Dr.-Ing. E.h.mult., Institut für Werkstoffkunde I, Universität Karlsruhe (TH), Postfach 6980, D-76128 Karlsruhe, Germany

Introduction

In components operating at high temperatures, transient temperature fields producing complex strain and stress fields are induced by start-ups, load changes and shut downs. As the sequence of these operation phases is repeated during service life it may cause thermo-mechanical fatigue (TMF) damage in the component and possibly failure of an entire system. The combustion chamber of gas turbines is a typical component whose lifetime is often limited by damage resulting from TMF loadings [*1,2*]. Frequently, data from isothermal strain controlled fatigue tests are used to predict the deformation behaviour and the lifetime of components exposed to TMF [*3*]. This procedure, however, involves considerable uncertainties; especially, if the development of the cyclic stress-strain response and the microstructure during isothermal and thermo-mechanical fatigue are different. In the present study, the TMF behaviour of the solid solution and carbide precipitation hardened nickel-base superalloy NiCr22Co12Mo9 which is commonly used as sheet material in gas turbines for power generation, is investigated. The deformation and lifetime behaviour as well as the development of the microstructure and the damage due to in-phase and out-of-phase TMF with different total mechanical strain amplitudes are analysed.

Material

The chemical composition of the nickel-base alloy NiCr22Co12Mo9 investigated (trade names Nicrofer 5520 Co and IN 617, respectively) was 0.069 C, 21.9 Cr, 11.65 Co, 8.75 Mo, 1.15 Al, 0.74 Fe, 0.46 Ti, balance Ni (all quantities in wt.-%). Hot rolled round bars with a diameter of 20 mm were annealed at 1475 K and water quenched. Solid round specimens were machined with a cylindrical gauge length of 10 mm, a gauge diameter of 7 mm and conical gripping heads. Within the gauge length the specimens were polished by hand with emery paper. The microstructure of the material consisted of twinned grains with a low dislocation density, incoherent M_6C carbides and Ti(C,N) carbonitrides in the interior and, more frequently at the boundaries of the grains [*4*]. The mean grain size was 160 μm.

Experimental Details

The mechanical loading was applied by a closed loop servohydraulic testing machine with a 63 kN capacity. Strain measurements were performed with a capacitive extenso-meter. For heating, an induction generator was used. Cooling was mainly achieved by thermal conduction into the specimen grips and could be forced by blowing compressed air on the specimens through a proportionally controlled valve. The temperature was measured and controlled with a Ni-CrNi thermocouple spot welded in the middle of the gauge length. Figure 1 illustrates the triangular temperature-time as well as strain-time courses chosen and the resulting stress-time course. The specimens are allowed to expand and contract at zero

stress during the initial heating from ambient temperature and during the first few thermal cycles, with the closed loop control operating at stress control. After this period, upon reaching the mean temperature T_m, the controller is switched over from stress to total strain control and the first thermo-mechanical cycle starts with heating up the specimen to T_{max}. The closed loop system allows the thermal strain-time course, $\varepsilon^{th}(t)$, which is accurately known from the first pure thermal cycles, to be superimposed by a chosen mechanical strain-time course $\varepsilon^{me}(t)$. In-phase (middle part of Fig. 1) and out-of-phase (lower part of Fig. 1) relations between temperature and mechanical strain ε^{me} were realized. During in-phase TMF, tensile stresses occur at high temperatures and compressive stresses at low temperatures, whereas during out-of-phase TMF stresses the contrary is true. The maximum cycle temperature, T_{max}, was 1123 K and the minimum cycle temperature, T_{min}, was 473 K in all tests. The total mechanical strain amplitude was varied between 0.15 % and 1.0 %. The temperature rate dT/dt was 14 K/s, resulting in a cycle period of about 93s.

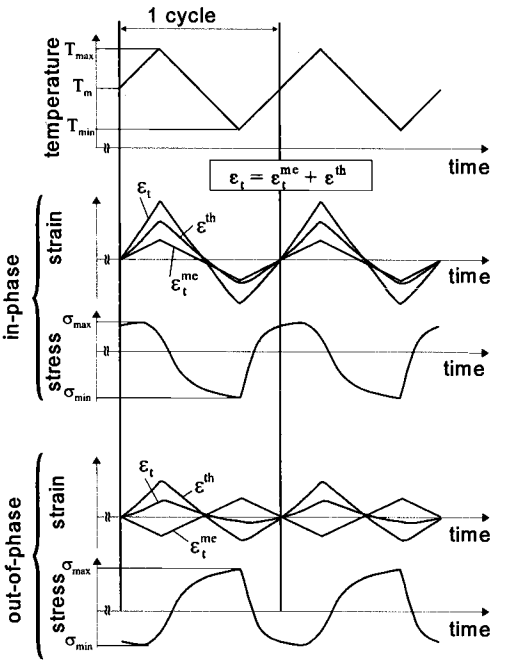

Figure 1 - *Temperature, strains and stresses during in-phase and out-of-phase thermal-mechanical fatigue loading as a function of time (schematicaly)*

Experimental Results

Hysteresis Loops

Figure 2 shows the influence of the total strain amplitude on the stress-mechanical strain hysteresis loops obtained at $N = N_f/2$ during in-phase and out-of-phase loading, respectively. The arrows indicate the circulation direction starting at the minimum temperature T_{min}. At $\varepsilon_{a,t}^{me} = 0.15$ % the absolute values of the stress increase continuously in the tensile as well as in the compressive range up to the maximum of the mechanical total

strain. However, at $\varepsilon^{me}_{a,t} \geq 0.25$ % stress relaxation occurs during heating up under both loading conditions. With growing total strain amplitudes the onset of stress relaxation appears at higher stresses, but smaller temperatures and the amount of the relaxation increases. Hence, the maximum stresses during in-phase and the minimum stresses during out-of-phase loading appear at temperatures which depend on the mechanical strain amplitude. Regarding in-phase and out-of-phase loops obtained from a given mechanical strain amplitude, they are more or less mirrored at the origin of the stress-mechanical strain ordinates. However, the measured mean stresses are negative regarding in-phase loading and positive with respect to out-of-phase loading.

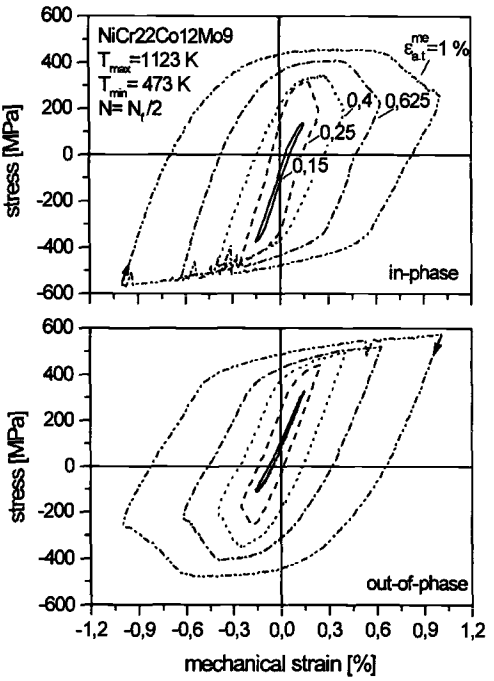

Figure 2 - *Mechanical strain hysteresis loops at N/2 for different $\varepsilon^{me}_{a,t}$ at in-phase and out-of-phase loading*

Cyclic Deformation Behaviour

In Fig. 3 the development of the stress amplitude σ_a and the mean stress σ_m evaluated from the peak values within the cycles as well as the plastic strain amplitude $\varepsilon^{me}_{a,p}$ during in-phase and out-of-phase loading, respectively, at different total strain amplitudes is given. At $\varepsilon^{me}_{a,t} > 0.15$ % the stress amplitude increases continuously with the number of cycles up to the macro-crack formation indicating cyclic hardening. For example σ_a increases from 300 MPa to 540 MPa during out-of-phase loading at $\varepsilon^{me}_{a,t} = 1.0$ %. Furthermore, cyclic hardening continuously reduces the plastic strain amplitudes, as can be seen at the bottom of the figure. Only at $\varepsilon^{me}_{a,t} = 0.15$ % during in-phase loading the maximum stresses and during out-of-phase loading the absolute values of the minimum stresses decrease with an increasing number of cycles. This is a consequence of the cyclic shift of the hysteresis loops to larger compressive (in-phase loading) or tensile (out-of-phase loading) stresses, which also result in the formation of compressive and tensile mean stresses, respectively, as shown in the upper diagrams in Fig. 3. The ratio σ_m/σ_a decreases strongly with increasing $\varepsilon^{me}_{a,t}$ values. Thereby, only at $\varepsilon^{me}_{a,t} = 0.15$ % do the mean stresses exceed 100 MPa.

As shown in Fig. 4 for total mechanical strain amplitudes of 0.15, 0.4 and 1.0 %, the development of the stress and plastic strain amplitudes during in-phase and out-of-phase

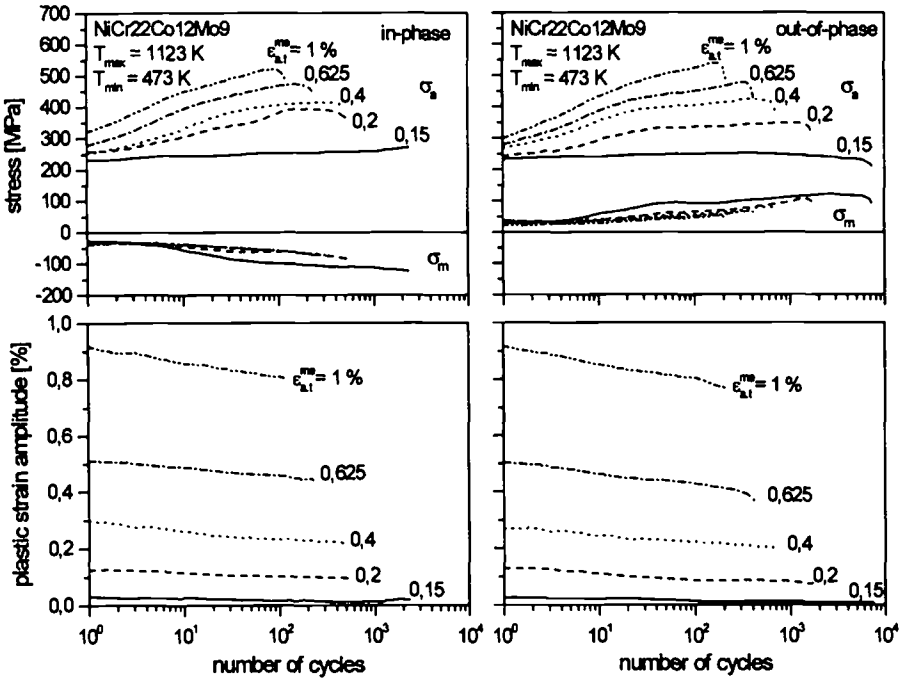

Figure 3 - *Development of the stress amplitude and the mean stress as well as the plastic strain amplitude for different $\varepsilon^{me}_{a,t}$ during in-phase and out-of-phase loading*

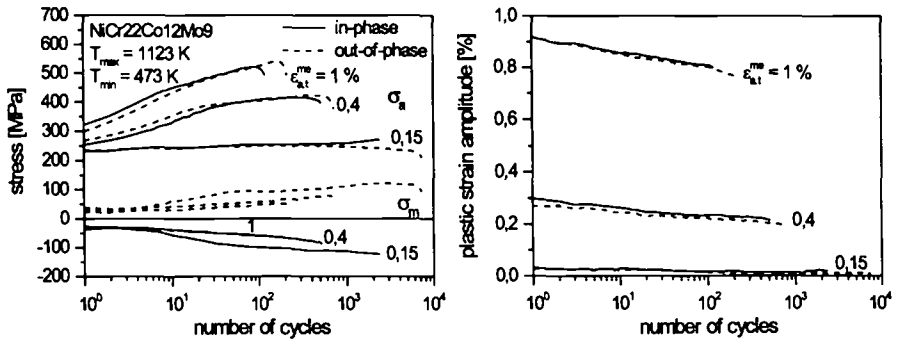

Figure 4 - *Development of σ_a and σ_m as well as $\varepsilon_{a,p}$ for different $\varepsilon^{me}_{a,t}$ during in-phase and out-of-phase loading*

TMF is almost perfectly the same. Again, it becomes visible that compressive mean stresses are formed during in-phase TMF and tensile ones during out-of-phase TMF. The absolute values of the mean stresses measured at a given mechanical strain amplitude and a given number of cycles do hardly depend on the phase relationship between temperature and strain.

Lifetime Behaviour

The relationships between total mechanical strain amplitude and number of cycles to failure given in Fig. 5 prove that in-phase loading always results in lower lifetimes than out-

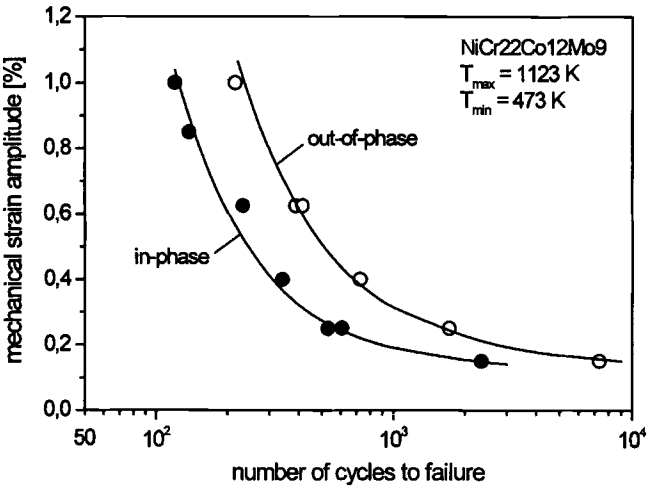

Figure 5 - *Wöhler curves from in-phase and out-of-phase TMF tests*

of-phase loading. By plotting these results and the relationships $\varepsilon^{me}_{a,e}$-N_f as well as $\varepsilon^{me}_{a,p}$-N_f in double logarithmic scaling in Fig. 6, it is shown that the lifetime behaviour is described well by the combination of the Basquin and Coffin-Manson relationship

$$\varepsilon^{me}_{a,t} = \frac{\sigma_f}{E} \cdot N_f^{-\beta} + \varepsilon_f \cdot N_f^{-\alpha} \qquad (1)$$

where α, β, σ_f/E and ε_f are material constants. Their values are given in Table 1. With respect to in-phase loading the intersection of the lines given by the Basquin and the Coffin-Manson relationships occurs at a lower number of cycles compared to out-of-phase loading.

Table 1 - *Values of α, β, σ/E and ε_f for in-phase and out-of-phase loading*

	σ_f/E	β	ε_f	α
in-phase	0.0028	0.095	7	1.4
out-of-phase	0.0035	0.1	6.2	1.22

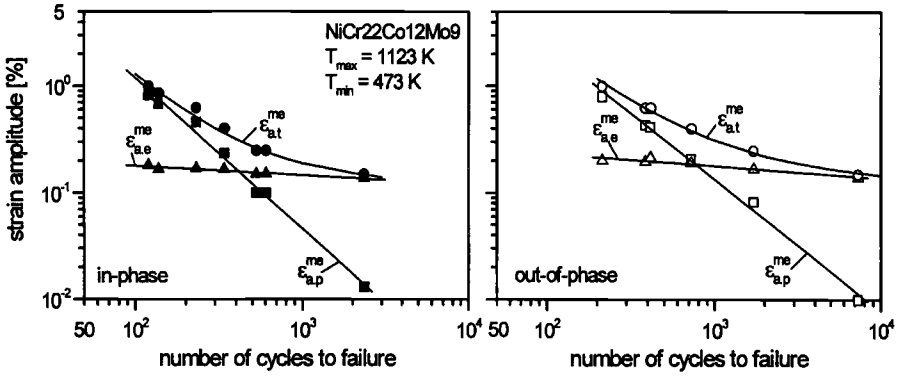

Figure 6 - *Total, elastic and plastic strain amplitudes at N/2 versus the number of cycles to failure for in-phase and out-of-phase loading*

Development of the Microstructure

In Fig. 7 the microstructure in the as received state (a)) and after fracture due to in-phase TMF at T_{max} = 1123 K, $\varepsilon^{me}_{a,t}$ = 0.15 % (b)) as well as $\varepsilon^{me}_{a,t}$ = 1.0 % (c)) is shown. During TMF, small coherent carbide particles precipitate at grain boundaries and glide planes. The interaction of dislocations with these carbides during cyclic plastic deformation results in a strong increase of the dislocation density and cyclic hardening, which is much more pronounced compared to isothermal fatigue at 1123 K and with the same total mechanical strain amplitudes [5]. During later stages of TMF, subgrain structures, visible in Fig. 7b) and c), develop as a result of recovery processes, but this does not occur in the whole specimen volume. The dislocation density within the subgrains is still rather high. TEM examinations of a large number of broken specimens do not show any significant influence of the phase relationship between temperature and mechanical strain on the development of the microstructure. However, there is an influence of the mechanical strain amplitude. At $\varepsilon^{me}_{a,t}$ = 0.15 % well formed subgrains are found within the grains as well as close to the grain boundaries, whereas at $\varepsilon^{me}_{a,t}$ = 1.0 % only initial stages of subgrain

formation are observed (compare Fig. 7b) and c)). Since the number of cycles to failure decreases with increasing mechanical strain amplitude, it should be noted that the microstructures existing after fracture are also influenced by different durations of the thermo-mechanical loadings. In any case, the dislocation density within the subgrains is significantly lower than the one within the areas with planar dislocation arrangements which also appear [*6*].

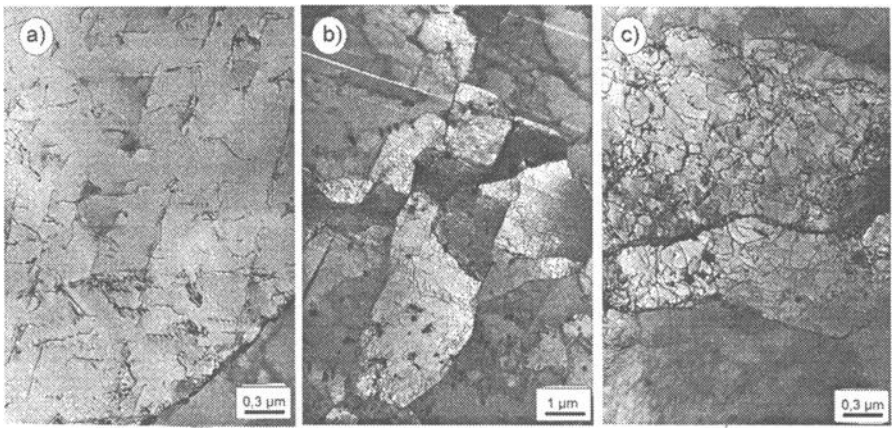

Figure 7 - *Microstruture a) in the as received state and after failure of specimens subjected to in-phase TMF at b)* $\varepsilon^{me}_{a,t}$ *= 0.15 % as well as c)* $\varepsilon^{me}_{a,t}$ *= 1.0 %*

Development of Damage

Figure 8 shows optical micrographs taken from longitudinal cuts close to the surface of specimens fractured by in-phase (left hand side) and out-of-phase (right hand side) TMF at $\varepsilon^{me}_{a,t}$ = 0.15 % (top) and $\varepsilon^{me}_{a,t}$ = 1.0 % (bottom). After all tests numerous small carbides at grain and twin boundaries as well as at parallel slip bands are observed. At $\varepsilon^{me}_{a,t}$ = 1.0 % the twin boundaries are curved indicating severe plastic deformations within the grains. During in-phase loading, micro-cracks propagate both inter- and transgranularily. In the latter case, slip bands are the preferential crack propagation paths. During out-of-phase loading the micro-cracks grow predominantly transgranularily.

To examine the development of micro-cracks, in-phase tests at $\varepsilon^{me}_{a,t}$ = 0.25 % as well as in-phase and out-of-phase tests at $\varepsilon^{me}_{a,t}$ = 0.625 % were interrupted after different numbers of cycles and the specimens were examined by an optical microscope. In Fig. 9 the evaluated micro-crack densities and mean crack depths are plotted as a function of the ratio N/N_f. Every data point in these diagrams required the evaluation of a new micrograph. The diagrams on the left show that during in-phase loading at $\varepsilon^{me}_{a,t}$ = 0.25 %, the first microscopic cracks were formed after about 40 % of the lifetime. The crack density and the mean crack length then increase continuously with N/N_f. The diagrams on the right prove that at $\varepsilon^{me}_{a,t}$ = 0.625 % micro-cracks appear somewhat earlier at about 28 % of the lifetime irrespective of

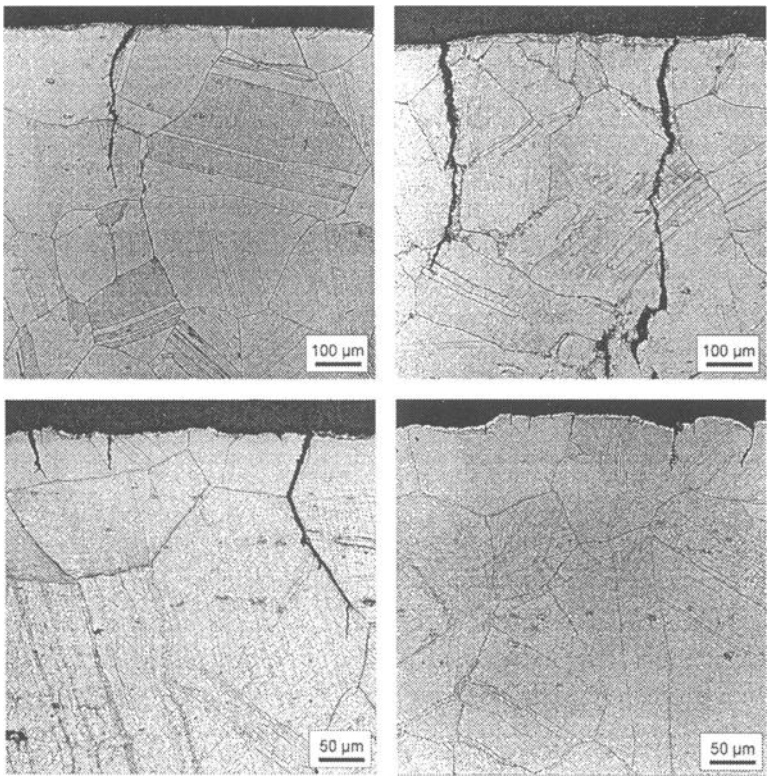

Figure 8 - *Micrographs from longitudinal cuts close to the surface of the specimens fractured by in-phase and out-of-phase loading at* $\varepsilon^{me}_{a,t}$ *= 0.15 % and 1.0 %*

the phase-relationship. At later stages of TMF, in-phase loading always results in smaller number, but larger mean depth of micro-cracks than out-of-phase loading. At a given ratio N/N_f during in-phase loading, the number of micro-cracks at $\varepsilon^{me}_{a,t}$ = 0.15 % is smaller and their mean depth is larger than the corresponding values at $\varepsilon^{me}_{a,t}$ = 0.625 %.

Analysis of fractured specimens proves that the number of micro-cracks per mm edge of the micrograph increases and the mean depth of the micro-cracks decreases with growing total mechanical strain amplitude (see Fig.10). Out-of-phase loading produces high micro-crack densities with comparatively small mean crack lengths. About 10 to 20 % of the cracks show intergranular propagation. On the other hand, in-phase loading produces fewer but longer micro-cracks about 50 to 70 % of which propagate intergranularly.

Figure 11 shows the development of the intergranular damage in the interior of specimens at $\varepsilon^{me}_{a,t}$ = 0.25 % (left) and 0.625 % (right) as a function of the ratio N/N_f. Even after fracture, no internal grain boundary damage is detectable after out-of-phase loading. During in-phase loading internal damage develops only in the second half of the lifetime.

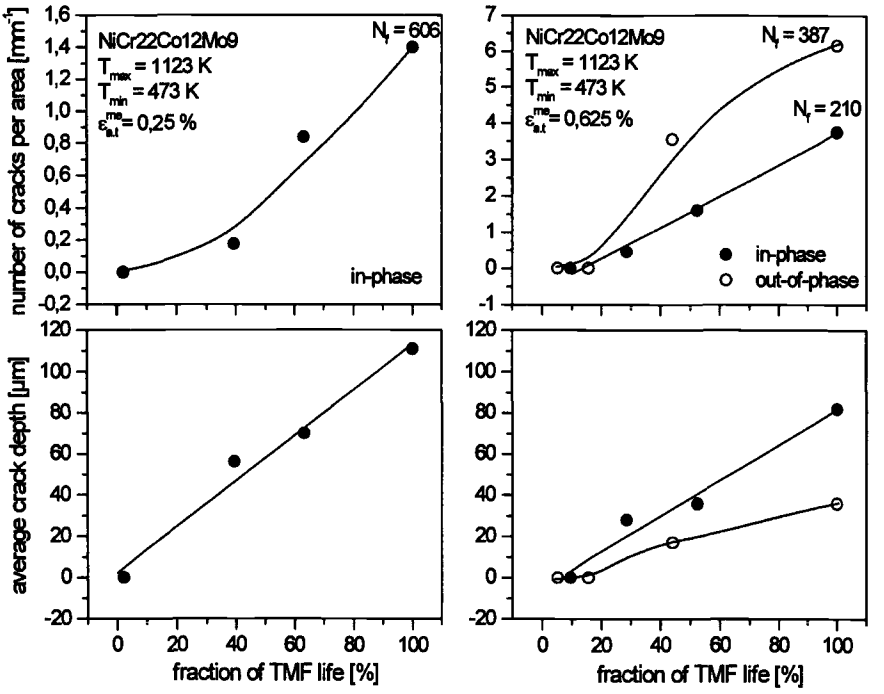

Figure 9 - *Micro-crack density and mean crack depth versus the ratio N/N_f at in-phase and out-of-phase loading for $\varepsilon^{me}_{a,t}$ = 0.25 % (left) and 0.625 % (right)*

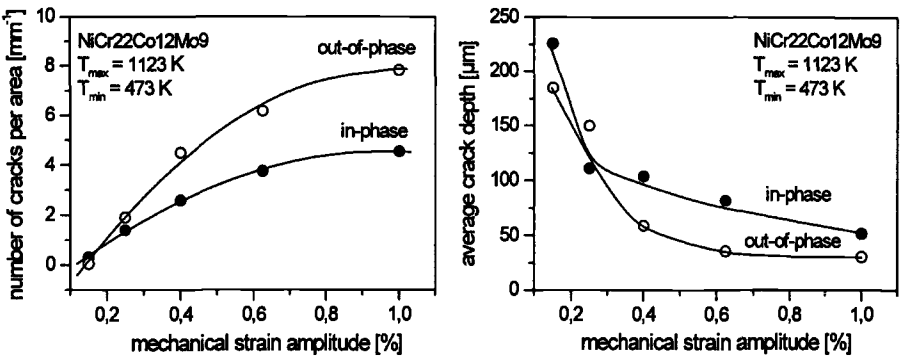

Figure 10 - *Micro-crack density and the average crack depth versus mechanical strain amplitude at in-phase and out-of-phase loading*

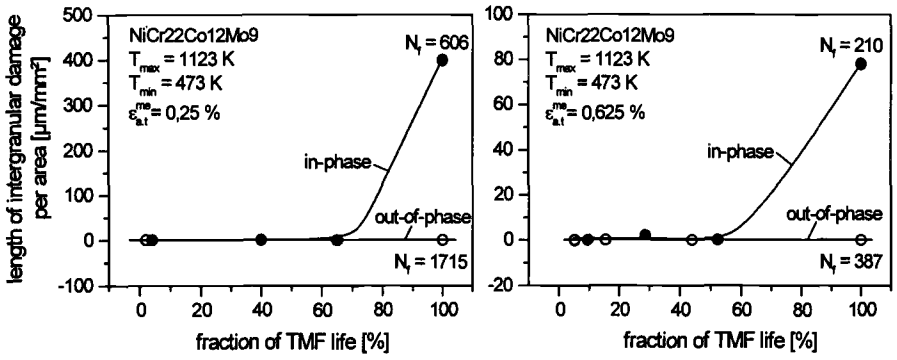

Figure 11 - *Intergranular damage versus the ratio N/N_f at in-phase and out-of-phase loading for $\varepsilon^{me}_{a,t}$ = 0.25 % (left) and 0.625 % (right)*

The influence of the mechanical total strain amplitude on the intergranular damage determined after fracture is shown in Fig. 12. During out-of-phase TMF, no internal damage is formed at any of the total strain amplitudes investigated. However, after in-phase loading

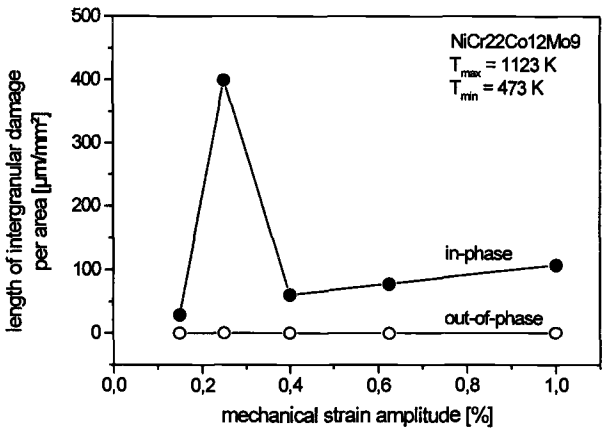

Figure 12 - *Intergranular damage after fracture versus mechanical strain amplitude at in-phase and out-of-phase loading*

internal damage appears at all total strain amplitudes, but particularly at $\varepsilon^{me}_{a,t}$ = 0.25 %, which was confirmed by repeated experiments and which is combined with a large number of pores and rather long cracks along grain boundaries. According to Fig. 10, there is no

correlation between this high intergranular damage and the micro-crack density at the surface.

Discussion

The development of the microstructure during TMF with fixed minimum and maximum cycle temperatures depends on the amount of cyclic plastic deformation, the plastic strain rate and the duration of the test. Increasing $\varepsilon^{me}_{a,p}$ results in increasing dislocation density and increasing cyclic hardening. On the other hand, at a given frequency, $\dot{\varepsilon}_p$ is the lower the lower $\varepsilon^{me}_{a,t}$ and, as a consequence, the lower $\varepsilon^{me}_{a,p}$ is. From the cyclic deformation curves in Fig. 3 it can be concluded that the values of $\dot{\varepsilon}_p$ vary by more than one order of magnitude. At low $\dot{\varepsilon}_p$ time-dependent diffusion controlled deformation becomes important and, in connection with the increased lifetime, results in pronounced subgrain formation visible in Fig. 7 b).

Due to the recovery processes occurring in every TMF cycle at the maximum temperature of 1123 K, the differences in the dislocation densities observed after fracture are rather small, even though the plastic strain amplitudes and the lifetime differ considerably (see Fig. 3). The sign of the mean stresses which are formed during TMF results first from the temperature dependence of the yield strengths, that decrease continuously with growing temperature [7] and second from the phase relation between the temperature and the mechanical strain. Hence, compressive mean stresses are formed during in-phase TMF and tensile mean stresses during out-of-phase TMF. In both cases, the absolute values of mean stresses increase during TMF due to the cyclic shift of the hysteresis loops which is promoted by the cyclic relaxation processes at high temperatures. The development of the mean stresses in the cyclic deformation curves in Fig. 3 reflects the differences of the material condition at the temperatures at which σ_{max} and σ_{min} appear. These are relatively low during tests with $\varepsilon^{me}_{a,t} \geq 0.25$ % at which the minimum stresses uniformly are found at 473 K and maximum stresses appear between about 950 K and 1020 K (see Fig. 2). Hence, the mean stresses also remain low. At $\varepsilon^{me}_{a,t} = 0.15$ % the highest absolute values of the mean stress occur, because the extreme values of the stress appear at the maximum and the minimum temperature, respectively.

In Fig. 13 the mean value of the plastic strain amplitude $\bar{\varepsilon}^{me}_{a,p}$ is plotted versus the lifetime in double logarithmic scaling for in-phase and out-of-phase loading. For both cases the data could be described well with straight lines. Therefore, the Coffin-Manson relationships for in-phase TMF

$$\bar{\varepsilon}^{me}_{a,p} = 7.0 \cdot N_f^{-1.40} \qquad (2)$$

and for out-of-phase TMF

$$\bar{\varepsilon}^{me}_{a,p} = 6.2 \cdot N_f^{-1.22} \qquad (3)$$

apply. It should be noted, however, that all TMF tests in this investigation were performed with constant minimum and maximum cycle temperatures. This obviously results in dominating deformation mechanisms, development of microstructures and damage mechanisms which do not differ qualitatively with regard to the wholeness of tests performed.

The absolute values of the exponents in Eq. 2 and 3 are significantly higher than those evaluated from isothermal fatigue tests. At temperatures between 295 K and 1123 K Coffin-Manson exponents between 0.75 and 0.94 were determined [*5,8,9*]. Partly, this difference might be caused by the usual definition of the plastic strain amplitude as half of the width of the stress-mechanical strain hysteresis loop at the actual mean stress. Regarding TMF the augmentation of the plastic strain amplitude connected with an increase of the total strain amplitude is mainly caused by the plastic deformation appearing at the higher temperatures of the cycle.

The fact that the results of in-phase and out-of-phase tests in Fig. 13 can not be assessed by a unique Coffin-Manson relationship is due to different crack propagation mechanisms. During in-phase loading tensile stresses at high temperatures cause distinctive grain boundary damage and relatively fast intergranular crack propagation. During out-of-phase TMF tensile stresses at low temperatures promote mainly transgranular crack propagation. The dotted line in Fig. 13 which refers to the upper abscissa shows that the ratio $N_{f,OP}/N_{f,IP}$ increases with decreasing plastic strain amplitude, and thus, increasing TMF life. Similar observations exist for other materials [*10*]. This behaviour is caused by the development of intergranular damage during in-phase TMF which is supported by creep processes and, therefore, is time-dependent. On the other hand, intergranular damage hardly affects out-of-phase TMF life.

In out-of-phase tests, the number of the micro-cracks at the surface after fracture increases stronger with increasing total strain amplitude than in in-phase tests (see Fig. 10). This is a result of the tensile stresses growing with $\varepsilon^{me}_{a,t}$. The decrease of the mean length of the micro-cracks after fracture can be attributed to the lifetime reduction due to increasing

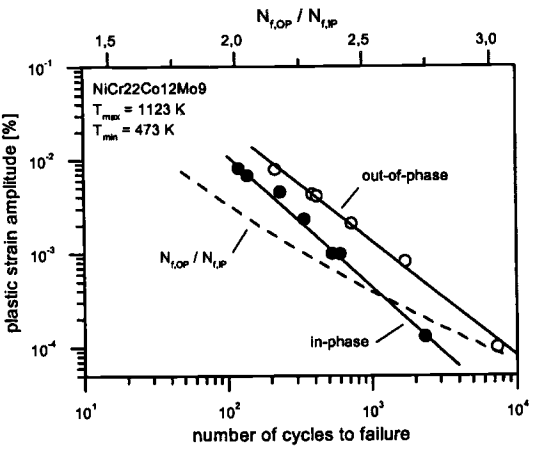

Figure 13 - *Coffin-Manson relationship from in-phase and out-of-phase TMF tests*

total strain amplitudes. At $\varepsilon^{me}_{a,t} = 0.15$ % only a few cracks develop which are relatively long at fracture due to the long duration of the test. At $\varepsilon^{me}_{a,t} = 1.0$ % a lot of short micro-cracks are formed due to the high tensile stresses but they do not grow significantly, possibly because of the fast propagation of the main crack. These relationships are confirmed by the results given in Fig. 9 which shows that during in-phase loading at $\varepsilon^{me}_{a,t} = 0.625$ % the number of the micro-cracks is always larger and their mean length is always smaller than at $\varepsilon^{me}_{a,t} = 0.25$ %, and that the mean length of the micro-cracks increases almost linearly in both cases up to fracture.

Intergranular grain boundary damage in the interior of the specimens develops during in-phase TMF only at relatively high numbers of cycles (see Fig. 11). According to microscopic investigations they are mainly caused by grain boundary separation due to creep supported plastic deformation processes. Since creep processes are time-dependent, pores and cracks at grain boundaries are formed in a rather late TMF stage. The extremely high amount of intergranular volume damage at $\varepsilon^{me}_{a,t} = 0.25$ % is caused by the combined effects of a long test and rather high tensile stresses arising at high temperatures. According to Fig. 2 the tensile stresses are much higher at $\varepsilon^{me}_{a,t} = 0.25$ % than at 0.15 %. On the other hand, at $\varepsilon^{me}_{a,t} = 0.4$ %, the maximum tensile stresses are even higher than at 0.25 %. However, in this case macro-crack propagation intervenes before a larger amount of grain boundary damage is formed.

Conclusions

From the results obtained in this study, the following conclusions can be drawn:

i During in-phase and out-of-phase thermo-mechanical fatigue (TMF) tests there is hardly any influence of the phase-relationship between the temperature-time and the mechanical-time course on the development of the microstructure, the stress amplitude, and the plastic strain amplitude. However, compressive mean stresses develop during in-phase loading and tensile mean stresses develop during out-of-phase loading.

ii The cyclic stress-strain response is governed by cyclic hardening which become very pronounced at high mechanical strain amplitudes. Cyclic hardening results from strong dislocation-dislocation and dislocation-particle interactions during plastic deformation at lower temperatures of the TMF-cycles. Dislocation-particle interaction is enhanced by the precipitation of small, semi-coherent carbides at elevated temperatures of the TMF-cycles.

iii The lifetime determined in both types of TMF tests do not fit in unique Basquin and Coffin-Manson relationships, but are adequately described by seperate ones. Even though compressive mean stresses develop during out-of-phase TMF, in-phase tests always yield smaller lifetimes than out-of-phase tests. This is due to the different development of intergranular damage, which is favored during in-phase loading by tensile stresses acting at high temperatures.

Aknowledgement

The financial support of this investigations by the "Deutsche Forschungsgemeinschaft" within the "Sonderforschungbereich 167: Hochbelastete Brennräume - Stationäre Gleichdruckverbrennung" is gratefully acknowledged.

References:

[1] Coles, A., "Material Considerations for Gas Turbine Engines," *Proc. 3rd Int. Conf. Mech. Behaviour of Materials (ICM3)*, Vol. 1, Pergamon Press, Oxford, 1979, pp. 3-11.

[2] Skelton, R. P., "Crack Initiation and Growth in Simple Metal Components during Thermal Cycling," *Fatigue at High Temperature*, 1983, pp. 1-62.

[3] Vogel, W.H., Soderquist, R.W. and Schlein, B.C., "Prediction of Crack Initiation in Combustion Chamber Liners," *J. Aircraft*, 14, 1977, pp. 1076-1080.

[4] Richter, F., "Thermophysikalische Eigenschaften des hochwarmfesten Werkstoffes NiCr22Co12Mo (INCONEL 617)," *Mat.-wiss. u. Werkstofftech.* 19, 1988, pp. 55-61.

[5] Merckling, G., "Kriech- und Relaxationsverhalten ausgewählter metallischer Werkstoffe bei höheren Temperaturen," *Dr.-Ing. Thesis*, Universität Karlsruhe (TH), 1989.

[6] Kleinpass, B., Lang, K.-H., Löhe, D., Macherauch, E., "Thermal-Mechanical Fatigue Behaviour of NiCr22Co12Mo9," J. Bressers and L. Rémy (Eds.), *Fatigue under Thermal and Mechanical Loading*, Kluwer Academic Publishers, Dordrecht-Boston-London, 1996, 327-337

[7] Viereck, D., "Das Zug- und Relaxationsverhalten von Hochtemperaturblechwerkstoffen im Temperaturbereich 78 K≤T≤1473 K," *VDI Fortschrittsberichte,* Reihe 5, Nr. 202, VDI-Verlag, Düsseldorf, 1990.

[8] Merckling, G., Lang, K.-H., Macherauch, E., "Das Ermüdungsverhalten von NiCr22Co12Mo9 im Temperaturbereich 295 K ≤ T ≤ 1473 K," *Z. Metallkd.*, 84, 1993, pp. 844-853.

[9] Moalla, M., Lang, K.-H., Löhe, D., Macherauch, E., "Isothermal High Temperature Fatigue Behaviour of NiCr22Co12Mo9 under superimposed LCF and HCF Loading," K.T. Rie and P.D. Portella (Eds.), Proc. 4th Int. Conf. on *Low Cycle Fatigue and Elasto-Plastic Behaviour of Materials*, 7.-11. September 1998, Garmisch-Partenkirchen, Elsevier Science Ldt., Oxford, UK, 1998, pp. 27-32.

[10] Beck, G. Pitz, K.-H. Lang, D. Löhe, "Thermal-mechanical and isothermal fatigue of IN 792 CC," *Materials Science and Engineering,* A234-236, 1997, pp.719-722.

Stress-strain Response Experiments and Modeling

Huseyin Sehitoglu,[1] Tracy J. Smith,[1] and Hans J. Maier[2]

Thermo-mechanical Deformation of Al319 - T7B with Small Secondary Dendrite Arm Spacing

Reference: Sehitoglu, H., Smith, T. J., and Maier, H. J., **Thermo-mechanical Deformation of Al319 - T7B with Small Secondary Dendrite Arm Spacing,"** *Thermo-mechanical Fatigue Behavior of Materials: Third Volume, ASTM STP 1371,* H. Sehitoglu and H. J. Maier, Eds., American Society for Testing and Materials, West Conshohocken, PA, 2000.

Abstract: Thermomechanical fatigue and isothermal deformation experiments were conducted on cast Al 319 alloys with small secondary arm spacings (SDAS) in the range of 25 to 35μm. The alloy was studied in the overaged state designated as T7B. In the case of the T7B treatment the material possesses dimensional stability, but incurs considerable loss of strength with time and cyclic deformation at temperatures exceeding 250°C. A two-state variable unified constitutive model was developed to characterize the stress-strain response for the material. The model handles temperature and strain rate effects and captures the microstructurally induced changes on the stress-strain response. The thermomechanical fatigue response under in-phase (TMF IP) and out-of-phase (TMF OP) conditions was simulated and the material exhibited a decrease in the stress range by as much as 50% with continued cycling. The decrease in strength was attributed to the significant coarsening of the precipitates at high temperatures and was confirmed by transmission electron microscopy.

Keywords: aluminum alloy, thermomechanical fatigue, dimensional stability, precipitate coarsening, thermal recovery, constitutive modeling.

Background

The present work stems from the need to understand the mechanical behavior of cast Al 319 alloys at high temperatures. These materials are used for the cylinder heads in automobile engines with the critical location being the valve bridge area, in which operating temperatures can potentially reach close to 300°C. These alloys derive their strength from Al-Cu precipitates, and depending on the heat treatment and thermal exposure in service, the precipitate morphology changes, which in turn alters the mechanical properties.

The T7B heat treatment (495°C for 8 hours, boiling water quench, followed by aging at 260°C for 4 hours) produces an overaged microstructure that yields dimensional stability (resistance to thermal growth). In the peak aged treatment, designated as T6, the

1. Professor and graduate student, respectively, Mechanical Engineering Department, University of Illinois at Urbana-Champaign, 1206 West Green Street, Urbana, IL 61801, USA.
2. Professor, Universität-GH Paderborn, Lehrstuhl für Werkstoffkunde, FB 10, Pohlweg 47-49, 33098, Paderborn, Germany.

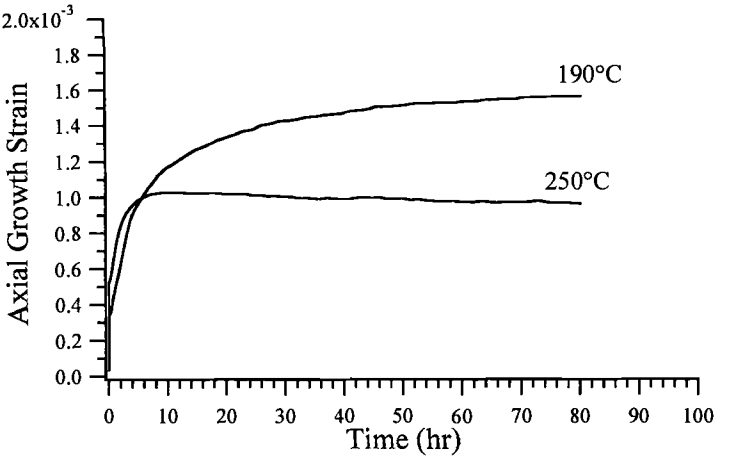

Figure 1- Axial growth of a sample during exposure of the material to 190°C (T6 aging temperature) and to 250°C (T7B aging temperature) after solutionizing at 495°C for 8 hours.

material is aged at 190°C for a period of five hours. To understand the dimensional stability or thermal growth, cylindrical specimens were solutionized at 495°C and subsequently quenched. One group of specimens was rapidly heated to 250°C while the other group was heated to 190°C and held at the elevated temperature for 80 hours. Upon removing the thermal strain from the measured total strain, it was possible to study the growth strains (dimensional change of the specimen) as a function of time. The results are summarized in Figure 1 and have been confirmed with companion specimens. As the precipitates nucleate and grow, for an initially solutionized material, the growth strains at 250°C (typical of T7B treatment) reach 1.0 x 10^{-3} and then decrease slightly due to relaxation of stress fields near the obstacles. At 250°C the material has undergone a growth strain of 0.95 x 10^{-3} after 4 hours and the growth strain has nearly stabilized. Therefore, this material is expected to be dimensionally stable in service. On the other hand, the specimen exposed to 190°C (typical of T6 peak aged treatment) undergoes growth strains exceeding 1.6 x 10^{-3} at the 80 hour point. After 5 hours, the growth strain reaches only 0.96 x 10^{-3}. Therefore, this material will exhibit dimensional changes if temperatures exceed 190°C in service.

Upon long-term exposure to high temperatures precipitates coarsen and dissolve back into solution and the strength levels decrease *[1-3]*. Predicting service conditions is possible upon a better understanding of the details of the material behavior as influenced by the solidification rate, composition, heat treatment, and service conditions. The secondary dendrite arm spacing is influenced by the solidification time. This paper is concerned with the deformation behavior of cast Al 319 alloys with a secondary dendrite arm spacing in the range 25 to 35 microns that corresponds to a solidification time of approximately 60 seconds. In earlier work, specimens were also taken from slowly solidified regions that correspond to a large secondary dendrite arm spacing. The

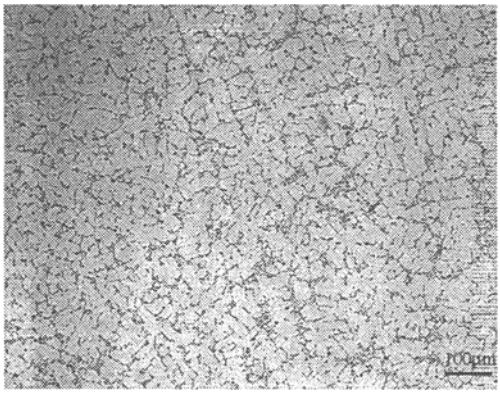

Figure 2 - Optical micrograph showing the small dendritic structure with an average spacing of 30μm.

microstructure of the Al 319 material with small secondary dendrite arm spacing is shown in Figure 2. The grain size (not shown) spans several millimeters.

A strong correlation exists between solidification time and the formation of primary theta, which in turn influences the amount of Cu remaining in solution. The rapid solidification times diminish the primary theta content and subsequently result in a higher Cu content in solution. For this class of materials, the Cu content in solution is nearly 4% for the small SDAS and decreases to 2.5% for the large SDAS. Consequently, the small secondary dendrite arm spacing microstructures of Al 319 produce the most superior properties in this class of alloys. The porosity levels for the small SDAS materials (the average area porosity levels were 0.04%) and the intermetallic volume fraction are also significantly lower than for the higher SDAS microstructures.

Although there has been previous work on the high temperature fatigue of aluminum alloys *[4-5]*, very few studies have investigated their thermomechanical fatigue deformation behavior *[6-7]*. Our previous work on Al 2xxx-T4 alloys considered the thermomechanical fatigue deformation behavior *[7]*, but the processing routes, the material composition and the aging conditions in the current study are quite different. The high temperature work of Bhat and Laird *[5]* demonstrated the dissolution of θ' precipitates at 250°C under cyclic straining conditions thereby leading to softening. In a companion study, Calabrese and Laird *[8]* showed that when the interparticle spacing (θ' spacing) was small, the dislocations shuttled between the precipitates and were accumulated at the interfaces. When the θ' spacing was large (exceeding 1 micron), the dislocations were stored in the matrix in the form of a cell structure similar to pure metals. Using these ideas, Calabrese and Laird obtained a first order estimate of the saturation stress behavior of these alloys which they found to equal 200 MPa for interparticle spacings in the range 0.2 to 0.5 microns. The strengthening levels in the present study are higher partly because of the contribution from solution hardening.

The TEM picture of the precipitates after the T7B treatment is shown in Figure 3(a). Note that the precipitates are mostly θ' and are located on [001] habit planes. Figure 3(b) shows the precipitate structure of the material after exposure to 300°C for 80 hours. This

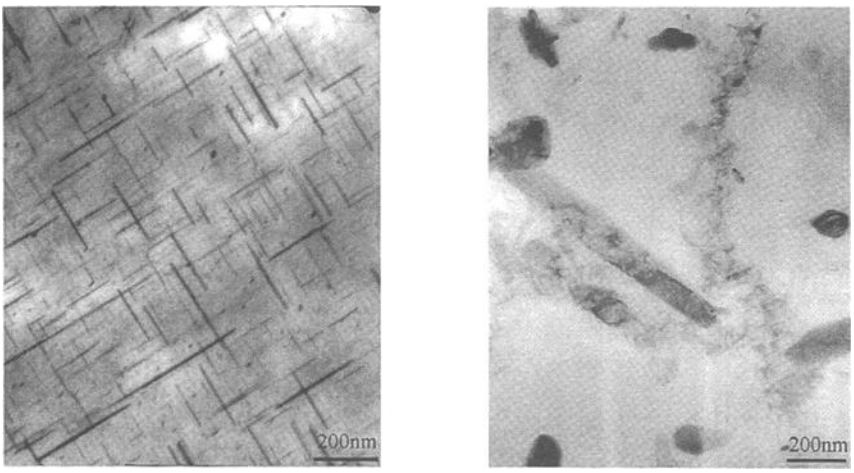

Figure 3 - TEM micrographs showing the precipitates in the T7B microstructure (a) undeformed (virgin) sample and (b) after exposure to 300°C for 80 hours.

is representative of the microstructure of Al 319 at the conclusion of the long TMF experiments. The micrograph shows that the interparticle spacing has increased and the precipitates have begun to deviate from their [001] habit planes and lose their plate-like shape. To gain insight into the role of the aging treatment, we compare the stress-strain response of Al 319 at room temperature after rapid quenching, room temperature (natural) aging, T6 treatment, and for the T7B treatment. The results are summarized in Figure 4. We note that the stress-strain response for the quenched case (Cu in solid solution) is substantially lower than the T7B case. However, after natural aging at room temperature for a period of one week the strength of the solutionized material exceeds the T7B case. We note that the strength (hardness) saturates after a period of 30 hours in the natural aging case. For comparison purposes, the stress-strain curve corresponding to the T6 treatment (peak aged treatment, 190°C for 5 hours) is also included in Figure 4. As expected this treatment produces the highest strength levels. It is worth noting that the precipitates that form after these treatments (overaging - predominantly θ'), peak aging (θ'') and natural aging (GPI zones) are different and this is treated further in the 'Discussion'.

This paper focuses primarily on the stress-strain response of the Al 319 material with small secondary dendrite arm spacing (SDAS) in the overaged condition. Some baseline comparisons with other treatments are also provided. The deformation behavior under unidirectional and cyclic loading cases is examined. Fatigue life information is included in several thermomechanical fatigue loading cases. The experiments range from isothermal (constant temperature, 250°C) and thermomechanical loading (varying temperature over 100°C to 300°C) to high temperature thermal exposure effects on room temperature deformation. A unified stress-strain model that incorporates creep and plasticity as inelastic strain was developed to describe the material response in the overaged state.

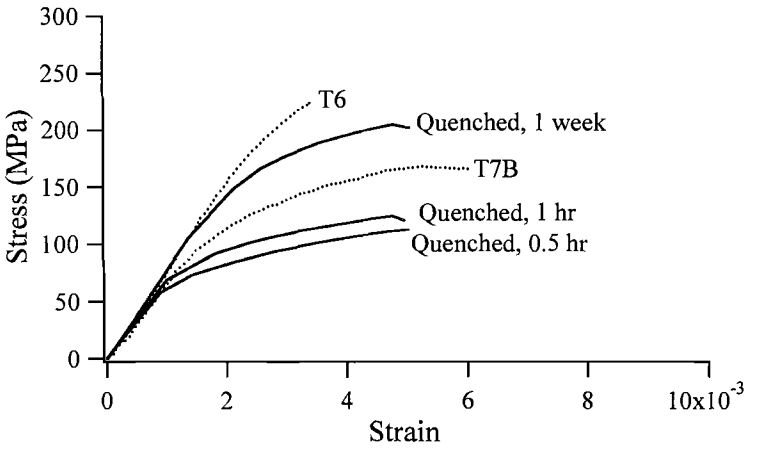

Figure 4 - Comparison of T7B, T6, solutionized and naturally aged material stress-strain response.

Material and Experimental Procedures

Specimens were sectioned from a sand cast wedge. The geometry of the wedge has been published in previous work *[9]*. The design of the wedge allowed the machining of samples with predetermined secondary dendrite arm spacings (SDAS). Specimens near the tip of the wedge have the small SDAS (30μm). The specimens for the thermomechanical fatigue deformation experiments were machined with a diameter of 7.6 mm and a gage length of 25.4 mm. The chemical composition of the material is given in Table 1. The alloy has an average composition of 3.33% Cu and 7.43% Si. The iron content of 0.38% is considered low compared to the higher Fe contents of 0.8% that are being considered for cylinder block applications.

Table 1 - *Material Composition of Al 319 in Weight Percent*

Element	Si	Cu	Mg	Fe	Mn	Zn	Ti	Cr	Sr	Al
wt (%)	7.43 ±.34	3.33 ±.16	0.22 ±.03	.38 ±.04	0.24 ±.02	< 0.25	.12 ±.02	< 0.05	0.03 ±.01	Bal.

Strain-controlled isothermal fatigue tests were performed at a temperature of 250°C with a strain rate of 5×10^{-5} s^{-1}. In addition, higher frequency tests were conducted for life information but these results will not be discussed in this paper. A wide range of mechanical strain ranges was considered (0.0007 to 0.0012) in the testing program.

A servohydraulic test machine with computer control was used in the thermomechanical fatigue experiments. The computer control unit was capable of handling load, strain, and temperature control. The data acquisition rate allowed 600 data points per cycle. A Lepel induction generator was used to heat the test specimen during the TMF experiments. The induction coil configuration was designed to minimize the

temperature gradients in the gage section. Temperature was measured using a Raytek noncontact infrared pyrometer. The temperature was controlled within ±3°C. In the present study, the mechanical strain rate was near 5 x 10^{-5} s^{-1}. The specimens were first heated to 200°C at zero load. The control was then switched to strain and the specimen was heated to 300°C, with $\dot{\varepsilon}_{ij}^{net}$ (net strain rate increment) applied to give the desired mechanical strain rate according to Equation [1]. Once 300°C was reached cooling to 100°C followed. In the thermomechanical fatigue experiments, two baseline TMF tests were considered in the present study: out-of-phase where the maximum mechanical strain coincides with the minimum temperature and in-phase where the maximum mechanical strain is attained at the maximum temperature. In the out-of-phase TMF loading, the maximum tensile stresses occur at minimum temperature end, while in the in-phase TMF loading, the material undergoes tensile stresses at maximum temperature. The key equation in TMF studies is *[7]*

$$\dot{\varepsilon}_{ij}^{net} = \dot{\varepsilon}_{ij}^{mech} + \dot{\varepsilon}_{ij}^{th} \qquad [1]$$

where the net (total) strain rate $\dot{\varepsilon}_{ij}^{net}$ is separated into the mechanical strain rate $\dot{\varepsilon}_{ij}^{mech}$ and thermal strain rate $\dot{\varepsilon}_{ij}^{th}$. For one-dimensional loading the subscripts can be dropped. The mechanical strain rate is the sum of elastic and inelastic strain rate components. In thermomechanical deformation, the phasing is defined as the ratio of mechanical to thermal strain rate ($\dot{\varepsilon}^{mech} / \dot{\varepsilon}^{th}$). This ratio is –1 for an out-of-phase loading and +1 for an in-phase loading.

Unified Constitutive Model for Al 319 Small SDAS

A unified constitutive model proposed by Sehitoglu and Slavik *[7,10]* and recently modified for Al 319 alloys *[1-3]* was utilized to describe the stress-strain behavior of Al 319-T7B. In the unified theories, the creep and plastic strains are combined as inelastic strain, and the concept of a yield surface is replaced by a stress surface. Inelastic flow is permitted inside the stress surface although its magnitude is small. Also, the stress state is allowed outside the stress surface in this model. This model utilizes two state variables: back stress and drag stress. The back stress describes the directional (internal) stress fields due to dislocation pile-ups at precipitates, grain boundaries and local stress fields due to obstacles. The drag stress is introduced to characterize the material strength due to the number of blocked dislocations, and depends on dislocation morphology, such as cell size. The forms of the constitutive relations are summarized in Table 2.

In Table 2, the $\dot{\varepsilon}_{ij}^{net}, \dot{\varepsilon}_{ij}^{e}, \dot{\varepsilon}_{ij}^{in}$ and $\dot{\varepsilon}_{ij}^{th}$ represent the total strain rate, elastic strain rate, inelastic strain rate and thermal strain rate, respectively. The expressions for all of these strain rates are listed in Table 2. In the elastic strain rate expression Poisson's ratio and the elastic modulus, E, are the material constants. In the thermal strain rate, β is the thermal expansion coefficient. In the inelastic strain rate expression (the flow rule), the material constants are A_o, the frequency factor, the activation energy, ΔH, and the exponents n_1 and n_2. The stress tensors are S_{ij}, deviatoric stress, and S_{ij}^{C}, deviatoric

Table 2 - *Summary of the Unified Constitutive Model*

Strain Components

$$\dot{\varepsilon}_{ij}^{net} = \dot{\varepsilon}_{ij}^{e} + \dot{\varepsilon}_{ij}^{in} + \dot{\varepsilon}_{ij}^{th}$$

$$\dot{\varepsilon}_{ij}^{e} = \left[(1-\nu)\dot{\sigma}_{ij} - \nu\dot{\sigma}_{kk}\delta_{ij}\right]\frac{1}{E} - \left[(1-\nu)\sigma_{ij} - \nu\sigma_{kk}\delta_{ij}\right]\frac{\partial E}{\partial T}\frac{\dot{T}}{E^2}$$

$$\dot{\varepsilon}_{ij}^{in} = \frac{3}{2} f\left(\frac{\bar{\sigma}}{K}\right)\frac{S_{ij} - S_{ij}^{c}}{\bar{\sigma}}$$

$$f\left(\frac{\bar{\sigma}}{K}\right) = \begin{cases} A_o\left(\dfrac{\bar{\sigma}}{K}\right)^{n_1} \exp\left(-\dfrac{\Delta H}{RT}\right) & \left(\dfrac{\bar{\sigma}}{K}\right) < 1 \\ A_o \exp\left[\left(\dfrac{\bar{\sigma}}{K}\right)^{n_2} - 1\right]\exp\left(-\dfrac{\Delta H}{RT}\right) & \left(\dfrac{\bar{\sigma}}{K}\right) \geq 1 \end{cases}$$

$$\dot{\varepsilon}_{ij}^{th} = \beta\dot{T}\delta_{ij}$$

$$E = e_1 - e_2 T$$

Back Stress Evolution

$$\dot{S}_{ij}^{C} = \frac{2}{3} h_\alpha \dot{\varepsilon}_{ij}^{in} - [r_\alpha^{D}\dot{\bar{\varepsilon}}^{in} + r_\alpha^{s}]S_{ij}^{C}$$

$$h_\alpha = \begin{cases} a_1 \exp\left\{-\left[a_2(\alpha_0 + \bar{\alpha})\right]^{a3}\right\} & \text{if} \quad \dot{\varepsilon}^{in}\cdot\alpha \geq 0 \\ a_1 \exp\left\{-\left[a_2(\alpha_0 - \bar{\alpha})\right]^{a3}\right\} & \text{if} \quad \dot{\varepsilon}^{in}\cdot\alpha \leq 0 \end{cases}$$

$$a_1 = const., \quad a_2 = A_{2_i}' \exp\left[-\frac{\Delta H}{RT}\right], \quad a_3 = A_{3_i}' \exp\left[-\frac{\Delta H}{RT}\right]$$

$$A_{2_{i+1}}' = A_{2_i}' + \left(A_{2_i}' - a_{2_{sat}}\right)a_2\Delta t \quad \text{and} \quad A_{2_1}' = a_2$$

$$A_{3_{i+1}}' = A_{3_i}' + \left(A_{3_i}' - a_{3_{sat}}\right)a_3\Delta t \quad \text{and} \quad A_{3_1}' = a_3$$

$$a_{2_{sat}} = const., \quad a_{3_{sat}} = const.$$

$$r_\alpha^{s}(\alpha, T) = 0$$

$$r_\alpha^{D}(\bar{\alpha}, T, \dot{\bar{\varepsilon}}^{in}) = c(\bar{\alpha})^{d_1}\left(\dot{\bar{\varepsilon}}^{in}\right)^{d_2}$$

$$c = c' \exp\left[-\frac{\Delta H_C}{RT}\right]$$

Drag Stress Evolution

$$\dot{K} = h_k - r_k + \theta\dot{T}$$

$$h_{kD} = B(K_{sat} - K)\dot{\bar{\varepsilon}}^{in}$$

$$r_k = A_3(K - K_{rec})$$

$$\theta = \frac{\partial K_o}{\partial T}$$

internal (back) stress. The effective stress, $\bar{\sigma}$, is defined as $\bar{\sigma} = [3/2(S_{ij} - S^c_{ij})(S_{ij} - S^c_{ij})]^{1/2}$ and the effective back stress is defined as $\bar{\alpha} = [3/2\, S^c_{ij} S^c_{ij}]^{1/2}$. The flow rule, $f(\bar{\sigma}/K)$, has a power law form in the creep regime and an exponential form in the time dependent plasticity regime with a smooth transition between these two extremes.

The deviatoric internal (back) stress, S^C_{ij}, is used to capture the Bauschinger effect, the transient creep effects, and the strain hardening behavior of the material. The term h_α represents the inelastic modulus and its magnitude decreases in an exponential manner with increasing values of $\bar{\alpha}$. The constants used in describing h_α are a_1, a_2, and, a_3 and evolve as a function of time and temperature. A decrease in a_1 represents a decrease in h_α with thermal exposure. The internal stress decreases due to dynamic recovery effects and is represented by the $c(\bar{\alpha})^{d_1}(\dot{\bar{\varepsilon}}^{in})^{d_2}$ term in which the constant c is temperature dependent, and the exponents d_1 and d_2 are material constants.

The drag stress, K, is a measure of the strength of the material. There are three key values of K that are determined from experiments. The first one is K_o that corresponds to the initial strength of the undeformed (virgin) material. There is a direct correlation between K_o and $\bar{\sigma}_{ys}$ (yield strength) via the flow rule relationship. Given the inelastic strain rate and temperature we can determine K_o and the $\bar{\sigma}_{ys}/K_o$ ratio by inverting the flow rule as follows $\bar{\sigma}_{ys}/K_o = f^{-1}\left(\dot{\bar{\varepsilon}}^{in} / A_o \times \exp(-\Delta H/RT)\right)$. The saturated drag stress, K_{sat}, is obtained from cyclic experiments under isothermal conditions. In the case of Al 319 alloys in the T7B condition cyclic softening is observed at all temperatures although the amount of cyclic softening is more pronounced at high temperatures (>250°C). As a result, the magnitude of K_{sat} is lower than K_o. The evolution of K under rapid cycling follows $\dot{K} = B(K_{sat} - K)\dot{\bar{\varepsilon}}^{in}$. Finally, K_{rec} is determined by exposing the material to high temperatures for a prolonged time, cooling to room temperature and subsequently conducting a tension experiment at room temperature. If significant coarsening occurs at

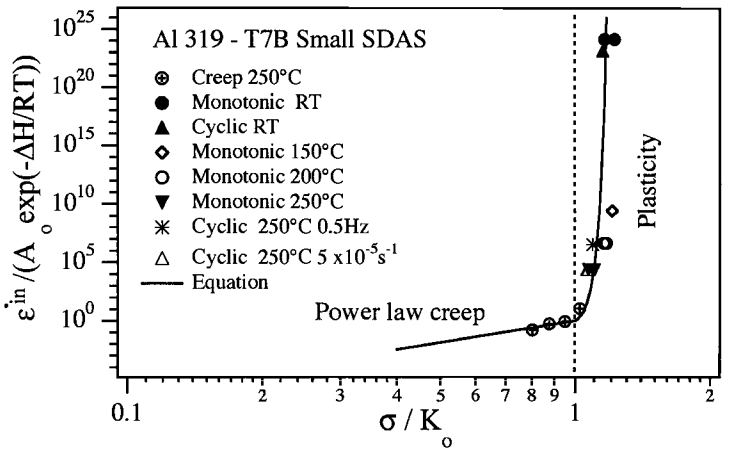

Figure 5 - The flow rule for Al 319 small SDAS in T7B condition.

high temperatures, K_{rec} will be significantly lower than K_o. In many cases the material coarsening may not reach the K_{rec} limit and the value of K decreases according to $\dot{K} = -A_3(K - K_{rec})$. The recovery rate is strongly dependent on the current value of $\bar{\sigma}/K$ with the rate of recovery being higher at high $\bar{\sigma}/K$ values. The last term in the drag stress evolution equation is $\theta = \partial K_o/\partial T$ which describes the change in the drag stress variable with temperature change only. The material constants for the Al 319 T7B material are listed in Table 3. The values obtained for the exponents and constants are consistent with previously published results on Al319 alloys under different aging conditions *[1-3]*.

To establish the flow rule, $f(\bar{\sigma}/K)$, in the model, monotonic tensile experiments were conducted at 20°C (strain rate independent), and at 150°C, 200°C, and 250°C with a strain rate of 5 x 10^{-5} s^{-1}. To complete the flow rule representation creep experiments at 250°C under constant load were also performed on the material. The flow rule, $f(\bar{\sigma}/K)$, for Al319-T7B is shown in Figure 5. The vertical axis is $\dot{\bar{\varepsilon}}^{in} / A_o \exp(-\Delta H/RT)$ and the horizontal axis is $\bar{\sigma}/K$. Some variation in the experimental results is noted in Figure 5 and is typical of the flow behavior cast materials. The constants and the exponents that describe this curve are provided in Table 3.

Table 3 - *Material constants for Al 319 Small SDAS.*

$n_1 = 6.2$	$c' = 3.90 \times 10^6$ / sec
$n_2 = 25.3$	$\Delta H_c = 33.0 kJ / mol$
$A_0 = 4.6 \times 10^{12}$ / sec	$d_1 = -0.7,\ d_2 = -0.25$
$\Delta H = 213.7 kJ / mol$	$B = 2.1$
$\beta = 2.16 \times 10^{-5} / ^o C$	$K_{sat} = 72.2 - 0.135T(^oC)$ (MPa)
$e_1 = 77000 MPa,\quad e_2 = 24.1 MPa / ^o C$	$A_3 = 4.6 \times 10^{-7}$ / sec $\quad if \dfrac{\bar{\sigma}}{K} \le 1.112$
$K_o = 77.6 - 0.0361T(^oC)$ (MPa)	$A_3 = 2.3 \times 10^{-5}$ / sec $\quad if \dfrac{\bar{\sigma}}{K} > 1.112$
$\alpha_0 = 150.0 MPa$	$K_{rec} = 81.0 - 0.219T(^oC)$ (MPa)
$a_{10} = 5.0 \times 10^5 MPa,\ a_{20} = 0.0066 / MPa,\ a_{30} = 1.95$	
$a_{1sat} = 5.0 \times 10^5 MPa,\ a_{2sat} = 0.015 / MPa,\ a_{3sat} = 1.32$	
$c_1 = 0,\ c_2 = -8.65 \times 10^7$ / sec, $c_3 = -3.90 \times 10^{-3}$ / sec	
$\Delta H_2 = 135.0 kJ / mol,\ \Delta H_3 = 20 kJ / mol$	

Simulations of Thermomechanical and Isothermal Fatigue Behavior of Al 319-T7B

The capabilities of the constitutive model are checked against several experiments. Simulations of the stress-strain response for Al 319-T7B small SDAS during isothermal fatigue at high temperature (250°C) and low strain rate (5x10^{-5} s^{-1}) are shown in Figure 6. The gradual softening of the material is predicted well with the model. A simulation of the cyclic stress-strain behavior under out-of-phase TMF loading was also conducted. The mechanical strain range in this TMF experiment was 0.6%. The comparison of simulation and experiment is given in Figure 7. It can be seen from Figure 7 that the stress-strain

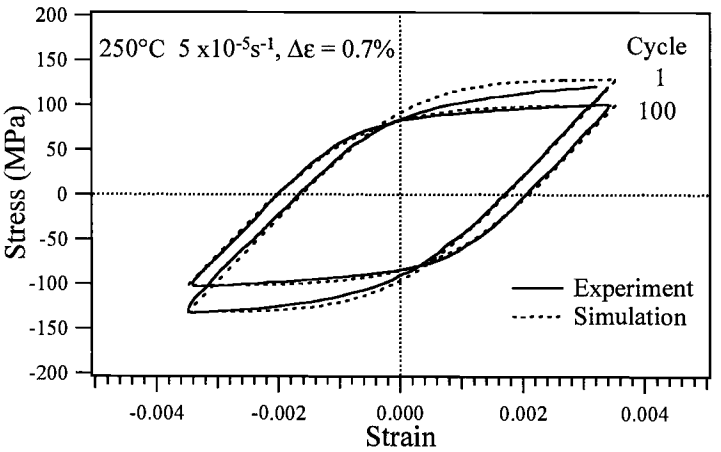

Figure 6 - Isothermal fatigue simulation and experiment at 250°C for a strain range of 0.7% and a strain rate of 5 x 10^{-5} s^{-1} for Al 319-T7B small SDAS.

response at the low temperature end of the cycle is predicted accurately. The stress response at the high temperature end is also close to the simulations. The fatigue life in this case was 1776 cycles. The simulation of stress-strain response for the thermomechanical in-phase case is given in Figure 8. The simulation is also satisfactory. Some of the differences between experiment and simulation arise from the variation of the elastic modulus in the specimens. The experimental results show a higher elastic modulus at the low temperature end than that used in simulations. This difference partly explains the higher inelastic strain range in the experiments compared to the simulations

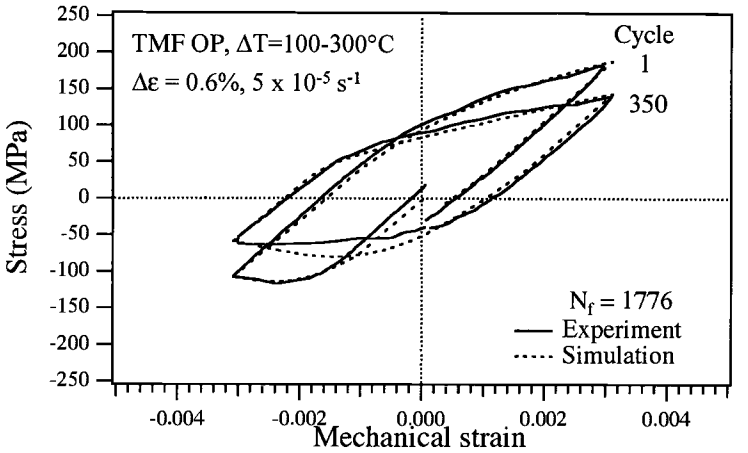

Figure 7 - TMF OP simulation and experiment for Al 319-T7B small SDAS material.

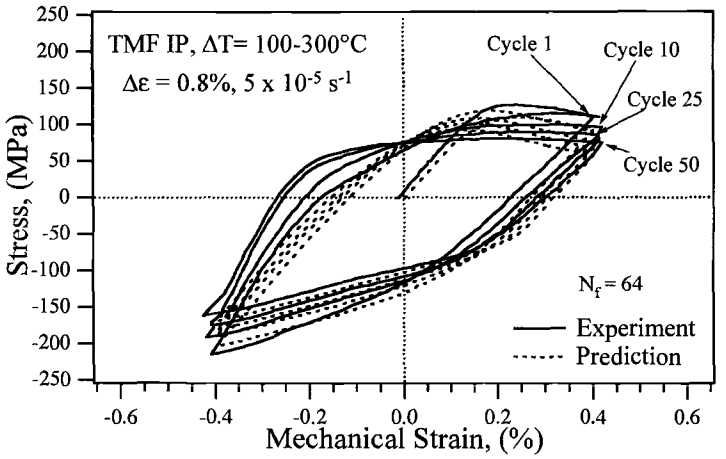

Figure 8 - TMF IP simulation and experiment for Al 319-T7B small SDAS material.

as shown in Figure 8. We also note that cyclic softening in Figure 8 is not as pronounced as in Figure 7. The fatigue life in this case was 64 cycles. Shorter lives were observed in all the TMF IP experiments compared to the TMF OP cases.

To gain insight into the experimental results and simulations, the stress range in all the TMF experiments are plotted against the mechanical strain range on a log-log plot as shown in Figure 9. The stress ranges for the first cycle ($N=1$) and for the half-life ($N_f/2$) are summarized for TMF OP and TMF IP cases. The stress ranges for the first cycle are similar for the TMF OP and IP cases. The solid line provides the predictions while the

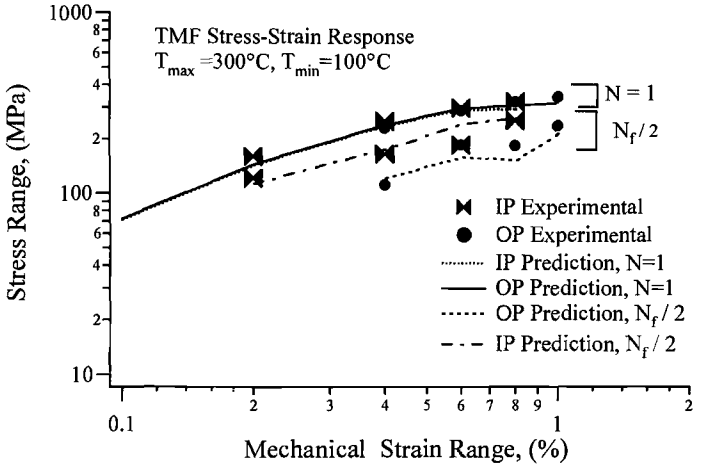

Figure 9 - Prediction of stress range for all TMF experiments for the first cycle ($N=1$) and at half-life ($N_f/2$).

data points represent the experimental results. The stress ranges for OP and IP cases are considerably different at half-lives. This difference is because the fatigue lives for the TMF IP cases are considerably shorter (by as much as a factor of ten), consequently, failure occurs before a significant decrease is observed in stress amplitudes. Overall, the decrease in stress range is almost a factor of two in some of the TMF OP cases. This is similar to the decrease observed under monotonic tension tests at room temperature after exposure to high temperatures for long periods of time.

To examine the capabilities of the model to simulate drag stress recovery, a virgin specimen was exposed to 300°C for a period of 192 hours (8 days), then the specimen was subsequently deformed in tension at room temperature. The experimental results (stress vs. inelastic strain) are shown in Figure 10 and are compared to the T7B material (with no thermal exposure, the highest curve on the plot), and the solutionized material (tested 0.5 hr after quench). The experimental results for the thermally exposed specimens exhibited apparent elastic modulus far lower than expected. Therefore, the data was reduced in two ways. The observed modulus of 30 GPa and also the expected modulus of 70 GPa were used and both results are included in Figure 10. There is a deviation between the two curves in the low strain regime but at higher strains the two curves converge. The simulations are shown for both the thermal exposure experiments and the T7B specimens with no thermal exposure. The simulations for thermal exposure experiments provide an upper bound on the experimental data. We note the remarkable agreement between the stress-strain curves of the solutionized material and the thermally exposed material. This points out the possibility that matrix behavior dominates the stress-strain response when there are no effective obstacles. Also, the agreement between the simulation and the experiment for the T7B treatment is remarkably close. We note that the strength level at room temperature (after thermal exposure) is nearly 2.5 times lower than that of the T7B aging treatment.

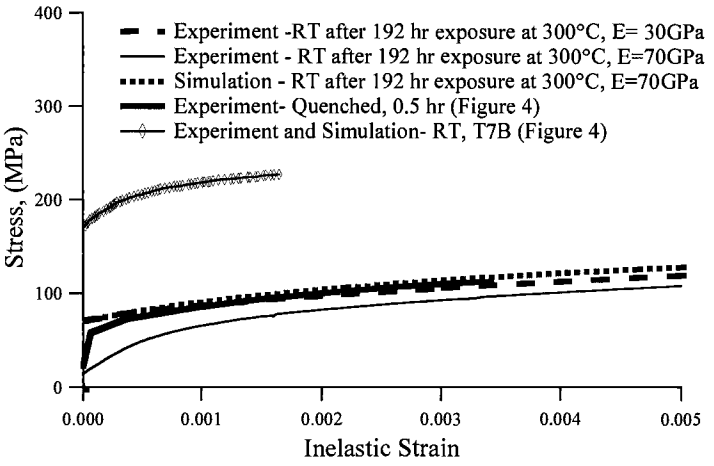

Figure 10 - Stress-strain response of small SDAS Al 319-T7B material after high temperature exposure as compared to the virgin material.

Discussion of Experimental Results

A two-state variable (back stress and drag stress) unified constitutive model was proposed to describe the stress-strain behavior of Al 319-T7B small SDAS under thermomechanical loading. This constitutive model provided successful simulations of the stress-strain response under a variety of conditions. We noted that significant recovery occurs in both the drag stress and the back stress due to thermal exposure at high temperatures for prolonged periods.

The work shows that the alloy with precipitates exhibits higher strength compared to the solid solution conditions (Figure 4). Mott and Nabaro *[11]* were the first to investigate the role of solute atoms in the strengthening of crystals. Their treatment considered the motion of a dislocation in the presence of solute atoms with a varying internal stress field. The average amplitude of the stresses over the dislocation segments was non zero and was found to be linearly dependent on the volume fraction of solute atoms, f, and the lattice mismatch strain. Their model predicted strengthening on the order of 10^{-2} G (where G is shear modulus) in Al-Cu alloys which is significantly higher than that observed experimentally. Mott and Nabarro's results were independent of the size of the obstacles. Later refinements for solid solution hardening resulted in a $f^{2/3}$ dependence *[12]*. Friedel and Fleischer's treatment *[13-14]* predicts a $f^{1/2}$ dependence and $\varepsilon^{3/2}$ dependence where ε is a measure of the misfit strains. Thermal activation effects have been disregarded in these models.

The strength of Al-Cu alloys, that have undergone aging to produce coherent precipitates, is strongly dependent on the precipitate lattice mismatch, the volume fraction and, the precipitate size. The lattice mismatch strains for the precipitates in Al-Cu alloys are non-spherical and for θ' precipitates the constrained strain in the [001] direction (normal to the precipitate plane) is as high as 0.34. A detailed discussion of the strengthening due to precipitates has been undertaken by Gerold and colleagues *[15]* and also by Nembach *[16]*. Upon calculating the force exerted by the obstacle on a dislocation, it has been shown that the strength depends on $(\varepsilon)^{3/2}(r.f)^{1/2}$ where ε is the lattice mismatch strain, and r, f denote the precipitate radius and volume fraction respectively. These results are applicable to coherent precipitates. We note that when both solid solution hardening and precipitation hardening is present, the resultant strengthening is measured in the experiments.

The Orowan relationship is most suited for the case of non-coherent precipitates. In this case the precipitates serve as pinning nodes for the dislocation lines and the strengthening is inversely proportional to the average distance between the particles. The strengthening is approximately proportional to $\sqrt{f}/r$. In the overaging case, the strengthening decreases with particle size in an inverse relationship. When cyclic softening occurs for the T7B microstructure over temperature and time the underlying precipitates lose their [001] habits and coarsen considerably. In the limit, when the distance between the precipitates become large, and large volume fraction of precipitates go back into solution the stress-strain response of the two microstructures approach each other. Other approaches to strengthening include the 'geometrically necessary' dislocation concept forwarded by Ashby *[17]* where the θ' plates rotate and create interface

dislocations in the matrix to maintain compatibility. Laird and colleagues predicted saturation stress levels of 200 MPa (corresponding to a plastic strain of 0.01) in Al-4% Cu alloys with θ' plates. In our case the strengthening levels at room temperature exceed the 200 MPa levels at plastic strain levels as low as 0.003. The Orowan relationship also resulted in strengthening levels of nearly 200 MPa. It is difficult to make quantitative comparisons with the present material because of additional contributions from Si and other elements via solid solution hardening.

The thermomechanical fatigue experiments demonstrated the marked softening in the Al 319-T7B alloys. The degree of softening is similar in the TMF OP and TMF IP experiments. However, since the TMF OP experiments exhibited much longer lives cyclic softening occurs to a larger extent in this case. The observations of cyclic softening are not limited to the TMF cases where maximum temperature was 300°C. In isothermal fatigue experiments at 250°C cyclic softening has also been considerable but the softening rate in the TMF case is more pronounced. The experiments at 150°C and at room temperature also exhibit cyclic softening but to a much lower degree than at the high temperatures.

The hardness of an Al-Cu alloy changes markedly upon holding at room temperature after quenching (Figure 4). This is attributed to the formation of copper enriched clusters, known as GP I zones. They have a plate-like shape, with the habit plane parallel to (100), and are continuous in structure (i.e. coherent) with the parent solution. Because the activation energy for nucleation and the critical nucleus size are very small for GP I than for the other three precipitates at low temperature, GP I forms athermally in quenched specimens. Therefore, when a comparison is made between the virgin specimens and those exposed to high temperatures the difference in the underlying precipitate structure should be noted.

The presented unified model possesses the minimum features to capture some of the complex material behavior trends observed experimentally. These are the gradual decrease in both the strength and the strain hardening upon exposure to high temperatures. Future modeling efforts will be needed to directly incorporate the volume fraction and precipitate spacing into the stress-strain relations. We note that the determination of interparticle spacing requires examination of numerous areas with different tilt angles using TEM. This is left aside for future research.

Summary

1. A two-state variable unified constitutive model is applied to describe the stress-strain response of Al 319-T7B small SDAS under thermomechanical loading. All material constants used in the model were established from experiments. The constitutive model can handle different strain rates, thermomechanical loading, and predict the marked softening in these alloys.
2. Because the fatigue lives observed under TMF OP cases are considerably longer than the TMF IP cases the degree of softening was significantly higher for the OP case. The stress-strain model captured these general trends accurately.

Acknowledgments

The work is supported by Ford Motor Company. Several experiments leading to the flow rule were conducted at Ford Research Laboratory (creep tests), Metcut (monotonic tests), and Westmoreland (high rate cycling tests). The support of Dr. John Allison and Mr. John Lasecki of Ford Motor Company is gratefully acknowledged.

References

[1] Smith, T.J., Maier, H.J., Sehitoglu, H., Fleury, E., and Allison, J., "Modeling High – Temperature Stress-Strain Behavior of Cast Aluminum Alloys," *Metallurgical and Materials Transactions A*, Vol. 30A, 1999, pp. 133-146.

[2] Sehitoglu, H., Qing, X., Smith, T.J., Maier, H.J., and Allison, J., "Stress-Strain Response of a Cast 319-T6 Aluminum under Thermomechanical Loading", *to appear in Metallurgical and Materials Transactions A*, 1999.

[3] Smith, T.J., Sehitoglu, H., Qing, X., and Maier, H.J., "The Influence of SDAS on the TMF Response of Al 319 Alloys," *Low Cycle Fatigue and Elasto-Plastic Behavior of Materials*, K-T. Rie, P. D. Portella, Eds., 1998, Elsevier Pubs., pp. 167-172.

[4] Baik, S. and Raj, R., "Wedge Type Creep Damage in Low Cycle Fatigue," *Metallurgical and Materials Transactions A*, Vol. 13, 1982, pp. 1207-1214.

[5] Bhat, S. and Laird, C., "Cyclic Stress-Strain Response and Damage Mechanisms at High Temperature," *ASTM STP 675*, 1979, pp. 592-623.

[6] Calabrese, C. and Laird, C., "Cyclic Stress-Strain Response of Two Phase Alloys, Part II. Particles not Penetrated by Dislocations," *Materials Science and Engineering*, Vol. 13, 1974, pp. 159-174

[7] Sehitoglu, H., "Thermal and Thermomechanical Fatigue of Structural Alloys," *Handbook on Fatigue and Fracture*, ASM (American Society for Metals), Ch. 19, 1996, pp. 527-554.

[8] Karayaka, M. and Sehitoglu, H., "Thermomechanical Fatigue Studies on Particulate Reinforced Al 2124," *Metallurgical and Material Transactions A*, Vol. 22A, 1991, pp. 697-708.

[9] Boileau, J., "The Effect of Solidification Time and Heat Treatment on the Tensile and Fatigue Properties of a Cast 319 Aluminum Alloy," *Proceedings of the 5th International AFS Conference on Molten Aluminum Processing*, AFS Inc. Des Plaines, IL, pp. 157-172.

[10] Slavik, D. and Sehitoglu, H., "A Constitutive Model for High Temperature Loading Part I.- Experimental Based Forms of Equations," *Thermal Stress, Material Deformation, and Thermomechanical Fatigue*, Sehitoglu, H. and Zamrik, S.Y., Eds., ASME PVP 123, 1987, pp. 65-73.

[11] Mott, N. F. and Nabarro, F. R., *Conference on Strength of Solids*, Physical Society of London, 1947, pp. 1-9.

[12] Labusch, R., "Statistische Theorien Der Mischkristallhartung," *Acta Metallurgica*, 1972, Vol. 20, pp. 917.

[13] Friedel, J., *Les Dislocations*, Gauthier-Villars, Paris, 1956.

[14] Fleischer, R. L., *The Strengthening of Metals*, Peckner, D., Ed., Reinhold Press, 1962, pp. 93-139.

[15] Gerold, V. and Haberkorn, H., "On the Critical Resolved Shear Stress of Solid Solutions Containing Coherent Precipitates," *Solid State Physics*, Vol. 16, 1966, pp. 675.

[16] Nembach, E., "Hardening by Coherent Particles having a Lattice Mismatch: The Effect of Dislocation Splitting," *Scripta Metallurgica*, Vol. 18, 1984, pp.105.

[17] Ashby, M.F., "The Deformation of Plastically Non-homogeneous Materials," *Philosophical Magazine*, Vol. 21, 1970, pp. 399-424.

R. P. Skelton,[1] G. A. Webster,[1] B. de Mestral,[2] and C.-Y. Wang[3]

Modelling Thermo-mechanical Fatigue Hysteresis Loops from Isothermal Cyclic Data

Reference: Skelton, R. P., Webster, G. A., de Mestral, B., and Wang, C. -Y., **"Modelling Thermo-mechanical Fatigue Hysteresis Loops from Isothermal Cyclic Data,"** *Thermo-mechanical Fatigue Behavior of Materials: Third Volume, ASTM STP 1371,* H. Sehitoglu and H. J. Maier, Eds., American Society for Testing and Materials, West Conshohocken, PA, 2000.

Abstract: A simple TMF facility is described which is capable of 'in-phase', 'out of phase' and 'diamond' type strain-temperature cycling. Typical TMF loops are presented for the 'diamond' type cycle for the nickel-base alloys IN100, Nimonic 90, IN738 and directionally solidified CM247LC-DS over the temperature range 400 °C-1000 °C. Alongside these results, isothermal cyclic stress-strain data are provided for ascending and descending strain amplitudes at discrete temperatures encompassing the strain and temperature range of the TMF tests. Testing on any individual specimen was terminated after a fixed energy consumption.

By superimposing the symmetrical isothermal loops about a common origin, the isothermal data are then used to predict the observed (asymmetrical) TMF behaviour. The method works well for materials which show history independence such as IN100. However, for some of the materials, slight modification to the procedure is required. The sensitivity of the method to the form of isothermal data is demonstrated.

Keywords: cyclic stress-strain response, isothermal testing, thermo-mechanical testing, counter-clockwise-diamond cycle, nickel-base superalloys

Introduction

Many components in service experience thermal transients during start-up and shut-down operations. Components can vary in thickness from 150 mm (e.g. pressure vessels and piping in conventional and nuclear power plant) to only several mm (gas turbine vanes and blades in modern aircraft and combined-cycle electric plant). It is therefore remarkable that of all the low cycle fatigue (LCF) tests at elevated temperature that have been undertaken in the past thirty years in support of lifetime calculations, relatively few have allowed the temperature to vary as well as the mechanical strain. The isothermal test is

[1]Research Fellow and Professor, respectively, Department of Mechanical Engineering, Imperial College, Exhibition Road, London SW7 2BX, UK.

[2]Engineer, Swissmetal Boillat, 2732 Reconvillier, Switzerland.

[3]Mechanical Engineer, Stork Comprimo Singapore Pte. Ltd., 4 Loyang Lane, #03-02, Singapore 508914.

certainly more simple to carry out, and the argument is usually put forward that isothermal data can be manipulated to predict service cycles of varying shape and magnitude. In contrast, a thermo-mechanical (TMF) test must be used to re-create a separate laboratory cycle to match every new service cycle that is introduced, for example, when maximum temperatures are increased in the interests of plant efficiency.

The uniaxial TMF test simulates a 'volume element' in components undergoing thermal transients and is generally complex, requiring computer control and careful experimental attention. In this paper, a simple TMF facility is described which is capable of 'in-phase' (IP), 'out-of-phase' (OP) and 'diamond' cycling. The latter cycle more faithfully reproduces conditions experienced by a gas turbine blade [*1*]. We are concerned with cyclic stress-strain (CSS) response and not cycles to failure but will nevertheless use the terms 'LCF' and 'TMF' for convenience. Great benefits can ensue if it can be demonstrated that TMF hysteresis loops can be predicted from LCF data. In this work, typical TMF loops are presented for the 'diamond' type cycle for some nickel-base alloys when cycled over the temperature range 400 °C-1000 °C. Alongside these results, isothermal CSS data are provided for ascending and descending strain amplitudes at discrete temperatures over the temperature range of the TMF tests. These isothermal data (where hysteresis loops are symmetrical) are then used to predict the asymmetric shape of the diamond TMF loops. Only relatively few specimens were tested owing to material availability. In accordance with previous work [*2*] testing on any individual specimen was terminated after an energy consumption of typically 0.25 J/mm^3 had been reached, to ensure that crack initiation had not occurred.

The purpose of this paper is therefore to investigate whether TMF loops may be predicted from isothermal data in several further alloys, as has been demonstrated already for IN100 [*2*].

Materials

Materials tested were (a) IN100, (b) Nimonic 90, (c) IN738 and (iv) directionally solidified CM247LC-DS. A chemical analysis is provided (Table 1). The Nimonic material was supplied as extruded bar which was further heat treated for 8 h at 1080°C followed by air cooling and 16 h at 700°C again followed by air cooling. Alloy IN100 was supplied as a cast billet of 75 mm diameter and no further heat treatment was given [*2*]. Alloy CM247LC-DS was supplied as offcuts from a cast slab [*3*] while the IN738 material was originally in the fir-tree root region of a cast industrial turbine blade that was not put into service [*4, 5*]. It was necessary here to friction-weld extension pieces (of Nimonic 115) to the extracted samples to provide laboratory specimens. All these materials are polycrystalline except for the CM247LC-DS alloy which had its [001] axis in the stress axis direction [*3*].

Table 1 - *Analysis of Alloys (wt-%), Balance Ni*

No.	Co	Al	Ti	Cr	Mo	V	Fe	Zr	W	Mn	Si	C	B
(a)	15	5.5	4.75	9.5	3.0	0.95	0.2	0.06	0.04	0.01	0.05	0.18	0.02
(b)	15	0.8	1.8	18.0	...	...	3.0	...	...	1.0	1.5	0.13	...
(c)	8.5	3.4	3.4	16.0	1.75	...	...	0.05	2.6	...	...	0.11	0.01
(d)[1]	9.2	5.6	0.7	8.1	0.5	...	...	0.02	9.5	...	...	0.07	0.02

[1]Also 1.5 Hf

Experimental Method

Isothermal Tests

The gauge length and diameter of the specimens were 12.7 mm and 6 mm respectively, except for Nimonic 90 specimens which were of 8 mm diameter. Heating was by means of RF induction, using a coil of approximately six turns with a gap to accommodate a side-contacting extensometer for strain measurement and control. The detector was of the capacitance type (unaffected by RF radiation) and the contacting arms were of high quality alumina for insulation against the RF coil. Reverse-load tests under symmetrical positive and negative strain limits were carried out on a machine of 100 kN capacity. Multiple step tests [*6, 7*] were carried out at a strain rate of 2×10^{-4}/s generally beginning in the elastic region, ascending to a total strain range not exceeding 1% (see below for CM247LC-DS), then descending to the elastic state. Some ten to fifteen strain steps were allowed in both ascending and descending modes with four cycles at each step. Hysteresis loops were recorded on the fourth cycle, giving the total strain range, $\Delta\varepsilon_t$, plastic strain range, $\Delta\varepsilon_p$ and the stress range, $\Delta\sigma$. Tests were carried out in the range 400 °C to 1000 °C, usually at 50 °C intervals but in some cases at 25 °C intervals. Limited numbers of specimens were available (six of IN100 and IN738; four of Nimonic 90 and two of CM247LC-DS) and in each case tests were grouped into neighbouring temperature bands as far as possible. Tests were stopped when energy consumption (cumulative areas of hysteresis loops) reached a level of 0.25 J/mm^3. Previous work [*2*] has shown this to be a reliable limit to guard against the onset of fatigue crack initiation which would invalidate the CSS results.

No periods were allotted to investigate possible evolutionary cyclic hardening and softening behaviour as previous experience has shown remarkable stability with these types of alloys [*8-10*]. However, in the case of Nimonic 90, fairly rapid initial softening was noted in the range 600 °C to 900 °C and this was allowed to be largely complete before embarking on a CSS determination. Also in the case of this alloy, *bi-thermal* types of tests were carried out whereby after four cycles at 800 °C, say, the temperature was quickly reduced to 600 °C at zero load, and careful attention paid to the first hysteresis loop at the lower temperature. The sequence was repeated in the reverse direction, and also for other temperature combinations. Such results were used in an attempt to refine the TMF loop predictions described later.

At each temperature, plastic strain range and stress range data from the hysteresis loop steps were fitted by least mean squares analysis to the power law equation:

$$\Delta\sigma = A\Delta\varepsilon_p^{\beta} \tag{1}$$

where A and β are constants. These values were obtained from tip-to-tip values of stress and corresponding plastic strain and is known as the locus method [*6, 7*]. Distinction was made between ascending and descending values of A and β.

Very limited testing was performed at one strain range only on alloy CM247LC-DS and the constants were determined from the actual *shape* of the tension-going curve, taking peak compressive stress as the origin. It was therefore more convenient to fit the relation:

$$\Delta\varepsilon_t = \Delta\sigma / E + (\Delta\sigma / A)^{1/\beta} \tag{2}$$

where E is Young's modulus determined from the linear unloading part of the loops at the respective temperature.

TMF Tests

Our TMF rig has features in common with other uniaxial facilities which have been developed over the past thirty years, in that the mechanical strain, ε_m, is defined as the difference between the total strain, ε_t, and the thermal strain, ε_{th}:

$$\varepsilon_m = \varepsilon_t - \varepsilon_{th} \tag{3}$$

Most systems employ hollow specimens in order to prevent transverse temperature gradients when temperature rise times are of the order 50 °C/s. But with more modest temperature rise and fall times of 4-6 °C/s in our work, the same solid specimens as are used for LCF tests could be employed. For the same reason, additional air cooling was not required to cool the specimen as lower temperatures were attained, the water-cooled grips being sufficient. Thus the convenient combination of a gauge-length expansion which is almost linear with temperature combined with (i) linear ramp rates supplied from the temperature controller and (ii) the programmable load-strain facility on the mechanical testing machine both facilitated development of a simple LCF rig for TMF purposes. In the case of non-linear expansion coefficients, corresponding mechanical ramp rates could be split into matching smaller linear segments, as desired. An inevitable gradient of some 10 °C existed *along* the gauge length and this was calibrated by comparing the output of thermocouples situated near the shoulder region of a dummy specimen with that of a thermocouple spot welded at the gauge centre.

Referring to the strain-temperature diagram (Figure 1) the working principle is as follows. Suppose the counter-clockwise diamond (CCD) path shown as the full lines is required (i.e. the mechanical component). Over the temperature range from T_{min} to T_{max} the free expansion and contraction are represented by the broken line (thermal component). According to Eq 3 the actuator on the testing machine must respond to ε_t which is given as the *sum* of the mechanical and thermal components. The controls are thus set to trace the offset diamond given as the bold lines in Figure 1. Conversely, the X-Y recorder requires only the mechanical component to display a meaningful loop, and arrangements must be made to *subtract* appropriate values of ε_{th} at each stage of the cycle by a suitable 'back off' signal.

To do this, a small computer program was written and connected to the system via an analogue/digital converter. In a typical test, the specimen is cycled from T_{min} to T_{max} and back again with the control system set to zero load. The thermal response is recorded continuously, overwriting each successive cycle. When the response has stabilised (usually after ten cycles), as becomes evident from chart recorders and the computer monitor, the output for the latest cycle is saved. This is 'played back' during each cycle during the test proper i.e. when mechanical straining takes place. Thus the correction was applied as a function of cycle time, and was reset at the start of each cycle. In fact the temperature controller, testing machine and computer all work from their own internal clocks which are synchronised at the beginning of each cycle by means of a pulsed signal. Finally, it may be noted that the 'thermal' signal does not necessarily indicate a true thermal expansion coefficient for the specimen gauge itself since it may contain the (stabilised) response of the extensometer detection unit and legs during cycling. The important point is that the thermal signal is eliminated, whatever the source. Repeated runs suggested an error of about 0.02% in total strain during the course of a day. Paradoxically, diamond type cycles were more convenient to carry out than either the IP or OP type because T_{min} occurs at the strain origin (see Figure 1).

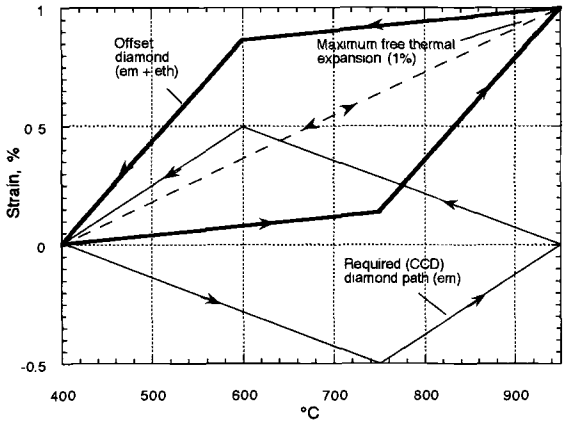

Figure 1 - *Generation of TMF Control Loop for IN738*

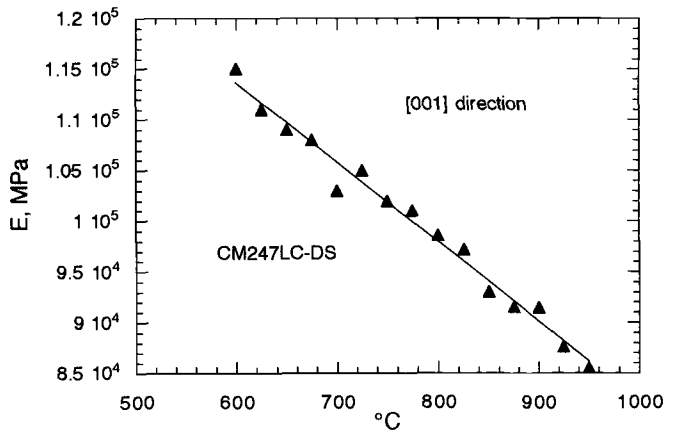

Figure 2 - *Example of Modulus of Elasticity Variation with Temperature*

Results

Isothermal Data

Values of Young's modulus at each temperature were determined from the linear unloading part of hysteresis loops (average of tension and compression arms). They were fitted to the following relation:

$$E = a - bT \tag{4}$$

where T and E are in MPa and °C respectively and a and b are constants. Values of a and b are provided (Table 2).

Table 2 - *Elastic Modulus Constants*

Alloy	a, MPa	b, MPa/°C	Example of Modulus at 800°C, MPa
IN100[1]	2.50×10^5	101	1.69×10^5
Nimonic 90	2.46×10^5	124.8	1.46×10^5
IN738	2.31×10^5	92.2	1.57×10^5
CM247LC-DS	1.61×10^5	78.5	9.82×10^4

[1]Ref. [2]

It is noted that the directionally solidified alloy gave a lower modulus value at all temperatures (Table 2 and Figure 2), in keeping with single crystal materials with the [001] direction aligned along the specimen axis [9].

As regards the elastic-plastic response (Table 3), locus values of A and β are listed for IN738 and curve-shape values for CM247LC-DS. The curve-shape method was also employed for the Nimonic 90 specimens (Table 4) which also gives representative values for the bi-thermal tests, discussed in more detail later. Values of A and β for alloy IN100 have been given in full in a previous paper [2]. Correlation coefficients in most cases were in excess of 0.95 for a typical set of fifteen data points. For lack of space, it is not possible to graphically summarise isothermal response for the alloys here: trends cannot be discerned from the curve-fitted values of A and β which should not be considered in isolation. The most satisfactory method is to use Eq 1 to calculate values of a 'cyclic yield stress' at a proof strain of say 0.0005 (0.05%) and plot these against temperature [2].

Hysteresis Loops Produced in TMF

In this work we restrict our examination to the CCD cycle, although tests on other forms have been completed. Referring to the required diamond path in Figure 1 (which applies to our tests on IN738), it is seen that peak tensile and compressive strains, ε_{max} and ε_{min}, do not occur at the temperature extremes of the cycle. Furthermore, these peaks (i.e. at 600 °C and at 750°C in the example of Figure 1) may be set to any values according to the

modelling application. In the present work, asymmetrical values have been used (Table 5). This means that strain rates differ in the various arms of the diamond, but these were arranged to be consistent with the isothermal values (1-2 × 10^{-4}/s). This corresponded to a loop cycle time of 2-4 min according to mechanical strain range and temperature span.

Table 3 - *Constants in Power Law (Locus)*

Temp., °C	IN738 (Ascending strain steps)		IN738 (Descending strain steps)		CM247LC-DS (Curve shape at maximum strain)	
	A, MPa	β	A, MPa	β	A, MPa	β
400	2683	0.108	54935	0.549	...	...
450	2776	0.107	44511	0.510	...	...
500	3818	0.156	27536	0.454	...	...
550	2992	0.126	3975	0.161	...	...
600	3161	0.135	4735	0.188	3861	0.121
625	...	...	...	...	2061	0.027
650	2335	0.082	4519	0.178	2393	0.046
675	...	...	...	...	11484	0.261
700	3537	0.145	10629	0.311	1821	0.008
725	...	...	...	...	14916	0.288
750	4623	0.185	16417	0.393	39764	0.383
775	...	...	...	...	23706	0.357
800	9109	0.335	11318	0.373	14417	0.298
825	...	...	...	...	31083	0.430
850	5844	0.293	18785	0.477	27221	0.430
875	...	...	...	...	12589	0.358
900	2956	0.215	4873	0.295	10701	0.358
925	...	...	...	...	11442	0.386
950	2927	0.250	10372	0.448	6926	0.321

Table 4 - *Power Law Constants for Nimonic 90 (Curve Shape)*

Temp., °C	Isothermal data		'Bithermal' data (UP)		'Bithermal' data (DOWN)	
	A, MPa	β	A, MPa	β	A, MPa	β
600	2225	0.107	3908	0.176	1753	0.083
650	2485	0.116	2464	0.123	2464	0.123
700	2399	0.110	2318	0.110	1857	0.082
750	2414	0.119	2163	0.111	2627	0.139
800	1530	0.085	1800	0.102	2144	0.132
850	1295	0.126	1338	0.130	1967	0.119
900	853	0.111	1692	0.161	1692	0.161

The experimental IN100 loop (Figure 3) was determined elsewhere [*11*] using a hollow specimen and air cooling in a totally computer-controlled facility and is included here for comparison with the present tests and also because our predictive method was quite successful for this alloy (Figure 3), see later. The plastic strain range at zero load was 0.26%. In contrast, the plastic strain for the Nimonic 90 alloy under less onerous conditions (Table 5) was 0.39% (Figure 4) while that for the IN738 alloy was similar at 0.296% (Figure 5). In complete contrast, the plastic strain range for the directionally-solidified alloy (Figure 6) was about 0.11%, at a much greater applied mechanical strain range. This was as a consequence of the low modulus value (Figure 1 and Table 2).

Table 5 - *Parameters of TMF Loops in CCD Cycling*

Alloy	ε_{max}, %	ε_{min}, %	T_{max}, °C	T_{min}, °C	Temp. at ε_{max}, °C	Temp. at ε_{min}, °C
IN100[1]	0.5	-0.5	1050	600	700	900
Nimonic 90	0.45	-0.45	900	600	700	800
IN738	0.5	-0.5	950	400	600	750
CM247LC-DS	0.8	-0.8	950	600	700	850

[1]Ref. [2]

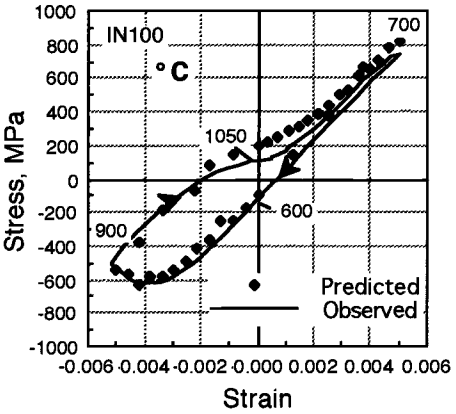

Figure 3 - *CCD Loops for IN100 [2]*

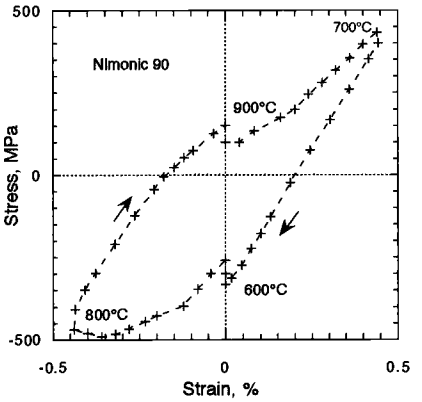

Figure 4 - *Observed CCD Loop for Nimonic 90*

For satisfactory rig operation, a dwell time of several seconds was necessary in each cycle at zero strain for synchronisation of clocks. For loops with large plastic strain this sometimes resulted in a short period of stress relaxation (Figure 4). Further, it might appear from these plots that the plastic strain range is somewhat greater in compression. However the strain at any point (other than at zero load) includes the elastic contribution from the

change in modulus with temperature, Eq 4. Between any two points 1 and 2 on a tension-going or compression-going curve it may be shown that this elastic contribution, δ, is given by:

$$\delta = \frac{\sigma_1 - \sigma_2}{b(T_1 - T_2)} \ln\left(\frac{a - bT_1}{a - bT_2}\right) \tag{5}$$

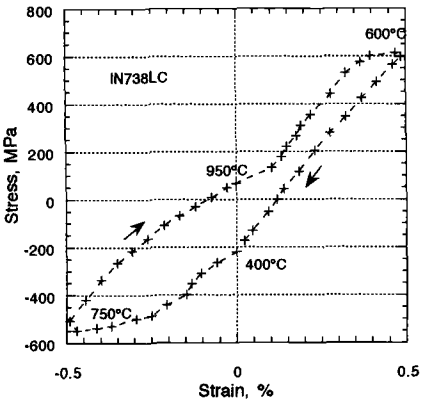

Figure 5 - *Observed CCD Loop for IN738LC*

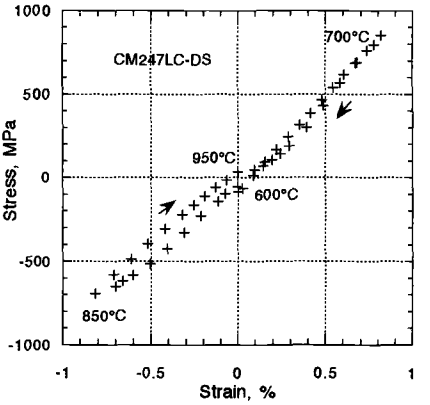

Figure 6 - *Observed CCD Loop for CM247LC-DS*

Prediction of TMF Loops

In order to construct TMF loops from symmetrical LCF loops, the latter are superimposed about their 'centroids' (Figure 7). The total strain range of each loop is equal to that of the TMF loop to be modelled. The method has been described previously [2] and the predicted results for IN100 are shown as individual points in Figure 3. The basic assumption is that in undergoing anisothermal cycling, deformation 'memory' of a material is independent of prior history. Thus in jumping from one loop to another at discrete strain intervals, deformation proceeds as if the material had always been on the new loop. The path taken among the loops can be pictured geometrically by superimposing the individual points of Figure 3 upon Figure 7. In practice one uses a strain-temperature diagram such as the required path shown in Figure 1, starting at peak compression and working anticlockwise towards peak tension, noting the increasing strain range at 25 °C intervals. At each station, Eq 2 is solved numerically and the corresponding stress *range* recorded. These are later converted to *actual* stresses and strains, having regard to sign. At peak tension a new origin is set up and the process repeated at the same temperature intervals (which do not necessarily imply equal increments of strain) until the cycle is completed.

If experimental data have only been collected at 50 °C intervals, to obtain sufficient points it is necessary to interpolate values of A and β. This technique has also been described fully elsewhere [2]. The most convenient method of solving Eq 2 is to set up a

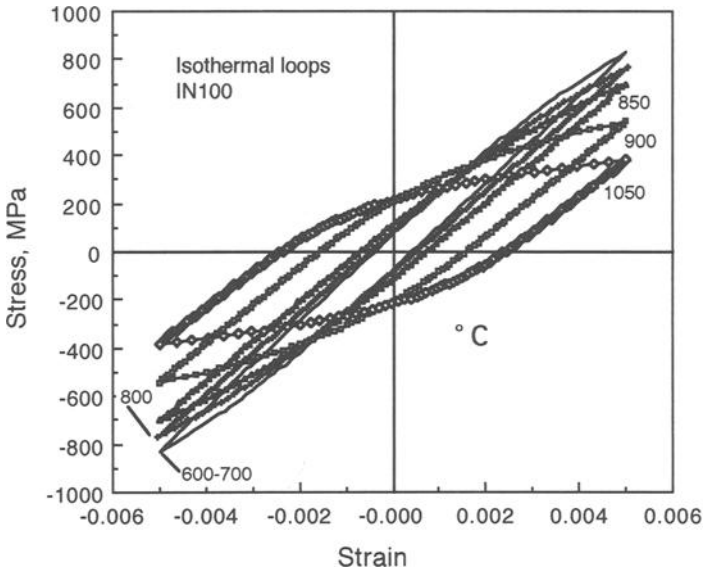

Figure 7 - *Superposition of Isothermal Loops for TMF Prediction [2]*

spreadsheet of values of temperature, strain range, E, A and β. In working round the diamond of Figure 1 it is apparent that each temperature (and corresponding E, A and β values) appears twice though of course the corresponding mechanical strains are different.

Using the above techniques, TMF loops were constructed for the remaining alloys. Using the 'ascending' parameters for IN738 in Table 3, the stress range is overpredicted (Figure 8), although the plastic strain range (0.26%) is in reasonable agreement, compare Figure 5. Using the 'descending' parameters, the stress range is similarly overpredicted (Figure 9), although the plastic strain range is now reduced at 0.17%. Using the data for CM247LC-DS from Table 3, the predictions are very good (Figure 10) as regards both the stress range and plastic strain range (0.15%), compare with Figure 6.

Attempts to simulate the loop for Nimonic 90 were not quite so successful. Using the 'isothermal' data from Table 4, several data points on the predicted TMF loop were subject to some scatter (Figure 11), the stress range was overpredicted, and the plastic strain range underpredicted at 0.21%, compare with Figure 4. In an attempt to refine the loop, 'bithermal' tests were conducted, some results having already been presented in Table 4. This work will be reported in detail separately. In conducting these tests, the idea was to 'freeze in' the microstructure in passing from a chosen high temperature to low temperature ('down' data in Table 4) or in the reverse direction ('up' data in Table 4). Appropriate values of A and β are selected from these tests according to the direction of temperature rise or fall in the TMF loop. The result (Figure 11) was a slightly wider loop (0.27% plastic strain range) at a somewhat lower stress range but still subject to scatter. This scatter was not present in the original isothermal and 'bithermal' curves.

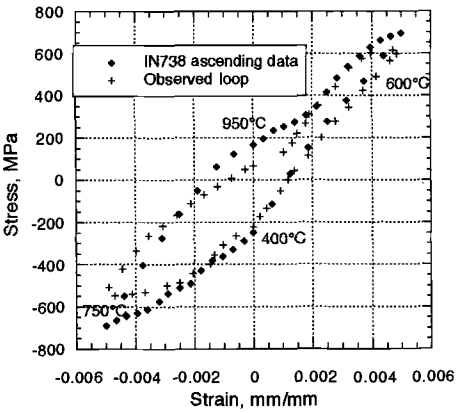

Figure 8 - *Predicted and Observed Loops for IN738 (i)*

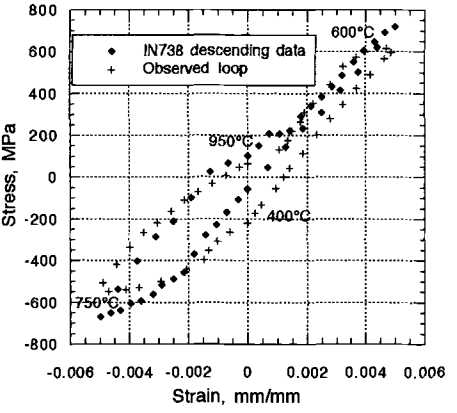

Figure 9 - *Predicted and Observed Loops for IN738 (ii)*

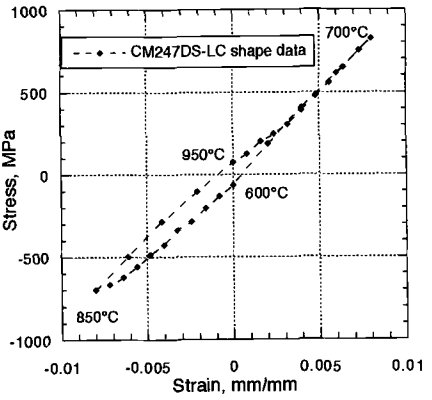

Figure 10 - *Predicted Loop for CM247DS-LC, compare Figure 6*

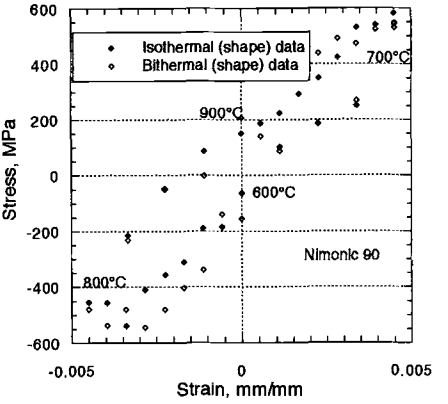

Figure 11 - *Predicted Loop for Nimonic 90, compare Figure 4*

To demonstrate the trend more clearly, the data were reworked using a one-element model and a kinematic hardening rule in ABAQUS [*12*]. This required fitting a bi-linear relation to power-law data. The method has been described previously [*11*] and results in a further smoothing out of the individual curves. The predicted TMF loop (Figure 12) is now more in line with the observed loop (Figure 4), the isothermal data giving a plastic strain range of 0.25% compared with 0.29% from the 'bi-thermal' data. This values still lie below the observed value of 0.39% (Figure 4). It is possible that since the TMF tests were performed after the LCF tests on the same specimens, further softening had occurred in Nimonic 90, unlike the case with the other alloys.

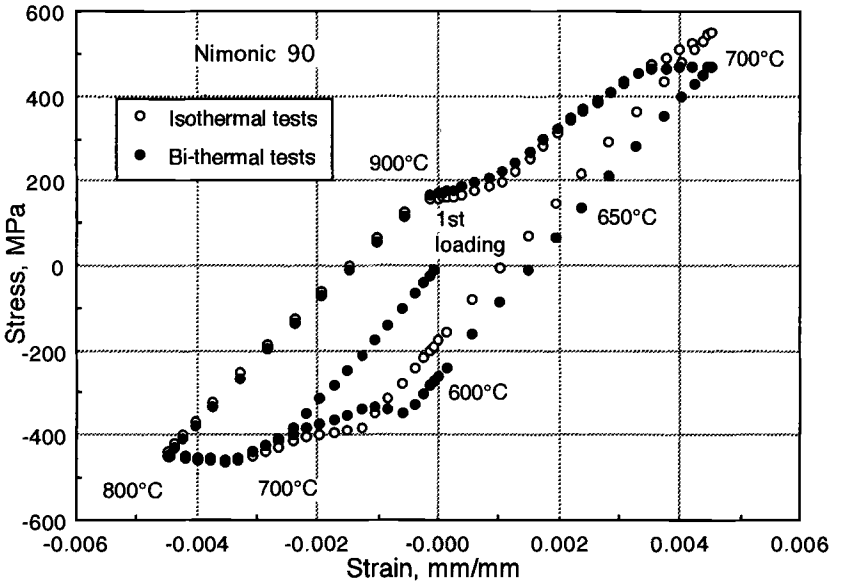

Figure 12 - *ABAQUS Calculation showing Sensitivity of Isothermal and Bi-thermal Approaches, compare Figure 4*

Discussion

As noted above, the testing rig was able to demonstrate IP, OP and clockwise diamond (CD) tests, though space reasons preclude a full discussion here. The first observation of note was that the OP test was not a mirror image of the IP test, as occurs for 1CrMoV steel for example [*13*], nor was the CD cycle in IN738 a mirror image of the CCD loop shown in Figure 5. Similar effects have been reported for TMF of a single crystal nickel-base alloy [*14*]. Key features of the loops for the IN738 alloy have been summarised (Table 6).

Table 6 - *Characteristics of IN738 in TMF at* ± 0.5% *between* 400° C *and* 950 °C

Cycle type	Turning point stress, MPa		Peak stress, MPa	Strain at peak stress, %	Plastic strain range, %	Loop energy[1], J/mm^3
CD	525	-610	575	0.43	0.35	2.48×10^{-3}
IP	350	-655	425	0.33	0.36	3.65×10^{-3}
OP	655	-360	-425	-0.36	0.32	2.92×10^{-3}

[1]Energy of CCD loop in Figure 5 is 2.31×10^{-3} J/mm^3

It is noteworthy that although the tests were conducted at the same total strain range of ± 0.5%, the energies expended per cycle (as denoted by hysteresis loop areas) were different and appeared to be most damaging for the IP cycle, see below.

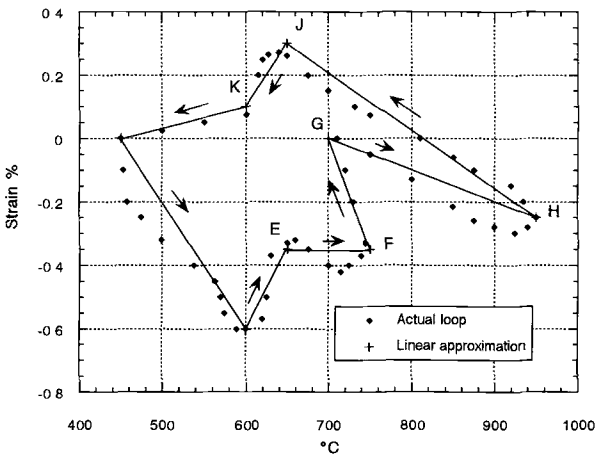

Figure 13 - *Representation of 'Industrial' Cycle [15, 17, 18] by Linear Steps*

The cycle experienced by industrial gas turbine blades [*15, 16*] is somewhat more complex (Figure 13); this example being taken from an experimental simulation [*17, 18*]. At point F there is an intermediate decrease in temperature and reduction of strain range to zero after initial start-up conditions before a continuation of the cycle at G during a more gentle loading towards the maximum temperature of the cycle. This loop was approximated in our rig by the eight steps shown as the straight lines in Figure 13, taking 6.75 min to achieve a closed cycle. The resulting hysteresis plot (Figure 14) contains a subsidiary loop FGH as has also been demonstrated by others [*17, 18*]. By comparing paths EFGJK in both Figures 13 and 14 the path round the complete cycle may be traced. Of course, in any

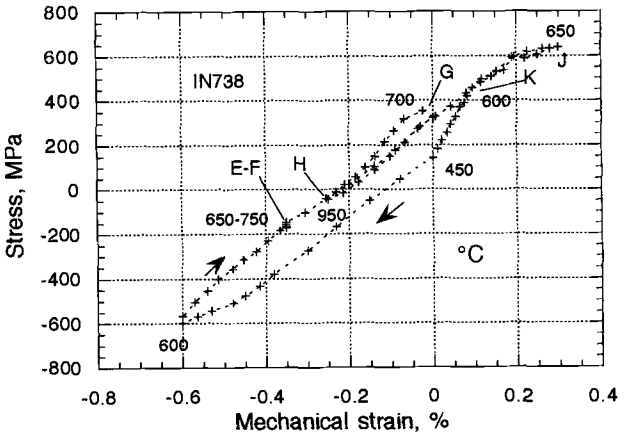

Figure 14 - *Observed 'Industrial' Cycle following Linear Paths of Figure 13*

assessment of fatigue damage based on energy considerations [2] the energy described in such subsidiary loops must be included. In principle it should be possible to predict this complex cycle from the construction shown in Figure 7 by setting up extra reference 'turning points' at G and H, in Figures 13 and 14.

As noted in Table 6, the measured cyclic energy of the CCD loop of Figure 5 is 2.31×10^{-3} J/mm^3. The energy of the predicted loop of Figure 8, which uses entirely the 'ascending' constants in Table 3 is, 2.50×10^{-3} J/mm^3 while that of the loop in Figure 9 which uses entirely the 'descending' constant is 1.63×10^{-3} J/mm^3 . As may be expected, a hybrid loop (not shown) which uses ascending constants for the tension-going direction and vice-versa for the compression-going direction has an intermediate energy of 2.04×10^{-3} J/mm^3.

In some TMF tests between 400 °C and 900 °C on precisely the same cast of IN738, Engler-Pinto found [*4, 5*] that cyclic energies were also greater for IP than for OP tests, the values at a total strain range of 0.7% being 7.0×10^{-4} J/mm^3 and 4.5×10^{-4} J/mm^3 respectively. At a lower strain range of 0.5% the values were 7.1×10^{-5} J/mm^3 and 3.3×10^{-5} J/mm^3 respectively. This implies that the loops cannot be mirror images. In contrast, other OP and IP work [*19*] on a separate cast of IN738 and at a much larger strain range of 1.5% shows a mirror image effect with a corresponding cyclic energy of 5.1×10^{-3} J/mm^3 though it should be noted that the temperature range was only between 750 °C and 950 °C. These observations have clear implications if energy summation is used as a fatigue damage parameter and a comprehensive investigation on the effect of strain range would be valuable. Some experiments show in fact that IP cycling is less damaging than OP cycling [*4, 5, 19*] while others show the opposite effect [*15*].

Conclusions

It has been shown that, for temperature rise and fall times in the range 4-6 °C/min, an existing LCF facility can be converted at moderate expense to produce TMF data for a variety of cyclic shapes. Use of isothermal cyclic stress-strain data in the same range tends to over predict the stress range and under predict the plastic strain range for the materials and hysteresis loops examined. These discrepancies can be reconciled to some extent by use of a cyclic energy parameter, which involves the counterbalancing product of stress range and plastic strain range giving a cyclic energy prediction close to that determined experimentally.

Acknowledgments

The authors would like to thank Drs. C. C. Engler-Pinto and F. Rézaï-Aria for supply of the cast materials. A discussion by one of us (R. P. S.) with Dr. B. Nath is gratefully recorded.

References

[1] Malpertu, J. L., and Rémy, L., "Thermomechanical Fatigue Behaviour of a Superalloy," *Low Cycle Fatigue, ASTM STP 942*, H. Solomon, Ed., American Society for Testing and Materials, West Conshohocken, Pa, 1988, pp. 319-341.

[2] Skelton, R. P., and Webster, G. A., "History Effects on the Cyclic Stress-strain Response of a Polycrystalline and Single Crystal Nickel-base Alloy," *Materials Science & Engineering*, Vol. A216, 1996, pp. 139-154.

[3] Blüm, M., Engler-Pinto, C. C., Jr., Meyer-Olbersleben, F., and Rézaï-Aria, F., "Grain Orientation and Size Effects on Thermal Fatigue Behaviour of CM247LC-DS," *Materials for Advanced Power Engineering, Part 2*, D. Coutsouradis, Ed., Kluwer Academic Publishers, Dordrecht, 1994, pp. 1099-1108.

[4] Engler-Pinto, C. C., Jr., Härkegård, G., Ilschner, B., Nazmy, M., Noseda, C., and Rézaï-Aria, F., "Thermo-Mechanical Fatigue Behaviour of IN738LC," *Materials for Advanced Power Engineering, Part 1*, D. Coutsouradis, Ed., Kluwer Academic Publishers, Dordrecht, 1994, pp. 853-862.

[5] Engler-Pinto, C. C., Jr., "Étude de L'Endommagement en Fatigue Thermo-Méchanique de Superalliages à Base de Nickel," PhD Thesis, 1996, EPFL, Lausanne.

[6] Skelton, R. P., "Cyclic Stress-strain Properties during High Strain Fatigue," *High Temperature Fatigue: Properties and Prediction*, Elsevier Applied Science, London, 1987, pp. 27-112.

[7] Skelton, R. P., "Bauschinger and Yield Effects during Cyclic Loading of High Temperature Alloys at 550°C," *Materials Science & Technology*, Vol. 10, 1994, pp. 627-639.

[8] Reger, M., and Rémy, L., "High Temperature, Low Cycle Fatigue of IN-100 Superalloy I: Influence of Temperature on Low Cycle Fatigue Behaviour," *Materials Science & Engineering*, Vol. A101, 1988, pp. 47-54.

[9] Gabb, T. P., Welsh, G., Miner, R. V, and Gayda, J., "The Low Cycle Fatigue Deformation Response of a Single Crystal Superalloy at 650°C," *Materials Science & Engineering*, Vol. A108, 1989, pp. 189-212.

[10] Milligan, W. W., Jayaraman, N., and Bill, R. C., "Low Cycle Fatigue of MAR-M200 Single Crystals with a Bimodal γ' Distribution at 760 and 870°C," *Materials Science & Engineering*, Vol. 82, 1986, pp. 127-139.

[11] Mallet, O., Engler-Pinto, C. C., Jr., Rézaï-Aria, F., Skelton, R. P., Nikbin, K., and Webster, G. A., "Influence of Material Stress-strain Characteristics on Thermomechanical Fatigue Analysis of IN100 Superalloy," *Materials at High Temperatures*, Vol. 13, 1995, pp. 47-54.

[12] 'ABAQUS 5.2 User Manual', Hibbitt, Karlsson & Sorensen, 1992.

[13] Beauchamp, D. J. and Ellison, E. G., "A Rig for Controlled Cyclic Strain and Temperature Testing," *Journal of Strain Analysis*, Vol. 17, 1982, pp. 45-52.

[14] Kraft, S., Zauter, R., and Mughrabi, H., "Aspects of High-Temperature Low-Cycle Thermomechanical Fatigue of a Single Crystal Nickel-Base Alloy," *Fatigue & Fracture of Engineering Materials & Structures*, Vol. 16, 1993, pp. 237-253.

[15] Viswanathan, R., *Damage Mechanisms and Life Assessment of High Temperature Components*, ASM International, Ohio, 1989, p. 433ff.

[16] Bernstein, H. L., Grant, T. S., McClung, R. C., and Allen, J. M., "Prediction of Thermal-Mechanical Fatigue Life for Gas Turbine Blades in Electric Power Generation," *Thermomechanical Fatigue Behaviour of Materials*, H. Sehitoglu, Ed., American Society for Testing and Materials, West Conshohocken, Pa, 1993, pp. 212-238.

[17] Meersmann, J., Ziebs, J., and Kühn, H.-J., "The Thermo-Mechanical Behaviour of IN738LC," *Materials for Advanced Power Engineering, Part 1*, D. Coutsouradis, Ed., Kluwer Academic Publishers, Dordrecht, 1994, pp. 841-852.

[18] Meersmann, J., Ziebs, J., Kühn, H.-J., Sievert, R., Olschewski, J., and Frenz, H., "The Stress-Strain Behaviour of IN738LC under Thermomechanical Uni- and Multiaxial Fatigue Loading," *Fatigue under Thermal and Mechanical Loading*, J. Bressers, Ed., Kluwer Academic Publishers, Dordrecht, 1996, pp. 425-434.

[19] Chen, H., Chen, W., Mukherji, D., Wahi, R. P., and Wever, H., "Cyclic Life of Superalloy IN738LC under In-phase and Out-of-phase Thermo-mechanical Fatigue Loading," *Zeitschrift für Metallekund*, Vol. 86, 1995, pp. 423-427.

Michael W. Woodmansee and Richard W. Neu[1]

Response of 60Sn-40Pb Under Thermal and Mechanical Cycling

Reference: Woodmansee, M. W. and New, R. W., **"Response of 60Sn-40Pb Under Thermal and Mechanical Cycling,"** *Thermo-mechanical Fatigue Behavior of Materials: Third Volume, ASTM STP 1371,* H. Sehitoglu and H. J. Maier, Eds., American Society for Testing and Materials, West Conshohocken, PA, 2000.

Abstract: An understanding of the internal mechanisms responsible for the enhanced deformation and degradation under combined thermal and mechanical fatigue in solder alloys is sought. Inelastic deformation can accumulate simply during unconstrained thermal cycling, –55°C to 125°C, in solder alloys due to the heterogeneous microstructure, the variation in properties, primarily the coefficient of thermal expansion, among the different phase and crystallographic grains, the low flow strength, and microstructural instability. To separate the effects driven by thermal cycling versus those driven by mechanical cycling, the local deformation and microstructural changes are tracked using independent interrupted thermal cycling and isothermal fatigue experiments. The deformation is measured by tracking surface roughness using a confocal scanning laser microscope. The accumulated deformation in 60Sn-40Pb under a –55°C to 125°C thermal cycle is significant. The accumulated deformation observed in two Sn-Ag base solder alloys as well as polycrystalline Sn under the same thermal cycle is notably smaller.

Keywords: thermomechanical fatigue, isothermal fatigue, thermal fatigue, lead-free solder, 60Sn-40Pb, confocal scanning laser microscope, heterogeneity, coefficient of thermal expansion mismatch

Introduction

Soldered interconnects in electronic packaging applications are expected to maintain an electrical, mechanical, and thermal connection between a component and a substrate. However, many electronic packages are subjected to moderate to extreme combined thermal and mechanical cycling conditions due to either the internal heating and cooling of the package itself or harsh external environmental conditions such as "under-the-hood" applications in automobiles. In addition, a better understanding is sought of the deformation and degradation behavior of solder alloys to determine the reliability of electronic packaging in aging weapons and advanced military systems as well as in the consumer electronics industry, which is continuously striving for smaller, more environmentally friendly packaging.

When designing electronic packaging, one potential failure mode that an engineer must consider is the aging and fatigue of the solder interconnects. The current industrial state-of-the-art methodology for evaluating this failure mode involves building prototypes of the proposed package design and subjecting these units to environmental loads and conditions which equal or supercede the harshness of the anticipated operating environment. To accelerate this process, wider temperature and strain ranges are often

[1] Graduate research assistant and assistant professor, respectively, The George W. Woodruff School of Mechanical Engineering, Georgia Institute of Technology, Atlanta, GA 30332-0405.

thought to compensate for using faster strain- and temperature-rates. The term "accelerated fatigue life testing" has been coined to describe this process. However, it is well recognized that different microstructural processes will govern a deformation depending primarily on its temperature, strain, strain rate, and previous deformation history. The validity of using a specific model will depend on the application for which it is being used.

Continuum mechanics-based models using an equivalent measure of the plastic strain amplitude are often used to predict fatigue lifetime, though, with various levels of success. When analyzing the behavior of small volumes such as solder interconnections, the continuum mechanics approach breaks down as the distribution of local stresses becomes highly heterogeneous when the reference scale is within one or two orders of magnitude of the characteristic microstructural length scale. Microstructurally based models are now being developed to better describe constitutive behavior when it is no longer valid to average local stresses over the bulk of the material.

In the case of 60Sn-40Pb, a ubiquitous solder alloy, the homologous temperature is high even at room temperature ($T / T_{melt} = 0.63$). The melting temperature of solder alloys is anywhere from 180°C to 300°C depending on the composition with 60Sn-40Pb being near the lower end. Soldered interconnects in an electronic packaging can be exposed to temperatures ranging from –55°C to 125°C (T / T_{melt} ranging from about 0.45 to 0.90), depending on the specific application. In fact, solder alloys are often employed at significantly higher homologous temperatures than other traditional "high" temperature structural alloys. For example, the homologous temperature ranges typical of titanium alloys and nickel base superalloys are 0.25 to 0.55 and 0.20 to 0.70, respectively. Because of the high homologous operating temperature, the deformation and degradation mechanisms of solder alloys are much more likely to be dominated by time-dependent and thermally-activated processes such as creep, stress relaxation and microstructural instability when compared to these other traditional high temperature structural alloys.

As background for understanding the thermal and mechanical behavior of solder alloys, it is fruitful to revisit the classical work of Boas and Honeycombe [*1*]. They studied the inelastic deformation in non-cubic metals (99.85Sn, 99.97Zn, 99.97Cd) and a cubic metal (99.99Pb) under unconstrained thermal cycling between 30°C and 130°C. They found that local deformation accumulates under unconstrained thermal cycling in the polycrystalline non-cubic metals but not in cubic metals. They further provided convincing evidence that the mechanical actuation of this deformation is due to the anisotropy in the coefficient of thermal expansion (CTE) in the non-cubic metals. In a polycrystalline metal, a local mismatch in CTE occurs resulting in the generation of local stress. This behavior is also likely to be observed in metal alloys where the adjacent phase grains also will have different CTE (and possibly anisotropic ones). For example, the CTE of Pb is $29.3 \times 10^{-6}\ C^{-1}$ and that of Sn along two orthogonal axes are $32.9 \times 10^{-6}\ C^{-1}$ and $16.6 \times 10^{-6}\ C^{-1}$. In fact, the observations of Boas and Honeycombe led them to coin the term "thermal fatigue" to describe this phenomenon.

In the case of Sn, it was found that the majority of the inelastic deformation induced by the thermal cycling was due to grain boundary migration, a high temperature creep mechanism. The motion of the grain boundaries was tracked by examining impressions left by the grain boundary as it moved from cycle to cycle. Based on their observations, it was theorized that the grain boundary migration was most active during the cooling part of the thermal cycle. This is presumably the part of the cycle when the most thermal energy was available in the material to drive dislocation climb.

In more recent work on the alloy of 60Sn-40Pb, the microstructure was found to coarsen homogeneously during unconstrained thermal cycling between –55°C and 125°C but coarsened heterogeneously along bands when constrained to produce a shear-dominated thermomechanical cycle [*2*]. Although no damage accumulation (i.e., cracking) was observed during the thermal cycling experiment, cracks initially formed within the coarsened bands inside Sn-rich phase, at Sn-Sn grain boundaries when exposed to thermo-

mechanical shear loading. Cracks across Pb-rich regions formed only after the Sn-rich phase failed. It has also been shown that such cracks propagate initially through Pb-rich phases [*3*] and primarily along phase grain boundaries [*4*]. Others have found that cracking occurs between Sn-Sn grain boundaries as well as along boundaries between the Sn-rich and Pb-rich phases [*5*]. Frear et al. [*2*] hypothesized that the coarsening of the material within the bands made it more susceptible to damage because the large-grained Sn-rich phase could no longer accommodate the imposed shear stresses by rotating and sliding along grain boundaries. Roughened bands developed on the surface parallel and perpendicular to the direction of shear. These roughened bands also correlated the coarsening of the phases. The crystallographic grains within the Sn-rich phase were found to grow from an initial size of 0.4 μm to a final size of 3 μm after 2000 thermomechanical cycles. While the extrinsic CTE mismatch between components in an electronic package is most often mentioned as a cause of failures in electronics packages, no discussion is made of the intrinsic CTE mismatch within the solder either between the Pb and the Sn phase. Nor is any discussion made regarding the directional CTE mismatch within the Sn phase due to crystallographic anisotropy as a driver for enhanced deformation and degradation.

In more traditional high temperature structural materials, the evolution of the microstructure has also been observed during thermomechanical fatigue. For example, precipitate phases can partially dissolve at elevated temperatures and re-precipitate at lower temperatures [*6*], rafts may form on glide planes [*7*] or plates may form perpendicular or parallel to the stress axis for uniaxial tension or compression tests, respectively. In addition, the arrangement of dislocations can be dependant on the cyclic phasing and on the temperature range and extremum [*8*].

The homologous temperature is sufficiently high for a diffusion-controlled mechanism to govern phase grain coarsening near and above room temperature. Significant phase grain coarsening in 63Sn-37Pb easily detectable in an optical microscope has been observed in near eutectic Sn-Pb alloys with exposure to room temperature after one year, though this coarsening continues and significant changes have been seen after 15 years [*9*]. Any elevated temperature above room temperature accelerates the coarsening process. A quantitative correlation between the coarseness of the microstructure and a steady-state creep rate can be determined [*9*]. In the early stages of isothermal aging at room temperature, the flow strength of 60Sn-40Pb decreases logarithmically with aging time [*10*].

This paper summarizes some unique experiments aimed at better understanding and quantifying the heterogeneous deformation and degradation and aging processes in solder alloys under both unconstrained thermal cycling and isothermal fatigue by tracking both inelastic deformation and coarsening. This type of experimental information may be useful in identifying the differences in the deformation and degradation processes between traditional and nontraditional solder alloys in electronic packaging applications. In addition, well-controlled experimental methods are needed to help develop and verify more sophisticated reliability models that take into account the heterogeneous nature of the deformation and degradation processes usually occurring at a scale just below the size of the interconnect itself.

Experimental Method

Thermal Cycling Procedure

Specimen Preparation – Small flat plate specimens (approximately 9 mm x 14 mm x 2 mm) were cast from 60Sn-40Pb, 96Sn-4Ag, 99.9Sn, and 96.2Sn-2.5Ag-0.8Cu-0.5Sb (Castin™) bar stock using a three-piece sandwich-type screw mold [*11*]. The liquidus temperatures of these metals and alloys are approximately 190°C, 228°C, 232°C, and 215°C, respectively. The mold consisted of a thin stainless steel stencil containing the

outline of 12 specimens sandwiched between two large blocks of aluminum. Small pieces of solder were cut from the bar stock and placed in a large threaded hole on one of the aluminum sides. A screw was inserted and the mold was heated over a hot plate. The temperature was monitored using a thermocouple placed between the mold halves. Once the mold reached a temperature 30°C above the liquidus temperature, the mold was stood upright so that when the screw was turned, the molten solder was driven into the cavity formed by the stencil from the bottom and forced air out of the top. Once the mold cavity had been filled with molten solder, the mold was quenched in cool water. The mold was then disassembled and the specimens were removed.

The specimens were then prepared for manual grinding and polishing by mounting two at a time onto the flat side of an aluminum block using double sided tape. The specimens were ground on a manual polisher / grinder using progressively finer grits of silicon carbide wet / dry sandpaper (500, 1200, 2400, and 4000 grit) and constant water lubrication. Polishing was then performed using a cloth embedded with a 0.4 μm colloidal silica polishing suspension. An oil-based lubricant was also used during the final polishing step to insure the appropriate friction. The specimens were then cleaned using ethanol and a cotton swab so that the surface was clear of residual silica suspension. Each specimen was carefully removed from the aluminum block using a knife. A light cross was etched into the surface of each specimen using a utility knife with light pressure to provide a reference to repeatedly locate the same area on the specimen for tracking the evolutionary changes. The microstructure of the as-cast 60Sn-40Pb, which is the main focus of this paper, is shown in Figure 1. The microstructure consists of Pb-rich (darker) phase grains in a Sn-rich (lighter) phase.

Thermal Cycling – The specimens were placed in a tube constructed out of Pyrex glass with stop cocks at each end. It was designed to be gas impermeable to provide an inert environment for the specimens during testing, so that the influence of oxidation on the surface could be minimized. Specimens were inserted and removed from the thermal

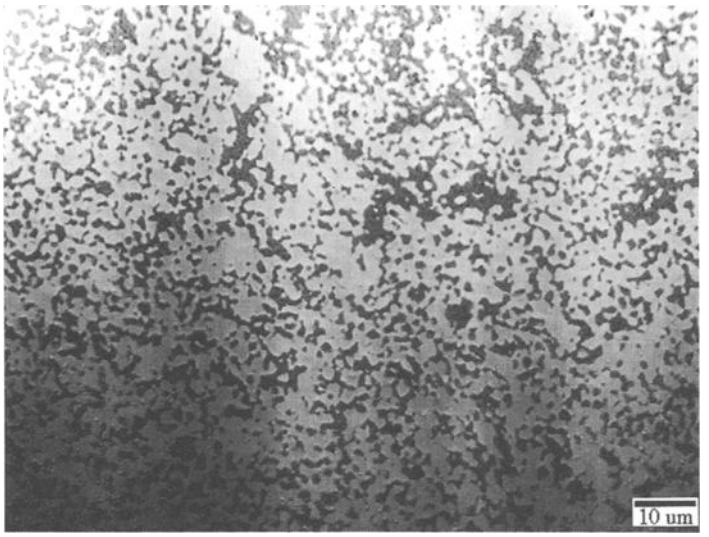

Figure 1 – *Microstructure of as-cast 60Sn-40Pb.*

cycling tube using a palate fabricated from brass. The tube was evacuated using a vacuum pump and backfilled with Argon gas.

The thermal cycling was performed in a Thermotron automatic thermal cycling oven (model ATS-320-DD-10-705-LN2, range 200°C / –73°C). The Thermotron is a three-compartment double-basket transfer system with nichrome heaters that provide heating for all three compartments and a refrigeration system in the center cold box. The cascade refrigeration system circulates chilled liquid refrigerant through evaporator coils in the cold box plenum. A liquid N_2 cooling system injects liquid nitrogen when the cooling demand is at full throttle. The three-compartment double-basket transfer system was designed so that as thermal cycling takes place the two boxes are 180° out of phase as they rotate between compartments essentially doubling the capacity of the system. The transfer system did not rotate continuously but operated in ramp and hold fashion. A gaseous N_2 purge injects gaseous nitrogen into the compartments to reduce the amount of moisture and oxygen present during heating. Cycle time was set to one hour, with 20-minute holds at the extremum temperatures of –55°C and 125°C. The temperature ramp time was deemed sufficiently slow enough such that the small flat plate specimens were continuously exposed to a quasi-static temperature environment with negligible thermal gradients within the specimen. The specimens were examined after 100, 200, 400, and 800 cycles to observe progressive changes on surface.

Isothermal Fatigue Procedure

Specimen Preparation – The isothermal fatigue tests were conducted on a conventional servohydraulic fatigue test system. Therefore, a modified-version cylindrical dumbbell specimen was used. First, the specimen blanks were cast from 60Sn-40Pb bar stock using a two piece, six-up, cylindrical cavity mold. The blanks were about 13 mm in diameter and 114 mm in length. Once the blanks had been reduced to a rough length of 104 mm on a vertical band saw, the ends were faced and center drilled on a manual lathe. Cylindrical dumbbell specimens were machined from the specimen blanks on a CNC lathe. The gage section diameter was 6.35 mm and gage length was 12.7 mm. Threads were also machined on the lathe to screw into the grips. The specimens were then modified for ease of polishing and tracking the surface changes. This was accomplished by manually milling two opposite sides of the specimen reducing the overall thickness along the entire length to 5.08 mm.

Each isothermal fatigue specimen was polished individually in the same manner as the thermal cycling specimens using an aluminum block with double sided tape and a cloth saturated with 0.4 μm colloidal silica suspension on a manual grinder / polisher. A light cross was etched into the surface of the polished gage section for reference in the same manner mentioned earlier.

Isothermal Cycling – Each dumbbell specimen was tested on a servohydraulic thermomechanical fatigue test system consisting of a 90 kN load frame with a 45 kN load cell, a MTS TestStar II control system, and a thermal chamber with its own control system. The thermal chamber was designed in-house specifically for isothermal and thermal cycling in the range of –60°C to 200°C. Both the temperature and the mechanical actuator were controlled independently by separate closed-loop control systems linked through the TestStar II control system. The desired temperature was maintained by controlling the flow rate of either hot or cold nitrogen gas through injection nozzles placed in the insulated thermal chamber. The nozzles were directed away from the specimen to minimize thermal gradients within the specimen during heating and cooling. Numerous thermocouples attached to a dummy specimen indicated that the temperature variation within the gage section of the test specimen was ±1°C. The use of liquid and gaseous nitrogen to control temperature also provided a nitrogen-rich atmosphere within the thermal chamber to mitigate surface oxidation on the specimen. The isothermal fatigue

tests were performed at a strain amplitude which would be approximately equivalent to the mechanically-induced strains under a complete thermal cycle. Based on the aggregate CTE of 60Sn-40Pb which is approximately 25. x 10^{-6} $°C^{-1}$, the thermal strain range under thermal cycling was 0.45% strain. This would also be the mechanical strain induced in a thermomechanical experiment where temperature was cycled –55°C to 125°C while the ends of the gage section were fully constrained. The testing was performed in displacement control to minimize bending due to the force of extensometer rods. The displacement range was calibrated to be equivalent to mechanical strain range of 0.45% in the gage section of the isothermal fatigue specimen. The ramp-rates and hold times imposed under isothermal cycling were the same as those experienced under thermal cycling. Therefore, the total cycle time was 1 hour. The isothermal tests were carried out to only 100 cycles due to time and resource constraints.

Surface Observation and Quantitative Methods

The purpose of this investigation was to obtain a quantitative measure of the local deformation and degradation after thermal cycling and isothermal fatigue. The criteria for selecting a method for tracking the heterogeneous deformation observed on the specimen surfaces included the need for a high-resolution z-axis scanning capability and an ability to track the evolution of the surface at a particular point. The z-axis is the direction out of the plane of the sample for surface topography measurements. The ability to provide visual imaging of the surface as well as topographical data was also important so that the heterogeneity of surface deformation could be correlated to the coarsening of the microstructure. Two newer microscopic methods were tried: the confocal scanning laser microscope and the atomic force microscope.

Confocal Scanning Laser Microscope (CSLM) – The confocal scanning laser microscope (Lasertec 1LM21) utilizes a He-Ne laser as a focused light source along with a focus scan memory to construct extended focus images of surfaces that have a large depth of field without sacrificing lateral resolution (0.25 μm resolution). The microscope operates by scanning the focal plane in the positive z-direction, across the surface of the specimen, by adjusting the stage position. A focused image is constructed by memorizing the stage position at which the CCD image sensor detects maximum intensity of laser light reflected from the specimen surface. A point of high intensity on the sensor represents the point of sharp focus. Special software developed for use with the CSLM creates grayscale images where shades of gray represented degrees of z-axis depth. These images were sectioned to give a surface profile that was characterized quantitatively by surface roughness, using the method described by ISO 4287/1. The process of acquiring a digital image, converting it to a topographic grayscale image and taking surface profiles from that grayscale is illustrated in Figure 2. The as-polished surface of the isothermal fatigue specimens had an initial arithmetic roughness (R_a) of 0.10 ± 0.02 μm and a RMS roughness (R_q) of 0.13 ± 0.04 μm. For the thermal cycling specimens, the initial R_a was 0.033 ± 0.004 μm and the initial R_q was 0.040 ± 0.006 μm.

It is most likely that the discrepancy between the initial roughness for the isothermal fatigue specimens and that for the thermal cycling specimens is due to a combination of the limited resolution of the CSLM and some tilt which was present in the larger isothermal fatigue specimens which was not present in the thermal cycling specimens, due to differences in their fabrication processes. Any tilt in the specimen led to detectable surface roughness increases despite the application of a "mean line" feature in the software that compensated for large wavelength trends on a linear surface profile. Smooth sloped surfaces are read by the CSLM as small step profiles when the readings are the same order of magnitude as the resolution and these step profiles are transformed into saw tooth profiles by the mean line feature. The portion of the surface roughness due to these saw teeth was an artifact of the microscope. Still, it was fortunate that the

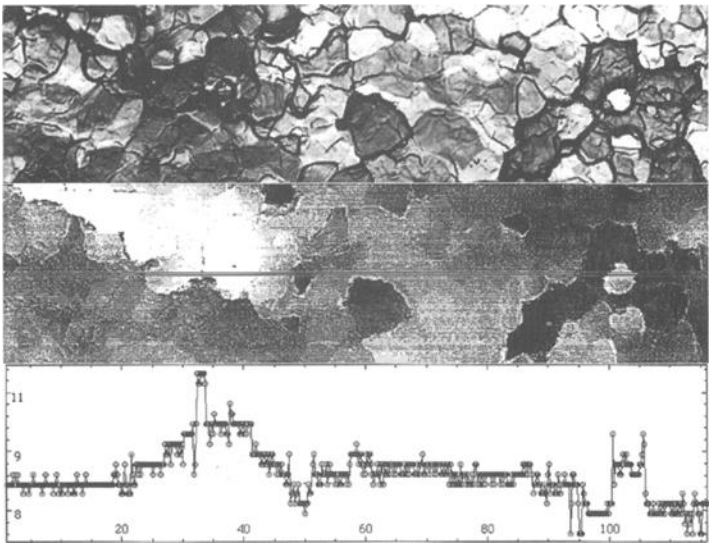

Figure 2 – *Surface profilometry using a confocal scanning laser microscope (units are in μm).*

isothermal fatigue samples began with some surface tilt. Even with careful alignment of the load train, the flat dumbbell specimens still tended to exhibit non-uniform deformation along the gage length with some buckling after a number of fatigue cycles. Fortunately, the relative changes in the surface roughness in the isothermal fatigue tests were found to provide a good measure of the relative surface deformation since the tilt in both the initial and final surfaces affects the mean line feature in the same manner. In the case of the thermal cycling, the samples maintained a flat surface within the resolution of the CSLM so the changes in roughness measurements could also be attributed to the surface deformation from thermal cycling.

Atomic Force Microscope (AFM) – The atomic force microscope used in this study (Burleigh, Metris 2000) employed a sharp silicon nitride probe attached to a cantilever type spring. During contact scanning mode as the probe traverses the sample, the specimen is raised and lowered by a PZT actuator in order to maintain a constant atomic force between the tip of the probe and the sample surface. A laser light detector is used to measure the deflection of the probe and this information is used as the input for the closed-loop actuator controller. The AFM generates topographical images that have a published z-axis resolution which ranges from 0.2 μm for the greatest X-Y scan range (70 μm x 65 μm area) to 0.005 μm for the smallest. For this application, the greatest scan range was employed. The specimen was rigidly mounted inside the AFM and could not be moved without retracting the probe sensor from the surface of the specimen. Image acquisition times ranged from a few minutes to a number of hours depending on the settings used and the desired resolution to be achieved. The quality of the image also depended on the settings used on the PID controller and this varied from surface to surface.

Evaluation of Methods – An increase in surface roughness can be attributed to deformation occurring between phases or grains due to grain boundary sliding or migration

or deformation within grains due to the development of persistent slip bands or the migration of dislocation subgrains and cells. Of the methods evaluated to monitor changes in surface roughness and microstructure, the CSLM was found be the most fruitful. The conventional optical microscope was only able to provide qualitative image information and was utilized as means to supplement data from the atomic force microscope, had it been used as the primary tool. The AFM that was used had a number of limitations including a sample size limit, a relatively small maximum flatness tolerance, scan times upwards of 100 minutes needed to acquire useable image data, and it had no surface imaging capabilities accompanying the topographical information needed to differentiate between phase grains. In addition, it was nearly impossible to return to the same place on the specimen surface to make sequential observations (i.e., after cycle blocks) using the AFM. The CSLM was found to provide the ideal combination of optical surface pictures and high-resolution topographical data without any of the aforementioned limitations associated with the AFM. In addition, the CSLM generated optical images far superior to the conventional light microscope because of the deep focal range utilized by the CSLM. The complete scan time was about 10 seconds. Therefore, the CSLM was utilized as the primary tool since it provided both quantitative data in the form of surface profiles and roughness measurements as well as qualitative information in the form of high magnification images with a wide focal depth. The particular CSLM unit that was used produced a minor artifact on each of the optical images that can be seen as a shaded field in the lower right and left corners. It is likely that the CCD image sensor used to detect laser light reflected from the specimen surface was not uniform for the unit used for this work. However, this artifact did not appear to influence the microscope's ability to construct accurate z-axis grayscale images.

The surface roughness was monitored at four different locations defined by the four quadrants of the cross etched on the surface near the center of each specimen. The spacing between the locations was about 400 μm. At each location, four linear profiles were taken at 0°, 45°, 90°, and 135° rotation from the 88 μm by 115 μm field of view (100x objective magnification) for a total of 16 linear profiles per specimen, per block of cycles. The profile values, provided directly by the imaging software on the CSLM, were then averaged to find a RMS roughness height and a 95% confidence interval for the sample.

Experimental Results and Discussion

Qualitative Observations

Thermal Cycling – After 800 thermal cycles from –55°C to 125°C, the surface appearance from the CSLM is shown on the left side in Figure 3. The surface appeared to increase in roughness from the initial as-cast state (i.e., the appearance in Figure 1). Z-axis grayscale images were collected on the CSLM to evaluate the topography of the specimen surface such as shown in Figure 2, which was taken from the same specimen. It could generally be seen by inspection of the corresponding optical and grayscale images that much of the deformation in the thermally cycled specimens occurred along phase grain boundaries and the enhancement of the phase grain boundaries reflects a shadow developed by a step caused by the protrusion of one of the phase grains. In addition, the cycled 60Sn-40Pb specimen was bifurcated using a utility knife and one half was polished to obtain a better view of the final phase grain distribution. This micrograph is shown on the right side in Figure 3. In this figure and all subsequent figures showing both the surface and microstructure, it should be pointed out that the locations are not exactly the same, but they are in the same general region.

Isothermal Fatigue – The changes in the CLSM surface appearance and phase grain distribution after 100 isothermal fatigue cycles at –55°C, 35°C, and 125°C are shown in Figures 4-6, respectively. For all isothermal mechanical cycling images, the

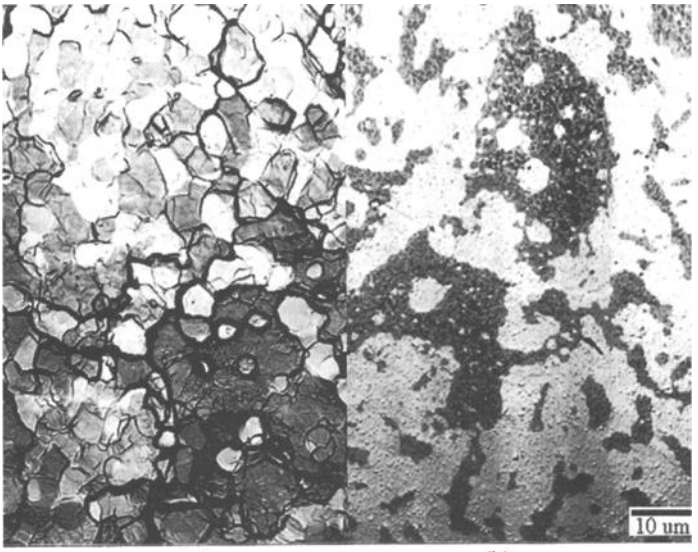

Figure 3 – *Unpolished (a) and polished (b) surface of 60Sn-40Pb after 800 thermal cycles.*

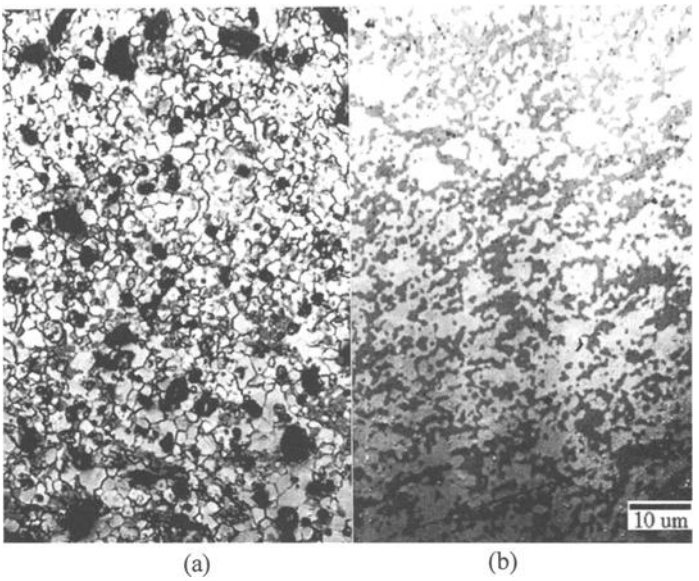

Figure 4 – *Unpolished (a) and polished (b) surface of 60Sn-40Pb after 100 isothermal cycles at –55°C.*

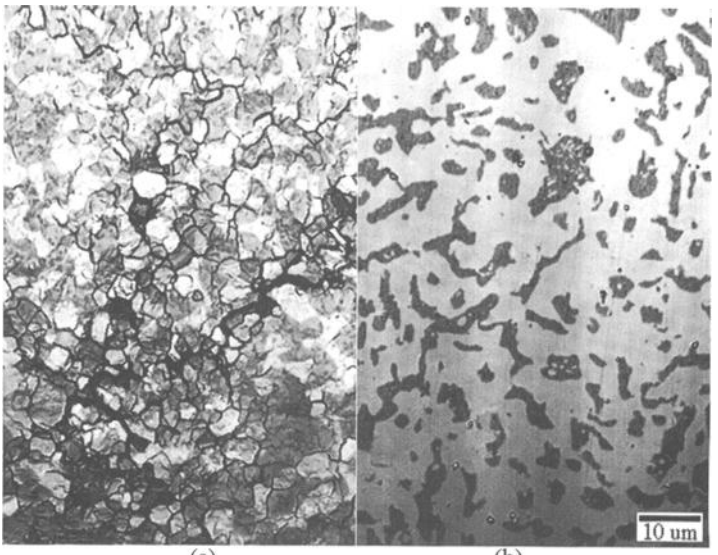

Figure 5 – *Unpolished (a) and polished (b) surface of 60Sn-40Pb after 100 isothermal cycles at 35°C.*

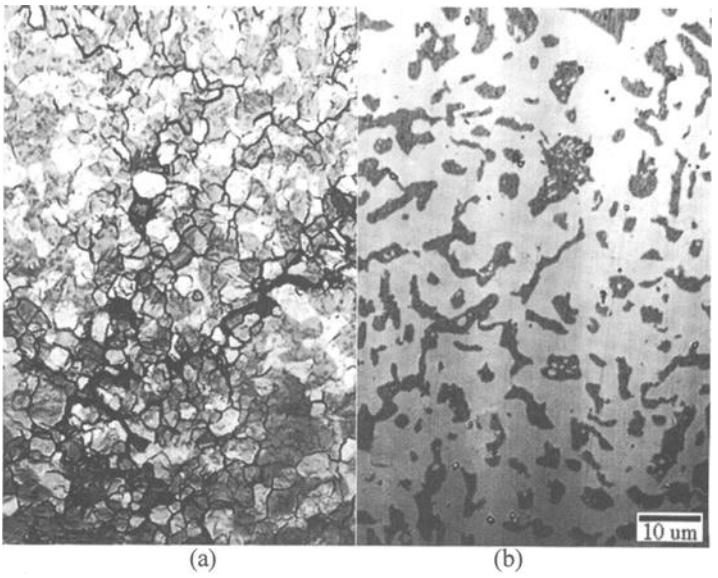

Figure 6 – *Unpolished (a) and polished (b) surface of 60Sn-40Pb after 100 isothermal cycles at 125°C.*

loading direction is horizontal. Similar to thermal cycling, the gray scale images of isothermal mechanical cycling also indicated that the enhanced phase grain boundaries represent steps caused by a protrusion of one of the phase grains. Compared to the initial microstructure (Figure 1), the Pb-rich phase grains coarsened somewhat at 35°C and even more at 125°C but maintained their size or possibly became slightly refined during isothermal deformation at –55°C.

Under isothermal fatigue at 125°C, the deformation looked similar to that at 35°C very locally (of the order of the phase grain scale) where deformation appeared to be concentrated near phase grain boundaries. However, at a lower magnification (higher scale), the deformation was concentrated primarily along nearly randomly oriented bands (Figure 7). The bands were spaced about 50 μm apart, on average. Specifically, the deformation appeared to be concentrated locally along phase grain boundaries within the bands with cracking occurring perpendicular to the loading direction along the bands. This cracking may be observed in Figures 4-6. Because the scan resolution of the CSLM is generally larger than the width of most microstructural cracks, it is non-trivial to distinguish between cracks in the microstructure and steps in the surface topography. The dark lines seen in the micrograph of the roughened surface after 800 thermal cycles probably represent steps in the surface that appear dark due to how they reflect the laser light during scanning in the CSLM. Most of these lines are wider than the scan resolution of 0.25 μm, but are not detected by the CSLM as cracks. On the other hand, the lines appearing on the micrographs of the solder surface after 100 isothermal fatigue cycles are most likely cracks because their orientation is perpendicular to the loading axis and similar cracks have been previously observed after isothermal fatigue [*2-5*]. The lines seen on the surface after the thermal cycling experiment are too thick to be cracks. The banding observed at 125°C was not observed after isothermal fatigue at 35°C or –55°C or after 800 thermal cycles.

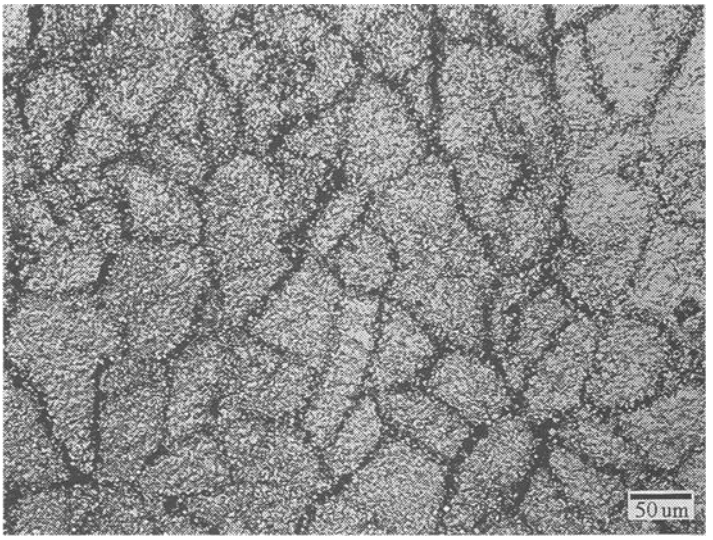

Figure 7 – *Lower magnification of unpolished surface of 60Sn-40Pb after 100 isothermal cycles at 125°C.*

Surface Roughness

The measurement of surface roughness for isothermal fatigue is shown in Figure 8. The increase in the RMS roughness (R_q - R_{qo}) is plotted where R_{qo} is the initial RMS roughness. For isothermal fatigue, the specimen surface roughened after cycling at all three temperatures. It is important to take care in interpreting the confidence intervals at each data point as they cannot simply be considered "error bars" here. As mentioned earlier, the mean RMS roughness height is determined from sixteen separate cross-sectioned surface profiles taken at four different orientations. For a cross section taken from a heterogeneously deformed surface, the exact roughness value determined will depend on what topographical surface features are cut by the cross section. For example, a roughened band seen at 125°C such as the one seen in Figure 7 might be cut by a 0° cross section, but would be missed by a 45° cross section. Therefore, part of the spread seen by the confidence interval is determined by the heterogeneity of the surface roughness.

Even the term "confidence interval" is somewhat incorrect, since the use of it often implies some true value. This is not the case here since the roughness of a heterogeneously deformed surface will change depending on the location and magnification of the observation taken. The term is used here for simplicity since the calculation is the same as for a true confidence interval of a sample population. Still, part of the spread seen in the confidence intervals will be due to some systematic experimental error since the surface height differences being measured were often the same order of magnitude as the resolution of the CSLM. For the samples we examined, the true surface height changes – as well as the portion of the confidence interval that is attributed to heterogeneity of the surface – were deemed to be greater in magnitude than the systematic error due to the resolution limitations of the CSLM. For the purposes of interpreting the data for these experiments, it is logical to conclude that larger confidence intervals are a signal that there is more heterogeneity in the surface topography.

For purposes of illustration, it is useful to consider the confidence interval about the data point at 35°C as representative of the experimental error since the deformation here was observed to be more homogeneously distributed than at the other temperatures. The confidence interval seen at –55°C is more representative of spread that may be seen due to heterogeneity of the surface topography. However, there is reason to believe that much of the increase in surface roughness during the –55°C isothermal test is due to surface deposits which can be seen in Figure 4, a by-product of this low temperature test in particular. For this reason, this data point probably does not reflect the increase in surface roughness due to inelastic deformation. On the other hand, approximately half of the confidence interval at the 125°C data point is most likely due to the heterogeneous roughening which was seen on the surface as opposed to systematic error or surface deposits. The other half of the confidence interval, which is about the same magnitude as the confidence interval at 35°C, is most probably due to experimental error.

Another factor to consider when analyzing the spread of the confidence intervals for the net increase in surface roughness is that this variable is obtained by subtracting two pieces of experimental data, initial roughness and final roughness, which each have a confidence interval of their own. When the difference was taken between the initial and final values of roughness, their confidence intervals were summed to obtain the net 95% confidence interval.

The increase in surface roughness due to thermal cycling for the alloys tested is shown in Figure 9. Confidence intervals are not plotted since they are of the order of the size of the marker. All the alloys and 99.9Sn exhibited an increase in surface roughness as the number of thermal cycles increased. However, the 60Sn-40Pb alloy showed a markedly greater increase in surface roughness as compared to the other lead-free alloys. Both 99.9Sn and Castin exhibited the slowest increase in surface roughness with

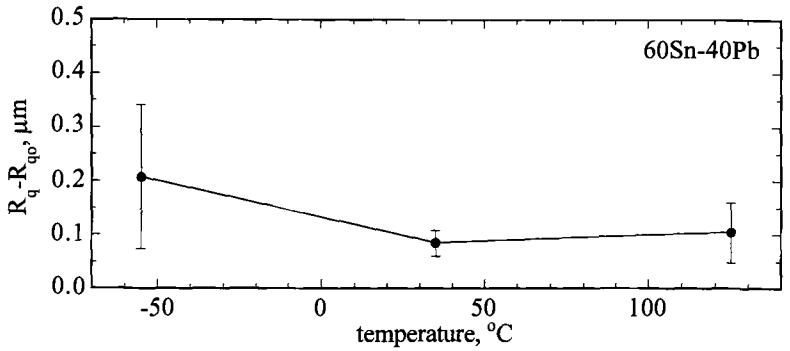

Figure 8 – *Surface roughness after100 isothermal fatigue cycles.*

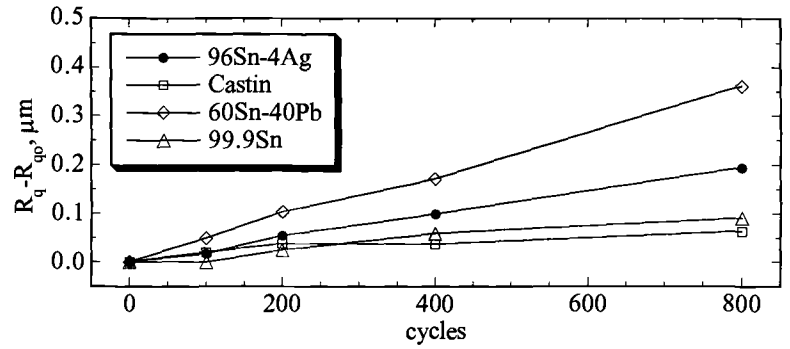

Figure 9 – *Surface roughness after thermal cycling from –55°C to 125°C.*

increasing number of thermal cycles. It is also noteworthy that the surface roughness appears to increase linearly with increasing cycle count for all of the alloys tested. In addition, the surface roughness measured after about 200 unconstrained thermal cycles is approximately equivalent to the roughness measured after 100 isothermal fatigue cycles at 35°C where the fatigue cycle consisted of a R = –1 loading at a strain amplitude equivalent to the thermal strain amplitude for a –55°C to 125°C thermal cycle. Therefore, the deformation observed under unconstrained thermal cycling can not be considered insignificant since it is of the same order in magnitude as the deformation measured under isothermal fatigue.

Phase Grain Growth

The growth of the phase grains was tracked by measuring the average spacing between phase grain boundaries. A stencil containing ten parallel lines, representing 100 µm in length in the digital micrograph, was laid over each image. The number of phase boundaries intersecting each line was counted in the same fashion described by the Heyn Lineal Intercept Procedure (ASTM E112-96). Although the Pb-rich grains were not always regularly shaped in the microstructure, they did appear to be distributed isotropically throughout the material. The average phase boundary spacing found in both

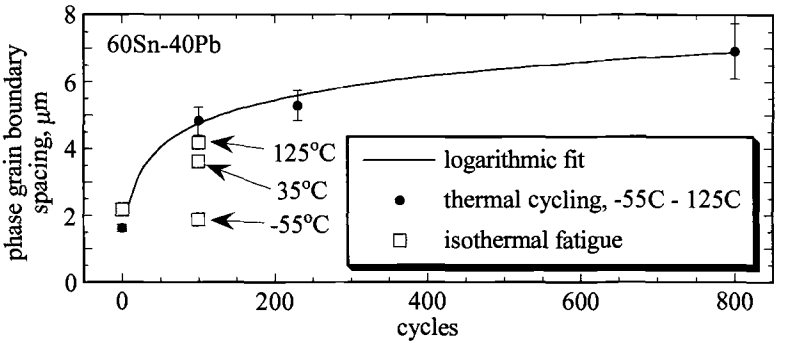

Figure 10 – *Average phase grain boundary spacing.*

the thermal cycling and isothermal fatigue specimens is reported in Figure 10. The confidence intervals for the isothermal fatigue data are not shown as they are smaller than the markers. The data for 100 and 200 thermal cycles was collected from images of the roughened surfaces where it was more difficult to distinguish between phase grain boundaries and steps in the surface profile. Still, the significant increase in the phase grain spacing quantitatively supports direct observation of the polished surface after 800 cycles (Figure 3). The 95% confidence intervals are also noted. The spread of the confidence interval may be interpreted as a sum of the systematic error and the variability of the phase grain size distribution (i.e., the larger the confidence interval, the more variability in the phase grain size distribution).

The isothermal fatigue specimens were found to have a slightly coarser initial microstructure than the thermal cycling specimens. This is a reasonable finding since the dumbbell specimens were much thicker than the flat plate specimens (13 mm outer diameter on the cylindrical blanks for the isothermal fatigue specimens versus 2 mm overall thickness for the flat plate specimens) and therefore would solidify more slowly during quenching in water. Longer cooling times are directly correlated to a coarser microstructure.

The phase grain boundary spacing, δ, of the thermally cycled specimens appears to increase logarithmically with cycles. The equation determined by a least mean squares analysis is $\delta = 1.027\ln(N) - 0.004$ where δ is measured in μm and N is the number of thermal cycles. It is interesting to compare this finding with that of Scott [*10*] who found that the tensile strength decreases logarithmically with isothermal aging time. In addition, the coarsening appears to be slightly attenuated under thermal cycling considering the time spent at the elevated temperatures under thermal cycling is less than that during isothermal fatigue at 125°C. For isothermal test at –55°C, the microstructure appears to be unchanged or possibly refined slightly from the as-cast condition. Based on past work [*9*], a continuation of coarsening is expected in all conditions except isothermal fatigue at –55°C if these tests are carried out for a longer period.

Further Discussion

The deformation contributing to the observed roughening of the surface in 60Sn-40Pb appears to be concentrated at phase grain boundaries and within the Sn-rich phase. The deformation observed in Sn, which was shown to be driven by the mismatch in the CTE between grains [*1*], is very similar to that seen in 60Sn-40Pb. It is likely that the isotropic CTE mismatch between the Sn-rich and Pb-rich phase grains in 60Sn-40Pb is driving the deformation at the phase boundaries while the directional CTE mismatch is

driving the deformation between crystallographic grains within the Sn-rich region. Considering that the amount of accumulated deformation in 60Sn-40Pb is four times as great as that in polycrystalline 99.9Sn, it is logical to conclude that the isotropic CTE mismatch between phases is more significant due to the accumulation of inelastic strains in 60Sn-40Pb than the directional CTE mismatch within the Sn-rich phase. In addition, the majority of the observed local deformation in 60Sn-40Pb is concentrated at the phase grain boundaries, rather then the crystalline boundaries within the 99.9Sn. The surface deformation seen in 60Sn-40Pb is much greater than that seen in 99.9Sn although both materials do show some inelastic surface deformation. In the case of 99.9Sn, since there are no phase boundaries to preferentially accumulate inelastic deformation, the deformation concentrates at the crystallographic grain boundaries. The presence of a soft Pb-rich phase in 60Sn-40Pb may allow the material within this phase to yield plastically at lower stresses than what would be required for yielding in the harder Sn-rich phase. This mechanism would allow the grains within the Sn-rich phase to "ratchet" through the Pb-rich phases as they expand and contract at different rates. The fact that the Pb-rich regions were generally recessed on the surface of the thermally cycled 60Sn-40Pb specimen supports this theory.

The lead-free solder alloys roughened substantially less than the 60Sn-40Pb when exposed to the same thermal cycle. This could be attributed to both a lesser degree of CTE mismatch within the microstructure over the bulk material of the lead-free alloys and a decreased susceptibility to accumulating inelastic deformation during thermal fatigue. Since the flow stress of 60Sn-40Pb is lower than that of Castin [*12*], Castin is more resistant to deformation for a given CTE mismatch between phase grains. The fact that the Sn and lead-free solder alloys did not roughen as substantially as the leaded solder suggests that the anisotropy of the CTE in the Sn-rich phase grains does not drive the accumulation of inelastic strain as strongly as the mismatch in CTE between Sn-rich and Pb-rich phase grains and the lower thermally-activated flow strength along the phase boundaries in the 60Sn-40Pb alloy.

It has been postulated by Frear et al. [*2*] that sites of high local strain will tend to occur at phase boundaries where accumulation of plastic strain is the greatest. It is likely that the presence of highly ductile Pb-rich phases allow plastic deformation near phase grain boundaries, increasing the apparent strain at these boundaries. Inhomogeneous deformation similar to this has been observed as an increase in surface roughness under isothermal cyclic shear deformation; however, inhomogeneous phase grain coarsening was also observed in the banding [*13*]. In alloys, the coarsening behavior is significant at high homologous temperatures $T / T_m > 0.6$ and this was confirmed for 60Sn-40Pb. It has been shown in previous work [*13*] that microstructural coarsening is a precursor to the accumulation of microstructural damage in solder alloys under shear loading. Although coarsening occurred in our uniaxial experiments, no coarsening was observed to occur preferentially within the roughened bands. Had the microstructure reflected the mesoscopic banding observed under isothermal fatigue at 125°C in any way, it would then be logical to conclude that there was a stronger interaction between local microstructure and local inelastic strain. This begs the question of whether phase boundaries in a coarsened region are sites where enhanced local deformation nucleates or whether it is the localized isothermal deformation that is a precursor to accelerated coarsening. Our data suggest the former, but it is also possible the tests may not have been run long enough to observe any measurable change in preferential coarsening within the bands of deformation. A study of microstructural coarsening during isothermal fatigue versus the coarsening seen during aging in absence of mechanical cycle could confirm this point with stronger resolution.

Cracks were observed along the phase boundaries where the grains had coarsened throughout the material surface after isothermal fatigue. These cracks tended to run perpendicular to the loading direction and did not appear to form in any type of banding but rather as somewhat random delamination between adjacent phase grains and

crystallographic grains within the Sn-rich phases. Similar cracking has also been observed under tension-tension uniaxial loading where the damage tended to accumulate along shear bands 45° to the loading direction [*5*]. During shear loading, a single crack was found to nucleate within a coarsened band and propagate [*2*]. Some dark lines were observed in the optical image obtained from the unconstrained thermal cycling test, but these lines were found to be merely artifacts of the imaging process rather than actual cracks. The grayscale image of the thermal cycling test showed no signs of cracking. The appearance of cracks along phase grain boundaries during isothermal fatigue loading supports the theory that local strains are concentrated there under these conditions. The absence of cracking during unconstrained thermal loading is an indicator that an additional global traction, either normal or shear, may be required to make it energetically favorable for cracks to nucleate along deformed phase or crystallographic grain boundaries.

It is clear that advances in deformation and degradation modeling must capture a number of lower scale features. Such features include the evolution of the phase grain size and distribution, the kinetics of thermally activated processes (particularly phase grain boundary migration and sliding) and the differences in the coefficient of thermal expansion. It is anticipated that these experimental cases with well-controlled boundary conditions can be used to establish and verify deformation and degradation modeling that takes into account these lower scale features. However, one important feature that could not be established is when it becomes energetically favorable for accumulated inelastic deformation along a phase grain boundary to become a crack. Clearly, past work shows that when cracks do form, they tend to form on the phase grain boundaries that experience the greatest accumulated inelastic strain [*2, 5*]. So to predict damage, one will need to track the accumulated deformation along the phase boundaries. While microstructural coarsening has been found to be a precursor to the accumulation of actual damage, the exact driving force leading to the nucleation of damage has yet to be resolved.

Conclusions

Thermal cycling behavior is an inherent property of an alloy. To understand why metals experience accelerated degradation under combined thermal and mechanical fatigue, we must first understand the microstructural mechanisms enabling local inelastic deformation during unconstrained thermal cycling. Clearly, thermal cycling cannot be assumed to be stress-free on the microstructural level in solder alloys. It is likely that differences of coefficient of thermal expansion (CTE) between phase grains and the anisotropy of the CTE in the crystallographic grains are the main drivers of accumulated inelastic strain during thermal cycling. The confocal scanning laser microscope is shown to be a reasonable method for tracking the evolution of heterogeneous surface deformation both quantitatively and qualitatively. The inelastic deformation mechanism in 60Sn-40Pb appears to be due to a creep mechanism that primarily involves phase grain boundary migration and sliding. The accumulated deformation in 60Sn-40Pb under a –55°C to 125°C thermal cycle is significant and is of the same order in magnitude as that observed under isothermal fatigue. 60Sn-40Pb is particularly susceptible to heterogeneous deformation under thermal cycling compared to Sn and selected lead-free solder alloys.

Coarsening of the phase grains is also significant during isothermal fatigue at 35°C and 125°C and thermal cycling. Under isothermal fatigue at 125°C, deformation is further localized along mesoscale bands, spaced about 50 μm apart. The bands of deformation in the 125°C isothermal test do not correlate to any type of mechanically driven microstructural coarsening. Some cracking is observed along phase grain boundaries after isothermal fatigue, with cracks running perpendicular to the loading direction.

Acknowledgments

The authors wish to acknowledge Dr. Hiroki Nanko, Ted Jackson, and Joel Panek of the Institute of Paper Science and Technology, Atlanta, Georgia, for their generosity in allowing our use of and assisting us with the confocal scanning laser microscope and proprietary surface profilometry software. The Thermotron thermal cycling oven is located in the Packaging Research Center at the Georgia Institute of Technology and the assistance of Paul Houston with the thermal cycling oven is appreciated. We also would like to thank Melinda Pierce, who was funded through an Undergraduate Summer Research Fellowship sponsored by the Materials Council of Georgia Tech, for her dedicated work in conducting the thermal cycling experiments.

References

[1] Boas, W. and Honeycombe, R. W. K., "The Plastic Deformation of Non-cubic Metals by Heating and Cooling," *Proceedings of the Royal Society. A*, Vol. 186, September 1944, pp. 57-71.

[2] Frear, D., Grivas, D., and Morris, J. W., Jr., "A Microstructural Study of the Thermal Fatigue Failure of 60Sn-40Pb Solder Joints," *Journal of Electronic Materials*, Vol. 17, 1988, pp. 171-180.

[3] Wolverton, W. M., "Mechanisms And Kinetics Of Solder Joint Degradation," *Brazing and Soldering*, No. 16, 1987, pp. 33-38.

[4] Bangs, E. R. and Beal, R. E., "Effect of Low Frequency Thermal Cycling on the Crack Susceptibility of Soldered Joints," *Welding Research Supplement*, No. 10, 1975, pp. 377s-383s.

[5] Cutiongco, E. C., Vaynman, S., Fine, M. E., and Jeanotte, D. A., "Isothermal Fatigue of 63Sn-37Pb Solder," *Journal of Electronic Packaging*, Vol. 112, 1990, pp. 110-114.

[6] Cailletaud, G. and Chaboche, J.-L., "Macroscopic Description of the Microstructural Changes Induced by Varying Temperature: Example of IN100 Cyclic Behavior," *ICM 3*, Vol. 2, Cambridge, England, 1979, pp. 23-32.

[7] Kraft, S., Zauter, R., and Mughrabi, H., "Aspects of High-Temperature Low-Cycle Thermo-mechanical Fatigue of a Single Crystal Nickel-Base Superalloy," *Fatigue and Fracture of Engineering Materials and Structures*, Vol. 16, No. 2, 1993, pp. 237-253.

[8] Zauter, R., Christ, H.-J., and Mughrabi, H., "Some aspects of Thermo-mechanical Fatigue of AISI 304L Stainless Steel: Part I. Creep-Fatigue Damage," *Metallurgical and Materials Transactions*, Vol. 25A, 1994, pp. 401-406.

[9] Ross, R. G. and Wen L.-C., "Solder Creep-Fatigue Interactions with Flexible Leaded Surface Mount Components," *Thermal Stress and Strain in Microelectronics Packaging*, J. H. Lau, Ed., Van Nostrand Reinhold, 1993, pp. 607-647.

[10] Scott, D. T., "Phenomenological Modeling of the Deformation Behavior of Solders," Master's Thesis, Georgia Institute of Technology, 1998.

[11] Woodmansee, M. W., "Thermal Cycling and Rate-Dependent Stress Relaxation Behavior of Solders," Master's Thesis, Georgia Institute of Technology, 1999.

[12] Whitelaw, R. S., Neu, R. W., and Scott, D. T., "Deformation Behavior of Two Lead-Free Solders: Indalloy 227 and Castin Alloy," *Journal of Electronic Packaging*, Vol. 121, June 1999, pp. 99-107.

[13] Tribula, D., Grivas, D., Frear, D. R., and Morris, J. W., Jr., "Observations on the Mechanisms of Fatigue in Eutectic Pb-Sn Solder Joints," *Journal of Electronic Packaging*, Vol. 111, 1989, pp. 83-89.

Robert Kühner,[1] Jarir Aktaa,[1] Leonardo Angarita,[2] and Karl-Heinz Lang[2]

The Role of Temperature Rate Terms in Viscoplastic Modelling: Theory and Experiments

Reference: Kühner R., Aktaa J., Angarita L. and Lang K.-H., **The Role of Temperature Rate Terms in Viscoplastic Modelling: Theory and Experiments,"** *Thermomechanical Fatigue Behavior of Materials: Third Volume, ASTM STP 1371,* H. Sehitoglu and H. J. Maier, Eds., American Society for Testing and Materials, West Conshohocken, PA, 2000.

Abstract: To describe inelastic material behaviour under nonisothermal loading conditions on the base of a viscoplastic model it is not sufficient to use only temperature-dependent model parameters. Also the temperature rate in the evolution equations of the internal variables must be considered. To investigate the influence of the temperature rate, experiments should be defined in which the model response shows a remarkable dependence on the temperature rate. Such experiments could be performed on a coupled "two-bar system" under thermal and complex thermomechanical loading, respectively. Using a recently developed testing facility experiments with a coupled "two-bar system" are realized. This allows different temperature paths to be applied to the two bars which can be coupled to produce the same total strain throughout the experiment. At the same time, the sum of the forces of the two bars is controlled as a function of time. In addition it is possible to perform suitable thermomechanical experiments on an "one-bar system." Here experiments with loading conditions similar to those observed at the "two-bar system" can be performed. The results show that temperature rate terms are necessary to model ratchetting effects correctly. Therefore, approaches taken from the literature were investigated and modified to achieve best agreement between modelling and experiment.

Keywords: modelling, viscoplasticity, ratchetting, thermomechanical loading

[1]Research Scientist and PhD., Group Leader, respectively, Forschungszentrum Karlsruhe, Institut für Materialforschung II, Postfach 3640, D-76021 Karlsruhe, Germany.

[2]Research Scientist and PhD., Group Leader, respectively, Universität Karlsruhe, Institut für Werkstoffkunde I, Postfach 6980, D-76128 Karlsruhe, Germany.

Introduction

In many areas of technology where components are subjected to varying mechanical and/or varying thermal loadings progressive plastic deformation can occur. This so-called ratchetting must be quantitatively predictable because it may lead to failure of component parts. For this purpose constitutive equations are required, being able to describe alternating plastic deformation under cyclic thermomechanical loading. Most of the advanced viscoplastic models however are not suitable for predicting ratchetting [*1*]. In particular those which use the linear kinematic hardening rule by Prager because in these models after a short transition period ratchetting stops [*2*]. The Chaboche model which uses a nonlinear kinematic hardening law is able to simulate ratchetting effects in principle. But quantitatively there is a significant overestimation of the ratchetting strain. Under cyclic thermal-mechanical loading temperature rate terms in the equation of kinematic hardening lead to a distinct improvement of the modelling of the ratchetting behaviour.

Thermoviscoplasticity Model

The investigations of the present paper base on the Chaboche model [*3*]. Here the total strain

$$\varepsilon_{tot} = \varepsilon_{el} + \varepsilon_{in} + \varepsilon_{th} \tag{1}$$

is additively decomposed into an elastic strain ε_{el}, an inelastic strain ε_{in} and a thermal strain ε_{th}. The elastic strain is given by Hook' s law

$$\sigma = E\varepsilon_{el} \tag{2}$$

where σ is the stress and E is the young's modulus. The thermal strain rate is defined by the thermal expansion law

$$\dot{\varepsilon}_{th} = \alpha\dot{T}, \qquad \varepsilon_{th}(T = T_0) = 0 \tag{3}$$

where α is the thermal expansion coefficient and $\dot{T}$ is the temperature rate. The inelastic strain rate is given by the evolution equation

$$\dot{\varepsilon}_{in} = \left\langle \frac{|\sigma - \Omega| - k - k_0}{Z} \right\rangle^N \operatorname{sgn}(\sigma - \Omega) \tag{4}$$

where Z is the viscosity and N is the isotropic exponent. Ω is the kinematic hardening variable, and k_0 is the initial value for the isotropic hardening variable k. The rate of the isotropic hardening variable is given by

$$\dot{k} = C(k_s - k)|\dot{\varepsilon}_{in}| \tag{5}$$

with the model parameters C and k_s. Here k_s is the saturation value for the isotropic hardening. For the kinematic hardening Ω evolution equations with different temperature rate terms were examined in this work to gain access to ratchetting behaviour. This so-called back stress Ω which was originally introduced to describe kinematic hardening can be regarded as a directed inner stress induced by deformation. The Bauschinger effect or, in general, the deformation induced anisotropy appearing under cyclic loading conditions is caused by this directed inner stress. For the Chaboche model the evolution equation for Ω runs:

$$\dot{\Omega} = H\dot{\varepsilon}_{in} - D\Omega|\dot{\varepsilon}_{in}| - R\Omega^m + \frac{\partial H}{\partial T}\frac{\Omega}{H}\dot{T}. \tag{6}$$

H, D, R and m are model parameters depending on material and temperature. The first term corresponds to the linear kinematic hardening rule by Prager [*4*]. Dynamic and static recovery effects are taken into account by the second and third terms, respectively. For the sake of simplicity, we have only investigated loading conditions with negligible static recovery. Therefore, the temperature rate independent terms are identical with the non-linear kinematic hardening rule by Armstrong-Frederick [*5*]:

$$\dot{\Omega} = H\dot{\varepsilon}_{in} - D\Omega|\dot{\varepsilon}_{in}|. \tag{7}$$

To obtain a better description of the deformation behaviour under nonisothermal loading the evolution equation for Ω was modified by Sievert [*6*] as follows:

$$\dot{\Omega} = H\dot{\varepsilon}_{in} + \frac{\partial H}{\partial T}\frac{\Omega}{H}\dot{T} - \frac{\Omega}{\Omega_s}\left\langle H|\dot{\varepsilon}_{in}| + \frac{\partial H}{\partial T}\frac{|\Omega|}{H}\dot{T}\right\rangle \tag{8}$$

where $\Omega_s = H/D$. Here another modification is proposed in order to improve the description of the ratchetting behaviour under thermomechanical loading:

$$\dot{\Omega} = H\dot{\varepsilon}_{in} - D\Omega|\dot{\varepsilon}_{in}| + \frac{\partial H}{\partial T}\frac{\Omega}{H}\dot{T} + \frac{\partial D}{\partial T}\Omega|\varepsilon_{in}|\dot{T}. \tag{9}$$

This modification was developed in the framework of the present investigations. The first three terms are identical with the nonlinear Chaboche rule. The idea for the second temperature rate term in this equation is derived from a nonlinear exponential approach for the back stress Ω. The evolution equations (7), (6) and (8), that are proposed by Armstrong-Frederick, Chaboche and Sievert are thermodynamically consistent formulations. The thermodynamically consistence of the modified evolution equation (9) proposed in the present work must be proved. The model parameters E, α, H, D, C, k_s, k_0, N and Z are material and temperature dependent. These parameters are shown in (Ta-

ble 1) for fife temperature points. Between these temperature points the model parameters are linearly interpolated. The model parameters were determined from strain controlled isothermal tensile experiments with hold times and strain controlled isothermal cyclic experiments that were performed on a one-bar system. The parameters for the Chaboche model and the parameters for the modified models are identical. The modified models contain no extra model parameters in comparison to the Chaboche model.

Table 1 – *Model parameters*

T	α	E	N	Z	H1	D1	k_0	C	Ks
°C	1E-5/K	N/mm²	-	$N/mm^2 s^{1/N}$	N/mm²	-	N/mm²	-	N/mm²
200	1.71	170000	3.7	380	35000	550	97	13	100
300	1.75	149700	3.54	354.5	30560	512.2	90.3	12.34	92
400	1.78	140000	3.4	340	28000	490	85	11.76	87
500	1.8	134700	3.3	334	26200	481	80.59	11.34	83
650	1.83	130000	3.2	330	24000	480	75	11	80

Experimental Procedures

The basic material for the specimens used in the present investigations is a plate of AISI 316L(N), DIN 1.4909 of the Creusot-Marrel (CRM) charge 11477. The thickness of the plate is 40 mm. The chemical composition (in wt - %) is: 0.02 C, 17.34 Cr, 12.5 Ni, 2.4 Mo, 1.8 Mn, 0.32 Si, 0.12 Cu, 0.080 N, 0.042 Nb+Ta, 0.030 Co, 0.02 P, 0.018 Al, 0.008 Ti, 0.0014 B, 0.0006 S. The state of material as supplied was solution treated (1100°C, vacuum) [7].

To develop temperature rate terms that allow a satisfactory description of ratchetting behaviour under cyclic thermal-mechanical loading it is important to have suitable ratchetting experiments. For this purpose suitable experiments on a two-bar system and on a one-bar system were defined and performed. The *one-bar system* was realised on base of an electromechanical INSTRON 8062 testing machine with digital control shown in Figure 1. This testing machine was completed by a heating system with digital temperature control. So nearly any thermal-mechanical loading can be realised. The specimens are heated by direct passage of current and the cooling results from water-cooled specimen grips as well as from thermal radiation and convection. The generation of the nominal value as well as the recording of the experimental data are performed synchronous for the testing machine and the heating system by a PC. This PC is equipped with a Microstar Data Acquisition Processor - Board. A NiCr-Ni thermocouple element weld on the specimen is used for temperature measurement. For strain measuring an extensometer with the gauge length of $l_0 = 6$ mm is directly clamped on the specimen.

The construction of the *two-bar system* is based on two servohydraulic MTS 810 testing machines. A schematic representation is given in Figure 2. The strain-measuring is realised with two extensometers with the gauge length of $l_0 = 12$ mm that are directly clamped on the specimens. The specimens are inductively heated by a Hüttinger

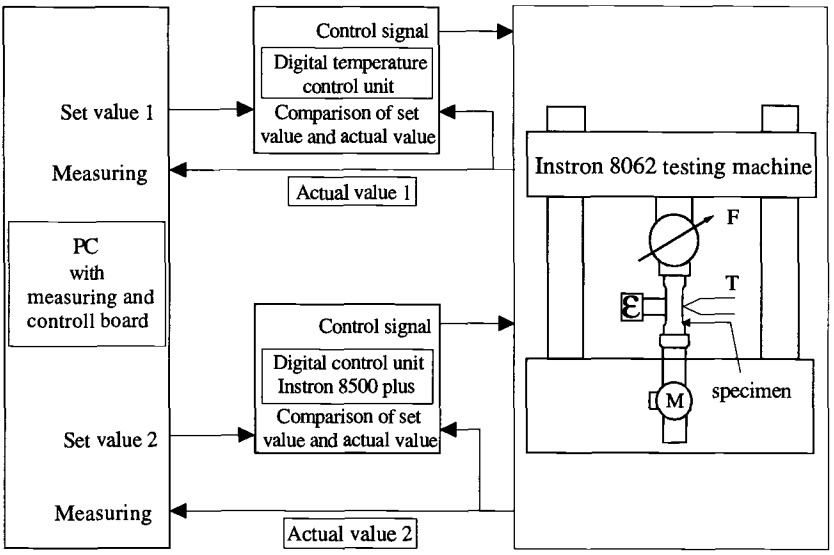

Figure 1 - *One-bar system*

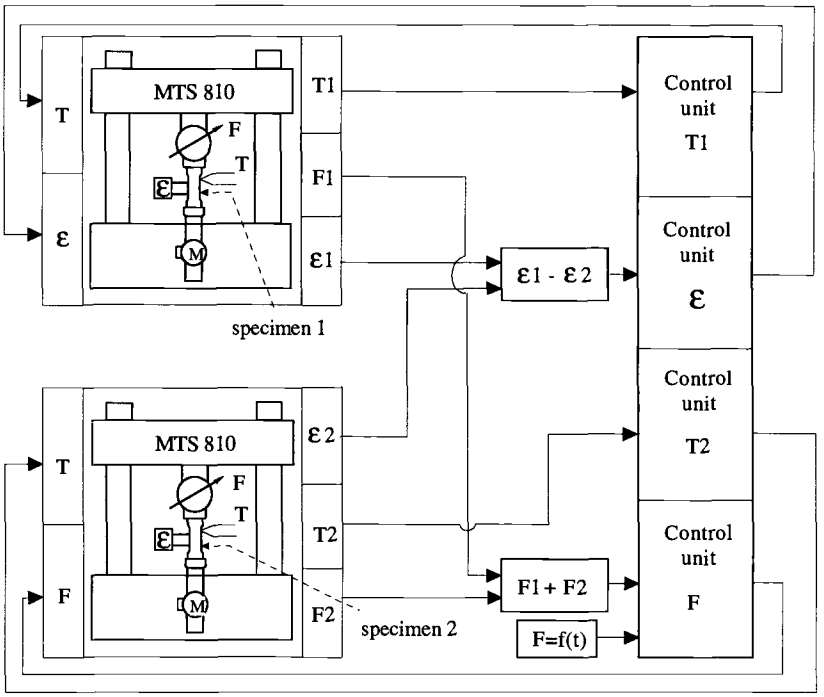

Figure 2 - *Two-bar system*

TIG 5/300 high-frequency generator and a water-cooled copper spool. The specimens are cooled by water-cooled specimen holders, by thermal radiation, convection and if necessary by pressure air. A NiCr-Ni thermocouple element weld on the specimen is used for measurement of temperature. The control of the total system is managed by the four channel digital controller "MTS Test-Star II" [8]. Another representation of the two-bar system is shown in Figure 3. This picture makes clear, that at the two-bar system two specimen are coupled the way, that the following boundary conditions are realised:

$$\varepsilon_{tot1} = \varepsilon_{tot2} \quad \text{and} \quad \sigma_1 + \sigma_2 = 0 .$$

It is possible to apply a temperature path to each of the specimen. From this thermal loading history together with the boundary conditions mentioned above the loading conditions for the specimen are determined.

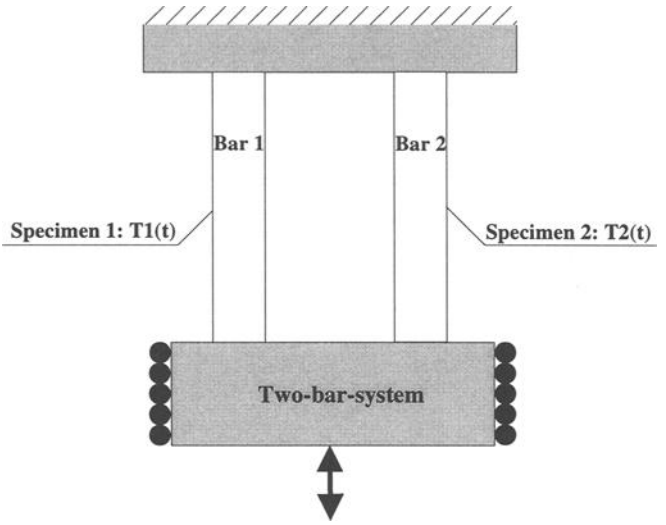

Figure 3 - *Loading conditions for the two-bar system.*

Results and Discussion

To investigate the role of temperature rate terms in modelling the inelastic material behaviour thermomechanical experiments were performed on the one-bar system and on the two-bar system. For the tests performed at the *one-bar system* stress and temperature controlled loading conditions without mean stress were chosen. The loading history of test I is shown in Figure 4. In this diagram the stress and the temperature respectively are plotted over time. In this experiment the stress and the temperature of the specimen are cycled out of phase. In Figure 5 the experimental and numerical results for this out of

phase test can be seen. Here the mean strain is plotted over the number of cycles. The experiment shows a small amount of ratchetting strain that saturates after a few cycles. The simulation by the modified model is quantitatively very close to the experiment and it also shows a saturation of ratchetting strain. The other simulations distinctively over-predict the ratchetting strain observed in the experiment. These model predictions do not show a saturation of ratchetting strain.

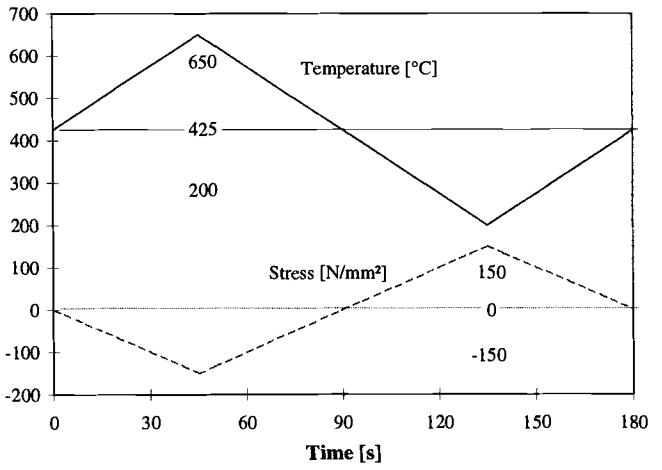

Figure 4 - *Loading conditions for test I.*

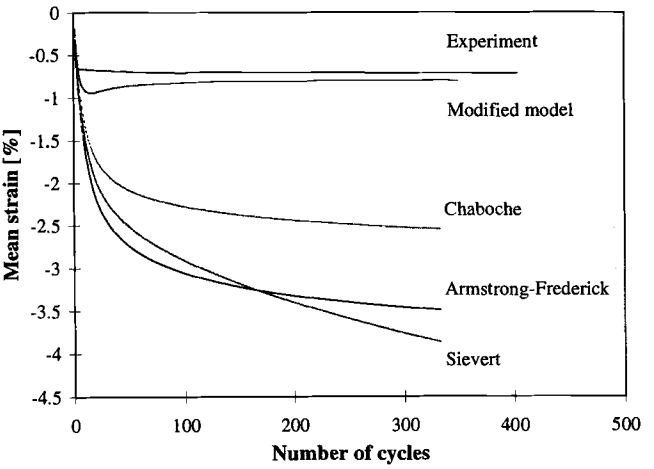

Figure 5 - *Experimental and numerical results from test I.*

The temperature rate term in the evolution equation proposed by Chaboche leads to an improvement of the model prediction in comparison with the Armstrong-Frederick (AF) formulation without temperature rate term. The temperature rate term proposed by Sievert leads to no improvement of the model prediction by the AF formulation of the evolution equation of the kinematic hardening rule without $\dot{T}$ - Term. The loading conditions of test II are shown in Figure 6 where the stress respectively the temperature are plotted over time. In this experiment stress and temperature are cycled in phase.

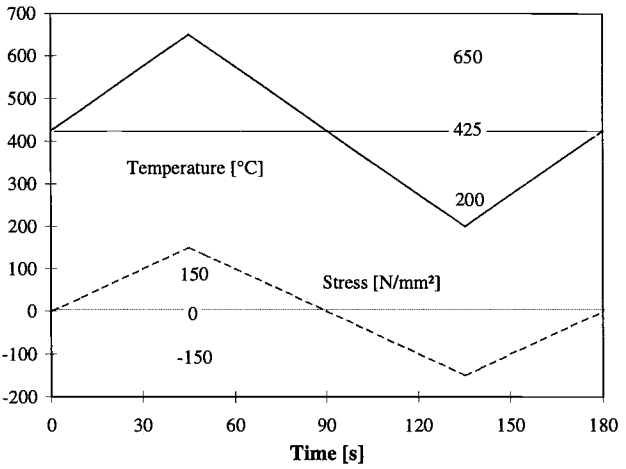

Figure 6 - *Loading conditions for test II.*

The numerical and experimental results are represented in Figure 7 where the mean strain is plotted over the number of cycles. Here again the prediction of the modified model is very close to the experimental result. Both the experimental result and the model prediction by our modified model show a saturation of ratchetting strain. The other model predictions produce too much ratchetting strain and they do not simulate the saturation of ratchetting observed in the experiment. In test I as well as in test II a tendency of the model to overshoot before saturation can be observed. In the presented evolution equations of the rate of the kinematic hardening that are of the Chaboche type the dynamic recovery term

$$-D\Omega|\dot{\varepsilon}_{in}|$$

is responsible for the ratchetting behavior. For thermocyclic loadings this term leads to an overprediction of the ratchetting strain. Especially the temperature-rate term proposed in the modified model is limiting the ratchetting strain produced by the dynamic recovery term under thermal loading conditions. This temperature rate term is growing with a growing amount of inelastic deformation. For this reason the influence of this term at the beginning of the inelastic deformation is small in comparison to the influence of the dy-

namic recovery term. When the overshoot is decreasing the influence of the temperature rate term is larger than the influence of the dynamic recovery term on the ratchetting behavior. When the ratchetting strain is saturated the influence of the dynamic recovery term and the influence of the temperature rate term on the ratchetting strain is balanced.

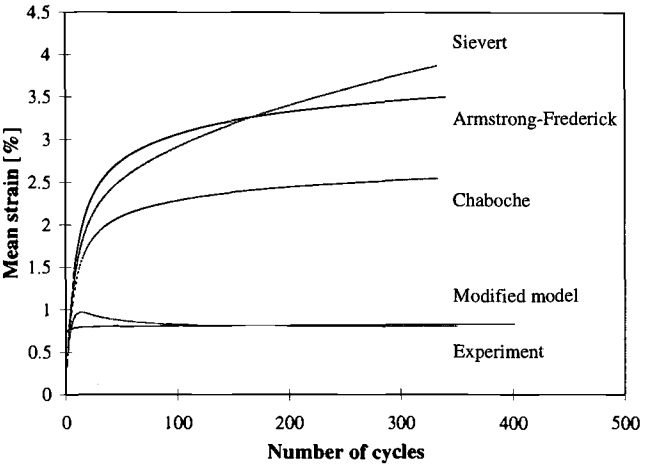

Figure 7 - *Experimental and numerical results from test II.*

Now a comparison of experiment and model prediction for three different loading conditions at the *two-bar system* is presented. The loading history of test III is shown in Figure 8 where the temperature is plotted over the time.

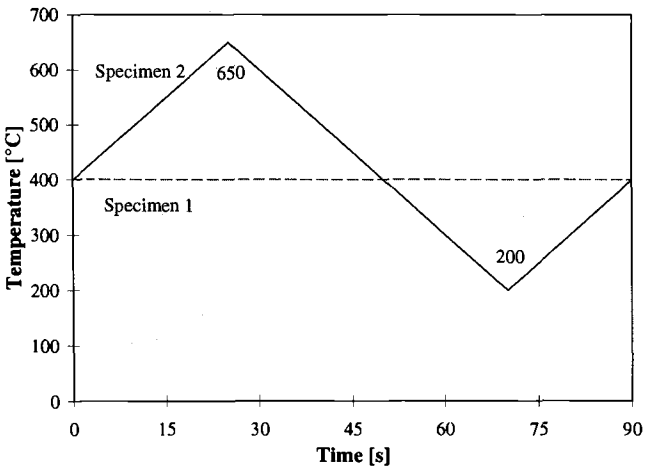

Figure 8 - *Loading conditions of test III.*

Before this test both specimen were heated up to 400°C at zero load. During this test the temperature of specimen 1 is held constant at 400°C while the temperature of specimen 2 is cycled between 650°C and 200°C. The experimental and numerical results are presented in Figure 9 where the mean strain is plotted over the number of cycles.

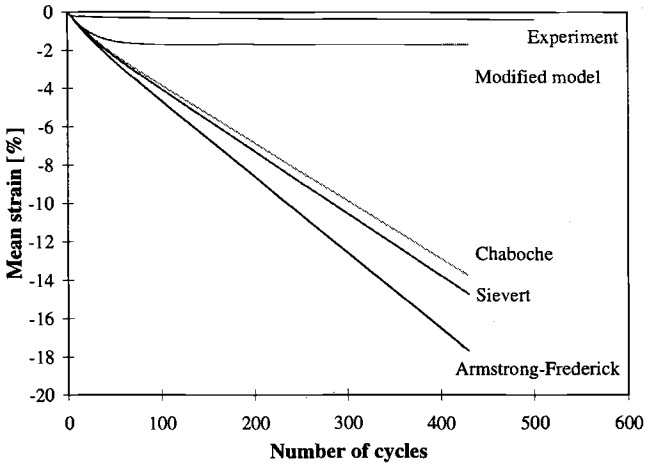

Figure 9 - *Experimental and numerical results from test III.*

Here again our modification of the temperature rate term of the evolution equation of the kinematic hardening leads to the model prediction that is quantitatively and qualitatively closest to the experiment. This model prediction shows saturation of ratchetting strain as it can be observed at the experiment, too. The other model predictions show a very large overprediction of the ratchetting strain observed in the experiment. They do not simulate the saturation of ratchetting strain that occurs in the experiment. The temperature rate terms proposed by Sievert and Chaboche lead to a slight improvement in comparison with the kinematic hardening rule by Armstrong Frederick that does not have a temperature rate term in its evolution equation.

The loading conditions of test IV can be seen in Figure 10 where the temperature is plotted over time. Before this test specimen 1 and specimen 2 are heated up to 425°C and 650°C, respectively, at zero stress. In this test the temperature of specimen 1 is held at constant 425°C whereas the temperature of specimen 2 is cycled between 650°C and 200°C. The experimental and numerical results of test IV are displayed in Figure 11 where the mean strain is plotted over the number of cycles. For this loading conditions the experiment shows a small amount of ratchetting strain with a saturation after a few cycles. The model prediction by the modified model is closest to the experiment. It shows a saturation of ratchetting strain as it can be observed in the experiment. The other model predictions simulate a ratchetting strain without saturation. Therefore there is a great difference in the mean strain predicted by this models and the mean strain observed in the experiment.

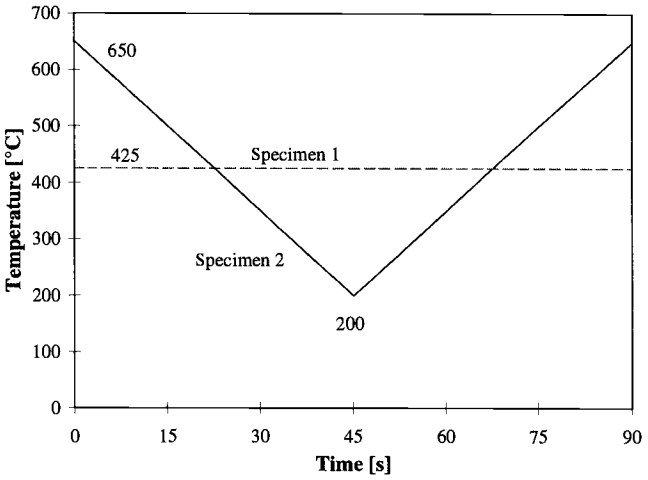

Figure 10 - *Loading conditions of test IV.*

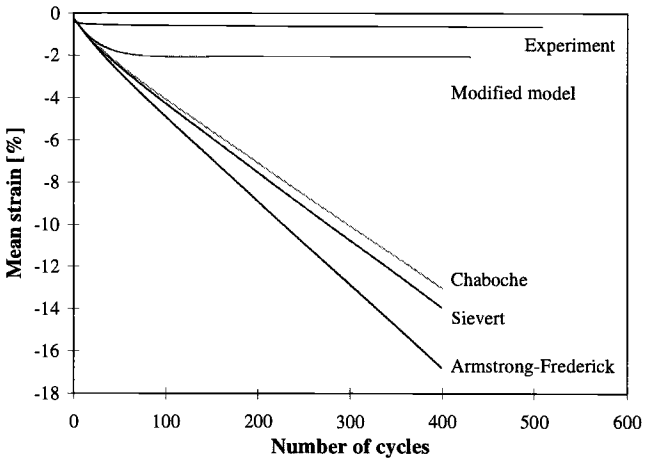

Figure 11 - *Experimental and numerical results from test IV.*

The loading conditions of test V are shown in Figure 12 where the temperature is plotted over the time. Before the test both specimens were heated to 200°C at zero stress. Then the temperature of specimen 1 and specimen 2 were cycled between 200°C and 400°C and between 200°C and 650°C, respectively, in phase. The results derived from experiment and calculation for test V are presented in Figure 13. In this plot the mean strain is plotted over the number of cycles. The comparison between experiment and model prediction for this test shows the same tendency as discussed in the tests before. Here again the prediction of the modified model is closest to the experimental result.

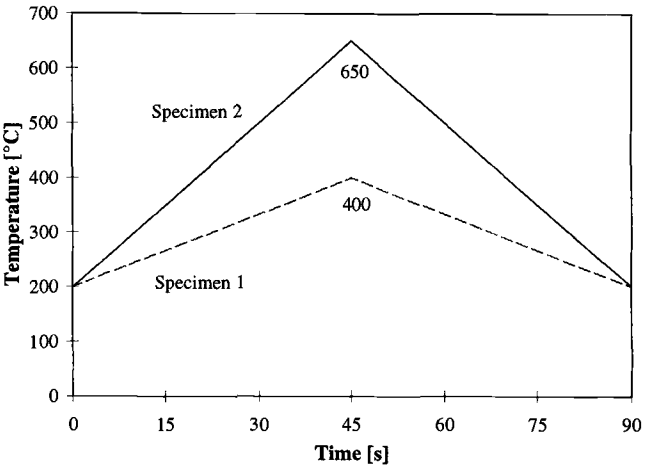

Figure 12 - *Loading conditions of test V.*

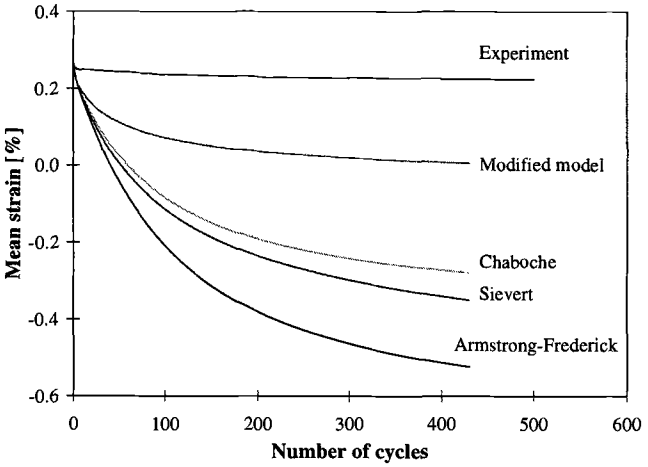

Figure 13 - *Experimental and numerical results from test V.*

Conclusions

Many advanced constitutive models with nonlinear hardening rules, like the Chaboche model, distinctively overpredict the ratchetting strain observed in experiments under thermal-mechanical loading conditions. These models either have no temperature rate terms or their temperature rate terms are too weak. This could be confirmed by ap-

plying models known from the literature to describe the ratchetting behaviour of AISI 316L(N) in thermomechanical tests. The conditions of the tests performed were selected so that the influence of mean stress on the ratchetting behaviour is excluded or minimized, respectively. It has been shown, that the temperature rate term proposed by Chaboche slightly improves the model prediction by the Armstrong-Frederick formulation of the evolution equation of the kinematic hardening that contains no temperature rate term. The temperature rate term proposed by Sievert leads to an improvement of the model prediction in comparison to the prediction by Armstrong-Frederick but there is no improvement in comparison with the model prediction by Chaboche. The $\dot{T}-$term presented in the modified model leads to a distinct improvement in predicting the ratchetting strain observed in the experiment under thermomechanical loading without mean stress.

Acknowledgements

This work was supported by the ministry of science, research and art of Baden-Württemberg. A special thanks is dedicated to R. Sievert from the BAM for his advisory, his discussion and his interest in this work.

References

[1] N. Ohno, "Current State of the Art in Constitutive Modelling for Ratchetting," *14 th International Conference on Structural Mechanics in Reactor Technology (SMiRT)*, Lyon, France, August 17-22, pp. 201-212, 1997.

[2] M. Sester, R. Mohrmann and H. Kordisch, Fraunhofer Institut für Werkstoffmechanik, March 97, T 1/97.

[3] J. L. Chaboche, "Time-Independent Constitutive Theories for Cyclic Plasticity," *International Journal of Plasticity*, Vol. 2, No 2, pp. 149-188, 1986.

[4] W. Prager, "Recent Developments in the Mathematical Theory of Plasticity," *Journal of Applied Physics* 20: 235-241, 1949.

[5] P. J. Armstrong and C. O. Frederick, "A Mathematical Representation of the Multiaxial Bauschinger Effect," CEGB Report: RD/B/N731. Berkeley Nuclear Laboratories, 1966.

[6] R. Sievert and J. Olschewski, "Modellierung thermisch-mechanischen viskoplastischen Verfestigungsverhaltens und Lebensdauerabschätzung bei mehrachsiger Hochtemperaturermüdung am Beispiel von IN738LC," Karaman-Auditorium, RWTH Aachen, Februar 1997.

[7] M. Schirra and S. Heger, "Zeitstandfestigkeits- und Kriechversuche am EFR-Strukturwerkstoff 316L(N), DIN 1.4909," KFK 4767, Institut für Material- und Festkörperforschung, Kernforschungszentrum Karlsruhe, September 1990.

[8] G. Pitz, K.-H. Lang and D. Löhe, "Konzeption und Realisierung eines Prüfsystems für komplexe thermisch-mechanische Belastung," Werkstoffprüfung 1995, Bad Nauheim, DVM, Berlin (1995), 69-78.

Life Prediction

Sam Y. Zamrik[1] and Mark L. Renauld[2]

Thermo-mechanical Out-of-Phase Fatigue Life of Overlay Coated IN-738LC Gas Turbine Material

Reference: Zamrik, S. Y. and Renauld, M. L., **" Thermo-mechanical Out-of-Phase Fatigue Life of Overlay Coated IN-738LC Gas Turbine Material,"** *Thermo-mechanical Fatigue Behavior of Materials: Third Volume, ASTM STP 1371,* H. Sehitoglu and H. J. Maier, Eds., American Society for Testing and Materials, West Conshohocken, PA, 2000.

Abstract: Thermomechanical fatigue (TMF) is a unique type of fatigue process in which a component is simultaneously subjected to fluctuating loads and temperature. Isothermal life prediction techniques are often not applicable to TMF conditions since mechanical properties are temperature dependent with different damage mechanisms. There are two major cycles in TMF: the in-phase (IP) cycle where the maximum strain peak coincides with the maximum temperature and the out-of-phase (OP) cycle where the maximum strain and the lowest temperature coincide.

Experimental and analytical methods are developed to address the effect of thermomechanical strain cycling on coated nickel base superalloy IN-738LC material which is a γ' (Ni_3Al) strengthened material used primarily for land based gas turbine blades. The coating system was a NiCoCrAlY overlay type. Tubular specimens in the two conditions, coated and uncoated, were primarily tested in out-of-phase (OP) TMF loading with a temperature range of 482-871°C. Using a viscoplastic concept which accounts for strain/temperature cycling response of substrate and coatings in terms of hysteresis loops which characterize the evolution of stress/strain/cycle up to mid-life cycle, a life prediction model was developed incorporating the effect of creep (strain hold-period), environment, and temperature. Test results show the OP TMF type cycle is the most damaging cycle for the coated IN-738LC material when compared to both in-phase and isothermal cycles. All experiments were strain-controlled with a triangular waveform and a strain-ratio $A = \varepsilon_{amp}/\varepsilon_{mean} = \infty$.

Keywords: thermomechanical fatigue (TMF), IN-738LC, NiCoCrAlY, out-of-phase, cycle, energy, coating

[1]Professor Emeritus, Department of Engineering Science and Mechanics, The Pennsylvania State University, University Park, PA 16802.

[2]Research Engineer, United Technology Research Center (Pratt & Whitney), Materials and Structures Technology Department, East Hartford, CT 06108.

Introduction

Most life prediction methods are focused on isothermal fatigue under constant or variable strain cycling; however, a new fatigue process has emerged as a result of temperature and strain cycling and has become a major contributor to industrial component failure. One such component is the gas turbine blade which undergoes various thermomechanical cycles depending on the location along the blade, i.e. at the root, the leading edge or the trailing edge. This process of failure is known as "thermomechanical fatigue (TMF)". For example, the leading edge cycle, has been found to generate severe TMF cracking and limit blade life (Bernstein et al., Arana et al., Pejsa and Cowles, and Linask and Derberger [*1-4*]). As the component is heated and compressed, stress relaxation occurs and tensile mean stresses are developed on turbine shut down. Also, when a strain is imposed in compression at the peak temperature in the TMF cycle and was held for a period of time, additional stress relaxation and environmental damage occur. Hence, thermomechanical fatigue (TMF) is a unique type of fatigue, where isothermal life prediction techniques are not applicable, since mechanical properties are typically temperature dependent and different damage mechanisms arise. There are two types of TMF cycles: in-phase (IP) TMF occurs when the maximum strain and peak cycle temperature coincide and out-of-phase (OP) TMF where the maximum strain and lowest cycle temperature coincide. Based on IP and OP test results, the OP TMF cycles are found to be the most damaging factor on the leading edge of a gas turbine blade from repeated turbine starts and stops and where damage is the highest.

Numerous life prediction models have been developed to address the thermomechanical fatigue of superalloys materials. The approaches can be categorized as strain-based approach such as the Manson-Coffin relation, energy-based approach such as the Ostergren [*5*] hysteretic energy approach, the Nissley [*6,7*] damage and crack growth approach and the damage approach such as the ones proposed by Remy et al. [*8*], Neu and Sehitoglu [*9*] approach, or Chaboche and Lesne [*10*] who developed a continuous fatigue damage model for thermomechanical fatigue with the damage accumulation rate as a function of maximum stress, σ_{max}, mean stress, $\bar{\sigma}$, an effective temperature, T* and the current damage in the material, D.

Material and TMF Test Procedure

Material and Specimen Preparation

The material used in this investigation is a nickel base superalloy IN-738LC which is γ' (Ni_3Al) strengthened material used primarily for land based gas turbine blading due to its high Cr content and correspondingly high corrosion resistance. This alloy was cast in the form of 25.4 mm diameter rods 165.1 mm long and subsequently solution treated at 1120°C for two hours. Fatigue test specimens, in the form of hollow cylindrical bars, were machined by a low stress grinding process and polished only in the axial direction to minimize the residual stresses and stress concentrations in the gage section. The tubular

specimens were then aged in a horizontal tube furnace at 843°C for 24 hrs in a vacuum (1 x 10^{-5} Torr) with specimen temperature monitored by a thermocouple junction inserted in the hollow fatigue specimen and placed in the middle of the gage section. After the 24 hr exposure at temperature, specimens were cooled in argon below 500°C prior to air exposure. Gage section oxidation was nearly eliminated by following the above procedure and by wrapping the gage section of each specimen in tantalum foil. This standard casting and heat treatment procedure produced the microstructure with an average grain size of 1.85 mm. This grain size corresponded to an average of 0.8 grains across the gage section wall thickness of the fatigue specimens. The NiCoCrAlY is an overlay coating applied to specimens by a low-pressure plasma spray (LPPS) by Chromalloy Turbine Technology according to specifications. Specimens were coated over the gage length as shown in Figure 1.

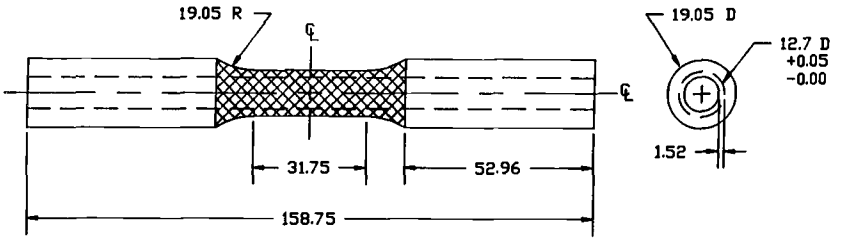

Figure 1— *IN-738LC TMF Test Specimens with Full Gage Length Coating*

After plasma spraying, the coated specimens underwent further processing such as heat treating to develop coating microstructure and coating adherence to the substrate, shot peening to enhance coating density and polishing to improve fatigue and aerodynamic characteristics. The coating thickness was 157 μm (6.3 mil) with approximately a diffusion zone thickness of 15 μm (0.6 mil) as shown in Figure 2 for a tested specimen.

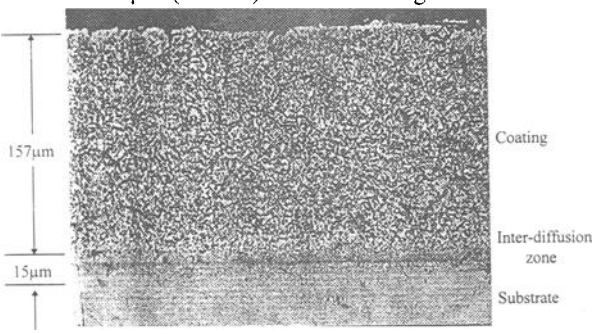

Figure 2— *Microstructure of NiCoCrAlY Overlay Coating after Testing*
$\Delta\varepsilon_{mech}$ = 0.7%, OP TMF, 482-871°C, t_h = 90 sec (comp), N_{90} = 160

Test Procedure

The thermomechanical testing system used an MTS biaxial fatigue equipment where the system contained three closed-loop control loops, one for temperature control and two for mechanical actuator control (axial and torsional). The temperature loop consists of a temperature controller induction heater (Lepel model T-2.5-1-KC-BW with a 2.5kW capacity), load coils, a command signal and a feedback signal. Temperature was measured with 6 type K thermocouples pulled against the specimen with alligator clips and springs. One thermocouple served as a feedback to the temperature controller while the other 5 monitored the specimen temperature at three locations within the extensometer rods and two locations outside the gage section, one above and one below. These five readout thermocouple signals were passed through Analog Device AD595 chips to linearize and amplify the thermocouple output within the temperature range of interest.

The TMF testing procedure is outlined in Figure 3 (a) and (b) for out-of-phase cycling with and without a compression hold.

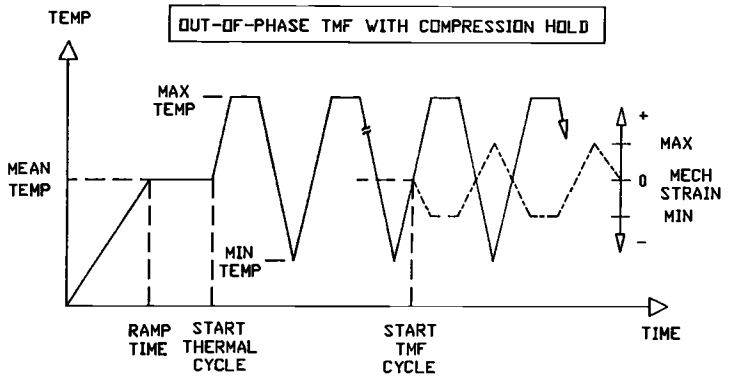

Figure 3a— *Relationship between Thermal and Mechanical Strains at Start-up of OP TMF Test with Compression Hold Time*

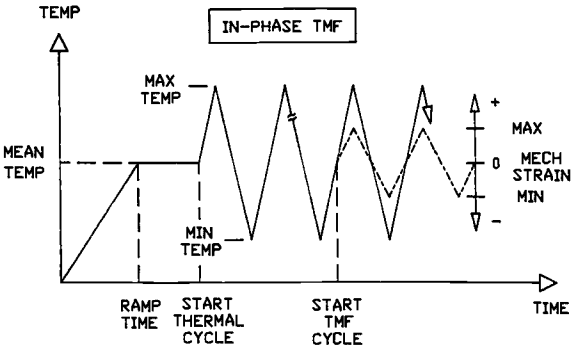

Figure 3b— *Relationship between Thermal and Mechanical Strains at Start-up of TMF Test*

In all cases, specimens are slowly raised to the mean cyclic temperature at which point the extensometer output is zeroed. The specimen is then heated and cooled between the selected temperature endlevels while the thermal expansion of the specimen is recorded from the extensometer output. This process is performed under zero load (free expansion condition) to ensure the collection of accurate strain data. Figure 4 shows the temperature command for TMF cycling. The command signal initiates specimen heating or cooling prior to the desired temperature peak or valley since the system response time does not allow instantaneous temperature changes. The coil design consists of three individually adjustable induction heater coils which are used to maintain gage section temperature within acceptable margins (±8°C) and to ensure that temperature inside the gage section is hotter than outside the gage section. The tubing is covered with an insulating fiberglass sleeve and painted with high temperature (704°C) spray paint.

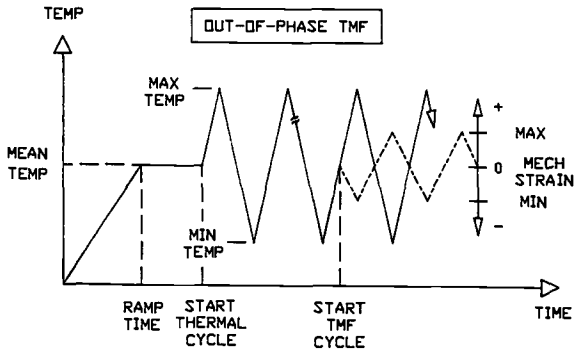

Figure 4— *Temperature Command Signal and Resulting Specimen Response during TMF Experiment without Hold-Time*

All experiments were strain-controlled with a triangular waveform and a strain ratio of ($A = \varepsilon_{amp}/\varepsilon_{mean}$) = ∞. Under isothermal conditions, the continuous cycle frequency was maintained at 10 cycles/minute. When a 90 second strain hold-time at the maximum tensile or compressive endlevel was introduced, the tensile- and compressive-going ramp times were maintained at 3 second each. For the TMF experiments without a hold-time, the continuous cycle frequency was set equal to 210 seconds/cycle, whereas for cycles with a 90 second strain compressive hold, the tensile-going and compressive-going strain ramps were increased to a total of 240 seconds/cycle. This slower ramp rate under hold-time TMF conditions was used to minimize the temperature fluctuations during the hold-time. For all tests, fatigue failure was defined at the cycle N_i at which a deviation from the stabilized peak tensile stress, σ_{sat}, was first observed. N_{90} represents the cycle at which a 10% load drop from σ_{sat} occurred.

Test Results

Uncoated IN-738LC Thermomechanical Fatigue (TMF) Tests

Uncoated specimens were tested at an operating temperature of 482-816°C, two OP TMF tests were cycled at mechanical strain ranges ($\Delta\varepsilon_{mech}$) of 0.5% and 0.7% and one IP TMF test at $\Delta\varepsilon_{mech}$ = 0.5%. At the same strain range of 0.5%, the IP life was at least twice as long as that of the OP life apparently due to the mean stresses developed, -166 MPa and 149 MPa, for the IP and OP specimens, respectively.

Increasing the temperature range to 482-871°C, a total of eight OP TMF tests were cycled at strain ranges of 0.3%, 0.5% and 0.8% with and without 90 second compressive hold-times. A comparison of continuous cycle fatigue lives at $\Delta\varepsilon_{mech}$ = 0.5% between the OP TMF test at 482-816°C (N_{90} = 5427) and the OP TMF test at 482-871°C (N_{90} = 1139), showed a significant reduction in life. When the peak temperature was raised 55°C, fatigue life was reduced by nearly a factor of 5.

Mid-life hysteresis loops are also shown in Figure 5 (a) and (b) for the 0.8% strain range tests and Figure 6 (a) – (d) for the 0.5% and 0.3% strain range experiments conducted at 482-871°C. These loops show a significant tensile mean stress due to the increasing elastic modulus with decreasing temperature and compressive stress relaxation at the high temperature of the TMF cycle. All mechanical hysteresis loops show a limited inelastic strain range, for instance at $\Delta\varepsilon_{mech}$ = 0.8%, the inelastic strain range (0.066%) is less than 10% of the total strain range and at 0.5% and 0.3% no inelastic strain range is detectable. Referring to an orientation scale in Figure 6, the total strain hysteresis loops for the 0.8% strain range are slanted in the + ϕ^* direction, whereas the 0.5% and 0.3% total loops are aligned in the - ϕ^* direction. This indicates that the magnitude of the thermal strain component over the temperature range 482-871°C was between 0.8% and 0.5%. In fact, the thermal expansion strain as measured prior to each fatigue test was typically 0.67%. Small deviations between the tensile- and compressive-loading are noticeable in the total strain loops, particularly at the endpoints most total strain loops and in the entire 0.8% and 0.3% hold-time loops. These departures from a smooth curve indicate that the thermal strains were not perfectly out-of-phase with the mechanical strains. This was especially true at minimum and maximum strain levels where the specimen temperature was expected to change instantly from heating to cooling or cooling to heating. Although the thermal mismatches could not be eliminated, they were minimized using the temperature decouples. These mechanical/thermal strain deviations have been discussed in greater detail in a previous publication with the conclusion that decouples are an appropriate means to minimize the deviations, Zamrik et al. [*11*]

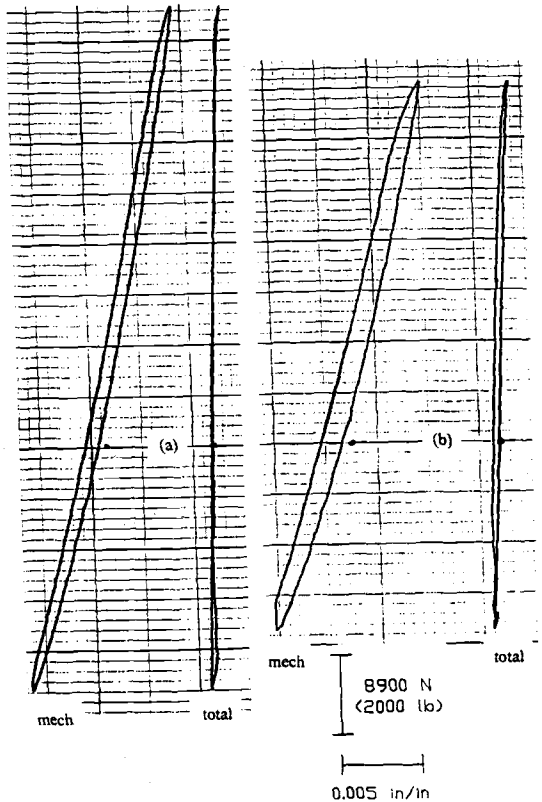

Figure 5— *Mid-life Hysteresis Loops (Mechanical and Total) for IN-738LC OP TMF Tested at a Temperature Range of 482-871°C*

(a) $\Delta\varepsilon_{mech}$ = 0.8%, t_h = 0 sec, and (b) $\Delta\varepsilon_{mech}$ = 0.8%, t_h = 90 sec (comp)

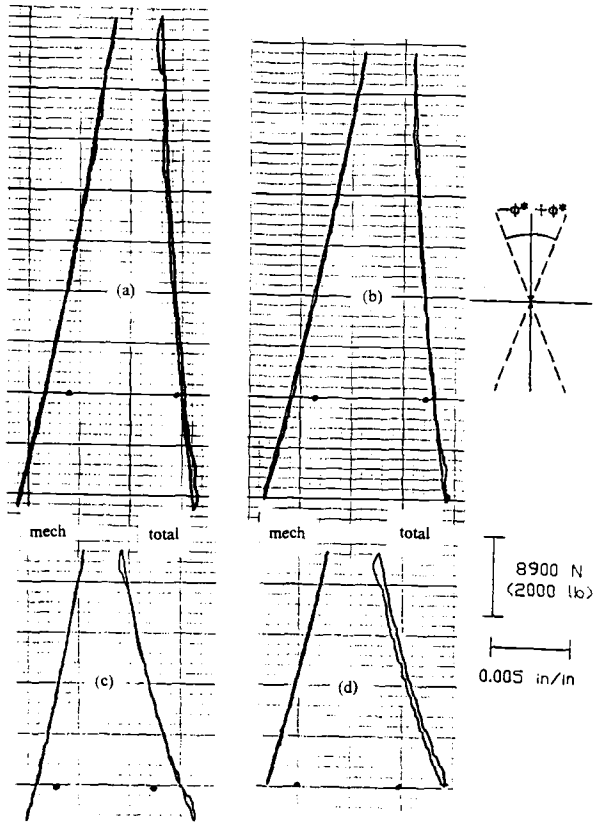

Figure 6— *Mid-life Hysteresis Loops (Mechanical and Total) for IN-738LC OP TMF Tested at a Temperature Range of 482-871°C*

(a) $\Delta\varepsilon_{mech}$ = 0.5%, t_h = 0 sec, and (b) $\Delta\varepsilon_{mech}$ = 0.5%, t_h = 90 sec (comp), and (c) $\Delta\varepsilon_{mech}$ = 0.3%, t_h = 0 sec, and (d) $\Delta\varepsilon_{mech}$ = 0.3%, t_h = 90 sec (comp)

NiCoCrAlY Coated IN-738LC Thermomechanical Fatigue (TMF) Tests

All coated TMF specimen results are shown in Figure 7. Ten tests were conducted at mechanical strain ranges of 0.3%, 0.4%, 0.5% and 0.7% with and without a 90 second compressive hold-time. The introduction of hold-time consistently reduced fatigue life by a factor of 2 at all strain ranges tested. Comparing the fatigue lives of coated and uncoated specimens, lower lives were observed for the coated specimens. For example, for the strain range of 0.5%, hold-time test showed a slightly lower life, N_{90} = 960 and N_{90}= 1113; however, at 0.3% the hold-time test showed a 35% lower coated life, N_{90} = 4512 as compared to N_{90} = 6924 cycles.

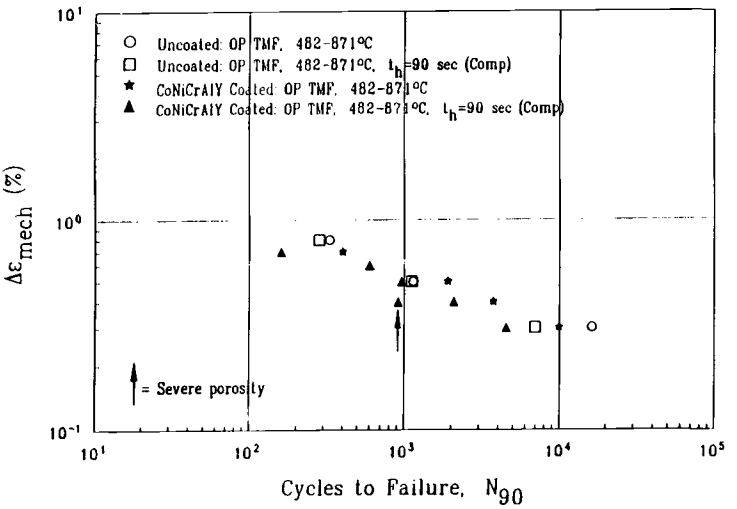

Figure 7— *Comparison of OP TMF Results on Uncoated and NiCoCrAlY Coated IN-738LC*

Mid-life loops are shown in Figure 8. The coated specimens test hysteresis response closely resembled comparative loops from uncoated substrate indicating the coating and coating processing had only a small effect on the stress-strain response of the substrate. The failure mode consisted of crack penetration into the coating with several cracks developing on the surface and linking to one major crack. For example, at 0.5% strain range with and without compressive hold-time, fatigue cracks typically grew over halfway through the coating thickness with several cracks particularly in the no-hold test propagating into the substrate as shown in Figure 9 and Figure 10a and for the hold-time test shown in Figure 10b. Also, the microstructure of a coated specimen tested at 0.7% strain range was shown in Figure 2.

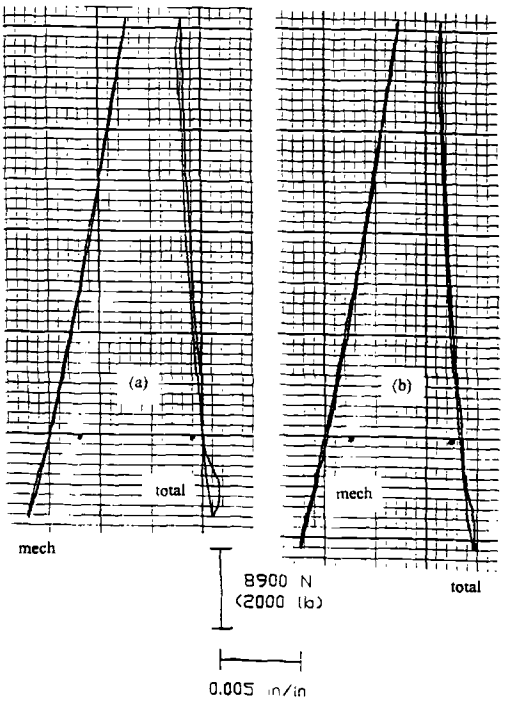

Figure 8— *Mid-life Hysteresis Loops (Mechanical and Total) for NiCoCrAlY Coated IN-738LC Tested in OP TMF at a Temperature Range of 482-871°C (a)* $\Delta\varepsilon_{mech}$ *= 0.5%,* t_h *= 0 sec, and (b)* $\Delta\varepsilon_{mech}$ *= 0.5%,* t_h *= 90 sec (comp)*

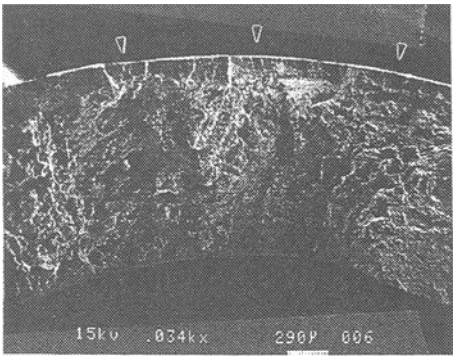

Figure 9— *SEM Fractograph Showing Fatigue Crack Initiation and Growth in NiCoCrAlY Overlay Coating*
$\Delta\varepsilon_{mech}$ = 0.5%, OP TMF, ΔT = 482-871°C, N_{90} = 1899

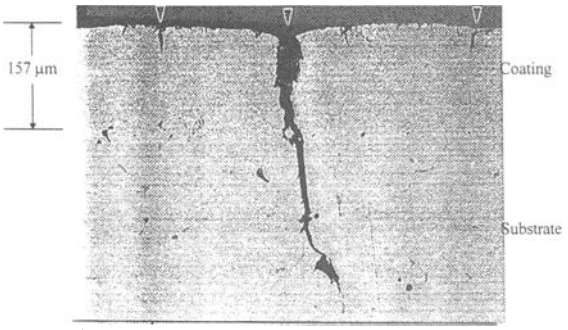

Figure 10a— *Optical Micrograph Showing NiCoCrAlY Overlay Coating Crack Initiation with Subsequent Crack Growth into IN-738LC Substrate*
$\Delta\varepsilon_{mech}$=0.5%,ΔT=482-871°C,N_{90}=1899
Crack Lengths: 15μm to 394μm (170X)

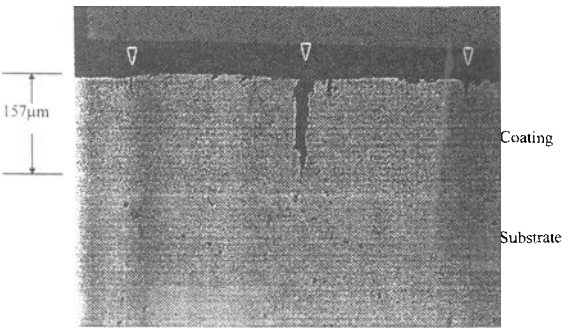

Figure 10b— *Optical Micrograph Showing Deep Fatigue Cracks in NiCoCrAlY Overlay Coating*
$\Delta\varepsilon_{mech}$ = 0.4%, OP TMF, ΔT = 482-871°C, t_h = 90 sec (comp), N_{90} = 2073
Crack Lengths: 27μm to 156μm (170X)

TMF Life Prediction Model Development

Based on the review of models discussed in the introduction and the experimental results, an energy-based approach was selected in the development of a TMF life prediction model for IN-738LC gas turbine material. The basic elements of the model are two parameters, σ_{max}, and ε_{ten}, incorporated in a tensile hysteresis energy module. Another reason for selecting an energy approach is the result of plotting published data [*12-15*] on the basis of strain vs. cycles to failure which showed a highly inaccurate prediction of fatigue life with a scatterband of 20x as shown in Figure 11.

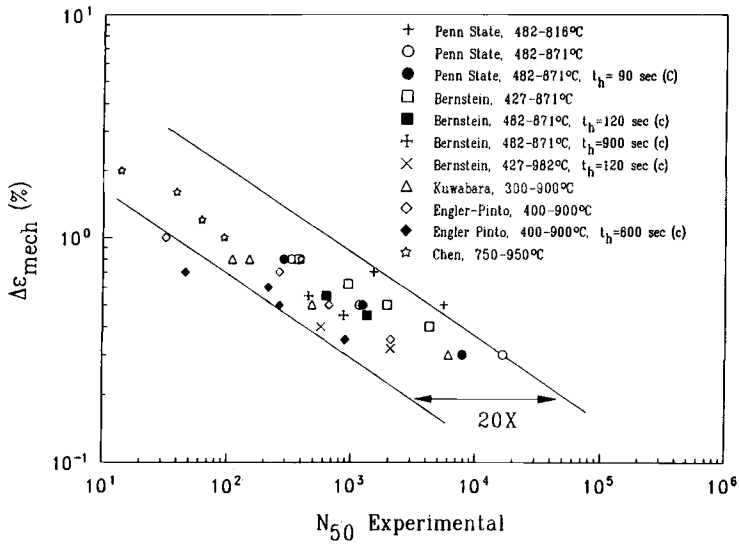

Figure 11— *Out-of-Phase Thermomechanical Fatigue Lives of IN-738LC Cannot be Accurately Predicted Using the Applied Mechanical Strain Range as the Only Correlating Parameter*

As a result of this inaccuracy, a life prediction model is developed on the basis of a frequency modified energy failure criterion by Ostergren [5] expressed as:

$$N_f = AW_T^{\beta} f^C \tag{1}$$

where W_T is the tensile inelastic hysteresis energy and f is the cycle frequency. The drawback of this approach is the restricted requirement that the inelastic energy should be predicted accurately. For the IN-738LC material, the hysteresis loops for OP TMF showed that the inelastic strain range is so small that large errors arise when attempting to either measure experimentally or predict analytically the inelastic strain range. As a result of this restriction, the Ostergren approach has to be modified on the basis of maximum tensile strain range rather than the inelastic strain range and to include the maximum tensile stress, the inclusion or exclusion of a compressive hold-time and the maximum cycle temperature. A schematic illustration of the mid-life hysteresis OP loops for both types of materials is shown in Figure 12 (a) and (b).

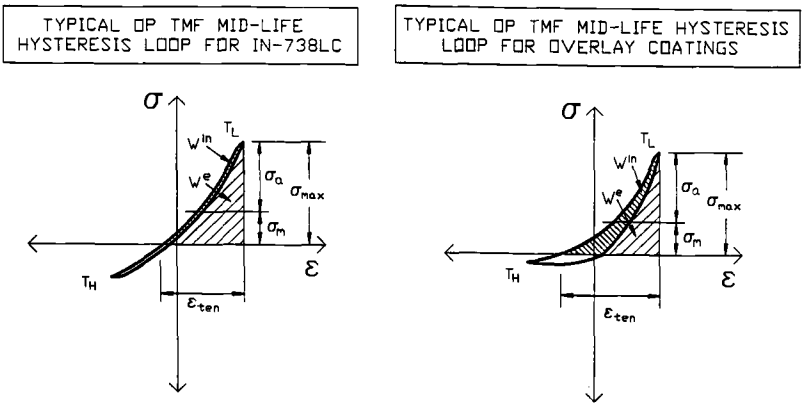

Figure 12— *Schematic Illustration of OP TMF Tensile Elastic Energy, W^e, and Tensile Inelastic Energy, W^{in}, on Typical IN-738LC and Overlay Coating OP TMF Hysteresis Loops*

Hence, the fatigue life cycle can be expressed as:

$$N_f = f(\Delta W, h(t), r(T)) \tag{2}$$

where ΔW represents an energy function, h(t) represents a creep or environmental effect due to hold-time and r(T) represents an elevated temperature effect. These three components are then combined for the cyclic life as:

$$N = A(\Delta W)^B (h(t))^C (r(T))^D \tag{3}$$

The parameter, ΔW, is selected as a ratio of cyclic fatigue energy, W_f, to static energy, W_t, as measured under monotonic tensile loading at the temperature of maximum tensile stress. The fatigue energy in this case is mostly the elastic energy, W_e, which is a good measure since the plastic energy component is negligible. Therefore, the parameter ΔW can be expressed as:

$$\Delta W = \frac{W_f}{W_t} \approx \frac{\sigma_{max}\,\varepsilon_{ten}}{\sigma_u \varepsilon_f} \tag{4}$$

where: σ_{max} = maximum tensile stress in mid-life hysteresis loop
ε_{ten} = tensile strain range in mid-life hysteresis loop for which the stress is tensile
σ_u = ultimate strength measured under monotonic tensile loading
ε_f = elongation to failure measured under monotonic tensile loading

The hold-time function can be expressed by:

$$h(t) = \left(1 + \frac{t_h}{t_c}\right) \tag{5}$$

where: t_h = length of compressive hold-time
t_c = length of total cycle time including hold-time

This hold-time function equals 1 under continuous cycling conditions and approaches 2 for cycles with hold-time lengths which approach the total cycle time.

The elevated temperature function can be written as:

$$r(T) = \exp\left(\frac{-Q}{R(T_{max} - T_0)}\right) \tag{6}$$

where: Q = activation energy for high temperature damage
R = gas constant
T_{max} = maximum temperature in TMF cycle
T_o = reference temperature

The elevated temperature parameter accounts for the exponentially increasing creep and/or environmental damage with increasing temperature. The reference temperature, T_o, is taken as the temperature at which the material's yield strength begins to decrease with temperature. Substituting Equations (4-6) into (3), the cyclic fatigue life is expressed as:

$$N = A\left[\left(\frac{\varepsilon_{ten}}{\varepsilon_f}\right)\left(\frac{\sigma_{max}}{\sigma_u}\right)\right]^B \left(1 + \frac{t_h}{t_c}\right)^C \exp\left(\frac{-Q}{R(T_{max} - T_0)}\right) \tag{7}$$

For out-of-phase TMF, σ_{max} corresponds to the low temperature of the TMF cycle. Also, the static energy components, ε_f and σ_u , are computed at the low temperature of the TMF cycle using the equations in Figure 13. The minimum and maximum cycle temperatures may be varied, so ε_f and σ_u must be known as a function of temperature.

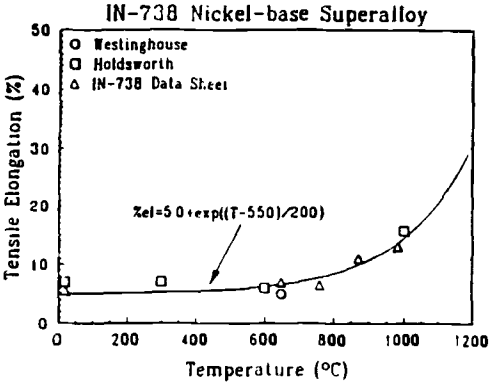

Figure 13a— *Dependence of Tensile Elongation on Temperature for IN-738 Nickel-base Superalloy*

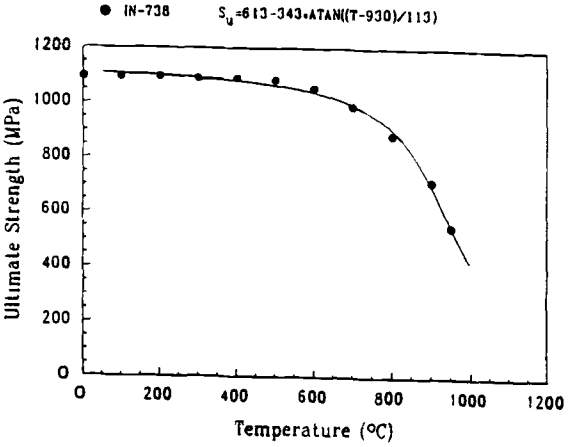

Figure 13b— *Dependence of Ultimate Strength to Failure on Temperature for IN-738 Nickel-base Superalloy*

The Application of the Model to TMF

The application of Equation (3) requires that the equation constants are determined. For each TMF cycle condition ($\Delta\varepsilon_{mech}$, T_{max}, T_{min}, etc.), the cyclic energy is evaluated using a viscoplastic model developed by Freed [*16*] to predict the mid-life hysteresis loop and calculate ε_{ten} and σ_{max}.. The model constants, A, B, C and Q are then calculated using a program to optimize the constants based on a sum of least squares error. As a result, all

fatigue data in Figure 11 are replotted in Figure 14a using ΔW and r(T), the elevated temperature damage component, where the scatterband is reduced to around 5x. However, when all three damage components, ΔW, h(t) and r(T), are incorporated, the scatterband is reduced to 3x (Figure 14b).

The criterion for failure is a 50% load drop from the peak stabilized load since most data was reported on that basis. However, data published by Kuwabara et al. [*13*] and Engler-Pinto et al. [*14*] were reported on 25% and 5% load drops, respectively. Based upon load drop data on tests conducted by the authors, the 25% and 5% load drop lives were increased by 5% and 15%, respectively, to estimate the additional number of cycles to 50% load drop. It is evident that the developed energy-base life prediction approach has correlated most of the TMF data generated under a range of testing conditions within a factor of three. The data obtained from Kuwabara et al. and Engler-Pinto et al. generally fall at the upper bound of the scatterband. These are the two references from which life data were increased to represent a 50% load drop situation. If the actual cycles to a 50% load drop were greater than the percentages used, the overall scatterband would decrease, and if the OP TMF data based on a 10% load drop failure criterion is used, the overall scatterband can be considerably reduced.

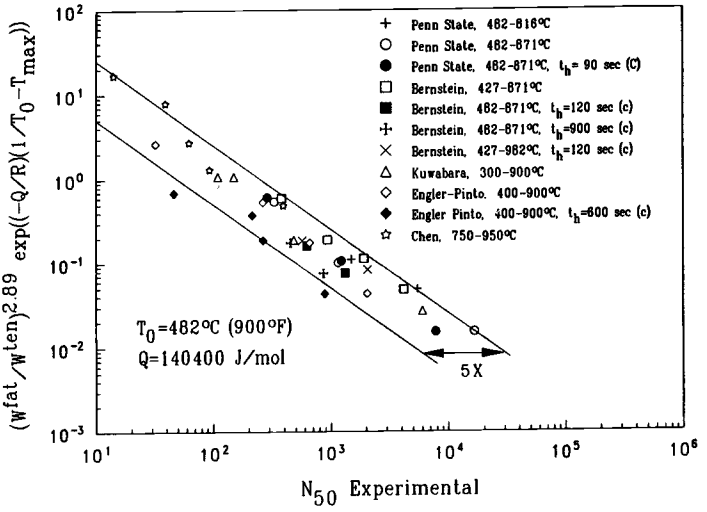

Figure 14a— *Correlation of Uncoated IN-738LC OP TMF Data Using ΔW, the Ratio of Cyclic to Static Energy and r(T), the Elevated Temperature Damage Component*

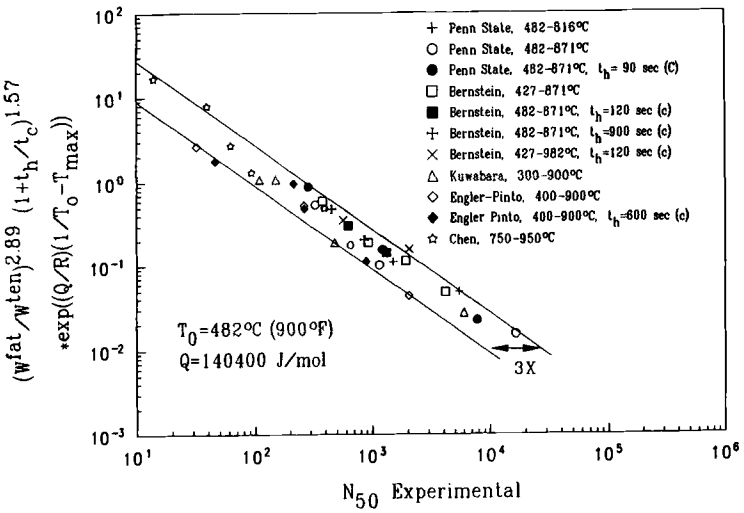

Figure 14b— *Correlation of Uncoated IN-738LC OP TMF Data Using Proposed Life Prediction Model Consisting of Three Damage Components: ΔW, the Ratio of Cyclic to Static Energy, h(t), the Hold-Time Damage Parameter, and r(T), the Elevated Temperature Damage Component*

Conclusions

The development of the uniaxial life prediction model included a viscoplastic model. The largest discrepancies between the viscoplastic model predictions and experimental data is observed under high-temperature compression loading at a high strain range ($\Delta\varepsilon_{mech}$ = 0.8%) loading as shown in Figure 15. Figure 15 also illustrates that the high-temperature compressive stress relaxation is under-predicted with strain hold-times. This relaxation error may result from the use of steady-state creep data in the viscoplastic flow rule analysis since steady-state creep rates are slower than primary creep rates and stress relaxation strain rates, whereas for 0.3 and 0.5% strain ranges, the model showed good accuracy in its prediction as shown in Figure 16. It should be noted that the viscoplastic model deficiencies have little impact in the overall TMF life prediction model since only the tensile fatigue energy is considered and the model predictions on the tension side of all hysteresis loops are excellent.

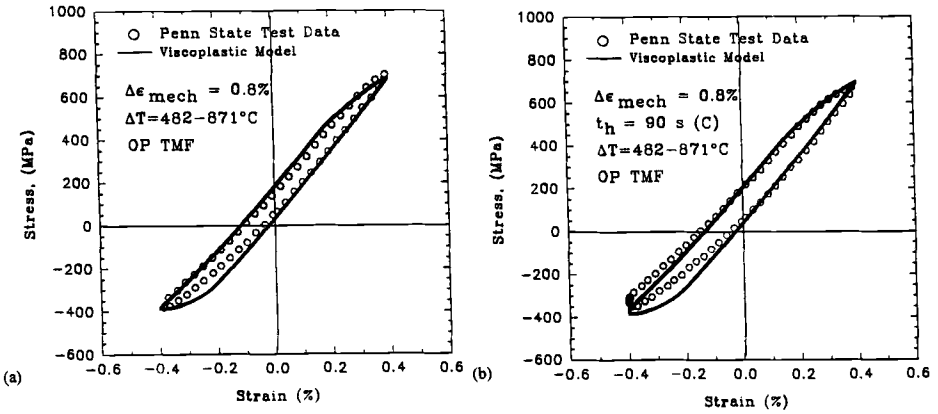

Figure 15— *Comparison of Experimental and Predicted Hysteresis Loops for IN-738LC Tested in OP TMF and ΔT = 427-871°C*
(a) $\Delta\varepsilon_{mech}$ = 0.8%, and (b) $\Delta\varepsilon_{mech}$ = 0.5%, t_h = 90 sec (comp)

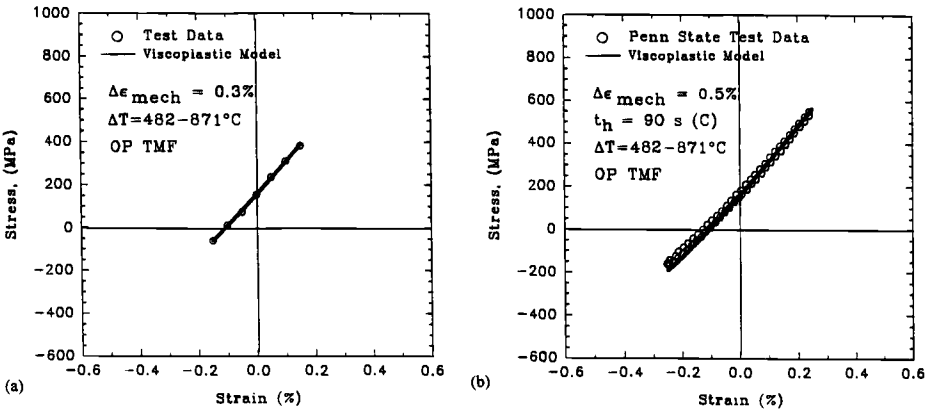

Figure 16— *Comparison of Experimental and Predicted Hysteresis Loops for IN-738LC Tested in OP TMF and ΔT = 427-871°C*
(a) $\Delta\varepsilon_{mech}$ = 0.3%, and (b) $\Delta\varepsilon_{mech}$ = 0.5%, t_h = 90 sec (comp)

The proposed life prediction method for overlay coated IN-738LC has shown the ability to correlate most of IN-738LC OP TMF data from numerous researchers into a 3x scatterband. This is an improvement over a Manson-Coffin strain approach where the scatterband for the same fatigue data was approximately 20x. In the proposed model, fatigue data generated under low to mid-level strain ranges ($\Delta\varepsilon_{mech}$ = 0.3% - 0.6%) show a good predictive agreement with experimental data (Figure 14b). However, at high strain ranges ($\Delta\varepsilon_{mech}$ > 0.8%) and low lives (< 100 cycles) numerous data points lie slightly outside the 3x scatterband. The life prediction model was developed such that the elastic and inelastic tensile energies were linearly added together, since under typical design applications with low to mid-level strain ranges, the elastic strain component of the total strain range dominates. Under high strain range loading, the inelastic component may be comparable to, or greater than, the magnitude of the elastic component. Under these conditions, a linear summation of tensile elastic and inelastic energies may not be appropriate. For the majority of the OP TMF data which is generated under more typical design strain ranges, the proposed life prediction model provides an excellent prediction capability.

The failure characteristics of the coated material showed that the coating affected the fatigue life by delaying crack growth into the substrate. It also enhanced the OP TMF life at high strain ranges but reduced the life at low strain ranges.

Acknowledgment

This paper is part of a comprehensive research program sponsored by DOE FETC through a cooperative agreement with South Carolina Energy Center under Contract No: AGTSR 93-01-SR012D on "Life Prediction of Advanced Materials for Gas Turbine Application". Also, the authors greatly appreciate the technical contributions made by Mr. John Junkin of Westinghouse Power Division in Orlando, FL, and Drs. Graham Webb and Tom Strangman of Allied Signal Aerospace Co., Engine Division in Phoenix, AZ. The program was administered by Dr. Dan Fant of South Carolina Energy Research Center.

References

[1] Bernstein, H.L., Grant, T.S., McClung, R.C. and Allen, J.M., "Prediction of Thermal-Mechanical Fatigue Life for Gas Turbine Blades in Electric Power Generation," *ASTM STP 1186*, American Society for Testing and Materials, Philadelphia, PA, 1993, pp. 212-238.

[2] Arana, M., Martinez-Esnaola, J.M. and Bressers, J., "Crack Propagation and Life Prediction in a Nickel-based Superalloy under TMF Conditions," *Fatigue under Thermal and Mechanical Loading*, J. Bressers and L. Remy, Eds., Kluwer Academic Publishers, Dordrecht, 1996, pp. 393-402.

[3] Pejsa, P.N. and Cowles, B.A., "Thermal Mechanical Fatigue Life Prediction for Advanced Anisotropic Turbine Alloys," *Journal of Engineering for Gas Turbines and Power*, Vol. 108, July 1986, 1986, pp. 504-506.

[4] Linask, I. and Derberger, J., "A Fracture Mechanics Approach to Turbine Airfoil Design," *75-GT-79*, 1979, pp. 1-8.

[5] Ostergren, W.J., "A Damage Function and Associated Failure Equations for Predicting Hold Time and Frequency Effects in Elevated Temperature, Low-cycle Fatigue," *Journal of Testing and Evaluation*, Vol. 4, No. 5, 1976, pp. 327-339.

[6] Nissley, D.M. and Meyer, T.G., "Life Prediction and Constitutive Models for Engine Hot Section Anisotropic Materials Program," *NASA, CR 189222*, August 1992.

[7] Nissley, D.M., "Thermomechanical Fatigue Life Prediction in Gas Turbine Superalloys: A Fracture Mechanics Approach," *AIAA Journal*, Vol. 33, June 1995, pp. 1114-1120.

[8] Remy, L., Bernard, H., Malpertu, J.L. and Rezai-Aria, R., "Fatigue Life Prediction Under Thermal-Mechanical Loading in a Nickel-Base Superalloy," *Thermomechanical Fatigue Behavior of Materials, ASTM STP 1186*, H. Sehitoglu, Ed., American Society for Testing and Materials, Philadelphia, 1993, pp. 3-16.

[9] Neu, R.W. and Sehitoglu, H., "Thermomechanical Fatigue, Oxidation and Creep: Part II. Life Prediction," *Metallurgical Transactions A*, Vol. 20A, Sept. 1989, pp. 1769-1783.

[10] Chaboche, J.L. and Lesne, P.M., "A Non-Linear Continuous Fatigue Damage Model," *Fatigue and Fracture of Engineering Materials and Structures*, Vol. 11, No. 1, 1988, pp. 1 - 17.

[11] Zamrik, S.Y., Davis, D.C. and Firth, L.C., "Isothermal and Thermomechanical Fatigue of Type 316 Stainless Steel," *Thermomechanical Fatigue Behavior of Materials: Second Volume, ASTM STP 1263*, M.J. Verilli and M.G. Castelli, Eds., American Society for Testing and Materials, Philadelphia, 1996, pp. 96-116.

[12] Bernstein, H.L., "Life Management System for General Electric Frame 7E Gas Turbine," *Life Assessment and Repair Technology for Combustion Turbine Hot Section Components*, R. Viswanathan and J.M. Allen, Eds., ASM International, Materials Park, OH, 1990, pp. 111-118.

[13] Kuwabara, K., Nitta, A. and Kitamura, T., "Thermal-Mechanical Fatigue Life Prediction in High-Temperature Component Materials for Power Plant," *Advances in Life Prediction Methods*, D.A. Woodford and J.R. Whitehead, Eds., ASME, 1983, pp. 131-141.

[14] Engler-Pinto, C.C., Jr., Harkegard, G., Ilschner, B., Nazmy, M.Y., Noseda, C. and Rezai-Aria, F., "Thermo-Mechanical Fatigue Behavior of IN-738LC," *Materials for Advanced Power Engineering, Part I*, Coutsouradis et al., Eds., Kluwer Academic Publishers, 1994, pp. 853-862.

[15] Chen, H., Chen, W., Mukherji, D., Wahi, R.P. and Wever, H., "Cyclic Life of Superalloy IN738LC Under In-phase and Out-of-phase Thermo-mechanical Fatigue Loading," *Z. Metallkd.* 86, 1995, pp. 423-427.

[16] Freed, A.D., "Thermoviscoplastic Model with Application to Copper," *NASA Technical Paper 2845*, 1988, pp. 1-15.

H. Ikuno,[1] S. Iwanaga, [1] and Y. Awano[1]

Thermo-mechanical Fatigue Behavior of Al-Si-Cu-Mg Casting Alloy

Reference: Ikuno, H., Iwanaga, S., and Awano, Y., **"Thermo-mechanical Fatigue Behavior of Al-Si-Cu-Mg Casting Alloy,"** *Thermo-mechanical Fatigue Behavior of Materials: Third Volume, ASTM STP 1371,* H. Sehitoglu and H. J. Maier, Eds., American Society for Testing and Materials, West Conshohocken, PA, 2000.

Abstract: This paper describes the thermo-mechanical fatigue behavior of Al-Si-Cu-Mg casting alloy. The alloy is widely used for cylinder heads and pistons of automobile engines. Repeated cycling between driving and resting, or low-power and high-power driving cause thermal cycling in the engine materials. The thermo-mechanical fatigue property is therefore very important to develop high-performance engines. This study aims to characterize the cyclic stress-strain behavior of this alloy and to clarify the factors dominating the fracture life. Results obtained are : (1) The stress-strain behavior changes remarkably during thermal cycling. Cyclic hardening and cycling softening occur in the higher and lower strain ranges, respectively. (2) A thermo-mechanical fatigue fracture limit diagram is obtained by connecting fracture points on the inelastic strain range - number of cycles relationship. (3) Consequently, in 10^3 - 10^4 cycles, it is considered that poor ductility and inelastic strain increase due to overaging dominate the thermo-mechanical fatigue life of the alloy.

Keywords: thermo-mechanical fatigue, cast aluminum alloy, stress-strain behavior, overaging, elastic strain range, hysteresis energy, fatigue limit diagram

Introduction

Al-Si-Cu-Mg casting alloy is generally used for cylinder heads and pistons of automobile engines, which are very important components that influence the engine performance. Cycling between driving and resting, or low-power and high-power driving causes thermal cycling in the engine materials. Because new high-performance engines aim to decrease fuel consumption, exhaust emissions and weight, the temperature and the stress have been fatally rising. Therefore, the thermo-mechanical fatigue properties have been more significant factors in developing high-performance engines.

[1]Researcher, Senior Researcher and Principal Researcher, respectively, Material Division 1, Toyota Central R&D Labs., Inc., Nagakute Aichi, 480-1192, Japan

Usually for ductile materials, the Manson-Coffin's law [*1*] which relates plastic strain range to the number of cycles to failure has bearing. However, for this Al-Si-Cu-Mg alloy, the plastic range is varying under severe conditions because overaging causes softening in this alloy. Therefore, we need a new relationship to represent the thermo-mechanical fatigue property under the severe conditions. On the other hand, there are very few thermo-mechanical fatigue studies of aluminum alloys [*2-6*].

This study aims to characterize the cyclic stress-strain behavior of this alloy and to clarify the factors dominating the fatigue life.

Material

The material evaluated was JIS (Japan-Industry-Standard) AC2B alloy shown in Table 1. Mixing 99.9% pure aluminum, Al-Si, Al-Cu, Al-Mg and Al-Fe base alloys produced the desired composition. The melted material was deoxidized with NaCl-25%AlF_3 flux at 750℃ and degassed under vacuum (around 10 Pa) for 1.2 ks. After that, 30 mm diameter and 170 mm long circular rods of 45 mm diameter and 85 mm long feeder head were sand-cast at 700℃. The heat treatment used was T6 (Table 1).

Table 1 - *Material*

Chemical composition (mass%)	Al- 6Si-3.5Cu-0.3Mg-0.25Fe
Solidification time	400 s (DAS* : 60 μ m)
Porosity	10^{-6} m^3/kg
Heat treatment	T6 (500 ℃ 18ks, W.Q. +160 ℃ 18ks)
Vickers hardness	130 (10kg)

* DAS : secondary dendrite arm spacing

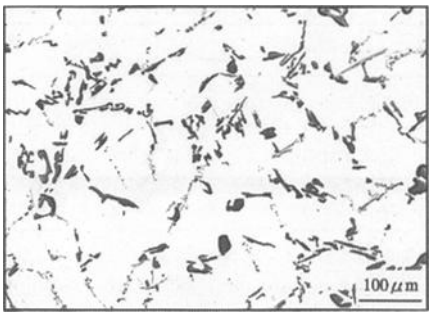

Figure 1 - *Microstructure of the JIS-AC2B Cast Aluminum Alloy*

Figure 1 shows the microstructure of the cast JIS-AC2B Alloy. It indicates a hypo-eutectic structure composed of an α-aluminum matrix, eutectic Si and Al-Si-Fe compound. θ '(Al_2Cu) and Mg_2Si metastable precipitates were dispersed in the matrix which was hardened by the T6 heat treatment. Figure 2 shows the thermo-mechanical fatigue specimen. The parallel part was machined to 10 mm diameter and 22 mm length and polished with #1000 wet emery paper to remove the shaving traces and make the surface roughness uniform.

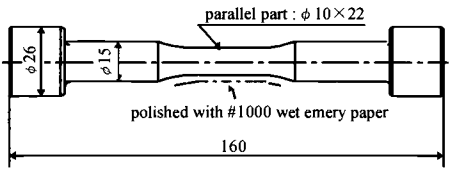

Figure 2 - *Specimen of Thermo-mechanical Fatigue Test*

Testing and Analysis

An electro-hydraulic machine performed the thermo-mechanical fatigue test. The specimen was heated with a high-frequency induction coil and cooled by blowing compressed air. A high temperature extensometer of 15 mm gage length was used for the longitudinal strain measurement. The machine used has a two-closed-loop analog control system. The temperature was measured and controlled by type-R thermocouples welded to the center of the gage length based on the signal from a function generator. The total (mechanical and thermal) strain was measured and controlled by means of a quartz rod extensometer based on the same signal from the function generator. The load was measured from a standard load cell.

Table 2 - *Conditions of Thermal Fatigue Test*

Test machine	Electro-Hydraulic type
Temperature	50 ~ 250 ℃
Mechanical strain range	0.4, 0.45, 0.6 %
Mean strain	0 %
Frequency, wave	240 s/cycle, triangle

Table 2 shows the test conditions. The lower temperature was 50℃ and the upper one was 250℃. The mechanical strain ranges were 0.4, 0.45 and 0.6 %. During the tests, mechanical strain and temperature were controlled out-of phase based on the signal from the function generator as shown in Figure 3. We selected these conditions

considering the practical use for an automobile engine material. After heating to 150℃ under stress free condition, control of the temperature and strain was begun for each target cycle. During the test, the temperature differences through the parallel part were less than 5℃.

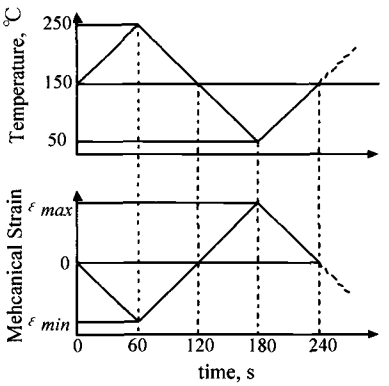

Figure 3 - *Target Thermal and Strain Cycle*

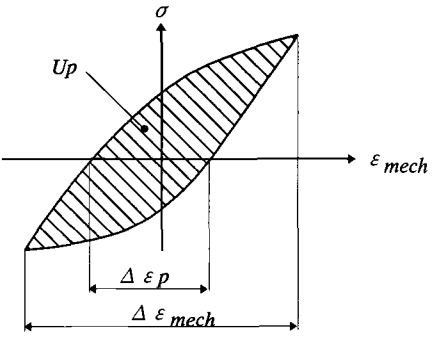

Figure 4 - *Stress-Strain Analysis*

The voltage signals that indicate the load and total strain were monitored with a data logging system. After the tests, the measured data were input into a computer for data analysis. The stress was calculated as the load divided by the initial cross section area. The following relation gave the mechanical strain.

$$\varepsilon_{mech} = (L-L_m) / L_o - \alpha (T- T_m) \quad (1)$$

where

L = instantaneous gage length
L_m = gage length at mean temperature
L_o = initial gage length at room temperature
T = instantaneous temperature
T_m = mean temperature
α = linear coefficient of thermal expansion

Figure 4 shows the analysis of stress-strain hysteresis. For engineering purposes, the inelastic strain range of a thermo-mechanical cycle can be determined to a first approximation by the following equation [7].

$$\Delta \varepsilon_{in} = \Delta \varepsilon_{mech} - (| \sigma_B | / E_b + | \sigma_c | / E_c) \quad (2)$$

where E_b and E_c are the elastic modulus at the maximum and minimum strain, respectively. In this test, the slopes of the stress-strain loops were almost constant

during unloading from maximum to zero strain and from minimum to zero strain. Therefore, the inelastic strain $\Delta \varepsilon p$ was defined as the strain range across the stress-free line. The hysteresis energy *Up* was the area in the hysteresis. $\Delta \varepsilon p$ corresponds to the plastic strain range because the creep strain is negligibly small in this test. *Up* is the energy consumed during a cycle per unit volume.

Experimental Results and Discussion

Figure 5 shows the relationships between the mechanical strain range $\Delta \varepsilon_{mech}$ and the number of cycles to failure N_f. N_f increases linearly with decreasing $\Delta \varepsilon_{mech}$ on the logarithmic graph.

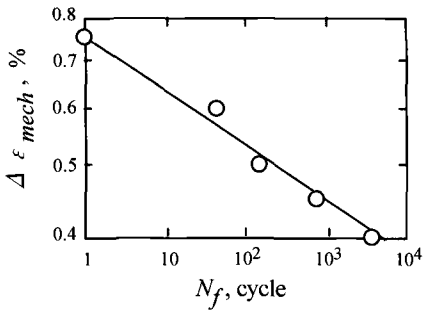

Figure 5 - *Mechanical Strain Range ($\Delta \varepsilon_{mech}$) - Number of Cycles to Failure (N_f) Relations*

Figures 6(a) and (b) show the change in the stress-strain hysteresis loops with thermal cycles for $\Delta \varepsilon_{mech}$ values of 0.6% and 0.4%, respectively. This stress-strain behavior is quite different in each case. For a $\Delta \varepsilon_{mech}$ of 0.6%, inelastic strain occurs during the first cycle and decreases with cycling, when the tensile peak stress tends to rise. On the contrary, for a $\Delta \varepsilon_{mech}$ of 0.4%, inelastic strain is negligible up to the first few hundred cycles and appears and increases at higher cycles, when the compressive peak stress is remarkably reduced.

Some alloys, as well as this alloy, show cyclic hardening and cyclic softening [*7,8*]. Especially, this alloy, which has been precipitation-hardened by near-peak aging at 160℃ in T6, then heated for a long time over the aging temperature(160℃) , undergoes precipitation enlargement resulting in alloy softening (overaging). Age-hardened aluminum alloys soften remarkably at temperatures over 200℃ due to overaging [*9*]. The maximum temperature 250℃ is too high for this alloy to soften.

The number of cycles to failure at a strain range of 0.6% is only about 40 cycles. Obviously, the examined material does not show any overaging effects in such short experiments. Therefore, the observed cyclic hardening is caused by the interaction of dislocations with each other and with the precipitates. At a strain range of 0.4%, the

number of cycles to failure is higher than 3000 cycles. Therefore, during the experiment, the material is held sufficiently long at high temperature so that overaging processes occur. Under the chosen conditions, the induced mechanical loading is not high enough to produce plastic deformation within the first cycles. Plastic deformation appears when the overaging processes have softened the material. Therefore, the overaging processes are exclusively responsible for the observed cyclic softening.

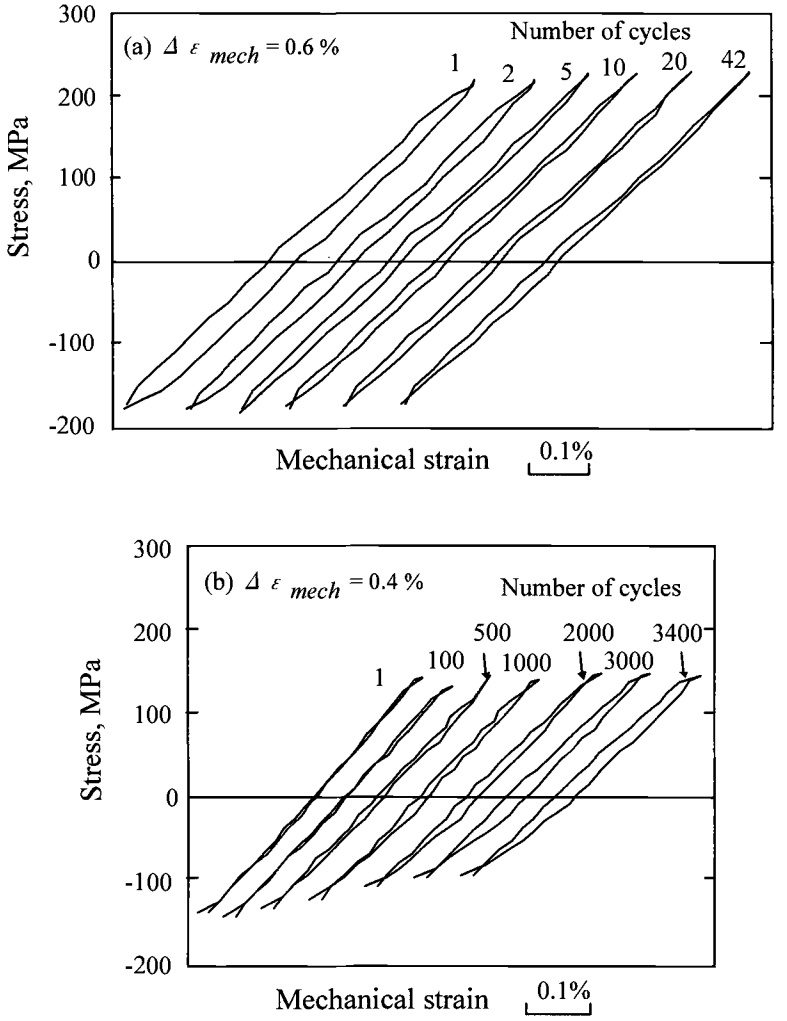

Figure 6 - *Change of Stress-Strain Hysteresis. The axis of mechanical strain is shifted to display the shape of the curves clearly. Envioronmental electromagnetic noise in the output signals from the test machine makes the loops appear wavy.*

Figure 7(a) shows the course in inelastic strain range $\Delta \varepsilon p$ with thermal cycling. For a $\Delta \varepsilon_{mech}$ of 0.6%, $\Delta \varepsilon p$ decreased with cycling until around the 10th cycle and remained almost constant after that. On the contrary, for a $\Delta \varepsilon_{mech}$ of 0.4% and 0.45%, $\Delta \varepsilon p$ disappeared up to a certain cycle and then rose and increased at the higher cycles. At lower $\Delta \varepsilon_{mech}$, inelastic strain appeared at higher cycles. The increasing rates of $\Delta \varepsilon p$ are almost the same under both conditions.

In Figure 7(a), connecting all fracture points produces a fracture limit diagram. The fracture limit of $\Delta \varepsilon p$ at the first cycle was defined as twice the tensile elongation. This diagram indicates that the fracture limit of $\Delta \varepsilon p$ is remarkably reduced for the earlier cycles and remains as small as 0.03-0.05% during the 10^3-10^4 cycles that should be generally warranted for an automobile engine material. It scarcely increased at the higher cycles and was only 0.05% at 10^4 cycles. Especially, the value at the 10^3 cycles, 0.03%, is remarkably lower than the values reported in other alloys [*4,10,11*]. This result indicates that the poor ductility at the higher cycles for this alloy reduces the thermo-mechanical fatigue life. In age-hardened aluminum alloys, softening due to overaging does not result in immediately increasing the ductility until the alloy softens sufficiently by heating for a long time [*9*]. In addition, because of the permanent expansion in volume causing enlargement of the precipitates due to overaging [*9*], internal stress is generated around the enlarged precipitates that cause brittleness of this alloy. Therefore, it is suggested that the poor ductility under severe conditions and the elastic strain increase due to overaging dominate the thermo-mechanical fatigue life of the cast aluminum alloy.

Figure 7(b) shows the accumulated inelastic strain $\Sigma \Delta \varepsilon p$ - N relationship. This figure produces another fracture limit diagram. The fracture limit of $\Sigma \Delta \varepsilon p$ remains constant up to a few tens of cycles and then it increases remarkably at higher cycles. This morphological feature is completely contrary to the $\Delta \varepsilon p$-N diagram.

Many studies are usually successful in adopting the ductility exhaustion law for life prediction of stainless steels [*12-14*]. The ductility exhaustion law defines that materials fail when the total of fatigue damage indicated by plastic strain range and creep damage reaches a constant value.

In this test, the limit value indicated as accumulated inelastic strain range is almost constant up to a few tens of cycles as shown in Figure 7a. Therefore, the life up to a few tens of cycles follows the ductility exhaustion law, where the creep damage is negligible because the temperature does not remain in the maximum and minimum temperatures.

On the contrary, after a few tens cycles, the limit value of accumulated inelastic strain range increased remarkably with increasing number of cycles. The maximum temperature, 523K (250℃), which corresponds to about 0.6 times the melting point in absolute temperature, is high enough to cause the mechanical strain to recover. Therefore, the recovery of mechanical strain causes an increase in the accumulated inelastic strain limit with increasing number of cycles after a few tens of cycles.

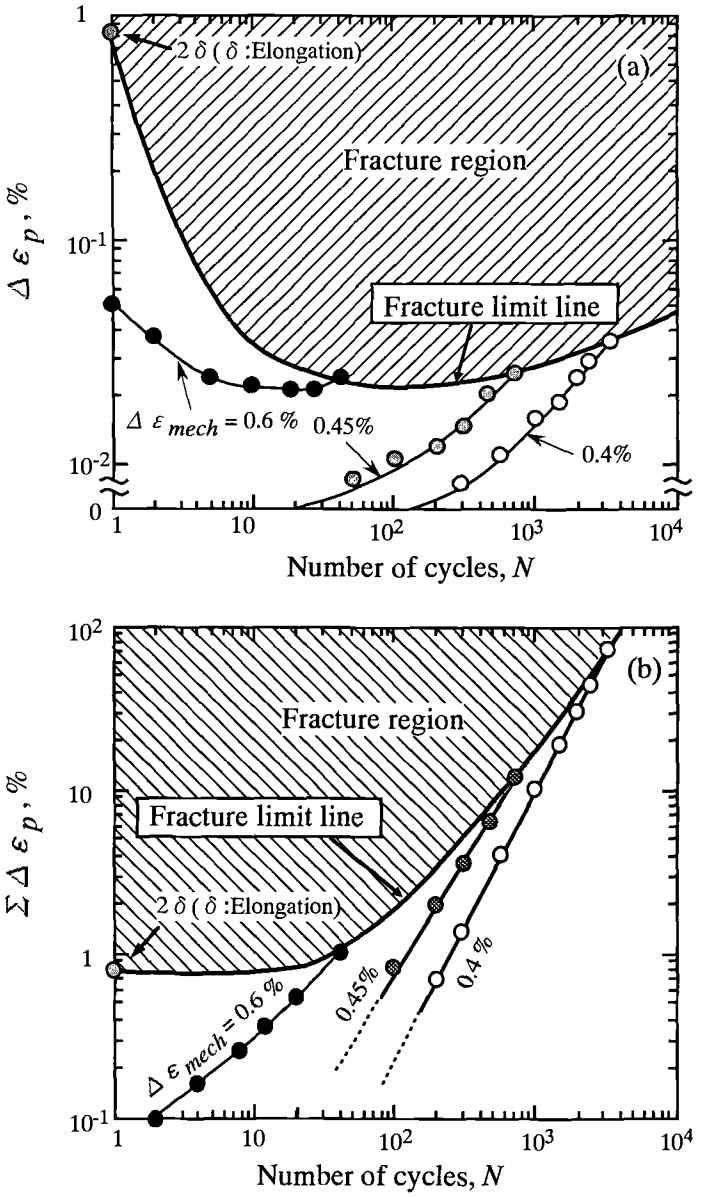

Figure 7 - *Thermo-mechanical Fatigue Limit Diagrams with Change in (a)Inelastic Strain Range Δ ε p and (b) the Accumulated Value Σ Δ ε p*

Assuming that the ductility exhaustion law is effective, Figure 7a shows the proportionally varying behavior between the given and recovered inelastic strain, which are the input and output of inelastic strain per cycle. When the input strain is larger than the output strain, the strain effectively remaining in the material should increase with cycling, and that causes the inelastic strain limit at which failure occurs to decrease with cycling. When the input and output strain balance, the inelastic strain limit should remain constant with cycling. When the output strain is larger than the input strain, the limit should increase with cycling. Figure 7a shows that the inelastic strain limit remained almost constant after a few tens of cycles; therefore, the given and recovered inelastic strain were balanced in this region.

The above discussion concludes that Figures 7a and 7b show fundamental behaviors that dominate the thermo-mechanical fatigue life of this alloy. In Figure 7a, the inelastic strain limit remained almost constant after a tens of cycles; therefore, increasing of the inelastic strain range due to overaging dominates the life. In Figure 7b, the accumulated inelastic strain limit remained almost constant up to a few tens of cycles. Therefore, the ductility exhaustion law is effective in this region because the recovery of inelastic strain is negligible.

We can utilize these Figures(7a and 7b) for life prediction of this alloy under the examined temperature conditions. For practical use, the fracture limit lines must be obtained from the experiments under the proper thermal cycle. The varying behavior also needs to be obtained by a computer-aided engineering (CAE) method using the cyclic stress strain behavior. Sehitoglu et al. reported the modeling of the stress-strain behavior of cast aluminum alloys [*15*]. This method can be used to estimate the cyclic stress-strain behavior.

$\Delta \varepsilon p$-N diagram (Figure 7a) is suitable for predicting a long life because the fracture limit is almost flat relative to the remarkable increase in $\Delta \varepsilon p$ at the higher cycles. On the contrary, the $\Sigma \Delta \varepsilon p - N$ diagram (Figure 7b) is suitable for predicting a short life because the fracture limit is almost flat relative to the remarkable increase in $\Sigma \Delta \varepsilon p$ at the lower cycles. Consequently, the $\Sigma \Delta \varepsilon p$-$N$ diagram and the $\Delta \varepsilon p$-N diagram are useful for short and long life predictions, respectively.

Figures 8 (a) and (b) also show thermo-mechanical fatigue limit diagrams using Up and ΣUp, respectively. Figures 7 and 8 appear similar because the stress range remained almost constant during this test. Inelastic strain has been defined variously, so that Figure 7 may limit wider application. On the contrary, Up is unified simply from the stress-strain hysteresis area and it also considers the stress change. Therefore, Up-N and ΣUp-N diagrams (Figure 8) can be applied more reliably.

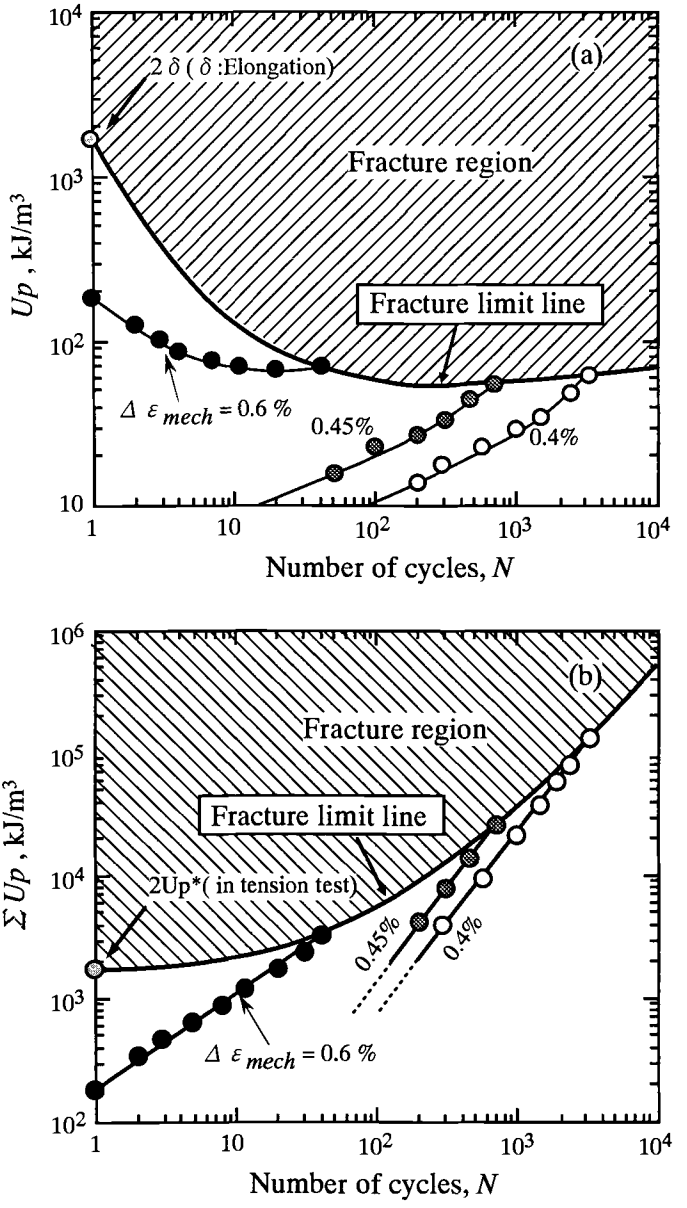

Figure 8 - *Thermo-mechanical Fatigue Limit Diagrams with Change in (a) Hysteresis Energy Up and (b) the Accumulated Value ΣUp*

Conclusions

(1) The stress-strain hysteresis loop changes with the number of thermal cycles for the Al-6Si-3Cu-0.3Mg casting alloy. Inelastic strain decreases in the early cycles; however, it increases at higher cycles.
(2) A thermo-mechanical fatigue fracture limit diagram is obtained by connecting the fracture points in the inelastic strain range - number of cycles relationship. The fracture limit of the inelastic strain range is very small in the 10^3 - 10^4 cycles corresponding to practical use cycles. This indicates poor ductility under severe conditions for this alloy.
(3) From these results, it is considered that poor ductility under severe conditions and inelastic strain increase due to overaging dominate the thermo-mechanical fatigue life of this alloy.

References

[1] Coffin, L. F. Jr., "A Study of the Effects of Cyclic Thermal Stresses on a Ductile Metal," *Trans. ASME*, 76(1954), pp. 931-950.

[2] Ikuno, H., Iwanaga, S., and Awano, Y., "Effect of Porosity on Thermal Fatigue Lives of AC2B Aluminum Alloy Castings," *Journal of Japan Institute of Light Metals*, 45(1995), pp.671-676.

[3] Ikuno, H., Iwanaga, S., and Awano, Y., "Development of Simple Thermal Fatigue Test Method Using Low-Thermal Expansion Restraining Holders," *J. Soc. Mat. Sci., Japan*, 45(1996), pp. 125-130.

[4]Flaig, B., Lang, K. H., Lohe, D., and Macherauch, E., "Thermal-Mechanical Fatigue of The Cast Aluminum Alloy GK-AlSi10Mg wa," *Fatigue Under Thermal and Mechanical Loading : Mechanisms, Mechanics and Modeling*, J. Bressers, L. Remy, M. Steen and J.L. Valles, Eds., Kluwer Academic Publishers, 1995, pp. 361-370.

[5] Watanabe, S., Isobe, T., and Iguchi, N., "Thermal Fatigue Resistance of Al-Si Casting Alloys for Pistons," *Journal of Japan Institute of Light Metals*, 22(1972), pp. 395-402.

[6] Tohriyama, S. and Kumano, M., "Influence of Material and Mechanical Properties on Thermal Fatigue Life of Aluminum Castings," SAE paper 950720.

[7] Sehitoglu, H., "Thermal and Thermomechanical Fatigue of Structural Alloys," *ASM Handbook vol.19: Fatigue and Fracture*, 1996, pp. 527-556.

[8] Lee, D. H. and Kwun, S. I., "Cyclic Hardening and Softening Behavior of a Fully Annealed Zircaloy-4," *Scripta Metallurgica et Materialia*, 31(1994), pp. 1475-1480.

[9] "Heat Treating of Aluminum Alloys," *ASM Handbook vol.4: Heat Treating*, 1991, pp. 841-879.

[10] Taira, S., Fujino, M., and Ohtani, R., "Collaborative Study on Thermal Fatigue of Properties of High Temperature Alloys in Japan," *Fatigue Engg. Mater. Struct.*, 1(1979), pp. 495-508.

[11] Taira, S., Fujino, M., "Studies on Thermal Fatigue Fracture of Metallic Materials," *J. Soc. Mat. Sci., Japan*, 25(1976), pp. 218-229.

[12] Priest, R. H. and Ellison, E. G., "A Combined Deformation Map-Ductility Exhaustion Approach to Creep-Fatigue Analysis," *Mater. Sci. Engg.*, 49(1981), pp. 7-17.

[13] Miller, D. A., "Fatigue-Creep Failure Mechanism Maps for 20%Cr/25%Ni/Nb Stainless Steel at 593 and 640℃," *Advances in Life Prediction Methods (ASME Conference)*, ASME, 1983, pp. 157-163.

[14] Hales, R, "A Method of Creep Damage Summation Based on Accumulated Strain for The Assessment of Creep-Fatigue Endurance, " *Fatigue Engg. Mater. Struct.*, 6(1983), pp. 121-135.

[15] Smith, T. J., Maier, H. J., Sehitoglu, H., Fleury, E., and Allison, J., "Modeling High-Temperature Stress-Strain Behavior of Cast Aluminum Alloys, " *Metall. Mater. Trans. A.*, 30A(1999), pp. 133-146.

Carlos C. Engler-Pinto, Jr[1] and Farhad Rézaï-Aria[2]

Thermo-mechanical Fatigue Investigation of Single Crystal Nickel Base Superalloy SRR99

Reference: Engler-Pint, C. C., Jr. and Rézaï-Aria, R., **" Thermo-mechanical Fatigue Investigation of Single Crystal Nickel Base Superalloy SRR99,"** *Thermo-mechanical Fatigue Behavior of Materials: Third Volume, ASTM STP 1371,* H. Sehitoglu and H. J. Maier, Eds., American Society for Testing and Materials, West Conshohocken, PA, 2000.

Abstract: This paper deals with the comparison between thermal fatigue (TF) and thermomechanical fatigue (TMF) testing for SRR99 superalloy. First, a measured TF mechanical strain-temperature (ε_m-T) profile between 200°C and 1100°C has been reproduced on a TMF specimen to allow for an estimation of the stresses and inelastic strains which occur during TF. Thermal-fatigue-based (TFB) ε_m-T profiles were determined based on the measured TF profiles. These TFB cycles, together with the well-known out-of-phase profile, were employed for all of TMF tests. The comparison of the results reveals that the TF and TMF out-phase tests are more damaging in terms both of the applied stress and strain range, while the TMF out-of-phase test is more severe if the comparison is made in terms of the inelastic strain range. Finally, it is shown that the results can be rationalized quite well by plotting the fatigue lives as a function of the maximum stabilized stress (σ_{max}).

Keywords: thermomechanical fatigue, thermal fatigue, nickel base superalloy, single crystal.

Introduction

Thermal gradients arising during transient regimes of start-up and shutdown operations produce a complex thermal and mechanical fatigue loading which limits the life of turbine blades [*1*]. The need for higher efficiency on gas turbines has led to higher and higher operating temperatures, which cause a more severe non-isothermal damage. In fact, for some advanced aircraft, the temperature changes from about 520°C to 1090°C in only 5 to 8 s during the heating and cooling phases [*2*].

The isothermal low cycle fatigue (LCF) design philosophy has been extensively adapted for design procedures and residual lifetime assessment of turbine blades. It is

[1] Post-doctoral Researcher, Escola de Engenharia de São Carlos (USP), Departamento de Engenharia de Materiais, São Carlos, Brasil.
[2] Research Associate, École Nationale Supérieure des Techniques Industrielles et des Mines d'Albi-Carmaux, Centre Matériaux, 81013 Albi, France.
(Both authors were formerly with LMM, EPFL, Lausanne, Switzerland).

generally [*3*] assumed that isothermal LCF tests at an "equivalent temperature" (maximum, mean or any other temperature within the thermal cycle) can represent the behavior and the life of an alloy subjected to a non-isothermal fatigue scenario. Nevertheless, there is no consensus for this equivalent temperature, as it can vary if different alloy systems and test conditions are considered.

More accurate and reliable assessment under non-isothermal fatigue becomes therefore mandatory. The strain–temperature history of a critical element from a blade can be simulated in the laboratory by either thermal fatigue (TF) or thermo-mechanical fatigue (TMF) tests. These two methodologies have become a useful tool to access the damage of specimens under more realistic conditions due to the simultaneous variation of temperature and strain (or stress) during a cycle. It is important to emphasize that TF is closer to reality because of the higher heating and cooling rates achieved as well as of the sample geometry, which is closer to blade geometry. TMF tests are particularly useful for the development of mechanical behavior and life-prediction models. Both TF and TMF tests may be used to determine fatigue lives under non-isothermal loading.

While the stress-strain loops must be calculated for blade-shaped TF specimens, they are directly measured under TMF tests. The results of the calculation are extremely dependent upon the constitutive law and boundary conditions considered [*4*]. In the beginning of TMF investigations only the simple in-phase (TMF-IP) and out-of-phase (TMF-OP) cycles were used. However, the cycles experienced by a real component in service may be different from that. More realistic and hence more complicated cycles such as diamond [*5*] and non-symmetric diamond [*6*] cycles were later proposed. TMF investigations have revealed that the behavior and resistance of superalloys are dependent on the strain–temperature cycle used. Therefore it is not possible to suggest a universal strain–temperature cycle since service conditions and design philosophies differ.

Irrespective of the fact that TF and TMF are two complementary laboratory tests to investigate the non-isothermal fatigue behavior of superalloys, the obtained results are generally compared solely to the available high temperature isothermal LCF results. No systematic comparison or link has been established yet between TF and TMF mainly because of the difficulty in measuring stresses and strains on blades or blade-shaped specimens under TF loading. To overcome this obstacle, a special device has been developed at the Laboratory of Mechanical Metallurgy at the Swiss Federal Institute of Technology in Lausanne, to measure the strain during thermal cycling at the wedge tip of TF blade-shaped specimens [*7–9*].

In the present work, the basic cycle used for the TMF investigation is deduced from the measured TF strain–temperature loops. The advantage of this approach is that the TF stresses at the wedge tip of the blade-shaped specimens can, to some extent, be determined experimentally. Furthermore, the life and the behavior under TF and TMF may be compared under relatively similar strain-temperature histories.

This paper aims to compare the fatigue lives of SRR99 obtained from TF, TMF-OP and TMF-TFB tests, where the latter presents a special strain-temperature (ε_m-T) profile derived from the TF measurements (TFB stands for thermal-fatigue-based).

Material and Experimental Procedures

The alloy was received as cast solid bars (Ø20 mm and 150 mm length) in the fully heat-treated condition with cubic γ'-precipitates of about 360 nm edge length. The nominal composition of SRR99 is given in Figure 1. SRR99 is a first generation single crystal superalloy, introduced in the beginning of the 80's. Nowadays, it is the single crystal superalloy mostly used in Europe for the fabrication of aircraft turbine blades [*10*].

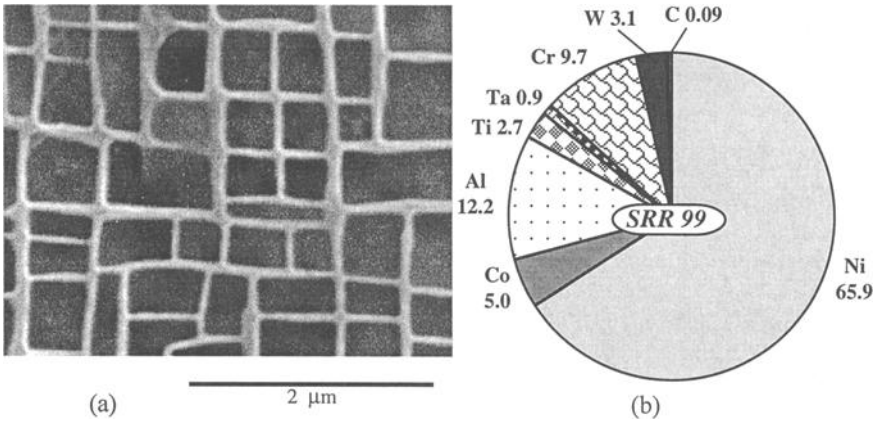

Figure 1 — *(a) Cubic γ'-precipitates and (b) nominal composition of SRR99 in atomic %.*

The TMF tests were performed on hollow specimens with a 11 mm external diameter and a wall thickness of 1 mm. The hole was cut by electrical-discharge-machining (EDM) and honed. The external surface was turned and mechanically polished along the longitudinal direction (1 μm diamond paste).

The tests were performed in a conventional closed-loop servo-hydraulic fatigue testing machine MFL (100 kN) specially adapted for TMF tests under total strain control. A Hewlett-Packard microcomputer (Apollo 715) connected to a Data Acquisition System (HP3852A) monitored the experiments. The specimens were heated by a HF generator (Hüttinger IG5/200, 6.0 kW, 200 kHz), connected to a Eurotherm 906S closed loop temperature controller. The computer was used to generate two synchronous analogic curves, which were provided to be the regulating signals for both temperature and strain control. The software was developed using the Hewlett-Packard VEE-Test environment. A schematic representation of the test equipment is shown in Figure 2. A 10°C/s linear heating and cooling rate was used for temperatures higher than 600°C leading to a thermal gradient of less than 10°C through the 1 mm thickness. From 600°C to 200°C the specimen is naturally cooled. The total period of the thermal cycle is 100 seconds for the 600–1100°C cycle and 368 seconds for the 200–1100°C cycle. A Maurer QPMR 85-d bicolor pyrometer monitored the tests between 600–1100°C, while a Chromel-Alumel thermocouple (type K) with Ø 0.3 mm wires separately spot-welded at the center of the gauge length monitored the 200–1100°C tests. A weak flow of argon was introduced

through the internal hole to reduce the oxidation at the internal surface as well as the thermal gradient through the thickness.

The TMF results are compared to the TF life previously obtained on self-constrained blade shaped specimens cycled between 200°C and 1100°C [*7-8*]. The TF tests were carried out on blade-shaped single edge wedge specimens, which are externally totally unconstrained during thermal cycling. Two similar thermal fatigue rigs consisting of a high frequency (HF) oscillator for heating and a nozzle for forced air cooling were developed. Two solid state induction generators working at two different frequencies (200 kHz and 3000 kHz) were employed. The different skin depth lead to two different thermal gradients without changing the specimen geometry. Therefore, two different strain–temperature histories were generated at the wedge tip of the TF specimens for an identical temperature-time cycle at the specimen surface (see Figure 3). The strain at the wedge tip was measured as a function of time and temperature over 20 mm within the central part of the TF specimen (see reference [*8*] for details).

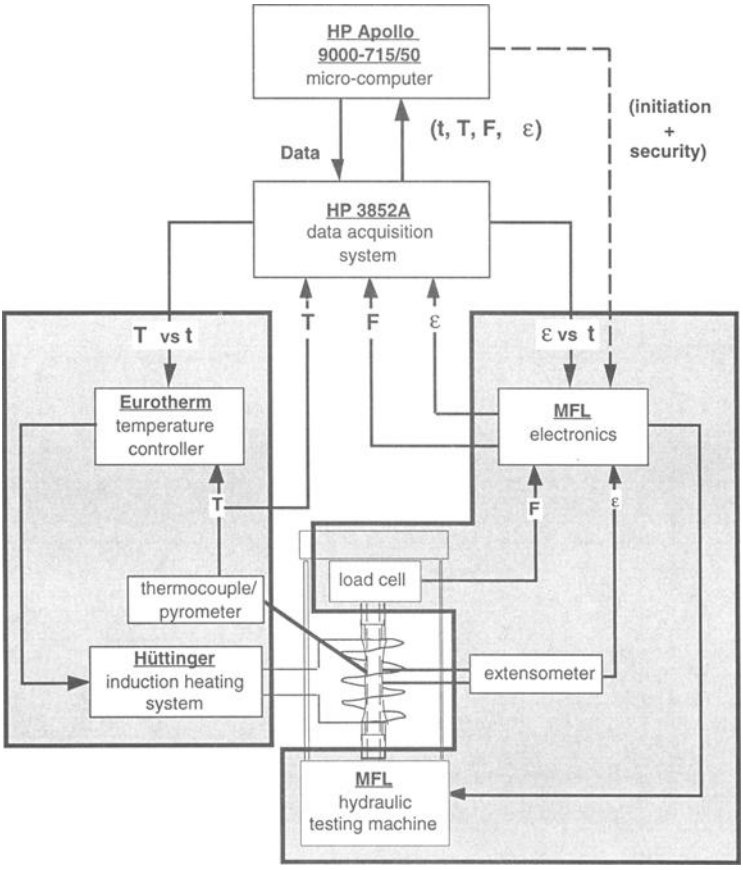

Figure 2 — *Schema of the TMF test facility.*

In order to compare the TF and TMF lives under similar conditions, two TMF strain-temperature profiles were deduced from the TF measurements: the TMF-TFB1 and TMF-TFB2 cycles, indicated in Figure 4. The minimum temperature of 600°C was used because of the pyrometer limitation (the use of a spot welded thermocouple was avoided in this case because it could initiate a premature crack). TFB1 was used first, and it has a maximum strain (and stress) at a temperature higher than what actually occurs during a TF test. Therefore, other tests were performed with the TFB2 cycle, in which the maximum strain (stress) occurs at 600°C which is equal to the TMF–OP test and closer to the TF test.

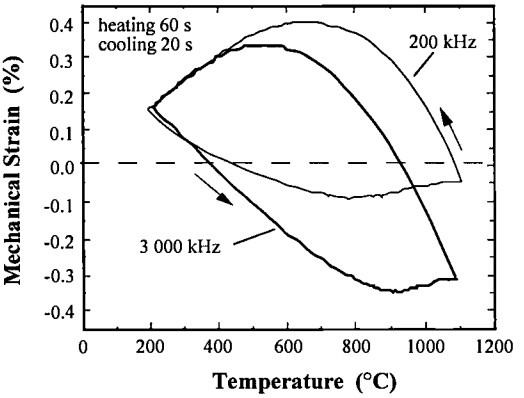

Figure 3 — *Strain-temperature cycles measured a the specimen surface during TF testing.*

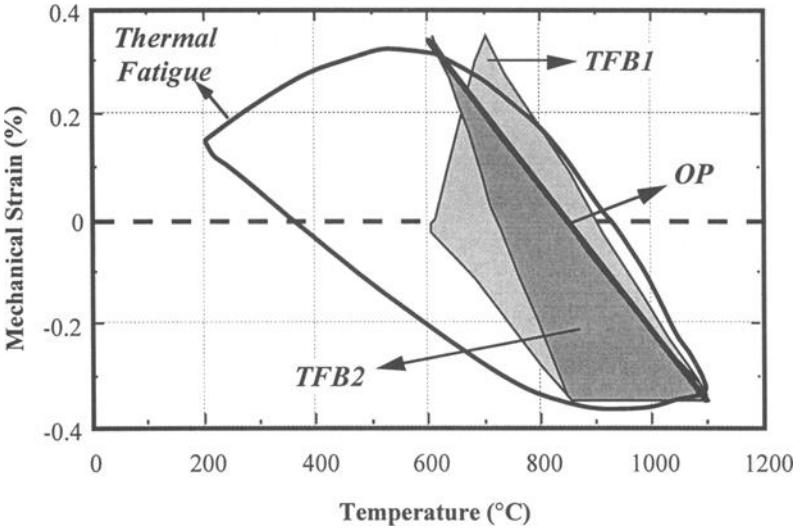

Figure 4 — *Strain-temperature cycles used in this investigation.*

Results and Discussion

TF Simulation under TMF

To evaluate the stress-strain behavior at the wedge tip of the TF specimen, the mechanical strain-temperature loop measured in the central region of the of a SRR99 TF specimen during a test in 3000 kHz rig between 200°C and 1100°C was applied in a TMF test. This simulation allows the experimental determination of the inelastic strain range and stress range for a TF test. The measured stresses are reported in Figure 5. Note that, as the hottest part of the cycle occurs in compression, there is a stress relaxation (or creep deformation) in compression during each cycle, until the peak compression stress stabilizes. As a consequence of that, a positive mean stress developed. The main factor that can affect the mechanical response in such a test is the sensitivity of the alloy to the strain rate [*11-13*]. In fact, the strain rate at the very beginning of heating and cooling under TF ($-2.4 \cdot 10^{-3}$ s^{-1} and 10^{-2} s^{-1} respectively) is much higher than under the TMF experiment ($-2.5 \cdot 10^{-4}$ s^{-1} and $1.5 \cdot 10^{-4}$ s^{-1}). At the end of heating and cooling, however, the strain rates for both TF and TMF tests are of the same order.

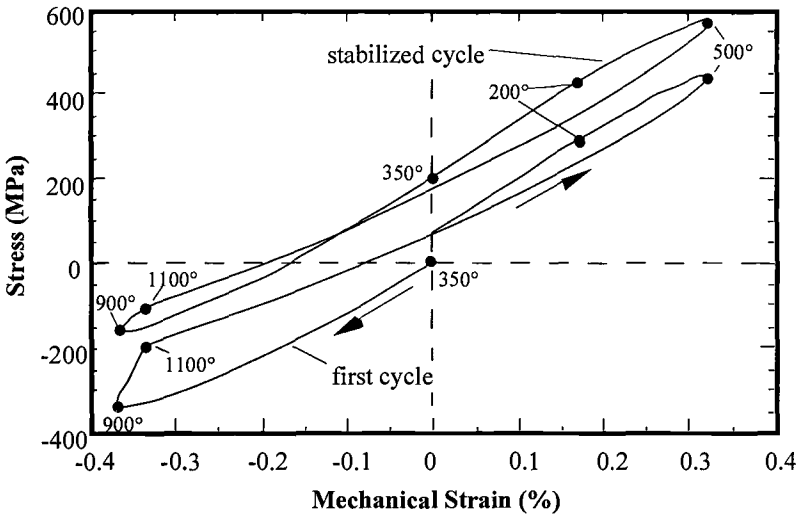

Figure 5 — *Stress-strain loops obtained in TMF for the measured strain-temperature TF-cycle under the 3000 kHz TF-rig.*

Crack Initiation Mechanisms

Apart from the TF simulation under TMF, all other TMF tests were performed between 600°C and 1100°C. Cracks initiate in all cases by a complex interaction between

the porosity and oxidation. A higher crack density was observed for the TMF-TFB1 and TMF-TFB2 as compared to the TMF-OP cycles.

During thermal cycling and prior to crack initiation, an oxide-scale and its corresponding γ'-depleted zone (DZ) are created. The stress concentration ahead superficial pores combined with the loss of the strength of the DZ and with the fragility of the oxide scale constitute the predominant mechanism of crack initiation for the conditions investigated [*8*].

Figure 6 shows a longitudinal cut of a TMF specimen with a very small crack. This specimen has been submitted to 2890 TMF-TFB1 cycles (600–1100°C, $\Delta\varepsilon_m$ (ε_{mmax} - ε_{mmin})= 0.7%) It can be observed that the crack initiates from a microporosity. It is also observed that the crack is filled with oxide. This photo was taken from another single crystal superalloy, CMSX-6, which behaves similar to the SRR99 superalloy under these TMF conditions, and it is shown here to illustrate the mechanism of crack initiation.

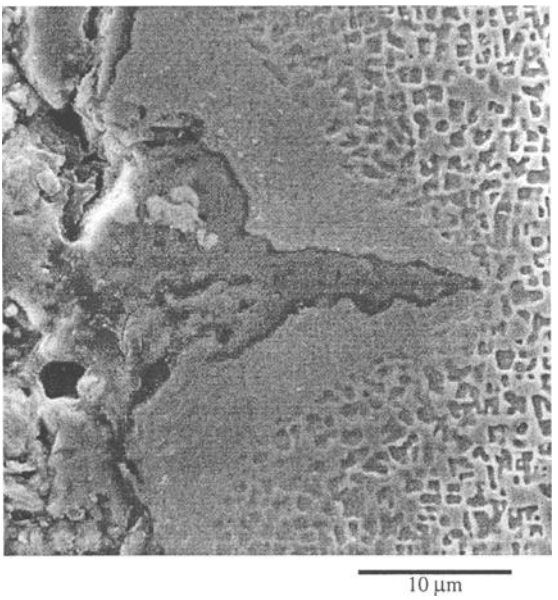

Figure 6 — *Polished and etched cross section of a CMSX-6TMF specimen showing a small crack initiated on an oxidized cast microporosity through the γ-depleted zone (loading is vertically).*

TMF and TF lives

The definition of fatigue life is a matter of controversy even for simple isothermal LCF experiments. It is still more complicated for non-isothermal fatigue tests. In this investigation, N_5 was adopted as the total fatigue life for both TMF and TF, which is defined as follows:

TMF — number of cycles where a decrease of 5% in the maximum stress is observed. A 5% reduction in stress corresponds approximately to the formation of a single 1 mm crack depth (~3 mm at the surface), which matches with the specimen wall thickness.

TF — number of cycles to form a 1 mm crack depth, measured directly on the specimen by regular test interruption and inspection (only 2 tests among 12 TF tests performed are reported here, see reference [*8*] for more details).

The results of all tests are given in Tables 1 and 2. For the thermal fatigue tests, the mechanical strain ranges were measured directly during testing and the stresses were either obtained from the TMF test or calculated elastically, as stated in Table 2.

Table 1 — *TMF results for the SRR99 superalloy (600–1100°C).*

ε_m-T profile	$\Delta\varepsilon_m$ (%)	$\Delta\sigma$ (MPa)	σ_{max} (MPa)	$\Delta\varepsilon_{in}$ (%)	N_5
	0.49	514	460	0.003	8787
	0.70	742	660	0.004	1588
OP	0.70	680	605	0.010	2735
	0.85	838	705	0.009	1276
	1.00	1018	820	0.015	370
	0.71	711	553	0.014	5237
TFB1	0.85	890	711	0.026	1770
	1.02	1026	826	0.037	933
TFB2	0.70	762	632	0.022	2321
	1.01	1010	835	0.041	880

Table 2 — *TF results for the SRR99 superalloy (200–1100°C).*

induction frequency	$\Delta\varepsilon_m$ (%)	$\Delta\sigma$ (MPa)	σ_{max} (MPa)	$\Delta\varepsilon_{in}$ (%)	N_5
200 kHz	0.48 [1]	532 [2]	—	—	10000
3000 kHz	0.69 [1]	743 [3]	576 [3]	0.028 [3]	1520

[1] directly measured during TF testing.
[2] calculated elastically: $\Delta\sigma = \Delta[E(T) \cdot \varepsilon_m(T)]$.
[3] obtained from TMF testing (Figure 5).

The comparison of the results reveals that the TF test is more damaging in terms of the applied mechanical strain ($\Delta\varepsilon_m$) or stress ($\Delta\sigma$) range, as shown in Figures 7 and 8, as compared with the TFB tests. The TF tests are presented here with a solid line to distinguish them from the TMF tests. It can be observed that the TF life lies very close to the TMF-OP life.

On the other hand, the TMF-OP test is more severe than all other tests if the comparison is made in terms of the inelastic strain range ($\Delta\varepsilon_{in}$), see Figure 9. Only one point is presented for TF because the simulation was only made for the test performed in 3000 kHz TF-rig. It is observed that the TMF-OP test leads to the shortest lives in this case. It can also be noted that the inelastic strain range correlates well all other points. This seems to indicate that the damage mechanisms are similar for TF and TMF-TFB tests due to the similarities of their ε_m-T profiles.

Finally, it is shown in Figure 10 that the maximum stress (σ_{max}) correlates well with all TMF points. In this case, the TF point lies below the TMF results. This trend will be further discussed in the next section, based on observations of the precipitate morphology.

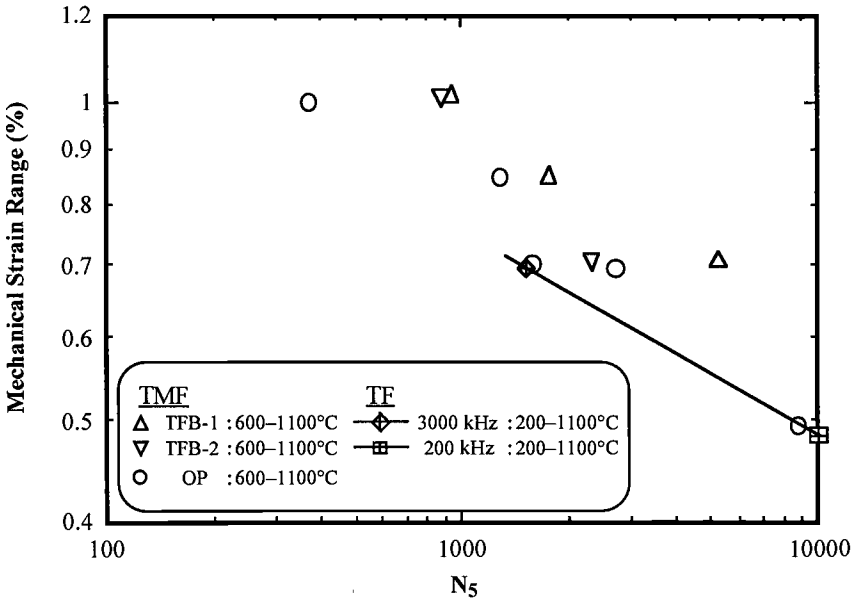

Figure 7 — *Fatigue life as a function of the mechanical strain range.*

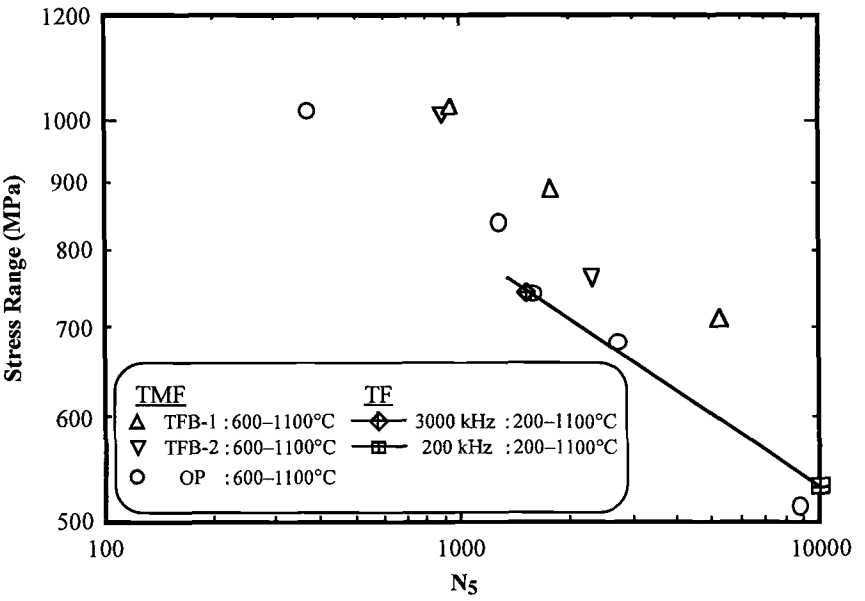

Figure 8 — *Fatigue life as a function of the stress range.*

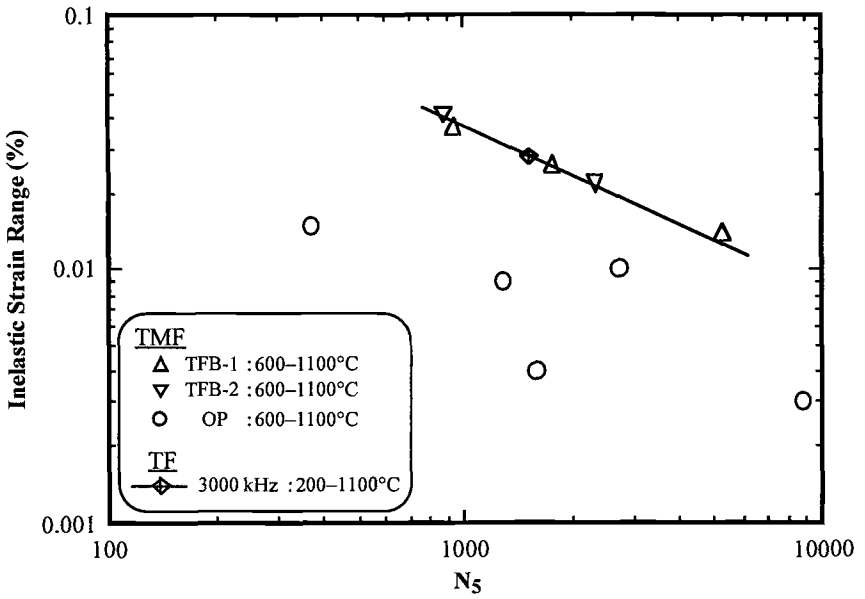

Figure 9 — *Fatigue life as a function of the inelastic strain range.*

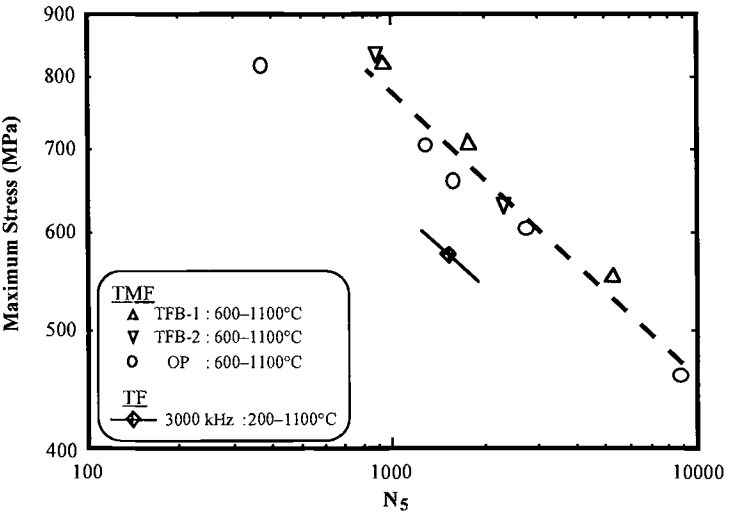

Figure 10 — *Fatigue life as a function of the maximum stabilized stress.*

Microstructural observations

Figure 11 and 12 shows the γ-γ' structure after two TMF tests and TF test performed in 3000 kHz TF-rig, respectively. It was observed that, for all TMF tests, the SRR99 superalloy develops a rafted γ-γ' structure parallel to the stress axis, which is typically observed after creep under compression. This clearly indicates that the alloy was actually under compression at the highest temperatures of the thermal cycles.

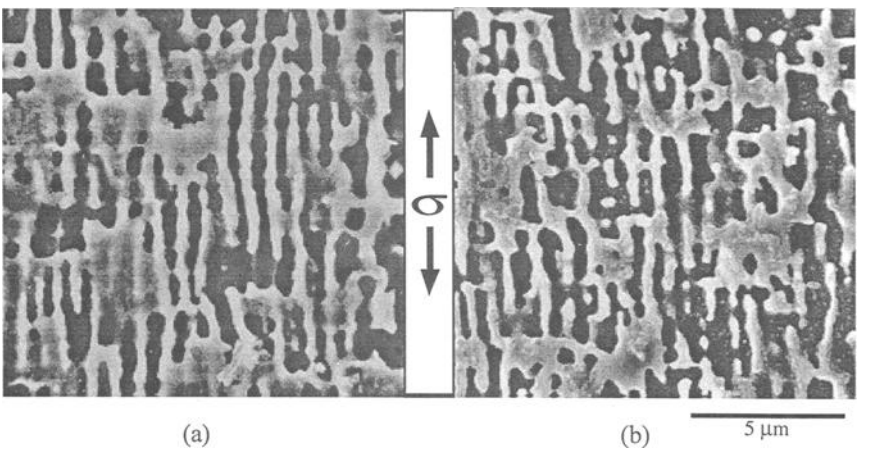

Figure 11 — *γ-γ' microstructure after TMF testing: (a) OP 600–1100°C, $\Delta\varepsilon_m$ = 0.7% (1600 cycles), and (b) TFB-2 600–1100°C, $\Delta\varepsilon_m$ = 0,7% (2325 cycles).*

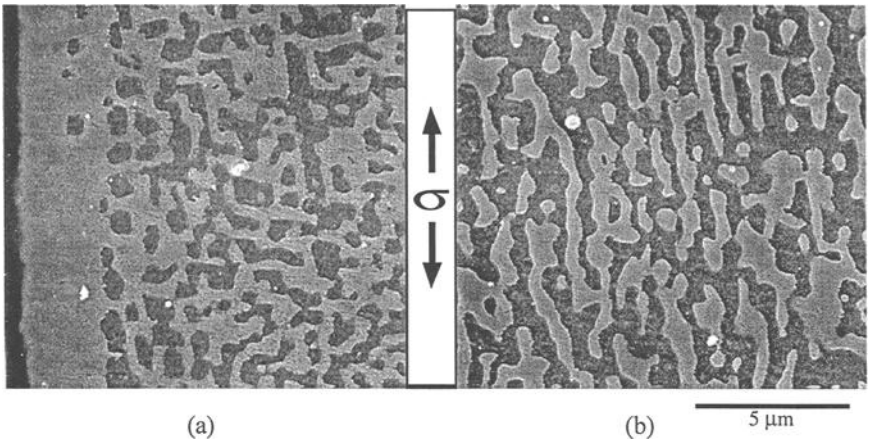

Figure 12 — *γ-γ' microstructure after 2000 TF cycles (3000 kHz, $\Delta\varepsilon_m$ = 0.69%): (a) near to the surface, and (b) 100 µm from the surface.*

A similar γ' morphology is observed the TF sample at a distance of 100 µm from the surface (Figure 12b). However, if we look at the γ' precipitates near to the surface of the TF specimen (Figure 12a), where cracks actually initiated, we observe that the γ' phase coarsened without a preferential orientation. This corresponds to what occurs when a nickel based superalloy are exposed to high temperatures without stress applied to it. Therefore, one may assume that the stress at the higher temperatures of the TF cycle near to the surface was actually closer to zero.

As described before, the TF test is characterized by a transition from a low strain rate at the end of heating to a very fast strain rate at the beginning of cooling. Mughrabi et al. [*13*] have shown (for isothermal LCF of CMSX-6, a nickel base superalloy which behaves similar to the SRR99) that the cyclic deformation behaviour depends upon the strain rate. If one assumes that the TMF simulation underestimated the maximum TF stress (high strain rate) and the TF stress relaxation in compression (low strain rate) then the maximum stress should correspond to the measured (or elastically calculated) stress range.

Following the above assumptions, Figure 13 replots N_5 vs. σ_{max}, where the stress range is used as the maximum stress for the TF tests. It should be noted that this corresponds to the upper limit for σ_{max} under TF (it should actually be slightly shorter). All points now seem to fit in a single curve. The same tendency has been reported by Kraft *et al.* [*5*] , who investigated the TMF behavior of the CMSX-6 superalloy under four different ε_m-T profiles. They associated this dependency of the fatigue life on the maximum stress to the development of soft γ-matrix channels, where dislocation movement is less constrained, leading to more localized slip than in a regular structure of cuboidal γ' particles.

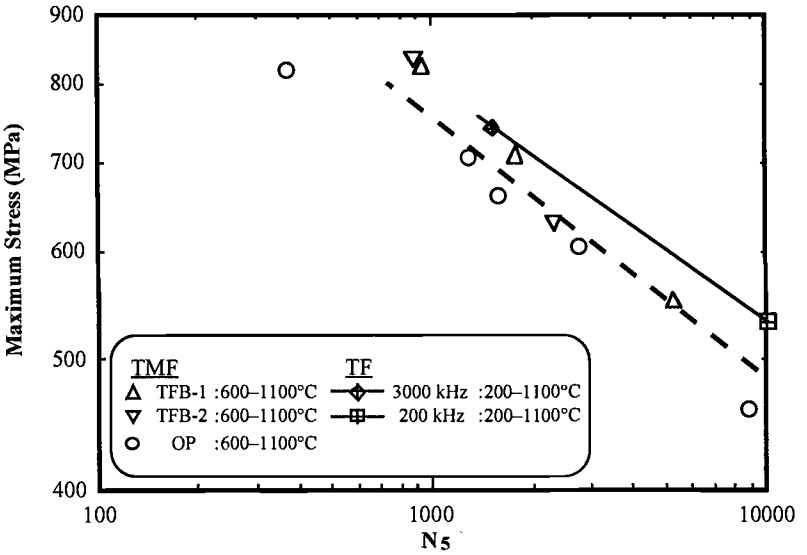

Figure 13 — *Fatigue life as a function of the maximum stabilized stress (corrected for the TF tests).*

Non-isothermal fatigue behaviour and microstructural evolution (raft structure here) of single crystal nickel base superalloys are dependant not only upon the strain-temperature-histrory but as well to the strain rate sensitivity of these alloys. One way to improve the TMF-simuation of the stress-strain behaviour of TF wedge-shaped specimens or a real blade is to perform the high strain TMF tests.

Conclusions

The thermomechanical fatigue and thermal fatigue behavior of SRR99 was compared under similar conditions. The strain–temperature profiles measured at the wedge tip of TF specimens were reproduced by TMF tests. On the basis of the TF strain measurements, new TMF cycles were introduced. The same crack initiation mechanism was identified for both TF and TMF, consisting of a complex interaction between oxidation, porosity and fatigue. The results could be rationalized quite well by plotting the fatigue lives as a function of the maximum stabilized stress (σ_{max}).

Finally, it is interesting to emphasize the importance of performing both TF and TMF tests, if possible under similar conditions. In this manner, the results of TF and TMF tests may be crosschecked with the results obtained from calculations. This would contribute to the development or improvement of existing TMF models. In fact, if one wants to use TMF results to predict real blade behavior, the model used for doing so must also be capable of predicting the behavior of a much simpler specimen under thermal fatigue loading.

References

[1] Coney, M. H., "Thermal Fatigue Cycling in Turbine Blades," *High Temperature Technology*, Vol. 8, No. 2, May 1990, pp. 115-120.

[2] Busso, P. and McClintock, F. A., "Thermal Fatigue Degradation of an Overlay Coating," *Materials Science and Engineering*, vol. A161, 1993, pp. 165–179.

[3] Taira, S., "Relationship Between Thermal Fatigue and Low-Cycle Fatigue at Elevated Temperature," *Fatigue at Elevated Temperatures, ASTM STP 520*, American Society for Testing and Materials, 1973, pp. 80-101.

[4] Mallet, O., Kaguchi, H., Ilschner, B., Nikbin, K., Rézaï-Aria, F., and Webster, G. A., "Influence of Thermal Boundary Conditions on Stress-Strain Distribution Generated in Blade-Shaped Samples," Int. Fatigue, Vol. 17, N° 2, 1995, pp. 129-134.

[5] Kraft, S., Zauter, R., and Mughrabi, H., "Aspects of High-Temperature Low Cycle Thermomechanical Fatigue of a Single Crystal Nickel-Base Superalloy," *Fatigue and Fracture of Engineering Materials and Structures*, Vol. 16, No. 2, 1993, pp. 237-253.

[6] Malpertu, J. L. and Rémy, L., "Influence of Test Parameters on the Thermal-Mechanical Fatigue Behaviour of a Superalloy," *Metallurgical Transactions A*, Vol. 21A, Feb. 1990, pp. 389–399.

[7] Meyer-Olbersleben, F., "Thermische Ermüdung Einkristalliner Nickelbasis-Legierungen," Dissertation thesis No. 1255, Swiss Federal Institute of Technology, Lausanne, June 14th, 1994..

[8] Meyer-Olbersleben, F., Engler-Pinto, C. C., Jr., and Rézaï-Aria, F., "On Thermal Fatigue of Nickel-Based Superalloys," *Second Symposium on Thermo-Mechanical Fatigue Behavior of Materials, ASTM STP 1263*, Michael J. Verrilli and Michael G. Castelli, Eds., American Society for Testing and Materials, West Conshohocken, PA, 1996, pp. 41–55.

[9] Engler-Pinto, C. C., Jr., Meyer-Olbersleben, F., and Rézaï-Aria, F., "Thermo-mechanical Fatigue Behaviour of SRR99," *Fatigue under Thermal and Mechanical Loading — Mechanisms, Mechanics and Modelling*, Kluwer, 1996, pp. 151–157.

[10] Curtis, R. V., Ghosh, R. N., and McLean, M., "Analysis of Creep Data for the Single Crystal Superalloy SRR99-<001> and Complex Orientations," *Creep and Fracture of Engineering Materials and Structures*, The Institute of Materials, London, 1993, pp. 199-208.

[11] Coffin, L. F., Jr., "Fatigue at High Temperature," *Fatigue at Elevated Temperatures, ASTM STP 520*, American Society for Testing and Materials, 1973, pp. 5–34.

[12] Gabrisch, H., Kuttner, T., Mukherji, D., Chen, W., Wahi, R. P., and Wever, H., "Microstructural Evolution in the Superalloy SC16 Under Monotonic Loading," *Materials for Advanced Power Engineering, Part II*, D. Coutsouradis *et al.*, Eds., 1994, pp. 1119-1124.

[13] Mughrabi, H., Kraft, S., and Ott, M., "Specific Aspects of Isothermal and Anisothermal Fatigue of the Monocrystalline Nickel-Base Superalloy CMSX-6," Superalloy 1996, R. D. Kissinger, D. J. Deye, D. L. Anton, A. D. Cetel, M. V. Nathal, T. M. Pollock and D. A. Woodford, Eds., The Minerals, Metals & Materials Society, 1996, pp. 335-344.

Composites

Arnd Jung,[1] Hans J. Maier,[2] and Hans-Jürgen Christ[1]

Effect of SiC-Reinforcement on Thermo-mechanical Fatigue of a Dispersion-Strengthened High-Temperature Aluminum Alloy

Reference: Jung, A., Maier, H. J., and Christ H.-J., **"Effect of SiC-Reinforcement on Thermo-mechanical Fatigue of a Dispersion-Strengthened High-Temperature Aluminum Alloy,"** *Thermo-mechanical Fatigue Behavior of Materials: Third Volume, ASTM STP 1371,* H. Sehitoglu and H. J. Maier, Eds., American Society for Testing and Materials, West Conshohocken, PA, 2000.

Abstract: Isothermal and thermo-mechanical fatigue (TMF) behavior of a dispersion-strengthened aluminum alloy has been studied between room temperature and 350 °C. Cyclic stress-strain (CSS) response was found to be dominated by dispersoid-dislocation interactions, and thus, the effect of an additional SiC reinforcement on CSS behavior was only minor. As the dispersoids are thermally very stable, identical microstructures were observed to form independent of the actual loading conditions. Consequently, CSS response under TMF conditions could be accurately predicted from isothermal tests only. Damage evolution, by contrast, was found to depend drastically on the type of test. A microcrack propagation model could be successfully used to correlate all tests performed on the unreinforced alloy. In the SiC-reinforced material, however, both creep damage and oxidation damage were more severe under TMF conditions than predicted from isothermal tests, and life prediction is nonconservative, if only based on isothermal tests.

Keywords: aluminum alloy, crack propagation, creep-fatigue interaction, dispersoids, fatigue life prediction, microstructure, modeling, oxidation, stress-strain behavior, thermo-mechanical fatigue

Introduction

Discontinuously reinforced aluminum alloys have attractive properties for aerospace and automotive industries, and much effort has been directed towards understanding the effect of ceramic reinforcements on mechanical properties. Elevated temperature use, however, is restricted if conventional *precipitation-hardened* aluminum matrices are employed [*1*]. *Dispersion-strengthened* aluminum matrices, by contrast, have excellent microstructural stability at elevated temperatures [*2*], and an additional discontinuous reinforcement enhances their attractiveness for structural applications because of the resulting increase in stiffness to weight ratio. Many of the envisioned applications will involve both thermal and mechanical transients, and thus, thermo-mechanical fatigue (TMF) becomes an important design aspect. At present, however, data on TMF behavior of such alloys are still rather limited. TMF experiments performed on SiC-reinforced *precipitation-hardened* aluminum al-

[1]Graduate Research Assistant and Professor, respectively, Institut für Werkstofftechnik, Universität–GH Siegen, D–57068 Siegen, Germany.
[2]Professor, Lehrstuhl für Werkstoffkunde, Universität Paderborn, D-33095 Paderborn, Germany.

loys have shown that the mismatch in coefficient of thermal expansion between SiC particles and the matrix significantly changes the internal stress fields during TMF loading [*3*]. On the other hand, processing-induced internal stresses were reported to dominate TMF behavior of a *dispersion-strengthened* aluminum alloy [*4*]. The effect of SiC reinforcement on fatigue behavior not only depends on the type of matrix, but also on the control mode of the test and the actual loading conditions. Further, as TMF tests are expensive and time consuming, TMF life is often predicted from isothermal tests only, or from TMF tests run under conditions substantially more severe than those encountered in actual service. From this, the objectives of the present paper were defined as follows:

- Develop a model that accurately predicts CSS response under both isothermal and TMF loading conditions. The model should be closely related to microstructure, but fit parameters should be kept minimum as to clearly reveal any distinctive features of TMF.
- Identify the role of the SiC particulates and the relevant damage mechanisms from fatigue experiments conducted on both a SiC–reinforced material and the same alloy without SiC particles.
- Model damage evolution to predict TMF fatigue life. The model should use a physically measurable quantity to characterize damage evolution.
- Compare model predictions with experiments and discuss the implications for life predictions under conditions not covered by the actual experiments.

Experimental Details

A dispersion-strengthened high-temperature aluminum alloy (Al–8Fe–4Ce, in wt pct) and the same alloy reinforced with 12.5 vol. pct SiC particles were employed for this study. Both alloys were obtained from ALCOA in the form of hot extruded bars that had been produced via a powder-metallurgy route from rapidly solidified gas-atomized powders. After solidification, the thermally very stable equilibrium phases $Al_{13}Fe_4$ and $Al_{10}Fe_2Ce$ are present, and the volume fraction of these finely dispersed incoherent phases is reported to be as high as 0.23 for this material [*2*]. For a more detailed microstructural characterization of the matrix material the reader is referred to references *2* and *5*. The SiC particles present in the reinforced material were found to have an average diameter of about 3 μm. Metallographic inspection of the as-received reinforced material indicated excellent bonding at the SiC/matrix interface and also an almost homogeneous distribution of the SiC particles. Further, the SiC particles appeared to have no effect on dispersoid distribution or grain size, and an average grain size of about 1 μm was determined for both materials.

For both fatigue and creep testing, smooth specimens with 7 mm gage diameter were machined from the as-received materials such that the stress axis was parallel to the extrusion direction. Prior to testing the gage length was polished mechanically with 1 μm diamond paste. Creep testing was done under constant stress conditions and at test temperatures (T) of 300 °C and 350 °C, respectively. In order to ease comparison between isothermal and TMF data, both types of tests were conducted in symmetrical push-pull true plastic strain control using a triangular command signal. Thus, the absolute value of the plastic strain rate was kept constant throughout

each cycle instead of the more commonly used type of testing with constant total strain rate. Details on the experimental set-up required to perform true plastic strain-controlled TMF tests and a discussion on the effect of the control mode on stress-strain response have been given elsewhere [6]. The plastic strain amplitudes ($\Delta\epsilon_{pl}/2$) employed in the fatigue tests were in the range from 2.5×10^{-4} to 4×10^{-3}, and plastic strain rates ($\dot{\epsilon}_{pl}$) were in the range from $10^{-5}\,s^{-1}$ to $10^{-2}\,s^{-1}$.

Isothermal fatigue tests were performed at room temperature, 150 °C, 300 °C, and 350 °C. The elevated test temperatures were generated using a conventional induction heater. To compensate for the rather weak magnetic coupling of the aluminum-based alloys, thin iron foils were wrapped around the samples outside of the actual gage length. This provided for significantly improved heating and an axial temperature gradient in the gage length less than 5 °C under isothermal test conditions could be routinely obtained by careful design of the induction coil. Thermocouples that were spot welded onto the gage length were found to cause premature fatigue crack initiation. Thus, test temperature was controlled with thermocouples held in place using thermocouple wire insulation. Spot welded thermocouples were used only as a means to check the accuracy of the temperature measurements.

The TMF tests were conducted with the temperature either increasing (in-phase (IP) tests) or decreasing (out-of-phase (OP) tests) with increasing plastic strain. In the TMF tests reported here, the temperature range was 200 °C, and the maximum temperatures were 300 °C and 350 °C, respectively. As a result of the rather low free convection cooling rate of the alloy studied, the plastic strain rate had to be limited to $10^{-5}\,s^{-1}$ to ensure that both the temperature and the plastic strain followed the triangular command signal accurately.

Fatigue crack growth was studied using single edge notch bend specimens loaded in 4-point bending. The specimens were machined such that the orientation of the crack plane was identical to that in the cylindrical bulk samples. These tests were intended to provide base line fatigue crack growth data unaffected by environmental effects. Therefore, all tests reported here were run at room temperature and a rather high frequency of 170 Hz. In order to minimize the influence of crack closure, a stress ratio $R = \sigma_{min}/\sigma_{max}$ of 0.7 was employed in these tests.

Microstructural studies were performed on a transmission electron microscope operated at a nominal accelerating voltage of 120 kV. For transmission electron microscopy (TEM), thin slices were cut both normal and parallel to the external stress axis of the fatigued samples. The TEM samples prepared from the unreinforced material could be thinned using conventional twin-jet electropolishing. Relatively large electron transparent areas were obtained with a solution consisting of 70 vol. pct CH_3OH and 30 vol. pct HNO_3 when electropolishing at -23 °C and a potential of 10.5 V. The SiC-reinforced material had to be thinned by dimple grinding followed by ion-milling. To minimize preparation-induced artifacts, a rather low angle of 2° was employed during ion-milling in the final stages.

Scanning electron microscopy (SEM) was used to study the damage mechanisms in the fatigued samples. The fracture surfaces were sputter-coated with gold in most cases in order to enhance image contrast. To study void growth within the bulk, fatigued samples were sectioned longitudinally. In order to clearly reveal fine voids, those samples were repeatedly polished and etched with 30 pct HNO_3.

Results

Isothermal Tests

Creep Behavior—In all creep tests initial hardening in the primary creep stage was followed by pronounced steady state creep. Even in tests run at 350 °C the microstructure appeared to be stable as no indication of any significant amount of softening was apparent up to creep strains of 5 pct. At 300 °C, the creep rate of the SiC-reinforced material was found to be slightly higher than that of the unreinforced alloy. In creep tests run at 350 °C, the creep rate was identical within the experimental error for both materials tested. In Fig. 1 data obtained from creep tests and isothermal low-cycle fatigue tests, respectively, are compared for the SiC-reinforced material. Apparently, the low-cycle fatigue tests performed at $\dot{\epsilon}_{pl} = 10^{-5}\,s^{-1}$ are still dominated by creep processes, and the transition between creep deformation and plasticity occurs at a strain rate higher than $10^{-5}\,s^{-1}$. For the unreinforced material, by contrast, this transition was found to take place well below $\dot{\epsilon}_{pl} = 10^{-5}\,s^{-1}$.

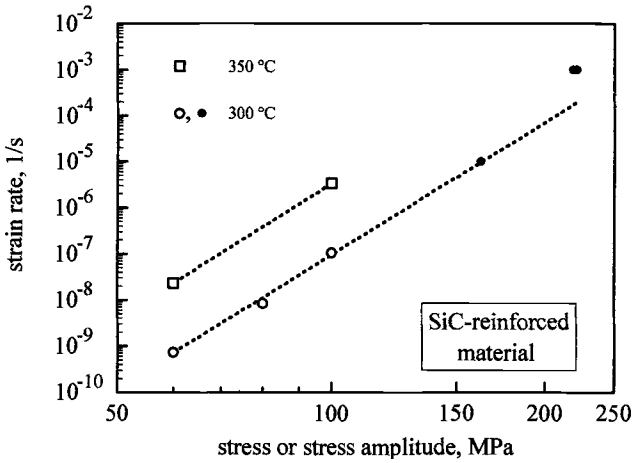

Figure 1 — *Steady-State Strain Rate Versus Stress for SiC-Reinforced Material. Open Symbols Refer to Creep Tests, Full Symbols Denote Stress Amplitudes of Low-Cycle Fatigue Tests.*

Cyclic Stress-Strain Response—As expected, stress amplitudes in plastic strain-controlled fatigue tests were slightly larger for the SiC-reinforced material than for its unreinforced counterpart, *cf.* Fig. 2. The difference in stress-strain response, however, diminished as temperature was increased and/or strain rate was decreased. Figure 2 also reveals that the SiC-reinforced material always failed suddenly in a macroscopically brittle manner. The unreinforced material, by contrast, showed a continuous drop in stress amplitude when macrocrack growth set in. The effects of temperature and strain rate on fatigue life that are visible in Fig. 2 will be addressed later.

Except for the room temperature tests on the SiC-reinforced material (labeled "A" in Fig. 2), no pronounced cyclic hardening or softening was observed in any

fatigue test. However, slight particle coarsening has been reported to occur in the unreinforced material in creep tests run at 316 °C [2]. The authors, however, also noted that cyclic stressing has a much smaller effect on particle coarsening than creep. In order to check whether significant microstructural changes do occur in the fatigue tests, a sample was cycled at $T = 300°C$, $\dot{\epsilon}_{pl} = 10^{-3}\,s^{-1}$ and $\Delta\epsilon_{pl}/2 = 4 \times 10^{-3}$ into cyclic saturation. Next, the test was interrupted at zero plastic strain, and the sample was cooled to room temperature immediately. When cycling was continued, the hysteresis loop obtained then was identical to that of samples cycled at room temperature only. Hence, it can be concluded that no substantial microstructural changes have occurred, and that the slight initial cyclic hardening or softening seen in Fig. 2 is mainly caused by rearrangement of dislocations.

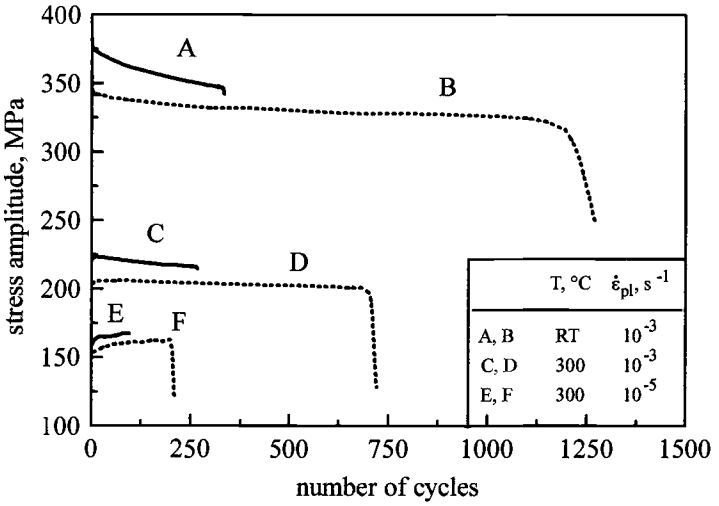

Figure 2 — *Cyclic Stress Response Curves of Unreinforced Material (Dashed Lines) and SiC-Reinforced Material (Solid Lines), Respectively.* $\Delta\epsilon_{pl}/2 = 4 \times 10^{-3}$ *in All Tests Shown.*

Fatigue crack growth—If analyzed in terms of the cyclic stress intensity factor range (ΔK), fatigue crack growth rate (da/dN) was found to be lower for a given value of ΔK in the SiC-reinforced alloy as compared to the unreinforced material. Similarly, the threshold value of ΔK determined at $da/dN = 10^{-11}$ m/cycle was found to be higher in the presence of SiC particles. In order to be able to use the data to describe fatigue crack growth in the LCF specimens as well, the data were reanalyzed in terms of the effective cyclic J-Integral [7], also referred to as Z_{eff}-Integral [8], using

$$da/dN = C \times (Z_{eff})^m = C \times \left(\Delta K_{eff}^2 \times \frac{1-\nu^2}{E}\right)^m \tag{1}$$

where ν is Poisson's ratio, E is Young's modulus, and ΔK_{eff} is the effective value of ΔK corrected for crack closure. Measurements confirmend that crack closure effects

are negligible at $R = 0.7$, i.e. $\Delta K_{\text{eff}} \approx \Delta K$. Table 1 lists the crack propagation constants C and m determined at room temperature. Fatigue life is obtained upon integrating Eq. 1 between the initial crack length in the first cycle ($a_{N=1}$), *cf.* Table 1, and the final crack length at failure ($a_{N=N_f}$). The effect of variations in initial crack length on fatigue life prediction will be discussed in a later section.

When plotted in terms of Z_{eff}, the difference in $\mathrm{d}a/\mathrm{d}N$ between both materials became small, and within the Paris regime $\mathrm{d}a/\mathrm{d}N$ data were almost identical within the experimental error limit. This indicates that most of the difference in $\mathrm{d}a/\mathrm{d}N$ results from the increase in elastic modulus caused by the ceramic reinforcement. Moreover, SEM studies performed on samples sectioned parallel to the loading axis through the crack plane showed that the fatigue cracks tried to avoid the SiC particles, i.e. the crack growth mechanism during most of fatigue life is similar whether SiC-particles are present or not. Therefore, the fatigue crack growth data obtained at room temperature and high test frequency were used to describe pure fatigue crack growth in the LCF samples. For plain strain conditions an approximation for Z_{eff} that is valid for semi-circular surface cracks is [*8*]:

$$Z_{\text{eff}} = (2.9W_{\text{el, eff}} + 2.5W_{\text{p}}) \times a = Z_{\text{D}} \times a \tag{2}$$

where a is the crack length, $W_{\text{el, eff}}$ and W_{p} are elastic and plastic deformation strain energy densities, respectively.

Table 1 — *Crack Propagation Constants Obtained at Room Temperature and* $R = 0.7$. *Note That Constants Given Yield* $\mathrm{d}a/\mathrm{d}N$ *in* m/cycle *for* Z_{eff} *in* $\mathrm{J/m^2}$. *Crack Length in the First Cycle* ($a_{N=1}$) *Was Obtained from Isothermal Tests. See Text for Details.*

Material	C, m/cycle	m, [/]	$a_{N=1}$, μm (fractography)	$a_{N=1}$, μm (best fit to life data)
unreinforced	1.2×10^{-12}	1.94	5 – 40	6 – 20
SiC-reinforced	7.4×10^{-13}	1.95	15 – 25	18 – 38

Thermo-mechanical Fatigue Behavior

As a consequence of the good microstructural stability that was seen in the isothermal fatigue tests, no significant microstructural changes were expected to take place during TMF loading. Figure 3 shows that the absolute value of the stresses measured at the minimum and maximum temperature of a TMF cycle were indeed very similar to the stress amplitudes obtained in isothermal fatigue tests at the respective temperatures. For SiC-reinforced material, the absolute values of the stresses in TMF tests were even closer to those obtained in the respective isothermal fatigue tests.

Despite the microstructural stability and the similarity in stress-strain response, fatigue life was significantly different under TMF loading and in isothermal tests, respectively. As expected, the effect of test mode on fatigue life of both alloys studied was only minor at large plastic strain amplitude. At small plastic strain amplitudes, however, OP TMF testing was much more damaging in the SiC-reinforced material than either IP TMF tests or isothermal tests conducted at the maximum temperature

of the TMF cycle, *cf.* Fig. 4. By contrast, IP TMF tests yielded lowest fatigue lives in tests performed on the unreinforced alloy. The effect of test mode on fatigue life, however, was less pronounced in this material. If compared based on plastic strain amplitude, the ceramic reinforcement always caused a reduction in fatigue life independent of the actual test conditions.

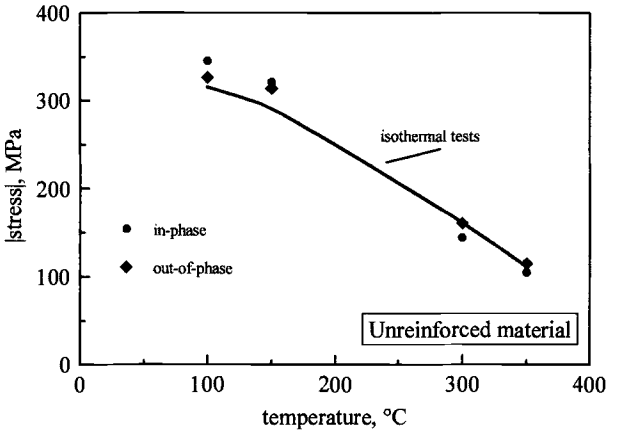

Figure 3 — *Stress Response of Unreinforced Material in TMF Tests as Compared to Isothermal Tests. All Tests Shown Were Conducted at* $\Delta\epsilon_{pl}/2 = 4 \times 10^{-3}$ *and* $\dot{\epsilon}_{pl} = 10^{-5}\,s^{-1}$. *The Temperature Range in the TMF Tests Was* 200 °C, *and Maximum Test Temperatures Were* 300 °C *and* 350 °C, *Respectively. See Text for Details.*

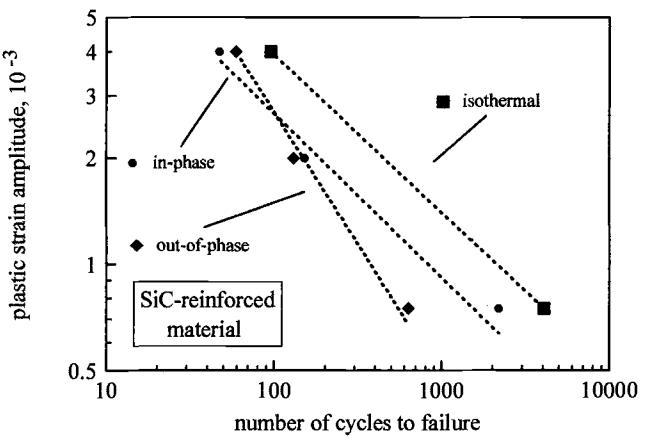

Figure 4 — *Effect of Test Mode on Plastic Strain Amplitude Versus Cycles to Failure Data for SiC-Reinforced Material. Both the TMF Tests and the Isothermal Tests Were Conducted at a Plastic Strain Rate of* $10^{-5}\,s^{-1}$. *Temperature Was Varied Between* 100 °C *and* 300 °C *in the TMF Tests. The Isothermal Tests Were Run at* 300 °C.

Microstructure

As revealed by TEM, stress-strain response is governed by the interaction between dislocations and dispersoids. Independent of the test temperature, strain amplitude or strain-temperature phasing, dislocation arrangements as observed by TEM were found to be similar to the one shown in Fig. 5a. The only exception were subgrain boundaries detected occasionally in isothermal fatigue tests conducted at 300 °C. These subgrain boundaries were found to be pinned by the dispersoids, and thus, subgrain boundary migration is insignificant. Similarly, grain boundary sliding is hindered by the dispersoids as well. The TEM studies also showed that the SiC particles had no significant influence on dislocation arrangement. Moreover, an increase in dislocation density at the SiC/matrix interface reported for dispersoid-free reinforced aluminum alloys [*9*] was not observed.

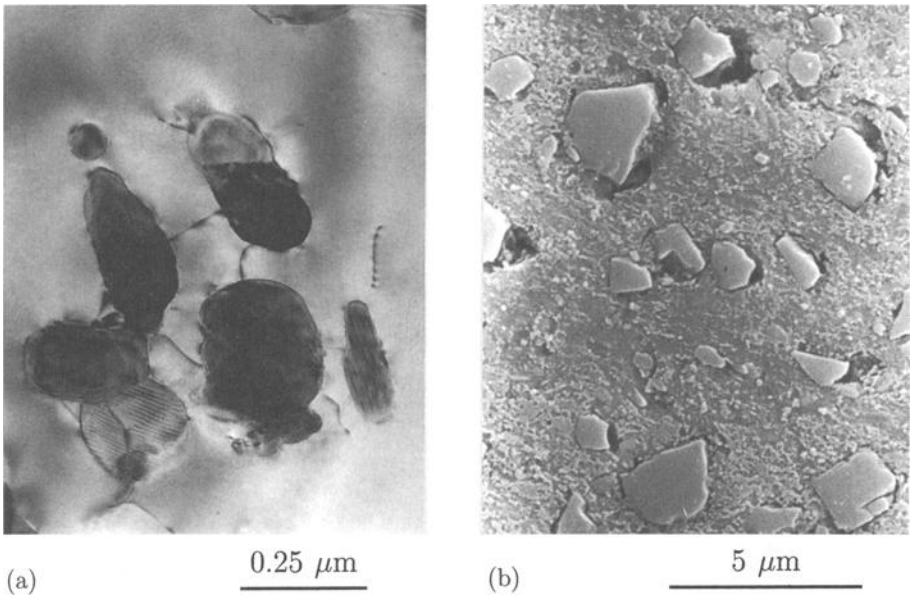

Figure 5 — *Two-Beam Bright Field TEM Micrograph (a) and SEM Micrograph (b) Showing Dispersoid–Dislocations Interactions and Void Formation at SiC Particles, Respectively. Note That Both Images Were Recorded from Areas Remote from the Crack Plane. Stress Axis Is Horizontal in (b). TMF In-Phase Test at* $\dot{\epsilon}_{pl} = 10^{-5}\,s^{-1}$ *and* $\Delta\epsilon_{pl}/2 = 4 \times 10^{-3}$. *Temperature Was Varied Between* 100 °C *and* 300 °C.

SEM studies showed numerous cracked SiC particles on the fracture surfaces of specimens fatigued at ambient temperature. It should be noted, however, that as long as the crack depth was smaller than 100 to 200 μm the fatigue cracks tended to avoid the SiC particles, i.e. crack propagation during most part of fatigue life occurred within the matrix.

At test temperatures above about 250 °C cracking of particles was observed rarely and void formation at the SiC/matrix interface became dominant. As ex-

pected, void formation was even more pronounced in tests conducted at low plastic strain rate ($\dot{\epsilon}_{pl} = 10^{-5}\,s^{-1}$). Void formation was not restricted to the immediate vicinity of the crack plane but is a bulk phenomenon instead, as could be shown in SEM studies on samples sectioned parallel to the loading axis. Again, it should be noted that for most part of fatigue life, crack propagation occurred preferentially within the matrix. Crack extension by link-up with the voids formed at the SiC interfaces was limited to longer rapidly propagating cracks. As seen in Fig. 5b, void formation at SiC particles did occur in TMF tests as well despite the fact that temperature is quite low during most part of the TMF hysteresis loop. As plastic strain amplitude was decreased, void formation became less prominent. At $\Delta\epsilon_{pl}/2 = 7.5 \times 10^{-4}$ voids at SiC particles could still be detected on the fracture surface, as local plastic strains are rather high there, but were no longer observed in the bulk. Void formation at the SiC particles could not be detected in any of the OP TMF tests. Obviously, void formation is inhibited as the high-temperature part of the cycle coincides with compressive stresses in this test mode. Similarly, no voids were observed in the unreinforced material in any test as grain boundary sliding is suppressed by the dispersoids.

SEM studies intended to identify the crack initiation site, yielded less clear results. In most cases fatigue cracks were found to have initiated in areas that were rich in iron. The actual size of the initial defects, however, could not be defined very accurately. Estimates based on the fractographic observations, are given in Table 1.

Modeling

Cyclic Stress-Strain Response

Microstructural heterogeneity is a feature common to most fatigued alloys, and local variations in yield stress are present even in fatigued single-phase materials [*10*]. Multi-component or composite models do take this heterogeneity into account. In the present paper, a modified Masing-type model was used to describe cyclic stress-strain (CSS) response under both isothermal and TMF loading conditions. In the actual model employed, the variation in local yield stress within the microstructure is represented by elements that have different yield stress. Each element is modeled with elastic perfectly plastic deformation behavior, which is a reasonable assumption at least at intermediate plastic strain amplitudes [*11*]. The distribution of the critical flow stress (σ_{if}) of the elements is described by a probability density function $f_p(\sigma_{if})$. The striking advantage of this approach is that the properties of all the individual elements can be obtained directly from an analysis of one branch of a stabilized hysteresis loop using

$$f_p(\sigma_{if}) = -\frac{2}{E^2}\frac{d\sigma_r}{d\epsilon_r} \tag{3}$$

where σ_r and ϵ_r are stress and strain in relative coordinates, respectively. For further details see e.g. [*12-14*]. The original Masing model, which was developed to explain the Bauschinger effect, only considers the athermal component of the yield stress. If the material is strained at a finite rate, however, the flow stress is increased by an effective or thermal component (σ_{th}). It should be noted that the analysis of the hysteresis loop shape based on Eq. 3 does not allow for a direct evaluation of σ_{th}. In the following, it is assumed that σ_{th} is the same for each element. This seems to be reasonable based on the TEM observations, which showed that the

main microstructural variation that affects the local yield stress is the interparticle spacing. Various methods have been proposed to determine the actual value of σ_{th}. At low temperatures and high strain rates, σ_{th} can be obtained with sufficient accuracy using either the simple approach outlined in reference [*15*], or the more detailed analysis of the hysteresis loop shape proposed by Polák et al. [*16*]. At high temperatures and low strain rates, which are the conditions of main interest in the present study, both methods fail as the yield stresses become too low. However, the change in the thermal stress component ($\Delta\sigma_{th}$) can still be determined accurately from two hysteresis loops if the strain amplitudes used are large enough so that all elements deform plastically, and both the microstructure and the deformation mechanism are identical in each tests. This can be be realized by first cycling the material into saturation and then changing the plastic strain rate instantaneously at the compressive load reversal point. Under such conditions $\Delta\sigma_{th}$ is equal to the difference in stress amplitude between the two tests. The plastic strain rates used in these tests had to be chosen such that deformation was not yet affected by creep processes. Figure 1 shows that at $T = 300\,^{\circ}\mathrm{C}$ this is indeed the case for $\dot{\epsilon}_{pl} \geq 10^{-3}\,\mathrm{s}^{-1}$.

The microstructure does no longer change once cyclic saturation is established. This also holds true within each individual cycle and the stress-strain response can then be simulated using a constant probability density function [*11*, *12*]. In order to model stress-strain response under TMF loading, it is assumed that the microstructure and deformation mechanism at each temperature of the TMF cycle are always identical to those in the corresponding isothermal tests [*13*, *14*]. This assumption of pseudo-isothermal behavior is substantiated by the TEM studies, which revealed that the microstructure remained constant irrespective of the actual test mode. For details on the actual implementation of the model see [*13*]. As the TMF tests included also deformation at low plastic strain rates and high temperatures, creep processes had to be taken into account. To minimize the amount of model parameters, only steady state creep conditions were considered. Furthermore, identical creep properties were attributed to all elements, and conventional power-law creep parameters were used to describe the creep behavior of the individual elements.

As a result of the good microstructural stability of the material tested, only few isothermal tests were required to predict CSS response under TMF loading conditions. The tests actually used to establish the parameters of the model are summarized in Table 2. A comparison between an experimentally obtained hysteresis loop and a prediction based solely on isothermal data is shown in Fig. 6. It should be noted that only isothermal tests run at $\dot{\epsilon}_{pl} \geq 10^{-3}\,\mathrm{s}^{-1}$ were used to establish the model parameters, whereas the hysteresis loop shown in Fig. 6 was obtained at $\dot{\epsilon}_{pl} = 10^{-5}\,\mathrm{s}^{-1}$. Still, the model predicts the main features of the experimentally obtained hysteresis loop rather accurately. The only significant deviations between experiment and prediction occur at high temperatures. At $300\,^{\circ}\mathrm{C}$ and $\dot{\epsilon}_{pl} = 10^{-5}\,\mathrm{s}^{-1}$, stress-strain response of the SiC-reinforced material is already dominated by creep processes (Fig. 1), and the differences seen between prediction and experiment at the high temperature end of the TMF loop result from the fact that only steady-state creep was considered in the model. Similarly, the model predicted slightly less rapid initial stress relaxation in dwell tests than obtained experimentally. As both IP and OP tests resulted in hysteresis loops that were close mirror reflections of each other, the accuracy of the predictions is not affected by strain-temperature phasing.

Table 2 — *Isothermal Tests Employed to Predict (a) CSS Behavior and (b) Fatigue Damage Under TMF Loading Conditions.*

Test conditions and data extracted	Number of tests [1]
a) cyclic stress-strain response, all tests on both alloys	
a1) LCF: RT, 150 °C, 300 °C; high $\dot{\epsilon}_{pl}$ of $10^{-3}\,s^{-1}$ ($f_p(\sigma_{if})$ as a function of temperature)	6
a2) LCF: 300 °C, high $\dot{\epsilon}_{pl}$ of $10^{-3}\,s^{-1}$ and $10^{-2}\,s^{-1}$ (strain rate dependence of thermal stress component)	2
a3) creep tests: 300 °C and 350 °C (power–law creep parameters)	10
b) damage	
b1) pure fatigue:	
FCG test at RT, unreinforced material only (crack propagation constants)	1
LCF: RT, $\dot{\epsilon}_{pl} = 10^{-3}\,s^{-1}$, both alloys (initial crack length)	8
b2) oxidation damage, unreinforced material only:	
LCF: 300 °C and 350 °C, $\Delta\epsilon_{pl}/2$: 0.075...0.4 pct, $\dot{\epsilon}_{pl}$ of $10^{-5}\,s^{-1}$ and $10^{-3}\,s^{-1}$ (oxidation damage parameters $\psi, m_{ox}, C'_{ox}, Q_{ox}$)	6
b3) creep damage, SiC–reinforced material only:	
LCF: 300 °C, $\Delta\epsilon_{pl}/2$: 0.075...0.4 pct, $\dot{\epsilon}_{pl}$ of $10^{-5}\,s^{-1}$ and $10^{-3}\,s^{-1}$ ($\Delta\epsilon_{cr}$)	6

[1] Some of the LCF tests were used to obtain data on both CSS behavior and damage evolution. Thus, a total of 31 tests was actually used to establish the complete model for both alloys.

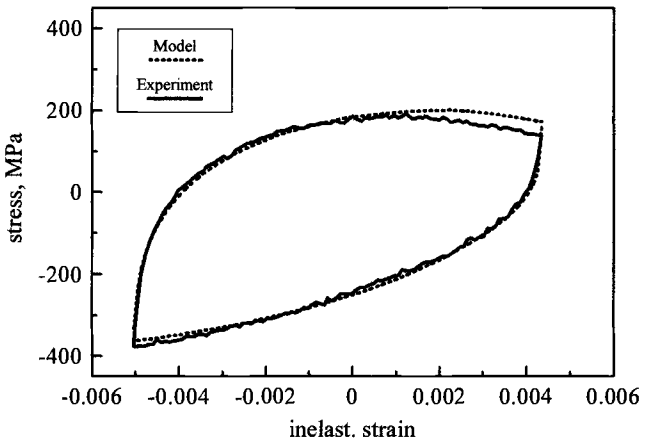

Figure 6 — *Comparison Betweeen an Experimentally Obtained Hysteresis Loop and Predictions Based on Isothermal Tests. TMF In–Phase Tests Between* 100 °C *and* 300 °C *on SiC–Reinforced Material at* $\dot{\epsilon}_{pl} = 10^{-5}\,s^{-1}$ *and* $\Delta\epsilon_{pl}/2 = 4 \times 10^{-3}$.

Fatigue Life

Crack initiation is rapid under cyclic loading conditions when relatively large plastic strain amplitudes prevail. Moreover, in the SiC-reinforced material, crack-like defects are already present prior to testing. Hence, it is reasonable to assume that fatigue life is governed completely by fatigue crack propagation for all tests reported here. The model used is similar to one proposed by Miller et al. [*17*], i.e. it is assumed that overall fatigue crack growth rate $(\mathrm{d}a/\mathrm{d}N)_{\mathrm{tot}}$ is the linear sum of terms resulting from pure fatigue, creep and oxidation.

Pure Fatigue Damage—Fatigue crack growth rate under pure fatigue conditions can be calculated directly from Eq. 1 using the data given in Table 1. As fractography has shown that crack propagation in the smooth specimens occurs within the matrix during most part of fatigue life, the data given in Table 1 was used for both the SiC-reinforced material and the unreinforced alloy. The actual value of Z_{eff} in Eq. 1 was obtained directly from analysis of modeled hysteresis loops using Eq. 2. Life prediction is not very sensitive to the value used for the final crack length, and $a_{N=N_{\mathrm{f}}} = 1\,\mathrm{mm}$ was always used. For both materials high strain rate *isothermal* fatigue tests conducted at *room temperature* were employed to obtain the initial crack length in the first cycle. It should be noted that life predicted is quite sensitive to the initial crack length. At first, $a_{N=1}$ as given in Table 1 was adjusted such as to merely fit the life data obtained. Fractographic observations, however, indicated that the scatter band obtained for $a_{N=1}$ from this fit was actually very close to the experimental observations (Table 1).

As the idea of pure fatigue damage assumes explicitly that crack propagation occurs independent of time and temperature, the procedure outlined above can be used to calculate fatigue crack growth rate resulting from pure fatigue damage under TMF conditions as well. In other words, fatigue crack growth rate only depends on crack length and strain energy densities, which are calculated using Eq. 2 from the shape of the modeled TMF hysteresis loop, and no further model parameters are involved.

Oxidation Damage—Miller et al. [*17*] have proposed that oxidation damage depends on temperature, time and cyclic loading conditions. In their model, the oxidation component of microcrack propagation is given by

$$\left.\frac{\mathrm{d}a}{\mathrm{d}N}\right|_{\mathrm{oxidation}} = C_{\mathrm{ox}}(Z_{\mathrm{eff}})^{m_{\mathrm{ox}}}\Delta t^{\psi} \tag{4}$$

where m_{ox} and ψ are material constants and Δt is the cycle time. The coefficient C_{ox} accounts for the temperature dependence of oxidation and will be discussed in more detail below. Fractography has shown that creep damage was negligible in all fatigue tests performed on unreinforced material. Therefore, the oxidation parameters were obtained by non-linear least squares regression to fatigue life data obtained in isothermal fatigue tests on *unreinforced* material. For the actual loading conditions of the tests used to establish the model parameters, see Table 2.

In the original model developed for high-strength Ni-base superalloys, Miller et al. [17] defined the coefficient C_{ox} as

$$C_{ox} = C'_{ox} \exp\left(\frac{-Q_{ox} - B\hat{\sigma}^k}{RT_{eff}}\right) \tag{5}$$

where C'_{ox}, B, k are all experimentally obtained constants. The apparent activation energy (Q_{ox}) for crack tip oxidation is made dependent on the stress ($\hat{\sigma}$) at minimum temperature of the TMF cycle. The modification of Q_{ox} is made to account for the observation that a material will oxidize more rapidly when subjected to a tensile stress. Similarly, an effective temperature (T_{eff}) was introduced to compensate for the varying temperature during the TMF test.

For the material tested in the present study, the situation appears to be somewhat different, as the oxide formed on aluminum alloys and Ni-base superalloys differ substantially. On aluminum alloys the oxide scale forms rapidly, but remains quite thin and thus rather ductile. In a TMF tests run at low strain rates ($\dot{\epsilon}_{pl} = 10^{-5}\,s^{-1}$ in the present study), the oxidation rate should always be governed by the maximum temperature of the cycle (T_{max}). Consequently, T_{eff} in Eq. 5 was replaced by T_{max}. If the oxidation rate is high and depends only on T_{max}, it should also be independent of cycle time at least in tests run at sufficiently low strain rate. Oxidation rate, however, should depend on plastic strain rate. Note that Eq. 4 could be reformulated easily in terms of $\dot{\epsilon}_{pl}$ instead of cycle time as the absolute value of $\dot{\epsilon}_{pl}$ was kept constant throughout each cycle in both the isothermal fatigue tests and the TMF tests. In other words, if the original formulation of Eq. 4 is used, Δt in a plastic strain controlled TMF test remains equal to the complete time of the cycle. Finally, the alteration in apparent activation energy in Eq. 5 predicts that more damage accumulates in an OP than during an IP TMF test. This reflects the fact that the oxide formed on Ni-base superalloys becomes more brittle at low temperatures, and thus, OP tests are most damaging as high tensile stresses occur at minimum temperature. By contrast, the oxide formed on the aluminum alloys studied in the present paper is rather ductile and overall stresses are quite low. One could, however, argue that conditions at the crack tip are quite different. Still, TMF tests on *unreinforced* material revealed that depending on the actual test conditions, IP TMF tests yielded identical or even slightly lower fatigue lives than OP tests. Therefore, the term $B\hat{\sigma}^k$ in Eq. 5 was always set equal to zero.

Creep Damage— At temperatures above about 250 °C, creep-damage was observed to occur in fatigue tests on SiC-reinforced material. Furthermore, fractography has shown that creep damage, i.e. void formation at SiC particles, takes places independently of fatigue crack growth during most of fatigue life. Hence, the damage parameter D_{CF} proposed by Riedel [18] should be suitable to describe fatigue crack growth under creep-fatigue conditions as it is explicitly assumed that both creep and fatigue damage occur independently of each other. Similar to Z_{eff}, the damage parameter D_{CF} is directly obtained from the shape of the hysteresis loop, and both parameters become equivalent at low temperatures. The critical parameter in calculating D_{CF} from a hysteresis loop is the determination of the creep contribution ($\Delta\epsilon_{cr}$) to overall inelastic strain. In case of isothermal fatigue test, $\Delta\epsilon_{cr}$ can be determined experimentally with reasonable accuracy using dwell tests or fatigue tests that employ instantaneous changes in strain rate [19]. In fact, D_{CF} could be used to

successfully correlate *isothermal* fatigue tests performed on the SiC-reinforced material, for details see [*19*]. Similar values for D_{CF} are obtained, if $\Delta\epsilon_{cr}$ is calculated using power-law creep data. Miller et al. [*17*] have noted that for TMF loading no solution for creep-damage parameters like D_{CF} do presently exist. Therefore, the authors proposed that the stress power release rate ($\hat{C}$) be used instead. In calculation of $\hat{C}$ the creep strain rate along the TMF hysteresis loop needs to be known. For a TMF tests run at $\dot{\epsilon}_{pl} = 10^{-5}\,s^{-1}$ between 100 °C and 300 °C, the creep strain rate is extremely small except for temperatures very close to T_{max}. Hence, the creep strain accumulated is small as well, and creep damage in such a test should be negligible. It is emphasized that this holds true for all methods that directly predict creep damage in such a TMF test from creep parameters obtained from conventional creep tests.

A comparison between experimentally obtained fatigue lives and predictions is shown in Fig. 7. Most of the tests shown were predicted within the generally used scatter of ± 2. Correlation between prediction and experiment was even better for the unreinforced material, and all tests were predicted well within a scatter of ± 2 of the median.

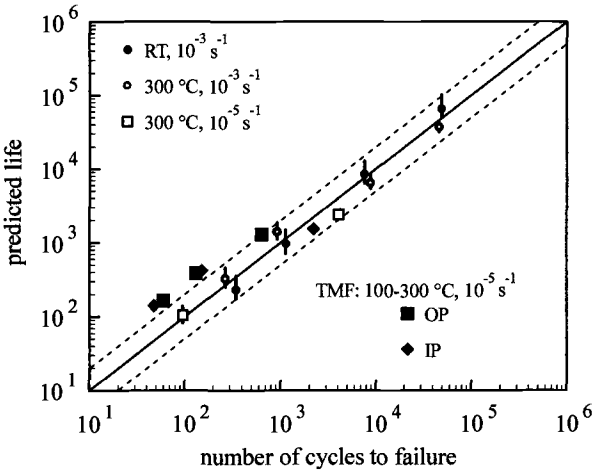

Figure 7 — *Life Prediction Results for SiC-Reinforced Material. Error Bars Shown Refer to Initial Crack Length ($a_{N=1}$) of* 18 μm *and* 38 μm, *Respectively. Whenever Error Bars Are Omitted, Scatter Predicted Is Less Than Symbol Size.*

Discussion

Stress-Strain Response

Masing-type composite models do inherently account for the Bauschinger effect, kinematic hardening [*20*], and memory of prior load history. More important, however, is the close correlation with microstructure. This is most evident from the prediction of the TMF loop (Fig. 6) obtained in a test run at $\dot{\epsilon}_{pl} = 10^{-5}\,s^{-1}$. The prediction is quite accurate despite the fact that in establishing the model parameters only isothermal tests at high strain rate ($10^{-3}\,s^{-1}$ and $10^{-2}\,s^{-1}$) were used and the

actual data base was rather small (Table 2). Note that the real advantage of the model is not the ability to accurately predict CSS response, as this is possible with continuum mechanics based models as well. Instead, differences between prediction and experiment can be directly used to discuss the distinctive features of TMF loading on microstructure [*13, 14*]. Such a direct correlation between microstructure and stress-strain response is more complicated with models that involve many parameters.

In the present paper, creep deformation was modeled assuming conventional power-law creep with a rather high stress exponent of about 10 (Fig. 1). It is known, however, that creep deformation in dispersion-strengthened materials is usually controlled by thermally activated detachment of dislocations from dispersoids [*21*]. For the material studied in the present paper, the dispersoid-dislocation interaction was reported to be relatively weak as compared to other dispersion-strengthened alloys, and thus, creep strength drops rapidly at higher temperatures [*21*]. Consequently, the creep equation used in the present model needs to be replaced, if stress-strain response at low strain rates and temperatures significantly exceeding 350 °C is to be predicted. As shown by Rösler and Arzt [*21*], their creep equation can be used to correlate experimental data obtained on Al–8Fe–4Ce up to 500 °C. However, TMF behavior up to 350 °C was of prime interest in the present study, and thus, no efforts were made to incorporate a more accurate creep equation into the model.

As microstructure determines the mechanical state [*20*], it is important to accurately model the change of microstructure as a function of temperature, time and plastic deformation, if stress-strain response is to be modeled under conditions not covered in the experiments used to establish the model parameters. In the present model, it was assumed explicitly that no changes in microstructure occurred at all in any test. Both the creep tests run at 350 °C and the fatigue experiments conducted at 300 °C did indeed demonstrate that microstructural changes are negligible for the test conditions studied. Further, as pseudo-isothermal behavior was assumed in predicting stress-strain response under TMF loading conditions, i.e. no fit parameters were involved, the accurate prediction of the TMF loops (Fig. 6) directly demonstrates that the microstructure is extremely stable under TMF test conditions as well. Angers et al. [*2*] have reported that the dispersoids coarsen substantially during creep tests run at 425 °C. Pseudo-isothermal behavior should again be a reasonable assumption for modeling deformation behavior of such a coarsened material, as CSS behavior will still be dominated by dispersoid-dislocation interaction. In other words, for accurate modeling of stress-strain response, the probability density function (Eq. 3) describing the initial microstructure, needs only to be replaced by one obtained from a sample with a coarsened microstructure.

It is also interesting to compare the dispersoid-strengthened SiC-reinforced material with conventional precipitation-hardened reinforced aluminum alloys. For an Al2xxx–T4 alloy reinforced with 20 vol. pct SiC particles, it was shown that the internal stress field is drastically altered by the SiC particles [*22*], and stress-strain response in OP tests differs substantially from that in IP tests [*22*]. Moreover, extra hardening under TMF conditions was observed, especially when alloys with small SiC particles were tested [*9*]. Dislocation pile-up was observed at the SiC/matrix interfaces, and it was concluded that blockage of plastic flow at the particles is important in explaining the increased strenghtening in TMF tests [*9*]. The observation that such extra hardening effects were found to be absent in the present dispersion-strengthened

SiC material, however, can only partly be attributed to the lower SiC particle volume fraction of 12.5 pct. At a volume fraction of 12.5 pct, SiC particles would still have a significant effect on matrix stress-strain response in *precipitation-hardened* alloys [*3*]. Furthermore, the effects should be largest at elevated temperatures as the property mismatch between SiC particles and matrix increases with temperature [*3*]. By contrast, the differences in stress-strain response of the *dispersoid-strengthened* SiC-reinforced material and that of the unreinforced matrix diminished at $T \geq 300\,^{\circ}C$. This lends further support to the TEM observations that stress-strain response in the present material is indeed dominated by dispersoid-dislocation interactions as a high volume fraction of disperoids is present.

Fatigue Life

The microcrack propagation model used to predict fatigue life assumes explicitly that the damage mechanisms are decoupled. As already noted by Miller et al. [*17*], however, a direct coupling between the various damage mechanisms may exist, but is difficult to quantify.

Pure Fatigue Damage—In prediction of pure fatigue damage, the only fit parameter involved was the initial crack length. The scatter band obtained for this fit parameter was, however, close to the fractographic observations for both alloys tested (Table 1). This indicates that the assumptions made in modeling pure fatigue damage, i.e. for both alloys fatigue life at room temperature is governed by fatigue crack propagation in the matrix, were indeed reasonable.

Oxidation Damage—As shown by fractography, creep damage was negligible in all OP TMF tests. Thus, it is to be expected that life prediction is equally accurate for both alloys. This, however, was not the case. Life prediction was very accurate for OP tests on unreinforced material, but nonconservative results were obtained for the SiC-reinforced alloy (Fig. 7). This difference cannot be attributed to scatter in initial crack length, as the fractographic observations have shown that initial crack length is much better defined in the reinforced alloy than in the unreinforced material. Further, the model showed that for both alloys life in the TMF tests was dominated by oxidation damage. The assumptions made in modeling oxidation damage under TMF conditions at first appear to be quite conservative, i.e. oxidation is dominated by the maximum temperature in the cycle and Δt in Eq. 4 remains equal to the complete cycle time in a TMF test. Still, nonconservative life prediction resulted for most tests on the SiC-reinforced alloy. Karayaka and Sehitoglu [*23*] have observed preferential crack tip oxidation in OP TMF tests run on a SiC-reinforced aluminum alloy, but not for IP TMF tests. It is often assumed that OP tests are most damaging as high tensile stresses coincide with low temperatures, where the material is rather brittle. Note that this is opposite to the trend observed for the unreinforced material. One might argue that locally much higher stresses and strains are present in the SiC-reinforced material [*24*]. However, all oxidation-dominated isothermal tests on SiC-reinforced material were predicted accurately, indicating that the effect of the SiC particulates on crack tip opening displacement and oxidation damage is properly accounted for when using Z_{eff} in Eqs. 1 and 4. Furthermore, fractography has shown that the fatigue cracks propagate within the matrix during most of fatigue life, again predicting a small effect of the SiC-reinforcement on oxidation. Currently, no simple model is available that correctly describes the physics of oxidation damage in SiC-

reinforced aluminum under TMF conditions. Obviously, a good fit can be obtained if the TMF tests are used to determine the parameters B and k in Eq. 5. It should, however, be noted that such an approach is then probably limited to conditions very closely resembling those used to establish the fit parameters.

Creep Damage—Grain boundary cavitation has been reported to occur in a *precipitation-hardened* aluminum alloy under test conditions similar to those used in the present study [*23*]. This type of creep damage is absent in the present material. The fine dispersoids not only hinder grain boundary sliding, which usually is considered a prerequisite for wedge-type crack formation, but seem to suppress or delay the nucleation of r-type voids on grain boundaries as well. Hence, void formation was only observed in fatigue tests on SiC-reinforced material. Note, that void formation was not observed in any OP test, i.e. voids do not simply form as a result of debonding at the SiC-matrix interface when high stresses are present. Instead, voids nucleated only under creep conditions, i.e. high tensile stresses, low plastic strain rates and high temperatures are all needed for void formation.

The present model accurately predicts creep damage in the isothermal tests, but again fails to predict fatigue life under IP TMF conditions (Fig. 7). Note that any model that calculates accumulation of creep strain based on conventional creep data would predict negligible creep damage for the conditions used in the IP test. At SiC particle corners *local* tensile stresses are high [*24*] and void nucleation in IP test is thus easily explained. However, high temperatures do prevail only during a small part of the TMF hysteresis loop and void growth and creep damage is expected to be small. The SEM studies have, however, clearly shown that voids grow substantially during IP TMF tests (Fig. 5b). Again, damage mechanisms appear to be strongly coupled, and thus, creep damage under TMF conditions is not predictable based on isothermal tests only. At present, life prediction of high-temperature components made out of SiC-reinforced aluminum alloys requires data obtained from TMF tests conducted under conditions closely resembling the actual service situation.

Summary and Conclusions

In the present study isothermal and thermo-mechanical fatigue (TMF) experiments were performed both on a dispersion-strengthened Al–Fe–Ce alloy and the same alloy reinforced with 12.5 vol. pct SiC particles. The main results of the present study may be summarized as follows:

1. Stress–strain behavior is dominated in both alloys by dispersoid–dislocation interactions. The effect of the ceramic reinforcement on stress–strain response is only minor.
2. The dispersoids are thermally very stable, and thus, identical microstructures are formed during cycling independent of the actual test condition. Consequently, stress–strain response under TMF conditions could be predicted quite accurately from few isothermal fatigue tests using a microstructurally based multi-component model.
3. A microcrack propagation model that accounts for pure fatigue, oxidation and creep effects, was successfully used to predict TMF life of the unreinforced material. For life prediction only data obtained from isothermal tests were required.

4. Similarly, all isothermal tests conducted on the SiC–reinforced material could be correlated with the model.
5. Damage mechanisms operating in TMF tests on SiC–reinforced material are strongly coupled, and thus, damage evolves differently than in isothermal tests. Consequently, life prediction for SiC–reinforced material is nonconservative if based on isothermal tests only.

Acknowledgment

Financial support of this work by Deutsche Forschungsgemeinschaft is gratefully acknowledged.

References

[1] Vyletel, G.M., van Aken, D.C., and Allison, J.E., "The Effect of Matrix Microstructure on Cyclic Response and Fatigue Behavior of Particle-Reinforced 2219 Aluminum: Part II. Behavior at 150°C," *Metallurgical and Materials Transactions A*, Vol. 26A, 1995, pp. 3155–3162.

[2] Angers, L., Fine, M.E., and Weertman, J.R., "Effect of Plastic Deformation on the Coarsening of Dispersoids in a Rapidly Solidified Al-Fe-Ce Alloy," *Metallurgical Transactions A*, Vol. 18A, 1987, pp. 555–562.

[3] Karayaka, M., and Sehitoglu, H., "Thermomechanical Deformation Modeling of Al2xxx–T4/SiC_p Composites," *Acta Metallurgica et Materialia*, Vol. 41, 1993, pp. 175–189.

[4] Beck, M., Kröpfl, I., Lang, K.-H., and Vöhringer, O., "Thermal and Thermal-Mechanical Fatigue of Dispersion Strengthened Al-Alloys," *Low-Cycle Fatigue and Elasto-Plastic Behaviour of Materials*, K.-T. Rie and P.D. Portella, Eds., Elsevier, Amsterdam, 1998, pp. 443–448.

[5] Angers, L., "Particle Coarsening in Rapidly Solidified Al-Fe-Ce Alloys," *Ph. D. Thesis*, Northwestern University, Evanston, IL, 1985.

[6] Christ, H.-J., Mughrabi, H., Kraft, S., Petry, F., Zauter, R., and Eckert, K., "The Use of Plastic Strain Control in Thermomechanical Fatigue Testing," *Fatigue under Thermal and Mechanical Loading: Mechanisms, Mechanics and Modelling*, J. Bressers and L. Rémy, Eds., Kluwer, Dordrecht, 1996, pp. 1–14.

[7] Dowling, N.E., "Crack Growth During Low-Cycle Fatigue of Smooth Axial Specimens," *Cyclic Stress-Strain and Plastic Deformation Aspects of Fatigue Crack Growth, ASTM STP 637*, American Society for Testing and Materials,Philadelphia, PA, 1977, pp. 97–121.

[8] Heitmann, H.H., Vehoff, H., and Neumann, P., "Life Prediction for Random Load Fatigue Based on the Growth Behavior of Microcracks," *Proc. of ICF6, Advance in Fracture Research '84*, S.R. Valluri, D.M.R. Tuplin, P.R. Rao, J.F. Knott and R. Dubey, Eds., Pergamon, Oxford, 1984, pp. 3599–3606.

[9] Sehitoglu, H., "The Effect of Particle Size on Thermo-Mechanical Fatigue of Al/SiC Metal Matrix Composites," *Fatigue under Thermal and Mechanical Loading: Mechanisms, Mechanics and Modelling*, J. Bressers and L. Rémy, Eds., Kluwer, Dordrecht, 1996, pp. 371–380.

[10] Mughrabi, H., "Dislocation Wall and Cell Structures and Long-Range Internal Stresses in Deformed Metal Crystals," *Acta Metallurgica*, Vol. 31, 1983, pp. 1367–1379.

[11] Holste, C., and Burmeister, H.-J., "Change of Long-Range Stresses in Cyclic Deformation," *Physica Status Solidi (a)*, Vol. 57, 1980, pp. 269–280.

[12] Polák, J., and Klesnil, M., "The Hysteresis Loop 1. A Statistical Theory," *Fatigue of Engineering Materials and Structures*, Vol. 5, 1982, pp. 19–32.

[13] Maier, H. J., and Christ, H.-J., "Modelling of Cyclic Stress-Strain Behavior under Thermomechanical Fatigue Conditions – A New Approach Based upon a Multi-Component Model," *Scripta Materialia*, Vol. 34, 1996, pp. 609–615.

[14] Maier, H. J., and Christ, H.-J., "Modeling of Cyclic Stress-Strain Behavior and Damage Mechanisms under Thermomechanical Fatigue Conditions," *International Journal of Fatigue*, Vol. 19, 1997, pp. S267–S274.

[15] Kuhlmann-Wilsdorf, D., and Laird, C., "Dislocation Behavior in Fatigue II. Friction Stress and Back Stress as Inferred from an Analysis of Hysteresis Loops," *Materials Science and Engineering*, Vol. 37, 1979, pp. 111–120.

[16] Polák, J., Klesnil, M., and Helešic, J., "The Hysteresis Loop 2. An Analysis of the Loop Shape," *Fatigue of Engineering Materials and Structures*, Vol. 5, 1982, pp. 33–44.

[17] Miller, M. P., McDowell, D. L., Oehmke, R. L. T., and Antolovich, S. D., "A Life Prediction Model for Thermomechanical Fatigue Based on Microcrack Propagation," *Thermomechanical Fatigue Behavior of Materials, ASTM STP 1186*, H. Sehitoglu, Ed., American Society for Testing and Materials, Philadelphia, PA, 1993, pp. 35–49.

[18] Riedel, H., *Fracture at High Temperatures*, B. Ilschner and N. J. Grant, Eds., Springer, Berlin, 1987.

[19] Jung, A., Maier, H. J., and Christ, H.-J., " Low-Cycle Fatigue Behaviour and Lifetime Prediction of a SiC-Particulate Reinforced Aluminium Alloy at Elevated Temperatures," *Proc. 12th Conf. on Fracture, ECF 12*, M. W. Brown, E. R. de los Rios and K. J. Miller, Eds., EMAS Ltd, UK, 1998, pp. 303–308.

[20] Asaro, R. J., "Elastic-Plastic Memory and Kinematic-Type Hardening," *Acta Metallurgica*, Vol. 23, 1975, pp. 1255–1265.

[21] Rösler, J., and Arzt, E., "A New Model-Based Creep Equation for Dispersion Strengthened Materials," *Acta Metallurgica et Materialia*, Vol. 38, 1990, pp. 671–683.

[22] Karayaka, M., and Sehitoglu, H., "Thermomechanical Cyclic Deformation of Metal-Matrix Composites," *Cyclic Deformation, Fracture, and Nondestructive Evaluation of Advanced Materials, ASTM STP 1157*, M. R. Mitchell and O. Buck, Eds., American Society for Testing and Materials, PHiladelphia, PA, 1992, pp. 101–120.

[23] Karayaka, M., and Sehitoglu, H., "Thermomechanical Fatigue of Particulate-Reinforced Aluminium 2xxx–T4," *Metallurgical Transactions A*, Vol. 22A, 1991, pp. 697–707.

[24] Llorca, J., Needleman, A., and Suresh, S., "An Analysis of the Effects of Matrix Void Growth on Deformation and Ductility in Metal-Ceramic Composites," *Acta Metallurgica et Materialia*, Vol. 39, 1991, pp. 2317–2335.

Gary R. Halford,[1] Bradley A. Lerch,[1] and Vinod K. Arya[2]

Thermal Strain Fatigue Modeling of a Matrix Alloy for a Metal Matrix Composite

Reference: Halford, G. R., Lerch, B. A., and Arya, V. K., **"Thermal Stain Fatigue Modeling of a Matrix Alloy for a Metal Matrix Composite,"** *Thermo-mechanical Fatigue Behavior of Materials: Third Volume, ASTM STP 1371,* H. Sehitoglu and H. J. Maier, Eds., American Society for Testing and Materials, West Conshohocken, PA, 2000.

Abstract: The Total Strain Version of the method of Strainrange Partitioning was used as the basis for modeling the thermomechanical fatigue resistance of the matrix material of the metal matrix composite, SCS-6/Ti-15-3. As prescribed by the model, the resistance was assessed through the use of bithermal creep-fatigue experiments. Bithermal temperatures of 205 and 427°C were imposed. A minimal number of strain limit-controlled, in-phase PP (pure fatigue, no creep) and CP (tensile creep) as well as out-of-phase PP (pure fatigue, no creep) and PC (compressive creep) experiments were conducted on conventional, axially-loaded, cylindrical-bar specimens. Inelastic strain range versus cyclic life curves for each of the Strainrange Partitioning bithermal cycles were evaluated and found to be nominally coincident. Cyclic elastic strain range versus inelastic strain range curves as well as elastic strain range versus life curves were documented for pure-fatigue and creep-fatigue conditions. The time-dependencies of these relationships were calibrated with the available data. These results enable the construction of total strain range versus fatigue life curves for thermomechanical fatigue for in- and out-of-phasing and for any arbitrary creep-time per cycle. Results are applicable to the cyclic life prediction of metal matrix composites using the Ti-15-3 matrix material.

Keywords: metal matrix composites, fatigue (metal), thermal fatigue, thermomechanical fatigue , bithermal fatigue, low cycle fatigue, high temperature fatigue, creep fatigue, life prediction, strainrange partitioning, crack initiation, thermal expansion

[1] Senior scientific technologist and research engineer, respectively, Lewis Research Center, NASA, Cleveland, OH 44135-3191.

[2] Research Professor, Department of Mathematical Sciences, University of Akron, Akron, OH 44325-3903.

Nomenclature

Symbols

A	General intercept constant
B	Intercept of elastic strain range–life relations
C	Intercept of inelastic strain range–life relations
C'	Intercept of inelastic line for combined creep-fatigue cycles
CP	Creep Plastic, Creep strain in tension, plastic strain in compression
K	Cyclic strain-hardening coefficient
N	Number of applied cycles
PC	Plastic Creep, Plastic strain in tension, creep strain in compression
PP	Plastic Plastic, Plastic strain in tension, plastic strain in compression
PPIP	PP - In-Phase
PPOP	PP - Out-of-Phase
CPIP	CP - In-Phase
PCOP	PC - Out-of-Phase
δt	Time per cycle of mechanical straining
V	Ratio, mean to alternating (applied to elastic strain herein)
Δ	Range of variable
ε	Strain

Subscripts

cp	Creep strain in tension, plastic strain in compression
eff	Effective
el	Elastic
fo	Failure with zero mean stress
fm	Failure with mean stress
ij	pp, pc, or cp
in	Inelastic
pc	Plastic strain in tension, creep in compression
pp	Plastic strain in tension, plastic strain in compression
t	Total mechanical

Superscripts

a	General power constant
b	Power for elastic strain range–life relations
c	Power for inelastic strain range–life relations
n	Cyclic strain-hardening exponent

Introduction

Continuous ceramic fiber reinforced, metal matrix composites for potential applications in high-temperature turbine engine components have been researched extensively during the decade of the 1990s [*1*]. Typically, strong, stiff fibers contribute their desirable characteristics to the composite when the fibers are aligned with the intended loading direction. Static tensile strength and stiffness increases of as great as 50 to 100 percent can be achieved depending upon the properties of the fiber and matrix and their volume fractions. Unfortunately, tensile strength in the transverse direction can be reduced to as low as 20 percent or less of that of the stand-alone matrix material. In the case of ceramic fibers, their low density is reflected in a composite of lower density than the matrix. Hence a zero-degree, aligned composite exhibits an even greater specific strength (strength to density) than the matrix material. Despite their severe degree of anisotropy in strength and stiffness, this class of composites appeared to offer strength advantages that might carry into the high-temperature creep-fatigue and thermomechanical fatigue regime.

The expectation that continuous fiber reinforced, metal matrix composites could be developed as materials for higher use temperatures than their matrix alloys alone has not materialized despite ~~a~~ decades of extensive funding by governmental and industrial sources. A major reason for the lack of fulfillment of promising expectations is the exceptionally high manufacturing, testing, and analysis costs. But, even if costs could be drastically reduced to an affordable level, there remain strong technical reasons why expectations cannot be met. Current high-temperature fiber reinforced metal matrix composites are, in fact, particularly ill-suited for resisting the inescapable thermal cycling component of high-temperature operation. This is because the inherent mismatch in the coefficient of thermal expansion between fibers and matrix creates an additional source of internally generated stresses and strains. These compound the severity of the conventional strains caused by mechanical loads and temperature gradients. In a comprehensive thermal/structural analysis reported by Halford and Arya [*2*] it was shown that the maximum induced cyclic strain range experienced in the metallic matrix material of <u>any</u> thermally cycled continuous fiber reinforced composite is always greater than would have developed in the stand-alone matrix material subjected to the same heat flux. Furthermore, the orientation of the maximum cyclic strain range invariably was found to be perpendicular to the fiber axis. This is by far the worst possible direction to sustain cyclic strain because of the notoriously weak bonding noted for most composites of this type. In this direction, fibers are a weakening influence on strength and not a strengthening benefit.

The above revelations should rule out any further interest in the use of metal matrix composites for severe thermal cycling environments wherein thermomechanical fatigue resistance is an important design criterion. However, because of certain unique design circumstances for which thermomechanical fatigue resistance of such composites is *possibly, but not necessarily*, the life-limiting concern, there is still merit in establishing life prediction modeling for thermal cycling of these material systems. This paper addresses a portion of the development of such a model. Its basis is the

framework originally proposed by Halford et al [*3*]. Only the salient features of the model will be presented.

Before discussing the model under current discussion, it should be pointed out that several thermomechanical fatigue life prediction models have been pursued. They are associated primarily with the organizations that have funded their development. The Wright Laboratories, Wright Paterson Air Force Base, have proposed variations of cycle fraction rule based models. The Wright Laboratories original model [*4*] assumes a linear summation of cycle fractions due to fatigue-dominated damage, creep-dominated damage, and an interaction between the two. The denominators of the life fractions were in turn related to the applied fatigue stresses according to empirical equations. Further development of the modeling led to a more general thermomechanical fatigue life prediction model, also based on cycle fractions [*5*]. Here, the fractions represented damage due to the matrix contribution and damage due to the fiber contribution. Again, the cyclic lives in the denominators were related empirically to applied fatigue stresses in the composite. The thermomechanical fatigue life prediction modeling contributions from the University of Illinois [*6,7,8,9*] go a step further and introduce another important damaging variable, oxidation. Oxidation's contribution was written in the form of a damage fraction that in turn could be added to the fatigue and creep damage fractions. Another important thermomechanical fatigue modeling effort is that based on the concept of Damage Mechanics that has association with the French Space Agency ONERA and the NASA Glenn (formerly Lewis) Research Center. The isothermal, isotropic modeling theory is complete and has been applied to unidirectional fiber reinforced composites [*10*]. Application to non-isothermal, isotropic conditions has also been reported [*11*]. Extension to the thermal cycling of anisotropic composites has yet to be reported

The continuous fiber reinforced, metal matrix composite systems that have received the greatest attention in recent years for potential high-temperature applications have used silicon carbide fibers with a designation of SCS-6. The fiber volume fractions studied have been in the approximate range of 0.20 to 0.36. The most common matrix materials have been titanium-based alloys, Ti-6Al-4V weight percent, Ti-15Mo-3Nb-3Al-0.2Si (referred to as β-21S or TiMetal-21S[1]) and Ti-15V-3Cr-3Sn-3Al (or simply Ti-15-3), and the titanium intermetallic, Ti-24Al-11Nb. Testing temperatures employed have ranged from room temperature to a maximum of 815°C, although 650°C is considered a practical upper temperature limit.

Background of Thermomechanical Fatigue Model

The life prediction model [*3*] of current interest to this paper treats a metal matrix composite as if it were a miniature structure, fully recognizing the constituents and their individual properties and how the constituents interact with one another. The mini-structural model identifies the fatigue-prone metallic matrix as the constituent for

[1] Registered trademark of Timet Corporation Henderson, NV.

tracking cycle-dependent changes in the composite during thermomechanical loading. These changes include the cyclic stress-strain inelastic constitutive flow behavior as well as creep-fatigue damage accumulation. Cyclic response changes in the matrix obviously alter the loads and strains incurred by the elastically responding fibers. The task of assessing fiber response, however, is simple if the response of the non-linearly behaving matrix can be calculated. This is because of the nature of the fibers. The principal metal matrix composites under serious consideration have used ceramic reinforcing fibers, and these are typically brittle and behave in a linearly elastic manner. They fracture abruptly when a maximum critical tensile strain [or stress = (strain x modulus of elasticity)] is imposed. Cyclic loading of the fibers *per se* has a negligible influence on their resistance to brittle fracture at the temperatures at which they would be utilized in typical applications. There may be some degradation of fiber strength due to interfacial sliding, but that would tend to occur rather late in the life after significant damage already has occurred in the composite by other mechanisms. Brittle materials of this nature do not experience classical cycle-dependent creep-fatigue crack initiation and propagation. This does not imply, however, that the stress-strain and fracture response of fibers doesn't influence the subsequent response of the adjacent matrix [*3*]

The Total Strain Version of Strainrange Partitioning is the creep-fatigue life prediction method used for assessing the thermomechanical fatigue resistance of the current matrix material. The thermomechanical fatigue resistance has been evaluated through a series of bithermal fatigue and creep-fatigue tests [*12*] to calibrate the model constants.

Experimental Details

The metal matrix composite material system of concern to the current study was used in a variety of programs at both NASA-Lewis and Pratt & Whitney [*13*]. Composite sheets were compacted from various numbers of plies of foil/fiber/foil. The matrix material was the titanium alloy commonly known as Ti-15-3. It had been selected initially for its ability to be rolled into thin foils. Stand-alone matrix material samples were fabricated for the current program by Hot Isostatically Pressing (HIPing) multiple layers of foils to attain a microstructure representative of that of the alloy as it would exist in the composite. Circular cross-section samples of the matrix material were machined to a diameter of 6.35 mm for axial thermomechanical fatigue loading. An axial extensometer measured strains on the uniform gage length samples that were loaded in state-of-the -art, axially-loaded, closed-loop, servo-hydraulic testing machines. The specimens were heated by direct induction. Temperature was measured and controlled by Type-K thermocouples in direct contact with the specimen surface. Four types of bithermal creep-fatigue tests (shown in idealized form in Figure 1) were conducted to document the thermomechanical fatigue resistance of the alloy. The bithermal temperatures were 205 and 427°C. Depending upon the test type and the location along the hysteresis loop within a cycle, the samples were under either strain

control or load control with either time-limits or strain-limits imposed. During all portions of the hysteresis loops for which plastic deformation was intended, the test was strain controlled at a total strain rate of approximately 0.001/s. When samples were allowed to creep at the maximum temperature, or during the zero load temperature excursions between the bithermal temperatures, the load was servo-controlled constant. Approximately 4.5 min./cycle were required for the zero load-controlled temperature changes (1.5 min. heating by induction, 3.0 min. without forced air cooling). The creep dwell times were not controlled constant from cycle to cycle nor from test to test. The dwell time/cycle was dictated by the amount of time required for the specimen to creep to the fix strain limit. Average cycle times, exclusive of the 4.5 min./cycle required for heating and cooling were determined for each test. All tests were conducted under computer control, with smooth mode switching between load and strain control. The bithermal tests were nominally completely reversed in mechanical strain. Specimen separation denoted failure.

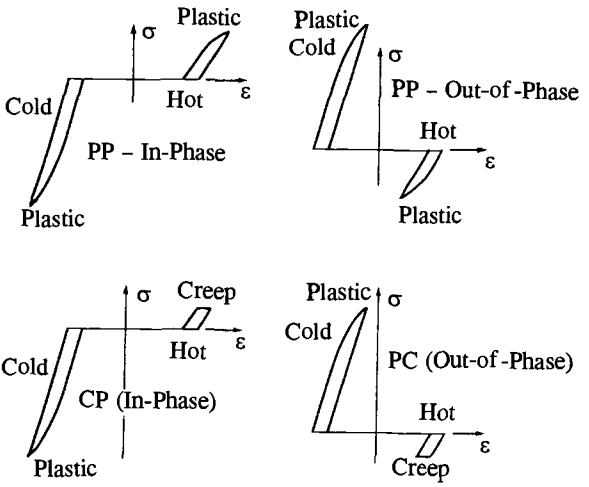

Figure 1 – *Idealized Bithermal Cycles*

Bithermal Results

Hysteresis loops taken at very near half-life were recorded and representative cyclic data recorded for analyses. Cyclic strain hardening was observed early in life but attained stabilization before the half-life was reached. Test results are summarized in Table 1. Pertinent data included mechanical total strain range, elastic strain range, inelastic strain range (and its partitioned creep and plastic components), ratio of the

mean to the amplitude of the elastic strain range, average active straining time per cycle including elastic, plastic and creep strains (exclusive of time to change temperature), observed cyclic life, and a calculated cyclic life representative of a zero mean stress (i.e., zero mean elastic strain) condition.

Table 1 – *Bithermal Test Results for Ti-15-3 at 205/427°C*

Spec #-Type	$\Delta\varepsilon_t$	$\Delta\varepsilon_{in}$	$\Delta\varepsilon_{pp}$	$\Delta\varepsilon_{cp}$	$\Delta\varepsilon_{pc}$	$\Delta\varepsilon_{el}$	$\Delta\varepsilon_{in}/\Delta\varepsilon_{el}$	V_{eff}	δt min/cyc	N_{fm} cyc	N_{fo} cyc
29-PPIP	0.0193	0.00080	0.00080	0	0	0.01850	0.043	≈ 0	0.5	416	416
30-PPIP	0.0149	0.00032	0.00032	0	0	0.01460	0.022	- 0.14	0.5	3 101	2 404
24-PPIP	0.0154	0.00020	0.00020	0	0	0.01520	0.013	- 0.41	0.6	5 640	2 846
28-PPOP	0.0186	0.00100	0.00100	0	0	0.01760	0.057	≈ 0	0.6	1 117	1 117
26-PPOP	0.0152	0.00017	0.00017	0	0	0.01500	0.011	≈ 0	0.5	3 108	3 108
20-PPOP	0.0144	0.00024	0.00024	0	0	0.01420	0.017	+0.18	0.5	1 803	2 514
23-PPOP	0.0144	0.00007	0.00010	0	0	0.01430	0.005	+0.28	0.5	1 710	2 846
22-PPOP	0.0112	≤0.00004	0.00010	0	0	0.01120	0.004	+0.54	0.4	2 299	5 703
21-PPOP	0.0111	≤0.00004	0.00010	0	0	0.01110	0.004	+0.56	0.6	2 235	5 703
31-CPIP	0.0180	0.00095	0.00057	0.00038	0	0.01700	0.022	≈ 0	1.3	1 059	1 059
32-CPIP	0.0147	0.00039	0.00014	0.00025	0	0.01430	0.017	≈ 0	15.0	2 500	2 500
41-PCOP	0.0185	0.00081	0.00057	0	0.00024	0.01767	0.014	≈ 0	3.0	626	626
44-PCOP	0.0165	0.00088	0.00053	0	0.00035	0.01560	0.022	≈ 0	15.9	1 721	1 721

Tracings of hysteresis loops taken near half-life are shown in Figure 2 for an example of each of the four types of bithermal creep-fatigue tests, PP - In-Phase (PPIP), PP - Out-of-Phase (PPOP), CP - In-Phase (CPIP), and PC - Out-of-Phase (PCOP.)

Cyclic Elastic Strain – Plastic Strain Behavior

The bithermal elastic-plastic cyclic strain-strain curve plots as a power-law strain hardening function (Figure 3),

$$\Delta\varepsilon_{el} = K_{pp}\,(\Delta\varepsilon_{pp})^{n} = 0.0490\,(\Delta\varepsilon_{pp})^{0.14} \qquad (1)$$

Note that the elastic strain range is the sum of the elastic strain in tension at one of the bithermal temperatures and the elastic strain in compression at the other. The plastic strain range is that portion of the inelastic strain range that contains no creep. The cyclic strain-strain curve is well-behaved and has a cyclic strain hardening exponent $n = 0.14$ which is within commonly encountered values for most alloys [*14*]. Of particular interest is that the bithermal PP - In-Phase (PPIP) and PP - Out-of-Phase (PPOP) test results as well as the bithermal CP - In-Phase (CPIP) and PC- Out-of-Phase

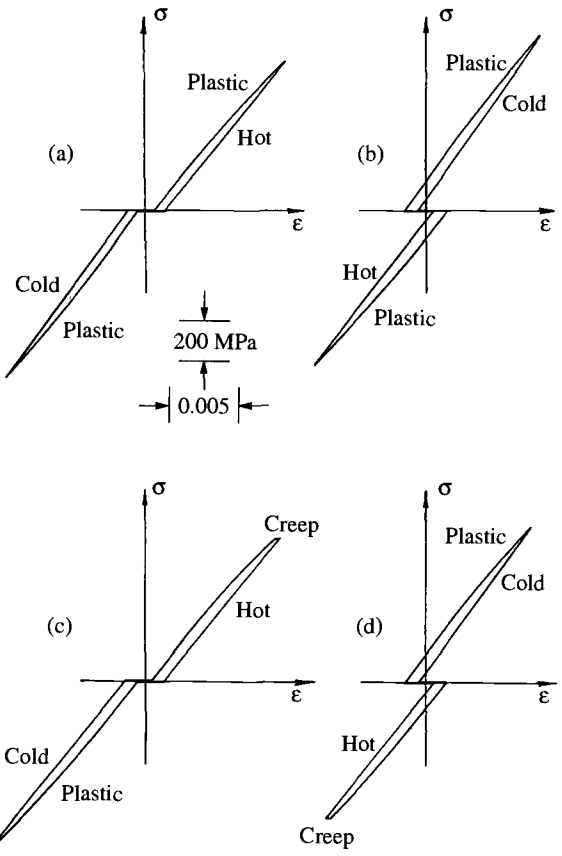

Figure 2 -- *Tracings of Hysteresis Loops for Ti 15-3 at 205/427°C Taken Near Half-life for Each of the Four Types of Bithermal Tests; (a) PP - In-Phase, Spec. 29, (b) PP - Out-of-Phase, Spec 28, (c) CP - In-Phase, Spec. 31, (d) PC - Out-of-Phase, Spec. 44*

(PCOP) results are essentially indistinguishable from one another. This limited data set implies that the presence of creep strains within the creep-fatigue cycles does not alter the elastic strain versus plastic strain relationship.

Strainrange Partitioning Life Relations

The Strainrange Partitioning life relations for the stand-alone matrix material, Ti-15-3 will have their greatest generality and applicability when they represent a zero

mean loading condition. This topic is discussed in detail in earlier treatments [*15,16*] of evaluating the life relations for other alloys. For isothermal evaluations either stress or elastic strain can be used as the parameter for establishing "mean" effects since the two terms are directly related by the isothermal modulus of elasticity. However, since the temperature-dependent modulus varies within a thermomechanical fatigue cycle, it

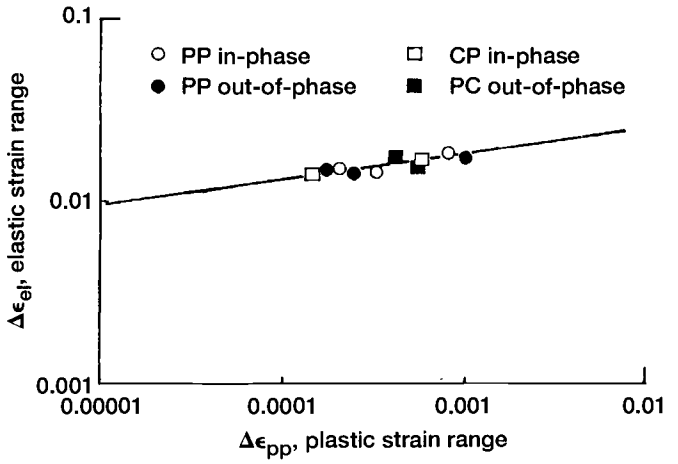

Figure 3 – *Bithermal Cyclic Strain-Strain Curve, Ti-15-3 at 205/427°C*

is more logical to deal with the mean elastic strain [*16*]. Mean elastic strains did develop during some of the virtually elastic cyclic loading conditions of the current bithermal tests. A measure of the extent of the mean elastic strain is given by the ratio of the mean elastic strain $\Delta\varepsilon_{el,m}$ to the elastic strain amplitude, $\Delta\varepsilon_{el}/2$. This ratio is designated V. The mean elastic strain (or mean stress) effectiveness criterion of Reference [*15*] was used to decide which tests required a correction to the measured cyclic life. The effectiveness of the mean elastic strain ratio V was computed using the transition equation proposed in [*15*] and given by the following equation.

$$V_{eff} = V \exp\left[-70(\Delta\varepsilon_{in}/\Delta\varepsilon_{el})^2\right] \quad (2)$$

Effects of mean elastic strain were computed using the recast-version [*15*] of the mean stress model of Morrow [*17,18*].

$$(N_{fo})^b = (N_{fm})^b + V_{eff} \tag{3}$$

where b is the magnitude of the negative slope of the elastic strain range versus zero mean stress fatigue life curve. The values of V_{eff} and N_{fo} (Table 1) were computed from equations (2) and (3).

PP - In-Phase and Out-of-Phase Elastic Life Relations – The elastic strain range life relation for PP cycling was found to be independent of the bithermal phasing for the matrix material (Figure 4). For these conditions, $N_{fo} = N_{pp}$. Iteration established the value of the slope to be *-0.16*, i.e., b is *0.16* in equation (4).

$$\Delta\varepsilon_{el} = B_{pp}\,(N_{pp})^{-b} = 0.0520\,(N_{pp})^{-0.16} \tag{4}$$

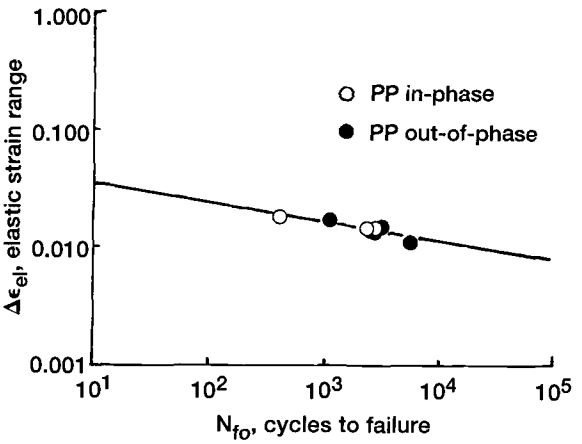

Figure 4 – *Bithermal Elastic Strain Range Life Relation for Ti-15-3 at 205/427°C*

As creep is added to a bithermal cycle (or any thermomechanical cycle), the inelastic strain range increases for a given elastic strain response. Alternatively for a given inelastic strain range, the elastic strain range decreases, as reflected by the intercept value, B, decreasing. The Total Strain Version of Strainrange Partitioning deals with the time-dependence of the B intercept through a series of equations explained in Reference [*19*]. Before presenting those results it is most convenient to first discuss the inelastic Strainrange Partitioning life relations.

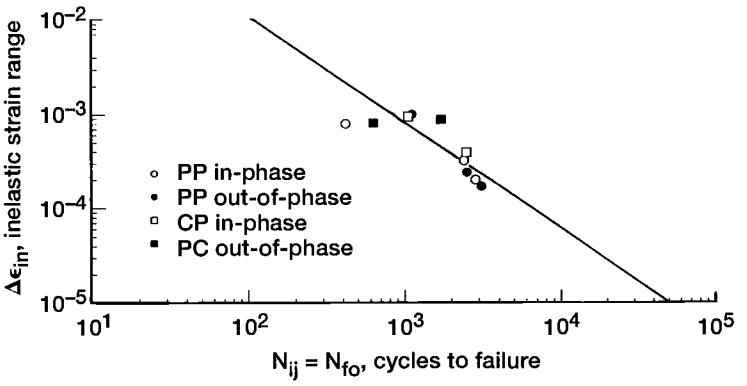

Figure 5 – *Bithermal Inelastic Strainrange Partitioning Life Relation for Ti-15-3 at 205/427°C*

In-Phase and Out-of-Phase Inelastic Life Relations – Figure 5 shows the inelastic strain range versus cyclic life results for all of the bithermal tests of Table 1. Inelastic strain ranges are at very low levels (≤ 0.001) leading to excessive scatter in the test results such that it is not possible to draw firm distinctions between the four types of bithermal test results. The absence of cyclic life degradation due to the imposition of creep strain coupled with the added exposure time for oxidation in the bithermal cycles was unexpected when the experiments were first conceived. A lack of degradation in life due to creep implies the deformation and cracking mechanisms for cyclic plasticity and cyclic creep are not appreciably different for this alloy within the temperature range studied. Data for inelastic strain ranges less than 0.00010 were not included in the curve fitting. A single curve fit equation is used to represent the entire data set.

$$\Delta\varepsilon_{in} = C_{ij}\,(N_{ij})^{-c} = 1.92\,(N_{fo})^{-1.12} \tag{5}$$

Compared to the 427°C isothermal PP life relation reported in References [*20*] and [*13*] (pp.307-315), the current slope is considerably steeper (*-1.12* versus *-0.60*). This observation implies a significant influence of thermal versus isothermal strain cycling on the cyclic resistance of this alloy. Although the slope is quite steep, the classical relation $n = b/c$ remains valid, i.e., $0.14 \approx 0.16/1.12$. Neither the addition of traces of observed surface oxidation nor the imposed creep strains had a discernible detrimental effect on the inelastic strainrange versus cyclic life to failure for the bithermal experiments. Yet, there is a substantial difference in behavior between isothermal and bithermal cyclic strain resistance.

The next step in the evaluation of the Total Strain Version of the Strainrange Partitioning model for thermomechanical fatigue life prediction of the stand-alone Ti-15-3 matrix material is the determination of how the elastic strain range versus cyclic life decreases as a result of time-dependent effects (principally creep).

Cyclic Elastic - Inelastic (Creep +Plastic) Strain Behavior

The dearth of data necessitates simplifying assumptions in order to analyze the current results. The first assumption is that only the intercept, K_{ij}, (and not the slope) of the elastic strain range versus inelastic strain range relation is affected by time through the effects of creep. The following power-law equation is used.

$$K_{ij} = A\ (\delta t)^{a} \tag{6}$$

Each of the four tests involving creep (two CP and two PC) were used to establish a line parallel to equation (1), thus yielding four intercepts for the respective values of δt. In turn, these intercepts were plotted on logarithmic coordinates against log (δt). The resultant expressions are as follows.

$$K_{cp} = K_{pc} = 0.0468\ (\delta t)^{-0.020} \tag{7}$$

Again, there is little distinction between the CP and PC behavior. From the equations governing the Total Strain Version of the Strainrange Partitioning) model [*3*],

$$B_{ij} = K_{ij}\ (C')^{n} \tag{8}$$

For the current material, $K_{ij} = K_{cp} = K_{pc} = 0.0468\ (\delta t)^{-0.020}$, and $C' = C_{ij} = 1.92$, and $n = 0.14$. Hence,

$$B_{ij} = 0.0468\ (\delta t)^{-0.020}\ (1.92)^{0.14} = 0.0513\ (\delta t)^{-0.020} \tag{9}$$

The elastic line for bithermal cycles involving creep can now be written as.

$$\Delta\varepsilon_{el} = 0.0513\ (\delta t)^{-0.020}\ (N_{ij})^{-0.16} \tag{10}$$

For rapid PP bithermal cycling with a $\delta t = 0.5\ min$, equation (10) properly reduces to the measured equation (4).

$$\Delta\varepsilon_{el} = 0.0520\ (N_{pp})^{-0.16} \tag{11}$$

It remains to evaluate the time-dependent partitioning equations for a general analysis.

Total Strain – Life Relation

The total strain range versus life relation for Ti-15-3 can now be written for thermomechanical fatigue cycling between 205 and 427°C.

$$\Delta\varepsilon_t = 1.92\ (N_{fo})^{-1.12} + 0.0513\ (\delta t)^{-0.020}\ (N_{fo})^{-0.16} \tag{12}$$

Knowing only the value of $\Delta\varepsilon_t$ (from, for example, an elastic structural analysis) and δt (from the projected mission usage) would be sufficient to predict the N_{fo} crack initiation life for the thermomechanical fatigue cycle of interest. Should a non-zero mean loading condition exist for the thermomechanical fatigue cycle, N_{fm} would then be calculated from equation (3). The crack initiation life N_{fo} calculated from equation (12) is compared to the experimentally deduced life N_{fo} (Table 1). The comparison is shown in Figure 6. These results represent the correlative capability of equation (12). With the exception of the longest life PP - Out-of-Phase result, calculated and measured results agree to within less than a factor of two in cyclic life.

To generalize equation (12) for a thermomechanical fatigue cycle with extreme temperatures differing from the bithermal characterization tests, three considerations must be addressed, particularly if no thermomechanical fatigue calibrating data have been generated for the new temperatures. These considerations are addressed below in a conjectural manner that can serve as a guide for further development.

1.) Temperature Dependence of Inelastic Strain Range–Life Relation - The principal reason governing a potential alteration of the inelastic life relationship by temperature would be if the deformation and damage mechanisms changed. An indication of deformation mechanism change is often reflected in changes in tensile ductility (time-independent plasticity) and creep-rupture ductility (time-dependent creep). The Ductility Normalized–Strainrange Partitioning equations [*21*] could be utilized to approximate shifts in the intercept of the inelastic life relation. With common mechanisms over a range of temperatures, equation (4) should suffice as written.

2.) Temperature Dependence of Elastic Strain Range–Life Relation - Below the creep regime temperature, the elastic line is typically independent of temperature. This is because the temperature dependency of strength and of modulus of elasticity are comparable and hence their ratio is nominally independent of temperature. Practical evidence of this is found in the ASME Pressure Vessel and Piping Codes (for example, Code Case N-47 for nuclear vessels) wherein a single strain fatigue curve is given to

represent a broad range of temperatures from room temperature to nearly 500 °C. For maximum temperatures into the creep regime, the elastic line tends to fall at a faster rate with increasing temperature than does the elastic modulus. Here, the relative change in the ratio of strength (yield or ultimate) to modulus serves as a useful indication of the extent the elastic line should be reduced. This shift applies only to the upper bound, elastic line that goes with PP type cycling. It is important to recognize that the elastic line for thermomechanical fatigue cycling has contributions from the low-temperature end of the cycle as well as the high-temperature end. The above adjustments should be made only to the high-temperature portion of the elastic strain range.

3.) Time Dependence of the Elastic Strain Range–Life Relation - With a higher maximum temperature, creep and relaxation occur more rapidly, thus the time-dependency of the elastic line gets to be very important. Going back to equations (8) and (6), it is seen that the time-dependency for the elastic line intercept is directly related to the cyclic strain-strain intercept value, K_{ij}, i.e., a flow property of the material as opposed to a failure property. In the absence of measured cyclic flow characteristics, relative changes with temperature and time of static strength properties could be used to guide the selection of constants for life prediction.

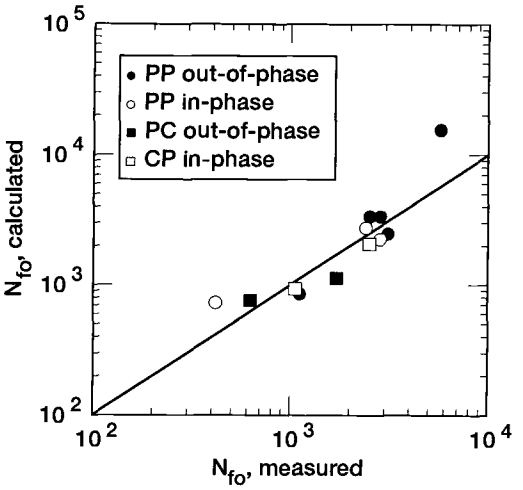

Figure 6 – *Correlation of Measured and Calculated Thermomechanical Fatigue Lives Based on the total Strain Version of Strainrange Partitioning, Ti-15-3 at 205/427°C*

Time-Dependent Partitioning of the Inelastic Strain Range

At the heart of the Strainrange Partitioning method is the ability to compute how much of the inelastic strain is partitioned into time-dependent creep and how much remains as time-independent plasticity. The most general approach to the determination of the partitioning is through a unified viscoplastic cyclic constitutive model [*21*]. Nicholas and Kroupa [*22*] , for example, have taken advantage of a recent version of the classical Bodner-Partom constitutive model to enhance the analysis of the internal stress-strain response of the metallic matrix material of their composite system, SCS-6/Ti-6Al-4V. An alternate approach to partitioning is through empirical correlation of data generated during the experimental evaluation of the cyclic material properties [*19*]. The very same information that aids in the partitioning of the inelastic strains is also of value in describing the elastic strain-inelastic strain cyclic relationship, and hence is of value in adjusting the time-dependencies of the elastic strain range versus cyclic life relation discussed above.

For the Ti-15-3 alloy of the current study, it is not necessary to be able to partition the inelastic strain range into its creep and plasticity components because the inelastic strain range life relationship appears to be independent of this partitioning.

Summary of Results

A limited-scope experimental program was conducted on the titanium alloy Ti-15-3 to evaluate its resistance to thermomechanical creep-fatigue loading. The objective was to calibrate the Total Strain Version of the Method of Strainrange Partitioning for predicting thermomechanical fatigue. For this purpose, bithermal creep-fatigue tests were performed at 205/427°C. The following results are summarized.

1. The inelastic strain range versus life relations for this alloy appear to be insensitive to the phasing of temperature and strain in the bithermal tests and to the partitioning of the inelastic strain ranges. Creep-fatigue strain ranges of CP and PC were found to be no more damaging than creep-free PP strain ranges.

2. The principal influence of creep on the bithermal creep-fatigue behavior is to alter the elastic strain (stress) response. The greater the creep strain, the lower the stress for a given inelastic strain and hence the lower the elastic strain versus inelastic response.

3. A preliminary calibration of the Total Strain version Strainrange Partitioning equations for thermomechanical fatigue has been achieved and they are ready for application to the life prediction of thermomechanically fatigued continuous fiber reinforced composites using the alloy Ti-15-3 as the matrix material.

4. Guidelines were discussed for extending and generalizing the thermomechanical fatigue life prediction equations presented for the titanium alloy Ti-15-3.

References

[1] *Life Prediction Methodology for Titanium Matrix Composites, ASTM STP 1253*, W. S. Johnson, J. M. Larsen, B. N. Cox, Eds., American Society for Testing and Materials, 1996.

[2] Halford, G. R. and Arya, V. K., "Thermal Stresses -- The Achilles' Heal of Continuous Fiber Reinforced Metal Matrix Composites," *Thermal Stresses `97, Proceedings of the Second International Symposium on Thermal Stresses and Related Topics*, Rochester Institute of Technology, NY, June 1997, pp. 41-44.

[3] Halford, G. R., Lerch, B. A., Saltsman, J. F., and Arya, V. K., "Proposed Framework for Thermomechanical Fatigue (TMF) Life Prediction of Metal Matrix Composites (MMCs)," *Thermomechanical Fatigue Behavior of Materials, ASTM STP 1186*, H. Sehitoglu, Ed., American Society for Testing and Materials, Philadelphia, 1993, pp. 176-194.

[4] Russ, S. M., Nicholas, T., Bates, M. and Mall, S., "Thermomechanical Fatigue of SCS-6/Ti-24Al-11Nb Metal Matrix Composite," *Failure Mechanisms in High Temperature Composite Materials*, ASME AD-Vol. 22 and AMD-Vol. 122, American Society of Mechanical Engineers, New York, 1991, pp.37-43.

[5] Nicholas, T., Russ, S. M., Neu, R. W., and Schehl, N., "Life Prediction of a [0/90] Metal Matrix Composite Under Isothermal and Thermomechanical Fatigue," *Life Prediction Methodology for Titanium Matrix Composites, ASTM STP 1253*, W. S. Johnson, J. M. Larsen, B. N. Cox, Eds., American Society for Testing and Materials, P1996, pp. 595-617.

[6] Neu, R. and Sehitoglu, H., "Thermo-Mechanical Fatigue, Oxidation and Creep: Part I-Experiments," *Metallurgical Transactions*, vol. 20A, 1989, pp. 1755-1767.

[7] Neu, R. and Sehitoglu, H., "Thermo-Mechanical Fatigue, Oxidation and Creep: Part II-Life Prediction," *Metallurgical Transactions*, vol. 20A, 1989, pp. 1769-1783.

[8] Sehitoglu, H. an Boismier, D. A., "Thermo-Mechanical Fatigue of Mar-M247: Part 2-Life Prediction," *ASME Journal of Engineering Materials Technology*, Vol. 112, 1990, pp. 80-89.

[9] Sehitoglu, H. and Karayaka, M., "Prediction of thermomechanical Fatigue Lives in Metal Matrix Composites," *Metallurgical Transactions*, Vol. 23A, July 1992, pp. 2029-2038.

[*10*] Kruch, S. and Arnold, S. M., "Creep Damage and Creep-Fatigue Damage Interaction Model for Unidirectional Metal-Matrix Composites," *Applications of Continuum Damage Mechanics to Fatigue and Fracture, ASTM STP 1315*, D. L. McDowell, Ed., American Society for Testing and Materials, 1997, pp. 7-28.

[*11*] Lemaitre, J. and Chaboche, L.-L., *Mechanics of Solid Materials*, Cambridge University Press, Cambridge, (English Translation), 1990, p.426.

[*12*] Halford, G. R., McGaw, M. A., Bill, R. C., and Fanti, P. D., "Bithermal Fatigue: A Link Between Isothermal and Thermomechanical Fatigue. Low Cycle Fatigue," *Low Cycle Fatigue, ASTM STP 942*, H. D. Solomon, G. R. Halford, L. R. Kaisand, and B. N. Leis, Eds., American Society for Testing and Materials, Philadelphia, 1988, pp. 625-637.

[*13*] *Reliability, Stress Analysis, and Failure Prevention - 1993, ASME, DE-Vol. 55*, R. J. Schaller, Ed., American Society of Mechanical Engineers, New York, 1993.

[*14*] Halford, G. R., "The Energy Required for Fatigue," *Journal of Materials*, Vol. 1, No. 1, 1966, pp. 3-18.

[*15*] Halford, G. R. and Nachtigall, A. J., "The Strainrange Partitioning Behavior of an Advanced Gas Turbine Disk Alloy, AF2-1DA," *Journal of Aircraft*, Vol. 17, No. 8, 1980, pp. 598-604.

[*16*] Halford, G. R., "Low-Cycle Thermal Fatigue," *Chapter 6, Thermal Stresses II*, R. B. Hetnarski, Ed., Elsevier Science Publishers B. V., Amsterdam, 1987, pp. 329-428.

[*17*] Morrow, J., "Fatigue Properties of Metals," *Fatigue Design Handbook, Sec. 3.2, SAE Advances in Engineering*, Vol. 4, Society of Automotive Engineers, 1968, pp. 21-29.

[*18*] Halford, G. R. and Manson, S. S., "Discussion of paper by J. Adams and M. Doner in Journal of Engineering for Power, ASME, Vol. 103, 1981," *Journal of Engineering for Power*, ASME, Vol. 104, April 1982, p. 411.

[*19*] Saltsman, J. F. and Halford, G. R., "An Update on the Total Strain Version of SRP," *Low Cycle Fatigue, ASTM STP 942*, H. D. Solomon, G. R. Halford, L. R. Kaisand, and B. N. Leis, Eds., American Society for Testing and Materials, Philadelphia, 1988, pp. 329-341.

[*20*] Gayda, J., Gabb, T. P., and Freed, A. D., "The Isothermal Fatigue Behavior of a Unidirectional SiC/Ti Composite and the Ti Alloy Matrix," *Fundamental Relationships Between Microstructure & Mechanical Properties of Metal-Matrix Composites*, P. K. Liaw and M. N. Gunger, Eds., The Minerals, Metals & Materials society, 1990, pp. 497-514.

[*21*] Halford, G. R., Saltsman, J. F., and Hirschberg, M. H., "Ductility Normalized-Strainrange Partitioning Life Relations for Creep-Fatigue Life Prediction," *Proceedings, Conference on Environmental Degradation of Engineering Materials*, R. P. McNitt and M. R. Louthan, Jr., Eds., Virginia Tech. Printing Dept., V.P.I. and State University, Blacksburg, VA, 1977, pp. 599-612.

[*22*] Nicholas, T. and Kroupa, J. L., "The Role of Inelastic Deformation in the Analysis and Life Prediction of Titanium Matrix Composites," *Advances in Computational Engineering Science*, S. N. Atluri and G. Yagawa, Eds., Tech Science Press, Forsyth, GA, 1997, pp. 45-50.

Ohchang Jin[1] and W. Steven Johnson[1]

The Role of Oxidation on the Thermo-mechanical Fatigue of Timetal 21S Matrix Composites

Reference: Jin, O. and Johnson, W. S., **"The Role of Oxidation on the Thermo-mechanical Fatigue of Timetal 21S Matrix Composites,"** *Thermo-mechanical Fatigue Behavior of Materials: Third Volume, ASTM STP 1371,* H. Sehitoglu and H. J. Maier, Eds., American Society for Testing and Materials, West Conshohocken, PA, 2000.

Abstract: Isothermal fatigue tests were performed on unnotched quasi-isotropic SCS-6/Timetal 21S (Ti-15Mo-2.6Nb-3Al-0.2Si) composites at room temperature, 400°C and 500°C with various hold times (0, 1 and 10 seconds). The specimen tested at 500°C showed significant oxidation, especially along the grain boundaries. In addition, there were changes in various physical properties of the composites at elevated temperatures: oxidation, phase transformation, viscoplastic flow of matrix, and interface reaction. The measurement of oxide thickness of both with and without load indicated that the oxidation of the matrix material was more severe with applied load than without load for the same amount of exposure time. Simple spectrum loading tests were conducted to examine the effect of test temperature on the formation of oxidation and its influence on the damage accumulation in the composites. Different numbers of applied cycles per block were used: n_1 and n_2 = 10, 100, and 1000 cycles. The change in temperature along with stress acted as thermal cycle that further introduced damages into the composites and reduced their life. As the number of applied cycles increased, the failure life of the composites was increased. The small number of cycles per block showed a shorter life due to more frequent changes in temperature level.

Keywords: titanium matrix composites, silicon carbide fibers, quasi-isotropic laminate, isothermal fatigue, spectrum loading, damage mechanisms, damage accumulation, oxidation, time dependent behavior.

[1] Graduate student and Professor, School of Materials Science and Engineering, Georgia Institute of Technology, Atlanta, GA 30332-0245

Background

Damage mechanisms of Titanium Matrix Composites (TMCs) at room temperature have been well characterized by various testing methods such as incremental tensile and fatigue tests combined with the in-situ and ex-situ characterization using microscopes [*1-5*]. This includes interface failure, matrix cracking and fiber fracture. In general, fatigue in TMCs at room temperature is characterized by extensive matrix damage prior to fiber failure [*3*]. This is due to the fact that the matrix can carry a significant portion of applied load at room temperature. Even though there are complex interactions between constituents under mechanical loading such as matrix microcracking and subsequent load transfer, the damage progress at room temperature is relatively straightforward since no time-dependent phenomena are involved in fatigue cycling.

However, TMCs at elevated temperatures undergo dramatic changes in physical properties since titanium is susceptible to environment. The degree of such changes depends upon the temperature level and the duration at that temperature. This is the reason that fatigue characteristics of TMCs at elevated temperatures are quite different from those at room temperature. Typical examples of such physical changes are oxidation [*6-16*], phase transformation, viscoplastic matrix flow, and changes in interfacial properties of the composite. Oxidation and interface reaction result in damage initiation and act as stress concentrators. Others induce the change in constituent response and alter the damage progression. Since the reinforcements (silicon carbide fiber) are ceramic material, there is no major change in fiber properties at elevated temperatures. However, titanium matrices have shown some temperature dependency at elevated temperatures [*5*].

Oxidation resistance of the matrix materials is the most crucial property in TMCs because the formation of oxide induces the difference in thermal expansion between the matrix and the oxide which produces residual stress between them. The key nature of the oxide is that it is brittle and cracks when its thickness reaches a critical value under loading and then continuously exposes matrix surface to the environment [*6-8*]. As a result, the formation of oxide reduces the composite's life significantly compared to the lifetime at room temperature. There are three possible mechanisms of metal oxidation: oxide scale formation on the surface, oxygen dissolution in interstitial sites in Ti [9], and oxidation along grain boundaries [*10,11*]. Oxygen dissolution can not be seen easily, however, it can cause matrix embrittlement.

What follows is a brief description of surface oxidation and grain boundary oxidation.

Surface Oxidation

Titanium dioxide is first formed on the matrix surface due to easy access of oxygen to the surface. Ti has been known to follow the parabolic law of oxidation up to 700°C [*12*]. X-ray diffraction studies have shown that the structure of TiO_2 is mostly Rutile structure without exceptions [*12*]. Further oxidation is limited by the oxide already

formed since the kinetics are dependent upon the diffusion rate of oxygen through the first formed oxide. Therefore, a sequence of layers of the different titanium oxides such as TiO, Ti_2O_3, Ti_3O_5 form even if the TiO_2 is thermodynamically the most stable oxide [*13*].

One important aspect of the oxide is that the rate of oxide formation depends not only on temperature and its duration but also on applied load. Antolovich et al. [*14*] showed that oxide formation is accelerated under mechanical loading. This is true because oxygen penetration is assisted by easy grain boundary movement under loading.

Grain Boundary and Interface Oxidation

Grain boundaries are known as an easy diffusion path for oxygen. When titanium is annealed at elevated temperatures before any application of load, the grain boundaries are oxidized as well. This type of oxidation induces embrittlement of grain boundaries so that application of the load will damage grain boundaries. If the matrix has good oxidation resistance, the most probable oxidation mechanism would be grain boundary oxidation. Indeed, this is the most frequent damage mechanism at elevated temperatures. Since there are several possible interfaces, the separation of the interfaces will provide the diffusion path for oxygen, especially if the composites contain off-axis fibers.

Materials and Test Procedures

Isothermal fatigue tests were performed to characterize the damage mechanisms and to evaluate the degree of oxidation at a particular temperature. This information is used to determine a dominant cause of composite failure in spectrum loading. The goals of spectrum loading were to examine the influence of oxidation at different temperatures on the composite life and to measure the effect of temperature alteration between the spectrum since it generates thermal cycling, inducing surface damage and ultimately reducing the life of composites.

Materials

Test materials were SCS-6/Timetal 21S. The composites were fabricated by a foil-to-foil process and Hot Isostatic Pressing (HIPing) at approximately 980°C at Textron Specialty, Lowell, MA. Ti-Nb crossweave wires were used to prevent the random movement of fibers. Heat-treatment was performed for all specimens at 621°C for 8 hours in vacuum to stabilize the α phase. For current study, quasi-isotropic laminates $[0/\pm45/90]_s$ with fiber volume fraction 0.36 were used.

Timetal 21S, also known as Beta-21S, is Timet's designation for Ti-15Mo-3Al-2.6Nb-0.2Si (wt %). Timetal 21S is a metastable β alloy that has been designed for improved oxidation resistance, elevated temperature strength, creep resistance, and

thermal stability compared to other Ti-based alloys such as Ti-15-3. SCS-6 fiber is produced by a chemical vapor deposition (CVD) process by Textron Specialty Materials Division. The modulus and ultimate strength of the fiber are typically 400 GPa and 3450 MPa, respectively [*15*]. The fiber is 142 μm in diameter, and it is a complex and mutilayered structure [*16*].

Experimental Procedure

The test conditions for isothermal fatigue were maximum stress, 350 MPa, stress ratio, 0.1, temperatures 400°C and 500°C, hold times 1, 10 and 100 seconds. The test waveform used was ramp-hold-ramp. For spectrum loading only 1 second hold period was inserted in the fatigue cycle to minimize the testing time. The waveform used for spectrum loading is shown in Figure 1. To monitor the temperature gradient along the specimen, three thermocouples (type K) were attached on each side of the specimen by spot welding. One was located on the center and the other two were attached at 0.5″ from the center. The temperature gradient along the 1″ gauge length was controlled within ±5°C for both isothermal fatigue and simple spectrum loading tests. An Ameritherm 2.5 kW induction heater was used for both isothermal fatigue and spectrum loading tests.

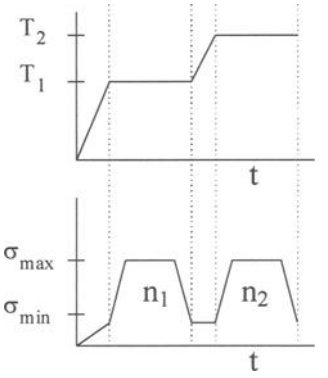

Figure 1—*Typical waveform for spectrum loading tests*

Before tests were started the specimens were soaked for 15-20 minutes to stabilize the temperature. For the spectrum loading tests, the heating and cooling rates were determined before the tests. The rates were 10°C and 2°C per second for heating and cooling, respectively. After failure of the composite, the fracture surfaces were examined by a Scanning Electron Microscope, Hitachi 500S. Finally, the microstructures of annealed specimens were compared to that of actual test specimens.

Results and Discussion

Mechanical Tests

The strain to failure of the composites was approximately 1 percent without exception, implying the brittle nature of composites. The results of isothermal fatigue tests are compared based on the influence of temperature and the effect of different hold times at different temperatures on the composite life. On the other hand, those of spectrum loading tests will be evaluated based on the effects of the number of applied fatigue cycles per block on the composite life.

Isothermal Fatigue—Results for isothermal fatigue tests are shown in Table 1. The composites tested at room temperature show a longer life compared to those tested at elevated temperatures. This resulted from the fact that elevated temperature somewhat changed the properties of composites, especially oxidation and phase transformation. As the test temperature increased from 400°C to 500°C, the number of cycles to failure of the composites reduced dramatically. This is because the higher temperature accelerated the kinetics of oxidation and reaction rate of the Ti-alloy.

Table 1—*Results of Isothermal Fatigue Tests at 400°C and 500°C with Various Hold Time*

	σ_{max} (MPa)	Temperature (°C)	Ht (sec)	N_f
1	350	25	0	70,818
2	350	25	1	34,443
3	350	400	0	22,256
4	350	400	1	29,348
5	350	400	10	51,844
6	350	400	100	12,462+
7	350	500	0	20,344
8	350	500	1	21,103
9	350	500	10	32,346

+ indicates run-out

Various hold periods resulted in different composite response at different temperatures. Hold period at room temperature reduced the composite life by introducing damages in the matrix. On the other hand, the hold period at 400°C and 500°C caused load transfer from the matrix to fibers rather than fatigue of the matrix at elevated temperatures. Especially, the composites at 500°C underwent some degree of time-dependent behavior. The specimen tested under 100 seconds hold time at 400°C did not show any damage progression, and the test stopped after 84 hours.

Spectrum Loading—Results of the spectrum loading tests are listed in Table 2. As the applied cycles per block increased, the composite life increased. This different composite life depending on the number of applied cycles resulted from the change in temperatures between 400°C and 500°C. More frequent change in temperature (n is small) caused more damage in the composite and produced a short composite life. The comparison of Table 2 with Table 1 indicates that the composites subjected to spectrum loading had a shorter life than isothermal fatigue. The presence of thermal cycles between mechanical loadings is responsible for the shorter composite life under spectrum loading.

Table 2—*Results of Spectrum Loading Subjected to Constant Amplitude Loading*

	σ (MPa)	Ht (sec)	n_1/400°C	n_2/500°C	N_f (Cycles)
10	350	1	10	10	8,074
11	350	1	10	10	13,712
12	350	1	100	100	19,800
13	350	1	100	100	13,955
14	350	1	1,000	1,000	17,919
15	350	1	1,000	1,000	23,004

Simple life prediction was made for spectrum loading based on Miner's linear damage rule [*17*];

$$\sum \frac{n_i}{N_i} = 1 \tag{1}$$

where N_i is the failure cycles at a particular stress and temperature and n_i is the number of applied cycles. The predicted life was 24,550 cycles for all spectrum loading. The prediction overestimates the life when n_i = 10 and 100, but is close to the experimental results when n_i = 1,000. Miner's rule does not account for the surface damage due to change in temperatures. In general, Miner's rule does not have the capability to take into account test variables other than stress. As long as the applied load is the same, the Miner's rule provides a good prediction of the composite life. Since the spectrum loading profile has thermal transitions, equation (1) has to be modified to include the contribution from thermal exposure.

Oxidation

Even if there are various forms of oxide, only the surface oxidation can be measured without using sophisticated analytical techniques. The grain boundary oxidation can be compared qualitatively based on the test conditions. There are two

important aspects regarding the oxidation of Timetal 21S. The first aspect is that the rate of oxidation is a function of applied load as well as temperature. The second one is that there are various forms of oxide other than TiO_2.

Without Loading—Based on the number of cycles to failure during the isothermal fatigue testing, the small specimens were annealed at 400°C and at 500°C. Microstructures are shown in Figure 2. These micrographs show extremely thin oxide scale (TiO_2) on the surface and other forms of oxides in subsequent layers. The sub-layer is relatively porous compared to the alloy itself. It is clear that the majority of the surface is not TiO_2. There are two possible explanations for this phenomenon. One would happen because TiO_2 acts as diffusion barrier of oxygen into the alloy resulting in an oxygen deficient compound. Two, further oxygen penetration causes dissolution of oxygen in the alloy. The result of both cases is matrix embrittlement.

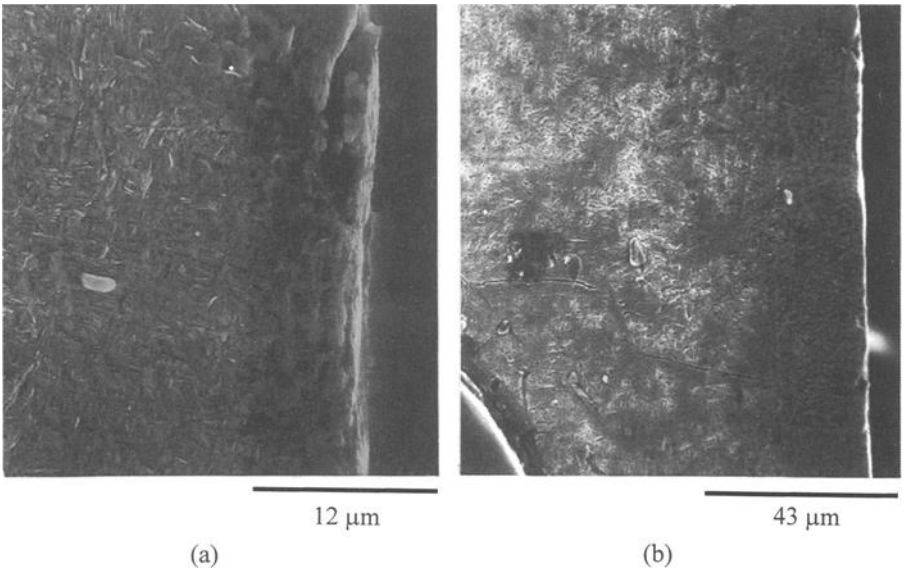

Figure 2—*Microstructures of annealed composite at 400°C a) for 16 hrs b) for 158 hrs*

The measured thicknesses of the oxide layer are given in Table 3. The relative amount of oxygen and titanium as determined by EDS (Energy Dispersive Spectroscopy) is also listed. The higher the annealing temperature, and the longer the annealing duration, the thicker the oxide scales. The oxide thickness for longer annealing duration shows a very slight increase. It may indicate that Timetal 21S has an excellent oxidation resistance. This is the reason that most studies regarding the oxidation behavior of Timetal 21S were done by measuring the weight gain in relation to time, not by oxide

thickness measurement. The relative ratio of oxygen to titanium was 2 to 1, indicating that the oxide was indeed TiO_2.

Table 3—*Amount of Oxygen and Titanium in Annealed Specimens at 400°C and 500°C Based on the Life of Isothermal Fatigue Tests*

	Oxygen (at%)	Titanium (at%)	Oxide Thickness (μm)
400°C/16 hrs	61.64	28.25	1.24
400°C/158 hrs	67.83	22.80	1.32
500°C/12 hrs	55.16	27.44	1.41
500°C/99 hrs	70.00	26.52	1.71

With Load—For the oxide measurement of actual specimens, the areas near the fracture surface were cold-mounted and polished. Figure 3 shows various forms of oxide near surface. The surface oxide is not identifiable in Figure 3a. However, the figure shows three distinctive oxide layers which resulted from the amount of oxygen diffused. Figure 3b is a magnified view of Figure 3a. The layer on the right has quite different microstructures from the left side, which contains the alloy structure. The oxide formation on the surface was not uniform; therefore it was difficult to measure.

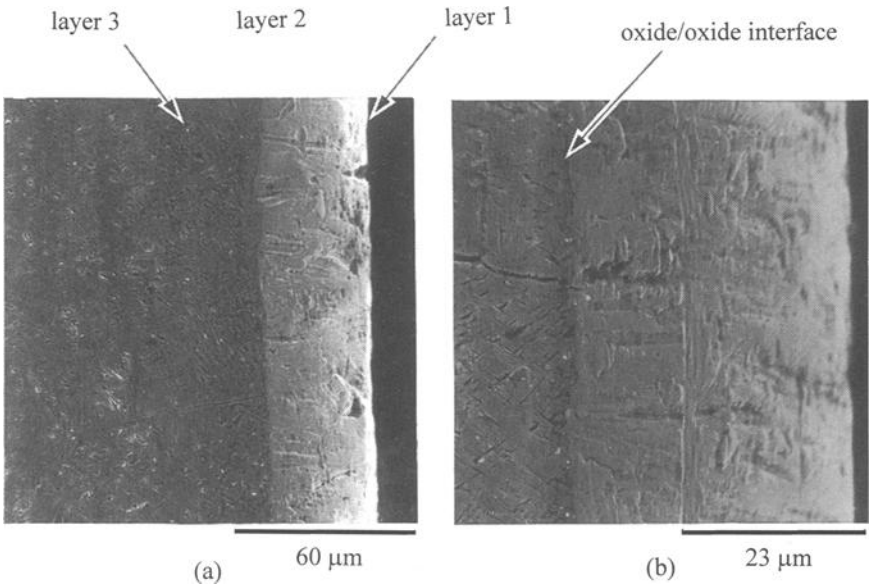

Figure 3—*Microstructures of Actual Test Specimens for 400°C and 1 Second Hold Period: Layer 1-Oxide Scale on the Surface, Layer 2 and 3 - Oxygen Deficient Layers*

Table 4 shows oxide thickness measurements of actual specimens. The trend is the same as the specimens without load. The thickness increase for longer exposure to the environment was rather large compared to the static exposure. This implies that the application of load makes oxygen diffusion easy. Diffussivity and activation energy were determined using the data: $D_0 = 1.088 \times 10^{-13}$ m^2/s and $Q = 25.61$ kJ/mol. The value of D_0 is extremely small compared to the reported value [*13*]. It should be noted that this value is based on the oxide scale on the surface.

Table 4—*Amount of Oxygen and Titanium Near Fractured Surface; Isothermal Fatigue at 400°C and 500°C*

	Oxygen (at%)	Titanium (at%)	Oxide Thickness (μm)
400°C/1 Ht	58.14	26.90	2.05
400°C/10 Ht	67.20	29.55	8.10
500°C/1 Ht	52.59	25.79	2.68
500°C/10 Ht	53.69	28.98	8.72

Fractography

Fractographic analysis provides information on the damage mechanisms and material degradation. The relative damages in matrix will be qualitatively compared based on test conditions. The effect of temperature on the damage accumulation will be identified by the degree of oxidation along grain boundaries. The fracture characteristics of the specimen subjected to isothermal fatigue conditions are first stated and then followed by spectrum loading.

Isothermal Fatigue

Most composites failed within or near the 1″ gauge length. The overall fracture mode was relatively flat. The fracture surface was different from the test conditions, especially depending on test temperature and hold period. Fatigue tests at room temperature showed significant matrix cracking. On the other hand, the tests at elevated temperature resulted in less matrix damage, indicating more load transfer to fibers. As the test temperature increased the matrix damage was less significant.

The specimen without hold period indicates more matrix damage than the one with hold period. As the hold period increased, less matrix damage was developed since the matrix experienced some degree of time dependent behavior at 400°C. When the composite was exposed to 10 seconds hold period at the maximum stress, the matrix started to suffer from oxidation along the grain boundaries.

Fatigue at 400°C—The fracture surface of the specimen with a 1 second hold period shows flat and brittle failure as shown in Figure 4. There are indications of shear failure along the 45° plies. It seems that 90° fibers were separated from the matrix in the early stage of loading. As shown in Figure 4a, the failure mode of the 0° fibers was brittle and the fiber failed rather suddenly. It is possible that the crack initiated from the inside of the composites, more specifically from the off-axis laminates, then grew toward the surface. On the other hand, there is some evidence of surface crack initiations. Figure 4b shows the deformed surface of the composite tested with 1 second hold time. The surface was damaged by several material degradations which are the viscoplastic matrix flow, phase transformation, and oxidation.

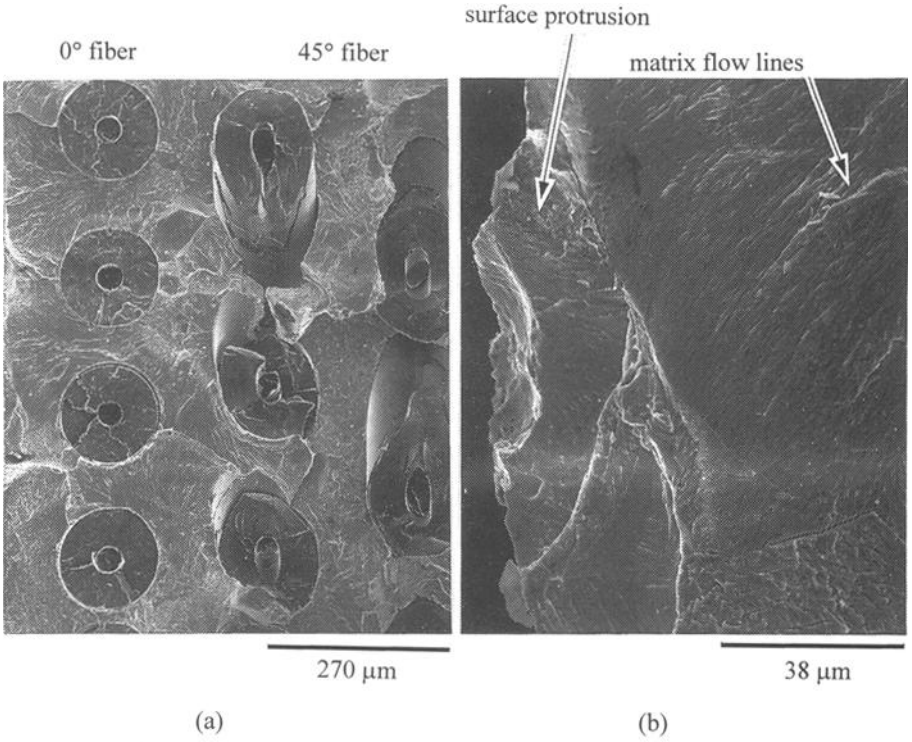

Figure 4—*Fracture Surface of the Specimen Tested at 400°C /1 sec Hold Time*

As the duration at a temperature increases, the environment plays a key role in changing the material properties. The chemical reaction between the fiber and matrix, that produces Ti_xSi_x or TiC [*18*], induced brittle failure around the 0° fibers. Figure 5a shows the crack initiated from the surface. The crack seems to be stopped near 0° fibers, because there is a change in fracture characteristics near 0° fibers: from a fast growing

surface crack (beach mark) to ductile dimple failure. Therefore, 0° fibers act as effective crack arrestors, especially for surface cracks. Figure 5b shows severe viscoplastic matrix flow when the composite was cycled under 10 second hold periods. This implies that the load was transferred from the matrix to fibers during the long hold time. This load transfer made the composite survive longer than the short period of hold time. In the case of the short hold period, there is not enough time for the matrix to transfer the load to fibers. So, the most damage due to applied load was introduced to the matrix.

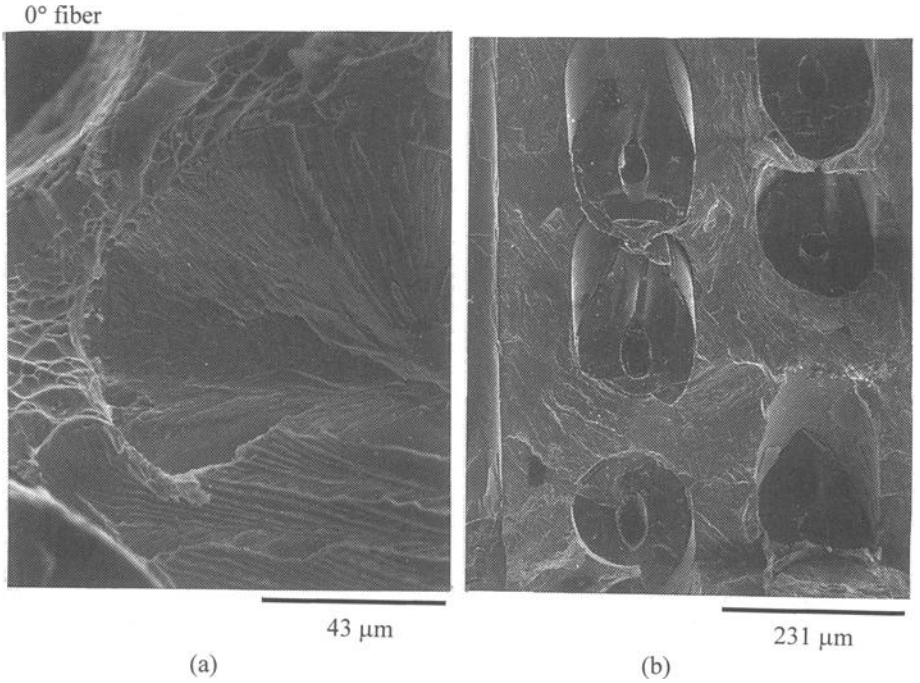

Figure 5—*Fracture Surface Tested at 400°C/10 s Hold Time*

Fatigue at 500°C—The trend in damage with increasing hold period is similar to isothermal fatigue at 400°C. However, the type of damage at 500°C is quite different since the degree of oxidation is greater than at 400°C. This difference is shown in the form of grain boundary oxidation. The extent of matrix damage is less at 500°C than at 400°C. At the same time, since the temperature 500°C is close to the transformation temperature, some α precipitates are observed along the grain boundary.

The overall fracture behavior was dominated by oxidation effects, especially along the grain boundaries and along the ply interfaces. Figure 6 shows the fracture surface of

the specimen with 1 second hold period. Oxide formed along the matrix grain boundary. Also, the grain boundary slipping is shown in the figure.

On the other hand, for the sample subjected to a 10 second hold time the fracture characteristics are somewhat different from the previously mentioned conditions. The overall fracture surface is shown in Figure 7. Intergranular fracture is an appropriate description of damage mode. The grain boundary decohesion is clearly shown in the figure. It is noteworthy that the intergranular failure dominated the matrix near off-axis fibers, but not near 0° fibers. This may occur when the off-axis fibers are debonded and held at the maximum load which opens the interface. The interface opening is an efficient diffusion path for oxygen. In the case of 0° fiber the surface oxide scale prevents significant oxygen penetration. Figure 7b shows a magnified view of Figure 7a. It is intergranular failure and shows some second phase precipitation along the grain boundary. The same mechanism can explain the longer life in the case of longer hold time, as in 400°C isothermal fatigue.

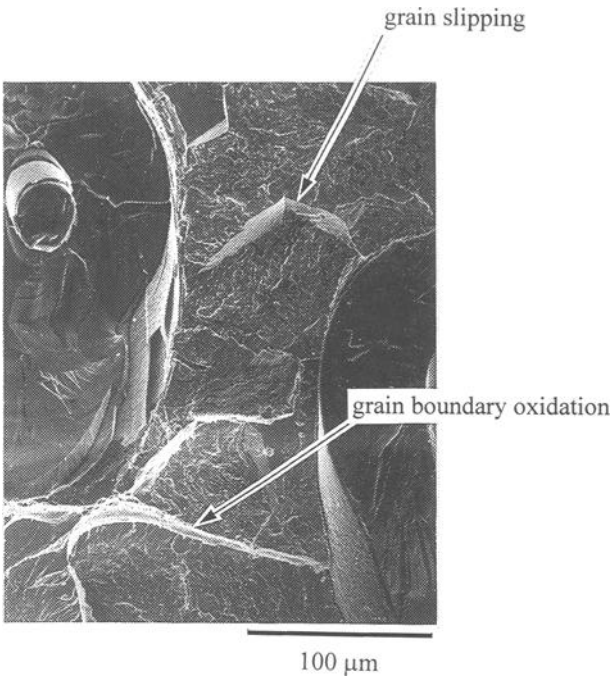

Figure 6—*Fracture Surface Tested at 500°C/1 s Hold Time*

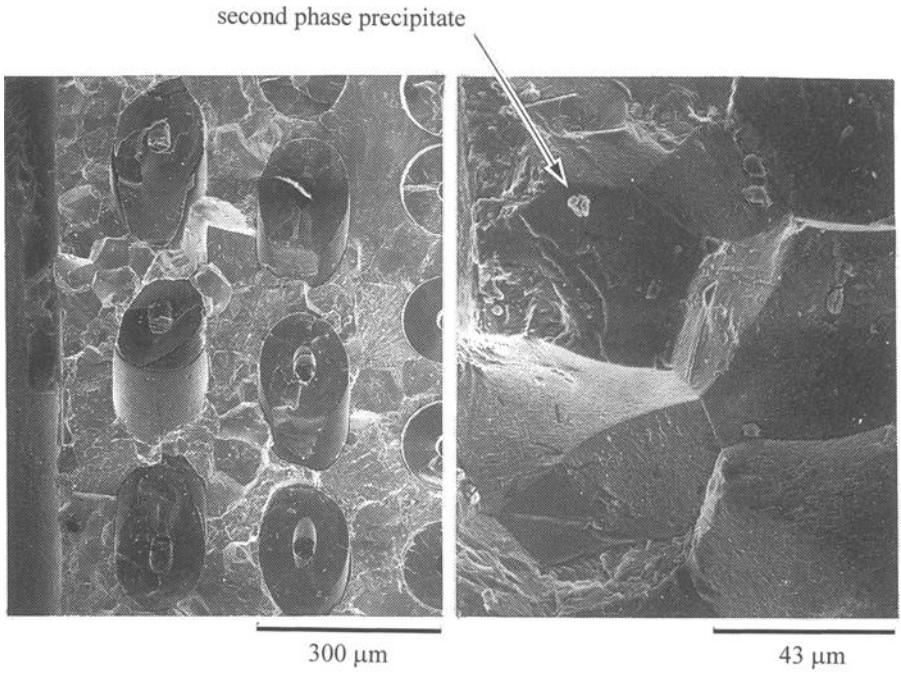

Figure 7—*Fracture Surface Tested at 500°C/ 10 s Hold Time*

Spectrum Loading

The location of failure was random compared to isothermal fatigue tests. The locations were seldom within the gauge length because the change in temperature induced random crack initiation. Each test condition has its own fracture characteristics that can be evaluated by the degree of matrix cracking and surface damage.

When the number of cycles per block is small, more surface cracks were induced by frequent changes in temperature. The change in temperature serves as thermal cycles that are as damaging as the mechanical cycles. The most important result was the observation that these thermal cycles result in surface cracking, which eventually reduces the life of the composites.

It is important to evaluate the role of higher temperature in damage progression because the rate of oxide formation is higher at higher temperature. As shown in isothermal fatigue, the oxidation was more severe at 500°C than at 400°C. The mechanical cycle at 500°C may determine the overall composite life. Another important

aspect of the exposure to higher temperature is time-dependent behavior of matrix material which induces grain boundary oxidation and easy grain boundary separation.

N = 10 Cycles—The fracture surface for spectrum loading with N=10 is shown in Figure 8. The fracture surface is relatively flat and brittle which is a similar failure mode to isothermal failure at 400°C. Figure 8a is the overall fracture surface of the composite. Showing cracks initiated from the surface of the composite. These surface cracks resulted from the change in temperatures. These surface cracks stopped growing near 0° fibers, which act as effective crack arrestors in the outer layer of the composites. This is mainly due to the fact that 0° fibers are the major load carrying constituent. Figure 8b shows the magnified view of the surface near the 0° fibers. The area near surface is extremely brittle indicating long exposure to the high temperature. In addition, the nature of matrix failure implies fast fracture. Cracks propagated to 0° fibers from all directions, especially from the off-axis fibers.

N = 1000 Cycles—Fracture surface of spectrum loading with N = 1000 cycles is shown in Figure 9. Overall, there is less surface crack initiation compared to N = 10 cycles. However, there is more evidence of intergranular failure as well as larger α precipitates, which indicate longer exposure to 500°C. When N is small, this type of damage is limited to 45° and 90° fibers. But in the case of N = 1000, such a feature is also shown in the area between 0° and 45° fibers. Figure 9b shows an expanded view of such an area.

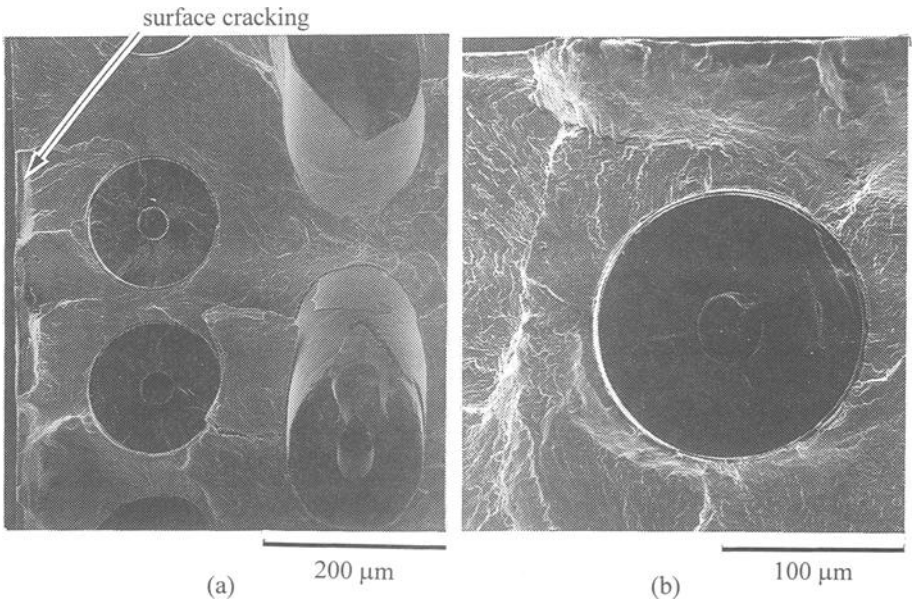

Figure 8—*Fracture Surfaces for Spectrum Loading with N = 10 cycles*

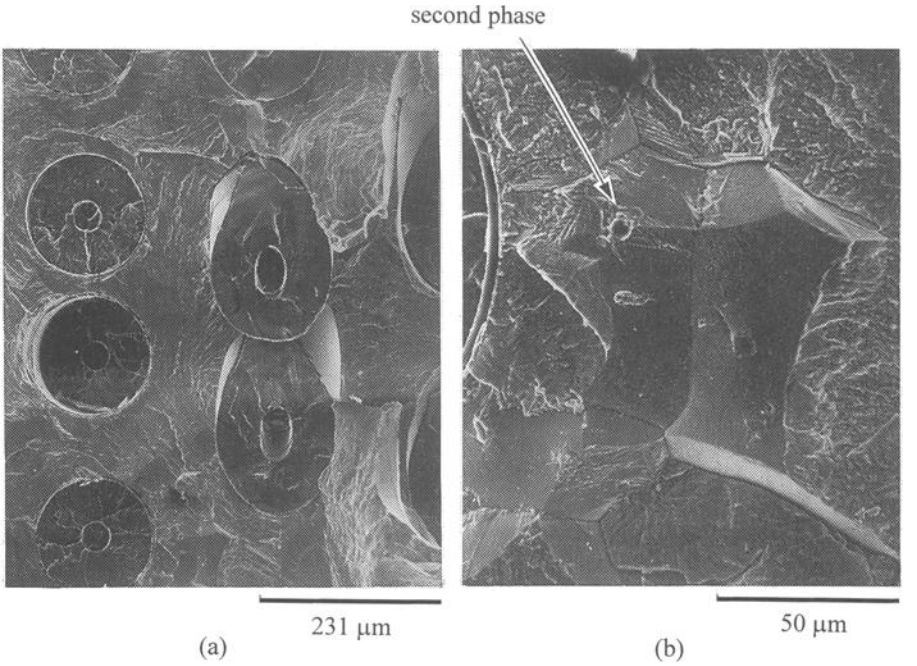

Figure 9—*Fracture Surfaces for Spectrum Loading When N = 1000 cycles*

Conclusion

Test results and fractographic analysis indicated that the matrix, Timetal 21S, has an excellent oxidation resistance. However, composite failure at elevated temperatures was still induced mainly by damage initiated in the oxide layer. It is clear that the oxidation is a function of applied load as well as temperature and exposure duration. The oxide thickness significantly increased under applied load compared to the specimens without load. Therefore, the applied load assists oxygen diffusion through the composite. Due to the kinetics of oxidation, TiO_2 was not the only oxide layer present. The surface oxide scale acted as a diffusion barrier that resulted in non-stoichiometric oxide compounds in the interior.

Isothermal fatigue tests characterized the oxidation behavior of the composite in terms of relative oxide formation on the surface and along the grain boundaries. The oxidation rate at 500°C was much faster than at 400°C. Therefore, the higher oxidation rate led to the reduction of composite life by matrix cracking and matrix embrittlement.

In spectrum loading, the thermal cycles between 400°C and 500°C caused thermal stress because of the difference in the coefficient of thermal expansion between the fiber and matrix and resulted in the reduction of the composite life. The damage produced by the thermal stress was shown in the form of surface cracking. This surface cracking was much more severe when the applied cycles per block was small than when it was large. Therefore, when the number of applied cycles is small, the life is controlled more by surface cracking than oxidation.

It is difficult to differentiate the fracture characteristics of spectrum loading from isothermal fatigue tests since the former is a combination of the latter at different temperatures. The obvious difference between the spectrum loading and isothermal fatigue is the degree of surface damage. The isothermal fatigue tests rarely show surface damage.

Acknowledgment

Funding for this work was provided by Accurate Automation Corp. (Program monitor Mr. Carl Lewis). The authors acknowledge the contribution of Mr. Rick Brown, research equipment specialist in the Mechanical Properties Research Lab at Georgia Tech.

Reference

[1] Johnson, W. S., Lubowinski, S. J., and Highsmith, A. L., "Mechanical Characterization of Unnotched SCS-6/Ti-15-3 Metal Matrix Composites at Room Temperature," Kennedy, J. M., Moeller, H. H., and Johnson, W. S., Eds., *ASTM STP 1080*, American Society for Testing and Materials, Philadelphia, PA, 1990, pp. 193-218.

[2] Johnson, W. S., "Fatigue Testing and Damage Development in Continuous Fiber Reinforced Metal Matrix Composites," in *Metal Matrix Composite: Testing, Analysis, and Failure Modes*, *ASTM STP 1032*, W. S. Johnson, Ed. , American Society for Testing and Materials, Philadelphia, PA, 1989, pp. 194-221.

[3] Saff, C. R., Harmon, D. M., and Johnson, W. S., "Damage Initiation and Growth in Fiber-Reinforced MMCs," *Journal of Metals*, Nov., 1989, pp. 58-63.

[4] Jin, O., Li, Y., Rabeeh, B. M., and Soboyejo, W. O., "An Investigation of the Effects of Interfacial Microstructure on the Fatigue Behavior of a Four-ply [75]4 Continuous Silicon Carbide Fiber-Reinforced Titanium Matrix Composites," *Metallurgical & Materials Trans*action, Vol. 28A, 1997, pp. 2583-2593.

[5] Boyer, R., Welsch, G., and Collings, E. W., Eds., Titanium Alloys, ASM International, 1994, pp. 921-942.

[6] Witting, L. A. and Allen, D. H., "Modeling the Effect of Oxidation on Damage in SiC/Ti-15-3 Metal Matrix Composites," *Journal of Engineering Materials & Tech*nologies, Vol. 116, 7/1994, pp. 421-427.

[7] Neu, R. W. and Sehitoglu, H., "Thermo-mechanical Fatigue, Oxidation, and Creep: Part I. Damage Mechanisms," *Metallurgical & Materials Trans*action, Vol. 20A, 1989, pp. 1755-1767.

[8] Neu, R. W. and Sehitoglu, H, "Thermo-mechanical Fatigue, Oxidation, and Creep: Part II. Life Prediction," *Metallurgical & Materials Trans*action, Vol. 20A, 1989, pp. 1768-1783.

[9] Chaze, A. M. and Coddet, C., "Influence of Alloying Elements on the Dissolution of Oxygen in the Metallic Phase during the Oxidation of Titanium Alloys," *Journal of Material Sci*ence, Vol. 22, 1987, pp. 1206-1214.

[10] Oshida, Y. and Liu, H. W., "Grain Boundary Oxidation and an Analysis of the Effects of Oxidation on Fatigue Crack Nucleation Life," *Low Cycle Fatigue*, Solomon, H. D. , Halford, G. R., Kaisand, L. R., and Lei, B. N., Eds., *ASTM STP 942*, American Society for Testing and Materials, Philadelphia, PA, 1988, pp. 1199-1217.

[11] Liu, H. W. and Oshida, Y., "Grain Boundary Oxidation and Fatigue Crack Growth at Elevated Temperature," *Theoretical & Applied Fracture Mech*anics, Vol. 6, 1986, pp. 85-94.

[12] Kofstad, P., Anderson, P. B., and Krudtaa, O. J., "Oxidation of Titanium in the Temperature Range 800-1200°C, " *Journal of Less-Common Metal*, Vol. 3, 1961, pp. 89-97.

[13] Allen, D. H., Foulk, J. W., Helms, K. L., and Lagoudas, D. C.," A Model for Predicting the Effect of Environmental Degradation on Damage Evolution of Metal-Matrix Composites," *Applications of Continuum Damage Mechanics to Fatigue and Fracture, ASTM STP 1315*, D. L. McDowell, Ed., American Society for Testing and Materials, Philadelphia, PA, 1997, pp. 29-45.

[14] Antolovich, S. D., Liu, S. and Baur, R., "Low Cycle Fatigue Behavior of Rene 80 at Elevated Temperature," *Metallurgical & Materials Trans*action, Vol. 12A, 1981, pp. 473-481.

[15] Mirdamadi, M. and Johnson, W. S., "Modeling and Life Prediction Methodology for Titanium Matrix Composites Subjected to Mission Profile," *Life Prediction Methodology for Titanium Matrix Composites, ASTM STP 1253*, W. S. Johnson, J. M. Larson, and B. N. Cox, eds., American Society of Testing and Materials, Philadelphia, PA, 1996, pp. 573-594.

[16] Lerch, B. A., Hull, D. R., Leonhardt, T. A., "Microstructure of a SiC/Ti-15-3 Composite," *Composites*, Vol. 21, No. 3, (3), 1993, pp. 216-224.

[17] Miner, M. A., "Cumulative Damage in Fatigue," *Journal of Applied Mechanics*, Vol. 12, 1945, pp. 159-164.

[18] Lerch, B. A., Gabb, T. P. and Mackay, R. A., "Heat Treatment Study of the SiC/Ti-15-3 Composite System," NASA TP-2970, NASA Lewis Research Center, Cleveland, OH 1990.

Experimental Techniques

Luc Rémy,[1] Alain Koster,[1] Eric Chataigner,[2] and Anny Bickard[3]

Thermal-mechanical Fatigue and the Modelling of Materials Behaviour Under Thermal Transients

Reference: Rémy, L., Koster, A., Chataigner, E., and Bickard, A., **"Thermal-mechanical Fatigue and the Modelling of Materials Behaviour Under Thermal Transients,"** *Thermo-mechanical Fatigue Behavior of Materials: Third Volume, ASTM STP 1371,* H. Sehitoglu and H. J. Maier, Eds., American Society for Testing and Materials, West Conshohocken, PA, 2000.

Abstract: Thermal-mechanical fatigue is addressed using the following methodology: volume element tests are used to check constitutive models as well as to investigate synergy effects and damage models. Structure tests as in thermal shock are used to validate models. This methodology is applied to two gas turbine materials: a wrought polycrystalline alloy, Superwaspaloy, for moderate temperature use, and aluminized single crystal AM1 superalloy for blades. The capabilities of viscoplastic constitutive models with internal variables are illustrated. A damage model is shown which describes the synergy between oxidation, creep and fatigue. Detrimental effects of aluminide coating for specific thermal mechanical loading paths are tentatively rationalized.

Keywords: thermal fatigue, thermal-mechanical fatigue, nickel base superalloys, constitutive equations life prediction

Introduction

The life assessment of components experiencing thermal transients is a major problem in high temperature machinery, in particular in gas turbines used in aircraft or in power plants. The usual procedure is to perform isothermal tests such as creep, low cycle fatigue or creep-fatigue tests to get the following models: firstly the stress-strain response under various loading conditions which allows identification of more or less complicated constitutive models; secondly rupture laws (i.e. creep rupture, S-N curves, Manson-

[1]Centre des Matériaux, Ecole des Mines de Paris, UMR-CNRS 7633, BP.87, 91003 Evry Cedex, France.
[2]Formerly with Centre des Matériaux, now with CREAS, 57360 Anneville, France.
[3]Formerly with Centre des Matériaux, now with SNECMA YKO, 77550 Moissy – Cramayel, France.

Coffin curves, etc.) which are used to identify damage models. Thermal and mechanical loads on the components are the input of a temperature and stress analysis, using finite element methods. The computed stress field is largely dependent upon the temperature interpolation or extrapolation of the constitutive equations. A damage analysis based on damage models previously fitted to the rupture database is generally made in a post-processor, which computes the life of the component.

The life prediction which is so achieved is however strongly dependent on the temperature dependence interpolation of constitutive and damage models and extrapolation to service conditions.

The simulation of thermal-mechanical loading of components in the laboratory is therefore of primary importance for life assessment. Two different tests are used: thermal-shock or thermal fatigue tests on simple structures [*1-3*] and thermal-mechanical fatigue (TMF) tests on volume elements [*4-6*].

Thermal-shock facilities were used for a long time and encompass burner rigs, fluidized beds, induction heating or lamp furnace heating and air cooling. Thermal-shock testing can simulate quite closely the behaviour of materials under service like thermal transients (for static parts); in particular fairly high temperature rates can be achieved and there is a strong temperature gradient. But at most temperature can be measured at some locations on structure surface. The temperature field and the stress and strain field have to be computed using a complete thermal and mechanical analysis as for real components. Thermal shock tests are useful to validate models predictions; the life predicted results from the convolution of constitutive and damage equations.

The TMF test involves simultaneous temperature and strain cycling, with no stress gradient across the specimen section. This is therefore a volume element provided that the temperature gradient across specimen section and along the gage length is kept to a minimum. The TMF test is becoming more popular and more practical with the development of microcomputer capabilities over the last 15 years. But it is often difficult to simulate real service conditions: the temperature rate is limited due to the constraint of no stress/temperature gradient in the gage length, the hold time duration is often shorter than steady operation periods, etc.

TMF is therefore useful to investigate synergy effects, which were not foreseen using isothermal creep or fatigue tests. TMF can be used to check independently the predictions of constitutive models and of damage models under thermal transients [*6*].

This methodology will be illustrated by two examples of gas turbine materials: Superwaspaloy, a wrought polycrystal nickel base superalloy, and AM1, a single crystal superalloy which is used for aluminide coated blades.

Constitutive Modelling of Superwaspaloy

Constitutive equations used for superalloys are often viscoplastic to account for creep. Equations with internal variables were developed among others in the group of Chaboche, to describe nonlinear kinematic hardening [*7*]. This is required by the Bauschinger effect which is quite important to describe stress redistribution in cyclically loaded superalloy components.The viscoplastic strain rate in uniaxial form is written as modified Norton' law:

$$\dot{\varepsilon}_v = \left\langle \frac{|\sigma - X_v| - R_v}{K} \right\rangle^n \text{sign}(\sigma - X_v) \qquad (1)$$

where K and n are constant at a given temperature, < > are Mc Caulay brackets (<U> = U if U>0 else 0), R_v is the radius of the plastic domain and X_v an internal variable that describes the position of the centre of the elastic domain in stress space. Both R_v and X_v are given by differential rate equations.

In the case of wrought Superwaspaloy, the following differential rate equations were used for kinematic hardening:

$$X_v = X_{v1} + X_{v2} \qquad (2)$$

with $X_{v1} = C_1\ \alpha_1$ and $\dot{\alpha}_1 = \dot{\varepsilon}_v$ (3)

and $X_{v2} = C_2\ \alpha_2$ (4)

where $\dot{\alpha}_2 = \dot{\varepsilon}_v - D_2\alpha_2\dot{v}$ with $\dot{v} = |\dot{\varepsilon}_v|$ (5)

And for isotropic hardening

$$R_v = R_{vo} + Q(1 - e^{Bv}) \qquad (6)$$

where $\dot{\varepsilon}_v$ is viscoplastic strain rate and v is the accumulated viscoplastic strain. C_1, C_2, D_2, R_{vo}, Q, B are constants at a given temperature. While a single kinematic hardening variable is often used in the form of Eq. (5) in the usual Chaboche equations, two kinematic hardening variables were necessary in the present alloy for the temperature and stress range investigated.

The material parameters were identified from LCF tests with various strain rates at different temperatures, using a dedicated software.

The prediction of this constitutive model is compared with a TMF stress-strain loop for a thermal cycle between 100 and 750°C using forced cooling (the cycle period is 260s). This constitutive model describes fairly well the shape of the TMF loops (Fig. 1). This constitutive model which has been tested against TMF stress-strain loops can be used with an improved degree of confidence in a finite element analysis of a component or of a simple thermal shock structure. Figure 2 displays the geometry of wedge specimens, standard and large, which are currently used on a thermal shock rig in our laboratory [*8*] using a lamp furnace and a removable cooling nozzle. A thermal shock was applied from room temperature to 750°C. During the thermal transient the temperature of the thin edge of the structure reachs the maximum (minimum resp.) on heating (cooling resp.) within 20s, for a total period of 90s.

A 2D heat transfer analysis. was made for two different specimen geometries, depicted in Fig. 2 using ZeBuLoN [*9*], the finite element code developed at Ecole des Mines in combination with SiDoLo [*10*], a commercial software for identifying parameters. The results of the heat transfer analysis [*8*] were used as input for the mechanical stress-strain analysis, using the identified constitutive equations. The computation is illustrated for a mechanically stabilised cycle cycle (20^{th}) for the two wedge geometries: Figure 3 shows the stress-temperature loops as well as the stress-mechanical strain loops in the area within 0.2 mm of the thin edge. The stresses are higher for the large geometry than for the standard geometry, and the same conclusions hold for the mechanical strain and

inelastic strain as well. The loops exhibit a mean tensile stress and mean compressive strain, which is rather sensitive to the amount of viscoplasticity and kinematic hardening.

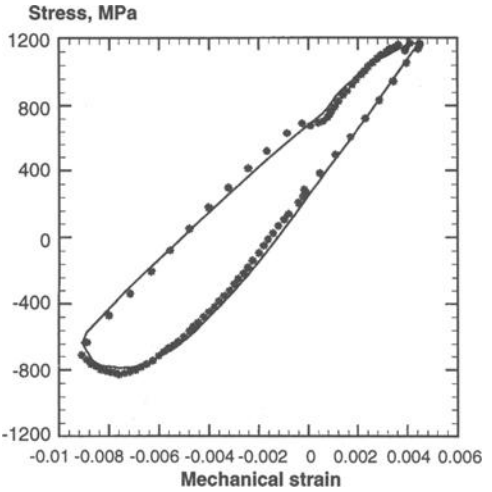

Figure 1 - *Comparison between constitutive model solid line and experiment (symbols) for hysteresis stress-strain loops of Superwaspaloy under thermal mechanical fatigue from 100 to 750°C (test frequency 5 10^{-3} Hz).*

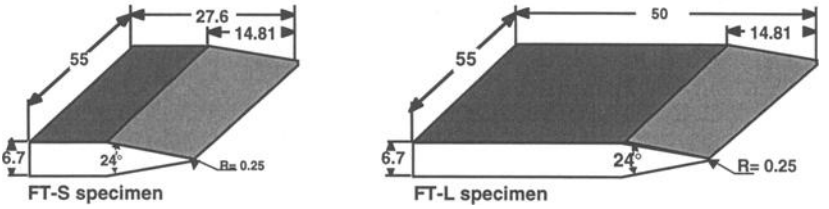

Figure 2 – *Geometry of thermal wedge specimens used for Superwaspaloy.*

Damage Modelling in Bare Superwaspaloy

Linear accumulation of creep and fatigue damage is widely used in the engineering practice to account for creep fatigue or thermal-mechanical fatigue. However in engineering alloys like superalloys, this is often inappropriate [*10*].

Continuum damage mechanics is an elegant way of describing nonlinear accumulation of creep and fatigue damage [*7, 11, 13*]. This theory uses a simplifying concept of an effective stress $\tilde{\sigma}$ which would produce the same strain in an undamaged volume element as the applied stress σ in the damaged element:

$$\tilde{\sigma} = \sigma/(1 - D) \qquad (7)$$

where damage D is such that $0 \leq D \leq 1$. Most authors like Lemaitre and Chaboche, Leckie and Hayhurst [*7, 12*] assume a linear summation of creep (dD_{cr}) and fatigue (dD_f) damage increments :

$$dD = dD_f(\Delta\sigma/2, \overline{\sigma}\ D) + dD_{cr}(\overline{\sigma}, D) \qquad (8)$$

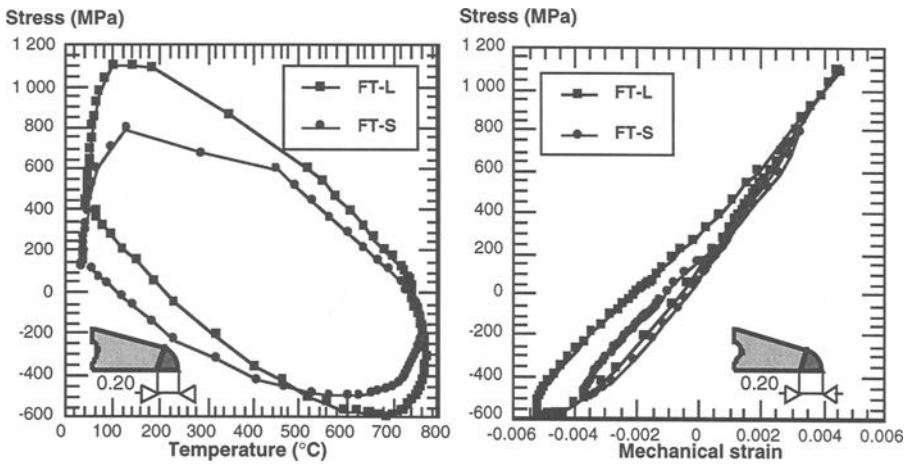

Figure 3 – *Calculated stress-temperature loops (left) and stress-mechanical strain loops (right) for the first element at the edge of the two geometries FT-S and FT-L depicted in Fig 2.*

Expressions for each increment are detailed in several references and $\Delta\sigma$, $\tilde{\sigma}D$ refer to the stress range, mean stress and damage respectively. Multiaxial loading is taken into account in different ways by authors. Damage is basically undefined and considered to be spread over the volume of a stressed element. Fatigue and creep damage obey two different rate equations but both damage forms are considered as additive with no distinction between them.

In our group, environmental attack of the surface of bare superalloys by oxidation was recognized to trigger surface crack initiation at high temperature, as shown by metallographic observations and by the reduction of life to crack initiation with respect to that in vacuum [*14, 15*]. The engineering life to crack initiation in cast superalloys was assumed to result from oxidation assisted microcrack growth [*16, 17*]. The models proposed can be written in the framework of continuum damage mechanics but here the fatigue damage is a, the length of microcracks. The oldest model [*14*] assumed a summation of crack growth rate increments :

$$da/dN = (da/dN)_f + (da/dN)_{ox} \qquad (9)$$

The fatigue increment was computed through Tomkins' model [*18*] but the oxidation contribution is a time-dependent term which was deduced from metallographic measurements of localised interdendritic oxidation [*14, 19*]. The major difference with Eq. 8 is that metallographic data are used in the model and not only mechanical tests.

The simple model of Eq. 9 can describe TMF or TF but it cannot account for oxidation-embrittlement. Such a phenomenon was evidenced by crack growth experiments on compact tension specimens which were precracked at a temperature, then oxidized at high temperature (without applied load) and finally cracked at the test temperature. An anomalous fatigue crack growth rate behaviour was observed in various superalloys and was attributed to a local reduction in fracture toughness induced by oxidation. It is therefore necessary to use a coupled equation to describe fatigue-oxidation interactions [*17*].

We used such a coupled model to describe oxidation-creep-fatigue interactions in wrought Superwaspaloy. Damage equation is written as:

$$da/dN = f(a, D_{cr}, \Delta\sigma/2, \sigma_c) \qquad (10)$$

where σ_c the critical stress to break a microstructure element of size λ is given by:

$$\sigma_c = g(l_{ox}, V) \qquad (11)$$

D_{cr}, is creep damage, l_{ox} is the depth of intergranular oxide, V is the volume parameter which describes the size effect, to account for the differences in element size in a finite element structure analysis and laboratory specimens used to identify the model parameters.

Damage is identified as the growth of a major microcrack which is described as failure of microstructure elements of size λ, using a local stress approach.

For pure fatigue, this description leads to:

$$da/dN = \lambda / N(\lambda) \qquad (12)$$

where the number of cycles to break a microstructure element, $N(\lambda)$ obeys Basquin's equation:

$$\Delta\tilde{\sigma}.N(\lambda)^b = 2\sigma_c \qquad (13)$$

$\Delta\tilde{\sigma}$ is an effective stress range, which is a function of crack length and specimen geometry (i.e. $\Delta\tilde{\sigma} = \Delta\tilde{\sigma}(a/w)$ in a compact form). σ_c is defined at an equivalent temperature under thermal transients.

Interaction with creep damage is described in the conventional Rabotnov-Kachanov way:

$$\Delta\tilde{\sigma} = \Delta\tilde{\sigma}/(1 - D_{cr}) \qquad (14)$$

$$\text{with } dD_{cr} = (1 - D_{cr})^{-k} \left(\frac{\sigma}{A}\right)^r dt \qquad (15)$$

where k, r, and A are three constants at a given temperature.

Parameters in these equations are fitted using LCF data at high frequency conducted to rupture (or interrupted before failure), creep data and LCF tests under vacuum.

Interaction with oxidation is described using experience accumulated in cast superalloys as well as in PM superalloys. There is a reduction of the critical stress σ_c from a constant value $\sigma_{c,virgin}$ in the material unaffected by oxidation to $\sigma_{c,embrittled}$ in the area embrittled by localised oxidation and a simple rule is used:

$$\sigma_c = \sigma_{c,virgin} (1 - Pl_{ox}/\lambda) + \sigma_{c,embrittled} (Pl_{ox}/\lambda) \quad (16)$$

where P is a constant. The depth of intergranular oxide l_{ox} is given by the rate equation, as shown previously for interdendritic oxide in cast alloys [*15-17*]:

$$d\left(l_{ox}^4\right) = \alpha^4(T)\, dt \quad (17)$$

where $\alpha(T) = \alpha_o \cdot \exp(-Q/RT) \cdot f(\Delta\varepsilon_p)$ (18)

where α_o is a constant, Q is an activation energy, R = 8.315J, T is temperature (in K) and f is a function which describes the interaction between oxidation kinetics and straining. α_o and Q are deduced from metallography of specimens sections which are oxidized in a furnace under no load, and f is deduced from the observation of strained specimens (if necessary, low frequency isothermal LCF tests can be used to check parameters). The application to thermal transients requires the integration of Eq. 17 over the whole thermal-mechanical cycle.

This model accounts for LCF lifetime under a large variety of testing conditions [*20*]. It has been observed to give a very good prediction of TMF life for a temperature cycle between 100 and 750°C.

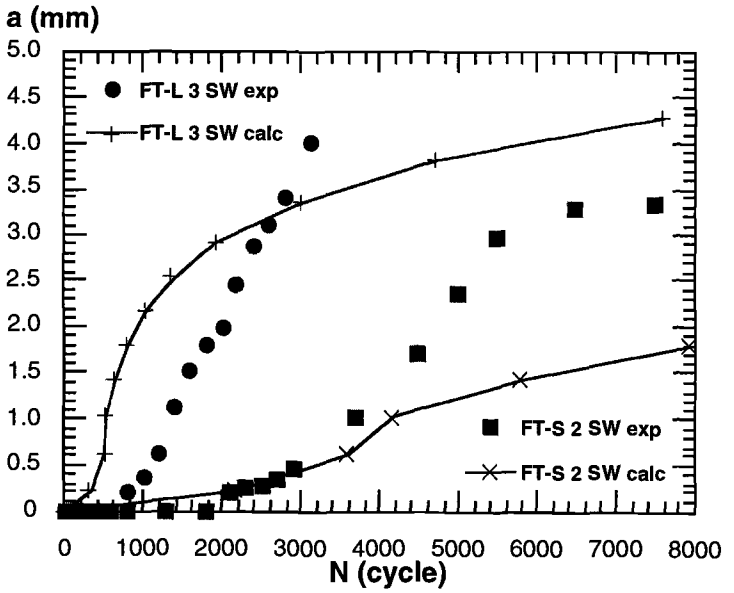

Figure 4 – *Depth of the major crack as a function of cycle number for the two wedge geometries in Superwaspaloy submitted to a thermal shock between 30 and 750°C: comparison between experiment and model predictions.*

Thermal shock experiments which have been discussed earlier in the paper, were used to check the predictions of this damage model in a component-like situation. Figure 4 depicts the comparison between the computed and experimental growth curve of the major crack for the two different geometries. A pretty good description of early crack growth is achieved up to 3 mm and 1 mm for the standard and large geometry respectively. One has to remember that this estimation is made in a post-processor of a stress analysis of an uncracked structure and it is therefore not expected to describe a long crack situation since stress redistribution due to crack growth is not taken into account.

Damage in Aluminized Single Crystals

The intrinsic resistance of superalloys to aggressive environment (involving oxidation as well as corrosion effects) is insufficient especially with advanced high strength directionally solidified polycrystals and single crystals. Overlay coating deposited by plasma technique and aluminide coatings (chemical vapor deposition) are widely used owing to their good oxidation resistance. They prevent loss of section, which can be especially important for thin walled component operating for long service conditions. A common practice is to use a coating a few tens μm in thickness and to design a component ignoring the presence of coating. This simplified procedure can be conservative or nonconservative according to the substrate-coating system and to the thermal-mechanical loading path. A NiAl coating was previously shown to give a slight increase in the TMF life of cast IN100 for a cycle which simulates the loading of a blade leading edge [*21*].

Intermetallic compound coatings, however, have a very low ductility near ambient temperature [*22*]. Brittle cracking is a primary risk for premature fatigue failure of coated components. This risk is often estimated using a measurement of tensile ductility [*23*], usually the strain to a macroscopic crack, as a function of temperature.

The ductile to brittle transition temperature can exceed 700°C for such NiAl type coating depending upon the aluminium content as well as upon alloying elements which diffuse from the substrate [*23*]. Figure 5 shows the ductility of C1A coating on AM1 single crystals for a [001] orientation: the tensile ductility varies from 0.65 to 1% when temperature increases from 20 to 750°C. Brittle cracking under tensile loading gives rise to large transgranular cracks typical of cleavage in aluminide coating at the surface of coated specimens.

TMF is in principle especially convenient to evidence synergy effects which can be expected with such a transition in ductility of the coating with temperature. In the case of [001] C1A coated single crystals of AM1 superalloys, TMF tests were carried out in the range 600-1100°C, using counter-clockwise diamond type cycle, as depicted in Fig. 6. No significant difference in the number of cycles to 1 mm crack depth was observed between bare and aluminized specimens even for the larger strain range (2%) where the peak tensile strain at 700°C slightly exceeds the ductility, on cooling (Fig. 7).

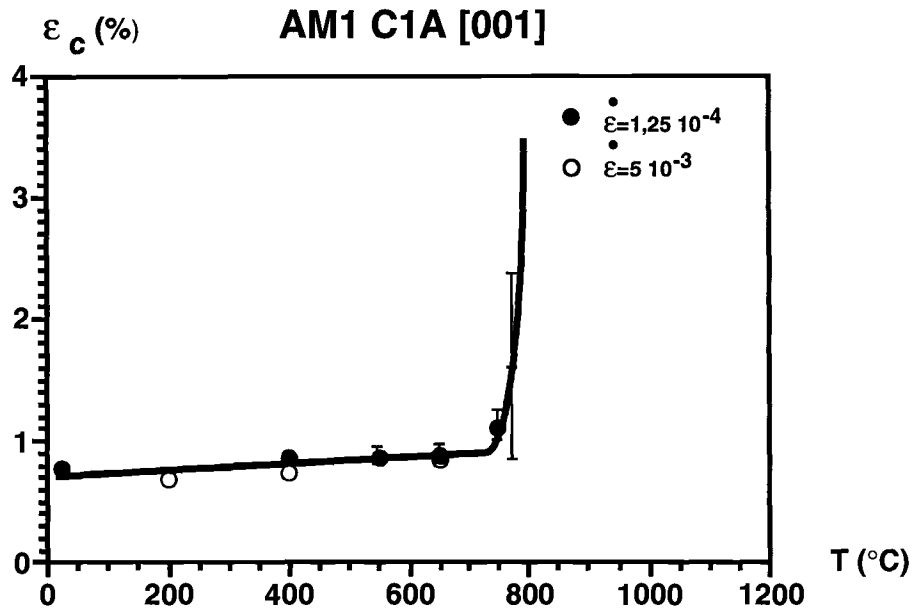

Figure 5 – *Variation of the ductility of C1A coating applied on single crystal AM1 substrate as a function of temperature ([001] orientation).*

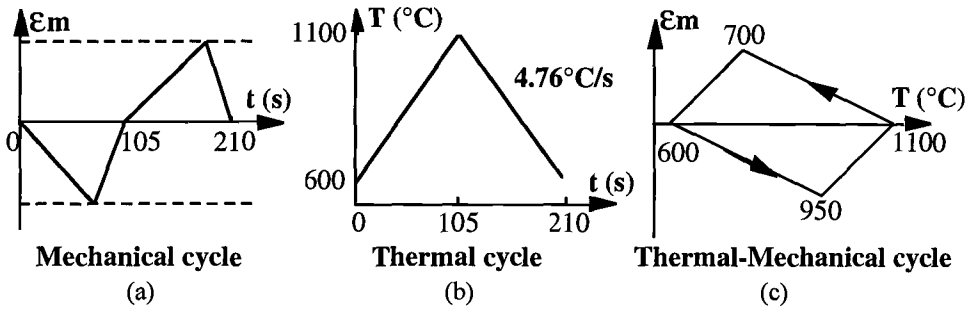

Figure 6 – *A simplified thermal-mechanical fatigue cycle for AM1 single crystals a) temperature versus time, b) mechanical strain versus time and c) mechanical strain versus temperature diagrams.*

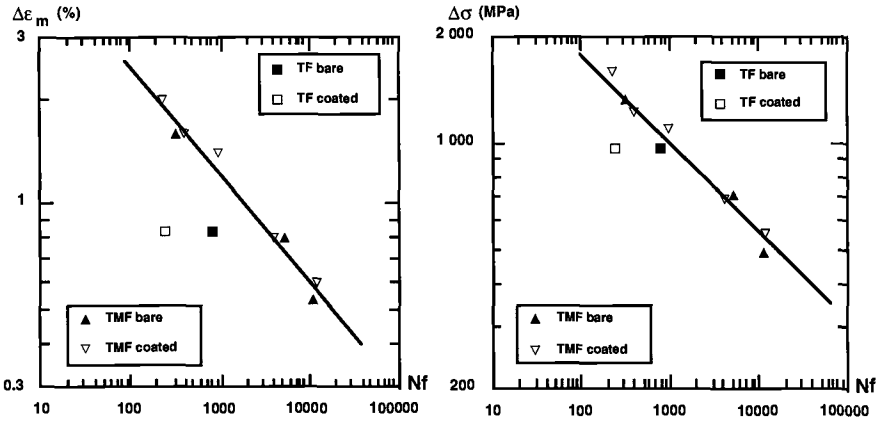

Figure 7 – *Variation of lifetime of AM1 superalloy single crystals as a function of mechanical strain range (left) and stress range (right) for bare and coated conditions, using the TMF cycle of Fig. 6. Points labelled TF refer to thermal fatigue of standard wedge specimens cycled between 30 and 1100°C.*

No brittle crack is actually observed on the surface of the highly strained TMF specimens using this diamond type cycle. Crack initiation in this material occurs mostly at subsurface casting pores whatever the condition, bare or aluminized [*19*].

This tensile strain ductility criterion does not seem to be very efficient to account for brittle fracture in the coating. In order to make a clearer demonstration, a TMF cycle was used with a purely compressive strain cycle in the same temperature range 600-1100°C using the same period, depicted in Fig. 8. When the mechanical strain varies from zero to a minimum value of – 1%, brittle cracking does not occur while long brittle cracks are observed for a minimum strain of – 1.2%.

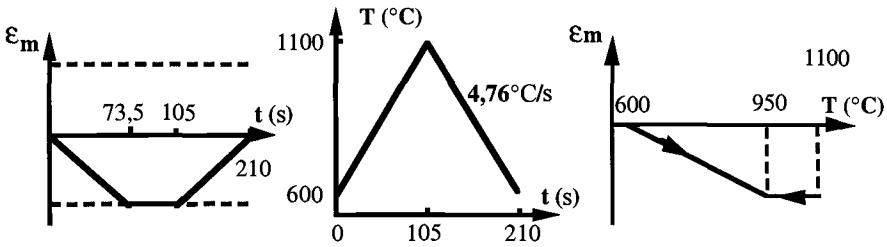

Figure 8 – *Compressive strain thermal-mechanical fatigue cycle used for C1A coated single-crystal AM1 superalloy: temperature versus time, mechanical strain versus time and mechanical strain versus temperature diagrams.*

Cleavage seems to be the dominant cracking mechanism in the aluminide. In monolithic brittle materials, cleavage is often described using a critical principal stress criterion [*24*]. The assessment of a critical stress criterion, requires first to estimate the stress state in the coating for the different thermal-mechanical loading paths.

The description of the layers, the external layer of aluminide which is enriched in alloying elements, together with the diffusion layer between aluminide and substrate is rather difficult and the actual constitutive behaviour cannot be obtained from direct mechanical tests. A rigorous treatment of the mechanical behaviour of the various layers seems to be rather unrealistic in view of all the uncertainties in geometry, chemical composition and local constitutive behaviour. The real situation was therefore approximated by a simple two-bar analysis. Two parallel elements were considered: one with the composition of the substrate, the other one supposed to be pure β-NiAl.

At every instant of the cycle, we assume

$$\dot{\varepsilon}_{substrate} = \dot{\varepsilon}_{coating} \tag{19}$$

The strain rate in the substrate is deduced from experimental measurements which are monitored throughout the tests (but this can be the result of the constitutive model identified for single crystal superalloy, in a component or a structure).

The C1A coating was assumed to have a viscoplastic behaviour at high temperature, which can be described by Norton's law.

Coefficients were taken from the data of Whittenberger on bulk NiAl of similar grain size [*25*]. The Young's modulus was measured at room temperature using a nano indenter ($E \simeq 155$GPa, measurements carried out at INSA, Lyon) and the temperature dependence was taken from literature [*26*]. The coefficient of thermal expansion was also deduced from literature data [*26*].

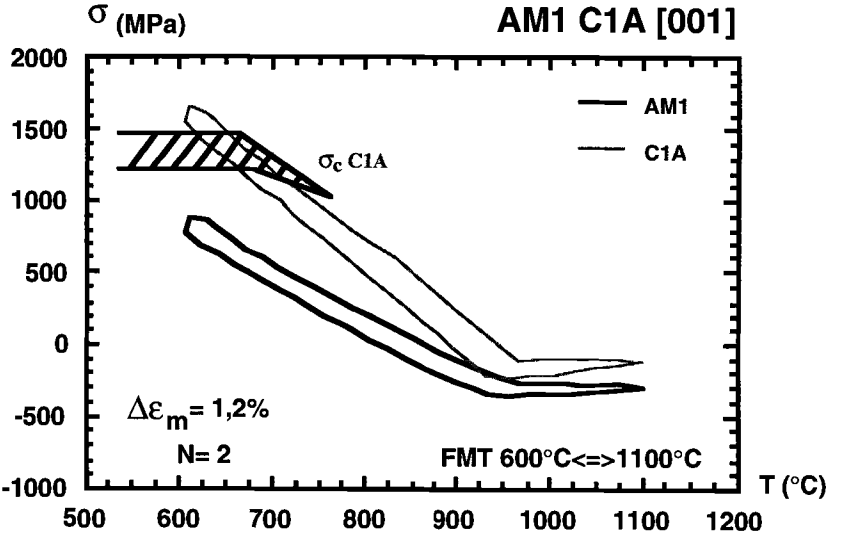

Figure 9 – *Stress versus temperature hysteresis loop for AM1 (experimental) and C1A (computed) using the thermal mechanical fatigue cycle shown in Fig. 8 for a minimum strain – 1.2%. Note the position of critical stress computed for C1A coating.*

The stress-temperature loops for C1A and the substrate AM1 are shown in Fig. 9 when a TMF cycle with a compressive strain is used. In the same diagrams, the critical stress corresponding to the tensile ductility curve of the coating is shown too. TMF gives

rise to a large relaxation of stresses at high temperature in the coating but at temperatures lower than about 800°C, a tensile stress is developing (even though mechanical strain is negative). A cycle with a minimum compressive strain of – 1% gives a tensile stress which does not exceed the tensile stress for cleavage in the coating. On the opposite for a minimum strain of – 1.2%, the peak tensile stress at 600°C exceeds the tensile stress for cleavage. These computations are consistent with the observation of brittle cleavage cracks for a peak strain of – 1.2% and of no crack for a peak strain of – 1%.

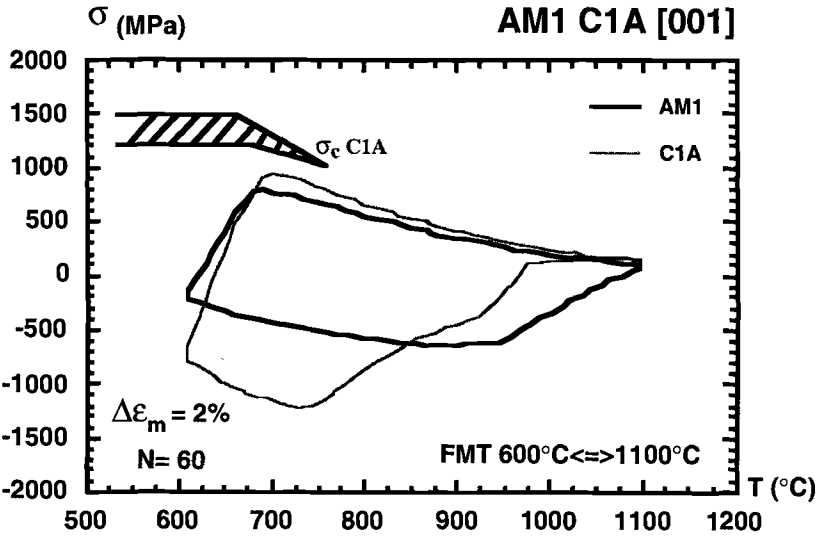

Figure 10 – *Stress versus temperature hysteresis loop for AM1 (experimental) and C1A (computed) using the standard diamond type thermal mechanical fatigue cycle shown in Fig. 5.*

The same computations were made for a diamond cycle between 600 and 1100°C (see Fig. 10). As shown in Fig. 10 this cycle shape gives rise to smaller tensile stresses on cooling and the tensile stress for cleavage is not reached even for a strain range as large as 2%. The comparison of the computed stress - temperature hysteresis loops for all the TMF cycles investigated and the tensile stress for cleavage is definitely consistent with the observations on the occurrence of brittle cracks. Therefore a critical tensile stress can be used to rationalize the onset of brittle cracking in aluminide coatings.

This criterion describes the worst situation where a brittle crack can form in a coating in a single cycle. However, for conditions where the stress in the coating is high but below the threshold for brittle cracking, a crack may propagate under fatigue loading and lead to a lifetime shorter than for the bare material.

This really occurs when a severe thermal shock is used between 30 and 1100°C on the AM1 single crystal coated by C1A. The crack initiation data are shown with the TMF diamond tests between 600 and 1100°C in Fig. 7. A dominant crack nucleates early on the coated structure, then stays almost still and then starts to grow again until it growth rate decreases (Fig.11), as usual for pure thermal shock situation [*17*], while the major crack initiates much later in the bare condition but then crack growth is regular. The

fracture surface of interrupted tests show clearly that cracking starts in the coating and then grows from the surface crack in the coating into the substrate.

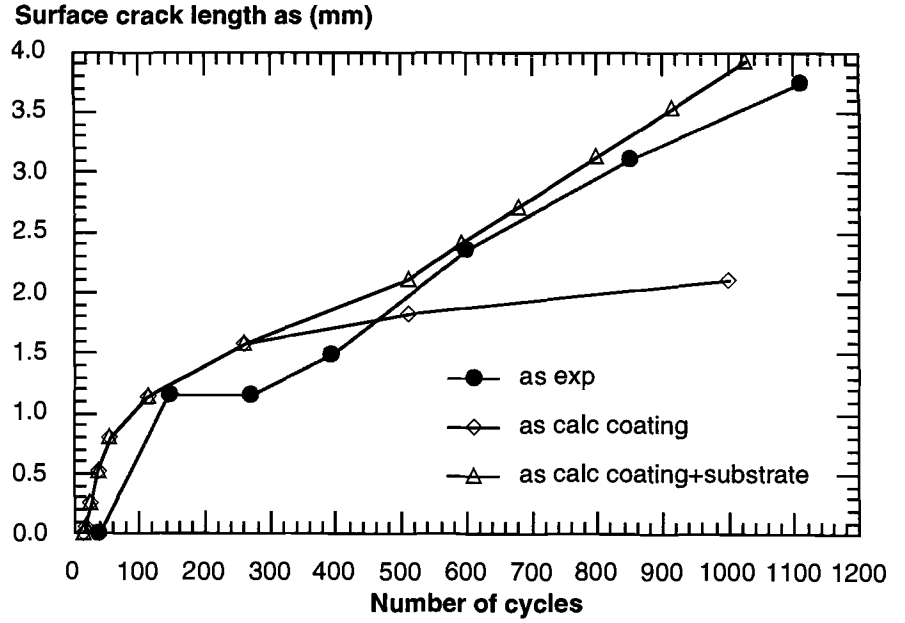

Figure 11 – *Comparison between model prediction and experimental crack depth (as measured on the surface) versus number of cycles between 30 and 1100°C on coated AM1. The early crack growth is governed by surface cracking in the coating and then crack growth is controlled by the substrate.*

Specimens with an original design used to investigate the tensile ductility of the coating were tested under low-cycle fatigue under strain-controlled conditions, in the brittle temperature range [*27*]. Using a two bar approximation as previously, S-N curves for the coating were obtained from the observations of specimens surface, interrupting the fatigue test at regular intervals. A Basquin type fatigue damage equation was deduced from these metallography observations [*27*].

Fatigue damage can thus be treated as a twofold damage mechanism: microcrack growth in coating using a fatigue equation deduced from these tests at low temperature, and microcrack growth in the substrate and from the surface, when the coating at the surface has a through-thickness crack. The oxidation-creep-fatigue model described earlier is used to describe damage in the substrate.

The predictions of such a model are shown in Fig. 11, where the early surface crack growth behaviour in the structure is dominated by fatigue cracking of the coating and then cracking is governed by the growth in the substrate.

Conclusions

Thermal-mechanical fatigue (TMF) is useful to check independently the predictions of constitutive models and damage models. But it can also be used to investigate synergy effects. Thermal shock or thermal fatigue tests are mostly applicable to validate models.

Viscosplastic constitutive models with internal variables can describe TMF stress-strains loops and can therefore be used with some confidence for structure analysis.

Damage models using continuum damage mechanisms can be used for superalloys experiencing thermal transients. But consideration of environmental effects is essential. The synergy between oxidation, creep and fatigue has been described for a wrought superalloy and included in a damage model.

Aluminized coatings can give rise to detrimental effects as shown for AM1 single crystals. Cleavage cracking in the aluminide can be described using a critical stress criterion.

At lower stresses, in the brittle temperature range, early fatigue crack initiation may occur but the anomalous crack growth behaviour can be rationalized using fatigue data for the aluminide coating.

Acknowledgments

The authors are grateful to SNECMA, SEP, and CNES for partial financial support of this work.

References

[1] Glenny, E., Northwood, J. E., Shaw, S. W. K. and Taylor, T. A., *Journal of the Institute of Metals*, vol. 87, 1958-1959, pp. 284-302.

[2] Glenny, E. and Taylor, T. A., *Journal of the Institute of Metals,* vol. 87, 1959-1960, pp. 449-461.

[3] Woodford, D. A. and Mowbray, D. F., *Materials Science and Engineering.* vol. 16, 1975, pp. 5-43.

[4] Hopkins, S. W., *"Thermal Fatigue of Materials and components", ASTM STP 612*, D.A. Spera and D.F. Mowbray (Eds), ASTM, Philadelphia, 1976, pp. 157-169.

[5] Koster, A., Fleury, E., Vasseur, E. and Rémy, L., *"Automation in Fatigue and Fracture: Testing and Analysis", ASTM STP 1231*, C.Amzallag (Ed), ASTM, Philadelphia, 1994, pp. 563-580.

[6] Rémy, L., *"High temperature fracture mechanisms and mechanics", EGF6*, P. Bensoussan and J.P. Mascarell (Eds), Mechanical Engineering Publications, London, 1990, pp. 353-377.

[7] Lemaitre, J. and Chaboche, J.L,. *"Mécanique des Matériaux Solides"*, Dunod, Paris, 1985.

[8] Koster, A., Laurent, G., Cailletaud, G. and Rémy, L., *"Fatigue under Thermal and Mechanical Loading"*, J. Bressers, L. Rémy, M. Steen and L. Valles (Eds, Kluwer, Amsterdam, 1995, pp. 25-35.

[9] Burlet, H., and Cailletaud, G., *Engineering Computations*, vol. 3, 1986, pp. 143-153.

[10] Pilvin, P., *Proc. Mecamat*, Besançon, 1988, pp 155-164.

[11] Rabotnov, Y. N., *"Creep problems in structural members"*, North Holland, Amsterdam, 1969.

[12] Leckie, F. A. and Hayhurst, D.R., *Acta Metallurgica,* vol. 25, 1977, p. 1059.

[13] Chaboche, J. L., *"Low cycle fatigue and life prediction", ASTM STP 770*, C. Amzallag, B. N. Leis and P. Rabbe (Eds), ASTM, Philadelphia, 1982, pp. 81-104.

[14] Reuchet, J. and Rémy, L., *Materials Science and Engineering*. vol. 58, 1983, pp. 19-32, pp. 33-42.

[15] Reger, M. and Rémy, L., *Materials Science and Engineering*. vol. A101, 1988, pp. 47-54; pp. 55-63.

[16] Reuchet, J. and Rémy, L., *Metallurgical Transactions,* vol. 14A, 1983, pp. 141-149.

[17] Rémy, L., *"Behaviour of defects at high temperatures", ESIS 15*, R.A. Ainsworth and R. P. Skelton (Eds), Mechanical Engineering Publications, London, 1993, pp. 167-187.

[18] Tomkins, B., *Philosophical Magazine,* vol. 18, 1968, pp. 1041-1066.

[19] Chataigner, E. and Rémy, L., *"Thermo-mechanical fatigue behavior of materials: 2nd volume", ASTM STP 1263*, M. J. Verrilli and M.G. Castelli (Eds), ASTM, Philadelphia, 1996, pp.3-23.

[20] Koster, A., Ph. D. Thesis, Ecole des Mines de Paris 1997.

[21] Bernard, H. and Rémy, L., *"Advanced Materials and Process", EUROMAT 89,* Edited by H. E. Exner and V. Schumacher, DGM, oberursel, vol. 1, 1990, pp. 529-534.

[22] Duret-Thual, C., Morbioli, R. and Steinmetz, P., "A guide to the control of high temperature corrosion and protection of gas turbine materials", Report EUR 10682 EN CEC, Luxembourg, 1986.

[23] Chataigner, E and Rémy, L., *"Fatigue et Traitements de surface"*, SF2M, Revue de Métallurgie, Paris, 1995, pp. 11-22.

[24] Knott, J., *"Fundamentals of Fracture Mechanics"*, Butterworths, London, 1973, p. 227.

[25] Whittenberger, J. D., *Journal of Materials Science,* vol. 23, 1988, pp. 235-240.

[26] Smeggil, J. G., United Technologies Research. Center, Contract N°62269-78 – C-0311, march 14, 1980.

[27] Bickard, A., Chataigner, E. and Rémy, L., unpublished results, Centre des Matériaux, 1996.

Gianni Filacchioni,[1] Claus Petersen,[2] Farhad Rézaï-Aria,[3] and Jens Timm[4]

A European Round Robin in Thermo-mechanical Fatigue Behavior of a 9% Cr Low Activation Ferrite-Martensite Steel

Reference: Filacchioni, G., Petersen, C., Rézaï-Aria, F., and Timm, J., **"A European Round Robin in Thermo-mechanical Fatigue Behavior of a 9% Cr Low Activation Ferrite-Martensite Steel,"** *Thermo-mechanical Fatigue Behavior of Materials: Third Volume, ASTM STP 1371,* H. Sehitoglu and H. J. Maier, Eds., American Society for Testing and Materials, West Conshohocken, PA, 2000.

Abstract: Test blankets of a thermo-nuclear fusion reactor are subjected during service to alternating thermal and mechanical stresses as a consequence of the pulsed reactor operation. Of particular concern is the thermo-mechanical fatigue (TMF) endurance of 9% Cr low activation ferrite-martensite steels. To design such blankets operating under the above loading conditions, for the time being fatigue life is predicted using design codes based on isothermal fatigue material data, but these codes will be verified with TMF data. Within the European Materials Long Term Programme for fusion research several laboratories are involved in performing TMF experiments using different facilities and samples. Results of a TMF-round robin of four European laboratories will be reported. Comparison of the various test data obtained will give a better understanding for these kinds of tests and enable an in-depth discussion of the scatter of the results, of its reason and what the implications are in terms of a TMF standard.

Keywords: thermo-mechanical fatigue, round robin, 9% Cr ferrite-martensite steel.

Structural components like test blankets for the international thermonuclear experimental (fusion) reactor ITER are subjected during service to alternating thermal and mechanical stresses as a consequence of the high heat fluxes and pulsed reactor operation, as well as coolant pressure, neutron irradiation, magnetic loads and temperature gradients.

[1]PhD, Senior Scientist, Ente per le Nuove Technologie l'Energia e l'Ambiente, Nuovi Materiali, Casaccia, via Anguillarese 301, I-00060 S. Maria di Galeria, Italy.

[2]Senior Scientist, Forschungszentrum Karlsruhe Technik und Umwelt, Institut für Materialforschung II, P.O. Box 3640, D-76021 Karlsruhe, Germany.

[3]PhD, Senior Scientist, École Nationale Superieure des Techniques Industrielles et des Mines d'Albi-Carmaux, Campus Jarlard, Route de Teillet, F-81013 Albi CT Cedex 09, France.

[4]Research Scientist, Joint Research Centre, Institute for Advanced Materials, P.O. Box 2, NL-1755 ZG Petten, The Netherlands.

The material of the structure must be dimensionally stable and retain adequate mechanical properties during exposure to the environmental conditions, if the required performance and prolonged endurance of the structure are to be achieved. Of particular concern is the fatigue endurance of ferrite-martensite steels under cyclic strains and stresses produced by the temperature changes. Along with radiation damage, this is currently considered as the most detrimental lifetime phenomenon for the structure [*1, 2*].

In order to design such structures operating under combined mechanical and thermal cycling, fatigue life has to be estimated with reasonable accuracy. Currently, fatigue life prediction analysis is based on isothermal fatigue data obtained at a chosen (often maximum operational) temperature. In some cases this approach is non-conservative. The generation of test data by thermal fatigue experiments, simulating more accurately the service conditions, has thus become necessary. Nevertheless, these experiments are very expensive; they are neither standardized nor applied in design codes. Therefore, thermal fatigue resistance still has to be predicted from isothermal fatigue data [*3*].

Of particular concern is the fatigue endurance of low activation ferrite-martensite (LAM) steels like the Japanese F82H modified (mod.) under cyclic strains and stresses produced by these temperature changes. This steel had been selected by the Fusion Matetials Long Term Programme of the European community as one of prime candidate materials for applications as a first wall of the blanket structure [*4, 5*].

Due to the missing standardization of the TMF test procedure on one hand and the necessity to compare TMF data from different European laboratories on the other hand a round robin between four laboratories was defined in 1995 [*6*]. The participants are: ENEA: Ente per le Nuove Technologie l'Energia e l'Ambiente, Casaccia, Italy; FZK: Forschungszentrum Karlsruhe Technik und Umwelt, Karlsruhe, Germany; ENSTIM: École Nationale Superieure des Techniques Industrielles et des Mines d'Albi-Carmaux, France; and JRC: Joint Research Centre, Petten, The Netherlands.

These four laboratories are running TMF experiments on four different kinds of samples and in four differnt kinds of test facilities. The TMF test conditions had been defined in the way that:

- Each laboratory performs the experiments with its sample size
- All samples are taken from one sheet of one heat of F82H mod. in as received tempered condition
- All samples are turned and polished with an inner and outer surface roughness of ≤ 2 µm by one manufacturer
- Out-of-phase test mode is used
- Heating and cooling rate is 5 K/s and test atmosphere is air.
- Temperature range is 200° C – 600° C, to give a total mechanical strain of about 0.5%.
- Mechanical clamping of the sample has to be performed at the lowest temperature (200° C) of the cycle.

Comparison of the various test data obtained will give a better understanding for these kinds of tests and enable an in-depth discussion of the scatter of the results, of its reason, and what the implications are in terms of a TMF standard.

Material and Samples

The material used in this TMF round robin was a ferritic-martensitic 7.8% Cr steel of a Japanese steel maker that fulfilled the so-called low activation criteria [7], with the chemical composition listed below (Table 1).

Table 1 - *Chemical composition of F82H mod. (Heat 9753) in wt % (Fe: Balance)*

C	Cr	Ni	Mo	V	Nb	Si	Mn	Ta	B	W	N
0.09	7.8	0.014	0.002	0.19	0.001	0.09	0.09	0.02	0.003	1.9	0.006

The material was delivered as a 25 mm thick plate in the tempered condition. After hot rolling the thermal treatment of the plate started with an austenitization of 1040° C / 40 min/ air cooling and was followed by the tempering 750° C / 60 min/ air cooling. For the four laboratories sample blanks had been cut from one piece of sheet perpendicular to the rolling direction, as can be recognized from the cutting plan (Figure 1).

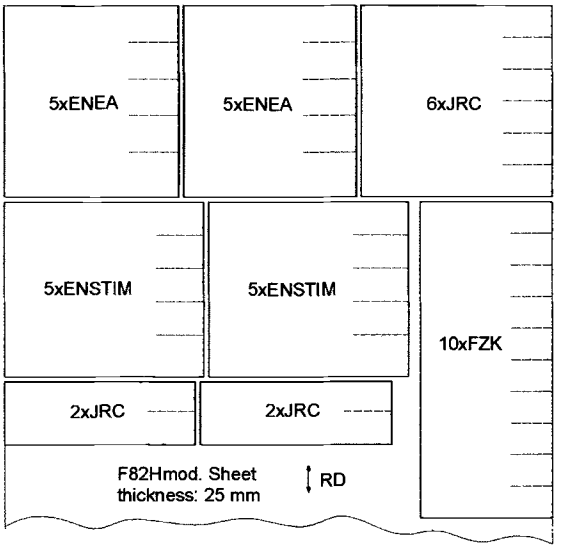

Figure 1 - *Cutting plan of the sample blanks for the four laboratories*

Samples of the different sizes of the four laboratories had been machined from these blank pieces. Simplified drawings of these samples are shown, where the main di mension can be depicted (Figure 2).

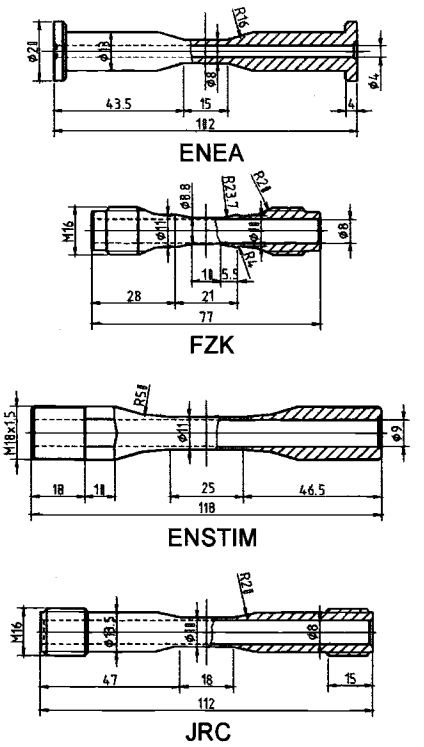

Figure 2 - *Simplified drawings of samples of the four laboratories*

The main sample dimensions (Table 2) vary in nearly all quantities from one laboratory to the other, but all laboratories use hollow cylindrical specimens.

Table 2 - *Main sample sizes of the four participating laboratories*

Dimensions in mm	ENEA	FZK	ENSTIM	JRC
Overall length	102	77	118	112
Cylindrical part	15	10	25	18
Gauge length	12.5	8.0	10.0	8.0
Outer diameter	8.0	8.8	11.0	10.0
Inner diameter	4.0	8.0	9.0	8.0
Wall thickness	2.0	0.4	1.0	1.0
Radius towards cylindrical part	R 16.0	R 23.7	R 50.0	R 20
Fixing	20x4	M 16	M 18	M16

Experimental Procedure

Principle Considerations

In TMF experiments, internal constraints inside the component caused by non-stationary temperature gradients are replaced by an external uniaxial constraint resulting in partial or total suppression of thermal strains. In the present round robin, during initial heating from room temperature to the minimum temperature T_{min}, specimens were allowed to expand freely in direction of the specimens axis at zero stress. After reaching T_{max}, the defined thermal cycle between ~ 200° C and 600° C with a heating and cooling rate of ~ ± 5 K/s was performed about 15 – 20 times to reach steady state conditions in the grips and pullrods and to measure the actual thermal strain of the sample. Then, in the case of closed loop testing facilities the control loop was switched over from stress or load control to total strain control or mechanically clamped in case of the FZK test facility.

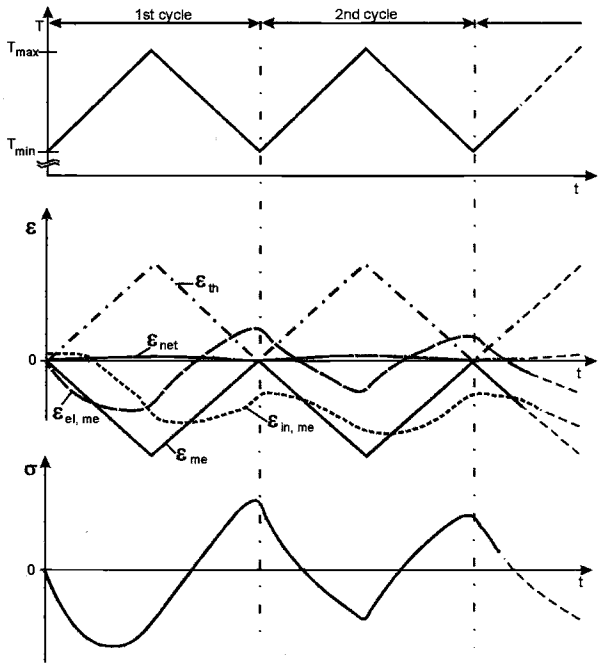

Figure 3 – *Time dependence of the measured quantities for the first and second cycle*

The main prerequisite of an out of phase TFM test is, that the cyclic mechanical strains are out of phase with the selected triangular temperature-time cycles. This is plotted qualitatively for the first and the second cycle (Figure 3). Due to the fact, that the sum

of the thermal strain ε_{th} and the mechanical strain ε_{me} has then to be constant, follows also the second condition $\Delta\varepsilon_{me} = -\Delta\varepsilon_{th}$. Thus, at the high temperature of each cycle a compressive stress is reached and at the low temperature a tensile stress. In case of ENEA, FZK, and JRC T_{min} was 200° C, at ENSTIM it was 230° C and T_{max} was kept in all laboratories to 600° C. At ENEA, FZK, and JRC the heating and cooling rate was ± 5 K/s and at ENSTIM it was ± 4 K/s. The condition $R_\varepsilon = -\infty$ could be realized in all laboratories. All tests had been performed up to failure of the specimen.

By definition, the net strain ε_{net}, at $T = T_{min}$ was set to zero at test start

$$\varepsilon_{net} = \varepsilon_{me} + \varepsilon_{th} = \varepsilon_{in,.me} + \varepsilon_{el,me} + \varepsilon_{th} = 0 \quad (1)$$

or

$$\varepsilon_{me} = \varepsilon_{in,.me} + \varepsilon_{el,me} = -\varepsilon_{th} \quad (2)$$

but in the real TMF experiment the condition $\varepsilon_{net} = 0$ is difficult to realize, therefore a net strain amount of less than 0.02% was detected, when reaching T_{max}.

From Eq. 2, the mechanical and also the sum of the inelastic and elastic strain generated by the total suppression of thermal strains were determined. During all performed TMF experiments, temperature T, thermal strain ε_{th}, net strain ε_{net}, mechanical strain ε_{me}, inelastic mechanical strain $\varepsilon_{in,me}$, elastic mechanical strain $\varepsilon_{el,me}$, and nominal stress σ are measured or calculated as a function of time.

In the TMF experiment the nominal stress is measured as a function of temperature (Figure 4, left side) and the stress-temperature hysteresis is evaluated. Because the thermal strain range $\Delta\varepsilon_{th}(T) = \alpha(T) \cdot (\Delta T)$, with α = thermal expansion coefficient, is completely compensated by the mechanical strain range $\Delta\varepsilon_{me}$, a stress-strain hysteresis loop as shown on the right side of the figure may be determined. These hysteresis loops can be used to draw the total strain range $\Delta\varepsilon_{me}$, the inelastic strain range $\Delta\varepsilon_{in,me}$, and the total stress range $\Delta\sigma$ (Figure 4, right side).

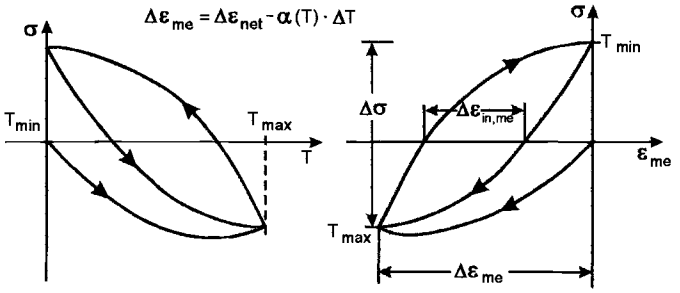

Figure 4 – *Evaluation of the out-of-phase thermo-mechanical test*

The total separation of the specimen, as the traditional measurement of fatigue life, was not considered suitable since it depends on the spacial distribution of initiated cracks which can lead to a larger scatter in number of cycles to failure. Therefore crack initiation was determined as the first deviation from linear best fit of the "steady-state" stress region (Figure 5), giving the number of cycles to crack initiation. As a measurement of the fatigue

life N_f, the number of cycles to a 5% drop from the stable linear cyclic softening behavior in tensile stress was used.

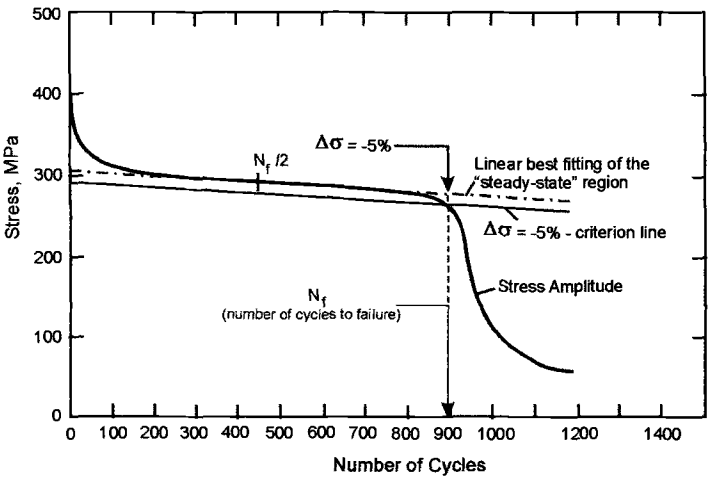

Figure 5 – *Example of evaluation of fatigue life from tensile peak stress versus number of cycles plot*

Due to the fact that rather different TMF testing facilities were used, a short description of each test facility together with some references will be given.

ENEA TMF Facility

The ENEA TMF test facility (Figure 6) has based on a PC-controlled electromechanical Mayes machine, with 100 kN capacity, with forced air cooling through the specimen and the grips during the cooling phase of the cycle. The heating system was a high frequency (160 kHz) generator of max. 5 kW, which was controlled by a temperature controller Eurotherm 900 and synchronised by the same PC, to heat up the specimen inductively by a water cooled copper coil. For temperature measurement and control a flattened 0.2 mm diameter "K"-type thermocouple was half wound around the specimen in the centerline. The statically measured axial temperature gradient over the gauge length was within ± 3° C. The net strain = 0 condition was controlled by a first extensometer with a gauge length of 50 mm, fixed on the grips of the specimen. Its deflection was measured in the cylindrical part of the specimen by an extensometer with a gauge length of 12.0 mm. With respect to strain behavior this TCF test includes complications not normally encountered with controlled TMF tests, because the mechanical strain is not a controlled quantity and therefore a variable. All tests were conducted in air until failure.

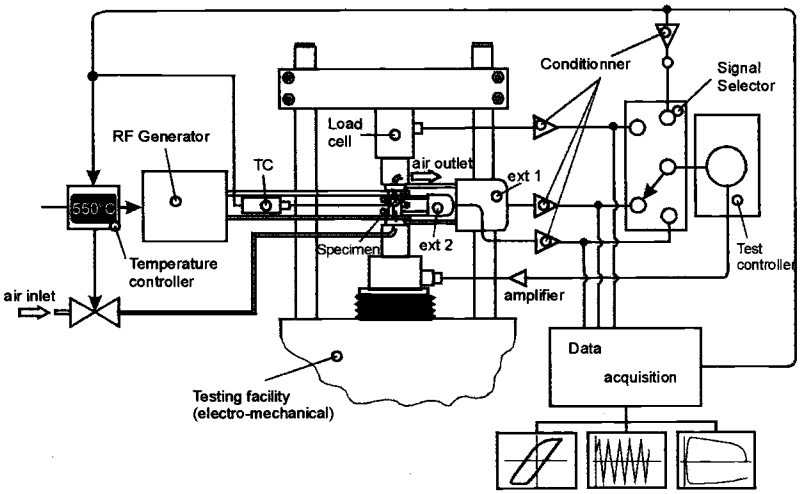

Figure 6 – *Scheme of the ENEA TMF testing facility*

FZK TMF Facility

The FZK TMF test rig (Figure 7) consists of a self-developed stiff load frame for mechanical clamping of the sample, which was directly heated by the digitally controlled ohmic heating device. The grips are water cooled. Temperature was controlled and measured by a Schuntermann & Benninghofen temperature programmer with a 0.1 mm thick NiCr-Ni-thermocouple, spot welded 5 mm above the mid-plane of the specimen, to avoid an influence on the fracture zone. For each test this thermocouple was attached to the specimen at exactly the same position. The maximum axial temperature gradient - statically measured - over the gauge length was within ± 23° C at 600° C. But if this measurement was performed dynamically the temperature gradient was reduced to ± 11° C. Load was measured by a load cell of 20 kN full scale and the deflection of the sample by an extensometer with a gauge length of 8 mm pulled against the sample from the opposite side by springs. Load and strain data are directly registered by a PC data acquisition system. With respect to strain behavior this simple TCF test includes complications not normally encountered with controlled TMF tests, because the mechanical strain is not a controlled quantity and therefore a variable [*8*]. All tests were conducted in air until failure.

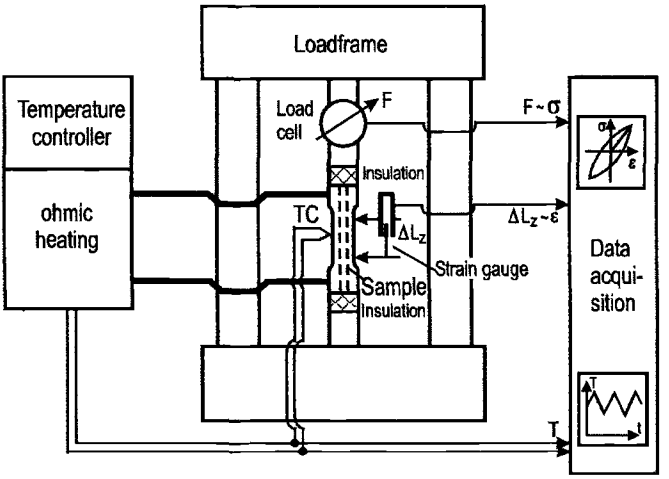

Figure 7 – *Scheme of the FZK TMF testing facility*

ENSTIM TMF Facility

The ENSTIM TMF test facility (Figure 8) is based on a PC-controlled Schenck Hydropuls machine with 250 kN capacity and water-cooled grips. The heating system was a Celes high frequency generator of 2 kW (100 to 400 kHz), which was controlled by a

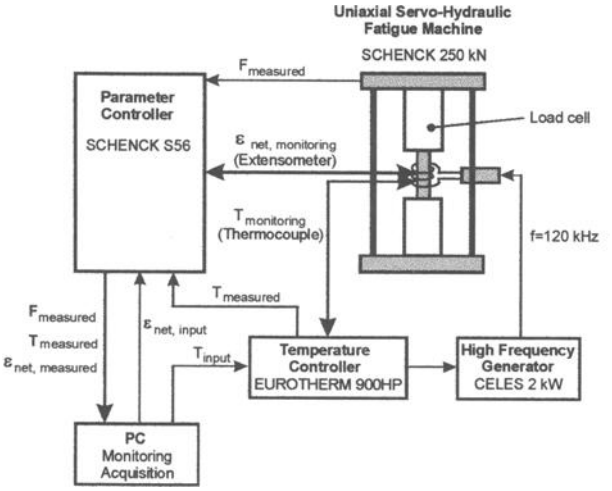

Figure 8 – *Scheme of the ENSTIM TMF testing facility*

temperature controller Eurotherm 900 HP and synchronised by the same PC, to heat up the specimen inductively by a water-cooled copper coil. The temperature was measured with two 0.2 mm diameter "K"-type thermocouples, spot welded 12.5 mm above and below the centerline of the specimen. The axial temperature gradient over the gauge length was within ± 10° C. The deflection of the sample is measured by an extensometer with a gauge length of 10 mm pressed to the sample with ceramic rods. All tests were carried out under total strain control and conducted in air until failure [*9*] occurred.

JRC TMF Facility

At JRC, TMF tests were carried out on a computer-controlled electromechanical closed loop universal testing machine from Schenck-Trebel, type RMC 100, of 100 kN load capacity. The test specimens were heated by means of high-frequency induction using a 6 kW RF induction heater. The coil configuration finally used was a multi-turn coil with one group of two turns concentrically surrounding each end of the specimen (Figure 9). The final axial temperature gradient over the gauge length was within ± 10° C at any in-

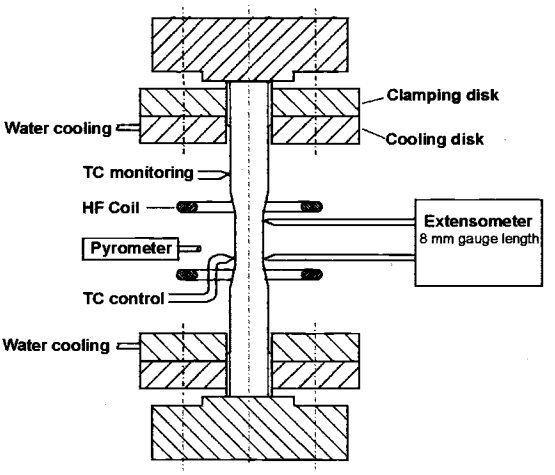

Figure 9 – *Test section of the JRC TMF testing facility*

stant in time within the cycle. The sample temperature was controlled by means of an N-type thermocouple (TC) spot-welded on the specimen outside the gauge length to avoid premature crack initiation in the gauge section due to spot welding damage. For each test this thermocouple was attached to the specimen at exactly the same position. The temperature controller used was a Eurotherm 900 EPC controller fed by the control computer. One further TC was attached outside the gauge length to monitor temperature. During the test an infrared pyrometer was used to double check the temperature in the

center of the gauge length. All tests were carried out under total strain control and conducted in air until failure [*10*].

Results and Discussion

Until now had been performed in this TMF round robin 14 experiments. These were 8 tests of ENEA, 2 tests of FZK, 2 tests of ENSTIM and 2 tests of JRC. Thermal strain ranges are measured directly in the gauge length of the samples fixed in the pull rods of the TMF test facilities during the warming up phase under load free conditions. Mean values are for ENEA with $\Delta\varepsilon_{th} = 0.54\%$, for FZK with $\Delta\varepsilon_{th} = 0.49\%$, for ENSTIM with $\Delta\varepsilon_{th} = 0.48\%$ and for JRC with $\Delta\varepsilon_{th} = 0.53\%$. The ENEA and JRC data show the highest values, but no correlation to sample dimensions or temperature measurement could be found.

The main test conditions and results are: minimum temperature T_{min}, maximum temperature T_{max}, number of cycles to failure at 5% drop of tensile peak stress $N_f(\Delta\sigma\text{-}5\%)$, mechanical strain range at half-life $\Delta\varepsilon_{me}(N_f/2)$, inelastic, mechanical strain range at half-life $\Delta\varepsilon_{in,me}(N_f/2)$ (Table 3), total stress range at half-life $\Delta\sigma(N_f/2)$, minimum stress range at half-life $\sigma_{min}(N_f/2)$, maximum stress range at half-life $\sigma_{max}(N_f/2)$ and mean stress range at half-life $\sigma_{mean}(N_f/2)$ (Table 4) were combined for comparison and statistical evaluation in

Table 3 – *Main TMF results of the four participating laboratories*

Test	T_{min} [°C]	T_{max} [°C]	$N_f(\Delta\sigma\text{-}5\%)$ [cycl.]	$N_f/2$ [cycl.]	$\Delta\varepsilon_{me}(N_f/2)$ [%]	$\Delta\varepsilon_{in,me}(N_f/2)$ [%]
ENEA 2	200	600	926	463	0.58	0.54
ENEA 3	200	600	993	497	0.59	0.56
ENEA 4	200	600	850	425	0.59	0.55
ENEA 5	200	600	925	463	0.52	0.49
ENEA 6	200	600	946	473	0.62	0.54
ENEA 7	200	600	1026	513	0.50	0.47
ENEA 8	200	600	900	450	0.61	0.57
ENEA 9	200	600	933	467	0.65	0.57
FZK J09	200	600	1541	770	0.38	0.108
FZK J10	200	600	1363	681	0.34	0.111
ENSTIM 3	230	600	1435	718	0.45	0.130
ENSTIM 1	230	600	960	480	0.55	0.220
JRC 2	200	600	1640	837	0.50	0.223
JRC 3	200	600	2670	1331	0.50	0.212

Table 3 (continued)

Test	$N_f(\Delta\sigma\text{-}5\%)$ [cycl.]	$N_f/2$ [cycl.]	$\Delta\varepsilon_{me}(N_f/2)$ [%]	$\Delta\varepsilon_{in,me}(N_f/2)$ [%]
Average	1222	612	0.527	0.378
Standard deviation	476	238	0.087	0.188
Standard error	127	64	0.023	0.050
Coefficient of variation [%]	38.97	38.94	16.56	49.58

Table 4 – *Main TMF results of the four participating laboratories*

Test	T_{min} [°C]	T_{max} [°C]	$\Delta\sigma(N_f/2)$ [MPa]	$\sigma_{min}(N_f/2)$ [MPa]	$\sigma_{max}(N_f/2)$ [MPa]	$\sigma_{mean}(N_f/2)$ [MPa]
ENEA 2	200	600	581	- 231	351	59
ENEA 3	200	600	582	- 235	348	57
ENEA 4	200	600	578	- 227	351	62
ENEA 5	200	600	575	- 228	347	60
ENEA 6	200	600	577	- 228	349	61
ENEA 7	200	600	573	- 225	348	62
ENEA 8	200	600	579	- 230	349	60
ENEA 9	200	600	589	- 234	355	61
FZK J09	200	600	508	- 194	315	61
FZK J10	200	600	508	- 194	315	61
ENSTIM 3	230	600	530	-210	320	55
ENSTIM 1	230	600	560	- 215	330	58
JRC 2	200	600	500	- 198	302	52
JRC 3	200	600	509	- 204	305	51
Average			553.5	-218	334.6	58.6
Standard deviation			32.8	14.7	18.6	3.5
Standard error			8.8	3.9	5.0	0.9
Coefficient of variation [%]			5.92	6.72	5.55	5.90

respect to their average values, standard deviations, standard errors and coefficients of variation.

The abandonment of a labwise or grouped statistical analysis was intentionally agreed between the four partners, because, if the data would be put in a data bank system the very specific information about the experiment normally will be lost.

The typical stress-strain behavior of an out-of-phase TMF test has been exemplary plotted from the data of test JRC 2 for the first cycle (Figure 10a) and for the saturation cycle (Figure 10b), that was equal to $N_f/2$.

The first cycle was only a ¾ cycle due to the test start at minimum temperature. From test start at zero levels stress and strain values were reaching a high compressive

stress of -390 MPa and an inelastic compressive strain of - 0.31%. After passing over T_{max}, temperature decreased and the elastic deformation part of the curve was reached. At T_{min} the maximum tensile stress value was detected together with zero mechanical strain.

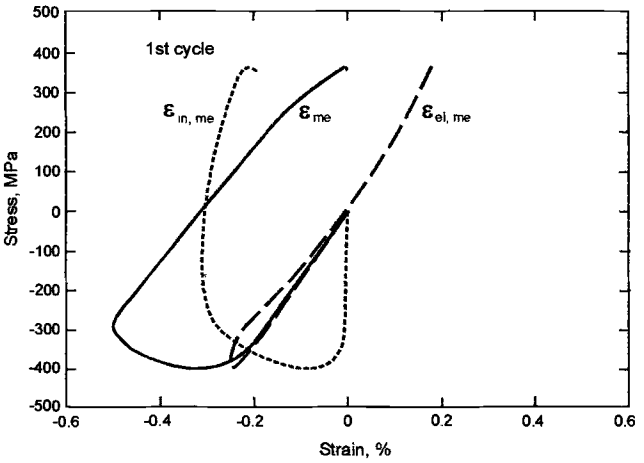

Figure 10a – *Example of the hysteresis loops of the first cycle of test JRC 2, evaluation of the three strain quantities*

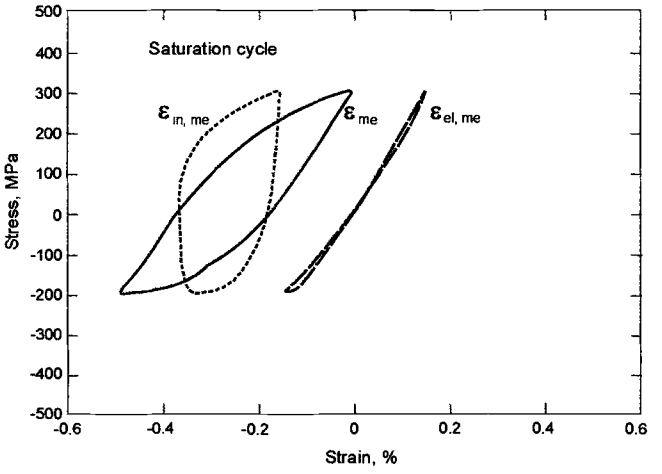

Figure 10b – *Example of the hysteresis loops of the saturation cycle of test JRC 2, evaluation of the three strain quantities*

During the saturation cycle the stress vs. mechanical strain and stress vs. inelastic mechanical strain hystereses represented another typical behavior of out-of-phase TMF

tests with the positive mean stress level of 52 MPa. Due to the nonlinarity of the temperature dependence of Young's modulus the elastic strain was not completely linear and hysteresis-free, but the effect was very low and therefore negligible.

The number of cycles to failure vary from the test ENEA 4 with $N_f = 850$ cycles, as the minimum value, to test JRC 3 with $N_f = 2670$ cycles, as the maximum value. The average value was calculated to 1222 cycles, the standard deviation to 476.26 cycles and the coefficient of variation to 38.97%. Compared to the normal scatter in cyclic tests, where one would see a scatter of one order of magnitude in N_f within a series of tests in a single laboratory, it seems to be a good result.

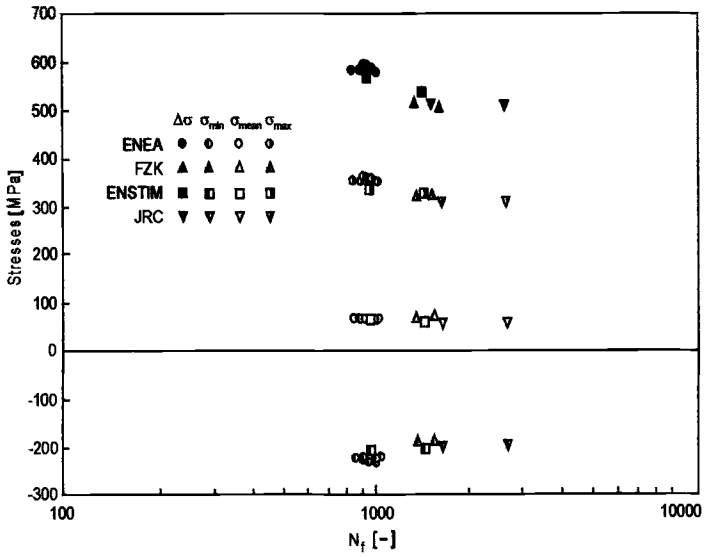

Figure 11 – *Stress range, maximum stress, mean stress and minimum stress as function of number of cycles to failure*

The evolution of the analysed stresses at half-life (Figure 11) results in a very consistent data set, where the mean stress $\sigma_{mean}(N_f/2)$ reveals the best accordance with an average value of 58.57 MPa, a standard deviation of 3.46 Mpa, and a coefficient of variation of 5.90%. With an average value of -218.07 MPa, a standard deviation of 14.66 Mpa, and a coefficient of variation of 6.72% follows in the accordance the minimum stress $\sigma_{min}(N_f/2)$ and the maximum stress $\sigma_{max}(N_f/2)$ with an average value of 334.64 MPa, a standard deviation of 18.56 Mpa, and a coefficient of variation of 5.55%. The total stress range $\Delta\sigma(N_f/2)$ consequently shows with an average value of 553.50 MPa, a standard deviation of 32.79 MPa and a coefficient of variation of 5.92% a slightly higher deviation.

The scatter of the measured strain values was much more pronounced, because the strain control or clamping situation in the four participating laboratories was different during the experiment. Two laboratories, ENEA and FZK, had performed the TMF tests by keeping the overall sample on a controlled length and clamping the sample rigidly in the

load frame, respectively. The measured strain in the gauge length of the sample had been taken as the mechanical strain according to Eq. 2.

The mechanical strain range $\Delta\varepsilon_{me}(N_f/2)$ of these both laboratories came up with an average value of 0.54 strain-%, a standard deviation of 0.099 strain-% and a coefficient of variation of 18.36%. The other two laboratories, ENSTIM and JRC, really compensated the thermal strain by a controlled applied mechanical strain. The mechanical strain range $\Delta\varepsilon_{me}(N_f/2)$ of the latter laboratories came up with an average value of 0.50 strain-%, a standard deviation of 0.035 strain-% and a coefficient of variation of 7.07%. Therefore the overall scatter of the mechanical strain range $\Delta\varepsilon_{me}(N_f/2)$ was higher (Figure 12), than expected from the above-mentioned stress situation. The mechanical strain range $\Delta\varepsilon_{me}(N_f/2)$ of all laboratories yielded in an average value of 0.53 strain-%, a standard deviation of 0.087 strain-% and a coefficient of variation of 16.56%.

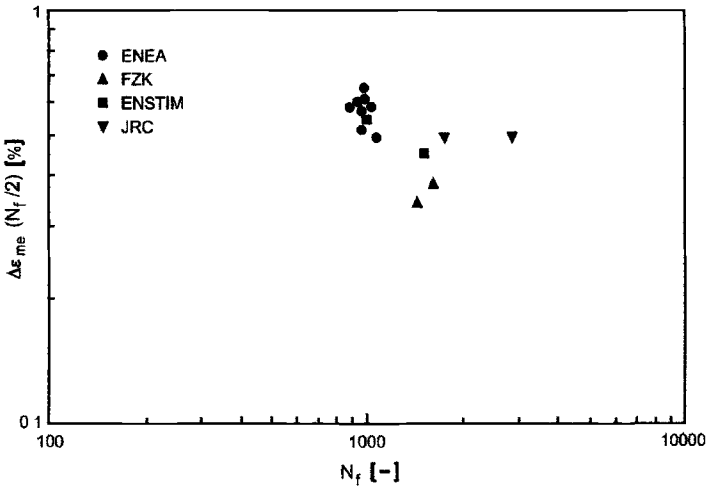

Figure 12 – *Mechanical strain range as function of number of cycles to failure*

Much more pronounced was the scatter in respect with inelastic mechanical strain range (Figure 13). The inelastic mechanical strain range $\Delta\varepsilon_{in,me}(N_f/2)$ of all laboratories reached an average value of 0.378 strain-%, a standard deviation of 0.188 strain-% and thus a very high coefficient of variation of 49.58%. The main amount arose from data of ENEA, with an average inelastic mechanical strain range $\Delta\varepsilon_{in,me}(N_f/2)$ of 0.536 strain-%, because the FZK, ENSTIM and JRC data were located nearer together with an average inelastic mechanical strain range $\Delta\varepsilon_{in,me}(N_f/2)$ of 0.167 strain-%, a standard deviation of 0.052 strain-% and a coefficient of variation of 30.82%. One of the reasons for the untypically high inelastic mechanical strain range values at ENEA is a shift and nonlinearity in strain vs. time behavior in relation to temperature vs. time behavior, i.e. an inadequate synchronization between temperature and strain. Because if one makes a strain correction by applying at maximum stress and minimum stress points in the stress-strain hysteresis, the Hook's line, calculated with the temperature dependent Young's moduli for each temperature, than reasonnable values for the inelastic mechanical strain range $\Delta\varepsilon_{in,me}(N_f/2)$ of

about 0.23 strain-% occur. ENEA's flattened thermocouple pressed against the sample surface can be the reason for the nonlinearity in strain response because the thermocouple has another time constant than the relatively thick wall (2 mm) of the tubular gauge length. This uncertainty still needs further investigation.

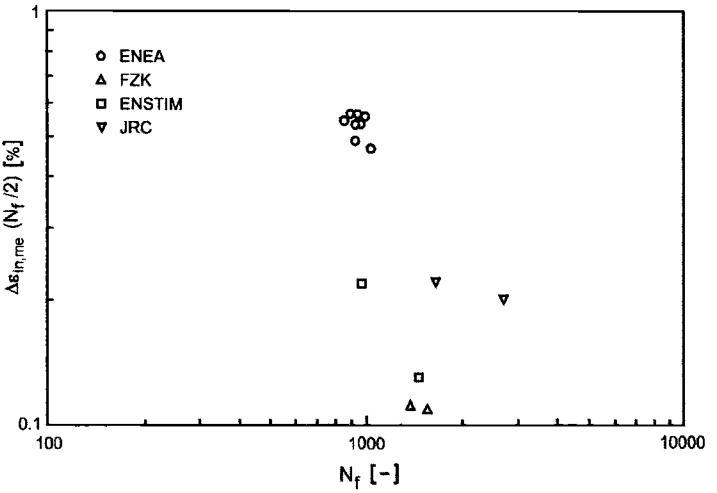

Figure 13 – *Inelastic mechanical strain range as function of number of cycles to failure*

Both tests of ENSTIM did not completely join the round robin conditions, because the temperature range was smaller and the heating and cooling rate slower. Nevertheless they had been included into the comparison, because the condition around the lower temperature was not so critical for the TMF experiment and the rate sensitivity is low.

The very preliminary character of the presented data sets with respect to amount of TMF experiments from the participating laboratories (ten had been planned from each laboratory) and to the statistical data processing should be emphasized. Therefore up to now no comparisons with other round robins in comparable areas had been drawn. If the complete data sets will be submitted, comparisons in the statistical variations can be made from similar studies organized by the likes of VAMAS, HTMTC and ASTM (to name a few).

Standardization efforts, like in ISO/TC164/ISC5/WG9 "Thermo-mechanical Fatigue Testing Method" are still necessary for better comparison, especially in the field of strain measurement, strain control, and analysis of obtained strain data.

Conclusion

During a European TMF round robin, out-of-phase TMF experiments on the Japanese low activation ferritic martensitic steel F82H, modified, had been performed in four laboratories at ENEA, FZK, ENSTIM, and JRC. With four different kinds of hollow cylindrical specimens on four different test facilities results had been obtained, which showed in number of cycles to failure an acceptable scatter, in stress values an agreeable low scat-

ter, but in strain values, especially in the inelastic strain values, larger differences at an unacceptably high scatter. Therefore the necessity for further steps in the direction of a well-defined standardization of these kind of experiments is still remaining.

Acknowledgements

This work was supported by the European Communities as part of the European Fusion Technology Programme under the auspicies of the Nuclear Fusion Project at the Forschungszentrum Karlsruhe.

References

[1] Diegele, E., Munz, D., and Schweinfurter, G., "Lifetime Prediction for the First Wall of a Fusion Machine," IAEA Coordinated Research Programme, Second Interim Report: Behavior of First Wall Components und Thermal Fatigue-Stress Analysis and Life Assessment, Technical Report KfK 5283, IMF II, Association FZK – Euratom, 1991.

[2] Alvarez-Armas, I., Armas, A. F., and Petersen C., "Thermal Fatigue of a 12% Chromium Martensitic Stainless Steel," *Fatigue & Fracture of Engineering Materials & Structures*, 17, 1994, pp. 671-681.

[3] Petersen, C., Schmitt, R., and Garnier, D., "Thermal and isothermal Low Cycle Fatigue of MANET I and II," *Journal of Nuclear Materials*, 233-237, 1996, pp. 285-288.

[4] Kohyama, A., Hishinuma, A., Gelles, D. S., Klueh, R. L., Dietz, W., and Ehrlich, K., "Low-activation ferritic and martensitic steels for fusion application," *Journal of Nuclear Materials*, 233-237, 1996, pp. 138-147.

[5] Daum, E., Ehrlich, K., and Schirra, M., "Proceedings of Second Milestone Meeting, Development of ferritic-martensitic steels," Technical Report FZKA 5848, IMF I, Association FZK – Euratom, 1997.

[6] Petersen, C., "Minutes of the Specialist meeting: Thermal Fatigue of fusion materials," unpublished report, 1995.

[7] Shiba, K., Hishinuma, A., Tohyama, A., and Masamura, K., "Properties of Low Activation Ferritic Steel F82H IEA Heat - Interim Report of IEA Round-Robin Tests (1) -," Technical Report JAERI-Tech 97-038 8 (in Japanese), JAERI, 1997.

[8] Petersen, C., and Rubiolo, G. H., "High Temperature Thermal Fatigue of Stainless Steels," Proceedings of FATIGUE 90, eds.: H. Kitagava and T. Tanaka, Honolulu,.USA, July 15-20, 1990, Vol. III, pp. 1559-1564.

[9] Miquel, B., "Etude du comportement et de l'endommagement en fatigue thermomécanique de l'acier F82H-MOD à 9% de chrome," Stage d'initiation à la recherche, DEA Génie Mécanique-Université Paul Sabatier, École des Mines d'Albi-Carmaux, Février-Juin 1998 (scientific training report in french).

[10] Arana, M., Martínez-Esnaola, J. M., and Bressers, J., " Crack Propagation and Life Prediction in a Nickel-Based Superalloy under TMF Conditions," Proceedings of International Symposium on: Fatigue under Thermal and Mechanical Loading – Mechanisms, Mechanics and Modelling, Petten, NL, May 22-24, 1995, eds.: J. Bressers and L. Rémy, Kluwer Academic Publishers, Dordrecht, 1996, pp. 393-402.

Josef Ziebs,[1] Jürgen Meersmann,[2] Hans-Joachim Kühn,[3] and Hellmuth Klinglehöffer[2]

Multiaxial Thermo-mechanical Deformation Behavior of IN 738 LC and SC 16

Reference: Ziebs, J., Meersmann, J., Kühn, H. J., and Klingelhöffer, H., " **Multiaxial Thermo-mechanical Deformation Behavior of IN 738 LC and SC 16,"** *Thermo-mechanical Fatigue Behavior of Materials: Third Volume, ASTM STP 1371,* H. Sehitoglu and H. J. Maier, Eds., American Society for Testing and Materials, West Conshohocken, PA, 2000.

Abstract: A study was undertaken to develop an understanding of the fatigue life on IN 738 LC under simple and simulated in-service operating thermomechanical cycling (TMF) in air. The experiments were conducted in the temperature ranges 450 - 950 °C, 450 – 760 °C and 600 – 850 °C. Results indicate that the lives differ with strain-temperature phasing. Diamond cycles gave the longest lives. A life prediction assessment is proposed based on the inelastic work $\sum MF\, \sigma_{ij}\, \Delta\varepsilon_{ij}^{in}$ at N_f. It is, shown that the J_2 theory is applicable to TMF loadings. Initial experiments on single crystal superalloy SC 16 prove that there is a non-uniform strain distribution in the plastic region along the circumference of [*001*] oriented specimens. These findings must be weighed when performing TMF tests.

Keywords: turbine engine simulation, multiaxial-thermomechanical fatigue, life prediction, IN 738 LC, SC 16

Introduction

High-temperature components such as turbine blades experience, during service, triaxial thermomechanical stress-strain fields. Predictions of blade behavior or life using only isothermal behavior or simple thermomechanical tests based on sequences of linear ramps may not be appropriate for many conditions due to the complex microstructural dependence on deformation and temperature history. Generally, the inelastic behavior of a metal is due to its past history of deformation and temperature exposure. Under repeated strain-temperature cycles a material may harden/soften or remain the same, depending on the initial state.

In low-cycle TMF the sequencing of loading and temperature variations can influence the fatigue life. Both shearing and normal strain/stresses under multiaxial loading are important in distinguishing the type of fracture.

[1] Senior Scientist,
[2] Research Scientist,
[3] Technical Specialist,
Federal Institute for Materials Research and Testing (BAM), Unter den Eichen 87, D-12205 Berlin

The majority of TMF tests have been carried out using simple thermal and mechanical cycles, such as the linear and diamond sequences [*1, 2*], Fig. 1. Accurate life testing of actual blade cycles, with and without hold times, has been carried out.

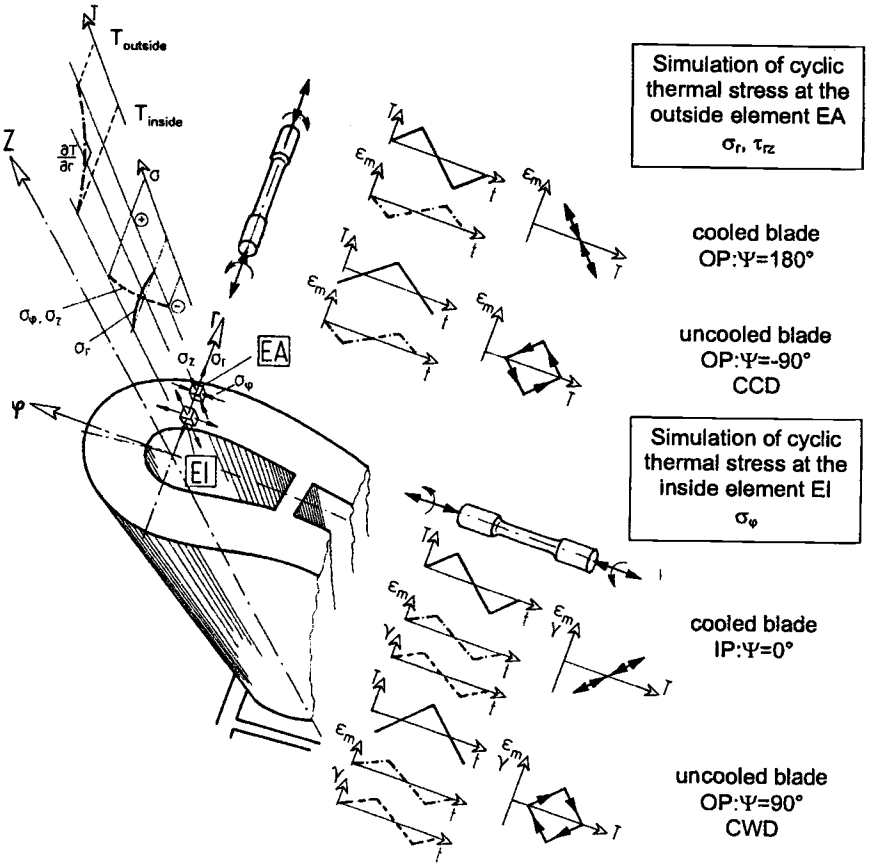

T	temperature	CWD	clockwise dir.
t	time	γ	shear strain
Ψ	phase	ε_m	mech. strain
IP	in-phase	$\tau_{f\varphi}$	shear stress
OP	out-of-phase	σ_φ	tang. thermal stress
CCD	counter-clockwise dir.	σ_f	radial thermal stress

Figure 1
Simulation of cyclic thermal stresses in a blade with simple thermomechanical cycles (linear and diamond)

The main purpose of the research reported in this paper is to develop a model to predict the TMF life of industrial gas turbine blades for multiaxial loading. The model developed is a semi-empirical model, similar to most engineering models that are actually used to predict low-cycle fatigue. A secondary objective of this research is to better understand the multiaxial TMF behavior of IN 738 LC and SC 16. The main features of the deformation behavior of the single cystal superalloy SC 16 are the anisotropic (structural and induced by the plastic flow) and inhomogeneous effects. A further objective of this research is to demonstrate how experimental results can give guidance to the development of time and temperature dependent constitutive models.

Material Details and Experimental Procedures

The materials studied were the cast nickel base alloys IN 738 LC and SC 16. The chemical composition and the heat treatment of the alloys are presented in Table 1.

Table 1 - *Chemical Composition of IN 738 LC and SC 16*

C	Cr	Co	Mo	Ta	Ti	Al	W	Si	Mn	Nb	Fe	Zn
IN 738 LC												
0.105	15.99	8.7	1.77	1.9	3.45	3.4	2.71	0.09	0.03	0.82	0.3	0.037
Solution treated at 1120 °C for 2 h, air cooled, aged at 850 °C for 24 h.												
SC 16												
0.01	15.4	0.17	2.8	3.5	3.48	3.45			<0.003	<0.003		
Solution treated at 1260 °C for 2 h, vacuum, high-temperature aging at 1100 °C for 4 h, final aging at 850 °C for 24 h, then finally air cooled.												

Thin-walled tubular specimens, 200 mm in total length, 50 mm gauge length, 26.5 mm outside diameter and 1.5 mm thickness in the gauge section were used. The specimens were supplied as cast-to-size tubes. The thermomechanical tests were conducted on an MTS tension-torsion-internal pressure closed-loop servohydraulic test machine under computer control. This system is equipped with an induction heating unit and a temperature monitoring device. The specimens can be subjected to controlled axial and shear strain displacement under a defined temperature-time history.

The test program comprised two groups of experiments: (1) uniaxial and tension-torsion thermomechanical fatigue with linear, diamond and sinusoidal cycling (simple TMF test) and (2) complex "bucket" uniaxial and tension-torsion thermomechanical tests [*1-3*]. As can be seen in Table 2, the simple TMF tests differ in the ε/γ-ratio and in the ε/T- as well as ε/γ-paths: tension-compression tests with ε/T phase angles $\varphi_T = 0°$, linear in phase (IP) and 180° out of phase (180 OP) and diamond ε/T-cyclings, ±90° (OP); torsion tests with γ/T phase angles $\varphi_T = 0°$ (IP) and $\varphi/_T = 90°$ (OP) diamond and circular cycling; proportional tension-torsion tests with ε/T and γ/T phase angles $\varphi_T = 0°$ (IP) and ±90° (OP) sinusoidal and diamond cycling; non-proportional tension-torsion tests with ε/T phase angles $\varphi_T = 180°$ and γ/T phase an-

Table 2 - *Details of simple and complex thermomechanical strain paths*

Temperature °C			Temperature rate K s^{-1}		Phase angle °		Strain versus temperature
T_1	T_2	T_s	$\dot{\varepsilon} = 10^{-4} s^{-1}$	$\dot{\varepsilon} = 10^{-6} s^{-1}$	ε - T	γ - T	
TMF Tensile-compressive strain				ε_m = 0,6 %, 0,5 %, 0,4 % (CCD, CWD ε_m=0,6 %)			
950	450	700	4,17	0,42	0, 180		
850	600	725	2,08	0,21	0, 180		
750	550	650	1,67	0,17	0, 180		
950	450	450	4,17		-90		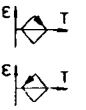
850	600	600	2,08		-90		
450	950	950	4,17		90		
600	850	850	2,08		90		
TMF Shear strain				$\gamma/\sqrt{3}$ = 0,6 %, $\dot{\gamma}/\sqrt{3} = \dot{\varepsilon}$			
950	450	700	4,17	0,42		0, 90	
760	450	605	2,58	0,26		0, 90	
450	950	950	4,17	0,42		90	
450	760	760	2,58	0,26		90	
TMF Proportional axial and shear strain $\bar{\varepsilon}_m$ = 0,6 %							
950	450	700	4,17	0,42	0	0	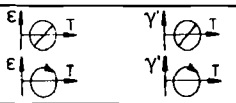
760	450	605	2,58	0,26	0	0	
450	950	700	4,17		-90	-90	
450	950	950	4,17	0,42	90	90	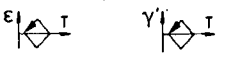
450	760	760	2,58	0,26	90	90	
TMF Nonproportional axial and shear strain $\bar{\varepsilon}_m$ = 0,4 %, 0,5 %, 0,6 %							
450	950	700	4,17		180	-90	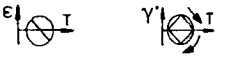
600	850	725	2,08		180	-90	

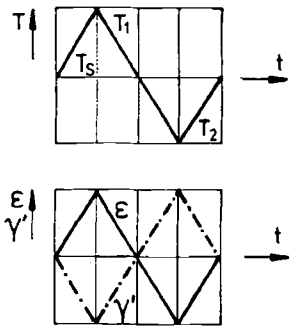

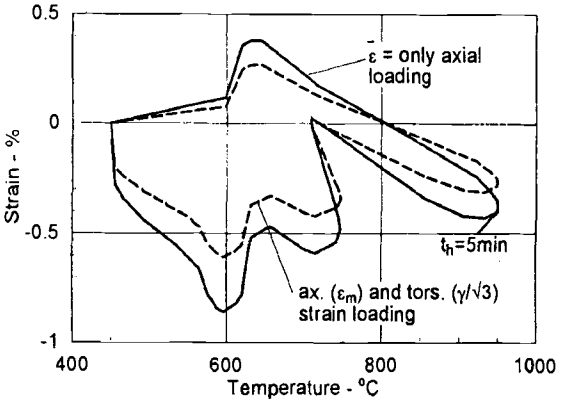

gles φ_T = -90° (diamond, sinusoidal). The complex "bucket" thermomechanical fatigue tests followed an assumed strain-temperature history representative of the leading edge of the first stage bucket in service. The tests were performed at equivalent strain ranges $\Delta\bar{\varepsilon}_m$ = 0.6%, 0.93%, 1.24%, equivalent strain rate $\dot{\bar{\varepsilon}}_m = 10^{-4}s^{-1}$, $10^{-5}s^{-1}$, the temperature range 450 °C < T < 950 °C and temperature rate $\dot{T}$ = 1.67, 2.08 and 4.21 Ks^{-1}.

An effective stress range $\Delta\bar{\sigma}$ and an effective plastic strain range $\Delta\bar{\varepsilon}$ based on the von Mises criterion, were used for correlating the multiaxial tension/torsion cyclic data:

$$\Delta\bar{\sigma} = \left[(\Delta\sigma)^2 + 3(\Delta\tau)^2\right]^{1/2} \tag{1}$$

and

$$\Delta\bar{\varepsilon} = \left[(\Delta\varepsilon_m)^2 + \frac{1}{3}(\Delta\gamma)^2\right]^{1/2} \tag{2}$$

where $\Delta\sigma$ and $\Delta\tau$ are the axial stress and shear stress ranges, respectively, and $\Delta\varepsilon_m$ and $\Delta\gamma$ are the corresponding components of the axial and shear strain ranges.

The total specimen strain, ε_{tot}, was calculated by adding the thermal ε_{th} and mechanical strains ε_m. The thermal strain was determined by

$$\varepsilon_{th} = \alpha\,(T)\,(T - T_o) \tag{3}$$

where T is the instantaneous temperature, T_o = 20 °C and α is the coefficient of thermal expansion. Based on experimental data α (T) could be approximated by

$$\alpha(T) = A_1 + A_2(T\text{-}T_o) + A_3(T\text{-}T_o)^2 \tag{4}$$

where A_1, A_2, A_3 are constants.

Details of the corresponding isothermal low cycle fatigue data along with the cyclic hardening and softening behavior can be found in [*4*].

Monotonous and sequential tension, torsion and tension-torsion loadings have been performed along the <001> direction and within the standard triangle type orientations on hollow specimens of SC 16 to demonstrate the various aspects of non-homogeneous deformation. Seven or eight strain gauge rosettes have been attached on the circumference of the cross section with respect to the orientation of the axis at RT. Each strain gauge had dimensions of 0.76 x 0.76 mm. The tests were conducted under axial and torsional strain or displacement (stroke) and angle position control.

Results

Simple TMF Tests

In addition to providing reference data for further study, these experiments were designed to investigate three points. Firstly, strain-temperature phase effects

were studied by using in-phase, out-of-phase and diamond TMF cycles, where the axial strain, shear strain or the axial and the shear strain amplitude were held constant, $\varepsilon_m = \bar{\varepsilon} = 0.4$, 0.5 and 0.6%. Does this result in different fatigue lives? Secondly, how do different temperature ranges 450–950 °C, 450–760 °C and 600–850 °C affect fatigue lives? Thirdly, can the isothermal data and the J_2 theory be used to describe the thermomechanical response of IN 738 LC? The results and the answers to these questions will also be used to assess the need of different life prediction techniques.

Strain-Temperature Phase Effect, Temperature Range

The longest lives were exhibited by those samples which had undergone diamond-type loadings [*5*]. For these tests, the strain at the maximum temperature was zero. The shortest lives were seen in those samples tested under sinusoidal, nonproportional strain paths. Different temperature-mechanical strain phasing, that is, linear out-of-phase or in-phase or in-phase-cycling, had a significant effect on fatigue lives in the temperature range 450 °C to 950 °C. A crossover of the linear TMF lines with temperature phasing of 0° or 18° is seen at about 10 cycles to failure, Fig. 2. The linear out-of-phase TMF cycle best simulates the complex blade TMF cycle for uniaxial loading (axial strain) because the highest temperatures occur while the surface is in compression. Nevertheless more damaging thermal mechanical loading was found in sinusoidal tension-torsion cycles with or without hold times. On the other hand, complex TMF tests gave longer lives at low strain ranges when compared with simple linear TMF tests. Since the high temperature deformation for complex TMF tests occur at a larger compressive inelastic strain, a shift in mean stress is seen in all tests.

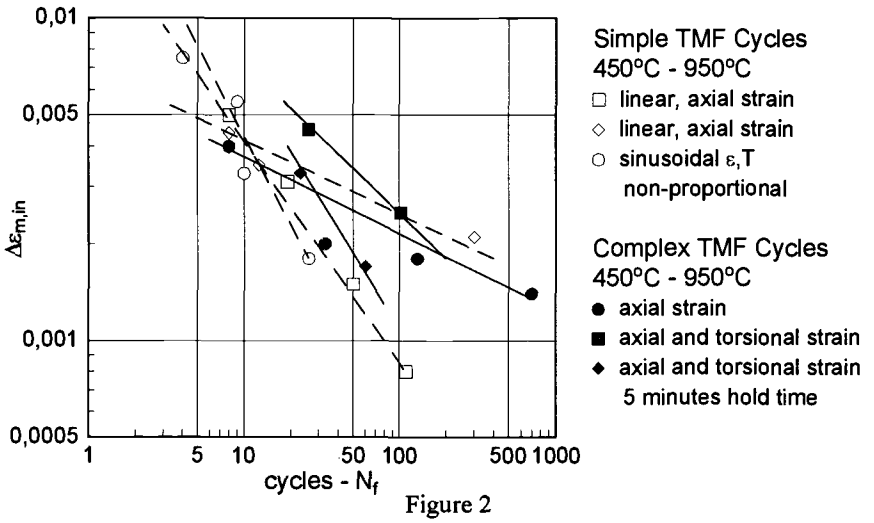

Figure 2

Inelastic strain range, $\Delta\varepsilon_{m,in}$, versus cycles to failure for simple and complex TMF tests of IN 738 LC, $\dot{\bar{\varepsilon}} = 10^{-4}s^{-1}$

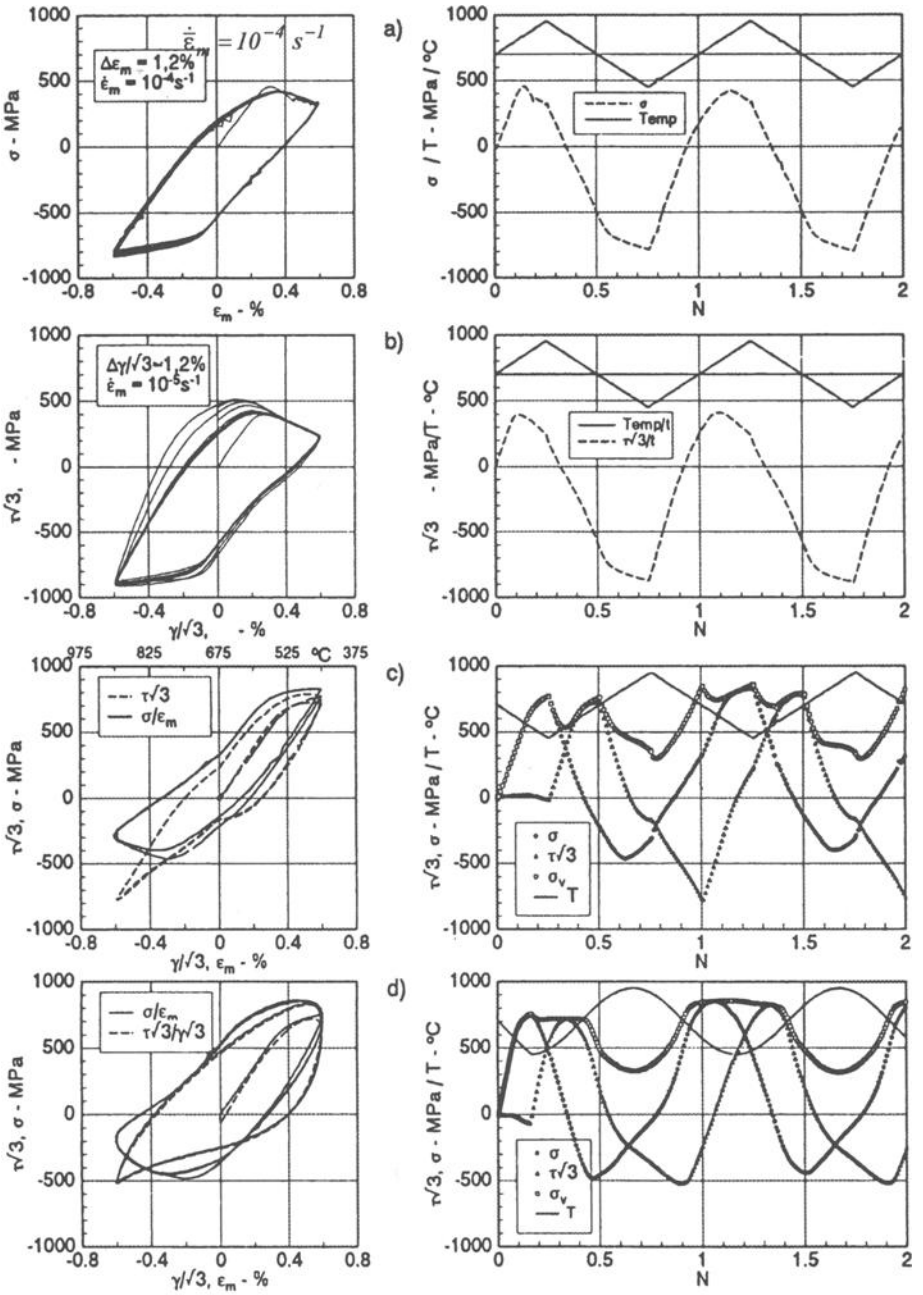

Figure 3

Stress- strain behavior and stress response versus cycles for simple TMF tests

The fatigue life for isothermal tests was found to be mainly spent in the propagation of microcracks. Fatigue lives for the different TMF cycles are significantly less than for isothermal cycles at the same maximum temperature [4]. This suggests that the thermal cycling introduces additional damage associated with thermal inhomogenities, either microscopically or macroscopically. Linear TMF tests conducted in the temperature range 450 °C to 750 °C gave lives, that were twice as long as the lives in the temperature range 450 °C to 950 °C [4]. However, the environmental attack should also be considered because it is greater at higher temperatures.

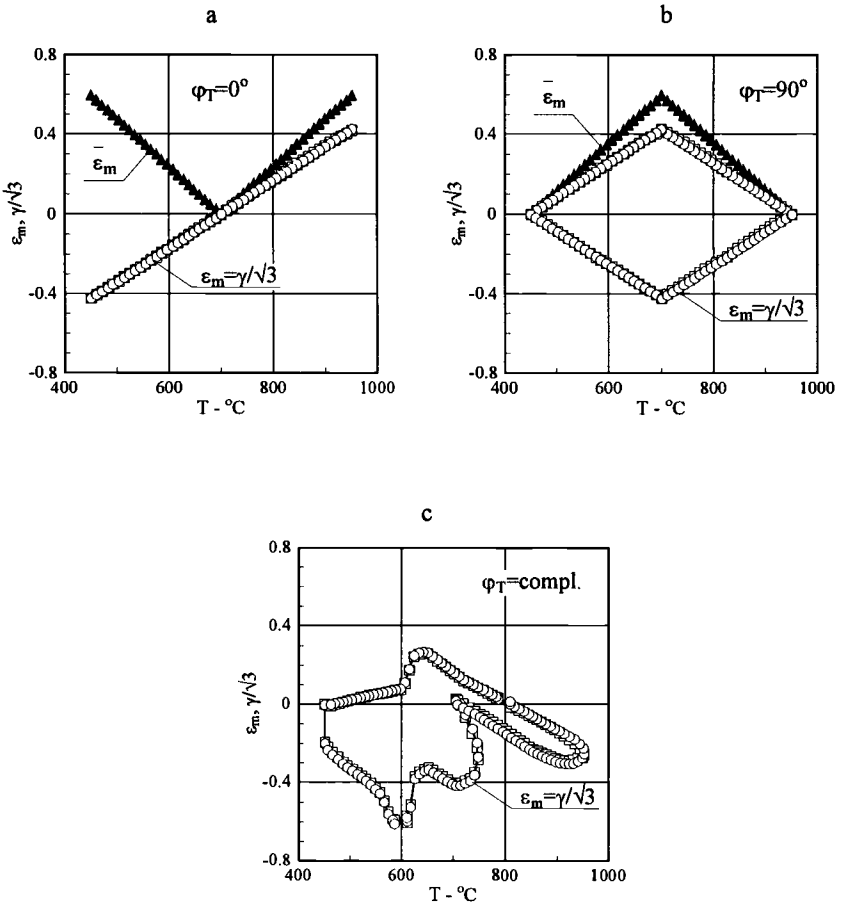

Figure 4
Applied strain and temperature phasings for simple and complex TMF tests

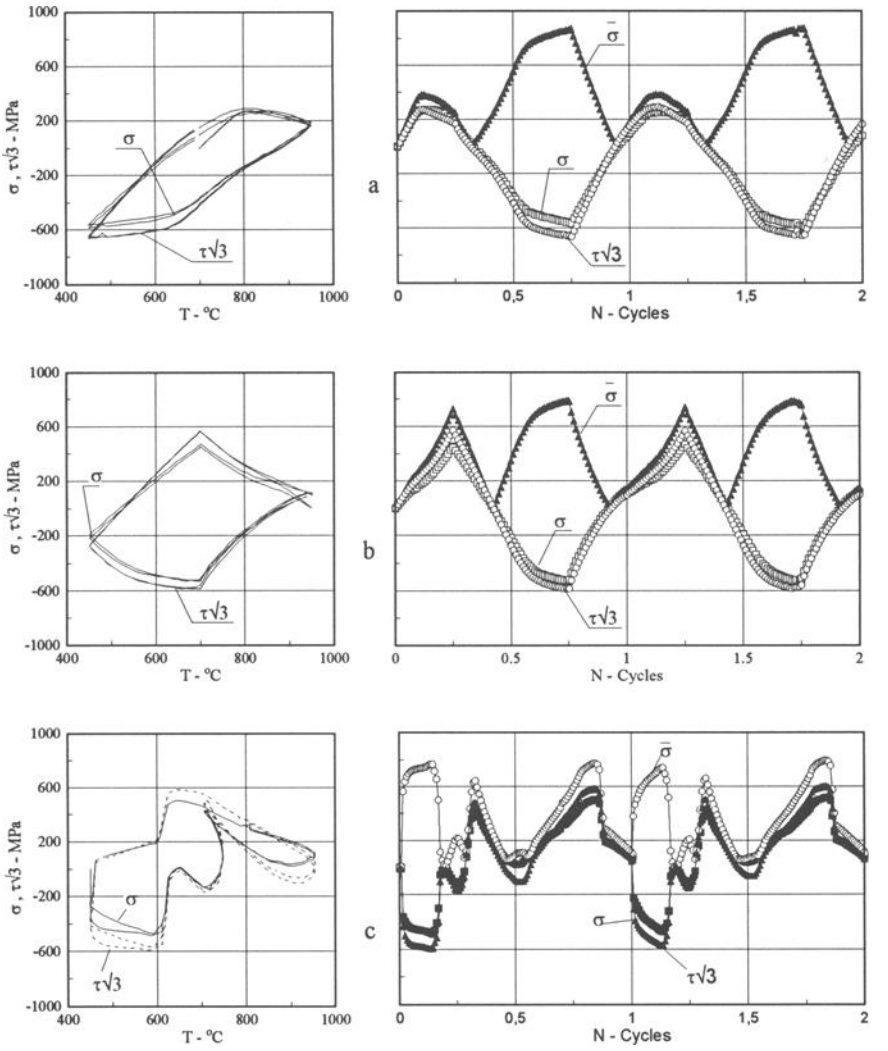

Figure 4 (continued)
Stress responses for simple and complex TMF tests with reference to the above applied strain temperature phasings

Some typical cyclic stress-strain curves for the linear TMF cycles are shown in Fig. 3: 450-950 °C, $\dot{\bar{\varepsilon}} = 10^{-4}\ s^{-1}$ (a) linear axial strain ramps ε-T IP; (b) linear shear

strain ramps, $\gamma/\sqrt{3}$-T IP; (c) linear axial and shear strain ramps, ε-T IP, $\gamma/\sqrt{3}$-T CWD; (d) sinusoidal axial and shear strain ε-T IP, $\gamma/\sqrt{3}$-T OP.

The applied axial-torsional strain temperature history for proportional tension-torsion, non-proportional diamond and complex "bucket" loadings and the resulting axial and shear stress temperature/cycles to failure responses are presented in Figure 4.

The applied in-phase ($\varphi_T = 0°$) proportional strain-temperature path results in an asymmetric stress response (Figure 4a). In the range of high temperatures, 750 °C to 950 °C, a significant stress relaxation is observed due to dynamic recovery. The stress response for tension and torsion is similar.

The non-proportional diamond ($\varphi_T = 90$ °) strain-temperature path achieves extremes of strain at T = 700 °C, Figure 4b. The TMF stress response coincides, at comparable mechanical strains, with the response of the isothermal tests in the temperature range 700 °C to 450 °C to 700 °C. In the 850 °C to 950 °C to 850 °C range softening is observed.

As shown in Figure 4c compressive stress peaks occur after warm-up, during acceleration and at base load for the blade strain temperature cycles. Tensile peaks occur before 'load' and during 'unload'. The largest inelastic strain is achieved after warm up. It is mainly reduced during the unload phase by tensile stress. The effects of different strain ranges ($\Delta\varepsilon$ = 1.24%, 0.93%, 0.60%) upon the fatigue lives are shown in Figure 5 for the complex bucket cycle. Peak stresses ($\overline{\sigma}$, σ_{max}, σ_{min}, τ_{max}, τ_{min}) are plotted versus the number of cycles. The hardening/softening behavior is similar to the behavior of the isothermal counterparts. However, the different strain ranges generate increasing tensile mean stresses. The effect of these tensile mean stresses on fatigue life typically increases as the total strain range increases. Note that the simple TMF tests generate compressive mean stresses in the hysteresis loops (Figure 4). However, the magnitudes of these compressive mean stresses are relatively small in comparison to the magnitudes of those generated in the 'bucket' cycles in the tension mode. The detrimental effect on the fatigue lives was already mentioned above.

Use of Isothermal Data for Predicting Nonisothermal Behavior

The question is often asked whether it would be possible to gain an understanding of the thermomechanical behavior of materials using isothermal experiments. Figure 6 shows the hysteresis loops on IN 738 LC subjected to linear in-phase TMF loading under a mechanical strain range of ± 0.6 percent and in a temperature range 450 °C to 950 °C, and also the hysteresis loops for other isothermal temperatures in the range of 450 °C to 950 °C under the same conditions. The isothermal loops are used to construct the hypothetical thermomechanical loop (broken line) assuming that the stress response of isothermal loading must be equivalent to nonisothermal loading for definite stress points of the hysteresis loops. Predicted and experimental curves show good correlation at the highest temperature 950 °C, although with 450 °C the predictions are slightly low. The predicted width of the hysteresis loop, however, is smaller than that observed. The shape of the experimental hysteresis loop tends to be more square.

The above-mentioned behavior was confirmed by sinusoidal nonproportional straining paths in tension-torsion tests at temperatures between 450 and 950 °C with an effective mechanical strain $\bar{\varepsilon} = 0.6\%$, Fig. 7. In this figure the solid line represents the stress loci of TMF tests in the $\sqrt{3}\,\tau - \sigma$ stress space and the broken lines (circles)

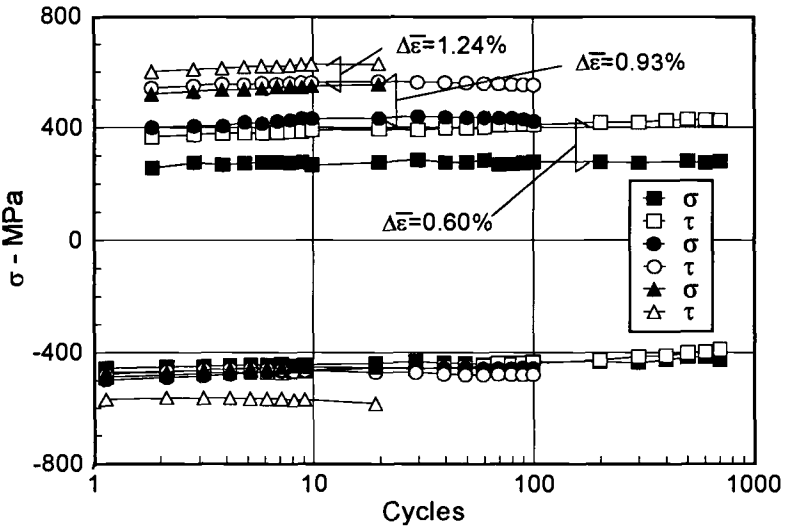

Figure 5
Axial and torsional stress versus number of cycles for 'bucket' cycles, $\Delta\bar{\varepsilon} = 0.6\%, 0.93\%, 1.24\%$

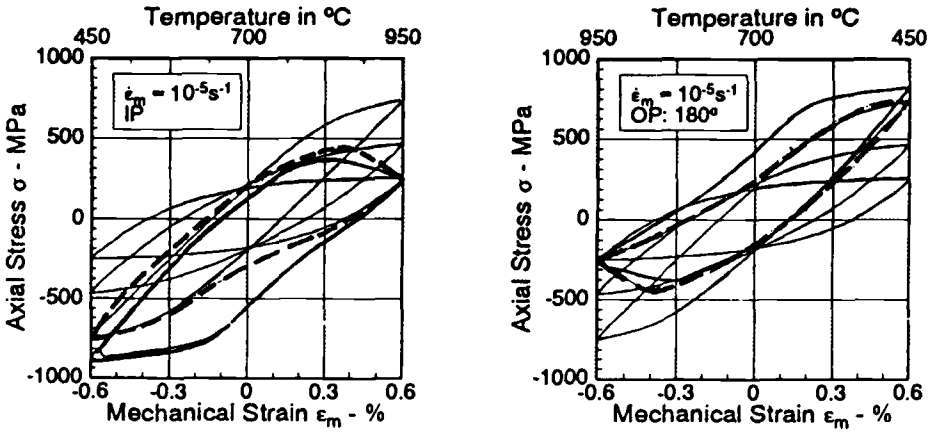

Figure 6
Comparison of TMF and isothermal hysteresis loops

the stress loci of isothermal tests under the same effective strain but at different temperatures.The experimental stress loci of the TMF and isothermal tests coincide at the highest and lowest temperatures, but discrepancies can be observed at other temperatures. The study of thermal history effects has brought out an important point about thermomechanical cycling. If the strain range and temperature levels activate similar deformation mechanisms, the isothermal values can be expected to model the TMF-response satisfactorily by interpolation. However, if different deformation mechanisms are activated, temperature history effects may be very important.

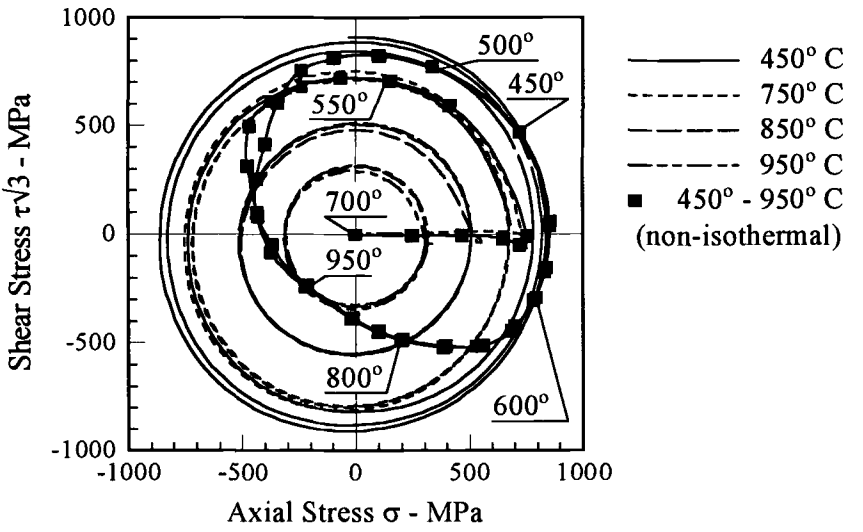

Figure 7
Comparison of TMF and isothermal stress responses for 90° out-of-phase strain cycling, $\bar{\varepsilon}$ = 0.6%, of IN 738 LC

Experimental Verification of the J_2 Theory for TMF Loading

The equivalent stresses and strains of simple and complex TMF loadings were calculated by the von Mises relation, Figure 8. The curves of equivalent stresses versus equivalent strains lead to very complex shapes because all values are positive. Therefore the curves were changed by signs to get the usual hysteresis loops. Pure tension-compression and torsion tests as well as tension-compression-torsion tests with $\varphi_T = 0$ (IP) are compared in Figure 8a. Figure 8b represents the OP-path with $\varphi_T = 90°$ and Figure 8c the complex path. In this diagram the pure torsional load is left. The equivalent stress values of pure tension-compression tests are about 100 MPa lower than the other. The deviations are inside the scatterband of this material. These diagrams verify that the von Mises hypothesis is altogether applicable to the deformation behavior of IN 738 LC at TMF loading.

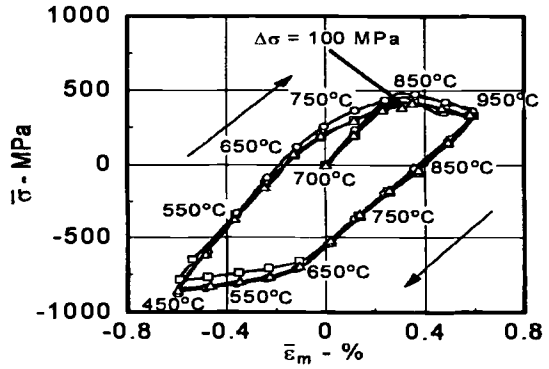

a) Phase angle φ_T = 0°

□ Tension - compr.
O Torsion
Δ Tension - compr. + Torsion

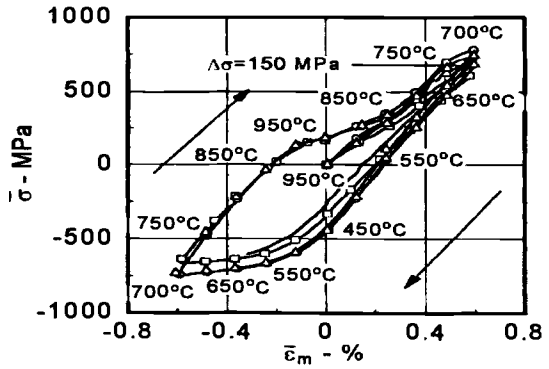

b) Phase angle φ_T = 90°

□ Tension - compr.
O Torsion
Δ Tension - compr. + Torsion

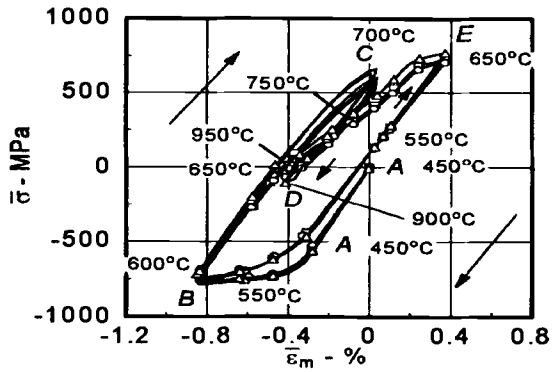

c) Phase angle φ_T = complex

□,O Tension - compr.
Δ Tension - compr.+ Torsion

$\overline{AB}$: Warm up
$\overline{BC}$: Acceleration
$\overline{CD}$: Load
$\overline{D}$: Base Load
$\overline{DE}$: Unload
$\overline{EA}$: Shut down

Figure 8
Comparison of uni- and multiaxial TMF tests (von Mises relation)
450 °C>T>950 °C, $\dot{\bar{\varepsilon}}_m = 10^{-4}$*1/s,* $\Delta\bar{\varepsilon}_m = 1.24\%$

Life Relations for Thermomechanical Fatigue

Although numerous life prediction methods have been forwarded for simple TMF tests [*6–9*], few studies were directly concerned with the fatigue life of 'bucket' TMF paths [*1*]. At elevated temperatures, under cyclic loading, the inelastic deformation of metals is comprised of both plastic and viscous components. Since both plastic and viscous deformation mechanisms can serve as driving forces for microcrack initiation and propagation, cumulative fatigue and creep damage mechanisms are intimately coupled under TMF loading. The driving force for the propagation of the nucleated cracks in metals is a function of the shear and normal stresses acting on the crack plane [*10*]. In multiaxial loading conditions the magnitude of the stresses depends on the strain paths. A global measure which includes all of the above mentioned parameters is the inelastic work.

Therefore the general form of the criterion is:

$$\sum \sigma_{ij} \Delta \varepsilon_{ij}^{in} = A N_f^m \tag{5}$$

where the coefficient A and the exponent m are calculated by linear regression for each TMF history. Figure 9 shows the data of five TMF histories with their straight-lines of regression. The most outside data points limit a scatterband with a N_f – width factor of 2.25 with respect to the scatterband midlife. N_f was defined as the cycle at which the maximum stress dropped off to 1% of a steady-state value including also points after saturation. As shown in Figure 9, the results of the uniaxial and biaxial TMF tests fall in a narrow band.

The quality of the lifetime prediction is also presented in Figure 9. As can be seen the correlation is generally within a factor of $\pm$ 2 of the medium between predicted and actual life.

Manson and Halford [*11*] proposed a stress based multiaxiality factor MF that modifies the inelastic work. The factor accounts for the change in ductility of a material as the state of stress changes.

$$\sum MF\, \sigma_{ij} \Delta_{ij}^{in} = AN_f^m \tag{6}$$

where

$$MF = \frac{1}{2 - TF}, \qquad TF \le 1 \tag{7}$$

$$MF = TF, \qquad TF \ge 1 \tag{8}$$

and

$$TF = \frac{\sigma_1 + \sigma_2 + \sigma_3}{\frac{1}{\sqrt{2}} \sqrt{(\sigma_1 - \sigma_2)^2 + (\sigma_2 - \sigma_3)^2 + (\sigma_3 - \sigma_1)^2}} \tag{9}$$

However, equation (6) estimates the fatigue lives with nearly the same degree of accuracy as without the multiaxiality factor.

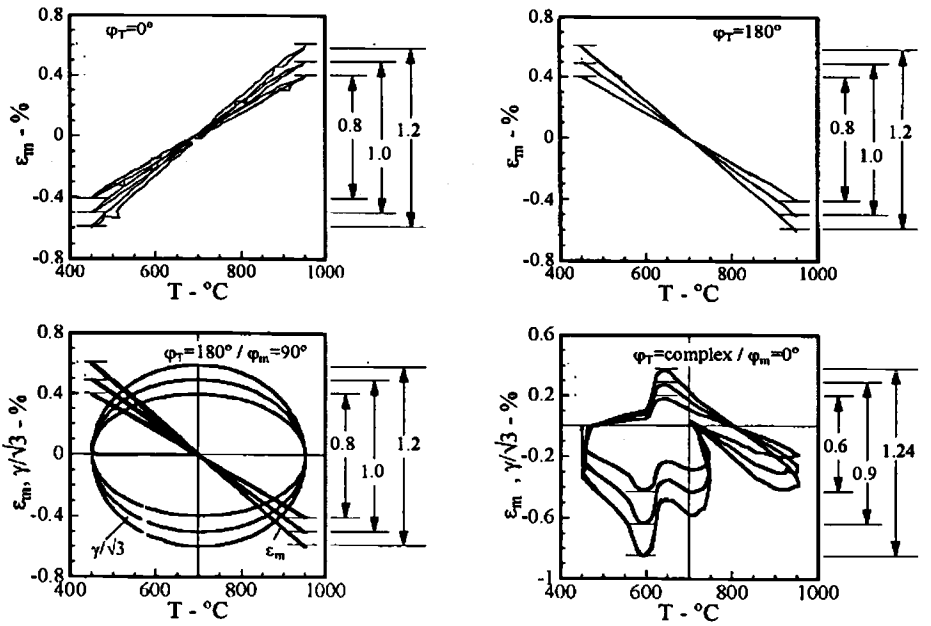

a : Identification paths ε_m/T

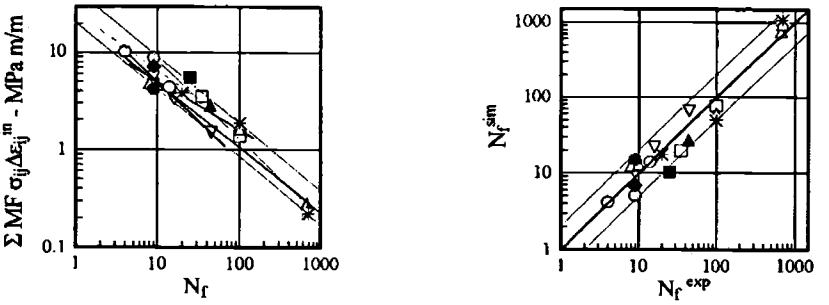

b : Determination of A, m by 1D-tests.

c : Verification of A, m.

Identification (ID-) - tests

tension-compr.
- ▽ Ψ_T = 0°
- □ Ψ_T = 180°
- △ Ψ_T = compl.

tension-compr.+ torsion
- ✳ Ψ_T = compl.
- ○ Ψ_T = 180°, sinus.

Verification-tests

- ▲ Ψ_T = 90°, Ψ_m = -, ΔT = 850 - 600°C
- ◆ Ψ_T = 180°, Ψ_m = 90°, ΔT = 950 - 450°C
- ■ Ψ_T = 180°, Ψ_m = 90°, ΔT = 850 - 600°C
- ● Ψ_T = 0°, Ψ_m = 0°, ΔT = 950 - 450°C

Figure 9

$\sum$ MF $\sigma_{ij}\,\Delta\varepsilon_{ij}^{in}$ *versus number of cycles for different tests including applied strain paths (at the top) and simulated versus experimental life*

Experimental Study of the Anisotropic and Non-Homogeneous Deformation Behavior of SC 16 Single Crystals

In order to take full advantage of nickel based single crystal superalloys it is necessary to understand the anisotropic and non-homogeneous deformation behavior. Therefore the local deformation characteristics of the SC 16 alloy were investigated via detailed studies of the local deformation with strain gauges at RT. The observations were analysed and interpreted in terms of crystallographic slip. In discussing TMF testing on single crystal superalloys it will be necessary to deal with non-uniform strain distribution along the circumference of different oriented tubular specimens under tension, torsion and tension-torsion loading.

Experimental Evidence of the Tensile Behavior

The mechanical response of SC 16 alloy in a tensile test depends on material orientation, temperature, strain and specimen shape and is quite different from that of a polycrystalline alloy. Initially round tubular specimens of different diameters (26.5 mm outside diameter, 1.5 mm thickness, 20 mm outside diameter, 1.5 mm thickness) in the near [001] or within the standard triangle type orientations deform into cross sections with a complex shape, Figure 10. At higher temperatures, 950 °C, the deformation is much more homogeneous. The experiment proves that more slip systems are activated. In contrast the post yield response of solid specimens shows a cross section with a circular or elliptical shape. There is not a clear explanation of this fact up to now. The reason is mainly to be found in the complexities of the deformation modes present in two-phase materials. The active deformation modes and their critical stresses depend on the composition, the temperature, the strain rate, the stress state and the previous deformation history. The work of Chin and Mammel [*12*] was the first attempt to do a systematic analysis of activated slip systems in the standard stereographic triangle. For {111} <101> slip systems, loading of fcc materials in or near the [001] direction will activate eight slip systems simultaneously if the stress is equivalent to the critical resolved shear stress (CRSS). Theoretical predictions of the combinations of active slip systems in a single crystal of a particular orientation have usually been based on one or two extreme sets of assumed boundary conditions. In the case of hollow specimens there could be particular boundary conditions on strain. The geometrical part of single-crystal plasticity is then the yield condition. This provides the basis for deriving which combination of slips will be activated among the many that are kinematically possible to achieve a given strain increment, and what particular stress state is necessary to activate this combination.

The interpretation of such non-homogeneous test results requires a finite element analysis as it has been done by Nouailhas and Cailletaud [*13*]. For that purpose experimental data, the macroscopic response of the material under tension or other loading conditions and, as much micromechanical information as possible, such as activated slip systems or local strains, must be introduced into the analysis.

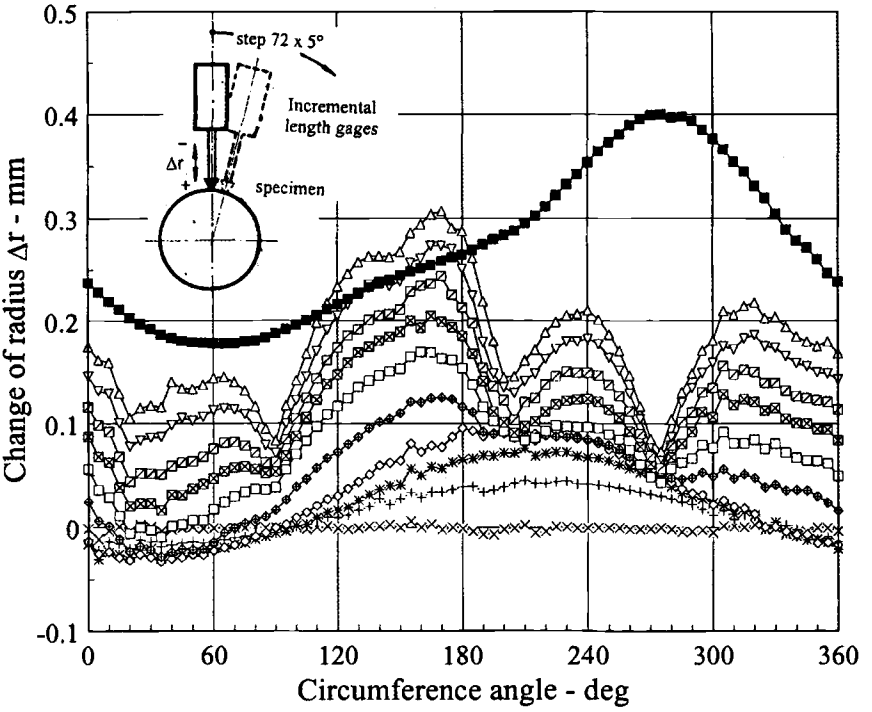

command:
s = axial stroke
ε = extensometer strain

T=RT, s=0mm
T=RT, s=0,1mm
T=RT, s=0,3mm
T=RT, s=0,6mm
T=RT, s=1,1mm
T=RT, s=1,6mm
T=RT, s=2,1mm
T=RT, s=2,.6mm
T=RT, s=3,1mm
T=RT, s=3,6mm
T=950°C, ε=4%

Figure 10
Change of radius of near [001] SC 16 tubular specimens in depedence of the circumference angle

Tension-Torsion Tests on <001> Specimens at RT

A completely non-symmetrical, non-homogeneous deformation behavior is observed under tension-torsion testing on [001] oriented specimens at room temperature. Eight strain gauge rosettes were attached along the circumference as above. One of them is located near a <100> direction, the others were regularly disposed. Axial and torsional strains were also measured by means of an axial-torsional extensometer attached to the specimen near [010]. Figure 11 shows the results of the strain gauges in the axial direction and at 45°. Different tension-torsion loading paths were measured. As can be seen in this diagram, the deformation is found to be non-uniform and non symmetrical. There are two 'soft' regions. When tension becomes predominant, quasi – uniform straining is obtained only in the axial directions.

These findings were confirmed by yield surface tests, Figure 12. The surface was determined by following radial (proportional) stress paths from the origin with an axial-torsional extensometer attached at different positions along the circumference. A small von Mises equivalent strain offset of yielding, ~ 10^{-5}mm/mm was selected. Octahedral slip (oblique segments) and cube slip (horizontal segments) are both involved in this diagram. The experiments prove, Figure 12a, that there is a non-uniform inelastic strain distribution along the circumference of <001> orientated specimens due to different slip systems (octahedral and cube slip). However, the assumption of homogeneous stresses in the specimen lead to the same experimental yield surfaces, Figure 12b. This diagram also confirms that a quadratic expression [*14, 15*] of a macroscopic yield criterion is not acceptable for a single crystal.

Summary

This study has demonstrated the versatility of the life prediction assessment. It can be applied to any arbitrary temperature-strain phasing. The sinusoidal TMF-time histories show the greatest inelastic works and result in the fewest cycles to failure. The scatterband with a N_f – width-factor is nearly the usual of 2.0.

Complex TMF cycle tests representing strain temperature time profiles in critical regions of a blade gave longer lives than simple linear TMF tests. Since this high-temperature deformation occurs at larger compressive strains, a shift in mean stress is seen in all tests. The approach used to describe fatigue with linear TMF cycles can therefore be expected to be conservative.

The damage on IN 738 LC is effectively only of crack propagation analysis, the crack closure effect has been recognized and the effective stress intensity has been used to describe the crack growth rate.

Since the saturated state of IN 738 LC is independent of the thermomechanical straining path, the maximum saturation stress range and the limiting values produced by linear straining paths. It is thus reasonable to conclude that in this case, simple TMF data are sufficient to evaluate some complex TMF cycles.

It was verified by experiments that the von Mises hypothesis is altogether applicable to the deformation behavior of IN 738 LC at TMF loading.

Initial experiments on single-crystal superalloy SC 16 prove that there is a non-uniform strain distribution in the plastic region along the circumference of [*001*]

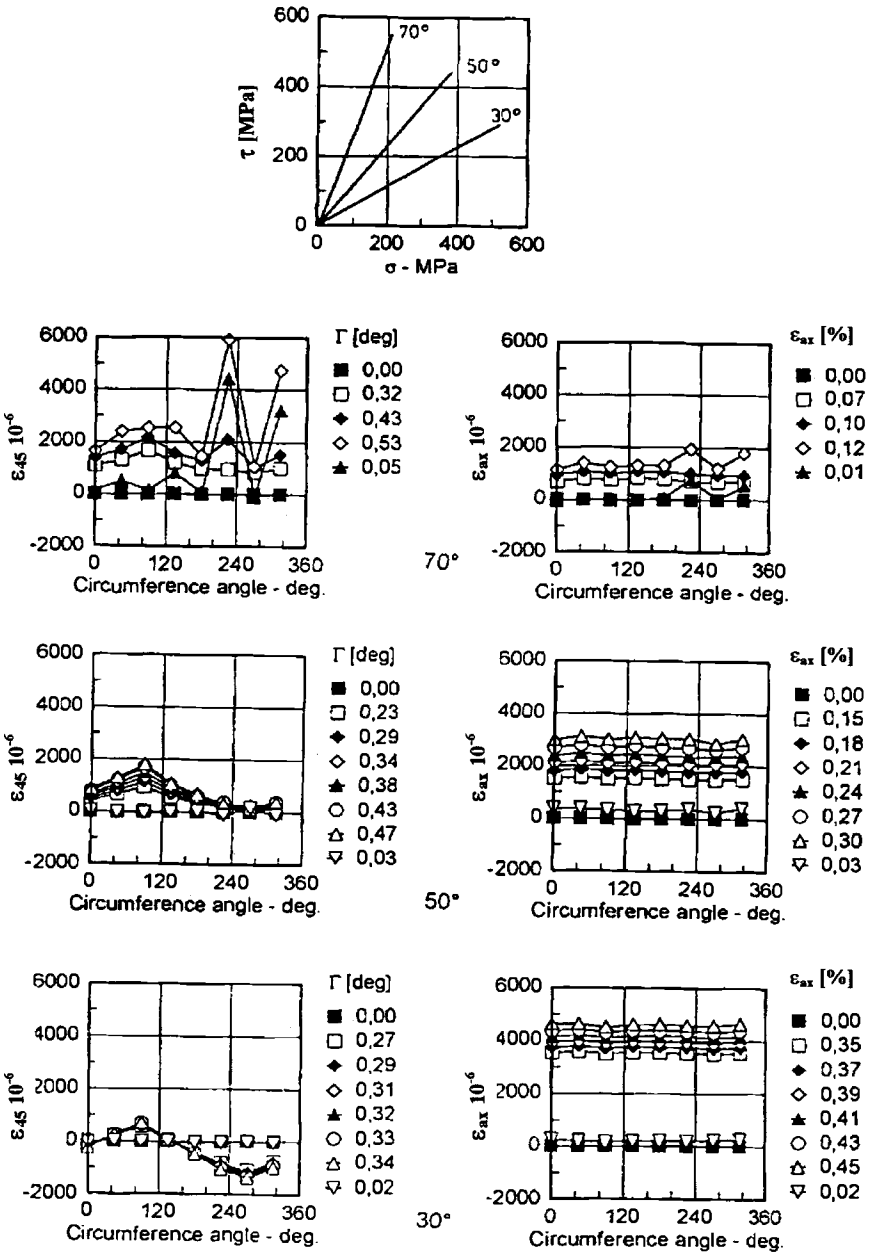

Figure 11

Readings of eight strain gauge rosettes in the axial direction and at 45° versus the circumference angle in dependence of the loading paths 30°, 50°, 70° (at the top)

a

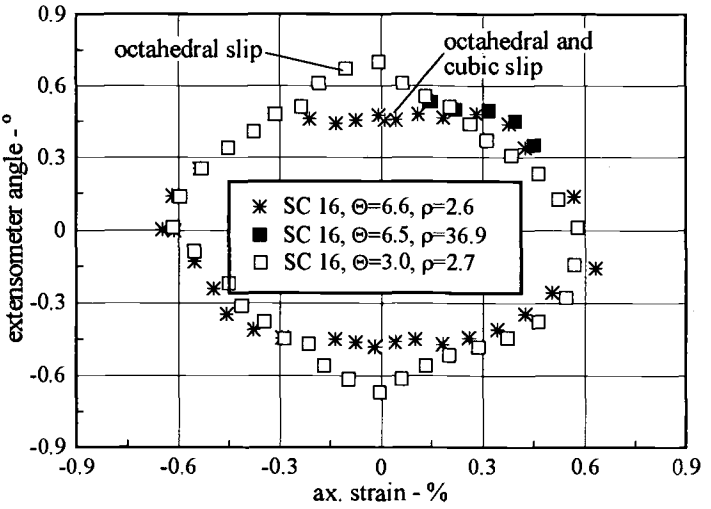

b

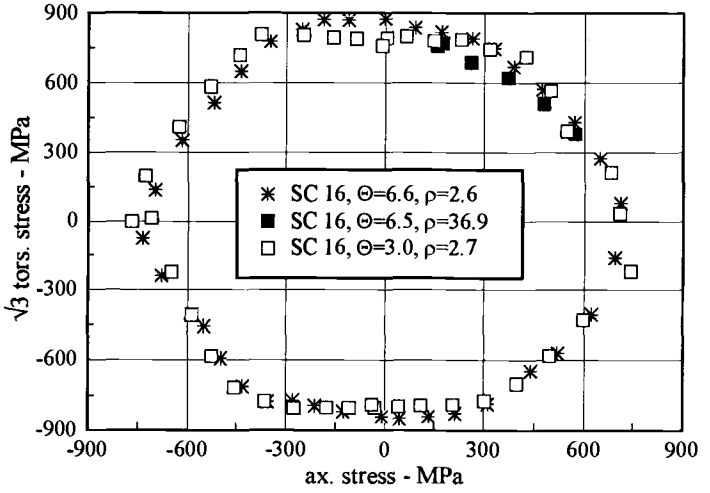

Figure 12

Yield surfaces of a [001] oriented specimens, a) applied axial-torsional strain paths, extensometer at different positions along the circumference; b) shear stress-axial stress plane (Θ, ρ: orientation of the crystal axes in terms of the angles Θ and ρ in the stereographic triangle)

orientated specimens under torsion or tension-torsion loading. This fact must be weighed when exact TMF tests are performed. The behavior reported can be explained in terms of slip on a finite number of slip systems.

Acknowledgments

The study presented here is part of an extensive investigation into IN 738 LC and SC 16 under multiaxial states of stress and temperature history. The financial support for this research, provided by Deutsche Forschungsmeinschaft (DFG), is gratefully acknowledged.

References

[1] Russel, E. S., "Practical Life Prediction Methods for Thermal-Mechanical Fatigue of Gas Turbine Buckets", *Proc. Conference on Life Prediction for High-Temperature Gas Turbine Materials*, V. Weiss and W.T. Bakker, Eds., EPRI AP-4477, Electric Power Research Institute, Palo, Alto, CA, 1986, pp. 3-1 – 3-39.

[2] Kuwabara, K., Nitta, A., Kitamura, T., "Thermal-Mechanical Fatigue Life Prediction in High-Temperature Component, Materials for Power Plant", *Proc. of the ASME International Conference on Advances in Life Prediction Methods*, Albany, NY, 1983, pp. 131 – 141.

[3] Bernstein, H.L., Grant, T.S. McClung, R.C., Allen, J.M., "Prediction of Thermal-Mechanical Fatigue Life for Gas Turbine Blades in Electric Power Generation", *Thermo-mechanical Fatigue Behaviour of Materials, ASTM STP 1186*, H. Sehitoglu, Eds., American Society for Testing and Materials, Philadelphia, 1993, pp. 212 – 238.

[4] Ziebs, J., Meersmann, J., Kühn, H.-J., Ledworuski, S., "High Temperature Inelastic Deformation of IN 738 LC under Uniaxial and Multiaxial Loading", *Low Cycle Fatigue and Elasto-Plastic Behaviour of Materials - LCF 3*, K.T. Rie, Eds., Elsevier Applied Science, 1992, pp. 248 – 255.

[5] Meersmann, J., Ziebs, J., Kühn, H.-J., "The Thermo-Mechanical Behaviour of IN 738 LC", *Materials for Advanced Power Engineering, Part I*, D. Coutsouradis et al, Eds., Kluwer Academic Publishers, 1994, pp. 841 - 852.

[6] Swanson, G.A., Linask, J., Nissley, D.M., Norris, P.P., Mayer, T.G., Walker, K.P., "Life Prediction and Constitutive Models for Engine Hot Section Anisotropic Materials Program", *NASA Report 179594, National Aeronauties and Space Administration*, Washington, D.C., 1987.

[7] Remy, L., Bernard, H., Malpertu, I.L., Rezai-Aria, F., "Fatigue Life Prediction unter Thermal-Mechanical Loading in a Nickel-Base Superalloy", *Thermomechanical Fatigue Behaviour of Materials for Testing and Materials, ASTM STP 1189*, H. Sehitoglu, Eds., ASTM, Philadelphia, 1993, pp. 3 – 16.

[8] Neu, R.W. and Sehitoglu, H., "Thermomechanical Fatigue, Oxidation and Creep: Part I. Damage Mechanisms, and Part II. Life Prediction", *Metallurg. Transactions A.*, vol. 20 A, 1989, pp. 1769 – 1783.

[9] Bakis, C.E., Castelli, M.G., Ellis, J.R., "Thermo-Mechanical Behaviour, Advances in Multiaxial Fatigue", *ASTM STP 1191*, D.L. Mc Dowell and R. Ellis,

Eds., American Society for Testing and Materials, Philadelphia, 1993, pp. 223 – 243.

[10] Socie, D., "Critical Plane Approaches for Multiaxial Fatigue Damage Assessment", *Advances in Multiaxial Fatigue, ASTM STP 1191*, D.L. Mc Dowell and R. Ellis, Eds., American Society for Testing and Materials, Philadelphia, 1993, pp. 7 – 35.

[11] Manson, S.S., Halford., G.R., "Discussion, Multiaxial Low Cycle Fatigue of Type 304 Stainless Steel", *J. Eng. Mat. Techn., ASME*, vol 99, 1971, pp. 283 – 286.

[12] Chin., G.Y., Mammel, W.L., "Computer Solution of the Taylor Analysis for Axisymmetric Flow", *Transactions Metallurg. Soc. AIME*, vol. 239, 1967, pp. 1400 – 1405.

[13] Nouailhas, D., Cailletaud, G., "Tension-Torsion of Single Crystals Superalloys: Experiment", *Int. J. Plasticity*, vol. 11, No. 4, 1995, pp. 451 – 470.

[14] Hill, R., "A Theory of the Yielding and Plastic Flour of Anisotropic Metals", *Proc. of the Royal Society of London, Series A*, 1948, pp. 281 – 297.

[15] Lee, D., Zaverl, F., "A Generalized Strain Rate Dependent Constitutive Equation for Anisotropic Metals", *Acta Metallurgica*, 1978, pp. 1771 – 1780.

Masakazu Okazaki [1] and Hiroshi Nakatani [2]

On the Significance of Environment in Thermal Fatigue of a Unidirectional SCS-6/Ti-24Al-11Nb Metal Matrix Composite

Reference: Okazaki, M. and Nakatani, H., **"On the Significance of Environment in Thermal Fatigue of a Unidirectional SCS-6/Ti-24Al-11Nb Metal Matrix Composite,"** *Thermo-mechanical Fatigue Behavior of Materials: Third Volume, ASTM STP 1371,* H. Sehitoglu and H. J. Maier, Eds., American Society for Testing and Materials, West Conshohocken, PA, 2000.

Abstract: Thermal Fatigue tests of a Ti-24Al-11Nb matrix composite unidirectionally reinforced with SiC fiber, SCS-6/Ti-24Al-11Nb, have been carried out without external load in air and in vacuum, under various thermal cycling conditions. The following characteristics of the material subjected to thermal fatigue and isothermal exposure were investigated: (i) crack nucleation and the change in density with thermal cycling; (ii) change of the fiber/matrix interface morphology by means of Electron Probe Micro Analyzer and Scanning Electron Microscope; (iii) change of the interfacial shear strength by fiber push-out tests, and (iv) effect of environment on the properties from (i) to (iii). Methodologies are also proposed for the characterization of damage due to thermal fatigue.

Keywords: Ti-24Al-11Nb matrix composite, SiC fiber, thermal fatigue, push-out test, interfacial shear strength, environment, depletion of carbon coating, crack density, damage assessment.

Introduction

Titanium alloy metal matrix composites (MMCs) have received considerable interest as materials for severe service conditions, because they generally possess many attractive characteristics: higher specific strength at high temperature and higher specific stiffness, compared with traditional monolithic materials [1,2]. For example, when this kind of MMC is applied to discs and blades in aero engines, up to a 70 % weight savings can be achieved, compared with the conventional components [2]. Thus, for the last decade many studies have been carried out to gain informa-

[1] Professor, Department of Metallurgy, The University of Tokyo, Hongo 7-3-1, Bunkyo-ku, Tokyo 113-8656, JAPAN.

[2] Chief Researcher, Gifu Technical Institute, Kawasaki Heavy Industries Ltd., Kakamigahara, Gifu 504-8710, JAPAN.

tion on mechanics and the mechanisms against several kinds of failures; fracture toughness under quasi-static loading [*3-5*], fatigue [*6,7*] and creep [*8,9*]. When applying MMCs at elevated temperatures, special considerations should be also paid to thermal stress which results from mismatches in elastic moduli and thermal expansion coefficient between the matrix and reinforcement [*3*], and the resultant thermal fatigue. Many efforts, therefore, have been made to understand thermal fatigue failure [*10-18*]. When MMCs were subjected to thermal cycling, significant reductions in retained tensile strength [*10, 15-17*], fracture strain [*15-17*], elastic properties [*15-18*] and resistance to stable crack growth [*18*] have been observed. On the other hand, many works to quantify the interfacial strength have been also conducted, because interfacial strength plays an intrinsic role in the above mechanical properties in most cases [*19-22*]. One of the typical evaluation methods is the fiber push-out test [*19-21*]. However, there still remain many problems to be clarified, regarding as thermal fatigue: for example, how the thermal fatigue damage should be defined and assessed; what is the relation between thermal fatigue damage and the interfacial strength; and how thermal fatigue life and the remaining life should be predicted.

In this work, thermal fatigue tests of a unidirectional SiC fiber reinforced Ti-24Al-11Nb matrix composite, SCS-6/Ti-24Al-11Nb, were carried out without external load in air and vacuum, under various thermal cycle conditions. The study explores the following: crack initiation and the change in crack density during thermal cycling; chemical analysis of regions near the matrix/fiber interface by Electron Probe Micro Analyzer (EPMA) and Scanning Electron Microscope (SEM); and interfacial shear strength changes via fiber push-out tests. Mechanistically-based mechanics models are presented for the assessment of damage.

Experimental Procedures

Material and Specimen

A Ti-24Al-11Nb matrix composite reinforced uni-directionally with continuous SiC fibers was investigated in this work. The fiber is a β-SiC fiber of 140 μm average diameter with a carbon rich graded silicon carbide coating on the surface, which was produced by Textron Specially Materials, Lowell, MA. These fibers were commercially bought in a form of woven preform. The 7-plies composite sheet of 180x40x1.5 mm was produced at Kawasaki Heavy Industries Co. Ltd., Kakamigahara, Gifu, Japan, by hot pressing at 1050℃ for 2 hrs. in vacuum alternating layers of thin-foils of the Ti-24Al-11Nb alloy and green tapes of the SCS-6 fibers so that the fibers were uniformly distributed as a hexagonal array in the matrix. The volume fraction of the fibers in the composite is about 33 %. The composite microstructure is given in Fig. 1. The detail of fiber/matrix interface will be given later.

From the composite sheet, plate specimens as illustrated in Fig. 1 were taken out by electro-discharge machining, with the SiC fibers aligned parallel to the longitudinal (60 mm) direction of the specimen. The gauge section of the specimen is the 10x30x1.5 mm portion of the plate center. The specimen surfaces were polished on a disc grinder. Some of fibers on the side and bottom surfaces (with 60x1.5 mm and 10x1.5 mm cross

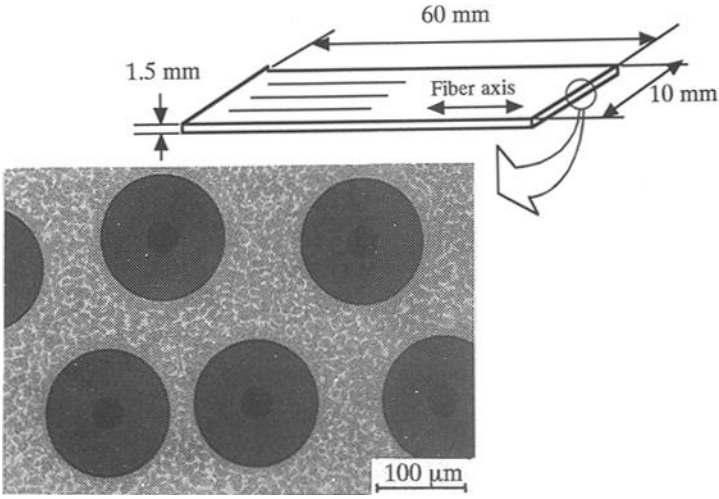

FIGURE 1 — *Thermal Fatigue Test Specimen and Composite Microstructure*

TABLE 1 —*Summary of Thermal Cycling Conditions.*

Condition	T_{max}* (°C)	T_{min}* (°C)	ΔT* (°C)	Environment	Heating rate (°C/s.)	Cooling rate (°C/s)
Condition A	450	150	300	vacuum	5.0	17.5
				air	5.0	11.1
Condition B	700	400	300	vacuum	5.0	18.5
				air	5.0	7.3
Condition C	700	150	550	vacuum	5.0	23.7
				air	5.0	14.7

sections, respectively) were directly exposed to air. However, the fibers were fully covered with the matrix within the bulk of the specimens which had rectangular 60 x 10mm cross sections.

Test Equipment and Test Program.

According to the test program summarized in Table 1, thermal fatigue tests were carried out by exposing the specimen (Fig. 1) to thermal cycling in vacuum and air, respectively, by means of a test equipment produced by authors [*18*]. The thermal cycles was repeated upto about 10^4 in maximum. In order to study the effect of

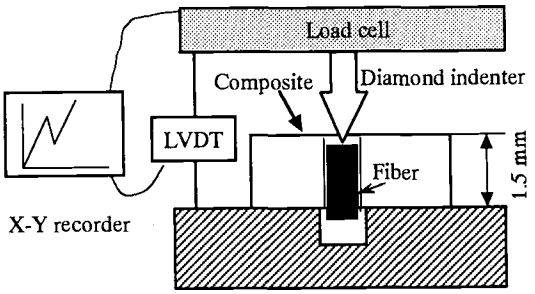

FIGURE 2 — *Push-out Test Apparatus*

environment the tests were performed not only in air but also in vacuum (10^{-3} Pa approximately). The test equipment consists of a high frequency induction heating system for heating, a heating tube in which the specimen was put and indirectly heated, and an air compressor for cooling in the tests conducted in air. During the thermal cycling the specimen was heated linearly by the induction heating system, and then cooled by controlling the compressed air flow into the heating tube in the air tests. In the vacuum tests, on the other hand, the specimen was cooled naturally. Thus, the cooling rate was not controlled constant strictly in the vacuum and air tests, hence, the cooling rates in Table 1 are merely average. However, effort was made in producing the heating tube, which allowed to obtain uniform temperature distribution within 5 ℃ on the specimen gauge section and to achieve almost linear cooling. This was performed by changing the heat capacity of the heating tube. The difference in the cooling rate between the vacuum and air tests in Table 1 is due to the difference of the heating tube. During the thermal cycling the temperature was monitored with three pairs of thermocouples that were spot welded directly onto the specimen gauge section. One of the thermocouples at the center portion of specimen gauge section was used to control the specimen temperature.

No external load was applied during the thermal cycling; thus, thermal stress is induced from the mismatch between the matrix and the fiber. The test condition in Table 1 was planned to investigate the effects of temperature range, ΔT, and maximum temperature in thermal cycling, T_{max}, on thermal fatigue damage. When the composite material is exposed to thermal cycling after the fabrication, thermal (i.e., residual) stress might be produced in the present composite in the following manner, on the basis of the fabrication point: while the material was processed at 1050℃, any residual stress while cooling from 1050℃ to the homologous temperature would be relieved due to significant creep of the matrix [*15*]. The homologous temperature of the present matrix alloy is approximately 600 ℃[*9,15*]. While cooling from 600 ℃ to room temperature no relaxation of residual stress occurs, thus the residual stress is produced in the composite. When the composite is heated up again during the thermal fatigue test, the residual stress is reduced depending on the thermal cycle condition. The stress in the matrix under the present thermal fatigue test is estimated (see Table 3), according to elastic analysis in Ref. 3 and assuming the homologous temperature being

TABLE 2 — *Mechanical Properties Used to Calculate Thermal Stress*

	Matrix			Fiber		
Temperature (℃)	E* (GPa)	ν*	α* (/℃)	E* (GPa)	ν*	α* (/℃)
R.T.	93.8	0.32	9.45 x 10^{-6} [22]	400 [15]	0.25 [15]	4.86 x 10^{-6} [15]
150 ℃	90.2					
400 ℃	77.5					
450 ℃	76.5					
550 ℃	72.2					

* E: Young's Modulus ν: Poisson ratio
α: Thermal expansion coefficient

TABLE 3 — *Estimation of Hoop and Axial Stresses in Matrix at Interface, σ_θ and σ_z, during the Thermal Cycle*

Condition	σ_θ at T_{max} (MPa)	σ_θ at T_{min} (MPa)	σ_z at T_{max} (MPa)	σ_z at T_{min} (MPa)
A	67	235	58	206
B	0	109	0	96
C	0	245	0	215

homologous temperature is assumed 600 ℃.

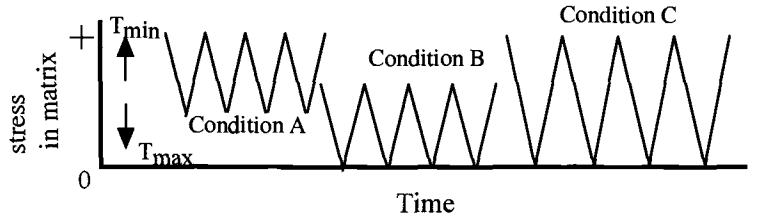

600 ℃. Table 2 displays the fiber and matrix properties used for this calculation [*15,22*], where most of mechanical properties are approximated constant independently of temperature, except Young's modulus of the matrix alloy. Note in Table 3 that the hoop stress in the matrix at the interface, σ_θ, and the axial stress along the fiber axis, σ_z, are always positive and that the former is slightly higher than the latter. The both σ_θ and σ_z increase as the specimen temperature goes down.

During the thermal fatigue tests, fatigue crack initiation and the change in density with thermal cycling was monitored by replicating the specimen surface within the gauge section with acetyl cellulose film. The fiber/matrix interface characteristics of the composite subjected to thermal cycling were also investigated by SEM and EPMA, with particular attention being paid to oxidation and chemical reactions.

Furthermore, fiber push-out tests [*19-21*] were also carried out to measure the change of interfacial shear strength of the composite with thermal fatigue, by means of an Akashi hardness tester (Model AVK) to which a diamond indenter was attached (Fig. 2). The indenter has a pyramidal angle of 136° and a 0.2x0.2 mm square basal plane, respectively. The fiber push-out test pieces with 1.5x1.5x8 mm were extracted from the mid-sections of the specimen subjected to thermal fatigue. The loading rate in the push-out test was approximately 10 N/s.

Results and Discussions

Cracks Induced by Thermal Cycling

As shown in Fig. 3, the following types of visible cracks were nucleated around the fiber by thermal cycling: the first is the longitudinal crack along the fiber/matrix interface parallel to the fiber axis; the second is the transverse, or circumferential crack in matrix normal to the fiber axis; and the third is the fiber breakage. The fiber breakage was very rare under the all test conditions. The first and second types of cracks are originated by σ_θ and σ_z, respectively. Damage progressed accompanied with the small crack initiation, the increase in density and the linkage with the thermal cycles, i.e., the fracture was not lead only by a few major cracks. Hence, it was difficult to quantitatively express the damage evolution by the crack growth rate, as in monolithic metallic materials. The extent of the damage was therefore quantified by the measurement of crack density with the surface replication technique. In this work the line density, D_L, was defined by

$$D_L = \Sigma(a_i) / A \qquad (1)$$

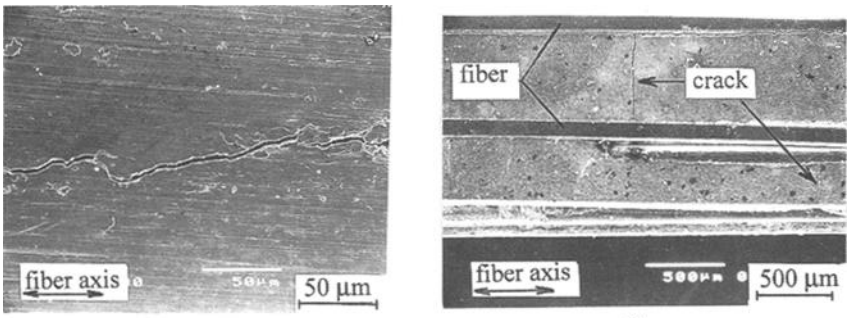

FIGURE 3 —*Cracks Nucleated by Thermal Fatigue: (a) Longitudinal Crack, (b) Transverse Crack*

where the $\Sigma(a_i)$ and A are the sum of crack length, and the measurement area, respectively. D_L expresses the sum of the crack length per unit area (hereinafter, D_L is called the crack density, for simplicity.). The changes of D_L of the longitudinal cracks and that of the transverse cracks is shown in Fig. 4. The followings can be pointed out from Fig. 4:

(i) Generally the crack initiated at an early stage of thermal cycling not only in air but also in vacuum. The density increased with increasing number of thermal cycles. These behaviors were the most pronounced under Condition C(; T_{max}=700℃, ΔT=550℃. Refer to Table 1.).

(ii) It is not easy to justify the effect of environment on thermal fatigue crack initiation, because some conflicting trends are found: for example, focusing on the longitudinal crack density given in Fig. 4(a), air atmosphere appears to accelerate the crack initiation under condition C cycling, however, the trend is contrary under the condition A (Fig. 4(a)). Under the condition B, the effect of environment is opposite between the both types of crackings; longitudinal and transverse crackings (compare Fig. 4(a) and Fig. 4(b)).

(iii) The longitudinal and transverse crack densities appear to vary with thermal cycling, interacting with each other (compare Fig. 4(a) and Fig. 4(b)). Under the condition C, for example, since the longitudinal cracking occurred previously in air, the transverse cracking seems to be relatively inferior, and vice versa under the condition B.

The reason of the feature (i) is due to the most severity of the thermal stress in the condition C (see Table 3). The effect of environment seen in the feature (i) is contrary to the results by Revelos et al. [*16*] showing that no interface-initiated cracking was formed in an inert atmosphere. The feature (iii) is attributed to the essence of mechanics of thermal stress: σ_θ and σ_z are not independent, and once one type of crack initiates the other type of crack can no longer evolve around there because of the local reduction of thermal stress. The synergetic effect between the feature (iii), maximum value of thermal stress, thermal stress range, test environment and the release of thermal stress due to cracking must make the feature (ii). While the features (i) supports that the crack density is a useful parameter to evaluate the thermal fatigue damage, the features (ii) indicates a limited ability of this parameter. It is also worthy to note that the crack density given in Fig.4 is no more than a parameter reflecting the surface damage.

Microstructural Morphology of Interface

A SEM micrograph of the matrix/fiber interface of the as-fabricated material is presented in Fig. 5, along with the result of the EPMA analysis. A carbon rich coating of a few micrometers in thickness, which had been originally deposited to achieve full strength by healing surface flaws of the fiber and to protect from the reaction with the matrix during the consolidation process of the composite [*23*], is found on the fiber surface in Fig. 5. The reaction layer, which consists of at least two layers, can be also identified between the carbon coating and the matrix. The thickness of inner and outer reaction zones are about 0.5 μm and 1.0 μm, respectively. The reaction zones have been shown by Baumann to be composed of $(Ti,Nb)C_{1-x}$

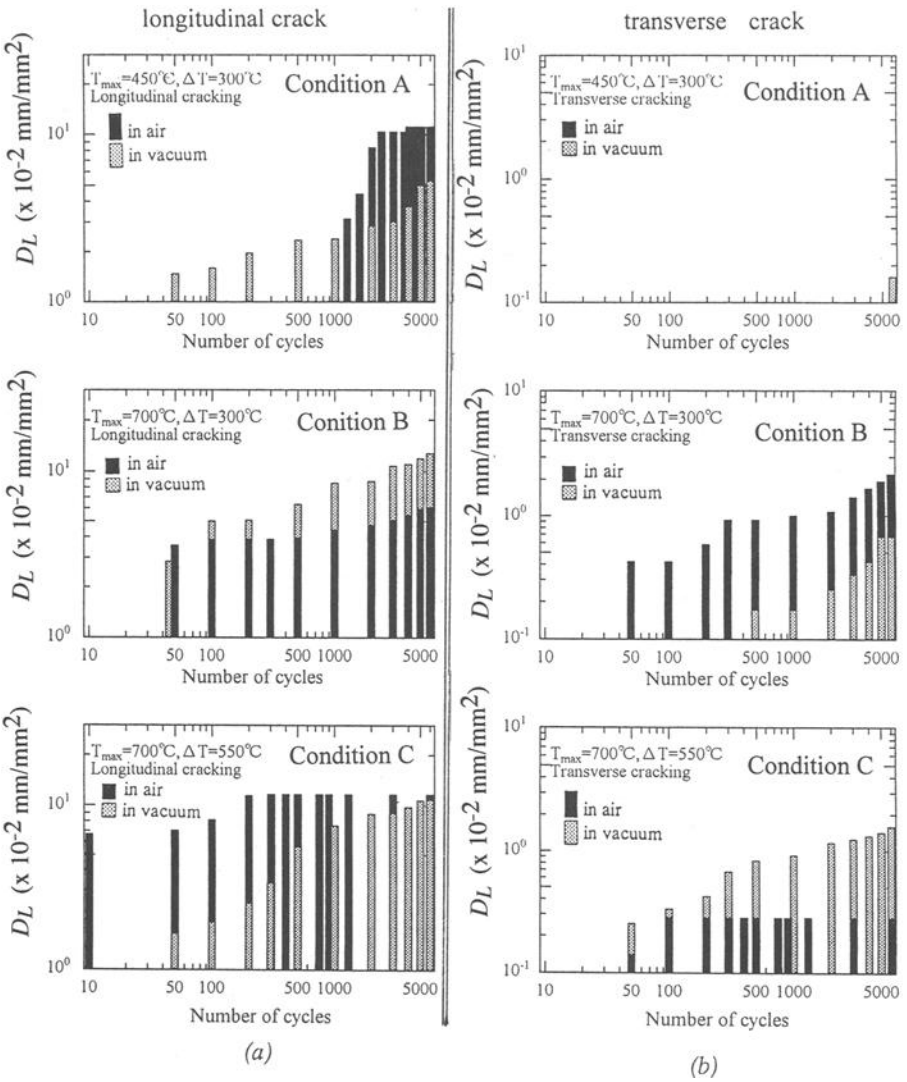

FIGURE 4 — *Change of Crack Density with Thermal Cycling: (a) Longitudinal Crack, (b) Transverse Crack*

+ $(Ti,Nb,Al)_5Si_3$, and $(Ti,Nb)_3AlC$ + $(Ti,Nb,Al)_5Si_3$ in a similar composite system [*23*].

When the material was subjected to either thermal cycling or isothermal exposure in air, some important changes were found in the interfacial regime, as shown in Figs. 6 (a) and (b). It is important to note that all of the above observations were carried out on pieces that were extracted from the mid-sections of specimens that were not

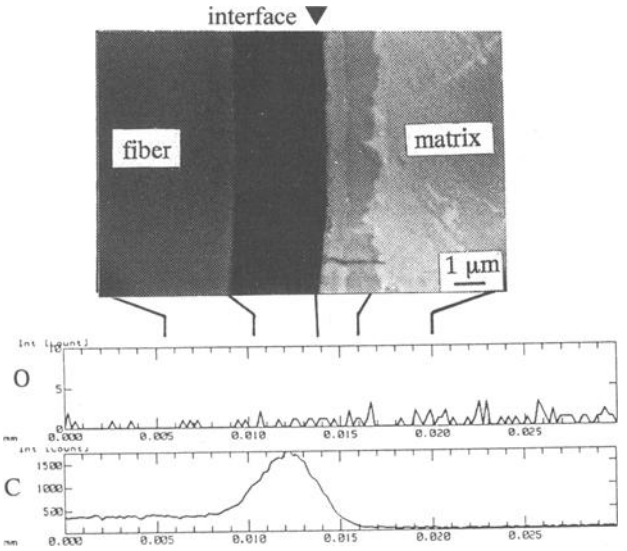

FIGURE 5 — *Microstructural Morphology of Interface and the EMPA Analysis of As-fabricated Material*

physically exposed to air. When the thermal cycling of the condition A in 6000 cycles was given to the material in air (Fig.6(a)), a significant increase of oxygen intensity was found near the fiber/matrix interface, while the C-rich coating was still identified on the fiber surface. This suggests that oxidation would get aggressive prior to the depletion of C coating during the thermal cycling, when maximum temperature of thermal cycling is relatively low. On the other hand, when the material was subjected to 6000 thermal cycles under the condition C (Fig. 6 (b)), not only the increase of oxygen intensity but also the depletion of C coating emerged. The similar damage were also observed in the case of the isothermal exposure at 700℃ for 200 hrs in air. It is also important to not in Fig. 6(b) that there is a physical clearance between the fiber and reaction layer. This is accordance with the severe cracking shown in Fig. 4.

In vacuum, however, any chemical changes near the interface were not observed in this work, even when the thermal cycling of the condition C, the most detrimental condition, was applied to the material for 6000 cycles. This was also the case in the isothermally aged material at 700℃ for 200 hrs in vacuum.

From these observations, it is confirmed that not only mechanical factors, such as thermal stress induced by thermal cycling, but also chemical factors; oxidation and depletion of carbon coating, play an important role in thermal fatigue failure in this composite.

Change of Interfacial Shear Strength

While the crack density measured in the previous section is a good scalar measure

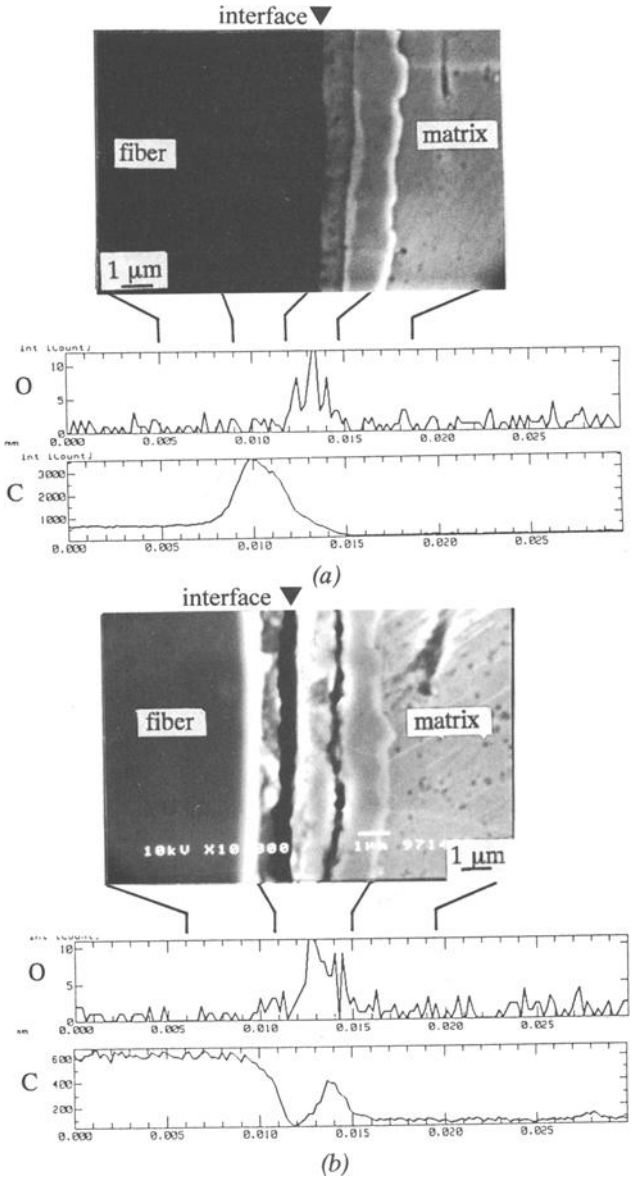

FIGURE 6— *Microstructural Morphology of Interface and the EMPA Analysis: (a) Condition A, 6000 cycles, in Air, and (b) Condition C, 6000 cycles, in Air*

of visible damage, it should be recognized that it may not provide an indication of the extent of damage inside the bulk of the material: i.e., damage inside of the material

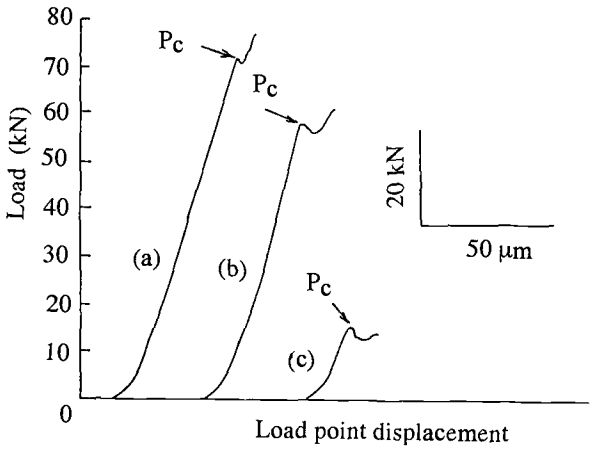

FIGURE 7— *Typical Load-Load Point Displacement Curves in Push-out Test: (a) As-fabricated Material, (b) Condition A, 6000 cycles, in Air, and (c) Isothermal Exposure, 700℃ in Air for 200 hrs.*

may not always evolve in the same manner as surface damage. On the other hand, it is also difficult to determine quantitatively the change of interface morphology shown in Fig. 6. In other words, another more sophisticated parameter is necessitated to assess the thermal fatigue damage. Thus, the interfacial shear strengths of the composites were determined by conducting fiber push-out tests at room temperature.

Some typical curves of load versus load point displacement in the push-outs are presented in Fig. 7. When the load reaches a critical value, P_c, load temporarily drops. This drop corresponds to the onset of debonding and sliding of the fiber. The interfacial shear strength, τ_{cr}, was simply determined from the P_c:

$$\tau_{cr} = P_c / (\pi \cdot d \cdot L) \qquad (2)$$

where d and L are the diameter of fiber and the length in the push-out test specimen, respectively. Strictly speaking, the fiber diameter would be possibly changed due to thermal cycling. In addition nobody can prove the uniform fiber extrusion along the interface during the push-out test. However, it is too difficult to quantitatively evaluate these matters. Thus, d and L in Eq. (2) are simply represented by the original fiber diameter and the specimen length in this work (0.14 mm and 1.5 mm, respectively).

It is natural that interfacial shear strengths should involve statistical scatter. In the present paper a Weibull function was assumed to hold. The distribution of interfacial shear strengths of the composite materials subjected to the isothermal exposure is given in Fig. 8 on a Weibull diagram, compared with that of the as-fabricated material. As can be seen in Fig. 8, the distribution of interfacial shear strength of the as-fabricated material can be well approximated by the Weibull function. The average of the as-fabricated material is approximately 100 MPa. This value is not either high or low, compared with the values in the same kind of composite [*7,21*]. When the material was isothermally exposed at 400℃ in air at which the carbon rich coating still remained on

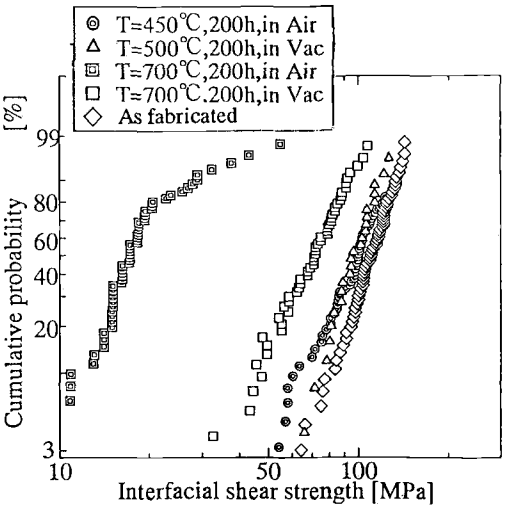

FIGURE 8 — *Change of Interfacial Shear Strength due to Isothermal Exposure*

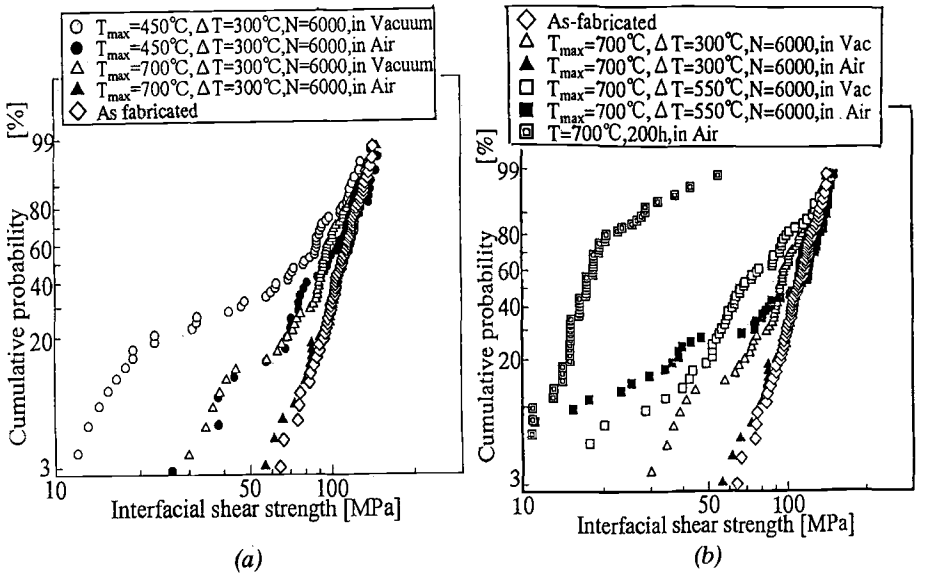

FIGURE 9 — *Change of Interfacial Shear Strength due to Thermal Cycling: (a) Conditions A and B, (b) Conditions B and C, and Isothermal Exposure*

the fiber surface, τ_{cr} is almost identical to that of the as-fabricated material. However, when the exposure temperature was higher, i.e., 700℃, the reduction of τ_{cr} was remarkable. Note that the depletion of the carbon coating was significant under this

condition (see Fig.10(b) shown later). It is worth noting that τ_{cr} changes in such a manner that the distribution of τ_{cr} shifts to the left hand side parallel to the abscissa; i.e. the τ_{cr} is reduced as a whole. This is a unique feature which was not be seen in the change due to thermal fatigue, as documented later. It should be also remarked in Fig. 8 that τ_{cr} is changed little when the material was isothermally aged in vacuum.

For simplicity τ_c is often expressed in the form [*3*]

$$\tau_{cr} = \mu \cdot \sigma_r + \tau_{re} \qquad (3)$$

where μ, σ_r and τ_{re} are the frictional coefficient between fiber and matrix, the interface pressure, and the bonding strength of the interface. Therefore, the thinning of carbon coating due to isothermal exposure results in a straightforward reduction of σ_r in Eq.(3) and hence the reduction of τ_{cr}.

When the material has experienced the thermal cycling, τ_{cr} was also varied, as shown in Figs.9(a) and (b). However, τ_{cr} reveals some interesting changing behaviors different from the one due to isothermal exposure, as follows. The first is that the change of τ_{cr} apparently emerges in the change of slope on the Weibull diagram; i.e. a change in the shape parameter in the Weibull function. This indicates the scatter of τ_{cr} became large by applying thermal cycling. As will be noted later (Fig. 11), the above change in slope may depend on the degree of thermal fatigue cracking. The second feature is that the change of τ_{cr} is found not only in air but also in vacuum: e.g., see the symbols △ and ▲ in Fig. 9(a), and □ and ■ in Fig. 9(b). The third noteworthy feature relating to the second feature is that the τ_{cr} of specimens subjected to thermal cycles in air is generally higher than that in vacuum; compare symbols △ and ▲, and ○ and● in Fig. 9 (a). This is apparently conflicting with the feature found in Fig. 8, which shows that isothermal exposure in air lowers the interfacial shear strength by the depletion of carbon coating. This point will be discussed later. The fourth one is that, as can be noted in Fig. 9(b) from the comparison between the materials subjected to isothermal exposure and thermal cycling in air (denoted by ▣ and ■, respectively), the former exhibits interfacial strengths lower than the latter, even when the exposure times are comparable. The fifth important feature is that, under the same maximum temperature in thermal cycle, the higher the temperature range, ΔT, is , the more the degradation of τ_{cr} is; compare between △ and □, and between ▲ and ■ in Fig. 9(b).

As already shown in Fig. 3, several types of cracks were nucleated under thermal cycling. After the cracks are nucleated, the thermal stress and the residual stress, σ_r in Eq. (3), should be reduced. This should result in a decrease of τ_{cr}. Thus, the above fifth feature can be reasonably interpreted by the severity of thermal stress (compare the thermal stresses between the conditions B and C, referring to the schematic illustration in Table 1.). The second feature also correspond to the results in Fig. 4, showing that the thermal fatigue crack originated not only in air but also in vacuum in a comparable density. On the other hand, the degree of thermal fatigue cracking may not be always uniform everywhere: the severer the degree of cracking is, the more the reduction of τ_{cr} should be. Hence, the above first feature can be also justified to be relevant to the inhomogeneous fatigue cracking. The reason why the changing behavior of τ_{cr} due to thermal fatigue is somewhat different from that due to isothermal exposure

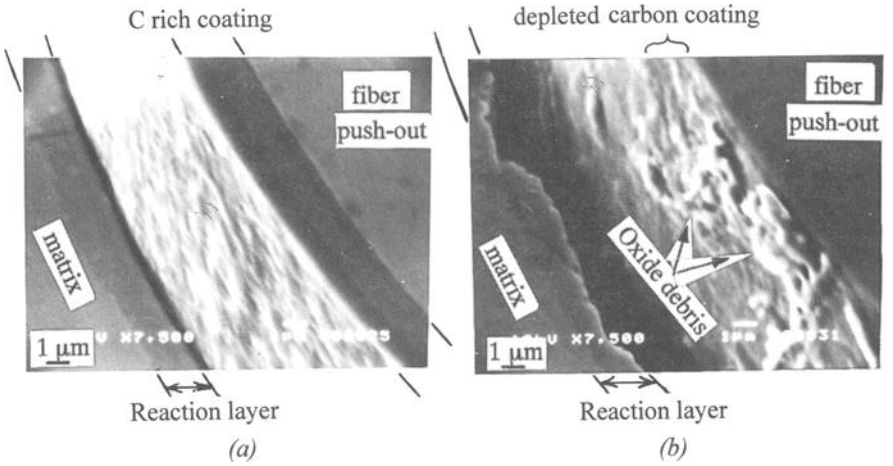

FIGURE 10— *Fibers Pushed-out from Matrix: (a) As-fabricated Material, (b) after Isothermal Exposure at 700℃ in Air for 200 hrs.*

(Fig. 8) is considered to be attributed to homogenity of damage: more homogeneous in the latter. The cause of the third feature will be discussed later.

Figures 10(a) and (b) present the fiber surface after the push-out test. Most of the fibers in the as-fabricated material were protruded at the carbon coating/reaction layer boundary; Fig.10 (a). Similar features were observed in almost all of the materials subjected to thermal cycling, when the maximum temperature was relatively low. On the other hand, when the material was exposed to the isothermal aging at higher temperature in air, or at 700℃ for 200 hrs. under which the carbon coating disappeared dramatically, the fiber surface can be seen directly, as shown in Fig. 10 (b). Oxide product which seems to promote the fiber asperity is also adhered on the fiber surface. Although the roughness of the fiber surface was not measured in this work, it is easy to suppose the asperity contact between the fiber and matrix in Fig. 10 (b), compared with Fig. 10 (a). The similar asperity to Fig.10(b) was also observed in the thermal fatigue test specimen in air, especially at the region where the fiber was bared due to the fatigue cracking.

Both the naked fiber and the adherence of oxide product on it in Fig. 10 (b) are likely to increase the frictional coefficient, μ, in Eq. (3), resulting in the increase of τ_{cr}. In the other words, air atmosphere which depletes the carbon coating on the fiber surface may have two conflicting roles: to increase τ_{cr} due to the increase of μ resulting from the asperity contact and the lack of lubricant, and to decrease resulting from the reduction of σ_r in Eq. (3). Hence, the third feature in Fig. 8 discussed above must be caused by the two conflicting phenomena.

Once τ_{cr} is degradated, it may lower the load transfer capability between fiber and matrix, resulting in the reduction of retained tensile strength of the composite[*10, 15-17*], fracture strain [*15-17*], elastic properties [*15-18*] and resistance to stable crack growth [*18*]. Therefore, it would be possible to correlate the change of τ_{cr} with that of the above mechanical properties. However, this need further quantitative study.

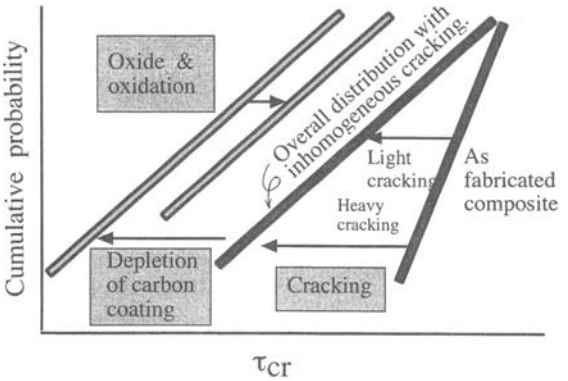

FIGURE 11— *Several Factors Contributing to the Change of Interfacial Shear Strength*

Many workers have confirmed that crack propagation behavior at the fiber/matrix interface strongly depends on how high τ_{cr} is [*19-22*]. According to the results by Fox et al. dealing with the similar kind of the composite [7], for example, while the crack propagation was significantly influenced by intact fiber bridging when it was about 80 MPa, the crack rapidly grew when τ_{cr} was high about 120 MPa. As shown in the previous section the thermal fatigue damage progressed accompanied with the small crack initiation and the increase in density, but not with a few major cracks. According to the measurements given in Figs. 8 and 9, τ_{cr} is no higher than 100 MPa in this work. It is considered that such a cracking manner is relevant to the level of τ_{cr}.

From the above arguments the changes in the interfacial shear strengths can be summarized as shown in the schematic in Fig. 11. Note that all the intrinsic thermal fatigue damages were largely reflected on the change of τ_{cr}. On the other hand, although the crack density can be easily measured on the surface and it is a good scalar measure of visible damage, it can only supply a limited information of the extent of damage inside the bulk of the material. Hence, the combination of two techniques is expected to provide more useful information on thermal fatigue life assessment and the remaining life estimation.

Conclusions

1. Thermal cycling results in interfacial crack nucleation. After crack nucleation, the crack density increases with increasing number of thermal cycles. The increase in crack density depends on the thermal cycle condition. Although the crack density is a good scalar measure of visible damage, it seemed difficult to quantitatively assess the damage only by this parameter.
2. The investigation on the fiber/matrix interface morphologies by means of SEM and EPMA revealed that environment played an intrinsic part in thermal fatigue damage, through the oxidation near the interface and the depletion of carbon coating on the fiber surface.

3. The interfacial shear strength of the composite, τ_{cr}, was significantly changed by applying the thermal cycling, depending on the test environment and on the temperature condition of thermal cycle. The value of τ_{cr} was also changed by the isothermal exposure in air. When the distribution of τ_{cr} was conventionally displayed on a Weibull diagram, the changes due to thermal fatigue and isothermal exposure emerged in a different manner: it did in the change of the shape parameter in the Weibull function in the former, and in that of scale parameter in the latter, respectively.
4. All the intrinsic thermal fatigue damages were reasonably reflected in the change of τ_{cr} in this work. Hence, useful information regarding thermal fatigue life assessment and estimation of remaining life may be provided by combing the measurements of interfacial strength and the crack density.

Acknowledgement

Authors express their great gratitude to the financial support by the Grant-in-Aid for scientific research by Japan Ministry of Education (No. 10555027).

References

[1] *Intermetallic Matrix Composites III,* Graves J.A., Bowman P.R. and Lewandoeski J.J. Eds., Material Research Society, PA, 1994.

[2] Ward-Close C.M. and Loader C., "PVD Processing of Fiber Reinforced Composites," *Recent Advances in Tatianium Metal Matrix Composites,* F.H. Froes and J. Storer Eds., TMS, Warrendale, PA, 1994, pp. 19-32.

[3] Budianski B., Hutchinson J. and Evans A.G., "Matrix Fracture in Fiber-Reinforced Ceramics," *J. Mech. Physc. Solids*, Vol. 34, 1986, pp. 167-189.

[4] Chiu H. and Yang J.M., "Effect of Fiber Coating On The Fracture and Fatigue Resistance of SCS-6/Ti_3Al Composites," *Acta Met.*, Vol. 43, 1995, pp. 2581-2587.

[5] Okazaki M., Tokiya M. and Nakatani H., "Stable Crack Growth and Damage Tolerance Evaluation of Ti-24Al-11Nb Matrix Composite Unidirectionally Reinforced with SiC Fibers," *Damage and Failure of Interfaces*, Rosmanith H.P. Ed., Balkema Publisher, Rotterdam, 1997, pp. 381-387.

[6] Davidson D.L., "The micromechanics of fatigue crack growth at 25 C in Ti-6Al-4V reinforced with SCS-6 fibers," *Metall. & Mater. Trans.-A* , Vol. 23-A, 1991, pp. 865-879.

[7] Fox K.M., Strangwood M. and Bowen P, " The Influence of Thermal Treatments on Interfacial Properties and Fatigue Crack Growth Resistance in SCS-6/Ti β21s Composite," *Composite.*, Vol. 7, 1994, pp. 684-691.

[8] Eggleston M.R. and Ritter A.M., "The transverse creep deformation and failure characteristics of SCS-6/Ti-6Al-4V metal matrix composite at 482 C," *Metall. & Mater. Trans.-A*, Vol. 24-A, 1994, pp. 2733-2744.

[9] Ohno N., Toyoda K., Okamoto N., Miyake T. and Nishide S., "Creep Behavior of A Unidirectional SCS-6/Ti-15-3 Metal Matrix Composite at 450 C, " *Trans. ASME*, J. Eng. Mat. Tech., Vol. 116, 1994, pp. 208-213.

[10] Russ S.W., "Thermal Fatigue of Ti-24Al-11Nb/SCS-6," *Metall. & Mater. Trans.*, Vol. 21-A, 1990, pp. 1595-1602.

[11] Neu R.W. and Sehitoglu. F., "Thermomechanical Fatigue, Oxidation and Creep: Part 2 Life Prediction," *Metall. & Mater. Trans.*, Vol. 20-A, 1989, pp. 1769-1783.

[12] Majumdar B.S. and Newaz G.M., "Thermo-Mechanical Fatigue of an Angle-Ply Metal Matrix Composite," *Composite materials: Fatigue and Fracture,* ASTM STP 1110, T.K. O'Brien Ed., Americal Society for Testing and Materials, Philadelphia, 1991, pp. 732-752.

[13] Gabb T.P., Gayda, and MacKay R.A., " Isothermal and Non-Isothermal fatigue Behavior of a Metal Matrix Composite," *J. Composite Materials*, Vol. 24, 1990, pp. 667-686.

[14] Halford G.R., Lerch B.A., Saltsman G.F. and Arya V.K., "Proposed Farmework for TMF Life Prediction of Metal Matrix Composites," *Thermo-Mechanical Fatigue Behavior of Materials,* ASTM STP 1186, H. Sehitoglu Ed., Americal Society for Testing and Materials, Philadelphia, 1993, pp. 176-194.

[15] Mall S, " thermal fatigue behavior of a Unidirectional SCS-6/Ti-15-3 Metal Matrix Composite," *J. Composite Mater*, Vol. 25, 1991, pp. 1668-1686.

[16] Revelos W.C. and Smith P.R., " Effect of Environment on the Thermal Fatigue Response of an SCS-6/Ti-24Al-11Nb Composite," *Metall. & Mater. Trans.*, Vol. 23-A, 1992, pp. 587-595.

[17] Smith P.R., Graves G.A. and Rhodes C.G., " Comparison of Orthorhombic and Alpha-Two Titatium Aluminides as Mtrices for Continuous SiC-Reinforced Composite," *Metall. & Mater. Trans.*, Vol. 25-A, 1994, pp. 1267-1283.

[18] Okazaki M., Hayashi K, and Nakatani H., "Thermal Fatigue Damage Mechanisms in a Unidirectional SCS-6/Ti-24Al-11Nb Metal Matrix Composite," *J. Soc. Mater. Sci., Japan,* Vol. 47, 1998, pp. 920-927.

[19] Yang C.J., Jeng S.M. and Yang J.M., "Interfacial Properties Measurement for SiC fiber-reinforced Titanium Alloy Composites," *Scrip. Met.,* Vol. 24, 1990, pp. 469-474.

[20] Chandra, N. and Anath C.R., "Analysis of Interfacial Behavior in MMCs and IMCs by the Use of Thin Slice Push-Out Test," *Composite Sci. Tech.,* Vol. 54, 1995, pp. 87-95.

[21] Guermazi M., "Temperature Dependence of Interfacial Shear Strength in SCS-6 fiber Reinforced Ti-24Al-11Nb Metal Matrix Composite," *Mater. Sci. and Technol.*, Vol. 10, 1994, pp. 399-405.

[22] Cox B.N., Dadkhah M.S., James M.R., Marshall D.B., Morris W.L. and Shaw M., " On Determining Temperature Dependence of Interfacial Shear Properties and Bulk Residual Stress in Fibrous Composites," *Acta Metall. Mater.*, Vol. 38, 1990, pp. 2425-2433.

[23] Baumann S.F., Brindley P.K. and Smith S.D., "Reaction Zone Microstructure in A Ti_3Al+Nb/SiC Composite," *Metall. & Mater. Trans.,* Vol. 21-A, 1990, pp. 1559-1568.

Günter Marci,[1] Klaus M. Mull,[2] Christian Sick,[2] and Marion Bartsch[3]

New Testing Facility and Concept for Life Prediction of TBC Turbine Engine Components

Reference: Marci, G., Mull, K. M., Sick, C., and Bartsch, M., **"New Testing Facility and Concept for Life Prediction of TBC Turbine Engine Components,"** *Thermo-mechanical Fatigue Behavior of Materials: Third Volume, ASTM STP 1371,* H. Sehitoglu and H. J. Maier, Eds., American Society for Testing and Materials, West Conshohocken, PA, 2000.

Abstract: A thermo-mechanical test facility is presented which enables testing of a cylindrical specimen under thermal and mechanical loading conditions which closely simulate the conditions in an aircraft engine. The principal features of the test facility are described. They include thermal shock during start-up and shut-down of an engine and cyclic loads comprising hold-times simulating the loading conditions during a usual flight of an aircraft. For such conditions, the life of physical vapor deposit (PVD) thermal barrier coatings (TBC) should be determined. A concept for life predictions for TBCs based on some minimum test results is presented.

Keywords: testing facility, turbine engine simulation, blade material, thermo-mechanical loading, life prediction, thermal barrier coating

Introduction

The task of testing and evaluating the service life of physical vapor deposit (PVD) thermal barrier coated (TBC) turbine blades was assigned to the authors. Available were the experience with servo-hydraulic testing machines and testing of aircraft structural materials under spectrum loading. It was decided to simulate turbine blade environment as far as possible. It required cyclic mechanical and thermal loading condition of a turbine blade during a flight to be simulated. The operating conditions of an CFM56-5C2 engine of a civil airliner during a normal flight were used as basis for the simulation. Due to the nature of thermal barrier coated (TBC) blades, dissimilar hybrid material, the thermal shock during start-up and shut-down of the engine had to be simulated. TBC on blades

[1]Senior Scientist, [2]Technical Specialist, [3]Scientist, Institute for Materials Research, DLR-German Aerospace Research Center, D-51170 Cologne, Germany

are intended either to increase the maximum operating temperature of the turbine engine or to increase the life of blades. The temperature on the surface of the TBC can be higher than the maximum temperature tolerable by the blade's metallic system, then the specimen has to be "cooled" by internal air flow. The air used for "cooling" has to be heated up to 500°C (770 K) in order to simulate the conditions in the engine. To simulate a blade, it was decided to use a hollow cylindrical specimen with a maximum wall thickness of 2 mm. The testing machine should be either load or displacement controlled, where the latter is taken off the specimen. Another consideration was that the ceramic coating should not be loaded by bending moments due to the gripping fixture.

Specimen and Gripping Fixtures

The specimen, Fig. 1, consists of a test section of 60 mm length with 8 mm outside and 4 mm inside diameter. On each side of the test section there is a 20 mm long transition region from 8 mm to 16 mm diameter in which a wrench way (14 mm) is machined. Both ends are threaded with M14 x 1. Because of the anticipated use of directionally solidified

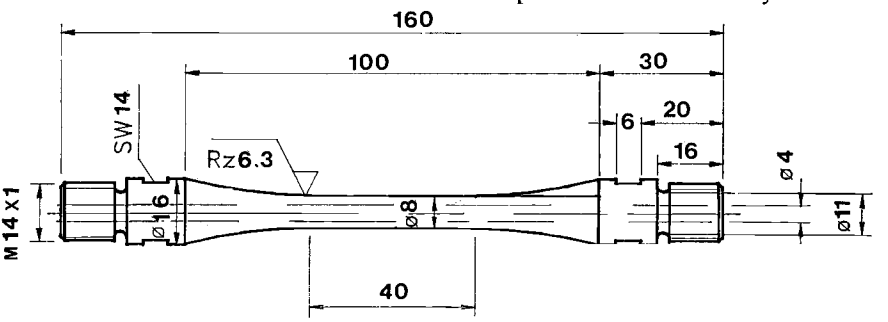

Figure 1 - Specimen configuration (dimensions in mm)

material as test specimen, the length of the specimen was limited to 160 mm. As can be seen in Fig. 2, the specimen (A) length is extended on both ends by an extension piece (B). The extension pieces allow the specimen to be mounted relative easily. A displacement gage can be fixed to these extension pieces, too. The extension pieces are tightly screwed into two spheres (C), into which, from the opposite side, the connection pieces (D) for the "cooling" air supply lines are screwed in. The spheres are flattened on opposite sides perpendicular to the specimen axis as to turn them with a corresponding wrench. Both connection pieces are furnished with thermocouples for temperature measurements. The spheres are held by two, concavely machined discs (E) with radius equal to that of the spheres. The two discs with the sphere between them are clamped inside the mounting rod (F) by a screwclamp (G). For mounting the "cooling" air supply line (H) and exhaust line (I), the mounting rods are slotted (K) above their clamping section. The mounting rods are connected to the cylinder rod on one side and the load cell on the other side. To protect the load cell from heat flow, a circular plate made of 2 mm copper sheet with 8mm copper tubing soldered on one side for water cooling is mounted below the load cell.

Heating, Thermo-Shock, and Internal Cooling Equipment

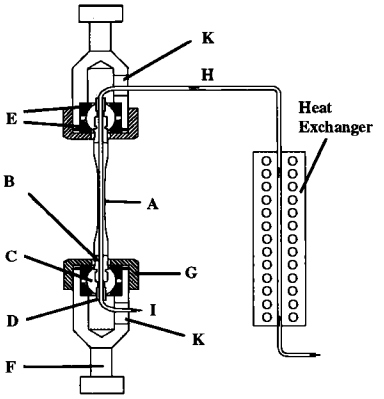

Figure 2 - Gripping arrangement for the thermo-mechanical specimen

The prime task of the equipment is to obtain experimental results that allow life prediction for TBC of blades. Therefore, radiation heating is used. Four halogen bulbs with 1000 W are used as heating source. Each of the four bulbs is positioned at one center of an ellipse and the specimen is placed in the other center of that ellipse, Fig. 3a. The major and minor diameters of the ellipses are 160 mm and 106 mm, respectively. As can be seen in Fig. 3a, the major axes of the ellipses are rotated 60 degrees against each other and an axis of symmetry going through the specimen position. The walls of the heating system are machined from brass (70Cu, 30 Zn). The walls are furnished with cooling channels machined and drilled in as shown in Fig. 3a and b.

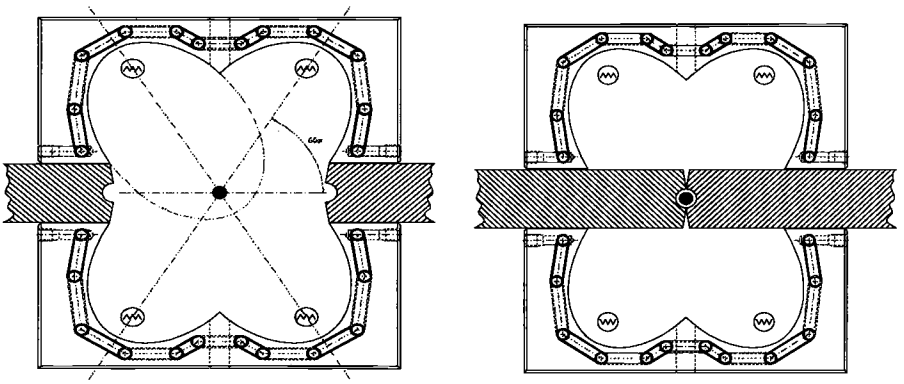

Figure 3 - Furnace: a) sliders - open *b) sliders - closed*

All inside surfaces of the heating system are gilded. The heating system as shown in Figs. 3a and b is covered by brass plates of 20 mm thickness that are water cooled. These cover plates are partitioned to allow each half of the heating system to be moved away from the specimen for easy mounting of the specimen. Each set of cover plates contains four holes for the light bulbs and one hole for the specimen. Each half of the heating system is mounted separately on a cradle with four glide bearings which slide on two glide

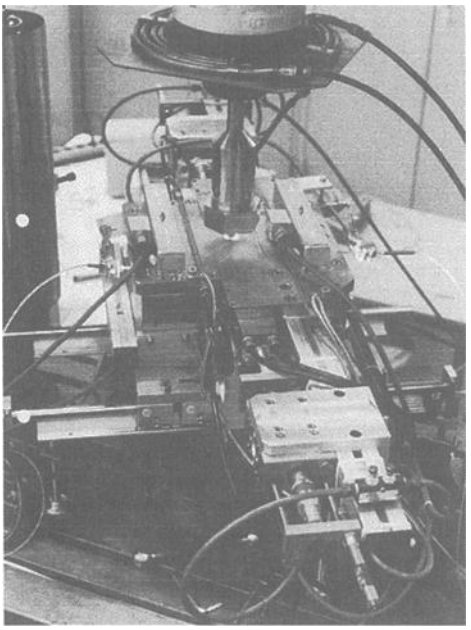

Figure 4 - Thermo-mechanical test facility

bars. Figure 4 is a photograph of the test facility.

The arrangement of the ellipses, Fig. 3a, is disrupted by a channel, symmetric around the specimen and mirror /and symmetric to the axes of the ellipses as shown in Fig. 3b. The channels have a rectangular cross section of 48 mm width and 60 mm height in which two sliders are moving. The "open" position of the sliders is shown in Fig. 3a, while Fig. 3b shows the sliders in the "closed" position. In the "closed" position the slider encloses the specimen in a cylindrical space of 20 mm diameter. This cylindrical space is coated with a black chromium-oxide as to achieve black body cooling of the radiating specimen. Black body cooling is intended for rapid cooling of the specimen in the temperature range between 1120°C and 730°C (1400K to 1000K). In addition, two rows of vents, with nine vents of 1 mm diameter equally spaced along the 60 mm test section are machined into each slider. The vents are used for rapid cooling of the hot specimen with cold air. The four rows of vents are in line with the major axes of the ellipses. This way, a thermal shock can be imposed on the TBC specimen. The slider is moved pneumatically and can switch between "open" and "closed" position in less than half a second.

High quality compressed air (water and oil free) with 700 kPa pressure is used and regulated via pressure gages and mass-flow meters as well as temperature measurements. This air goes into an electrically heated heat-exchanger, in which this air can be heated up to a maximum temperature of close to 500°C (773K). Via insulated tubing, this heated air is transferred to the specimen for internal "cooling". The temperature of the cooling air is measured before it enters the extension piece of the specimen and as it leaves the extension piece on the lower side.

Test Parameters and Their Control

Machine and system control as well as data acquisition are handled by a computer program build-up on the windows version of "DASYLab". The parameters for internal cooling of the specimen are set independently (cooling air flow and temperature). They are continuously measured and recorded by the computer program. Load or displacement,

surface temperature of the specimen, and thermo-shock condition are simultaneously controlled by the computer program.

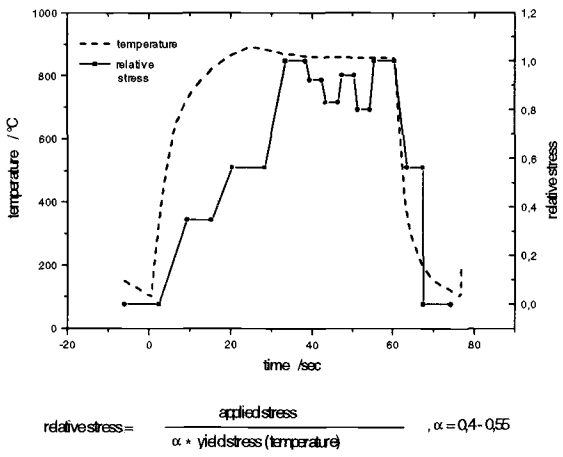

Figure 5 - Load and Temperature spectrum during thermo-mechanical tests

Figure 5 gives the thermo-mechanical loading spectrum schematically which simulates a normal flight for an CFM56-5C2 engine. The maximum stress in the specimen is attained twice during the flight spectrum, namely during "take off" and before landing. This maximum stress corresponds to 70% of the yield stress at 850°C (1123K). The test temperature of the metal surface was fixed for the directionally solidified IN 100 to be 850°C (1123K). An over-shooting of this temperature was allowed during the heat-up phase, since the corresponding stresses are relatively low then.

Thermoshock occurs by heating the specimen instantaneously with full heating capacity of the system at the start of an individual flight. This corresponds to the start-up of the turbine engine. Equivalently, the shut-down of the engine is simulated at the end of each flight by moving the sliders to enclose the specimen (see Fig. 3b). The specimen is rapidly cooled by black-body and air cooling. During the time the sliders enclose the specimen the heating system is continuously operating under power as if to maintain the "normal" maximum temperature. This is to obtain the maximum heat-up velocity during the start of the next flight. In Fig. 6, a comparison is made between the cooling rates:

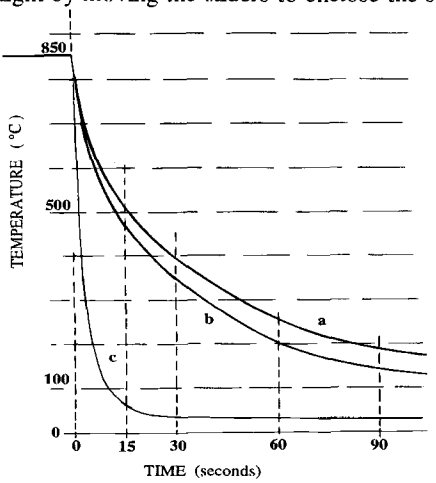

Figure 6 - Different cooling rates depending on cooling conditions

a) heating system shut-off (sliders in the "open" position, no air cooling).
b) heating system shut-off and sliders in the "closed" position (no air cooling).
c) heating system shut-off, sliders in the "closed" position and air cooling via 36 vent holes.

Figure 6 shows that even at a maximum temperature of 850°C (1123K) the influence of "black-body" cooling can be detected. "Black-body" cooling is only effective for

temperatures above approximately 700°C (973K). If the maximum temperature is increased to 1100°C (1373K), i.e. for testing single crystal specimen, the "black-body" cooling should furnish a substantial contribution to the cooling rate of the specimen.

Tests were made to investigate the thermal gradients under different conditions of specimen internal cooling conditions (air temperature and flow-rate of air). Figure 7 shows some of the test results for cooling air temperature equal to room temperature. Shown in Fig. 7 are the temperatures at the surface of the TBC, at the interface between bond coat and TBC and below the specimen's inside surface. All temperatures are plotted as functions of mass-flow-rate and temperature of the cooling air. Test results like these shown in Fig. 7 lead to selecting a cooling air temperature of 280°C (553K) (entrance temperature at the upper extension piece-position D in Fig. 2) and a mass-flow-rate of 45 standard liter per minute. These conditions were selected because small deviations from desired conditions have no measurable effect on the specimen temperatures.

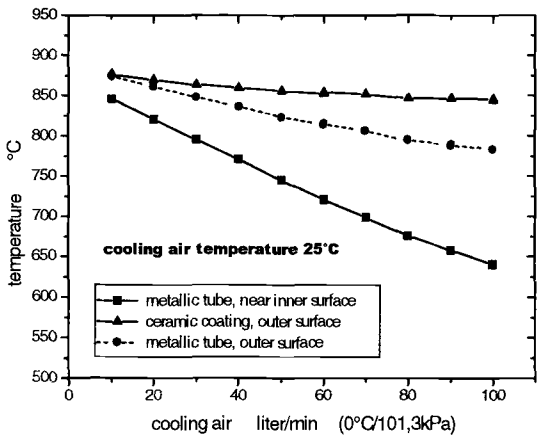

Figure 7 - Specimen temperatures in dependence on mass-flow-rate and temperature of the cooling air

Testing Concept

In a simplified view, design of turbine engine components is based today on two theoretical concepts that are often applied simultaneously. One is a Wöhler-type (low cycle) fatigue analysis and the other is a fracture mechanics concept denoted as "retirement for cause." Emphasis is placed on one or the other concept depending on the experience of the individual turbine engine designer. With the Wöhler-type fatigue analysis, there are also differences in criteria used to estimate the life of a component. From a scientific standpoint a defect-free component can hardly ever be manufactured. Nevertheless, such conditions are often presumed in a Wöhler-type analysis. Furthermore, defect initiation is often assumed to be an instantaneous event that defines the end of the fatigue design life. Bound by necessity and practical experience, pseudo "defect initiation" is often defined as crack or defect size of 0.7 mm largest dimension. In this case, the end of the fatigue life is defined by this size of defect. Other groups of designer use failure of the component as the end of the fatigue life analysis.

The fracture mechanics concept "retirement for cause" also has its limitations. Due to

the high thermo-mechanical load level, the calculated fatigue crack propagation (FCP) life depends largely on the nondestructive evaluation technique used to define the largest nondetectable defect as starting condition for the FCP life. Furthermore, to define the end of FCP life is not a clear-cut matter. With component testing to failure, and expressing the failure conditions in appropriate fracture mechanics terms, it must be insured that failure during testing does correspond to the failure in service. Plane strain fracture toughness K_{IC}, its counterpart for plane stress K_C and the fracture toughness J_C are available for characterization of failures. Failures of turbine engine components are anticipated to occur most likely under higher temperatures. The fracture mechanics failure criteria for the higher temperature regime, above 720°C (>1000 K) are certainly questionable from a scientific stand-point. Nevertheless, an engineering approach is used by selecting one of the parameter K_{IC}, K_C or J_C that fits best to describe the subject failure. Newer scientific results for Ti-alloys [*1*] shed strong doubts that either of the foregoing failure criteria is appropriate for Ti-alloys. The calculated design life is the number of thermo-mechanical cycles bringing the largest nondetectable defect to the size at failure. Creep and oxidation modify the FCP life in a nonlinear fashion.

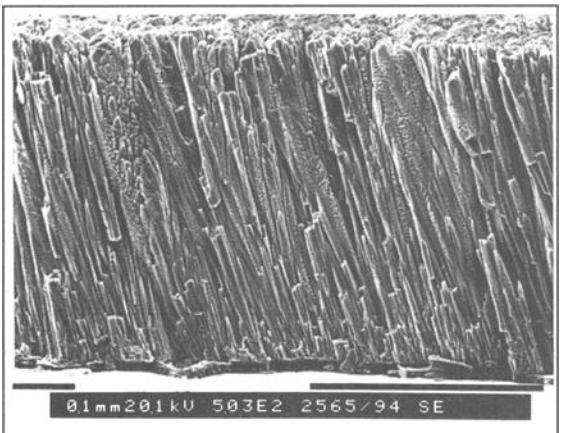

Figure 8 - Micrograph of PVD thermal barrier coating

The PVD thermal barrier coat of turbine blades with (ZrO_2 + Y) has a thickness of 200 to 300 μm and has columnar structure with the columnar structure perpendicular to the blade surface (Fig. 8). Between the thermal barrier coating and the blade material there is a so-called "bond coat" with approximately 100 μm thickness. The bond coat has the task to enhance the bond between the TBC and the blade material and secondly to provide oxidation protection of the blade material. It should be noted that the practical experience with TBC blades are such that the TBC has a much lower life than the blade material. Cracks in the TBC or in the interface "TBC and bond coat" supposedly do not grow into the blade material before failure of the TBC. Due to the lack of tools and knowledge about failure mechanisms of TBCs, it was decided by the authors that a fracture mechanics approach should not be attempted. Life predictions for thermal barrier coated turbine engine components are the prime task to be executed, particularly for blades. Therefore, a Manson-Coffin type analysis as was suggested in the "NASA HOST Program" [*2,3*] is to be used as basis for life predictions of TBCs.

In the first phase of the test program it is intended to obtain sufficient data to build a simple, reliable life predictive model for TBC coated specimens (blades). In order to use the results for the improvement of PVD TBC and to obtain some guide for TBC life under service conditions, the following concept is implemented. We start from the as-

sumption that in the near future TBCs are used to extend the life of the blades only. Furthermore, the life of the uncoated blade is taken as reference to which the life of the TBC is compared; the life of a blade is determined by the thermo-mechanical loading conditions in the most critical location. The life of the specimen without TBC is matched to that of the uncoated blade by simulating the thermal conditions of an engine as closely as possible and adjusting the mechanical load spectrum to which the specimen is exposed. If the life of a certain blade is 4500 hours service, then this corresponds to 3000 flights under the assumption that the average flight lasts 1.5 hours. Therefore, the uncoated specimen has to have a life of 3000 flights. Since the life of the uncoated thermo-mechanical specimen and the uncoated blade are identical, the thermo-mechanical loading conditions should be equivalent (Fig. 5). As far as the temperature spectrum is concerned, the reference temperature for the system (IN 100 + TBC) was chosen to be 850°C (1123K) on the outer metal surface of the specimen. It means that the specimen without TBC has 850°C on its outer, uncoated surface, while the specimen with TBC has 880°C on the TBC surface and 850°C at the interface of bond coat and TBC. The idea behind it is that the critical location of the metal blade determines temperatures and mechanical loading conditions of the blade which consequently are imposed on the TBC, too. Therefore, the life of TBC is expressed as fraction "F" of blade life, namely:

F = Life of TBC / Life of Blade

The thermo-mechanical loading conditions of TBCs are solely determined by these thermo-mechanical loading conditions which are the design base of the metallic blade. We have some conservatism in this approach, since the temperature of the outer metal surface of blades coated with TBC for life extension is lower than that of uncoated blades. Initial results for directionally solidified IN 738 LC-DS + bond coat and TBC were obtained.

Conclusions

The thermo-mechanical test facility designed and built by the authors furnishes the test conditions originally anticipated to be necessary for life prediction tests of TBCs on turbine engine components. The first test program on the system (IN 100 + bond coat + PVD-TBC) is presently executed.

References

[1] Marci , G., "Abnormal da/dN - ΔK Curves: New Failure Mode with Ti-Alloys," *Mat.-wiss. U. Werkstofftech.* No.28, 1997, pp. 51-58.

[2] NASA Lewis Research Center, Hot Section Technology (HOST) Program, 1986 - 1992.

[3] Meier, S.M., Nissley, D.M., and Sheffler, K.D., "Thermal Barrier Coating Life Prediction Model Development", *NASA Contractor Report 189111*, July 1991.

Leonardo Angarita,[1] Günter Pitz,[2] Karl-Heinz Lang,[3] and Detlef Löhe[4]

Realization of Complex Thermal-mechanical Fatigue by a Two-specimen Testing System

Reference: Angarita, L., Pitz, G., Lang, K.-H., Löhe, D., **"Realization of Complex Thermal-mechanical Fatigue by a Two-specimen Testing System."** *Thermo-mechanical Fatigue Behavior of Materials: Third Volume, ASTM STP 1371,* H. Sehitoglu and H. J. Maier, Eds., American Society for Testing and Materials, West Conshohocken, PA, 2000.

Abstract: Many components are exposed to high thermal and mechanical loadings. For example, the blades of gas turbines are subjected to thermally and mechanically induced strains and stresses at varying temperatures. The former arise from inhomogeneous temperature fields, which are due to start-stop cycles, resulting in thermal fatigue. The latter arise from centrifugal forces, which arise from the rotation of the turbine, resulting in mechanical low cycle fatigue and creep during service.

The combination of thermally induced loading and mechanically induced loading can neither be investigated in a conventional (strain controlled) thermal-mechanical fatigue (TMF) test nor in a conventional (stress controlled) creep test. Also the interaction between different volume elements within a component can not be investigated in a single specimen experiment. To simulate such "complex" thermal-mechanical fatigue loading, a two-specimen testing system was build up. At this testing system the thermal-mechanical loading of the specimens, each of them representing a distinct volume element of a component, is generated just by varying the temperature-time history of the two specimens and the coupling conditions between them. Furthermore, it is possible to superimpose an external force, e.g. representing the centrifugal force. The distribution of this force on the two specimens and the resulting deformation behaviour are the result of the interaction of the two specimens. The testing and interpretation methods as well as the results of first experiments with a 12% chromium steel and a 316 type stainless steel are presented.

Keywords: complex thermal-mechanical fatigue, cyclic deformation behaviour, 12% chromium steel, 316 type stainless steel

[1]M.S., Graduated Student, Institut für Werkstoffkunde I, Universität Karlsruhe (TH), Postfach 6980, D-76128 Karlsruhe, Germany

[2] Dr.-Ing, Daimler Benz AG, D-76742 Wörth, Germany

[3] Dr.-Ing, Institut für Werkstoffkunde I, Universität Karlsruhe (TH), Postfach 6980, D-76128 Karlsruhe, Germany

[4] Prof. Dr.-Ing, Institut für Werkstoffkunde I, Universität Karlsruhe (TH), Postfach 6980, D-76128 Karlsruhe, Germany

Introduction

Many components used in high temperature applications in the chemical industry, in energy producing plants or in engines are exposed to complex thermal-mechanical loadings during service. Frequently these loadings are a superposition of quasi static creep, low frequency thermally induced fatigue and higher frequency mechanically induced fatigue. In addition oxidation and/or corrosion may occur.

For the design of such components, all possible loading conditions and their interaction must be considered. Therefore, enormous efforts were and are done to determine the material behaviour under service relevant conditions. [*1*] gives a good summary of the current knowing in this area.

Experimental analysis of the thermal and mechanical loading of a components by the deformation and failure behaviour of the material using currently available single specimen testing arrangements is not(or only under strong restrictions) possible with respect to the interpretation and the transfer of the experimental results. In particular, stress rearrangements which appear at thermocyclical loadings within a component can change the loading conditions of a regarded volume element during the operating time. These effects cannot be reproduced in single specimen testing system sufficiently well.

Complex Thermal-Mechanical Loading

Thermal fatigue of components is caused by start-stop-cycles and load changes, i.e. in the above mentioned applications. Since the temperature changes which are associated with the operating conditions are not homogeneously in the entire material volume, thermally induced stress fields emerge. They are specified in particular by the geometry and the material behaviour of the considered component. In this context uncooled and cooled components must be distinguished. Fig. 1 schematically illustrates the situation when using an uncooled turbine blade [*2,3*]. When heated by the indicated gas flow, the temperature of volume element 1 at the surface reaches the service temperature relatively quickly, while the temperature of volume element 2 in the interior of the blade rises to a less

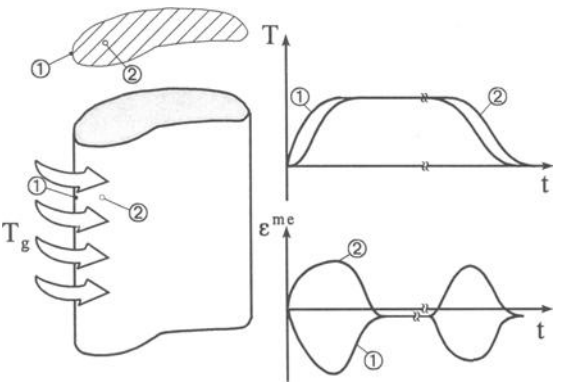

Figure 1 - *Temperatures and mechanical strains in an uncooled turbine blade*

degree. As a consequence, a difference in temperature develops for the volume elements 1 and 2, respectively. Assuming as a first approximation that the blade does not bend, the total strains of both elements must remain equal so that the different thermal strains are equalized by mechanically forced strains ε_1^{me} and ε_2^{me}.

A different situation occurs if the component is cooled, which is nearly always the case for the first rows of gas turbine blades. As Fig. 2 schematically shows, there is no temperature equalization between the volume elements 1 and 2 after reaching service temperature [*3*]. Temperature and mechanical strains of the "hot" volume element 1 are out-of-phase and those of the "cold" volume element 2 are in-phase. Taking into account that during service such components are exposed to a great number of these heating and cooling processes, it must be pointed out that a cyclic thermal loading exists, which (for volume element 1) could be described by a relatively large temperature range and a relatively high compressive mean stress, while for volume element 2, a relatively slight temperature range and high tensile mean stress is significant.

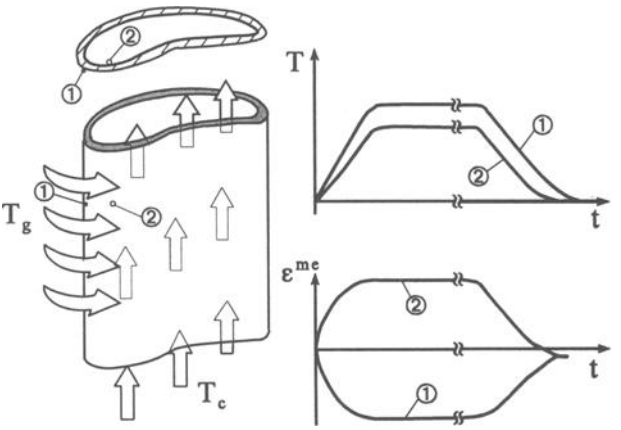

Figure 2 - *Temperatures and mechanical strains in a cooled turbine blade*

These thermal fatigue loading components are usually superimposed by mechanical loadings. So, creep loading is produced by constant forces, moments and/or pressures. As examples turbine blades can be identified which are exposed to high centrifugal forces. If the mechanical loadings are not constant or if component oscillations occur, mechanical fatigue loading also emerges. Usually, the number of thermal cycles occurring during the lifetime or application of a component is significantly smaller than the number of the mechanical cycles.

For the assessment of the deformation and failure behaviour of components, all existing loading components and their interaction must be considered. In order to evaluate thermally induced fatigue loading, characteristic relations between the deformation and the failure behaviour of the considered material obtained from experiments with cyclic thermal loading are necessary. To simplify the experiments, it is generally assumed that the thermally produced stresses come from the superposition of thermal extensions. Therefore, thermal fatigue loading is described as an isothermal cyclic strain loading. The obtained relations between loading amplitude and number of cycles to failure are in the simplest case described by a temperature-Wöhler curve. The Coffin-Manson relationship, which was originally developed for the evaluation of components under thermal mechanical loading [*4, 5*], is also frequently used to describe the material life.

In general, creep loading is evaluated by the material's response during isothermal creep testing. For this purpose data resulting from experiments with different loadings or temperatures are recorded [6]. The superposition of creep loading with thermal fatigue loading is usually described by so-called service life share rules or by procedures like "strain range partitioning" [7]. For the evaluation of high frequency fatigue loading, typically data from isothermal stress controlled cyclic deformation experiments are used.

However, there are several problems associated with the described procedure. First of all, the transformation of thermal cyclic loading into isothermal strain controlled cyclic loading raises the problem of the temperature choice. When using the conservative procedure, the maximum temperature of the thermal cycle to be described is often chosen. Thereby, service life under thermal cycling conditions may be overestimated by using isothermal fatigue data generated at the maximum temperature. This result is closely connected with the additional problem how thermal cyclic loading could be transformed into isothermal strain controlled cyclic loading. As during thermal cyclic loading different material resistances occur during each cycle, mean stresses are built up. If tension mean stresses emerge, the service life during thermal cyclic loading is shortened. Microstructural instabilities is a further problem. Although during thermal cyclic loading in each cycle a wide temperature range is covered, for isothermal cyclic loading the temperature remains constant except during start-up. It turns out that the requirements for the formation of precipitates are completely different. This, of course, may have an influence on the cyclic deformation and failure behaviour of the material. Finally, in coarse heterogeneous materials and in coated materials, cyclic stresses are always induced by cyclic temperature changes if different expansion coefficients of the phases and/or layers exist. This mechanism does not exist during isothermal fatigue. The evaluation of service life of thermocyclic loaded specimens or components on the basis of the results of isothermal fatigue tests can be non-conservative.

The interaction between "hot" volume element 1 and "cold" volume element 2 in Figure 1 and 2 can change during thermocyclic loading, if cyclic hardening and/or softening processes occur. If one assumes, for example, that the hot volume element cyclically softens as a consequence of the high maximum temperature and, on the other hand, the cold volume element cyclically hardens, the degree of extension suppression of the hot volume element increases during thermocyclic loading. This phenomenon can neither be reproduced by an isothermal LCF-test nor by a thermal cyclic experiment with fixed test conditions within the experiment.

The evaluation of the interaction between low frequency thermal cyclic loading, creep loading and/or high frequency stress controlled fatigue loading is particularly difficult. An experimental reproduction of this interaction by applying pure strain controlled or pure stress controlled test conditions is not possible. However, it is under these conditions that important technical applications proceed. The existing suggestions for solving this problem are insufficient. The mutual influence of the different loading components with regard to the occurring damage can only be considered in terms of service life share rules by empirical adjustment of the failure determining damage sum. Here, as well, the central problem remaining is, that thermocyclic loading and/or isothermal low cycle fatigue is strain controlled, whereas creep loading and high cycle fatigue are stress controlled. In the case of elastical-plastic material response the above mentioned procedures are not suitable to

describe the change of a thermally induced inhomogeneous and non-stationary stress field by a superimposed creep loading.

Experimental Concepts for Thermal-Mechanical Loadings

Complex thermal mechanical loading experiments consist of applying combinations of mechanical, thermal and partially also chemical reactions and of recording the deformation, damage and failure behaviour of the material investigated [*9*]. The loadings must correspond to practical applications, and it must be possible to measure the material response.

If mechanical loadings are induced in a component by temperature gradients the procedure is called *thermal fatigue* by internal constraint (see Fig. 1 and 2). Since this kind of loading is the most important one for components, material testing procedures are applied in which loading is produced by internal constraint. For reasons of time they are frequently simulated through thermal shock loadings. The main difficulty remains that the thermally induced stresses can not be measured and that the determination of the cyclic deformation behaviour can only by carried out by analytical techniques with suitable material models. However, the formation and the growth of cracks can be determined experimentally [*3*].

If mechanical cyclic loading is applied in addition to thermal cyclic loading, *thermal-mechanical fatigue* is generated. A simple method of TMF has been proposed by Coffin [*4*]. A hollow specimen, which represents the highest loaded volume element, is installed in a fixed load frame and is subjected to a temperature-time course. By changing the stiffness of the loading frame, the flexibility of the test arrangement can be modified and (within certain limits) can thus been adjusted so that different component loading situations may be simulated. Still, today, advanced experimental facilities after this principle are operated frequently in connection with direct electrical resistance heating [*10*].

A larger variety of testing possibilities will be obtained by substituting the fixed loading frame by a controlled testing machine [*11, 12*]. The internal constraint condition existing in a component can fundamentally be simulated by strain or stress controlled testing methods. As thermal fatigue is due to the suppression of cyclically appearing thermal extensions, strain control is used almost without exception. The advantage of these procedures is that the parameters of thermal cyclic loading can easily be changed within wide limits and that the resulting material response can be measured in terms of the developing stresses. A disadvantage, however, is that the multiaxiality of thermal cyclic loadings existing in components can not be realized in most cases and that changes in interaction between component elements which have different temperatures and result from cyclic hardening or softening processes cannot be taken into consideration. Typical loadings are "out-of-phase" and/or "in-phase" cycles for cooled as well as the "diamond-cycle" for uncooled components.

As discussed above, thermal fatigue is due to the suppression of cyclically appearing thermal extensions so that in practice, strain control is often used. For *complex thermal-mechanical fatigue*, stress controlled creep loading and/or high frequency fatigue loading must be applied as well. This can be realized by changing the control path during an

experiment. As a consequence, control and data collection require a much greater effort. Alternatively, for the implementation of very low frequency cyclic strain loadings with very long hold times the "packaged testing" technology was developed [*13*]. In this case, cyclic strain controlled fatigue segments and constantly stress controlled creep segments are summed up in packages. The strain controlled fatigue packages include standard low cycle fatigue loadings with abbreviated strain cycles. In the constant stress controlled creep packages, the stress relaxation loading appearing during the holding times of the strain cycles is described by equivalent tensile stresses.

Despite the abundant possibilities, which are offered by the already mentioned thermal mechanical fatigue test methods, important loading requirements still remain unsatisfied. The missing ability to realize changes of the internal constraint during thermal cyclic loading by emerging changes of the material states was already mentioned. In addition, highly loaded components are not only loaded thermally but also by external forces, moments and/or pressures. The superposition of thermally induced stresses and stresses induced by external loadings leads to difficulties in purely strain controlled or purely stress controlled testing conditions because one of the processes can not be simulated correctly. One possibility of simulating such processes is the so-called "three bar test" [*8*], where three specimens are coupled with each other by two stiff cross yokes, thus mutually constraining hindering themselves during thermal expansion. For example, the loading conditions given in Fig. 1 are realized by using two specimens which have a higher temperature than the third one. In addition, a mechanical loading can be realized applying an external force to the cross yokes. Due to the purely mechanical linkage, the experimental possibilities of this set-up are limited. Clearly more variations are possible with a two specimen test system [*14,15*], where two specimens are installed in two separate testing machines. One specimen is held at a constant temperature, while the other one is exposed to cyclic temperature loading with defined amplitude and frequency. With suitable linkage of both testing machines, the "three-bar-test" is exactly simulated.

Conception of a Testing System for Complex Thermal-Mechanical Fatigue

With the testing system schematically presented in Fig. 3, the interaction between low frequency (strain controlled) thermocyclic loading and (stress controlled) creep loading and/or high frequency fatigue loading in metallic materials as well as a component relevant linkage between a "hot" and a comparably "cold" volume element should be realized.

In general, the testing system should fulfil the following requirements:

1. Independent and (in a wide range) freely selectable temperature-time-courses for specimen 1 (hot volume element) and specimen 2 (cold volume element) with maximum temperatures up to 1200°C
   - ⇒ Consideration of different thermal loadings, component geometries, temperature conductivities and cooling conditions
2. Independent force-time-course for the sum of the forces acting on the two specimens
   - ⇒ Realization of creep loading and of stress controlled higher frequency

fatigue loading superimposed to thermal-mechanical loading

3. Linkage between the total strains of the specimens 1 and 2 with separate extension measurement and separate force measurement

⇒ Realization of the mutual thermal extension suppression, consideration of the thermal extension behaviour, recording of the stress distribution on specimen 1 and 2, recording of the cyclic deformation behaviour, the formation of cracks and the failure behaviour

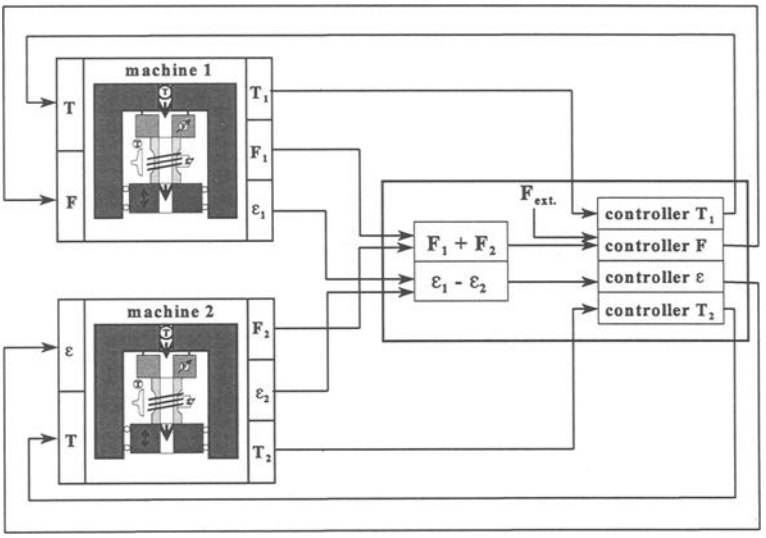

Figure 3 - *Experimental set-up (schematically)*

From these requirements the testing conditions and associated control circuit presented in Fig. 4 can be established. The temperatures T_1 and T_2, the forces F_1 and F_2 as well as the total strain $\varepsilon_{t,1}$ and $\varepsilon_{t,2}$ are measured separately and conveyed to the controller a common 4 channel digital controller. The two temperature control loops are independent of each other. However, the two control loops for specimen 1 and 2 are connected with each other. One testing machine is operated in strain control (controller ε) and the other is operated in force control (controller F). To the strain control loop the difference of the strains of specimen 1 ($\varepsilon_{t,1}$) and specimen 2 ($\varepsilon_{t,2}$) supplied. For the chosen boundary conditions this difference is held on zero. By that is ensured that the strain of both specimens is the same at every time. To the force controller the sum of the forces acting on specimen 1 (F_1) and specimen 2 (F_2) is supplied. This sum can either be held on the value zero simulating a system on which no external force has an effect. However, it is also possible to provide a time-course for the sum of the forces to take into account an external force. With that, for example, centrifugal forces of a turbine blade is simulated. The distribution of the external force on the two specimens yields from the system behaviour. It depends on the mechanical properties of the single specimens which change during the

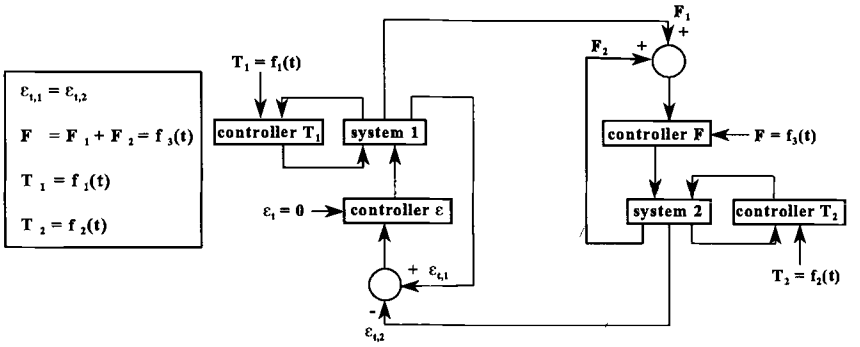

Figure 4 - *Control circuit*

temperature cycle and which may change during the experiment. Due to the coupling of the two mechanical control loops the retention of the above mentioned requirements is ensured.

Realization of the Testing System

The testing system was built on the basis of two MTS model 810 servo hydraulic testing machines with maximum cyclic force capacities of 100 kN. Specimen 1 (hot volume element) and specimen 2 (cold volume element) are installed in separate servo hydraulic testing machines which are equipped with hydraulic water-cooled grips. In Fig. 5 one of the loading frames, with a specimen, the grips, the induction coil and the cooling nozzles are shown. Both hollow and solid specimens can be used. Strain is measured directly at both specimens by means of air-cooled extensometers which are put on directly on the gauge length with ceramic bars. The inductive heating of the specimens is conducted with high frequency generators by Hüttinger, Type TIG 5/300. Cooling occurs mainly by heat conduction in the water-cooled specimen grips and, if necessary, additionally by blowing compressed air on the surface of the specimens and/or (for hollow specimens) by leading cooling gas through the specimens. The temperatures are measured with 6 NiCr-Ni-thermocouples which are directly welded to the surface of the specimens. From the 6 temperatures, single or mean values can be selected for temperature control. Fig. 6 illustrates the whole testing system.

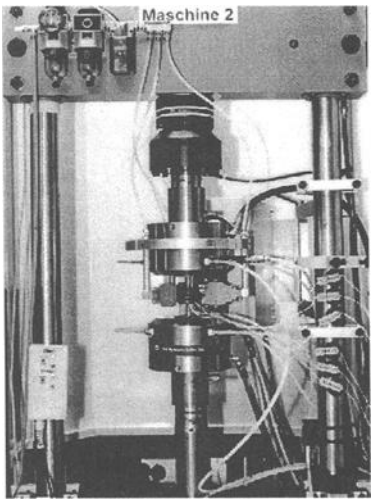

Figure 5 - *Loading frame with specimen, grips, induction coil and cooling nozzles*

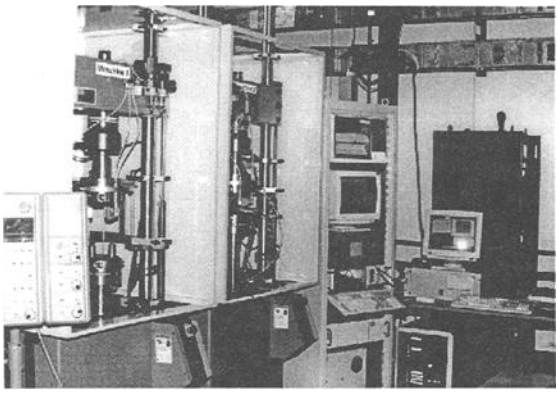

Figure 6 - *Total view of the testing set-up*

Control of the total system is achieved using a 4-channel digital controller MTS TestStar II. One channel is available for each of the two hydraulic actuators and one for each of the two heating and cooling systems. Due to regulation with one 4-channel-controller, the phase shifts between the controlling circuits can be minimized. The main task concerning the construction of the experimental set-up is the optimization of the testing system, particularly of the mechanical controlling processes $F = F_1 + F_2$ and $\varepsilon_{t,1} = \varepsilon_{t,2}$ as well as of the temperature control loops to achieve sufficient homogeneous temperature distribution especially along the longitudinal axis of the specimens.

Testing Methods and Interpretation

The first tests were performed with the 12% chromium steel X 22 CrMoV 12 1 and the 316 type stainless steel X2CrNiMoN 17 12 using solid round specimens with a cylindrical gauge length of 15mm and 8mm diameter within the gauge length. For strain measurement high temperature extensometers with a basis measurement length $l_0 = 12$mm were directly clamped on the gauge length of the specimens. For temperature measurement three NiCr-Ni-thermocouples were spot welded within the gauge length of each specimen.

Fig. 7 and 8 show some characteristic results obtained when specimens made of X22 CrMoV 12 1 are used. In the tests shown in the left and middle of Fig. 7 the results of thermal cyclic loading without additional external forces are presented. In the test shown in the right column of Fig. 7, an additional external force was superimposed. The upper row of diagrams shows the applied temperature-time-courses, and the middle row stands for the mechanical strain-time-courses. The row at the bottom of Fig. 7 illustrates the stress reactions of the two specimens.

In the following the test results are discussed in detail:

a) Investigation of the alternate extension suppression at equal phase but different maximum temperature of the two specimens (see left column of Fig. 7).

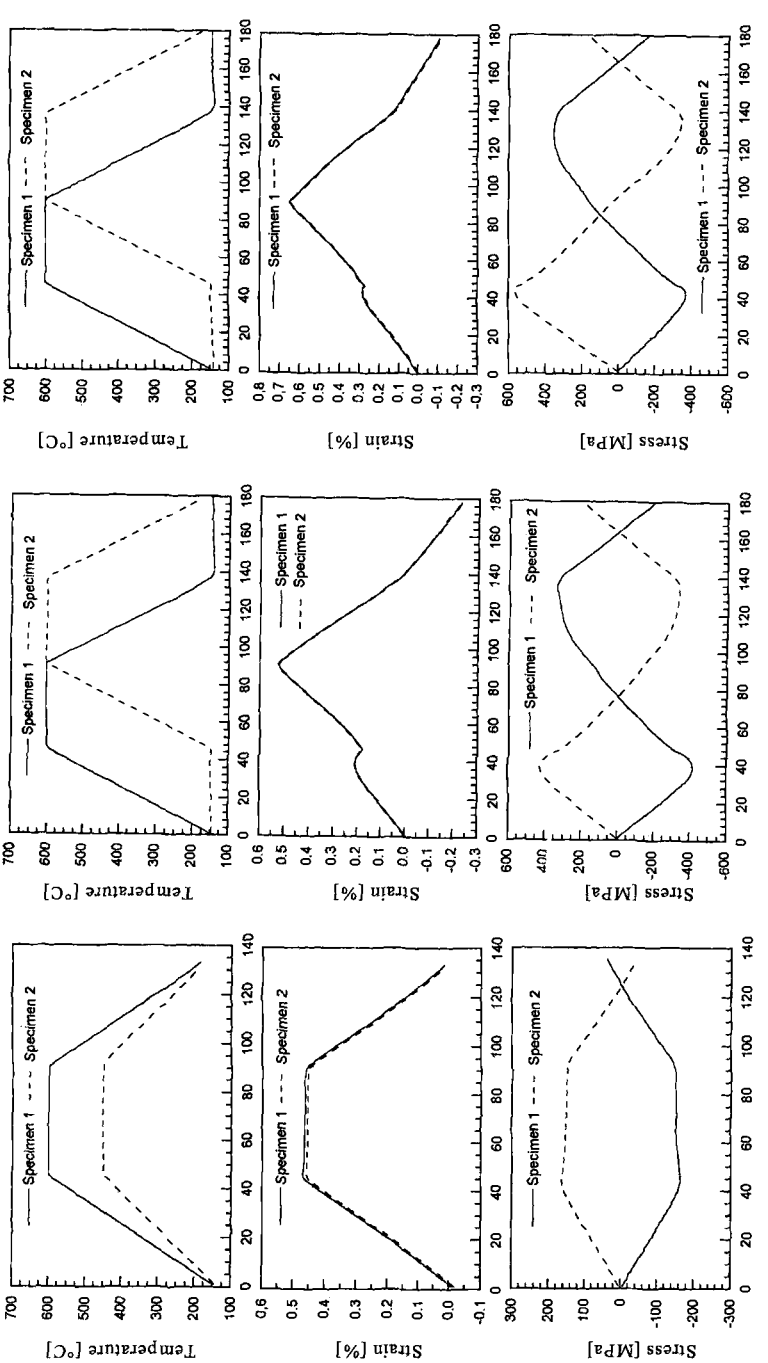

Figure 7 - *Results from experiments with 12% chromium steel X 22 Cr MoV 12 1 at different temperature-time-courses (upper row) and strain (middle row) as well as stress lower row) response of the material*

The volume elements of a cooled component are heated up more slowly and cooled down faster at the cooled surface (2) than those at the heated surface (1). They always reach a lower maximum temperature. A holding time t_{max} at the maximum temperature T_{max} was introduced. The different maximum temperatures T_{max} for specimens 1 and 2 and/or the temperature difference between both specimens as well as the duration of the holding time now constitute the testing parameters.

b) Influence of alternate extension suppression at equal maximum temperature but different phase relations between temperature and mechanical loading (see middle column of Fig. 7).

In an uncooled component, volume elements in the interior (2) are heated up and/or cooled down more slowly than those at the surface (1). The maximum temperatures reached are equal in both elements. In dependence on the heat conductivity and the geometry and a phase t_{Ph} shift between the temperature-time-courses of the two volume elements occurs. Assuming that $\varepsilon_{t,1} = \varepsilon_{t,2}$, alternating extension suppression is achieved. The holding times t_{max} at T_{max} and t_{min} at T_{min} are measured in such a way that cooling and heating of specimen 1 only takes place when T_{max} and T_{min}, respectively, are reached in specimen 2. Thereby, test parameters are the maximum temperature T_{max} and the phase shift t_{Ph}.

c) Consequences of an additionally superimposed external force F on the alternate extension suppression (see right column of Fig. 7).

For uncooled and cooled components external forces may appear which lead to an additional loading. In turbine blades centrifugal forces lead to creep loadings and dynamic pressure and/or bending forces lead to mechanical cyclic loadings. Considering the loading situation described in paragraph a) above, during the holding time t_{max} of the specimen 1 an external force F is superimposed, which leads to a creep loading in both specimens. This corresponds to the conditions that exist in an uncooled component which is loaded thermally and mechanically. The investigations focus on the influence of the external force F as well as on the load distribution in the two specimens (see bottom row of the right column of Fig. 7). Furthermore corresponding tests with temperature loadings like those in cooled turbine blades are planned. For the simulation of cyclic mechanical loadings, the static external force F imposed for this experiment shall be replaced by a cyclic component. Thus, both creep and fatigue components of the mechanical loading would be taken into consideration.

The interpretation of the tests is oriented towards generally known evaluation methods. The starting points are "out-of-phase", "in-phase" or "diamond-cycle" loadings out of the usual single-specimen thermal fatigue tests. The "out-of-phase" loading corresponds to specimen 1 according to test conditions b). The "in-phase" loading corresponds to specimen 2 according to test conditions b). Fig. 8, for example, shows the evaluation of the stress-mechanical strain-hysteresis loops of the first cycle according to these test conditions. The course of the total strain loops expressively shows that specimen 1 is supposed to out-of-phase loading whereas specimen 2 is in-phase loaded. The developing plastic strain loops demonstrate the higher plastic deformation of specimen 1 which is caused by the higher maximum temperature acting on this specimen. Cyclic

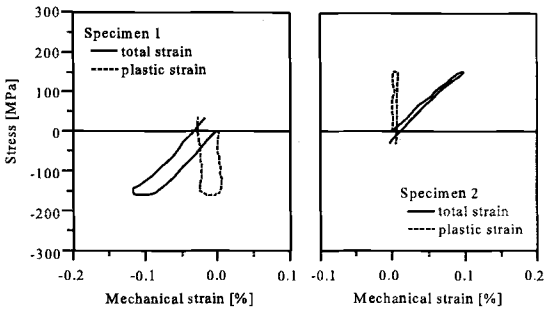

Figure 8 - *Stress-mechanical strain-hysteresis loops of the first cycle from experiments with the steel X22 CrMoV 12 1*

deformation curves as well as cyclic stress-strain curves of the regarded volume elements at the respective loading conditions could be obtained from such evaluations.

A loading similar to that of the "diamond-cycle" corresponds to the loading with alternate extension suppression and to the loading conditions of the specimens 1 and 2 in a). One has to consider that for specimen 1, the "diamond-cycle" is run in the counter-clockwise direction. This means that a negative mechanical extension occurs during heating up and, accordingly, a positive mechanical extension emerges when cooling down. For specimen 2 the "diamond-cycle" is run in a clockwise direction. In this case, a positive mechanical extension develops when heating up and a negative mechanical extension occurs when cooling down.

As an other example, Fig. 9 shows the loading conditions and the material reactions in the first temperature cycle. In this case specimens made of 316-type steel X2NiCrMoN 17 12 were used. The upper part of Fig. 9 represents the temperature courses. While specimen 1 is cycled between T_{min} = 200°C and T_{max} = 650°C,

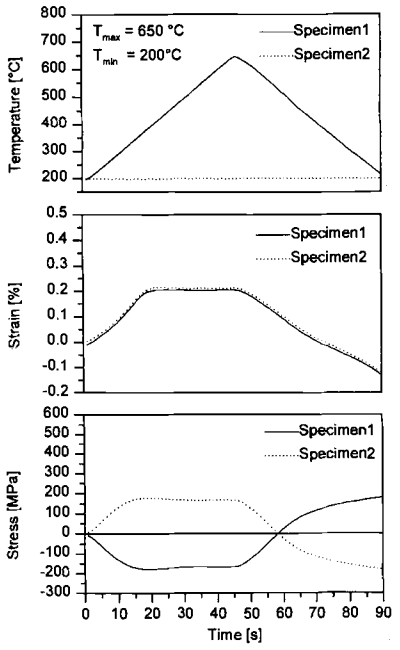

Figure 9 - *First cycle of an experiment with 316-type steel X2NiCrMoN 17 12. Top: temperature-time-course, middle: strain response, bottom: stress response*

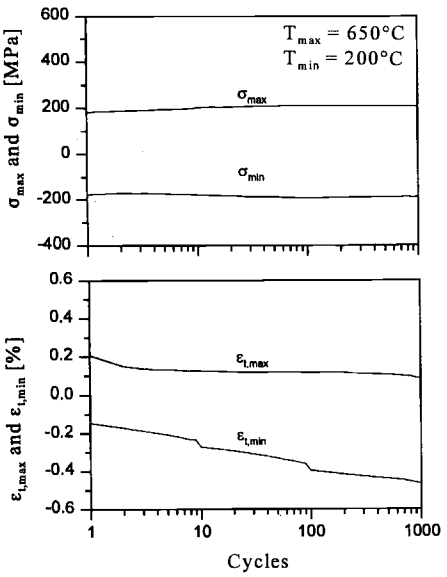

Figure 10 - *σ_{max}, σ_{min}, $\varepsilon_{t,max}$ and $\varepsilon_{t,min}$ as a function of the number of temperature cycles from an experiment with 316-type steel X2NiCrMo 17 12*

the temperature of specimen 2 is held at 200°C. The strain response in the middle part of Fig. 9 and the stress response in the lower part of Fig. 9 proof that the set-in of plastic deformation at a certain temperature restricts the developing strains and stresses. The plastic deformation mainly takes place in specimen 1 and lead to the development of tensile stresses in specimen 1 during cooling down to T_{min}. Due to the loading conditions specimen 2 produces stresses of the same absolute value as specimen 1, but of opposite sign. Figure 10 analyses in cyclic deformation curves the development of the minimum and maximum stresses (upper part) as well as of minimum and maximum total strains (lower part) with increasing number of temperature cycles. As you will see σ_{max} and σ_{min} remain relatively constant while $\varepsilon_{t,max}$ and $\varepsilon_{t,min}$ decrease continuously with increasing number of cycles. A hold time of 40 s introduced at the maximum temperature of specimen 1 intensifies the plastic deformation processes which lead to a greater decrease of the developing total strains (see Fig. 11).

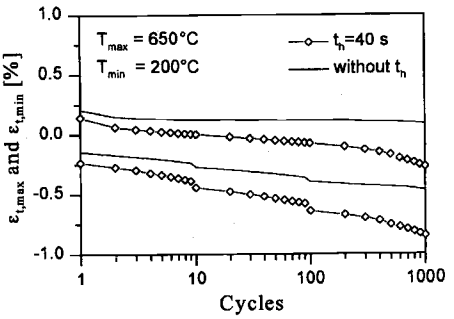

Figure 11 - *$\varepsilon_{t,max}$ and $\varepsilon_{t,min}$ versus the number of temperature cycles for tests with 316-type steel X2NiCrMo 17 12 without and with a hold time t_h*

Conclusions

In this contribution a new two-specimen testing system for the realization of complex thermal-mechanical fatigue experiments is introduced. With this testing system it is possible to investigate the interaction between two specimens representing two volume elements of a thermal-mechanical loaded component. Beyond this it is possible to examine the influence of a superimposed external force on the thermal-mechanical deformation and failure behaviour of two coupled specimens (volume elements). The different modes of operation of the testing system is explained and first results to the cyclic deformation behaviour of two different steels are introduced. The main task is now to compare the deformation and the lifetime behaviour of the specimens in the two-specimen testing system with that one of comparable loaded specimens in single-specimen experiments. Furthermore, there are activities to model the cyclic deformation behaviour of the specimens in the two-specimen testing system [16].

Aknowledgement

The financial support by the "Deutsche Forschungsgemeinschaft (DFG)" is gratefully acknowledged.

References:

[1] Bressers, J., Rémy, L., Steen, M., and Vallés, J. L., Eds., *Fatigue under Thermal and Mechanical Loading. Mechanisms, Mechanics and Modelling*, Kluwer Academic Publishers, Dortrecht, The Netherlands, (1996).

[2] Spera, D. A., "Comparison of Experimental and Theoretical Thermal Fatigue Lives for Five Nickel-Base Alloys," *Fatigue at elevated Temperatures*, ASTM STP 520, A. E. Carden, A. J. McEvily, and C. H. Wells, Eds., American Society for Testing and Materials, (1972), 648-657.

[3] Löhe, D., "Thermische Ermüdung," *Rißbildung und Rißausbreitung unter mehrachsiger mechanischer und thermischer Belastung,* Berlin (1993), 33-48.

[4] Coffin, L. F., "A Study of the Effects of Cyclic Thermal Stresses on a Ductile Metal," *Trans. ASME* 76 (1954), 931-959.

[5] Manson, S. S., "Behaviour of Materials under Conditions of Thermal Stress," *NACA Report 1170*, Lewis Flight Propulsion Laboratory, Cleveland, (1954).

[6] Blum, W., Granacher, J., "Zyklisches Kriechen," *Festigkeit und Verformung bei hoher Temperatur,* DGM Informationsgesellschaft, Oberursel (1989), 165-181.

[7] Saltsman, J. F., Halford, G. R., "An Update of Total-Strain Version of SRP," *NASA Technical Paper 2499* (1985), 1-24.

[8] Manson, S. S., "Thermal Stress and Low Cycle Fatigue," McGraw Hill (1966)

New York.

[9] Spera, D. A., "What is Thermal Fatigue?" *Thremal Fatigue of Materials and Components,* ASTM STP 612, D. A. Spera and D. F. Mowbray, Eds., American Society for Testing and Materials, (1976), 3-9.

[10] G. Degallaix et al., "A Martensitic 10.6% Cr-Steel under Mechanical and Thermal Fatigue," *Fatigue under Thermal and Mechanical Loading*, M J. Bressers et al., Eds., Kluwer Academic Publishers, Dortrecht, The Netherlands, (1996), 445-455

[11] Flaig, B., Lang, K.-H., Löhe, D., and Macherauch, E., "Thermal-Mechanical Fatigue of Cast Aluminum Alloy GK-AlSi10Mg wa," *Fatigue under Thermal and Mechanical Loading*, M J. Bressers et al., Eds., Kluwer Academic Publishers, Dortrecht, The Netherlands, (1996), 361-370.

[12] Kleinpass, B., Lang, K.-H., Macherauch, E., "Zum thermisch-mechanischen Ermüdungsverhalten von NiCr22Co12Mo9," *Materialwissenschaft und Werkstofftechnik* 25, (1994), 389-398.

[13] Kloos, K. H., Granacher, J., Hartfiel, R., "Verhalten von Gasturbinenschaufelwerkstoffen unter langzeitiger Kriechermüdungsbeanspruchung," *Materialwissenschaft und Werkstofftechnik* 24 (1993), 250-257.

[14] Stentz, R. H., "A Study of Thermal Ratchetting Using Closed-Loop, Servo-Controlled Test Machines," *Cyclic Stress-Strain Behavior-Analysis, Experimentation, and Failure Prediction*, ASTM STP 519, American Society for Testing and Materials, Philadelphia (1973), 3-12.

[15] Morrow, D. L., "Component Simulations of a Pressure Vessel Subject to Thermal Fluxes," *Thermal and Environmental Effects in Fatigue: Design-Research Interface,* American Society of Mechanical Engineers (1983), 59-73.

[16] Kühner, R., Aakta, J., Angarita, L., and Lang, K.-H., "The Role of Temperature-Rate Terms in Viskoplastic Modelling: Theory and Experiments," *Thermo-mechanical Fatigue Behavior of Materials: Third Volume, STP 1371,* H. Sehitoglu and H. J. Maier, Eds., American Society for Testing and Materials, West Conshohocken, Pa, (1999).

Rémy Chieragatti[1] and Florin Paun[1]

A New technique for High Frequency Multiaxial Thermo-mechanical Fatigue Testing of Materials

Reference: Chieragatti, R., Paun, F., **"A New technique for High Frequency Multiaxial Thermo-mechanical Fatigue Testing of Materials,"** *Thermo-mechanical Fatigue Behavior of Materials: Third Volume, ASTM STP 1371,* H. Sehitoglu and H. J. Maier, Eds., American Society for Testing and Materials, West Conshohocken, PA, 2000.

Abstract: The proposed thermo-mechanical fatigue test rig is based on a rotating bending machine and employs a high and a low temperature sources. This permits imposing thermal and mechanical loading at relatively high frequencies on a portion of a surface generatrix of a tubular specimen.

Using this rig, a series of experiments was carried out on superalloy test specimens. These tests were conducted at various mechanical loadings with the temperature cycling between 600 and 1050°C in 10 seconds. The temperature distribution on the test specimen was measured under stabilized conditions and the same was calculated using a finite element code. Good correlation was found between the experimental and simulated temperature distributions. The thermal stress field, hence calculated, enables us to identify the critical crack initiation sites of the specimen and to calculate the applied thermo-mechanical cycle. In this way, an equivalent constant temperature can be defined and fatigue life has been predicted using isothermal fatigue results only.

Keywords: thermo-mechanical test rig, high frequency, equivalent stress model, fatigue, superalloy

[1]Département de génie mécanique, École Nationale Supérieure d'Ingénieurs de Constructions Aéronautique, Toulouse, France

Introduction

Thermo-mechanical fatigue (TMF) phenomena in the blades of jet engines or gas turbines, usually occur due to the interaction between mechanical loading and high frequency temperature gradients generated during transient operations.

The proposed test rig is based on a rotating bending machine and incorporates a high and a low temperature source (see figure 1). It presents some improvements with respect to already existing experimental devices [*1*]. For example, it allows a higher frequency fatigue load application than "volume element" type test benches [*2, 3*]. It also has a better stress-strain control than the "structural element" type test benches [*4, 5*]. With reference to "classical" cycles in TMF [*6, 7*], all elliptical cycles can be achieved with higher frequency. This development required a numerical simulation of the temperature field of a rotating tubular test specimen. The cyclic variations of temperature are brought about by a high frequency inductor and a cold air jet. The setting of these heating and cooling sources does not vary during an experiment.

The numerical simulation considers aspects including:

- the convection caused by the cold air jet
- the heat transfer by radiation between a black and a grey body through the air.

A mechanical simulation permits the calculation of stresses from thermal field data and applied mechanical loading.

A series of experiments was carried out on IN100 test specimens with the temperature varying between 600 and 1050°C in 10 seconds with different mechanical loading applied during each experiment. These test conditions are close to real service conditions of turbine blades. IN100, a nickel based superalloy, is one of the turbine blade materials.

Simulations and experimental results are presented and compared in this paper.

Experimental and Numerical Methods

The Test Rig and the Specimen

This test rig has already been presented in a previous article [*8*]. This is a rotating bending fatigue machine in which two thermal sources are incorporated.The heat source is a high frequency induction furnace whereas a cold air jet is used for cooling. The tubular type test specimen used in the study is made of IN100. Its composition in weight per cent is shown below (Table 1).

This specimen is a hollow cylinder of 6 mm inner diameter while the outer surface is conical with the mean diameter of the working zone equal to 8 mm. The total length of the test specimen is 95 mm. It is held in the machine at its two cylindrical ends. With a

suitable application of heating/cooling as well as of the rotating bending loading, high frequency thermo-mechanical fatigue cycles are produced in a small portion of a generatrix of this test specimen.

Table 1-*Composition of IN100 in Weight per Cent*

C	Cr	Co	Mo	Ti	Al	Zr	B	V
0.18	10	15	3	4.7	5.5	0.06	0.014	1

Four thermocouples are fixed on the same surface generatrix, respectively 0, 5, 10 and 15 mm away from the center of the most loaded zone.The temperature readings from all of four thermocouples are recorded throughout testing. The rotating frequency is approximately 0.1 hz.

The applied deflection is controlled with the help of a displacement gauge placed at one end of the specimen. Four levels of deflection are used i.e. 0, 0.2, 0.4, and 0.9 mm. The resulting force is measured with the help of a load cell.The two thermal sources are set to obtain temperature variations between 600°C and 1500°C on the central thermocouple.

The deflection is applied to the specimen at room temperature. The specimen is allowed to elongate axially during temperature field stabilization. As soon as the stable thermal cycle is attained, the axial displacement is blocked.

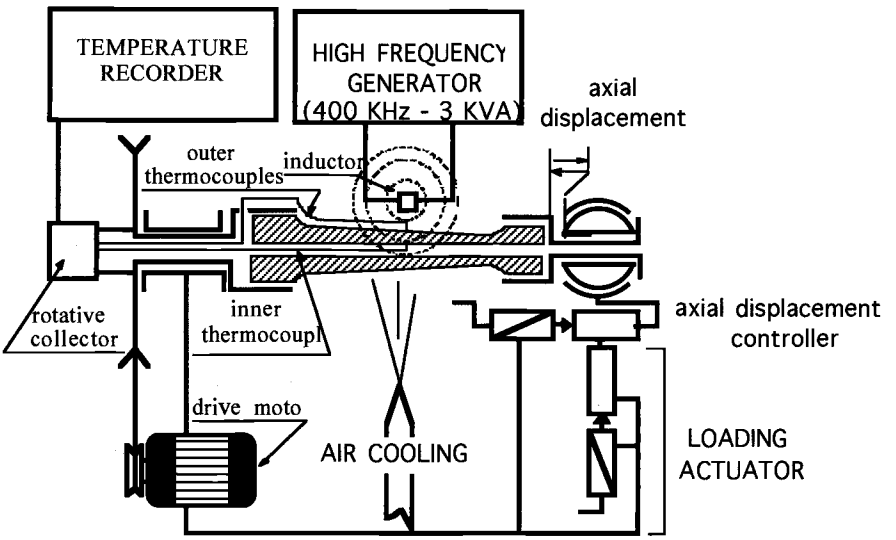

Figure 1 - *Schematic of Thermomechanical Fatigue Test Rig*

Simulation.

The test specimen was simulated with the help of SAMCEF finite elements

software.

Geometrical Model - In the geometrical model, the nodes and meshes were defined on a cross section in cylindrical reference axes with 20 angular steps and then repeated axially at decreasing distance intervals while approaching the high thermal loading zone. This zone is situated almost at the half length of the test specimen. Two ends of the specimen were also taken into account and the fillets were considered to be conical instead of circular (this approximation affects only a lightly loaded zone). Meshes are formed of quadrangle isoparametric element. These elements can be used for both thermal and mechanical analyses.

Thermal Model - This model is thoroughly described in the previous article [8]. The main conditions and results are reviewed here. Functions of heat transfer were associated to different facets of the geometrical model using THERNL module of SAMCEF (Figure 2). Four zones were considered for solving our problem:

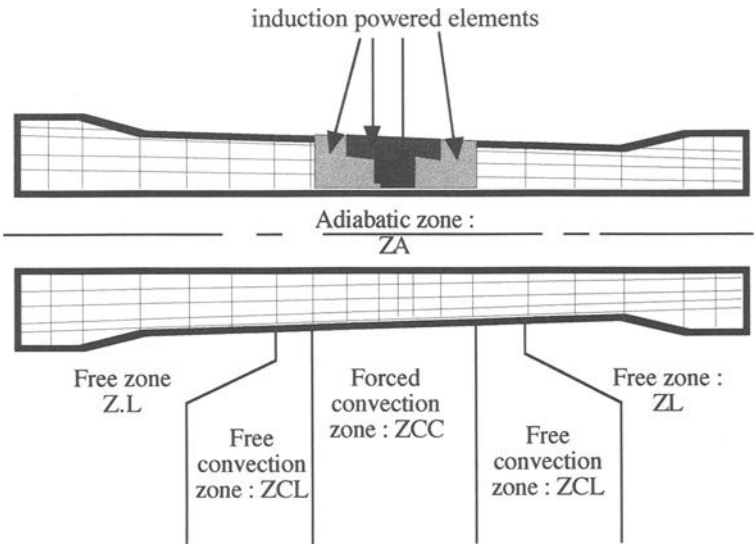

Figure 2 - *Schematic of Geometrical Model*

- Zone ZCC (Forced Convection Zone)

This is the central belt on which was simulated the convection caused by the cold air jet and the radiation through the air. Estimated to be 4 meshes wide, it covers a 8 mm distance along the specimen length

- Zone ZCL (Free Convection Zone)

This zone comprises two belts of 3 mm width each on both sides of the ZCC and serves as buffer zone between ZCC and ZL.

- Zone ZL (Free Zone)

This covers the remaining test specimen where heat transfers due to convection and radiation are small.

- Zone ZA (Adiabatic Zone)

It comprises all the internal facets of the test specimen, where heat transfer is condidered to be negligeable.

Underneath the ZCC and ZCL zones, volume elements were defined in order to absorb the power generated by the inductor. This power depends upon the distance between volume element and the source of induction. This induction source was modelled as being linear and perpendicular to the specimen axis. Fourier's law is used for the heat transfer in conduction and Fick's law is used for convection. Radiation was taken into account using Bolzmann's law.

Simulation of Cycles - Since the stabilized conditions are not obtained right from the first cycle, it was necessary to monitor the temperature evolution cycle after cycle. Therefore, every ZCC and ZCL type zone receives a variable thermal flux depending on its position on the generatrix and on the circumference. The same is true for volume element defined to absorb induction power. Two circumferencewise adjacent zones receive an equal thermal flux but out of phase. Two lengthwise adjacent zones receive unequal thermal flux but in phase. A software program for temperature feed back was developed. It takes temperature distribution at the end of every cycle and inputs it as the initial conditions of the next cycle.

Simulation of Mechanical Loading - When the specimen thermal field is calculated using THERNL module, it is translated into SADYNL module. Nonlinear calculations of thermal and mechanical loadings were carried out using this module. The load on the structure is applied in small increments but thermal loading is applied at the first increment. At every increment of load, the non-linear system of equations is solved using Newton-Raphson method. The material behaviour at each temperature value was described by experimental stress-strain curves modelled by linear segments. Von Mises equivalent stress was used to compare the calculated stress and strain fields to the experimental curves at each loading increment. Loading is applied only once on the specimen model which means that no cyclic evolution in stress-strain behaviour was taken into account.

Experimental and Numerical Results

Main Thermal Results

Comparison Between Experimental Measures and Simulation - In figure 3(a), the evolution of temperature, measured by the central thermocouple of all specimens over

one stabilized cycle, is compared to the simulated one. A good correlation between these two results can be noticed. In figure 3(b) , the highest temperatures measured by each thermocouple during one cycle, are compared to the corresponding simulated temperatures. A good correlation is obtained here as well with a deviation lesser than 10% for the lowest temperature and lesser than 0.5% for the highest ones.

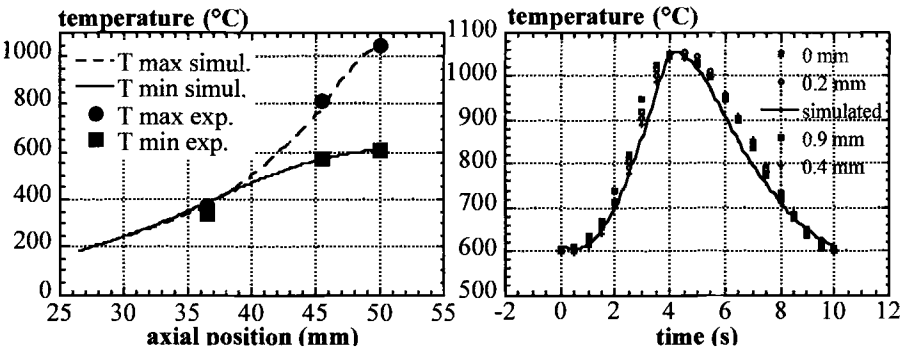

(a) (b)

Figure 3(a) - *Simulation and Experimental Highest Temperatures Measured by Outer Thermocouples on a Generatrix.*

Figure 3(b) - Simulation and Experimental Temperatures Measured by the Central Thermocouples of Different Specimen during a Cycle .

Main Fatigue Results

Table 2 - *Test Results*

deflection (mm)	crack initiation* (number of cycles)	fatigue life (number of cycles)
0	1300-1500	2300
0.2	1500-1600	2900
0.9	400-600	3400
0.4	1500-1700	4000

* 50 micrometers crack size was measured on outer surface by an optical system [9]

The results are reported on the table 2.

In this table, it is noticed that fatigue life does not change linearly with deflection; the longest fatigue life is obtained for a medium value of deflection (0.4 mm). It is noticed on fracture surfaces of these specimens that crack initiation is in the interior of the sample

when deflection is low (< 0.4 mm) and at the exterior when deflection is high (>0.4 mm).When deflection has a medium value, both kinds of crack initiation can be found. This is shown below (Figure 4).

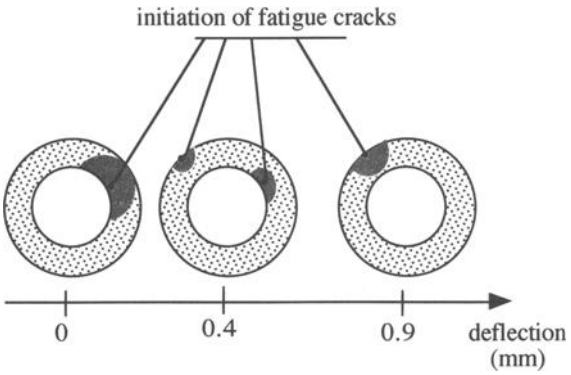

Figure 4- *Schematic Illustration of Crack Initiation Site versus Deflection on Fracture Surface of Specimens*

Results of Mechanical Simulation

The mechanical model was subjected to three deflections i.e. 0, 0.4 and 0.9 mm as previously described. The calculated stress field state is strongly three dimensional. In order to compare the stress-strain state to the material behaviour, a uniaxial equivalent stress criterion is needed. Von Mises criterion is proposed by SAMCEF software to be used for all isotropic metallic materials. From the analysis of the resulting stress field, critical sites can be determined in the central section at the internal and external sides of the numerical specimen as shown in figure 5.

Still, for zero deflection, the highest stressed sites are in the interior of the specimen but at a lower temperature than the maximum stressed outer site. So, a priori, the most critical site can not be defined without introducing equivalent criteria for temperatures and stresses.

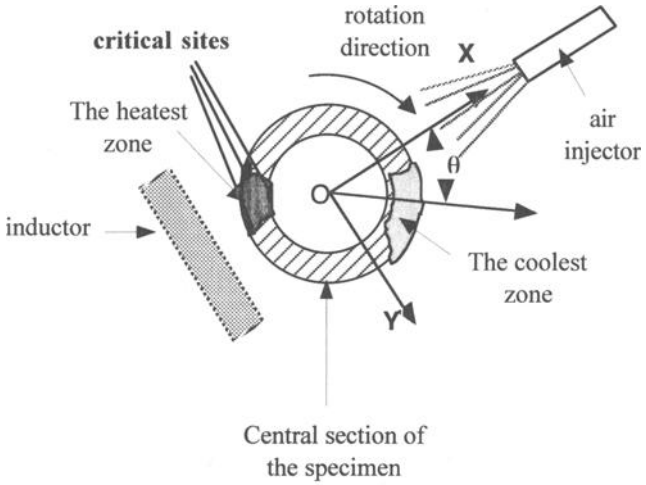

Figure 5 - *Schematic Illustration of the Location of the Critical Sites*

Model For Tension-Compression Equivalent Stress

Figure 6a shows the evolution of Von Mises equivalent stress with respect to temperature, during a cycle. The maximum variation of stress value, $\Delta\sigma$ max, is 180 MPa. For zero deflection simulation, the maximum stress is obtained at an inner site. However this stress amplitude would lead to more than 10^5 cycles to failure even if the highest temperature isothermal fatigue test is taken into account, as show in figure 6b. The experimental fatigue life was 4000 cycles to failure. Therefore in our case, Von Mises criterion seems to be ineffective in predicting fatigue life. That is why, another equivalent stress criterion is tested. It is derived from the Chaboche criterion [*10*]. Equivalent stress in the model proposed by Chaboche is calculated from a given stress tensor as written below:

$$\sigma eq = \alpha J0 + \beta J1 + \gamma J2$$

where:

σeq = the equivalent unidirectional stress

J0 = max <<σi>>, where si are the components of the stress tensor written in the principal directions (principal stresses)

J1 = the first invariant of the stress tensor (hydrostatic pressure)

J2 = the second invariant of the stress tensor (Von Mises stress)

α, β, γ = weighting coefficients

This model is modified for taking into account the effect of compression. This is done

by changing the expression of J0 by the following one:

$$J0' = \text{sign}(\sigma i) * J0$$

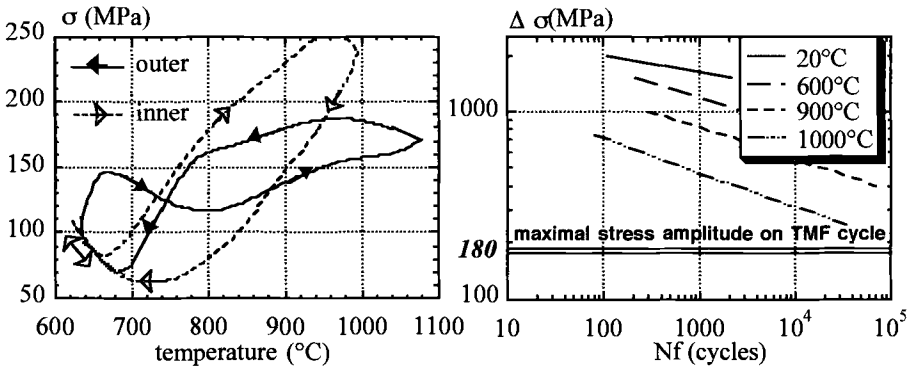

(a) (b)

Figure 6 a - *Evolution of Von Mises Equivalent Stress versus Temperature during a Cycle*

Figure 6 b - *Von Mises TMF stress Amplitude compared with isothermal LCF tests*

The weighting coefficients are calculated so as to obtain by this model, the same equivalent stress at maximum plastic strain as obtained through Von Mises criteron at critical inner and outer sites (i.e. -248.5 MPa and 185.8 MPa). The two following equations are obtained for the zero deflection simulation:

- inner site:

$$-\alpha(-283)+\beta(138.6)+(1-\alpha-\beta)(248.5)=-248.5$$

- outer site :

$$-\alpha(253.5)+\beta(-129.5)+(1-\alpha-\beta)(185.8)=185.8.$$

The solution is:

$$\alpha = 0.894 \qquad \beta = 0.192 \qquad \gamma = -0.086.$$

Similar calculations are made for two other deflections and results are gathered in table 3. The experimental results for 0.2 mm deflection are quite the same as the ones at 0.0 mm deflection, that's why this loading was not simulated.

It can be noticed that α, β and γ values are quite the same for all the deflection values. It means that this way of calculating an equivalent stress is compatible with the results of the non-linear calculation of stress-strain field made with Von Mises criterion.

In figure 7a, the evolution in one cycle of different invariants of the stress tensor, obtained on the inner site for zero deflection simulation, is plotted and compared with the evolutions of Chaboche-like or Von Mises equivalent stresses. The Chaboche-like equivalent stress follows well the evolution of J0. The amplitude of the evolution of this

equivalent stress is almost equal to 350 MPa. In figure 7b, this evolution is plotted against the corresponding temperature during a cycle for inner and outer sites. The amplitude of calculated equivalent stress for the inner site is higher than the one for the outer site.

Table 3. *Calculated Weighting Coefficients for the Simulated Deflections*

deflection (mm)	α	β	γ
0.0	0.894	0.192	-0.086
0.4	0.896	0.187	-0.083
0.9	0.902	0.185	-0.086

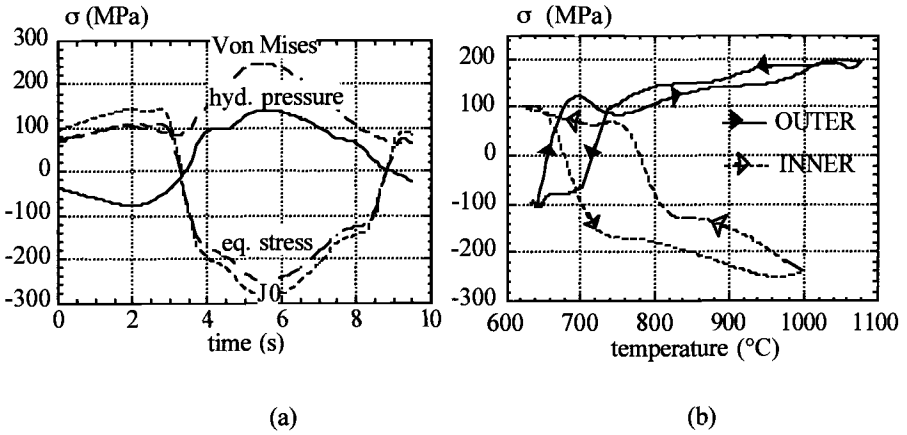

(a) (b)

Figure 7 a - *Evolution of equivalent stress and invariants of the stress tensor on the critical site during one cycle.*

Figure 7 b - *Proposed equivalent stress versus temperature*

Model For Equivalent Temperature.

TAIRA's criterion has been chosen in this study as proposed by Lemaître et Chaboche [*11*]. This criterion is based on the hypothesis that damage in thermo-mechanical fatigue can be compared with damage in isothermal fatigue at the equivalent temperature calculated over the fatigue cycle stress versus temperature.This criterion is represented by the following relation:

$$\frac{1}{N_F(S_M,\bar{S},T^*)} = \frac{1}{2}\int_{\bar{S}}^{S_M} \frac{\beta(T(S))dS}{(S-\bar{S})N_F(S,\bar{S},T(S))}$$

Where - S is the ratio $\sigma/\sigma_u(T)$, called reduced stress.

σ = the variable stress in the thermo-mechanical cycle

T = temperature corresponding to σ

σ_u = ultimate tensile stress at T [*12*]

- N_F is the number of cycles to failure at current S and T, taken from Low Cycle Fatigue tests
- S_M, $\bar{S}$ are respectively the maximum and the mean reduced stresses
- β is a temperature dependent coefficient [*12*]
- T* is the equivalent temperature for which the number of cycles to failure is calculated.

According to this model, a 1000°C temperature can be taken for all equivalent isothermal fatigue tests.

Discussion: Estimation of Fatigue Life

Figures 8a and 8b show the evolution of calculated equivalent stresses with respect to total strain on inner and outer sites for different simulated deflections.

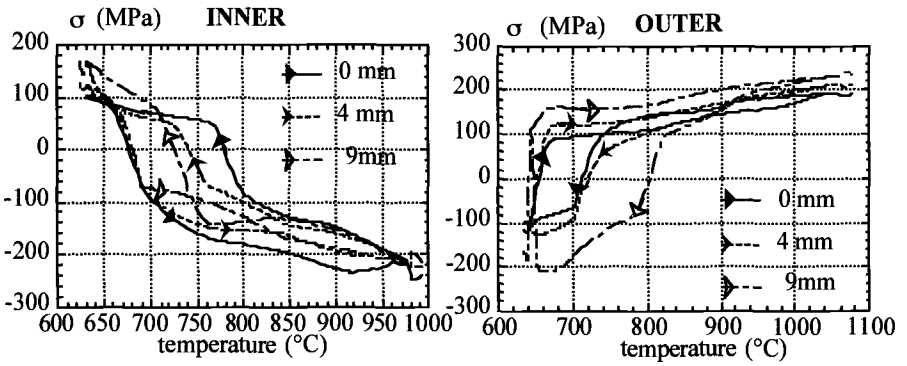

(a) (b)

Figure 8 a - *Proposed equivalent stress versus temperature for the different speciment on the inner critical sites.*

Figure 8 b - *Proposed equivalent stress versus temperature for different specimens on the outer critical sites*

Thermo-mechanical cycles are quite similar for each kind of sites. The stress

amplitudes, reported in table 4, can also be compared.

Table 4- *Simulated Stress Amplitude versus Simulated Deflection*

deflection (mm)	Δ σ inner site	Δ σ outer site
0.0	352 MPa	298 MPa
0.4	350 MPa	342 MPa
0.9	386 MPa	451MPa

These results show that the highest stress is inside the specimen when deflection is low and ouside when it is high; it agrees with the experimental data described in figure 4.

Figures 9a shows the evolution of equivalent stress on critical sites with respect to the applied deflection. It can be noticed that when deflection increases, the highest amplitude of stress (corresponding to inner site) starts decreasing slowly and goes on increasing strongly on the outer site. Considering the present specimen subjected to the present thermo-mechanical loading, stresses lower than 300 MPa cannot be applied. If an equivalent temperature of 1000°C according to TAIRA model is considered, highest achievable fatigue life is nearly 4000 cycles.

Figure 9b shows a quite good agreement between isothermal fatigue curve of IN100 at this temperature (1000°C) and experimental results using Chaboche-like equivalent stress.

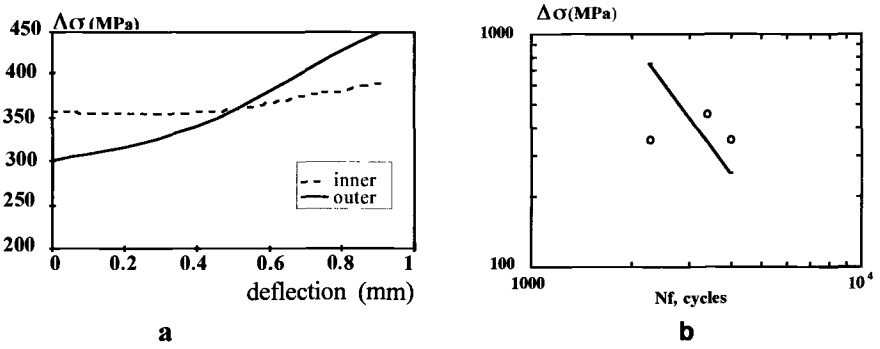

Figure 9 a - *Evolution of equivalent stress on critical sites versus deflection.*
Figure 9 b - *Comparison between LCF curve of IN100 at 1000°C and experimental results*

To improve the fatigue behaviour, a new type of specimen is simulated. By changing external and internal diameters to respectively 18 and 15 mm, thermal stresses decrease

below 150 MPa and a 10 000 cycles fatigue life can be achieved. A few experiments will be carried out to verify this simulation.

Conclusion

A new test rig is proposed to test materials under high frequency thermo-mechanical loadings. Good experimental repeatability and reliability are verified.

The development of a numerical simulation of the test permits satisfactory determination of the thermo-mechanical field of the specimen by using a new equivalent stress model for multiaxial fatigue damage.

However, a limitation on fatigue life is encountered under the present configuration.

Some modifications are suggested with the help of simulation results.

References

[1] Sehitoglu, H.,"Thermal and Thermomechanical Fatigue of Structural Alloys," *Fatigue and Fracture*, ASM Handbook, Vol. 19, American Society for Metals, pp. 527-556.

[2] Kadioglu, Y., "*Modelling of thermo-mechanical fatigue behavior in superalloys*, University of Illinois at Urbana - Champaign, - U.M.I. Order Number 9215833. 1992

[3] Remy, L., Bernard, H.,Malpertu,J.L., Rezai-Aria,F.,"Fatigue Life Prediction Under Thermal-Mechanical Loading in a Nickel-Base Superalloy," *Thermo-mechanical Fatigue Behavior of Materials, ASTM STP 1186*, Husseyin Sehitoglu, Ed., American Society for Testing and Matezrials, Philadelphia, 1993, pp. 3-16.

[4] Köster, A., Laurent, G., Cailletaud, G., Rémy, L.,"Analysis of Thermal Fatigue Tests for Superalloy Components," *Fatigue under Thermal and Mechanical Loading, Proc. of the symposium held at Petten, 22-24 May 1995,* J.Bressers and L.Rémy, Ed., Kluwer Academic Publishers, Dordrecht, 1996, pp 25-33

[5] Tretyachenko, G.,Karpinos, B.,Barilo,V.,Solovjova, N.,"Methods and Results of Biaxial Thermal Fatigue Testing with Non-Uniform Strain Distribution," *Proc., Fourth International Conference on Biaxial / Multiaxial Fatigue*, Paris, May 31- June 3, 1994, pp379-390

[6] Heine, J.E.,Ruano, E.,Delaneuville, R.E., "TMF life prediction, approach for turbine blade," *Thermal Mechanical Fatigue of Aircraft Engine Material,* AGARD, CP-569, 1996, 20.1-20.6.

[7] Lautridou, J.C., Guédou,J.Y.,Delarue, J., " Damage Mechanism Assessement on Turbine Blades Superalloys through TMF Tests," *Thermal Mechanical Fatigue of Aircraft Engine Material*, AGARD, CP-569, 1996, 10.1-10.6.

[8] Chieragatti,R.,Paun, F., Fournier, D., Lautridou, J. C., Lelait, L.," New type of experimental method in thermomechanical fatigue of materials with a high cycling frequency," *Proc, Thermec'97, International Conference on Thermomechanical Processing of Steels and Others Materials,* T. Chandra and T.Sakai Ed.,The Minerals, Metals &Materials Society, Wollongong, Australia, 1997,vol.2, p.1623.

[9]Alam, A.M., Chieragatti, R., Claude, A., "A crack monitoring system for fatigue testing," Proc., third France-Japan congress and first Europe-Asian Congress on Mechatronics, ENSMM, Université de Franche Comté, IMCF, Japan Socity for Precision Engineering, Besançon, oct.1-3, 1996, pp 176-178.

[10] Lemaître,J., Chaboche,J.-L., *Mécanique des matériaux solides,* Dunod, Paris, 1985, pp 378-381

[11] Lemaître,J., Chaboche,J.-L., *Mécanique des matériaux solides,* Dunod, Paris, 1985, pp 420-422

[12] Lemaître,J., Chaboche,J.-L., *Mécanique des matériaux solides,* Dunod, Paris, 1985, p 366

Author Index

Subject Index

ISBN 0-8031-2853-3